Spatio-temporal evolution of interictal epileptic activity : a study with unaveraged multichannel MEG data in association with MRIs.

Thesis

UNRESTRICTED

Spatio-temporal evolution of Interictal Epileptic Activity: a study with unaveraged multichannel MEG data in association with MRIs

Panagiotis D. Bamidis, Ptych.Phys. (Excel), MSc (Distinction)

A Thesis presented for the degree of Doctor of Philosophy

Department of Physics, The Open University,
Walton Hall, Milton Keynes, MK7 6AA, U.K.

May, 1996

Date of submission 1st May 1996
Date of award. 12th June 1996

Ο φαρος της Αλεξανδρουπολης.
The lighthouse of Alexandroupolis in Greece.

Η εργασια αυτη ειναι αφιερωμενη εξαιρετικα σε αυτους

που μ' αγαπουν και με υπομενουν.

This thesis is dedicated to those who love me and are being patient with me.

ABSTRACT

This thesis addresses issues relating to MEG modelling, analysis and interpretation of results. A source model employing current density distributions, namely Magnetic Field Tomography (MFT), is used to obtain the MEG results.

The first issue of concern refers to the registration of MEG data with structural MR images in an attempt to improve the localisation capability of MEG/MFT. Simulations testing some spatial and temporal aspects of the reconstruction capability of MFT are also provided. A novel way of conducting MFT studies in depth is suggested and implemented: the iterative use of a source space designed to cover deep situated structures on either side of the brain.

The main bulk of this thesis is concerned with research into interictal epileptic activity as recorded by means of multichannel MEG systems and analysed using MFT. The major aim is to investigate whether or not MFT analysis of unaveraged MEG data (single epochs) is feasible in cases of pathophysiological signals and more specifically interictal signals from patients with epilepsy of a complex partial type. The investigation is undertaken against the "traditional" view of the impropriety and absurdity of using single epoch records in the MEG analysis due to noise dominance; we provide evidence that analysis of single, unaveraged epileptic spikes is actually feasible: we demonstrate spatio-temporal coherence in the MFT results of the various single interictal events and show that activity extracted from the "averaged event" is made up of activity contributions which occur intermittently and at variable latencies. Our statements are drawn from the study of both superficial and deep activity.

We further exploit the above conclusions to study the spatio-temporal evolution of interictal activity during the course of unaveraged spike events in two cases of temporal lobe epilepsy. We observe the interactions between superficial and deep temporal structures: superficial activity is identified as preceding deep activity. These observations are reinforced using a novel technique of backavareging three dimensional MFT solutions. Furthermore, consistent propagation patterns of activation in the depth of the temporal lobe are revealed among the various spike events.

DECLARATION

None of the material contained in this thesis has been previously submitted for a degree or any other qualification to this or any other university or institution.

The analysis and interpretation of the results are entirely of my own. The experimental recordings used in Chapters 6 and 7 were kindly provided by Dr E. Hellstrand of the Neurophysiology Department, Karolinska Hospital, Stockholm, Sweden. The recordings of the first half of Chapter 8 are owned by Dr J. Volkmann of the Neurology Department, Heinrich-Heine-University, Düsseldorf, Germany, who kindly allowed their use herein. The auditory odd-ball recordings in the second half of Chapter 8 were part of an on-going experiment at the MEG laboratory of the Institute of Medicine at Jülich, Germany, in which I participated.

Parts of this thesis have been published in the following:

1. BAMIDIS P.D., HELLSTRAND E., LIDHOLM H., ABRAHAM-FUCHS K., IOANNIDES A.A. (1995), "MFT in complex partial epilepsy: Spatio-temporal estimates of interictal activity", NeuroReport, 7(1):17-23.

2. IOANNIDES A.A., LIU M.J., LIU L.C., BAMIDIS P.D., HELLSTRAND E., AND STEPHAN K.M. (1995), "Magnetic Field Tomography of cortical and deep processes: examples of "real-time mapping" of averaged and single trial MEG signals", International Journal of Psychophysiology, 20(3):161-175.

3. IOANNIDES A.A., HELLSTRAND E., BAMIDIS P.D., and ABRAHAM-FUCHS K. (1995). "Estimates of brain activity from unaveraged interictal multichannel magneto-encephalographic signals". In: Baumgartner C, Deecke L, Stroink G, Williamson SJ, eds. Biomagnetism: Fundamental Research and Clinical Applications, Proceedings of the 9th International Conference on Biomagnetism, Studies in Applied Electromagnetics, 7, Amsterdam, Elsevier, pp 326-329.

4. BAMIDIS P.D., HELLSTRAND E., IOANNIDES A.A. (1995), "MFT of deep activity from single epoch interictal epileptic data", Human Brain Mapping, Supplement 1:1, p. 381.

5. BAMIDIS P.D., HELLSTRAND E., LIU M.J., IOANNIDES A.A. (1994), "Interictal Epileptic Activity: a study with Magnetic Field Tomography using averaged and unaveraged MEG recordings", International Journal of Psychophysiology, 18(2):93.

6. BAMIDIS P.D., HELLSTRAND E., IOANNIDES A.A. (1994), "Spatio-temporal Evolution of epileptic activity as revealed from unaveraged interictal multichannel MEG recordings", IPSM & BES 1st Joint Annual Scientific Conference & Exhibition, Keele, UK, Book of Abstracts, p. 160.

7. BAMIDIS P.D., HELLSTRAND E., IOANNIDES A.A., "Propagation of epileptic activity during single (unaveraged) interictal spikes as studied with Magnetic Field Tomography", Book of abstracts, 10th International Conference on Biomagnetism, Santa Fe, USA, February 1996, p 292.

8. BAMIDIS P.D., IOANNIDES A.A., "Combination of point and surface matching techniques for accurate registration of MEG and MRI", Book of abstracts, 10th International Conference on Biomagnetism, Santa Fe, USA, February 1996, p. 14.

9. IOANNIDES A.A., BOLTON J.P.R., LIU M.J., BAMIDIS P.D, LIU L.C., DAMMERS J., GROSS J., AND MUELLER-GAERTNER H.W, "Magnetic Field Tomography: general principles and performance measures", Book of abstracts, 10th International Conference on Biomagnetism, Santa Fe, USA, February 1996, p. 136.

10. IOANNIDES A.A, MUELLER-GAERTNER H.W., BAMIDIS P.D., WEISE F., HACKLAENDER T., DAMMERS J., and LIU M.J., (1995), "The P300 Generators: Where and when are they activated. An MFT investigation using bihemispheric MEG signals", Human Brain Mapping, Supplement 1:1, p. 176.

11. BAMIDIS P.D., IOANNIDES A.A. (1993): "Relating function (MEG) to structure (MRI)", in "Recent Advances in Biomagnetism, 9th International Conference on Biomagnetism, Book of Abstracts" (ed) Deecke L et al, Vienna, pp 241-242.

Acknowledgements

I wish to take advantage of this great tradition of acknowledging the direct and indirect contributions of others to the outcome of the piece of work presented in this thesis.

I should, first of all, like to express my profound gratitude to Dr. Andy Ioannides, my supervisor, for his constant enthusiasm, impeccable guidance and advice, his unfailing interest, his instructive suggestions, and his continuous patience and encouragement throughout the whole period of my "PhD journey". It has undoubtedly been a privilege to "fly" with him! The fact that he has been a very hard worker himself never gave me the chance to "complain" that I was myself working very hard, and I would like to thank him for that, too. His expertise and "biomagnetic knowledge" is nothing short of excellence and it has proved indispensable at a number of cases in my project. The results presented herein are our joint efforts, which could not be separated in any way even if one wanted to do so. At times, he was my only friend around and at some other times he was advising me like a father. The warm environment that his family offered me was substituting very efficiently the absence of my family and I would like to thank them all for that. I will never forget them!

My thanks also go to Dr. Eric Hellstrand of the Neurophysiology Department at Karolinska Hospital in Stockholm, Sweden, for providing the bulk of the clinical data analysed in this thesis and having agreed to collaborate with us on the "MFT epilepsy project". He has effectively acted as an "informal co-supervisor" and his criticism at the other end of the phone line has been very constructive indeed. He also gave me a great welcome in his home when I visited Stockholm in February 1995.

The Physics Department of the Open University (OU) has not only provided an excellent working environment and friendly atmosphere, but has also funded the whole period of my PhD studies. Professor SJ Bell Burnell has always been there for advice and help on all kinds of problems and I should, therefore, like to say a special word of thanks to her. My thanks also go to Drs. Alan Cooper and Stuart Freake who read my first year report

and patiently examined me in the traditional first year "mock viva". Further help from Drs. Stephen Swithenby and John Bolton is also acknowledged. Sue Messham and Mike Watkins kept my teaching interests alive by giving me the chances to participate in various OU Physics summer schools and script marking sessions of Physics exams. I shall also mention the secretarial staff of the Physics department - especially Yvonne McKay - for their ever so kind help and friendly presence.

A word of thanks also goes to present and past members of the Biomagnetism group of the Open University. Everybody gave their own kind of input to my study and I would like to thank them all. It would, however, be a sin not to especially thank Dr. MingJun Liu, my friend and colleague whom I shared the office with for 3.5 years. He constantly supported my "computer needs" and he was a very good company in our common 10am-10pm "routine" timetable.

Help and support from the Academic Computer Services (ACS) unit of the OU is gratefully acknowledged too; in particular I wish to thank Steve Batie, Steve Daniels, David Clover, and Craig Howorth for their kind and prompt help.

I should also like to thank my colleagues at the MEG laboratory in Jülich, Germany, and especially Jürgen Dammers for his hard work as an experimentalist and subject - during the odd-ball experiment- but also as a guide to Germany during my visit there in December 1994. I should also mention Dr. Jens Volkmann who allowed me to analyse for the purpose of my thesis some of the myoclonus data he collected in Jülich.

I owe a special debt to my friends Iraklis Paraskakis and Stylianos Hatzipanagos here in Milton Keynes whose friendship, humour and lively discussions - especially during the "Talbot Club" meetings - kept me going. The Milton Keynes Hellenic Community also deserve an acknowledgement for allowing me to work as a part time Greek teacher at the local school, but also for making the "last Sunday of the month Liturgies" possible. A word of thanks should finally go to my friend Dimitris Pappas at MIT, my best "network" company for almost every single evening at the other side of the Atlantic, who kept me fully informed on all the exciting sport events.

I would further like to express my gratitude to the Bodosakis Foundation that funded the initial stages of my post-graduate studies in the UK.

Last but not least, I am grateful to my family and my fiancée for their constant encouragement and continuous love throughout the years. I am particularly indebted to them for being patient with me!

1. INTRODUCTION 1

1.1 HISTORY OF BIOELECTROMAGNETISM* 2

1.2 THE DEVELOPMENT OF MAGNETOENCEPHALOGRAPHY 3

1.3 ISSUES ON MEG MODELLING 7

1.4 SCOPE OF THE THESIS 9

2. IMAGING THE HUMAN BRAIN: BACKGROUND INFORMATION 11

2.1 NEUROMAGNETISM 1

2.2 THE ORIGIN OF THE SIGNALS 12

2.2.1 Organisation of the brain 12

2.2.2 Neuroelectric activity 14

2.2.3 Postsynaptic Potential 14

2.2.4 Action Potential 15

2.2.5 What is it that MEG detects? 16

2.2.6 The Equivalent Current Dipole Approach 17

2.3 BASIC BACKGROUND ELECTROMAGNETISM 19

2.3.1 Forward problem 19

2.3.2 Maxwell's Equations 19

2.3.3 Primary and secondary sources 20

2.3.4 Homogeneously Conducting Sphere 22

2.3.5 Other models of the conducting medium 23

2.4 NEUROMAGNETIC INSTRUMENTATION 24

2.4.1 Basics 24

2.4.2 Multi-SQUID considerations 27

2.4.3 Modern Systems 28

2.4.4 Digest 29

2.5 COMPARISON OF EEG AND MEG 29

2.6 TOPOGRAPHIC ELECTROPHYSIOLOGICAL MAPPING 31

2.7 OTHER FUNCTIONAL BRAIN IMAGING MODALITIES 32

2.7.1 X-ray CT 32

2.7.2 MRI 33

2.7.3 MRS 35

2.7.4 Radionuclide Techniques: PET and SPECT 35

2.7.5 EIT 37

2.7.6 NIRS 38

2.8 OVERVIEW: MEG VERSUS OTHERS 38

3. RELATING STRUCTURE AND FUNCTION **41**

3.1 In General 41
3.2 Localisation in MEG 42
3.3 Fundamental Principles of Registration 43
3.4 A Review of the Registration Techniques used in Medical Imaging 45
3.4.1 Point/Line-Matching *46*
3.4.2 Surface-based Methods *46*
3.4.3 Accuracy achieved by various methods. *48*
3.5 Registration studies at the OU* 49
3.5.1 Motivation *49*
3.5.2 Point Matching *50*
3.5.2.1 "PM-ALL" 51
3.5.2.1.1 The formulation 51
3.5.2.1.2 Results 54
3.5.2.2 "PM" 55
3.5.2.2.1 In General 55
3.5.2.2.2 Minimisation 56
3.5.2.2.3 Results 57
3.5.3 MEG-MRI Surface-Matching *59*
3.5.3.1 63
3.5.3.1 Examples 64
3.6 Discussions 69
3.6.1 In General *69*
3.6.2 The basis for future developments *75*
3.6.3 Synopsis *77*

4. INVERSE PROBLEM **78**

4.1 In General 78
4.2 Lead Fields 80
4.3 Current dipoles 82
4.3.1 Single Current Dipole *82*
4.3.2 Multi-dipole models *84*
4.4 Current distribution models 87
4.4.1 Fourier Imaging *88*
4.4.2 Lead Field Synthesis or Spatial Filter Imaging *89*
4.4.3 Minimum norm estimates *90*
4.4.4 Magnetic Field Tomography (MFT) *94*

5. MFT TESTS AND SIMULATIONS 100

5.1 "TRAINING" THE SYSTEM 100

5.1.1 Source space configuration and display definitions 101

5.1.2 Selecting the proper parameters 104

5.2 SENSOR NUMBER EFFECTS IN MFT ESTIMATES 113

5.3 RECOVERING DEEP ACTIVITY 122

5.3.1 Unilateral case 122

5.3.2 Bilateral Measurements 130

5.4 DYNAMIC SIMULATIONS 136

5.4.1 Recovering the temporal aspects of a single source 137

5.4.2 A superficial and a fairly deep source 139

5.4.3 Three nearby, fairly deep sources 141

5.4.4 Bilateral hippocampal activation 148

6. MFT STUDY OF UNAVERAGED INTERICTAL EPILEPTIC EVENTS 151

6.1 INTRODUCTION AND HISTORICAL REMARKS 151

6.2 TERMINOLOGY 152

6.2.1 Seizure types and electric patterns+ 152

6.2.2 Epileptic zones and relevance of interictal recordings 154

6.3 EPILEPSY NEUROIMAGING AND MEG 158

6.4 STUDYING INTERICTAL EPILEPTIC EVENTS WITH MFT 160

6.4.1 Materials and Measurements 161

6.4.1.1 Case history (Pat1) 161

6.4.1.2 Recordings and Methodology 161

6.4.1.3 MFT analysis 163

6.4.2 MFT - ECD comparison 166

6.4.3 MFT source-space comparison: cylinder versus partial hemisphere 173

6.4.4 The study of unaveraged interictal events 179

7. SPATIO-TEMPORAL EVOLUTION OF EPILEPTIC ACTIVITY DURING UNAVERAGED INTERICTAL EVENTS 195

7.1 INTRODUCTION AND RATIONALE 195

7.2 MATERIALS AND METHODS 196

7.2.1 Patients 196

7.2.1.1 Case history (Pat2) 196

7.2.1.2 Case history (Pat3) 197

7.2.2 Measurements and analysis 198

7.2.3 MFT analysis *200*
7.3 RESULTS 202
7.3.1 Neocortical and deep temporal interactions *202*
7.3.2 Propagation patterns at the depth of the temporal lobe *206*
7.3.3 Separate tests for bilateral activity *211*
7.4 DISCUSSION 216

8. BIHEMISPHERIC MFT STUDIES 221

8.1 INTRODUCTION 221
8.2 A CASE OF MYOCLONIC EPILEPSY 222
8.2.1 Motivation *222*
8.2.2 General Terminology *222*
8.2.3 The case *223*
8.2.4 Measurements and Analysis *223*
8.2.5 Results *225*
8.2.6 Discussion *234*
8.3 AUDITORY ODD-BALL STUDY 237
8.3.1 Aims and General Information *237*
8.3.2 Experiment and Measurements *238*
8.3.3 Analysis *238*
8.3.4 Results and discussion *239*

9. GENERAL DISCUSSION AND FURTHER WORK 250

APPENDIX A 258

THE SIEMENS 37-CHANNEL KRENIKON SYSTEM 258
THE BTI MAGNES SYSTEMS 259

APPENDIX B 262

AUDITORY ODD-BALL RECORDINGS (JÜLICH): EXPERIMENTAL PROTOCOL 262
Subjects *262*
Recording Preparation *262*
Measurements *263*

REFERENCES 265

FIGURE 1-1: RELATIVE PROPORTION OF VARIOUS SECTIONS OF BIOMAGNETISM DURING THE LAST FOUR INTERNATIONAL CONFERENCES OF THE "BIOMAGNETIC" RESEARCH COMMUNITY THAT TOOK PLACE IN NEW YORK (NY, 1989), MÜNSTER (MÜ, 1991), VIENNA (VIEN, 1993), AND NEW MEXICO (NM, 1996). SEE MAIN TEXT FOR THE REST OF ABBREVIATIONS. 5

FIGURE 1-2: CLASSIFICATION OF BIOMAGNETIC PAPERS INTO THREE MAIN CATEGORIES AND THEIR RELATIVE PROPORTIONS IN THE LAST FOUR CONFERENCES. SEE FIGURE 1-1 FOR ABBREVIATIONS. 6

FIGURE 1-3: THE THREE MAIN AREAS OF MEG APPLICATIONS AND THEIR RELATIVE PROPORTIONS OVER THE LAST FOUR BIOMAGNETISM CONFERENCES. SEE FIGURE 1-1 FOR ABBREVIATIONS. 6

FIGURE 2-1: BASIC PARTS OF THE HUMAN BRAIN ANATOMY AND DEMONSTRATION OF TWO TECHNIQUES CAPABLE OF RECORDING ITS ELECTRICAL ACTIVITY: MEG, WHICH MEASURES MAGNETIC FIELDS OUTSIDE THE HEAD, AND EEG WHICH MEASURES ELECTRIC POTENTIALS ON THE SCALP. 12

FIGURE 2-2: STRUCTURE OF A NEURON (MODIFIED FROM HÄMÄLÄINEN ET AL 1993). 13

FIGURE 2-3: IONIC PROCESSES OCCURRING IN AN EXCITATORY (E) AND IN AN INHIBITORY (I) SYNAPSE. 15

FIGURE 2-4: PROPAGATION OF AN ACTION POTENTIAL (AP) IN A NEURON. NOTE THE DEPOLARISATION AND REPOLARISATION FRONTS AND THE DISTRIBUTION OF IONS IN THE INTRACELLULAR AND EXTRACELLULAR SPACES. 16

FIGURE 2-5: THE BIOT-SAVART LAW. 18

FIGURE 2-6: DISTRIBUTION OF SPECTRAL DENSITIES OF VARIOUS MAGNETIC FIELDS ASCRIBED TO TYPICAL SOURCES OF BIOELECTROMAGNETISM AND NOISE. 25

FIGURE 2-7: BLOCK DIAGRAM OF A TYPICAL SQUID-BASED MAGNETIC SENSOR AND ITS ASSOCIATED ELECTRONICS. NOTE THE PART OPERATING IN CRYOGENIC TEMPERATURES. 26

FIGURE 2-8: THE MOST FUNDAMENTAL TYPES OF MAGNETIC SENSORS USED IN BIOMAGNETISM: (A) MAGNETOMETER, (B) FIRST ORDER AXIAL GRADIOMETER, (C) SECOND ORDER AXIAL GRADIOMETER, AND (D) PLANAR GRADIOMETER. 27

FIGURE 2-9: RELATIVE PROPORTION OF RESEARCH WITH THE VARIOUS FUNCTIONAL BRAIN IMAGING TECHNIQUES, AS JUDGED FROM PAPERS PRESENTED AT THE 1ST INTERNATIONAL CONFERENCE ON FUNCTIONAL MAPPING OF THE HUMAN BRAIN, HELD IN PARIS IN JUNE 1995. 39

FIGURE 3-1: REPRESENTATION OF A POINT IN TWO DIFFERENT CO-ORDINATE SYSTEMS. 44

FIGURE 3-2: THE RAY FROM THE "HAT" POINT **P'** TO A POINT BELOW THE "HEAD" (CIRCULAR DISKS) INTERSECTS THE "HEAD" AT POINT $\mathbf{P}_{INT}$. THE DISTANCE OF **P'** TO $\mathbf{P}_{INT}$ IS CONTRIBUTING TO THE COST FUNCTION. 47

FIGURE 3-3: THE ARROWS IN (A) SHOW THE VITAMIN PILLS USED TO PERFORM THE POINT-MATCHING. THE FIT OF THE MEG CO ORDINATES OF THE PILLS (BLUE CROSSES IN (B)) WITH THEIR MRI ONES (MARKED AS LITTLE RED CIRCLES IN (B)) IS PERFECT. HOWEVER, THE HEAD SHAPE OUTLINES IN THE SYSTEM (RED DOTS) DO NOT MATCH THE MRI SCALP OUTLINES (GREEN CONTOURS). 50

FIGURE 3-4: A POINT P^i IN THE NTH MRI SLICE AND ITS REPRESENTATION IN THE MEG SYSTEM. 51

FIGURE 3-5: THE CENTRE OF THE NTH SLICE IS DEFINED ACCORDING TO SLICE NO AND THE THIRD DIRECTIONAL UNIT VECTOR. 54

FIGURE 3-6: THE FIT OF THE MEG POINTS TO THEIR POINTS DEFINED IN THE MRI SYSTEM (SHOWN BY THE ARROWS IN (A)). THE X,Y SCALING FACTORS WERE ASSUMED TO BE DIFFERENT IN (B), WHILE THEY WERE TAKEN TO BE EQUAL IN (C)..... 55

FIGURE 3-7: THE ROTATED CORONAL SLICES WERE REGISTERED WITH THE SAGITTAL ONES. THEN POINTS ON THE MID-SAGITTAL LINE ON THE CORONAL SLICES WERE JOINED (RED LINE) AND SUPERIMPOSED ONTO THE MID-SAGITTAL SLICE. THE CONTOUR DEFINED BY THE "CORONAL" POINTS FITS PERFECTLY WITH THE SCALP OUTLINE IN THE MID-SAGITTAL SLICE. 58

FIGURE 3-8: FOR EACH MEG POINT A "HEAD" PATCH THAT CORRESPONDS TO IT IS FORMED. THEN THE SQUARED DISTANCE FROM THE MEG POINT TO THE PATCH IS CONTRIBUTING TO THE COST FUNCTION. ... 60

FIGURE 3-9: VISUALISATION OF THE REGISTRATION RESULT. POINTS IDENTIFIED ON (A) ARE SUPERIMPOSED ON (B), AND (C). IN (B) 69 POINTS WERE USED TO PERFORM THE REGISTRATION (FINAL1 ROW IN TABLE 3), WHILE 60 ADDITIONAL POINTS (TOTAL OF 129 POINTS) LYING ON THE MIDSAGITTAL AND MIDCORONAL SLICES WERE USED IN (C) (FINAL2 ROW IN TABLE 3-3)..... 63

FIGURE 3-10: IN THE TOP PLATE, THE HEADSHAPE MEG POINTS (DOTS) DO NOT FIT WITH THE MRI SKULL OUTLINES, DESPITE THE MATCHING OF THE MEG FIDUCIARY POINTS (CROSSES) WITH THE MRI FIDUCIARY POINTS (CIRCLES). IN THE BOTTOM PLATE, SURFACE MATCHING WAS PERFORMED TO RESOLVE THE PROBLEM. NOTE THE GOOD FITTING OF THE DOTS ON THE SKULL MRI OUTLINES. THE MISMATCH BETWEEN THE CROSSES AND THE LITTLE CIRCLES REVEALS THE ORIGIN OF THE INCONSISTENCY..... 64

FIGURE 3-11: THE MEG HEAD SHAPE POINTS (RED DOTS) WERE REGISTERED WITH THE MRI SCALP OUTLINES, AS THE LATTER WERE EXTRACTED FROM THE CORONAL MRI SLICES. THEN A POINT-MATCHING WAS EMPLOYED TO REGISTER THE CORONAL WITH THE SAGITTAL (IN (B)) AND AXIAL (IN (C)) SECTIONS. IN ALL CASES, THE MEG POINTS THAT LIE 2 MM FROM THE DISPLAYED MRI SLICES ARE DRAWN. THEIR FIT WITH THE MRI SCALP IS VERY SATISFACTORY IN ALL THREE CASES..... 65

FIGURE 3-12: VISUALISATION OF THE REGISTRATION RESULT IN DIFFERENT PERSPECTIVE ANGLES. IN THE TOP, ALL THE MRI OUTLINES (GREEN) ARE SUPERIMPOSED ON THE OVERALL MEG HEADSHAPE (RED) BUILT FROM OVER 12,000 POINTS. IN THE MIDDLE AND BOTTOM PLATES, THE MEG POINTS USED IN THE SURFACE MATCHING PROCESS ARE SHOWN AS BIG RED DOTS SUPERIMPOSED ON THE MRI SKULL OUTLINE POINTS (GREEN AS BEFORE). NOTE THE LACK OF MRI POINTS AT THE TOP OF THE HEAD (DUE TO LACK OF DATA DURING MRI ACQUISITION). THE FIT BETWEEN MEG AND MRI APPEARS EXCELLENT IN ALL VIEWS; HOWEVER, THE LAST FIGURINE IN THE SERIES, REVEALS THAT THERE MIGHT BE AN ERROR OF SOME 2-3 DEGREES IN ONE ANGLE (I.E. A MISMATCH OF SOME 4-5 MM). 67

FIGURE 3-13: ANOTHER EXAMPLE OF VISUALISING THE REGISTRATION RESULT IN DIFFERENT PERSPECTIVE ANGLES. MEG HEADSHAPE (RED) POINTS ARE SUPERIMPOSED ON MRI OUTLINES (GREEN). THE FIT BETWEEN MEG AND MRI APPEARS EXCELLENT THROUGHOUT. THE RMS MISMATCH PER POINT WAS 4 MM. SEE MAIN TEXT. 68

FIGURE 3-14: SKULL OUTLINES IN MRI (GREEN) AND MEG (RED) CO-ORDINATE SYSTEMS: BEFORE REGISTRATION (LEFT), AFTER POINT MATCHING (CENTRE), AND AFTER SURFACE MATCHING (RIGHT). SURFACE MATCHING IMPROVED THE FIT FOR SOME 3.5 MM. 72

FIGURE 3-15: (A) AXIAL MRI SLICE OF PATIENT JH AFTER SURGERY; (B, C, D) SKULL AND BRAIN TRACINGS FOR AXIAL, CORONAL AND SAGITTAL MRI SECTIONS OF THE SAME SUBJECT BEFORE SURGERY. AFTER ALIGNING ALL SECTIONS WITH THE MEG SYSTEM, THE PART REMOVED AT SURGERY IS OUTLINED IN THE 1 CM THICK SLICE (A), AND ITS CO-ORDINATES ARE TRANSFERRED ACROSS INTO THE 0.6 CM THICK COMPLETE SET OF MRIS (THICK LINE DRAWINGS). 73

FIGURE 3-16: INSTANTANEOUS MFT DISPLAYS FOR TWO NORMAL SUBJECTS, TB AT 25 MS AND KS 30 MS AFTER STIMULUS ONSET, AND FOR THE PATIENT JH AT 50 MS. A SAGITTAL PLANE IS SHOWN, THROUGH THE AMYGDALA AND HIPPOCAMPUS WHICH ARE SHOWN IN OUTLINE. THE LEVEL OF ACTIVITY AT EACH TIME-SLICE IS SHOWN AS COLOUR CODED CONTOUR PLOT OF THE MODULUS OF THE MFT ESTIMATE FOR THE PRIMARY CURRENT DENSITY $|J(R,T)|$ (YELLOW > RED > GREEN); AT THE POINT OF MAXIMAL STRENGTH AN ARROW IS PRINTED SHOWING THE PROJECTION OF J ALONG THE PLANE OF THE DISPLAY. FOR THE PATIENT, THE TRACING OF THE BRAIN OUTLINE AND AMYGDALA AND HIPPOCAMPUS WERE OBTAINED FROM MRI SLICES ACQUIRED BEFORE THE SURGERY. THE PINK DOTS MARK THE CO-ORDINATES OF THE EXCISED PART THAT LIE WITHIN 4 MM FROM THE DISPLAYED MRI SLICE. 74

FIGURE 3-17: INSTANTANEOUS MFT DISPLAYS SIMILAR TO THOSE IN FIGURE 3-16, BUT FOR THE PERIOD JUST AFTER THE P2 PEAK. IN THE TOP ROW THE ACTIVITY IN RESPONSE TO THE ODD STIMULUS FOR SUBJECT KS APPEARS TO HOVER IN THE AMYGDALA REGION BEFORE TUNNELLING THROUGH THE HIPPOCAMPUS AT A LATENCY OF 200 MS. IN CONTRAST FOR THE PATIENT THE ACTIVITY ARCHES TOWARDS THE AMYGDALA REGION WITHOUT MAKING PROGRESS, SINCE THE AREA WAS REMOVED AS INDICATED BY THE PINK REGION. 75

FIGURE 4-1: EXAMPLES OF SILENT SOURCES. (A) A RADIAL CURRENT DIPOLE IS MAGNETICALLY SILENT; (B) A CLOSED LOOP OF CURRENT IS ELECTRICALLY CURRENT; (C) A UNIFORM DISTRIBUTION OF CURRENT PERPENDICULAR TO A CLOSED SURFACE IS BOTH MAGNETICALLY AND ELECTRICALLY SILENT. 79

FIGURE 5-1: AN EXAMPLE OF MFT MODELLING AND DISPLAY. LEFT: THE SOURCE SPACE IS PART OF A 3-DIMENSIONAL HEMISPHERICAL VOLUME, REPRESENTED AS 9 SECTIONAL CUTS. THE DISTANCE BETWEEN THE MOST SUPERFICIAL LEVEL (9) AND THE DEEPEST LEVEL (1) IS 5.42 CM; THE OVERALL THICKNESS OF THE SOURCE SPACE IS 6.1 CM. HORIZONTAL BARS INDICATE SENSOR POSITIONS. THE CIRCLE DEPICTS THE PROJECTION OF THE CONDUCTING SPHERE ON THE SPECIFIC MRI OUTLINE PLANE, WHILE THE SMALL DOT THE CONDUCTING SPHERE CENTRE. RIGHT: EACH LEVEL IS ROTATED SO THAT IT IS FLAT ON THE PAGE; DISPLAYS AT SUCCESSIVE DEPTHS ARE PLACED BELOW EACH OTHER. ACTIVITY IS SHOWN AS A CONTOUR PLOT. A CROSS INDICATES THE POSITION OF A TEST CURRENT DIPOLE (SEE NEXT SECTION). FAR RIGHT: THE COLOUR SCALE CONVENTION USED THROUGHOUT THIS THESIS: STRONG ACTIVITY IS PLOTTED IN YELLOW, WEAK IN BLUE. 103

FIGURE 5-2: RECONSTRUCTIONS OF THE STANDARD CURRENT DIPOLE SET USING UNITARY REGULARISATION AND UNIFORM PROBABILITY WEIGHT. NOTE THAT ALTHOUGH VERY SUPERFICIAL DIPOLES ARE CORRECTLY RECONSTRUCTED, SENSITIVITY IS WASTED IN THE REGION UNDERNEATH THE SENSOR ARRAY, AND AS RESULT NOTHING CAN BE SAID ABOUT NON-SUPERFICIAL SOURCES. 106

FIGURE 5-3: IN THESE RECONSTRUCTIONS $\lambda_3 = 4.5\ cm$, AND DEEP SOURCES ARE CORRECTLY RECOVERED, BUT SUPERFICIAL AND MIDDLE-DEPTH ONES ARE "PUSHED" DEEPER. THE DEPTH-ENHANCEMENT IS TOO STRONG, AND λ_3, THE PROBABILITY DECAY PARAMETER, NEEDS TO BE HIGHER. 107

FIGURE 5-4: RECONSTRUCTIONS WHERE DEEP AND FAIRLY DEEP SOURCES ARE NOT CORRECTLY RECOVERED (THE EFFECT IS MORE OBVIOUS IN MIDDLE LEVELS), WHILE VERY SUPERFICIAL ONES ARE FULLY BENEFITED. THE DEPTH-ENHANCEMENT IS WEAK $\lambda_3 = 6.0\ cm$, AND THE DECAY NEEDS TO BE DECREASED. 108

FIGURE 5-5: RECONSTRUCTIONS WHERE THE DEPTHS OF MOST SOURCES ARE CORRECTLY RECOVERED; IN THIS CASE $\lambda_3 = 5.3\ cm$, AND IT IS THE APPROPRIATE CHOICE. 109

FIGURE 5-6: INVERSIONS WITH THE SELECTED PROBABILITY DECAY FACTORS, BUT FOR SMOOTHING S=1.0. THE RECONSTRUCTIONS SEEM REASONABLY CORRECT. 110

FIGURE 5-7: INVERSIONS WITH THE SAME PROBABILITY, BUT FOR SMOOTHING S=1.3. 110

FIGURE 5-8: THE SAME PROBABILITY IS USED, BUT SMOOTHING S=2.0. TRYING TO MAKE TOO FINE RECONSTRUCTIONS IN THE PRESENCE OF NOISE RESULTS IN EVENTUAL LOSS OF DETAIL. THIS SMOOTHING VALUE IS DEFINITELY UNACCEPTABLE. 111

FIGURE 5-9: THE FINAL RESULT WITH PROPERLY DEFINED PROBABILITY DECAY AND SMOOTHING PARAMETERS. THESE ARE, $\lambda_3 = 5.2\ cm$, and $s = 1.0 \Rightarrow \tilde{\zeta} = 0.1$. THESE VALUES ARE NOW FIXED, AND ARE THE ONES TO BE USED WITH ANY REAL DATA OF THE SAME EXPERIMENTAL SET-UP. 112

FIGURE 5-10: THE NUMBER OF SENSORS IN SET-UP 1 (37) IS PROGRESSIVELY LOWERED TO OBTAIN SET-UPS 2 AND 3 WITH 19 AND 13 SENSORS RESPECTIVELY. BIG DOTS REPRESENT PROJECTIONS OF THE SENSOR POSITIONS ON THE SOURCE SPACE DISPLAY. THE BIG CIRCLE CORRESPONDS TO THE BOTTOM SOURCE SPACE LEVEL, WHILE THE SMALL TO THE TOP (SUPERFICIAL) ONE - THE SMALL DOT IS THE CENTRE OF BOTTOM LEVEL. A MINIATURE TRIANGLE DEPICTING THE NOTE HELPS IN THE DEFINITION OF POSTERIOR (P) AND ANTERIOR (A) DIRECTIONS. 114

FIGURE 5-11: RECONSTRUCTIONS OF THE STANDARD DIPOLE SET FOR SET-UP 1 (NOISELESS DATA). 116

FIGURE 5-12: RECONSTRUCTIONS OF THE STANDARD DIPOLE SET FOR SET-UP 2 (NOISELESS DATA). 117

FIGURE 5-13: RECONSTRUCTIONS OF THE STANDARD DIPOLE SET (NO NOISE) FOR SET-UP 3. 118

FIGURE 5-14: RECONSTRUCTIONS OF "DEEP" DIPOLES IN THE PRESENCE OF 20% RANDOM NOISE FOR SET-UP 1. 119

FIGURE 5-15: RECONSTRUCTIONS OF THE "DEEP" DIPOLES IN THE PRESENCE OF 20% RANDOM NOISE FOR SET-UPS 2 (TOP) AND 3 (BOTTOM). 120

FIGURE 5-16: RECONSTRUCTIONS OF THE SUPERFICIAL DIPOLES IN THE PRESENCE OF 20% RANDOM NOISE FOR SET-UP 3. 121

FIGURE 5-17: SIMULATION OF UNILATERAL RECORDINGS WITH THE KRENIKON SYSTEM. SKULL AND BRAIN MRI OUTLINES OF A SUBJECT ARE SHOWN TOGETHER WITH APPROXIMATE MRI OUTLINES OF THE THALAMI AND HIPPOCAMPI. THE ORIGINAL SOURCE SPACE IS PART OF A HEMISPHERE, AND COVERS THE LEFT HEMISPHERE. DIPOLES ARE SHOWN AS THICK ARROWS AND ARE PLACED IN VARIOUS ANATOMICAL REGIONS (FROM TOP LEFT TO BOTTOM RIGHT): LEFT HIPPOCAMPUS (LHI); BRAIN STEM; RIGHT

HIPPOCAMPUS (RHI); LEFT CORTEX (LC) AND RHI TOGETHER; LEFT SUPERIOR THALAMUS (LTH); RIGHT SUPERIOR THALAMUS (RTH); RHI AND RTH TOGETHER; LC; LHI AND RHI. 125

FIGURE 5-18: CONTOUR PLOTS OF THE SQUARED CURRENT DENSITY ESTIMATES OF THE PREVIOUS SOURCES USING THE HEMISPHERICAL SOURCE SPACE. SUCCESSIVE MRI SLICES DIFFER BY 6 MM, AND ARE SELECTED ACCORDING TO THE POSITION OF THE MAXIMUM ACTIVITY (MARKED BY A DOT). SOURCES WITHIN THE SOURCE SPACE ARE SATISFACTORILY RECOVERED; WHEN STRONG GENERATORS ARE PRESENT BEYOND THE BOTTOM SOURCE SPACE LEVEL, SOLUTIONS APPEAR AS "FOCAL" (IN THIS CORONAL PERSPECTIVE) DEEP ACTIVITY. 126

FIGURE 5-19: PLOTS WHERE THE CURRENT DENSITY ESTIMATES ARE OBTAINED WITHIN A CENTRALLY - TO THE HEAD - PLACED SMALL CYLINDER AFTER THE PROBABILITY DECAY FACTORS WERE PROPERLY READJUSTED. PROVIDED THAT CONDUCTIVITY MODELLING IS CORRECT, WE CAN NOW SEE WHERE THE "FOCAL DEEP" ACTIVITY APPEARING IN THE PREVIOUS PLOTS IS COMING FROM. 127

FIGURE 5-20: RECONTRUCTIONS OF THE PREVIOUS SOURCES WITHIN THE SMALL CENTRAL CYLINDER USING THE SAME CONDUCTING CENTRE FOR BOTH THE FORWARD AND INVERSE PROBLEMS. 128

FIGURE 5-21: SMALL CENTRAL CYLINDER RECONTRUCTIONS OF THE PREVIOUS SOURCES WHERE THE CONDUCTING SPHERE CENTRE FOR THE FORWARD PROBLEM HAD A DIFFERENCE OF (-1 CM, +1 CM, -1 CM) FROM THE ONE USED IN THE INVERSE PROCEDURE. 129

FIGURE 5-22: RECONSTRUCTIONS OF THE DIPOLE SET DEFINED IN FIGURE 5-17 USING THE LEFT PROBE ONLY. EACH HORIZONTAL ROW REPRESENTS ONE TIMESLICE (I.E. A SINGLE OR DOUBLE DIPOLE). IN THIS PERSPECTIVE IS EASY TO VISUALISE WHICH CYLINDER LEVEL IS PROXIMAL TO THE SENSORS SIDE. 133

FIGURE 5-23: SAME AS BEFORE, BUT USING THE RIGHT PROBE ONLY. THE CONDUCTING SPHERE IS FITTED TO THE RIGHT SIDE ONLY. ALL THE RIGHT SIDE GENERATORS ARE RECOVERED SUCCESSFULLY; WHEN LEFT SIDE GENERATORS ARE ACTIVE, THE LEVEL OF ACTIVATION IS CORRECTLY RECOVERED. HOWEVER, WHEN BOTH LHI AND RHI ARE SIMULTANEOUSLY ACTIVATED (LAST ROW), ONLY RHI IS "SEEN". THIS INVERSION COMPLEMENTS THE INFORMATION OBTAINED FROM USING THE LEFT PROBE ALONE. 134

FIGURE 5-24: SAME AS BEFORE, BUT USING BOTH PROBES TOGETHER IN THE MFT PROCESS. THE CONDUCTING SPHERE IS FITTED TO BOTH SIDES. BOTH SIDE GENERATORS ARE RECOVERED; HOWEVER, THE IMAGES ARE DISTORTED A BIT, DUE TO THE PROXIMITY OF THE CONDUCTING SPHERE CENTRE. THE ADVANTAGE OF USING SUCH A COMBINATION IS THAT ONE CAN OBTAIN INFORMATION ABOUT BOTH SIDES IN ONE INVERSION, RATHER THAN COMBINING ELEMENTS FROM TWO SEPARATE (LEFT AND RIGHT SIDE) INVERSIONS. 135

FIGURE 5-25: A DIPOLE, LOCATED AT THE HIPPOCAMPUS OF A SUBJECT, IS ACTIVATED AT 10, 33, AND 65 MS WITH ACTIVATION DECAYS OF 5, 10, AND 20 MS RESPECTIVELY. THE DIPOLE STRENGTH PROFILE IS ILLUSTRATED BY THE GREEN CURVE. TOP: THE 9-LEVEL MFT SOLUTIONS FOR THE WHOLE PERIOD (EVERY FOURTH TIMESLICE IS SHOWN) WHEN 20% NOISE IS ADDED TO THE SIGNALS PRODUCED BY THE DIPOLE. MIDDLE AND BOTTOM: ON THE LEFT, INTEGRALS OF INTENSITY THROUGHOUT THE WHOLE PERIOD ARE SUPERIMPOSED ON THE SUBJECT'S MRI OUTLINE (BOTTOM FOR THE NOISELESS CASE, MIDDLE FOR THE 20% ADDED NOISE CASE); THE MFT MEASURES OF ACTIVATION WITHIN THE RECTANGULAR ROI ARE

DISPLAYED ON THE RIGHT (BLUE CURVES). THE DIPOLE IS MARKED BY CROSSES IN THE CYLINDER PLOTS AND BY ARROWS IN THE INTENSITY DISPLAYS. 138

FIGURE 5-26: MFT RESULTS IN THE PRESENCE OF 10% ADDED NOISE. RIGHT: THE RECONSTRUCTED ACTIVATION CURVES FOR THE PARIETAL (ORANGE) AND HIPPOCAMPAL (BLUE) REGIONS ARE IN TURN COMPARED WITH THE ACTUAL DIPOLAR PROFILES; IN THE TOP GRAPH THE TWO RECONSTRUCTED ACTIVATION CURVES ARE THEMSELVES COMPARED. LEFT: THE TWO ROIS TOGETHER WITH THE INTEGRALS OF INTENSITY OVER THE PERIODS MARKED BY DASHED VERTICAL LINES. 140

FIGURE 5-27: TOP: DIPOLES (ARROWS) ALONG THE HIPPOCAMPAL AXIS AND INTEGRALS OF INTENSITY OVER THE PERIODS THAT EACH SOURCE IS DISTINCTLY ACTIVE - MARKED BY VERTICAL DASHED LINES BELOW, ARE SUPERIMPOSED ON MRI OUTLINES. MIDDLE: MODEL PROFILES FOR EACH DIPOLE. BOTTOM: ROIS AND INTENSITY INTEGRATED OVER THE WHOLE PERIOD (LEFT) AND MFT ACTIVATION CURVES (RIGHT). 144

FIGURE 5-28: THE SAME DISPLAY AS IN FIGURE 5-27 BUT FOR A MORE COMPLICATED TEMPORAL EVOLUTION OF THE THREE SOURCES 145

FIGURE 5-29: MODEL STRENGTH PROFILES FOR THE ANTERIOR AND POSTERIOR DIPOLES (LEFT) TOGETHER WITH THEIR CORRESPONDING MFT ACTIVATION CURVES (RIGHT), IN SMALLER TIME INTERVALS, SO THAT TEMPORAL DIFFERENCES BECOME CLEAR. WHEN THERE IS A SIMULTANEOUS ACTIVATION (DASHED PARTS), THE MFT ACTIVATION CURVES ARE PEAKED TOGETHER. WHEN THERE IS A SEQUENTIAL TRANSITION IN THE ACTIVATION THERE IS A TIME LAG IN THE ASCENDING OR DESCENDING VALLEYS OF THE MFT CURVES. 146

FIGURE 5-30: TOP: THE CHANGES IN THE MAGNITUDE OF THE INSTANTANEOUS INTENSITY ARE DISPLAYED BY CONNECTING AREAS OF STRONG ACTIVITY WITH ARROWS. THIS TRANSLATES INTO AN IMAGE OF THE SEQUENTIAL SHIFTS OF STRONG ACTIVATION, THEREBY PROVIDING HINTS OF HOW THE VARIOUS ANATOMICAL REGIONS OF THE BRAIN MIGHT BE CONNECTED. ON THE LEFT, THE INTERVAL 10-30 MS OF THE MODEL IN FIGURE 5-28 IS ILLUSTRATED WHERE ACTIVITY PROPAGATES FROM THE ANTERIOR, THROUGH THE MIDDLE, TO THE POSTERIOR PARTS OF THE HIPPOCAMPUS. ON THE RIGHT, THE INTERVAL 30-50 MS OF THE SAME MODEL IS GIVEN WITH SEQUENTIAL SHIFTS OF ACTIVITY FROM POSTERIOR→ANTERIOR→POSTERIOR. BOTTOM: INTEGRALS OF INTENSITY OVER THE SPECIFIC EPOCHS. NOTE THEIR SLIGHTLY DIFFERENT SHAPE/ORIENTATION WHICH INDICATES THE OVERALL TREND IN THE SEQUENCE OF TRANSITIONS OVER THE PARTICULAR PERIODS. 147

FIGURE 5-31: RESULTS FROM MODELLING BI-HIPPOCAMPAL ACTIVATION. THE MFT ACTIVATION CURVES (RED) ARE COMPARED WITH THEIR CORRESPONDING MODEL DIPOLE PROFILES OF THE RIGHT (BOTTOM) AND LEFT (MIDDLE) HIPPOCAMPUS (GREEN). INTEGRALS OF INTENSITY OVER 10 MS (MARKED BY VERTICAL DASHED LINES) AND ROIS ARE PRESENTED ON THE LEFT PARTS. THE TOP ROW SHOWS THE DIPOLE POSITIONS INSIDE THE CYLINDRICAL SOURCE SPACE (LEFT), BUT ALSO THE TWO HIPPOCAMPAL MFT CURVES FOR EFFORTLESS COMPARISON 149

FIGURE 5-32. LEFT: CYLINDRICAL SOURCE SPACE AND SENSOR POSITIONS FOR THE TWO THE TWIN MAGNES BTI SYSTEM. RIGHT: MFT ACTIVATION CURVES (RED/BLUE) AND MODEL DIPOLE PROFILES (GREEN) FOR THE LEFT (BOTTOM) AND RIGHT (TOP) HIPPOCAMPUS. IN THE MIDDLE A DEPTH-TIME-PLOT ILLUSTRATES

FOR BETTER CLARITY). THE TWO RECTANGLES MARK THE SHORT PERIODS USED FOR THE MFT-ECD COMPARISON: JUST PRIOR TO THE TEMPLATE EVENT AND AROUND THE PEAK. THE EARLY PERIOD (LEFT RECTANGLE) IS STUDIED IN THE MIDDLE ROW, WHILE THE PERIOD AROUND THE PEAK (RIGHT RECTANGLE) IS GIVEN IN THE BOTTOM. REST OF ANNOTATIONS FOLLOW THE CONVENTIONS IN FIGURE 6-4. NOTE THE GENERALLY LOWER ECD CORRELATION COEFFICIENTS THAN THOSE OBTAINED IN THE AVERAGE SIGNAL (SNR WAS BETTER THERE), AND THE DISAGREEMENT BETWEEN MFT AND ECD IN THE BOTTOM ROW, INDICATING ANOTHER CENTRE OF ACTIVITY IN ANOTHER LOCATION (NOT REVEALED HERE THOUGH). ALSO NOTE THE "DEEPER" ECD LOCALISATIONS IN THE BOTTOM ROW. 171

FIGURE 6-6: SAME AS IN FIGURE 6-5, BUT FOR ANOTHER INTERVAL (SEE RECTANGLE) DURING THE FILTERED SIGNAL (TEMPLATE SHARP WAVE EVENT), DURING WHICH A DEEP AREA IS BECOMING ACTIVE AT THE PRESENCE OF A SUPERFICIAL SOURCE. THE ECD LOCALISATION IS COMPLETELY OUT OF PLACE, FITTING THE DATA MORE AND POORLY UNTIL IT FAILS TO PROVIDE A SENSIBLE SOLUTION (THREE DOTS IN THE PLACE OF THE CORRELATION COEFFICIENT). THE MFT SOLUTIONS, ON THE CONTRARY, VARY SMOOTHLY AS ACTIVATION OF THE DEEP AREA APPEARS AND GRADUALLY DIES OFF. 172

FIGURE 6-7: COMPARISON OF THE SOLUTION OBTAINED FROM THE CYLINDRICAL AND PARTIAL HEMISPHERICAL SOURCE SPACES. THE FILTERED TEMPLATE SIGNAL IS USED THROUGHOUT. SOLUTIONS ARE PROJECTED ON THE PATIENT'S MRI SLICES IN THE WAY USED SO FAR, BUT CONSIDERING ONLY THE TOP 3 LEVELS OF THE EACH SOURCE SPACE (LEVELS 7-9). NOTE THE SIMILARITY OF THE CORRESPONDING SOLUTIONS AND THE NEARLY SAME MRI LOCALISATIONS (THERE IS ONE MRI SLICE DIFFERENCE IN THE SECOND AND THIRD COLUMN, SEE TEXT). THE THREE TIMESLICES ARE 10 MS APART DURING AN INTERVAL AT WHICH ACTIVITY APPEARS IN BOTH SUPERFICIAL CORTEX AND DEEP STRUCTURES SIMULTANEOUSLY (1: T=1040 MS; 2: T=1050 MS; 3: T=1060 MS) 175

FIGURE 6-8: THE SAME AS IN FIGURE 6-7 BUT CONSIDERING THE DEEP LEVELS ONLY, THAT IS, LEVELS 1-4 FOR BOTH SOURCE SPACES. NOTE THE SIMILAR SHAPE AND LOCALISATION OBTAINED WITH THE TWO SOURCE SPACES AND ALSO THE DIFFERENT CURRENT DENSITY VALUES DUE TO THE USE OF COMPLETELY DIFFERENT SETS OF RECONSTRUCTION PARAMETERS (THE SAME HOLDS TRUE FOR FIGURE 6-7 AS WELL). INSTANCES SHOWN: 1: T=1040 MS; 2: T=1050 MS; 3: T=1060 MS) 176

FIGURE 6-9: TOP: FILTERED TEMPLATE SIGNAL (SUPERIMPOSED ARE THE STRONGEST CHANNELS). A RECTANGLE MARKS THE TIME INTERVAL USED BELOW (SHARP WAVE WITHIN LIGHT VERTICAL LINES). MIDDLE AND BOTTOM: 5 MS APART PLOTS FOR THE CYLINDER (MIDDLE) AND HEMISPHERE (BOTTOM). IT IS EASY TO SEE THAT THE LATTER ARE LESS FUZZY AND BETTER LOCALISED. AMBIGUITIES ENCOUNTERED WHEN ACTIVITY IS CLOSE TO THE CYLINDER-EDGES TOGETHER WITH "THE SUPERFICIAL ARTEFACTS" IN THE CYLINDER CASE ARE ELIMINATED BY THE WIDER COVERAGE THE HEMISPHERE PROVIDES (SEE TEXT). 177

FIGURE 6-10: ELIMINATION OF THE SUPERFICIAL ARTEFACTS BY THE WIDER COVERAGE AFFORDED BY THE HEMISPHERICAL SOURCE SPACE. NOTE THE SMOOTH DEVELOPMENT OF AN ACTIVATION JUST AT THE POSTERIOR BOUNDARIES OF THE CYLINDER - BUT WELL WITHIN THE HEMISPHERE - WHICH LEADS TO SUPERFICIAL ARTEFACT IN THE CYLINDER CASE (SEE THE ANTERIOR END OF THE MIDDLE COLUMN) WHICH IS ABSENT IN THE HEMISPHERE SOLUTIONS. 178

FIGURE 6-11: INTEGRALS OF INTENSITY OVER 20 MS FOR THE FIRST 80 MS OF THE SHARP WAVE EVENT WE HAVE EXAMINED SO FAR CORRESPONDING TO THE SOLUTIONS EXTRACTED FROM THE AVERAGED (TOP ROW), FILTERED (MIDDLE ROW) AND RAW SIGNALS (BOTTOM ROW). ONLY THE SUPERFICIAL LEVELS OF THE SOURCE SPACE (LEVELS 7-9) ARE DISPLAYED. THE SOLUTIONS ARE SUPERIMPOSED ON THE PATIENT'S MRI OUTLINES OF THE SKULL (BLUE), BRAIN (LIGHT BLUE), THALAMI (ORANGE), AND HIPPOCAMPI (PINK). ONE CAN SEE THAT THE THREE RECORDS SHOW SIMILARITIES IN GENERAL, BUT THESE ARE NOT MAINTAINED AT EACH TIME STEP (SEE THE MRI SLICE NUMBER PRINTED WITHIN EACH PLOT; INTERSLICE MRI DISTANCE IS 6 MM). THE SITUATION WOULD BE WORSE IF THE SINGLE TIMESLICES ARE CONSIDERED AT STEPS OF 2.5 MS RATHER THAN INTEGRATED SOLUTIONS OVER 20 MS. 184

FIGURE 6-12: SAME AS IN FIGURE 6-11 BUT FOR THE DEEP LEVELS OF THE SOURCE SPACE (LEVELS 1-4). SAME COMMENTS APPLY. 185

FIGURE 6-13: SAME AS IN FIGURE 6-11 BUT WITH THE INTENSITY INTEGRATED OVER 50 MS. THE SOLUTIONS FOR THE THREE DATASETS BEGIN TO LOOK MORE SIMILAR TO EACH OTHER. ONLY SUPERFICIAL LEVELS ARE CONSIDERED. 186

FIGURE 6-14: SAME AS IN FIGURE 6-13 BUT FOR THE DEEP LEVELS. 187

FIGURE 6-15: INTEGRALS OF INTENSITY OVER 100 MS FOR THE AVERAGED (LEFT COLUMN), FILTERED (MIDDLE COLUMN) AND RAW DATASETS (RIGHT COLUMN). SUPERFICIAL LEVELS ARE CONSIDERED AT THE TOP, DEEP ONES AT THE BOTTOM. NOTE THE MORE "SIMILAR APPEARANCE" OF THE THREE SETS OF SOLUTIONS. 188

FIGURE 6-16: LEFT HALF: 100 MS INTEGRATED MFT SOLUTIONS FOR THE SUPERFICIAL (LEVEL 9, TOP) AND DEEP (LEVEL 1, BOTTOM) LEVEL, AND FOR THE SOLUTIONS EXTRACTED FROM THE AVERAGE (LEFT) AND RAW (RIGHT) SIGNALS. A SMALL TRIANGLE IN THE DEEP LEVEL DENOTES THE NOSE, WHILE A SMALL DOT INDICATES THE NASION (NAS) IN THE SUPERFICIAL. THE SAME ROIS ARE USED IN BOTH RAW AND AVERAGED CASES, SEEN AS TWO RECTANGLES (ONE SUPERFICIAL AND ONE DEEP) IN RED AND BLUE COLOURS RESPECTIVELY. RIGHT HALF: ACTIVATION CURVES FOR THE SAME TWO ROIS (RAW IN RED, AVERAGED IN BLUE) FOR THE PERIOD OF THE SHARP WAVE EVENT. THE MAXIMA OF EACH CURVE ARE PRINTED WITH SUITABLE COLOURS IN ARBITRARY UNITS, WHILE DASHED VERTICAL LINES INDICATE THE TIME INTERVAL (FROM THE BEGINNING OF PERIOD SHOWN) USED FOR THE INTEGRATION. NOTE THAT THE RAW AND AVERAGED RECORDS SHOW SOME DISAGREEMENT IN EVOLUTION OF THE ACTIVITY, ESPECIALLY THE DEEP ONE: AROUND THE TIME OF THE SHARP WAVE MAXIMUM (1110 MS) THE AVERAGE RECORD EXHIBITS AN EXPLOSIVE BUILD UP AT THE DEEP LEVEL WHICH IS ABSENT IN THE CORRESPONDING ACTIVATION CURVE FROM THE RAW SIGNAL. 189

FIGURE 6-17: EPOCH SET 1. *TOP TWO ROWS*: AVERAGED (BLUE) AND RAW (RED) TEMPLATE; *REST*: 6 SIMILAR EPOCHS. LEFT: SIGNALS FROM ONE MEG CHANNEL. *MIDDLE*: ACTIVATION CURVES OF THE DEEP REGION. RIGHT: TIME-DEPTHPLOTS. AT THE INTERVAL OF PEAK AVERAGED ACTIVATION (PINK), EPOCHS REVEAL A CONSISTENT ACTIVATION, ALSO SEEN IN DEPTHPLOTS: SOME OF THE EPOCHS ARE WELL CORRELATED WITH THE AVERAGED (ROWS 4, 5, 6, 8 FROM TOP), WHILE SOME OTHERS (ROW 7) ARE NOT. SIMILAR EFFECTS CAN BE SEEN DURING ANOTHER INTERVAL CONTAINING THE SECOND MAJOR PEAK OF THE AVERAGED ACTIVATION (BROWN). 190

FIGURE 6-18: SAME AS IN FIGURE 6-17 BUT FOR EPOCH SET 2. THE CUMULATIVE EFFECT OF ACTIVATIONS AT INDIVIDUAL EPOCHS SEEMS AGAIN TO GIVE RISE TO THE APPEARANCE OF THE AVERAGED PEAK (PINK TIME WINDOW)..... 191

FIGURE 6-19: EPOCH SET 2: INTEGRALS OF INTENSITY (FOR THE DEEP LEVELS) OVER T=1010-1030 MS, THAT IS 10 MS ON EITHER SIDE OF THE ACTIVATION PEAK TIME FOR THE AVERAGED TEMPLATE, SUPERIMPOSED ON PROPER MRI OUTLINES. NOTE THE GENERALLY GOOD AGREEMENT BETWEEN AVERAGED (TOP LEFT) AND RAW (TOP, SECOND FROM LEFT) TEMPLATES EXTENDED IN THE SIMILAR EPOCHS DESPITE SOME EPOCH VARIABILITY (SEE EPOCHS 2, 3, 4). THE LATTER, HOWEVER, CAN BE PARTLY EXPLAINED BY THE EFFECT THE CENTRAL POINT OF THE INTENSITY INTEGRATION INDUCES, SINCE THE LATENCY 1020 MS IS NOT EXACTLY "CENTRAL" IN OUR TIME WINDOW FOR ALL EPOCHS..... 192

FIGURE 6-20: EPOCH SET 1; TOP ROW CORRESPONDS TO THE AVERAGED TEMPLATE, SECOND FROM TOP TO THE RAW TEMPLATE, WHILE REST TO THE SIMILAR EPOCHS. LEFT: SIGNALS FROM ONE MEG CHANNEL. RIGHT: ACTIVATIONS OF THE SUPERFICIAL ROI (SEEN IN FIGURE 6-16). THE BUILT UP OF THE PEAKS IN THE AVERAGED RECORD - THE TWO MAIN PEAKS ARE MARKED - CAN AGAIN BE EXPLAINED AS RESULTING FROM THE VARIABLE AMPLITUDE ACTIVATIONS OF THE ROI THROUGHOUT THE INDIVIDUAL EPOCHS IT IS ALSO WORTH NOTING THE GENERALLY LOWERED MAGNITUDES INVOLVED, ESPECIALLY IN THE ACTIVATION FOR THE AVERAGED EPOCH..... 193

FIGURE 6-21: EPOCH SET 1. INTEGRALS OF INTENSITY (FOR THE SUPERFICIAL LEVELS ONLY) OVER THE FIRST 80 MS OF THE INTERICTAL EVENTS SUPERIMPOSED ON CO-REGISTERED MRIS OF THE PATIENT. THE FIRST DISPLAY REFERS TO THE AVERAGED EPOCH, THE SECOND ONE TO THE RAW TEMPLATE, WHILE THE REST 6 TO THE SIMILAR RAW EPOCHS RESPECTIVELY. THE CONCORDANCE AMONG THE VARIOUS EVENTS IS CLEAR (NOTE ALSO THE MRI SLICE NUMBER WHICH WITH ONLY ONE EXCEPTION RANGES FROM 10 TO 13, I.E. GIVING AN OVERALL RANGE OF LESS THAN 1.8 CM SLICE RANGE)..... 194

FIGURE 7-1: EXPERIMENTAL SET UP FOR PAT2. TOP: THE SENSOR POSITIONS RELATIVE TO PATIENT ANATOMY. IN THE AXIAL AND CORONAL SECTIONS, A BAR REPRESENTS EACH GRADIOMETER SENSOR, WHILE IN THE SAGITTAL A DOT SHOWS THE PROJECTION OF THE GRADIOMETER ONTO THE DISPLAYED SLICE. THE CONDUCTING SPHERE USED TO MODEL THE CONDUCTIVITY OF THE BRAIN, AND THE SOURCE SPACE ARE ALSO MARKED. BOTTOM: AN INTERICTAL EPILEPTIC SPIKE EVENT IS SHOWN IN TWO DIFFERENT VIEWS. ON THE LEFT SIGNALS FROM ALL CHANNELS ARE DISPLAYED ACCORDING TO CHANNEL LOCATION, WHILE ON THE RIGHT, ONLY THE STRONGEST ONES ARE SUCCESSIVELY ILLUSTRATED..... 199

FIGURE 7-2: MFT OF DIFFERENT FILTERING REGIMES (PAT2). TOP: RAW DATA; RIGHT HALF: SUPERIMPOSED SIGNALS FROM ALL CHANNELS (TOP) AND CORRESPONDING FTS (BOTTOM); LEFT HALF: INSTANTANEOUS ESTIMATES OF INTENSITY SUPERIMPOSED ON AXIAL AND SAGITTAL MRI DRAWINGS (SEE TEXT). MIDDLE: SAME BUT, 1–20 HZ FILTERED DATA. BOTTOM: DATA IN THE THETA RANGE. ALL THREE DATASETS REVEAL ACTIVATION OF THE HIPPOCAMPAL COMPLEX. 201

FIGURE 7-3: TOP LEFT: INTERICTAL EVENT WITH SUPERIMPOSED SIGNALS OF 30 CHANNELS; TEMPLATE INTERVAL WITHIN HEAVY LINES; LETTERED VERTICAL LINES MARK THE TIMES USED FOR THE MFT ESTIMATES OF INTENSITY DISPLAYED IN THE BOTTOM PART OF THE FIGURE. TOP MIDDLE: THE TEMPORAL

EVOLUTION OF ACTIVITY IN THE LEFT HIPPOCAMPAL REGION (BLACK) AND IN THE TEMPORAL CORTEX (RED). TOP RIGHT: THE HIPPOCAMPAL AND CORTICAL REGIONS OF INTEREST. BOTTOM: MFT ESTIMATES OF INTENSITY INTEGRATED OVER 20 MS (I.E. 10 MS ON EITHER SIDE OF EACH LETTERED LINE). *AXIAL AND CORONAL DISPLAYS*: THE SOLUTIONS ARE SUPERIMPOSED ON DRAWINGS OF THE CLOSEST MR IMAGE; *SAGITTAL DISPLAY*: SOLUTIONS ON A FIXED MRI SLICE AT THE HIPPOCAMPAL LEVEL. NOTE L-LEFT SIDE, R-RIGHT SIDE, PROJECTIONS OF THE HEMISPHERICAL SOURCE, AND MODULUS OF $\mathbf{J}^p$ (IN ARBITRARY UNITS, BENEATH EACH SAGITTAL SECTION). 203

FIGURE 7-4: TOP HALF; PAT2; LEFT: LEFT-HEMISPHERE INTERICTAL SPIKE WITH SUPERIMPOSED SIGNALS OF ALL CHANNELS (NOTE TIME BARS A-C). RIGHT; *TOP ROW*: INSTANTANEOUS MFT ESTIMATES OF INTENSITY ON AXIAL MR IMAGES (NOTE TIME INSTANTS A-C AND $|\mathbf{J}^p|$ VALUES IN ARBITRARY UNITS); *BOTTOM ROW; MIDDLE*: GRAPH OF TEMPORAL EVOLUTION OF ACTIVITY IN THE LEFT HIPPOCAMPAL AREA (DOTTED LINE) AND TEMPORAL CORTEX (FULL LINE) (NOTE TIME BARS A-C); *BOTTOM ROW; LEFT AND RIGHT*: MR IMAGES OF ROIS AT THE LEVEL OF HIPPOCAMPUS (SAGITTAL VIEW) AND TEMPORAL CORTEX (CORONAL VIEW). BOTTOM HALF: SIMILAR, BUT FOR THE RIGHT HEMISPHERE OF PAT3. 204

FIGURE 7-5: TOP ROW: (PAT2); *LEFT*: SUPERFICIAL INTEGRALS OF INTENSITY OVER 100 MS, AFTER BACK-AVERAGING 18 SINGLE EVENT SOLUTIONS OF STRONG HIPPOCAMPAL ACTIVATION. TWO MAIN ROIS ARE REVEALED IN THE SAGITTAL VIEW: ONE FRONTO-INFERO-TEMPORAL AND ONE MORE POSTERIOR IN THE TEMPORO-PARIETAL REGION. *MIDDLE*: GRAPH OF ACTIVATIONS OF THE CORTICAL AND HIPPOCAMPAL ROIS. NOTE THE PRE- AND POST-HIPPOCAMPAL ACTIVATION OF THE CORTEX. *RIGHT*: SAGITTAL VIEW OF DEEP INTENSITY INTEGRALS AFTER BACK-AVERAGING. HIPPOCAMPAL ACTIVATION IS CLEARLY SHOWN. *EXTREME RIGHT*: SCHEMATIC AXIAL VIEW OF THE NEOCORTICO-MESIOBASAL INTERACTIONS EMERGING FROM THE BACK-AVERAGED SOLUTIONS; THE SEQUENCE APPEARS AS: ANTERIOR-CORTEX→POSTERIOR-CORTEX→ANTERIOR-CORTEX→HIPPOCAMPUS→ANTERIRO-CORTEX→POSTERIOR-CORTEX. BOTTOM: SIMILAR, BUT AFTER BACK-AVERAGING 19 SOLUTIONS FOR PAT3. ACTIVATION SEQUENCE APPEARING FROM THE BACK-AVERAGED SOLUTIONS (EXTREME RIGHT SCHEMATIC) INVOLVES: POST.-CORT.→ANT-CORT.→HI→ANT-CORT.→POST-CORT. THE CIRCLES IN THE SAGITTAL VIEWS ILLUSTRATE A PROJECTION OF THE APPROPRIATE SOURCE SPACES. 206

FIGURE 7-6: SEQUENCES OF EVENTS OF THE VARIOUS INTERICTAL SPIKES AT THE DEPTH OF THE LEFT TEMPORAL LOBE OF PAT2. TOP: SUPERIMPOSED SIGNALS OF FIVE INDIVIDUAL INTERICTAL SPIKES; A PAIR OF VERTICAL BARS MARK THE 60 MS PERIOD USED IN THE NEXT TWO ROWS FOR EACH SPIKE. MIDDLE: SHIFTS OF THE INSTANTANEOUS ACTIVITY (ARROWS) DURING THE 60 MS PERIODS. BOTTOM: MFT SOLUTIONS INTEGRATED OVER THE 60 MS PERIOD. SAGITTAL PLANE AS IN FIGURE 7-3 (SEE TEXT). 208

FIGURE 7-7: PAT2. (A) INTEGRATED INTENSITY OVER 60 MS IN A SAGITTAL LEVEL THROUGH HIPPOCAMPUS (LEFT). INSTANTANEOUS SHIFTS OF MAXIMUM ACTIVITY COMPUTED EVERY 2.5 MS (RIGHT). PROPAGATION FROM ANTERIOR TO POSTERIOR HIPPOCAMPUS IS OBSERVED. NOTE THE SHAPE OF THE INTEGRATED INTENSITY AND THE ACTIVATION CURVES FOR THE TWO INDICATED ROIS (BOTTOM RIGHT). ACTIVATION OF THE GREATER HIPPOCAMPAL AREA IS GIVEN IN BOTTOM LEFT. (B) SIMILAR BUT WITH ANTERIOR-POSTERIOR-ANTERIOR SEQUENTIAL SHIFTS. 209

FIGURE 7-8: SEQUENCES OF EVENTS DURING THE COURSE OF VARIOUS INTERICTAL SPIKES AT THE DEPTH OF THE RIGHT TEMPORAL LOBE OF PAT3. TOP: SUPERIMPOSED SIGNALS OF FOUR INDIVIDUAL INTERICTAL SPIKES; AS IN FIGURE 7-6, A PAIR OF VERTICAL BARS MARK THE PERIOD USED IN THE NEXT TWO ROWS FOR EACH SPIKE (SOME 56-74 MS IN EACH CASE). MIDDLE: SHIFTS OF THE INSTANTANEOUS ACTIVITY (ARROWS) DURING THE INDICATED PERIODS. THE FIRST TWO DISPLAYS SHOW ANTERIOR→POSTERIOR PROPAGATIONS; THIRD DISPLAY CORRESPONDS TO A POSTERIOR→ANTERIOR PROPAGATION; FINALLY, THE FOURTH DISPLAY DEMONSTRATES POSTERIOR→ANTERIOR→POSTERIOR SEQUENTIAL SHIFTS. BOTTOM: MFT SOLUTIONS INTEGRATED OVER THE ABOVE PERIODS. A FIXED SAGITTAL MRI SLICE AT THE LEVEL OF THE HIPPOCAMPUS IS USED THROUGHOUT. CIRCLES ILLUSTRATE A PROJECTION OF THE APPROPRIATE SOURCE SPACE LEVEL..... 210

FIGURE 7-9: EXAMPLES OF LOCALISED DEEP SOURCES FOR PAT2. CORONAL SECTIONS. A) INSTANTANEOUS MFT ESTIMATES (LEFT) OF RECORDED FOCAL DEEP ACTIVITY AND COMPUTER GENERATED DATA WITH A SINGLE DIPOLE PLACED IN THE RIGHT HIPPOCAMPUS (RIGHT). HEMISPHERICAL SOURCE SPACE IS USED. B) MFT ESTIMATES FOR SOURCE SPACE SHIFTED MEDIALLY (SEE TEXT; ALSO TESTS IN CHAPTER 5). *TOP PART*: LOCALES OF TEST DIPOLES (ONE IN EACH HIPPOCAMPUS). *BOTTOM PART*: MFT ESTIMATES FROM THESE TWO SETS OF SIMULATED SIGNALS. C) REAL DATA FOR THE ORIGINAL HEMISPHERICAL SOURCE SPACE (TOP), AND FOR THE DEEP CYLINDRICAL SOURCE SPACE (MIDDLE) FOR TWO SPECIFIC INSTANCES: ON THE LEFT, WITH ACTIVITY LOCALISED AT THE LEFT HIPPOCAMPAL REGION; AND ON THE RIGHT WITH FOCAL DEEPER ACTIVITY IDENTIFIED. *BOTTOM*: TEMPORAL EVOLUTION OF ACTIVITY IN THE LEFT (BLACK) AND RIGHT (GREEN) HIPPOCAMPAL REGIONS. THE HEMISPHERICAL SOURCE SPACE MODEL WAS USED TO OBTAIN THE ACTIVATION WITHIN THE LEFT HIPPOCAMPAL ROI (SEE, FOR INSTANCE, FIGURE 7-3), WHILE THE CYLINDRICAL MODEL FOR THE RIGHT HIPPOCAMPAL ACTIVATIONS (ROI COVERING THE WHOLE BOTTOM LEVEL OF THE CYLINDER)..... 213

FIGURE 7-10: TOP HALF: TIME-DEPTHPLOTS FOR THE SMALL CYLINDRICAL SOURCE SPACE (TOP) ALONG WITH THE ECG SIGNAL (BOTTOM) FOR PAT2. ZERO DEPTH CORRESPONDS TO L-HI, WHILE 5-6 CM DEPTH CORRESPONDS TO R-HI. BOTTOM HALF: AN EXPANDED TIME SEGMENT OF THE ABOVE PERIOD. THE FIRING OF THE R-HI AREA IS CLEARLY INDEPENDENT OF THE HEART CYCLE..... 214

FIGURE 7-11: PAT2: LEFT: SUPERIMPOSED SIGNALS FOR THREE INTERICTAL EVENTS. RIGHT: ACTIVATIONS IN THE LEFT CORTEX (RED) AND THE TWO HIPPOCAMPI (BLACK AND GREEN) FOR THE SAME THREE INTERICTAL EVENTS, AFTER COMBINING THE TWO SOURCE SPACE MODELS. ACTIVATIONS OF THE RIGHT HI WERE DERIVED FROM THE BOTTOM LEVEL OF THE "DEEP" CYLINDER, WHILE THOSE FOR LEFT CORTEX AND LEFT HI WITHIN THE SAME ROIS SHOWN IN PREVIOUS FIGURES. NOTE LIGHT VERTICAL BARS INDICATING THE MAXIMA OF EACH ACTIVATION CURVE. DESPITE SEQUENCES OF SUCCESSIVE ACTIVATIONS, NO SYSTEMATIC TIME RELATION IN THE ACTIVATION ONSET AND OFFSET OF THE TWO HIPPOCAMPI COULD BE OBSERVED. 215

FIGURE 8-1: EXPERIMENTAL SET UP AND ANALYSIS MODELS FOR THE MYOCLONIC PATIENT (BN). TWO HEMISPHERICAL SOURCE SPACES WERE USED IN THE MFT ANALYSIS, ONE FOR EACH PROBE. NOTE THE SOURCE SPACE ORIENTATIONS WITH RESPECT TO THE MEG HEADSHAPE OUTLINE (GREEN) AND THE

SENSORS (RED AND BLUE BARS FOR PROBES A AND B RESPECTIVELY). 4 LEVELS ARE GIVEN FOR SOURCE SPACE IN THREE PERSPECTIVE VIEWS. THE CONDUCTING SPHERES FOR EACH PROBE ASPECT ARE PLOTTED AS PINK CIRCLES; PINK DOTS DENOTE THE CONDUCTING CENTRES. 225

FIGURE 8-2: ANALYSIS OF PROBE B SIGNALS. TOP: RECTIFIED EMG (ORANGE) AND SUPERIMPOSED SIGNALS OF ALL MEG CHANNELS (BLUE). MIDDLE: PLOTS OF INTENSITY PROJECTED ON SAGITTAL MRI SLICES REVEALING A REGION AT THE POSTERIOR-INFERIOR PART OF THE PARIETAL LOBE: ON THE LEFT, INTENSITY IS INTEGRATED OVER 20 MS (FROM T=-50 TO T=-30 MS); ON THE RIGHT, AN INSTANTANEOUS SOLUTION AT THE TIME OF THE FIRST MAXIMUM ACTIVATION. BOTTOM: MRI OUTLINE SHOWING THE CHOSEN ROI (LEFT) AND GRAPH OF ITS ACTIVATION IN TIME (RIGHT). NOTE FIDUCIALS, DOTTED VERTICAL LINES DENOTING THE INTEGRATION PERIOD USED ABOVE, AND VALUE OF $|\mathbf{J}^r|$ IN ARBITRARY UNITS. 229

FIGURE 8-3: TOP: *LEFT*: MIDSAGITTAL MRI SLICE WITH SENSOR POSITIONS (RED BARS; PROBE A) AND DISPLAY OF TWO SOURCE SPACE LEVELS (1 AND 8; ORANGE CIRCLES); *MIDDLE AND RIGHT*: 20 MS LONG INTEGRALS OF INTENSITY THROUGH AN OBLIQUE AXIAL SLICE AT THE PLANE OF THE 8TH SOURCE SPACE LEVEL SHOWING ACTIVATION OF THE LEFT (30-50 MS POST-EMG ONSET) AND RIGHT (90-110 MS POST-EMG ONSET) SENSORIMOTOR AREAS (L-SM AND R-SM RESPECTIVELY). NOTE ANATOMICAL LANDMARKS (COLOURED DOTS), CENTRAL SULCUS TRACINGS (BLUE), L,R-SM ROIS, ROUGH OUTLINE OF THE MIDSAGITTAL SLICE (PINK; SEE FIGURE 8-4 FOR MORE "ORIENTATION" DETAILS), AND OBLIQUE AXIAL SKULL OUTLINE (BROWN). MIDDLE: *LEFT*: MEG SIGNALS FROM ALL CHANNELS OF PROBE A (RED) AND RECTIFIED EMG (ORANGE); *RIGHT*: ACTIVATION GRAPHS FOR THE L- AND R-SM ROIS; DOTTED VERTICAL LINES SHOW THE PERIODS USED ABOVE. BOTTOM: THE SAME 20 MS INTENSITY INTEGRALS ON SAGITTAL MRI SLICES. NOTE LOCATION OF CENTRAL SULCUS. 230

FIGURE 8-4: STUDY OF THE SM ACTIVATIONS DURING THE FIRST 100 MS FOLLOWING EMG ONSET. LEFT: INTEGRATED INTENSITY THROUGHOUT 100 MS. NOTE ORIENTATION OF A SAGITTAL SLICE THROUGH L-SM (MID-SAGITTAL PLANE IS A FEW MM TO THE RIGHT OF THIS SLICE, JUST WHERE THE CENTRAL SULCUS (CS) TRACES FROM LEFT AND RIGHT FORM AN ANGLE); SEE ALSO ANATOMICAL LANDMARKS, AND SOURCE SPACE LEVELS (1 AND 8). MIDDLE: CONNECTIVITY PLOTS FOR THE SAME PERIOD; THE SEQUENTIAL SHIFTS OF MAXIMUM INTENSITY CRISS-CROSS THE CENTRAL SULCUS. RIGHT: LOCALISATIONS OF STRONG INTENSITY MAXIMA THROUGHOUT THE SAME PERIOD. NOTE THEIR "DISTRIBUTION" ON EITHER SIDE OF THE CENTRAL SULCUS; ANATOMICAL LANDMARKS ARE NOT SHOWN TO AVOID CONFUSION. DOT COLOURS CORRESPOND TO DIFFERENT DURATIONS OF ACTIVITY IN EACH POINT (YELLOW LONGER THAN RED; RED LONGER THAN GREEN), WHILE DOT SIZE DIFFERENT INTENSITY STRENGTHS (THE BIGGER THE DOT THE STRONGER THE INTENSITY) 231

FIGURE 8-5: TOP: 20 MS LONG INTEGRALS OF INTENSITY THROUGH AN OBLIQUE AXIAL SLICE AT THE PLANE OF THE 8TH SOURCE SPACE LEVEL; TIME INTERVALS ARE BETWEEN 150-170 MS (LEFT) AND 230-250 MS (RIGHT) AFTER EMG ONSET. THE REGIONS REVEALED ARE ANTERIOR TO THE SM REGIONS SHOWN BEFORE, AND ARE WITHIN THE ANTERIOR PARTS OF THE SUPPLEMENTARY MOTOR AND/OR FRONTAL AREAS (L,R-SMA/FRONTAL). NOTE CS TRACES, SOURCE SPACE LEVELS, OBLIQUE AXIAL SKULL OUTLINE, AND ANATOMICAL LANDMARKS. MIDDLE: ACTIVATION CURVES OF THE TWO ROIS. NOTE THAT THE

ACTIVATION OF L-SMA IS MUCH STRONGER THAN THAT OF R-SMA. BOTTOM: THE PREVIOUS INTENSITY INTEGRALS (SHOWN ON TOP) AS PROJECTED ON PROPERLY SELECTED SAGITTAL MRI SLICES. NOTE CS MARKS, AND $|J^p|$ IN ARBITRARY UNITS. 232

FIGURE 8-6: ACTIVATIONS WITHIN ALL THE PREVIOUSLY MENTIONED REGIONS FOR SUMMARY AND/OR COMPARISON PURPOSES. NOTE THAT THE FIRST SIGNIFICANT ACTIVATION OCCURS IN THE LEFT IPL REGION (SOME 40 MS BEFORE EMG ONSET) FOLLOWED BY A WHOLE SEQUENCE OF EVENTS INVOLVING THE SM AND SMA REGIONS BOTH CONTRALATERALLY AND IPSILATERALLY. DASHED VERTICAL LINES MARK 100 MS APART LATENCIES TO AID COMPARISONS. 233

FIGURE 8-7: LEFT: INTEGRATED INTENSITY BETWEEN 70 AND 90 MS AFTER EMG ONSET. RIGHT: LOCALISATION OF THE INSTANTANEOUS MAXIMUM OF INTENSITY. THE LOCATION OF THE MAXIMUM IS IN THE SECOND SOMATOSENSORY AREA (SII) 234

FIGURE 8-8: EXPERIMENTAL SET UP FOR SUBJECT HMG (FRONTOLATERAL DEWAR POSITIONS) AND MFT SOURCE SPACE MODELS. TOP AND MIDDLE: TWO HEMISPHERICAL SOURCE SPACES WERE USED IN THE MFT ANALYSIS, ONE FOR EACH PROBE. NOTE THE SOURCE SPACE ORIENTATIONS WITH RESPECT TO THE MEG HEADSHAPE OUTLINE (GREEN) AND THE SENSORS (RED AND BLUE BARS FOR PROBES A AND B RESPECTIVELY). 4 LEVELS ARE GIVEN FOR SOURCE SPACE IN THREE PERSPECTIVE VIEWS. BOTTOM: THE "SMALL" CYLINDRICAL SOURCE SPACE USED IN THE SIMULTANEOUS STUDY OF BOTH PROBES. IN EACH PLOT, THE CONDUCTING SPHERE IS DRAWN AS A PINK CIRCLE WITH A PINK DOT MARKING THE CENTRE OF THE CONDUCTING SPHERE 242

FIGURE 8-9: MFT SOLUTIONS FOR THE AVERAGED ODD RESPONSE OBTAINED INDEPENDENTLY IN THE LEFT AND RIGHT SOURCE SPACES BETWEEN T= 325 MS AND T=340 MS AFTER STIMULUS ONSET (TO THE LEFT EAR). THE $|J^p|$ VALUES BENEATH EACH AXIAL SLICE CORRESPOND TO THE MAXIMUM OF THE DISTRIBUTION THROUGHOUT THE WHOLE OF THE LEFT AND RIGHT SOURCE SPACES AT THAT TIME INSTANT, WHILE THOSE BENEATH EACH SAGITTAL TO THE MAXIMUM OF THE 3 DEEP LEVELS ONLY IN EACH SOURCE SPACE. 243

FIGURE 8-10: MFT RECONSTRUCTIONS FOR THE SAME TIME INTERVAL AS THAT IN FIGURE 8-9, BUT REPEATED USING THE DEEP CYLINDER SOURCE SPACE MODEL (BOTH PROBES TOGETHER; SEE BOTTOM OF FIGURE 8-8). THE DISPLAY FORMAT IS THE SAME USED WITH THAT OF FIGURE 8-9, EXCEPT THAT ONLY THE OVERALL MAXIMA THROUGHOUT THE WHOLE CYLINDER ARE PRINTED BENEATH EACH AXIAL SLICE. 244

FIGURE 8-11: LEFT: THE DEEP CYLINDER SOURCE SPACE MODEL. RIGHT: TIME-DEPTHPLOTS FOR THE MFT SOLUTIONS PRESENTED IN FIGURE 8-10 (I.E. USING THE DEEP CYLINDER MODEL). TWO SCALES ARE USED: *IN THE TOP*, THE TIME-DEPTHPLOT INVOLVES ALL 9 LEVELS OF THE CYLINDER SPACE (I.E. FROM FAIRLY DEEP RIGHT TO FAIRLY DEEP LEFT REGIONS), WHILE IN THE *BOTTOM*, ONLY THE 5 DEEP LEVELS OF THE CYLINDRICAL SOURCE SPACE ARE INVOLVED; ARROWS DEPICT THE ASSOCIATION BETWEEN THE DEPTHPLOT EDGES AND THE INVOLVED SOURCE SPACE LEVELS; (SEE TEXT). ONE CAN NOTE THE AFOREMENTIONED "CROSSOVER" HAPPENING AROUND THE LATENCIES STUDIED IN THE PREVIOUS FIGURE. 245

FIGURE 8-12: MFT DISPLAYS INVOLVING THE LATENCIES FROM T=495 MS TO T=510 MS DURING THE ODD EPOCH 282. THE SAME CONVENTIONS ARE USED AS FOR FIGURE 8-9. NOTE AGAIN THE GENERAL AGREEMENT BETWEEN THE TWO INDEPENDENT MFT RECONSTRUCTIONS (LEFT AND RIGHT) IN THE

IDENTIFICATION OF DEEP MIDLINE ACTIVATION. SEE ALSO THE CORRESPONDING DEEP CYLINDER RECONSTRUCTIONS IN FIGURE 8-13. 246

FIGURE 8-13: MFT RECONSTRUCTIONS FOR THE SAME TIME INTERVAL AS THAT IN FIGURE 8-12, BUT USING THE DEEP CYLINDER SOURCE SPACE MODEL. SEE FIGURE 8-10 FOR CONVENTIONS. THE DISPLAYS ARE CONSISTENT WITH ACTIVATION OF THE CINGULATE WHICH SHIFTS FROM ANTERIOR TO POSTERIOR. 247

FIGURE 8-14: MFT DISPLAYS INVOLVING THE LATENCIES FROM T=315 MS TO T=330 MS DURING THE ODD EPOCH 297. THE CONVENTIONS VALID IN FIGURE 8-9 APPLY HERE TOO. NOTE AGAIN THE GENERAL AGREEMENT BETWEEN THE TWO INDEPENDENT MFT RECONSTRUCTIONS (LEFT AND RIGHT) IN THE IDENTIFICATION OF DEEP POSTERIOR MIDLINE ACTIVATION. SEE ALSO THE CORRESPONDING DEEP CYLINDER RECONSTRUCTIONS IN FIGURE 8-15. 248

FIGURE 8-15: MFT RECONSTRUCTIONS FOR THE SAME TIME INTERVAL AS THAT IN FIGURE 8-12, BUT USING THE DEEP CYLINDER SOURCE SPACE MODEL. SEE FIGURE 8-10 FOR CONVENTIONS. HINTS ARE PROVIDED FOR ACTIVATION AT THE POSTERIOR CINGULATE LEVEL ESPECIALLY IN THE AXIAL PROJECTIONS. 249

FIGURE A-1: THE BTI TWIN MAGNES SYSTEM (2X37 CHANNELS) INSIDE THE DEDICATED SHIELDED MAGNETICALLY ROOM AT JÜLICH RESEARCH CENTRE, GERMANY. THE COUCH USED AS THE SUBJECT "LYING-BED" IS SEEN BETWEEN THE TWO DEWARS. 260

FIGURE A-2: A TYPICAL SUBJECT/PROBE POSITIONING USED FOR AUDITORY RECORDINGS (TEMPORAL SENSOR PLACEMENT) WITH THE BTI TWIN MAGNES SYSTEM (2X37 CHANNELS) AT JÜLICH RESEARCH CENTRE, GERMANY. NOTE THE PROBE POSITION INDICATOR (PPI) MENTIONED IN CHAPTER 3 USED FOR "CLICKING" (MARKING) ANATOMICAL LANDMARKS (NASION IN THIS SPECIFIC CASE) 261

TABLE 3-1: RESULTS FROM "PM" (POINT-MATCHING). THREE POINTS WERE ROTATED AND TRANSLATED AWAY FROM THE TRUE POSITIONS (INITIAL ERRORS). PM TRIED TO "BRING THEM BACK" TO THEIR PROPER POSITIONS. AT THE END OF THE PROCESS THE "FINAL ERRORS" WERE EVALUATED. NOTE THE SMALL FINAL RMS MISFIT/POINT VALUES..... 57

TABLE 3-2: RESULTS FROM MEG/MRI SURFACE-MATCHING. A SET OF POINTS WAS ROTATED AND TRANSLATED AWAY FROM THEIR TRUE POSITIONS (INITIAL ERRORS). THE SURFACE-MATCHING PROGRAM WAS THEN ASKED TO RETURN THEM BACK TO THEIR ORIGINAL POSITIONS. AT THE END OF THE PROCESS THE "FINAL ERRORS" WERE EVALUATED. NOTE THAT THE VALUES FOR THE FINAL RMS MISFIT/POINT ARE LESS THAN 3 MM IN ALL CASES..... 61

TABLE 3-3: THE SIGNIFICANCE OF THE "QUALITY" OF POINTS; CORRECTION OF THE SAME INITIAL ERROR IS ATTEMPTED USING DIFFERENT NUMBER OF POINTS. IN THE FIRST CASE (69 POINTS), NO CARE WAS TAKEN IN THE SELECTION OF THE POINTS. IN THE SECOND (129 POINTS), 60 ADDITIONAL POINTS IN TWO PERPENDICULAR DIRECTIONS (MIDSAGITTAL LINE, MIDCORONAL LINE) WERE ADDED TO THE ORIGINAL 69. THE FIT IN THE SECOND CASE IS SIGNIFICANTLY IMPROVED (COMPARE ROWS FINAL1 AND FINAL2) OF THE LAST COLUMN..... 62

TABLE 6-1: LOCALISATION DETAILS FOR ECD AND MFT FOR 4 TIMESLICES OF THE AVERAGE SHARP WAVE SHOWN IN THE TOP ROW OF FIGURE 6-4 (TIME PERIOD IS MARKED BY THE TWO LIGHT VERTICAL LINES ON THE LEFT). THE CORRESPONDING SOLUTIONS CAN BE SEEN IN THE MIDDLE ROW OF FIGURE 6-4. THE MFT LOCALISATION DETAILS HAVE BEEN OBTAINED FROM THE POSITION OF THE MAXIMUM MODULUS OF THE CURRENT DENSITY. NOTE THE GENERALLY GOOD AGREEMENT BETWEEN MFT AND ECD. 170

TABLE 6-2: SAME AS IN TABLE 6-1, BUT FOR ANOTHER PERIOD WHEN DEEP ACTIVITY IS IDENTIFIED FROM BOTH METHODS (TIME PERIOD MARKED BY THE TWO RIGHT MOST VERTICAL LINES). THE CORRESPONDING SOLUTIONS CAN BE SEEN IN THE BOTTOM ROW OF FIGURE 6-4. NOTE THE GENERALLY GOOD AGREEMENT BETWEEN MFT AND ECD, DESPITE THE EXPECTED BLURRING OF THE MFT SOLUTIONS IN DEPTH..... 170

1. Introduction

Biomagnetism embraces a diverse range of activities, all made manifest by the presence of a magnetic field outside a body. Although different living organisms can indeed be included, research is mainly focused on human studies. Depending on the origin of the magnetic fields, biomagnetism is divided into Magnetoencephalography (MEG, brain), Magnetocardiography (MCG, heart), Magnetoneurography (MNG, peripheral nerve), Magnetogastrography (MGG, gastrointestinal tract), Magnetopneumonography (MPG, lungs), and Biosusceptometry (BLS, liver or BSS, spleen). All these biomagnetic methods have two distinctive qualities: they are completely non-invasive and they provide information about the function or the physical properties of the various organs. This thesis focuses on the measurement, analysis, modelling, and interpretation (in terms of physiology/pathophysiology) of MEG signals, with special emphasis on signals from epileptic patients.

The goal of this introductory chapter is to place this piece of research in the context of other work in the biomagnetic field, but also in the wider field of functional brain imaging. Since MEG signals are a result of the electrophysiological phenomena within the brain, the important milestones in the history of bioelectromagnetic measurements are reviewed. Following, the current state of MEG within biomagnetism is examined, and issues relating to MEG modelling discussed. At the end of this chapter, the scope and an outline of the remainder of the thesis are given.

1.1 History of bioelectromagnetism*

The Greeks are credited with the first recorded bioelectric observations some 2600 years ago thanks to Thales of Miletus, who commented on the severe shocks produced by electric fish, but also to Hippocrates, who just a little more recently (5th century BC) gave a written account of the numbing effects of Nile catfish's electric discharges. However, the scientific era of bioelectromagnetics did not start until 1600, when Gilbert defined and named electricity. In 1791 Galvani performed the first experiments on the stimulation of muscle contractions by electric fields, and progress was made in understanding the link between biology and electricity. Although Galvani's interpretations were challenged by Volta, it was obvious that the period of scientific experimentation had been initiated.

In 1820, Oersted accidentally discovered the connection between electricity and magnetism having observed the deflection of a magnetic needle due to a current. Soon after that, Ampere established the concepts we now call current and voltage, and proposed the use of a galvanometer based on them and eight years later Nobili actually developed a galvanometer sensitive enough to make precise measurements of currents in frog preparations. At about the same time the laws of electrical resistance were elucidated by Ohm and others, and finally in 1831, Faraday discovered the basis of all transformers and related devices, mutual induction, while Henry stated the principle of self-induction. Owing to the introduction of induced currents from magnetoelectric or electromagnetic machines, and the constant attempts of Duchenne, uses of "electrotherapy" also appeared. In parallel Bois-Reymond established many basic laws of bioelectricity, and his friend, Helmholtz, succeeded in precisely measuring the velocity of the nerve impulse - he got a value of 27.25 m/sec which is about the same as measured today. Helmholtz made theoretical contributions too. He was the first to point out (Helmholtz 1853), that it is impossible to deduce uniquely the spatial distribution of activity within a confined volume from measurements of the surface potential and/or the magnetic field outside the body, a statement known as "the non-uniqueness of the bioelectromagnetic inverse problem" (Helmholtz 1853).

The late 1800s witnessed a number of fundamental discoveries in physics and parallel technological innovations in the Western civilisation, that had an invaluable impact on bioelectromagnetics. For example, Tesla in 1888, made possible the industrial use of AC current and in the same year, Hertz demonstrated the existence of the electromagnetic waves as predicted by Maxwell in 1864. However, instrumentation in

---

* *where references are not explicitly made, the following books/papers have been used: Brazier 1984, Brazier 1988, Bischof 1994*

bioelectromagnetics remained quite unreliable and inaccurate well into the 1920s when vacuum-tube amplifiers and oscilloscopes came into more general use.

Although recordings were performed in animals, human "brainwaves" were not recorded from the surface of the scalp until 1924, when Berger, a German psychiatrist, was finally successful in his recordings, having been benefited from a double-coil galvanometer granted to him by Siemens. He used two large sheets of tinfoil, one on the forehead and one on the back of the head, to register the first human electroencephalogram (EEG)* , and claimed that he was able to discriminate between alpha and beta waves generated by currents inside the brain. For years he was trying to find a physiological basis for psychic phenomena, brain injury, epilepsy, and mental effort. His studies were later enriched with the discovery of delta and theta waves in 1935 and 1943 by Adrian and Walter respectively. Their efforts had undoubtedly established the era of EEG as a tool in neurology and psychiatry. Computing and other technological advances together with the need for more precise recordings have replaced Berger's 2 electrodes with as many as 64, 128 or even 256! Nowadays, there are more than 50 laboratories around world-wide using "high resolution systems" accommodating more than 64 electrodes (channels; Neuro Scan News 1995)

1.2 The development of Magnetoencephalography

Since the currents that Berger and others were measuring would also generate magnetic fields, it should be theoretically possible to measure them outside the head. However, very sensitive devices were needed for that purpose. In fact, the birth of biomagnetism is dated back to 1963 (Baule and McFee 1963) when Baule and McFee succeeded in measuring real "animal magnetism", the magnetocardiogram (MCG). However, the measurement of the magnetic equivalent of EEG, is attributed to Cohen. In 1968, he used room-temperature operated solenoid coils inside a magnetically shielded room, to detect the spontaneous alpha rhythm magnetically. Inside the room, environmental signals were reduced and the most dominant noise source interfering with the measurements were the coils themselves!

---

* *The term EEG is also attributed to Berger, whose humanistic educational background rejected the previously adapted "electrocerebrogram" due to the ugly linguistic mixture of Greek ("electro", "gram") and Latin ("cerebro") fragments. What Berger proposed in German was the term "Elektrenkephalogram", since the root "enkephalo" from the Greek is linguistically more correct than "encephalo" (Niedermeyer, 1993a).*

The following step was the advent of superconducting technology. The superconductivity effect, discovered in 1911 by Onnes, and theoretically exploited by Josephson (Josephson 1962), was used in 1970 by Zimmerman (Zimmerman et al 1970) for the construction of the Superconducting Quantum Interference Device (SQUID), a highly sensitive magnetic flux detector. Cohen collaborated with Zimmerman and Edelsack that same year, and used the SQUID to record the human MCG (Cohen et al 1970). Two years later, the recordings were carried out on epileptic patients (Cohen 1972). Cohen's pioneering studies were followed by those of Brenner and others (Brenner et al 1975), who were the first to present magnetic measurements of (visually) evoked responses/fields (VEFs). The single sensor (channel) used in those early days, though, was too laborious to use: to locate, even approximately, the activated area of cortex, it had to be repositioned around the head, and the recordings to be repeated; it is obvious that this was causing discomfort to the "immobile" patient/subject, and many phenomena, especially spontaneous activity, could not be adequately studied.

Over the past two decades, remarkable advances in instrumentation were made in the infant discipline of biomagnetism. The first generation of single channel systems gave its place to the second (oligochannel systems, 5-14 sensors), third (polychannel or multichannel systems, 19, 28, 37 sensors), and finally to the fourth generation (whole head systems, 64, 74, 122, 143, 147 sensors). There are currently three companies constructing commercial whole head systems: Neuromag (Finland), BTi (USA), and CTF (Canada). More than 18 laboratories world-wide are currently using multichannel systems of more than 19 sensors providing partial coverage of one or both sides of the head, and by the end of 1996 or soon thereafter, another 18 will be using helmet like systems. Various national projects are also under development. In Italy, a "small" MCG system facilitated with 55 channels, together with a helmet-like system featuring 153 channels (Pizzella 1995) are being constructed. The Japanese government had also launched a multi-company project at the Superconducting Sensor Laboratory of Japan (SSL), in order to construct a helmet system with more than 200 sensors, but also to drive from element technology to system integration for magnetometry (Kado 1995). Although the latter project was recently stopped, some other smaller scale programs seem to be running in Japan.

Obviously, helmet-like systems can only be used for MEG. However, all the previous generation systems were and are used in the broad field of biomagnetism covering numerous applications. We mentioned in the beginning of our introduction the diverse subsections sharing the common grounds of the biomagnetic science. It will be useful to examine the relative proportion of research that has been input into each one of those.

In trying to do so, we shall consider the papers presented at the last four "International Conferences of Biomagnetism", the most prestigious meetings that serve as forums of the biomagnetic field: the 1989 meeting in New York, the 1991 in Münster, the 1993 in Vienna, and the most recent one held in Santa Fe, New Mexico in February 1996..

Figure 1-1 shows that MEG has always been the main research topic, followed by MCG. A slight increase in the proportion of both MEG and MCG at the expense of the other sections is seen. Moreover, almost three times as many papers focused on brain investigations than on cardiac topics, an analogy kept almost constant throughout the years.

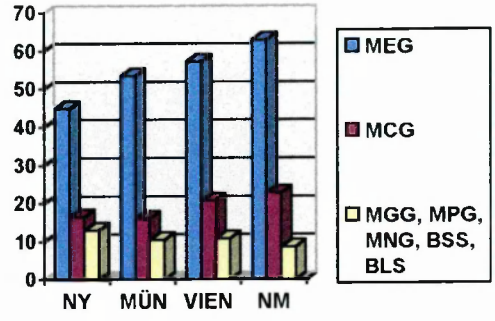

Figure 1-1: Relative proportion of various sections of Biomagnetism during the last four International Conferences of the "biomagnetic" research community that took place in New York (NY, 1989), Münster (MÜ, 1991), Vienna (VIEN, 1993), and New Mexico (NM, 1996). See main text for the rest of abbreviations.

Classifying the papers into categories according to the topics deemed to have benefited we can see that three main areas emerge: instrumentation, theory-modelling, and applications. The main bulk of research over the last few years has been thrown onto applications, as appreciated from Figure 1-2. Moreover, relatively few papers are presented on instrumentation, an effect explained by the fact that instrumentation has been mainly carried out more commercially (by companies) lately, rather than by individual research groups. An gradual rising in theory-modelling is also appearing, and is actually expected to increase more in forthcoming meetings, as a result of the introduction of new systems (e.g. helmets), which of course necessitate more advanced modelling methodologies.

Since this thesis is concerned with MEG as applied in epilepsy, we regard it appropriate to show in Figure 1-3 the relative distribution of MEG applications. Studies with evoked responses have been the main consideration so far, since they form a relatively easy, but

also traditional way of experimentation in cognitive neuroscience. Studies in epilepsy have remained almost constant throughout the years, but they are four times as fewer than evoked fields. However, they constitute the main clinical application ground of MEG (BioMagList 1995). Another trend that is illustrated in Figure 1.3, is the increase of cognitive applications. As Lloyd Kaufman pointed out in the opening speech of the Vienna Conference, "MEG has a real potential to study human cognition", and, therefore, such MEG applications are expected to expand further over the next few years.

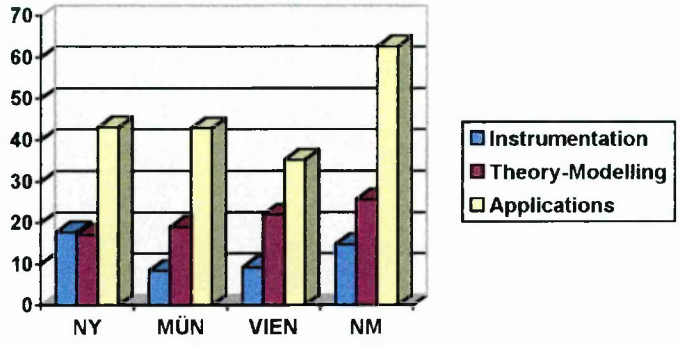

Figure 1-2: Classification of biomagnetic papers into three main categories and their relative proportions in the last four conferences. See Figure 1-1 for abbreviations.

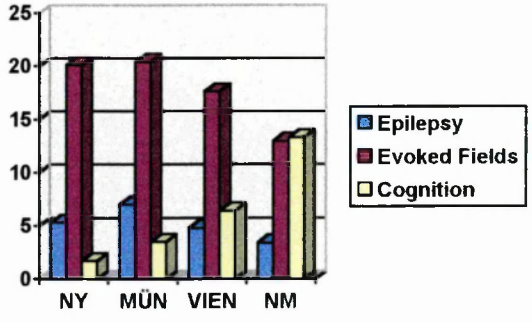

Figure 1-3: The three main areas of MEG applications and their relative proportions over the last four biomagnetism conferences. See Figure 1-1 for abbreviations.

1.3 Issues on MEG modelling

Images of brain activity are also produced by other methods like single photon emission tomography (SPECT), positron emission tomography (PET), and functional magnetic resonance imaging (fMRI). At present, the spatial resolution of these (especially the latter one) is sufficiently good to allow studies of brain function. However, all these techniques lack in temporal resolution; they can only trace brain activity in the order of seconds (or even minutes), which is far slower than the actual speed of brain processes. EEG and MEG offer the ability to study the dynamic topology of brain activity millisecond by millisecond. They are both completely non-invasive, since the subjects/patients are not exposed to any radioactivity, time varying, or strong steady magnetic fields. Moreover, MEG measurements are non-contact.

In addition, MEG's spatial resolution is a few millimetres for cortical, superficial sources. When calculating the distribution of currents in the brain from magnetic (or electric) fields (or potentials) outside the head, we are dealing with the so-called "inverse problem". Unlike in the case of the previously mentioned imaging techniques, however, the mathematics of the bioelectromagnetic inverse problem are inherently fuzzy. As mentioned before, Helmholtz had already shown in 1853, that the solution is not unique: an infinite number of diverse current distributions can explain a given magnetic field. Despite this mathematical hurdle, reliable estimates for the primary current distribution can in fact be obtained, if some prior knowledge and assumption about the form of the sources is given and the level of detail demanded in the reconstruction is not finer than the sensitivity of the sensors (Ioannides 1994).

Injecting *a priori* knowledge into the source reconstruction usually demands anatomical constraints. In the simplest of the cases, one should expect the sources of brain activity to lie within the brain volume! To gear even this simplistic task, correlation with images of anatomy (i.e. MRI/CT images) is necessary. Likewise, if certain regions are known to be activated at specific instances, the reconstruction volume could be defined by those regions. Obviously, the higher the degree of accuracy in correlating (registering) MEG with MRI/CT, the more precise the outcome.

Another way of introducing *a priori* information is through a model. To date, many source models have been proposed and developed. These can be basically classified into two categories. The first one, assumes that all primary activity is generated by a single or a few point sources, i.e. current dipoles, while the second one allows for the more general and realistic case of distribution of currents. The main bulk of this thesis, makes use of an imaging method that lies within the second category, namely, Magnetic Field Tomography (MFT). However, at some stages, comparisons of MFT with the more

widely used, though simplistic, single current dipole or equivalent current dipole (ECD) model, are performed.

The traditional view that (useless) background "brain noise" is eliminated by averaging signals, has been widely used to date, to improve the signal-to-noise ratio (SNR). When performing an evoked response experiment, there is a well (pre)defined epoch length with respect to a stimulus onset, and signal averaging across epochs, is very easily achieved. In the case of studying spontaneous activity when no stimulus is present, the task is more difficult, but one can still use target signal patterns, and then attempt a global spatio-temporal search to correlate epoch segments. For example, a clear epileptic spike could be used as a target (template) and then scanning can be conducted through the signal space, in order to identify similar appearances of the presumably same event. Averaging can then be performed across the identified time periods (Abraham-Fuchs et al 1990).

Arguments against treating background brain activity as noise have been appearing more frequently in recent years. It was shown, for instance, that pre-stimulus EEG tends to attain a phase-order pattern prior to expected stimulation (Başar et al 1989). In addition, importance has been drawn onto mind's "microstates" as opposed to the global general characteristics of the averaged signals (Lehmann 1989; Pascual-Marqui et al 1995). Furthermore, analysis of single epochs is emerging as a robust methodology of homing into brain's dynamics (Childers 1986; Liu LC and Ioannides 1995; Haig et al 1995).

The validity and reliability of the averaged signal have also been questioned when spontaneous epileptic recordings are considered (Sato 1992). In the early days, when a single or a few MEG channels were used, averaging was necessary if a map of signals were to be constructed outside the head. The most fundamental capability of multichannel systems, however, has been the ability to capture the magnetic field with no loss of spatio-temporal coherence. This allows analysis of single epochs (in evoked responses) or single spike events (in epileptic activity). One important consideration though must be taken into account: the model that one uses, has to be adequately robust to permit such analysis. ECD models have often failed to provide sensible source descriptions over data with low SNR, or at segments away from the main signal peaks. In fact, this has been the traditional link between ECD models and the use of averaged signals (Ioannides 1994). On the other hand, MFT has been proved to be immensely more powerful in studies of single auditory evoked responses (Liu 1995), especially through the use of integrals of intensity distributions.

1.4 Scope of the thesis

This thesis addresses the following issues relating to MEG modelling, analysis and interpretation of the results. First, to device strategies of accurately registering MEG data with structural images (e.g. MR images), thereby improving the localisation capability of MEG/MFT, but also provide the prerequisite for advanced modelling of specific brain structures (e.g. hippocampus). Secondly, to provide some tests on MFT's reconstruction capability in depth, especially when contemporary MEG equipment is used. Thirdly, to use MFT to test whether or not analysis of single trial pathophysiological data is doable. We shall show that analysis of single, unaveraged epileptic spikes is actually feasible, and compare such analysis with that of averaged spikes. Finally, we shall exploit this capability to study the spatio-temporal evolution of epileptic activity (especially in depth) and extract useful and physiologically meaningful information of the underlying generators.

To achieve the above goals, the remainder of the thesis is organised as follows. Chapter 2 is a review of the general background on imaging brain function. The multi-disciplinary field of neuromagnetism is defined, the origin of the electric sources is discussed, and the fundamental mathematical/physical/technical principles that govern the measurement and interpretation of such sources are given. Finally, MEG is placed on the more general context of functional brain imaging modalities.

Chapter 3 focuses on aspects of the registration of MEG and MRI. The mathematical background and the general strategies of registration are reviewed, followed by the implementation and the results of the methods developed. Their significance for MFT studies is also stated.

The issues specific to the biomagnetic inverse problem, including modelling with point-like sources or distributed current methods are discussed in chapter 4. Special emphasis is drawn on MFT, some tests of which are presented in the next chapter. Although both superficial and deep sources are regarded, prominence is shown in modelling deep sources, with both unilateral and bilateral (bihemispheric) sensor set-ups.

The condition of epilepsy and the "state of play" in imaging epileptic patients is introduced in chapter 6. In the same chapter, the feasibility of studying unaveraged, interictal spike events with MFT is presented through the demonstration of consistencies, in the case of complex partial epilepsy (CPE).

Chapter 7 is concerned with the spatio-temporal evolution of epileptic activity during unaveraged, interictal spikes recorded with the KRENIKON 37-channel system (unilateral recordings of CPE). Since activity initiated in the contralateral to the measurements side is identified, the following two chapters focus on simultaneous,

bilateral recordings. Due to the lack of such data with the KRENIKON system, the BTi twin MAGNES probe (2x37 channels) is used in two examples in chapter 8: in a case of a patient with myoclonic epilepsy, and in single case taken from a series of auditory odd-ball evoked responses.

A summary of the main findings and the conclusions drawn from this project together with suggestions for possible future work are finally presented in chapter 9.

2. Imaging the Human Brain: background information

2.1 Neuromagnetism

Electrical activity in the brain is caused by movements of specific ions inside and outside cellular membranes. Neuromagnetism is concerned with the study of the magnetic phenomena in neurons, the basic units of organisation of the central nervous system. Magnetoencephalography (MEG) refers to the detection and study of the magnetic fields produced by neural tissue or in other words the "neuromagnetic fields". On the other hand, an electroencephalogram (EEG) is a measurement of the potential difference also due to neural activity (Figure 2-1). Both techniques can record physiological signals in the millisecond range, a characteristic that distinguishes them from the rest of the imaging modalities, relating to large scale brain function.

In this chapter, we describe the mechanisms underlying the generation of electrical activity, and we then home into the physical principles governing such effects, together with the instruments used for their measurement. Although the presentation is specially adopted to MEG, we try to keep some "windows open" for EEG as well, so that the comparison of the two techniques, as given at a later stage in this chapter, becomes more comprehensive. Finally, the two techniques are compared with other functional brain imaging modalities.

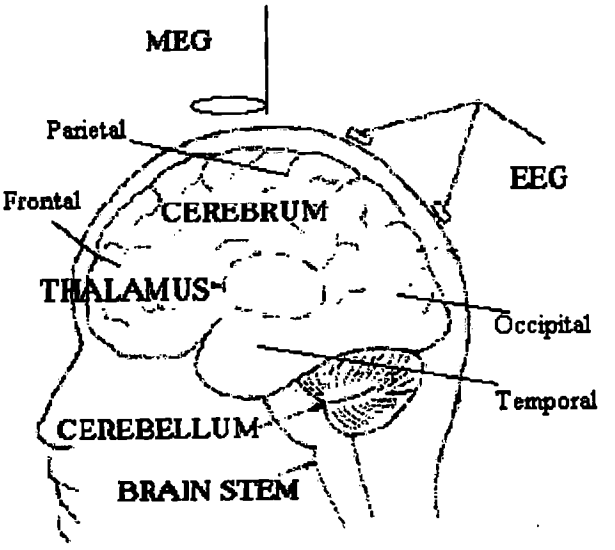

Figure 2-1: Basic parts of the human brain anatomy and demonstration of two techniques capable of recording its electrical activity: MEG, which measures magnetic fields outside the head, and EEG which measures electric potentials on the scalp.

2.2 The origin of the signals

2.2.1 Organisation of the brain

The three primary divisions of the human brain are brainstem, cerebellum, and cerebrum (Figure 2-1). The *brainstem*, the stalk of the brain, is the structure through which nerve fibres relay signals in both directions between higher brain centres and spinal cord. Two egg-shaped structures compose the *thalamus* at the top (superior) and to the side (laterally) of the brainstem, which is a relay station and important integrating centre for all sensory input to the cortex (except for smell). The *cerebellum*, which sits on top and to the back (posterior) of the brainstem is concerned with co-ordinating subconscious movements of skeletal muscles and with posture/equilibrium maintenance (Tortora and Anagnostakos 1990), although more recently it has been implicated in cognition and mental development too (Hashimoto et al 1995).

The large part of the brain remaining when brainstem and cerebellum are excluded is the *cerebrum*, accounting for seven-eighths of the total brain weight, and occupying most of the cranium. It is divided almost equally into two halves (*cerebral hemispheres*). The uppermost layer of the cerebrum, the *cerebral cortex*, is about 2-4 mm thick, and has a total surface area of some 2500 cm^2 folded in a complicated way, so that it fits the cranial cavity formed by the skull. There are four *lobes* in each cerebral hemisphere: *frontal, parietal, temporal,* and *occipital* (Figure 2-1).

Nerve cells (*neurons*) and glial cells (*glia*) are the principal building blocks of the brain. The glia (neuroglia) were believed to be mainly concerned with the structural support and protection of the brain tissue. Recently, however, suggestions were made for a more active role of neuroglia (Shea 1995). Neurons on the other hand, are responsible for conducting nerve impulses from one part of the brain to another; they are the basic information processing units. It is believed that as many as 10^{10}-10^{11} neurons are present in the human brain (Thomson 1985). Most neurons consist of three distinct portions (Figure 2-2): *cell body* (*soma* or *perikaryon*), *dendrites*, and *axon*. Soma is the neuronal portion containing the cell nucleus and much of the metabolic machinery and being necessary for the continuation of neuron's life. Dendrites are usually highly branched, thread-like extensions of the soma, that receive inputs from other neurons. The axon originates from the soma as a small conical elevation (*axon hillock*), and forms a large, trunk-like process that is highly specialised and conducts nerve impulses away from the cell body to other neurons.

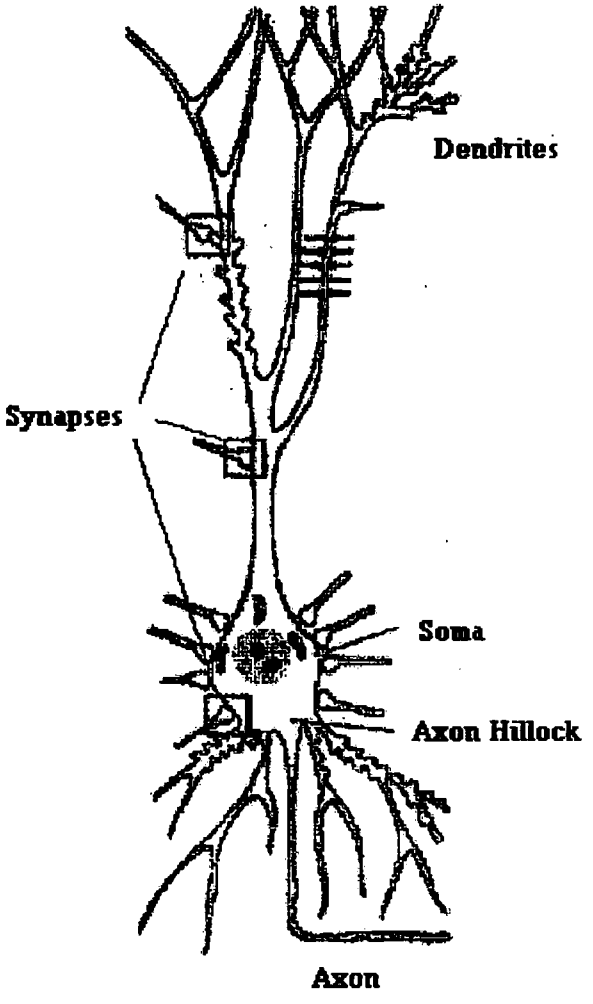

Figure 2-2: Structure of a neuron (modified from Hämäläinen et al 1993).

The cortex is composed of "grey matter", so called because of the predominance of cell bodies. Just below the grey matter is the "white matter", in which axons predominate. However, grey matter also exists in subcortical nuclei, like the thalamus.

2.2.2 Neuroelectric activity.

A neuron is surrounded by a 10 nm-thick insulating membrane, which divides the tissue into intracellular and extracellular compartments with different ion concentrations. In a non-excited neuron, the intracellular compartment is more negative than the extracellular one resulting in a potential difference across the membrane called resting membrane potential (RMP, ~-70mV); this is maintained by special protein molecules on the membrane that pump specific ions against the concentration gradient and also serve as passive ion channels. The most important is the Nα-K pump, which we shall come back to later.

A conventional neuron is bipolar in nature, designed to gather information at one end (one and only one dendrite) and to transmit data at the other (axon end). However, the vast majority of the brain neurons are multipolar, having several dendrites. Neurons in a neuronal pathway are not in actual physical contact, but are separated by a narrow gap known as *synapse*. By convention, the membrane of the axon terminal is referred to as the *presynaptic membrane*, and that of the neuron it connects with as the *postsynaptic membrane*. When electrical activity arrives along the axon, certain chemicals are released from the terminal into the synaptic cleft. These chemicals precipitate electrical activity in the dendrites of the receiving cell. For this reason, the presynaptic neuron refers to the transmitting terminal, while the postsynaptic neuron refers to the receiving dendrite.

2.2.3 Postsynaptic Potential

When the transmitting molecules released to the 50 nm-wide synaptic cleft arrive at the postsynaptic neuron, they cause a change in the permeability of the membrane for specific ions resulting in an alteration of the potential in the vicinity of the membrane (postsynaptic potential, PSP) which in turn causes an electric current along the interior of the postsynaptic neuron. Depending on the direction of flow two types of PSPs can be defined. The underlying chemical processes are extremely complex, but, in general, they can be described as follows. In one case, sodium channels open and the current flows into the cell, thereby, depolarising it. Once the transmembrane potential rises above a critical value, the cell is excited (excitatory PSP). In another case chloride channels are activated, current flows out (Figure 2-3), the postsynaptic cell is hyperpolarised and thus, inhibited (inhibitory PSP).

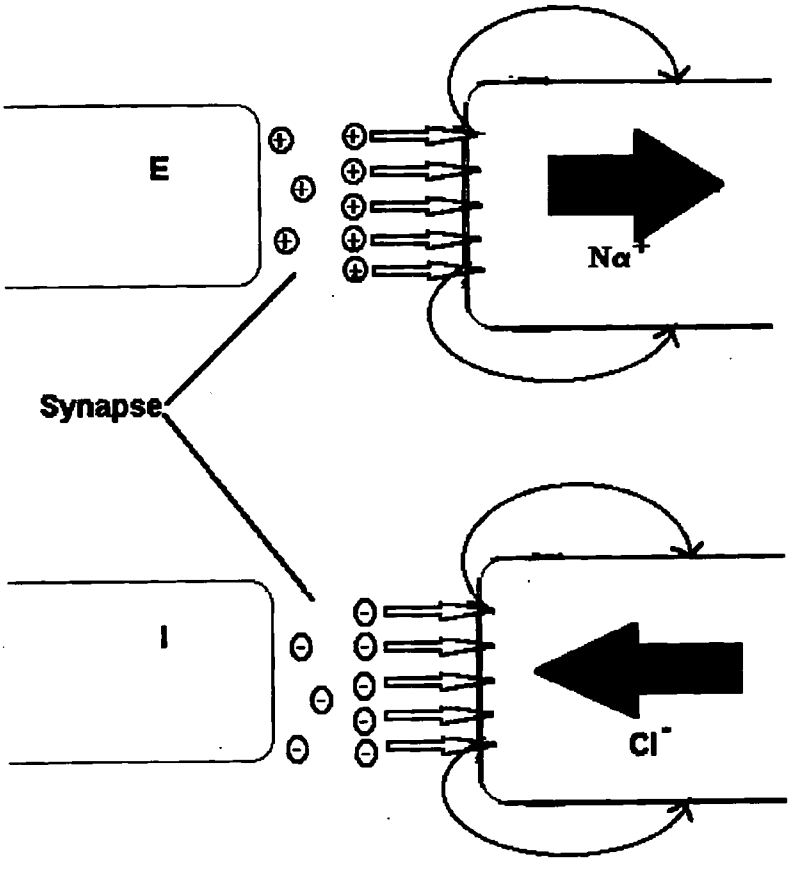

Figure 2-3: Ionic processes occurring in an excitatory (E) and in an inhibitory (I) synapse.

2.2.4 Action Potential

The action potential (AP) is a propagating excitation along a neuronal axon. It is initiated at the axon hillock when the net effect of multiple synapses to a neuron is sufficiently larger than the RMP value (~ -70mV) to exceed the necessary threshold (~ -40mV) (Santana de Sa 1991). During the first part of the action potential (depolarisation) voltage gated $N\alpha^+$ channels open and allow $N\alpha^+$ to enter the intracellular space. The process is fast, and as more $N\alpha^+$ channels open depolarisation is increased and more $N\alpha^+$ channels open (positive feedback); the membrane potential is ultimately reversed (~ +20mV). At this point the permeability of the membrane changes again, the $N\alpha^+$ channels are shut and an outward flow of K^+ ions is established (repolarisation) eventually restoring the initial state (RMP). The AP travels along the axon with undiminished amplitude like the wave of falling pieces in a chain of dominoes (Hämäläinen et al 1993). The moving ions give rise to currents within the cell, which can be described by current dipoles resulting in currents in the surrounding tissues, the so-called volume currents (Plonsey 1981).

The above description of AP emerges a picture where the leading front of the AP is represented by an intracellular current pointing in the propagation direction

(depolarisation front) and an intracellular current of opposite sign (repolarisation front) each accompanied by its own extracellular currents (Wikswo et al 1980) as in Figure 2-4.

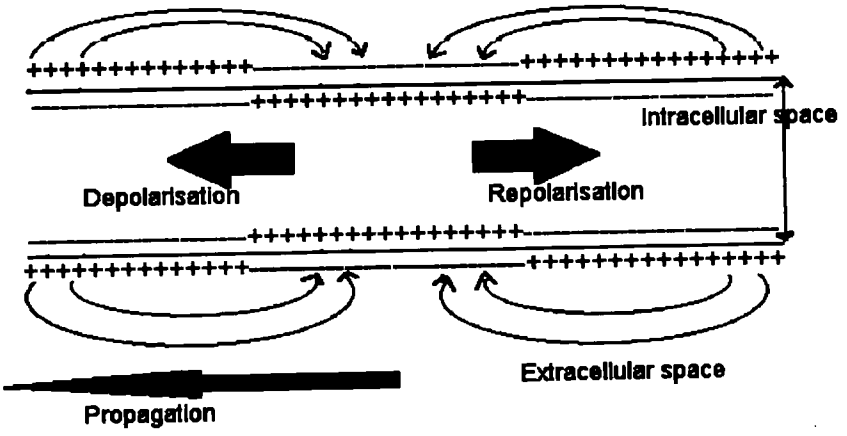

Figure 2-4: Propagation of an action potential (AP) in a neuron. Note the depolarisation and repolarisation fronts and the distribution of ions in the intracellular and extracellular spaces.

2.2.5 What is it that MEG detects?

Attempting a determination of the likely sources detectable by MEG, one has to take into account considerations regarding the strength of the various sources (with respect to detectable strengths), their temporal and spatial summations, as well as their geometrical arrangement. Although APs can be detected magnetically (Curio 1995) it is most unlikely that they are responsible for the macroscopic fields observed outside the brain, for a number of reasons. First, the two opposite dipoles composing an AP form a quadrupole whose magnetic field decreases rapidly with distance as $1/r^3$, as opposed to $1/r^2$ valid for a dipolar field such as the postsynaptic current flow. Cancellation of the fields associated with the two dipoles of an AP is very likely and will depend on the separation of the two fronts (~1 mm for an unmyelinated cortical axon). Furthermore, temporal summation of currents flowing in neighbouring fibres is more likely for synaptic currents, which last tens to hundreds of milliseconds (low-frequency region) than for APs lasting 1 ms only (high frequency region).

There is good histological evidence supporting the likely summation of the synaptic currents too. The cortex is organised in 6 layers parallel to the cortical surface. Each of these contains neurons with different sizes and soma shapes. The largest cell bodies are found in layers 5 and 6 (layer 1 being the most superficial) and have a definite pyramidal shape. These pyramidal cells have a linear structure with long dendrites that span most of the six layers and extent laterally along the cortex by as much as 0.5 mm in a parallel fashion (columnar organisation; Robinson D, 1992).

So activity in one cell is highly likely to be accompanied by activity in the cells around it. This correlation is attributable to the collateral processes of the cell synapsing preferentially on cells within its surrounding column; as a consequence the resultant direction of current flowing in the dendrites is perpendicular to the cortical sheet of grey matter. Moreover, this sheet is highly folded forming fissures/sulci in such a way, that it eventually becomes parallel to the head surface. As we discuss in the next few sections though, such a configuration is favourably prone to MEG (EEG) detection through the measurement of the magnetic fields (electric potentials) generated by such currents. Since one square millimetre of cortex contains as many as 10^5 pyramidal cells, the simultaneous activation of one synapse in a thousand over an area of 1 mm^2 would suffice to produce a detectable signal. In practice, 40-200 mm^2 of cortex may be activated in order for the magnetic fields to be detected (Chapman et al 1984; Hari 1990).

In conclusion, the consensus is that MEG (EEG) can detect the postsynaptic currents from the pyramidal dendrites. However, there have been only a few experimental studies (e.g. Okada 1988) on the microscopic mechanisms of field generation, and so one has to be cautious of the possibility of there being other field generation mechanisms. For example the earliest components of evoked responses and certain components of brain stem responses may well represent coherent volleys of action potentials.

2.2.6 The Equivalent Current Dipole Approach

To describe the relationship between neural activity and measured electric and magnetic field the approach of the equivalent current dipole model (ECD) is usually adopted, as has briefly been mentioned in previous paragraphs. A current dipole Q, is a short element of current I, of length L, and negligible cross-section. Being a vector, both its position and orientation in space are necessary for its determination. The dipolar strength or the magnitude of the "moment" Q is defined as Q=IL (units A-m). It is usually represented by an arrow pointing in the direction of current (see Figure 2-4 and Figure 2-5). This simplified description of the electrical properties of a biological source suffices when considering a small region of active tissue, where the largest linear dimension of the region is much smaller than its distance from the measuring point. However, wide distributions of activity may exist. In this case the superposition principle permits us to view the resulting field (potential) patterns as arising from a number of current dipoles distributed within the active area, and the field (potential) as being the sum of the individual dipolar contributions.

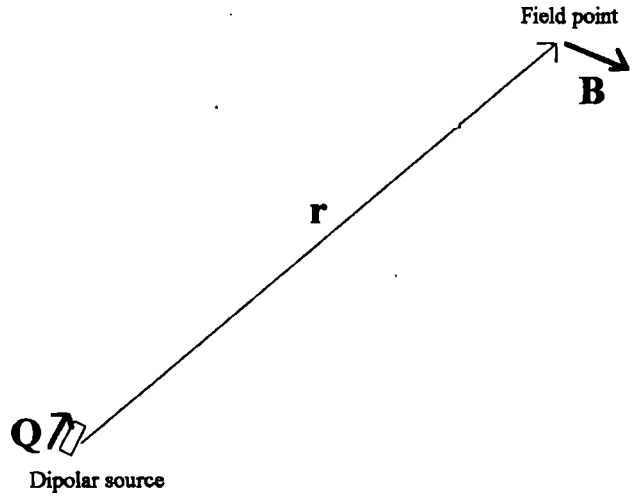

Figure 2-5: The Biot-Savart law.

The magnetic field (strictly speaking, the magnetic induction) **B**, is given by the Biot-Savart law:

$$\mathbf{B} = \frac{\mu_o}{4\pi}\frac{\mathbf{Q}\times\mathbf{r}}{|\mathbf{r}|^3} \qquad (2\text{-}1)$$

with μ_o being the permeability of free space ($4\pi\ 10^{-7}N/A^2$ in SI) and **r** being the vector joining the point where the field is evaluated with the dipole position (Figure 2-5). With the assumption that there are no ferromagnetic particles within the head, the permeability of biological tissue may be considered as equal to that of free space. Therefore, postsynaptic activity at a dendrite of a pyramidal cell (typically $Q=3\ 10^{-14}$A m) will generate a magnetic field of B≈0.002 fT, 4 cm away from the synapse. Such a weak field is not detectable, but if say, some 50,000 synapses were contributing coherently then the total magnetic field would have been (assuming they are almost parallel to each other, and pointing in the same direction)

$$\mathbf{B} = \mathbf{B}_1 + \mathbf{B}_2 + \ldots \mathbf{B}_{50,000} = 50,000\mathbf{B} = 100\,fT \qquad (2\text{-}2)$$

which is about the order of a typical measurement over the scalp in response to e.g. an auditory stimulation. However, as mentioned earlier, the activated area may occupy some 2 cm^2 to allow for the above number of simultaneous activated synapses. It is obvious, that the more extended the area is, the less accurate the description of the biological activity the ECD model provides will be (Williamson and Kaufman, 1990). The more general case would consider a distribution of current density, **J(r)** over a certain

brain volume. Within this terminology the current dipole moment can be thought of as a mathematical convention where $\mathbf{J}$ is concentrated to a single point $\mathbf{r}_Q$

$$\mathbf{J}(\mathbf{r}) = \mathbf{Q}\delta(\mathbf{r} - \mathbf{r}_Q) \tag{2-3}$$

where $\delta(\mathbf{r})$ is Dirac's delta function.

In summary, a current dipole is used in MEG (EEG) as an equivalent source for the unidirectional (primary, see next paragraph) current density that may extend over several square centimetres of cortex; this concept, however, involves slightly different physical concepts for MEG and EEG as we discuss below.

2.3 Basic Background Electromagnetism

2.3.1 Forward problem

In the previous section, we described examples where the source details (magnitude, position relative to detector) were known and so we were able to calculate the characteristics of the generated magnetic field. This procedure is known as the "biomagnetic forward problem". When the magnetic fields are measured and identification and characterisation of the source responsible for their generation must be deduced, we are dealing with the so-called "biomagnetic inverse problem" which will be the theme of discussion in another chapter. In this paragraph we concentrate on the forward problem.

2.3.2 Maxwell's Equations

When the conductivity σ and the electric current generators (sources) in the brain are known, it is feasible to calculate the electric field E and the magnetic field B using Maxwell's equations and the continuity equation $\nabla \cdot \mathbf{J} = -\frac{\partial \rho}{\partial t}$ ($\mathbf{J}$ and ρ are the total current density and the charge density, respectively). Assuming that the permeability of the medium is that of free space and the fact that $\frac{\partial \mathbf{E}}{\partial t}$ and $\frac{\partial \mathbf{B}}{\partial t}$ can be ignored as source terms (quistatic approximation[+]) Maxwell's equations can take the form:

[+] *This approximation is based on the assumption that the time derivative terms in Maxwell's Equations are very small. In other words,* $|\varepsilon \partial \mathbf{E}/\partial t| << |\sigma \mathbf{E}|$ *and* $\partial \mathbf{B}/\partial t$ *to be very small. One may prove that these two conditions are valid by taking into account the low range of frequencies involved in neuromagnetism (typically < 100 Hz) and the conductivity value for brain tissue (cf Hämäläinen et al 1993).*

$$\begin{aligned} \nabla \cdot \mathbf{E} &= \frac{\rho}{\varepsilon_o} \\ \nabla \times \mathbf{E} &= 0 \quad \text{or} \quad \mathbf{E} = -\nabla V \\ \nabla \cdot \mathbf{B} &= 0 \\ \nabla \times \mathbf{B} &= \mu_o \mathbf{J} \end{aligned} \tag{2-4}$$

where $\nabla = \hat{e}_x \frac{\partial}{\partial x} + \hat{e}_y \frac{\partial}{\partial y} + \hat{e}_z \frac{\partial}{\partial z}$ with ε_o being the permitivity of free space and V the electric potential. Using the above equations we can deduce expressions for **B** and V at a point **r** due to **J** existing at **r'**:

$$V(\mathbf{r}) = \frac{1}{4\pi\sigma} \int \frac{\mathbf{J}(\mathbf{r}') \times (\mathbf{r} - \mathbf{r}')}{|\mathbf{r} - \mathbf{r}'|^3} d^3 r' \tag{2-5}$$

$$\mathbf{B}(\mathbf{r}) = \frac{\mu_o}{4\pi} \int \frac{\mathbf{J}(\mathbf{r}') \times (\mathbf{r} - \mathbf{r}')}{|\mathbf{r} - \mathbf{r}'|^3} d^3 r' \tag{2-6}$$

For a dipolar source

$$V(\mathbf{r}) = \frac{1}{4\pi\sigma} \frac{\mathbf{Q}(\mathbf{r}') \cdot (\mathbf{r} - \mathbf{r}')}{|\mathbf{r} - \mathbf{r}'|^3} \tag{2-7}$$

and

$$\mathbf{B}(\mathbf{r}) = \frac{\mu_o}{4\pi} \frac{\mathbf{Q}(\mathbf{r}') \times (\mathbf{r} - \mathbf{r}')}{|\mathbf{r} - \mathbf{r}'|^3} \tag{2-8}$$

2.3.3 Primary and secondary sources

It is useful to divide the current density **J** into two components: the volume or return current $\mathbf{J}^U = \sigma \mathbf{E}$ which is the "passive" result of the macroscopic field on charge carriers in the conducting medium, and the primary current $\mathbf{J}^P$. Therefore:

$$\mathbf{J}(\mathbf{r}) = \mathbf{J}^P(\mathbf{r}) + \mathbf{J}^U(\mathbf{r}) = \mathbf{J}^P(\mathbf{r}) + \sigma(\mathbf{r})\mathbf{E}(\mathbf{r}) = \mathbf{J}^P(\mathbf{r}) - \sigma(\mathbf{r})\nabla V(\mathbf{r}) \tag{2-9}$$

We reiterate here, that $\sigma(\mathbf{r})$ is the macroscopic conductivity of the head. In other words, the whole cortex is supposed to be a homogeneous conductor.

The primary source within the conducting tissue (intracellular current) can be considered as a battery in a conducting medium composed of a pair of monopoles (a source and a sink) next to each other which are linked by a small line current element. In this case an Ohmic current flow is induced in the conducting medium: the return or volume current.*

---

* *It is important to realise that the physical nature of this concept is different for MEG and EEG (Ioannides 1994). For MEG, a monopole, i.e. a point source or sink of current produces no magnetic field, but it does*

The expression for the magnetic field generated by **J** can now be written as

$$\mathbf{B}(\mathbf{r}) = \mathbf{B}_o(\mathbf{r}) + \mathbf{B}^U(\mathbf{r}) \tag{2-10}$$

with $\mathbf{B}_o(\mathbf{r})$ given by Equation 2-6 for **J**=**J**^{P} and

$$\mathbf{B}^U(\mathbf{r}) = -\frac{\mu_o}{4\pi}\int \sigma(\mathbf{r})\left[\nabla' V(\mathbf{r}) \times \frac{(\mathbf{r}-\mathbf{r}')}{|\mathbf{r}-\mathbf{r}'^3|}\right] d^3r' \tag{2-11}$$

where $\nabla' = \hat{e}_x \frac{\partial}{\partial x'} + \hat{e}_y \frac{\partial}{\partial y'} + \hat{e}_z \frac{\partial}{\partial z'}$.

If the conducting medium is assumed to be composed of homogenous parts, $\nabla\sigma(\mathbf{r})$ is non-zero only at the boundaries and so, it is possible to expand $\mathbf{B}^U$ as a sum of surface integrals over boundaries, i.e. over all discontinuities in σ:

$$\mathbf{B}^U(\mathbf{r}) = \frac{\mu_o}{4\pi}\sum_{j=1}^{n}(\sigma_j^{out} - \sigma_j^{in})\int V(\mathbf{r}')\frac{\hat{n}(\mathbf{r}') \times (\mathbf{r}-\mathbf{r}')}{|\mathbf{r}-\mathbf{r}'|^3} dS_j \tag{2-12}$$

with σ_j^{in} and σ_j^{out} being the conductivities inside and outside the conductivity object of surface S_j, $\hat{n}$ being an outward unit vector normal to S_j, and dS_j a surface element.

The corresponding expression for $V^U(\mathbf{r})$ is given by:

$$V^U(\mathbf{r}) = \frac{1}{4\pi\sigma}\sum_{j=1}^{n}(\sigma_j^{out} - \sigma_j^{in})\int \frac{V(\mathbf{r}')\hat{n}(\mathbf{r}') \cdot (\mathbf{r}-\mathbf{r}')}{|\mathbf{r}-\mathbf{r}'|^3} dS_j \tag{2-13}$$

where σ denotes the electrical conductivity of the medium surrounding $\mathbf{r}$. The terms $(\sigma_j^{out} - \sigma_j^{in})V(\mathbf{r}')\hat{n}(\mathbf{r}')$ describe the equivalent surface current distributions on the boundaries of each S_j and are often called "secondary currents"; they are oriented perpendicular to the boundaries.

---

produce an electric potential. Since current conservation makes a monopole impossible, the next most fundamental structure is a pair of monopoles (a source and a sink in close proximity). Although the latter is the most basic source in EEG,it is still a "silent" source for MEG. If the construct, however, involves a connection of the source with the sink by means of an infinitesimal line element of current, then it becomes a legitimate MEG source too. When such a construct is embedded in a biological medium, it induces a flow of current to complete the circuit.

2.3.4 Homogeneously Conducting Sphere

The most elementary model of conductivity of the human head that takes account of its curvature is a sphere of uniform conductivity. This is the most widely used model in MEG. A more generalised model can include concentric shells of different conductivity to represent the cerebrospinal fluid, skull and dermis.

When a uniform conductor is spherically symmetric, the contribution of the volume currents to the radial component of the magnetic field vanishes. Thus, the radial component of the field at any distance above the surface of a conducting sphere can be attributed to the primary source alone. Therefore, B_r can be calculated from

$$B_r(\mathbf{r}) = \frac{\mu_o}{4\pi}\int \mathbf{J}^p(\mathbf{r}') \times \frac{(\mathbf{r}-\mathbf{r}')}{|\mathbf{r}-\mathbf{r}'|^3}\cdot \hat{e}_r\, d^3r' \tag{2-14}$$

or in the case of a current dipole $\mathbf{Q}$ at $\mathbf{r}_Q$

$$B_r = -\frac{\mu_o}{4\pi}\frac{\mathbf{Q}\times\mathbf{r}_Q\cdot\hat{e}_r}{|\mathbf{r}-\mathbf{r}_Q|^3} \tag{2-15}$$

Sarvas (1987) derived an analytic expression for $\mathbf{B}$ in rectangular co-ordinates:

$$\mathbf{B}(\mathbf{r}) = \frac{\mu_o}{4\pi}\frac{F\mathbf{Q}\times\mathbf{r}_Q - (\mathbf{Q}\times\mathbf{r}_Q\cdot\mathbf{r})\nabla F(\mathbf{r},\mathbf{r}_Q)}{F(\mathbf{r},\mathbf{r}_Q)^2} \tag{2-16}$$

where

$$F(\mathbf{r},\mathbf{r}_Q) = \alpha(r\alpha + r^2 - \mathbf{r}_Q\cdot\mathbf{r}) \tag{2-17}$$

and

$$\nabla F(\mathbf{r},\mathbf{r}_Q) = (r^{-1}\alpha^2 + \alpha^{-1}\mathbf{a}\cdot\mathbf{r} + 2\alpha + 2r)\mathbf{r} - (\alpha + 2r + \alpha^{-1}\mathbf{a}\cdot\mathbf{r})\mathbf{r}_Q) \tag{2-18}$$

with $\mathbf{a} = (\mathbf{r}-\mathbf{r}_Q)$, $\alpha = |\mathbf{a}|$, $r = |\mathbf{r}|$.

Although the above equations seem to be complicated, an important point directly seen from them, is that B_r vanishes if the primary current is radially oriented, and so does $\mathbf{B}$. This is true for any axially symmetric current in an axially symmetric conductor (Grynszpan and Geselowitz 1973). A source placed in the centre of the sphere will produce no magnetic field either. It is common to refer to such sources as "magnetically silent".

To resume, in a spherically symmetric conductor, MEG is sensitive only to the tangential component of the primary current. As a result, and as long as the assumption that PSP currents flow perpendicular to the cortical surface, the method is optimal for detecting

activity in fissures or in structures where geometry enhances current flow parallel to the surface (e.g. hippocampus).

The electric scalar potential V, on the surface of such a conductor is affected by the conductivity profile. In other words, if two good conducting bodies (brain, scalp) are interrupted by a poorly conducting layer (skull), V will be attenuated on the scalp and the potential pattern (e.g. due to a dipole inside) will be more widespread than in a homogenous sphere. Finally, another point to remember, is that both radial and deep sources contribute significantly to V.

2.3.5 Other models of the conducting medium

A number of other conducting models has been used in the biomagnetic research so far. The simplest of these treats the conducting tissue as a flat surface of infinite extent, with an insulating material on one side (e.g. air) and a uniform conductor on the other. This is called the conducting "half space" or "infinite half space", and can be considered as an asymptotic case of the spherically symmetric conductor discussed in the previous paragraph. Its relevance to brain studies becomes apparent when the primary source is very superficial so that its depth is much smaller than the radius of the head, so that the scalp curvature near the source can be locally neglected.

Both the half space and sphere models can be generalised to include multislab or concentric shells of different conductivities to represent the brain tissue, cerebrospinal fluid, skull, and scalp. A typical choice, developed mainly for EEC studies, makes use of three concentric and homogeneous spheres. Scalp and skull thickness followed by the ratio of conductivity between skull and brain/scalp are the most important modelling parameters especially when one considers the potential distribution on the scalp (Scherg 1990). However, these considerations are not essential for MEG modelling, since the currents in the skull and on the scalp contribute negligibly to **B** (Hämäläinen and Sarvas 1989). In support of this theoretical statement, Okada and Xu (1993) proved experimentally that magnetic fields are permeable to the skull: they compared animal somatic evoked fields (SEFs) over intact skull against the SEFs over the intact dura (i.e. with the skull removed) and found the two signals to be similar in topography and waveform.

Inaccuracies introduced by the spherical model may, however, be attributed to directional and/or spatial variability of brain conductivity or large conductivity variations (e.g. eye sockets). When measurements are conducted over a relatively small area of the head, the spherical model furnishes a neat description and there is no need to use more elaborate models. The need is stronger when a large area of the head is covered or multichannel probes covering both hemispheres are used. Lütkenhöner et al (1990)

showed that it is better to consider the local (to the measurements) curvature of the inner skull in the process of fitting it with a sphere; Hari and Ilmoniemi (1986) suggested that the curvature of the inner skull just above the source is of importance in the determination of the conducting profile. In this context, it proves useful to take into account different sphere models, one for each head region, or even one for each sensor.

More sophisticated and realistic models have also been and being developed, where the head is assumed to consist of arbitrarily shaped compartments with different (isotropic) conductivities. The brain surface, as derived from MRI or CT images, is usually triangulated and then the forward problem is solved by assuming this surface encloses (in the simple case) a medium with homogeneous conductivity, and the potential over several hundreds of triangles composing the surface together with the field outside it are evaluated. The feasibility of this method has been proved both theoretically (Hämäläinen and Sarvas 1987) and experimentally (Ducla-Soares 1989). Such a model might improve MEG modelling especially when deep sources are concerned or when the temporal or frontal brain regions are considered where the deviation from sphericity is sometimes large. However, as Hämäläinen and Sarvas noted (1989) there is no need to account for a realistic multi-layer medium when the magnetic fields are evaluated (whereas there is a definite such need when evaluating the electric potential over the scalp in EEG), although improvements in modelling deep source are indeed expected by using realistically shaped compartment models (Stok et al 1987).

The penalty, of course, in moving away from simple to sophisticated realistic models, is substantial increase in the complexity of the model and associated computations. Intermediate models can also be used alternatively by choosing a spheroidal head shape (Fieseler et al, 1995) for which expressions for the magnetic field calculation have been known for some time (Grynszpan and Geselowitzt 1973; Cuffin and Cohen 1977). The important message drawn from such studies is that the "silent space" of a perfect spherical conductor (sphere centre) is no more silent when such elaborate (and of course closer to reality) models are regarded, and so activity from structures close to the centre of the head might indeed produce detectable signals as evidenced from recent studies (Ribary et al 1991).

2.4 Neuromagnetic Instrumentation

2.4.1 Basics

The signal strengths associated with neural activity are extremely small, as mentioned already and as depicted in Figure 2-6, necessitating the use of ultra sensitive detection systems. To date, the only instrument fulfilling such requirements of sensitivity and

bandwidth is the SQUID magnetometer. The components of such a device are shown in Figure 2-7: a detection coil which senses changes in the external magnetic field and transforms them into an electric current; an input coil which transforms the resulting current into a magnetic flux; the SQUID sensor; and associated electronics dealing with further transformation of the flux into a room temperature voltage output. A refrigerant bath (liquid Helium, temperature below 4.7 K) is used to maintain the SQUID (and detection coil) in the superconducting state.

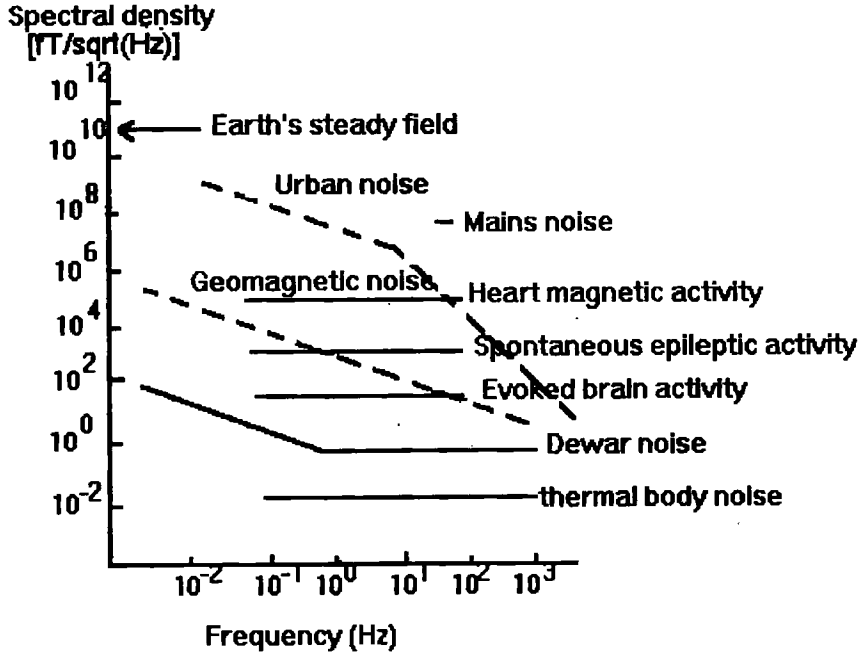

Figure 2-6: Distribution of spectral densities of various magnetic fields ascribed to typical sources of bioelectromagnetism and noise.

The term SQUID is an acronym of a Superconducting QUantum Interference Device which consists of a superconducting ring (loop) interrupted by one or more weak links (Josephson junctions) that are either resistive or have such a low critical current that become resistive far sooner than the rest of the loop. A weak link is characterised by a maximum value of current it can sustain without loss of superconductivity. Quantum mechanical phase coherence of charge carriers in a superconductor gives rise to flux quantisation in a solid ring; the magnetic flux through the loop must be an integer multiple of the so-called flux quantum, $\Phi_o = 2.07$ fWb $= 2.07\ 10^{-15}$ Tm^2. In an external magnetic field, the quantisation is accomplished by supercurrents that flow in the ring so as to precisely cancel any deviations from the quantisation condition. In a SQUID, the weak link limits these currents and, as a consequence, the degree of the external field compensation. In a dc-SQUID, i.e. when direct current is fed through the loop, the

voltage over the SQUID depends on the external flux threading the loop; dc squids: have better noise characteristics and are also used with dc amplifiers which in turn have less inherent noise than rf ones.

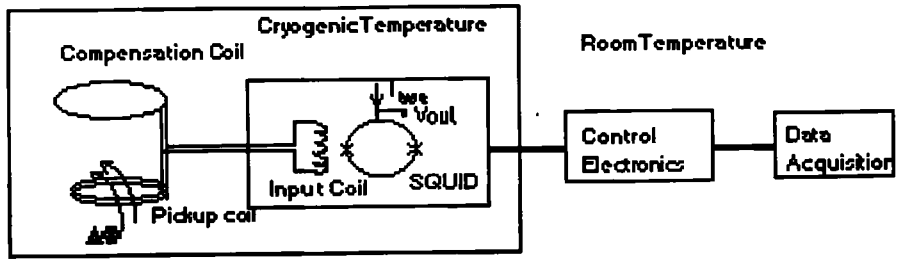

Figure 2-7: Block diagram of a typical SQUID-based magnetic sensor and its associated electronics. Note the part operating in cryogenic temperatures.

The detection coil (usually referred to as the pickup coil) together with its compensation coil (whenever present) and the input coil form what is called the flux transformer. When a magnetic field impinges on the pickup coil an electric current is set up in it; as a result of the mutual inductance between the input coil and the SQUID, the latter can sense a signal proportional to the original flux.

The use of flux transformers gives the biomagnetometer designers a considerable amount of freedom in designing the geometry of the sensors. Even a simple loop of wire coupled to the SQUID could be used (magnetometer). In this case though, the apparatus has to be placed in a shielded room to eliminate ambient noise. Usually gradiometers are used rather than simple magnetometers. A gradiometer is sensitive to nearby sources but insensitive to distant "noise" sources, because they couple with the same amplitude but opposite sign to the pickup and compensation coils, and they, therefore, sense the gradient of the field rather than the field itself.

Compared with the magnetometer (Figure 2-8 (a)) which has only one pickup coil, the gradiometer comprises a pickup coil and a compensating coil. In the case of Figure 2-8 (b), the gradiometer is sensitive to the field gradient in the z-direction, and it is, therefore, called "first order axial gradiometer", since it is only the first spatial derivative of the field that is involved. Even in this case, however, the devices still operate within a shielded environments to secure noise rejection. The noise level is conventionally quoted as a root mean square field noise per square root of the bandwidth, with a typical figure being a few $fT / \sqrt{Hz}$.

More sophisticated geometries are involved in a "second order gradiometer" (Figure 2-8(c) to reject both spatially uniform field and field gradients. "Third order gradiometers" are also available including virtual third order gradiometers using reference channels some distance away from the pickup coils. Such gradiometers have been used in the CTF

commercial instrument showing that no shielded room is required in this circumstance (Vbra et al 1995).

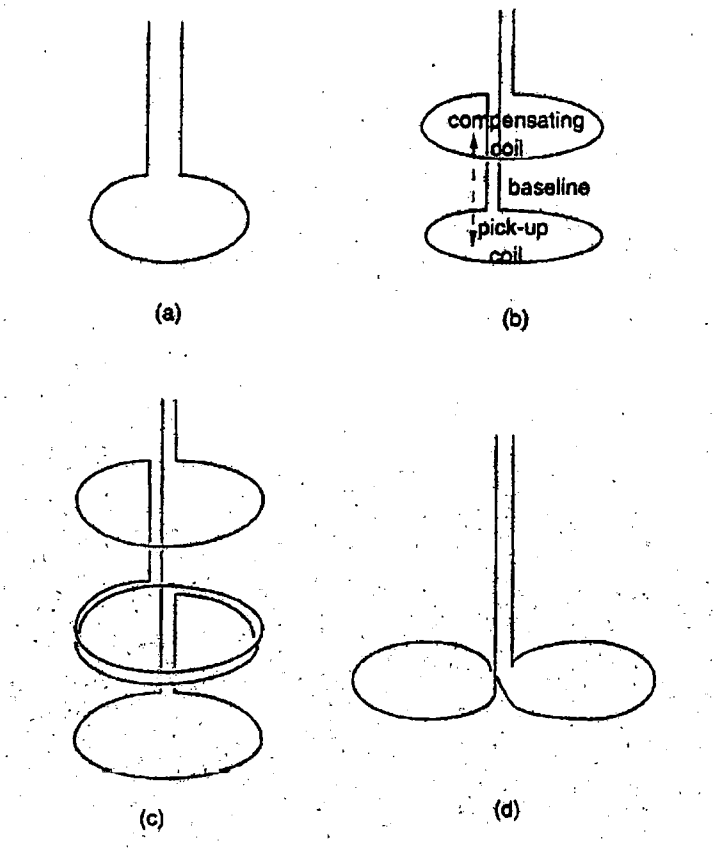

Figure 2-8: The most fundamental types of magnetic sensors used in biomagnetism: (a) magnetometer, (b) first order axial gradiometer, (c) second order axial gradiometer, and (d) planar gradiometer.

Although axial gradiometers have been traditionally used for most experiments world-wide, the coils can indeed be shaped differently in order to perform measurements of the vertical component of the field B_z along a transverse direction (x, y or both). Such devices are called planar gradiometers (Figure 2-8 (d)). The advantages of such configuration designs over the axial ones lie in that the double D construction is compact in size and can be easily fabricated with thin-film techniques (Josephs et al 1995). In addition, it provides better locating accuracy; it lacks, however, in depth sensitivity (Hari 1993).

2.4.2 Multi-SQUID considerations

Until about a decade ago, almost all biomagnetic measurements were carried out using single channel magnetometers. Under such conditions, multiple placements over the head were necessary to cover a sufficiently large patch. As a result, the recording

procedure was extremely time consuming, but also the temporal coherence of the data was lost. The advent of multichannel probes containing a number of sensors in one (or two) Dewar(s), and covering large areas (or even the whole head) simultaneously, changed the situation dramatically in favour of the use of MEG as a functional brain imaging tool.

Because of the unimaginable variety of likely current distributions in the human brain, general criteria for optimal magnetometer design do not exist. For a given source configuration, one would favour maximum sensitivity The latter is sometimes, however, contradictory to the requirement of good spatial resolution (locating accuracy). For example, increasing the pickup coil diameter improves field sensitivity, but deteriorates spatial resolution.

In addition, the size of the Dewar, the properties of the SQUIDs, the feasible number of channels, the distribution and strength of external noise sources, are all constraints restricting the previously mentioned design freedom.

2.4.3 Modern Systems

Since 1989, the generation of multichannel systems emerged, having typically more than 20 SQUID channels arranged over an area exceeding 10 cm in diameter. For years since then, the most commonly used systems were the 37-channel systems constructed by Siemens AG (Germany) or BTi (USA). They were both operating with axial gradiometers of first and second order respectively. In the last three years whole head coverage systems are available by Neuromag (Finland) and CTF (Canada). The Neuromag system has a total of 122 planar first order gradiometers (61 two-gradiometer units, measuring $\partial B_r/\partial x$ and $\partial B_r/\partial y$, while the CTF instrument consists of 64 axial first order gradiometers, which with the help of reference channels can be electronically operating as second or third order gradiometers; both systems employ a helmet like arrangement. Recently CTF upgraded their system; their new helmet version accommodates 143 channels.

BTi has also recently launched a twin probe system (2x37) with Dewars than can be independently positioned over each hemisphere to provide large coverage. In 1996, they are also going to release a whole head system employing 147 magnetometers.

More technical details are given in Appendix A for the Siemens 37 channel system (KRENIKON) and the BTi twin probe system (MAGNES) as data from these two instruments are used extensively in this piece of work.

A final point to be mentioned is that all systems are assigned a co-ordinate system defined by a set of fiduciary points. Probe position indicator devices are developed to facilitate this requirement. Using such a device, the sensor positions can be accurately

defined in the 3-dimensional space, and the MEG recordings can also be associated with MRI images of the same subject/patient to allow for studies of function with the correct anatomical background. A more detailed description of this topic is given in Chapter 3.

2.4.4 Digest

If the axis of a gradiometer is oriented perpendicular to the head so that it measures just the radial component of the magnetic field, then the measurement will only depend on the primary sources if the spherical head model is used. Tilting the gradiometer axis relative to the head, so that the tangential component of the field be also measured, will result in a magnetic field recording associated with both the primary and secondary sources (Stok et al 1987). Although in practice, the gradiometer axis is usually oriented perpendicular to the head, this is often not the case with the modern multichannel systems, which of course, cannot fulfil the requirement of having a large number of gradiometers arranged in a fixed curvature and all of them being perpendicular to all heads!

2.5 Comparison of EEG and MEG

Because of their common electrophysiological origin, EEG and MEG share many features and should be viewed as being complementary methods. In this section we highlight some of their differences and pinpoint the complementarity issue.

As mentioned in the beginning of the chapter, EEG records the difference in potential between two electrodes. The choice of the electrodes to be compared, therefore, becomes important. Three common reference connections are referred to as:

- unipolar: each electrode is connected to a single reference electrode, usually at a fixed location, which can be at an electrically quiet location on the scalp.
- bipolar: each electrode is referenced to its next one (electrode 1 to electrode 2, 2 to 3 etc.)
- Average reference: each electrode is referenced to a point which is calculated as the average of the potentials at more than one (e.g. the two ears) or even all electrode points (global average reference) or as the average of the nearest neighbours (source derivation).

The idea of assuming a scalp electrode as being electrically quiet suffers from obvious limitations, since locations commonly used, like the ears, might not be that electrically quiet during an auditory stimulation. There have been many studies that demonstrate that EEG wave forms are sensitive to the location of the reference electrode, and, as a result, individual investigators have their own preference for reference configurations.

This requirement is completely absent in MEG, since absolute values of the magnetic field can be recorded without any reference. (Of course the term "reference channels" can also be met in MEG but it is associated to distant noise elimination rather than being a recording necessity).

This problem though can be partially overcome by computing the surface Laplacian, which in its simplest form, can be performed by subtracting from a given recording one-fourth of the voltage signal recorded at each of the 4 surrounding electrodes to evaluate the Laplacian: $\partial^2 V / \partial x^2 + \partial^2 V / \partial y^2$. Such Laplacian EEG maps are essentially sharper than the original EEG potential maps, since they reveal patterns of the volume current emerging from the cortex, passing through the skull and scalp, and returning back to the interior.

However, sharpening the potential maps to eliminate reference electrode effects, reduces the sensitivity to deep sources but also fails to be accurate at the edges of the EEG array where the full Laplacian cannot be obtained, although some improved techniques using spline functions or spherical harmonics have been reported (e.g. Perrin et al 1987). Moreover, the missing exact knowledge of the various conductivities and thicknesses (scalp, skull, CSF etc.), essential for the electric potential calculation as mentioned previously, suggests that a sharper pattern does not imply that a more accurate estimation for the sources can be obtained (Wikswo et al 1993).

Moreover, one should remember that MEG is not sensitive in radial dipoles embedded in a perfect spherical conductor, while EEG is sensitive to both radial and tangential sources. Although this statement is usually regarded as an obvious disadvantage of MEG, it could be used as a facility to discriminate between two hypothesised sources, one of which would have a tangential component and the other of which would not (Hari et al 1984, Wood et al 1985). Since, however, the spherical model is not a perfectly realistic case, the selectivity of MEG is somewhat compromised, and dipoles oriented normal to the skull may as well contribute appreciably. On the other hand, this different emphasis between MEG and EEG on neuronal populations (e.g. sulci and gyri) may be particularly helpful - once the two methods are combined - in charting activity that spreads from one region to another, since it would be expected that the prominence of one modality would be followed by the other sequentially.

Other more practical differences are associated with the fact that EEG is based on contact measurements, since the electrodes applied to the scalp with conductive paste while the MEG recordings are conducted in a non-contact fashion. Entire head measurements were traditionally performed with EEG allowing for a complete scalp potential of spontaneous events like epileptiform discharges, while it is only recently that whole head MEG

systems became available. On the other hand, longer patient/subject preparation times were needed with EEG, but this is also minimised now with contemporary systems (Gevins et al 1991). In addition, continuous monitoring is easily accomplished with EEG, since the electrodes are small and secured to the head -while MEG demands immobile recordings inside shielded rooms; this enables the EEGer to study rare spontaneous events like for example seizures.

As far as localisation accuracies are concerned, it is expected that either technique have its own "preferred" direction in the localisation. It was in fact shown, both theoretically and experimentally (Cohen and Cuffin 1983), that in general the MEG maps should be tighter than the EEG ones (i.e. by at least one-third under certain configurations), favouring MEG's locating ability. Since then, there have been many studies on the subject, and fairly recently a controversy began concerning the relative localisation merits of the two techniques (Cohen et al 1990). Cohen and co-workers compared electric and magnetic measurements of signals from a source implanted in a patient's head and concluded that MEG is only marginally more accurate than EEG and practically offers no significant advantage in locating cerebral activity. The claim, however, was challenged by other researchers on methodological grounds (Williamson 1991; Hari et al 1991). Numerous conferences and symposia have subsequently discussed the topic delineating the minimum requirements for a satisfactory *in vivo* comparison of the ability to localise dipoles with EEG and MEG (Anogianakis et al 1992). The dust appears now to be settling due to recent reports on localisation tests (Nakasato et al 1994) and to what one would anticipate in terms of the basic electromagnetic theory (Ioannides 1994).

2.6 Topographic Electrophysiological Mapping

Despite the limitations mentioned so far, EEG and MEG offer a unique view of brain physiology at the millisecond temporal scale. They are both completely non-invasive and harmless and are perfectly suited to follow the dynamics of the various neurophysiological processes in a spatio-temporal coherent way - thanks to the modern multichannel systems - with a few millimetres accuracy at the cortical level. However, they can provide only functional information, or in other words unravel the underlying physiology, but not the anatomy as such. They, therefore, need to be associated with images of structure, i.e. CT or MR images (see next section, but also Chapter 3). The end product, is a powerful and fascinating depiction of the brain in action.

A number of studies have been performed in this way by researchers of both communities, ranging from tracking activity evoked by a stimulus (auditory, visual, somatosensory, pain) (Liégeois-Chauvel et al 1994; Singh et al 1994; Suk et al 1991), and recording of spontaneous activity of healthy subjects (Ribary et al 1995) or epileptic

patients (Bamidis et al 1995), up to unfolding memory or mentality associated activations (Salmelin et al 1994; Gevins and Smith 1995).

One of the drawbacks in the analysis of both techniques (but mainly of MEG) has been the model used to represent the underlying activity. To date, the majority of the MEG investigators use current dipoles (where the whole activity is collapsed into a point) to model the distribution of electrical sources within the brain (see for example Rogers 1994). The oversimplicity of such models has limited the range of physiologically interesting questions that MEG (and/or EEG) is capable of tackling and served as against the general acceptance of the technique, although when used along with stringiest selection criteria produced results of clinical usefulness. In the last ten years or so, but especially in the last five, more general and powerful techniques which allow for distributions of current density rather than point like generators of activity, have become available with names like Magnetic Field Tomography (MFT) or Minimum Norm Current distribution and others (see Chapter 4 for a more detailed description). Many brain functions involve the coherent activation of broad regions that are inconsistent with ECD models. In these cases, models that estimate the general distribution of current flow within the brain at many possible regions are of interest.

Finally, when both the MEG and the EEG, as well as their users, reach an equal stage of technical and physiological sophistication, it will undoubtedly be possible to obtain additional returns on the collective intellectual investments by fully merging the two techniques to obtain even more accurate and stable source reconstructions (Hasson 1991).

2.7 Other Functional Brain Imaging Modalities

Over the last two decades a formidable array of medical imaging methods have been generated. Notable among these and particularly relevant to our discussion are X-ray tomography (CT), Magnetic Resonance Imaging (MRI) and Spectroscopy (MRS), Single Photon Emission Computed Tomography (SPECT), Positron Emission Tomography (PET), Electrical Impedance Tomography (EIT), and Near Infra-Red Spectroscopy (NIRS). In this section we briefly describe each technique and we highlight their powers and limitations, in the general context of comparing them with the already mentioned EEG and MEG. Some more details of the various techniques as used in the study of epilepsy are also going to be given in Chapter 6.

2.7.1 X-ray CT

Developed in the early 70's (Hounsfield 1973), CT overtook the simple X-ray radiographs, and offered 3-dimensional sets of electron density maps. It was the first non-invasive (but radiation utilising) method to offer images of human anatomy with a

spatial resolution of about 1 mm and a density (linear attenuation coefficient of X-rays) discrimination of better than 1%. Fairly recently, the use of contrast agents and the development of spiral (or helical) CT has enabled the application of 3-dimensional CT angiography that offers exquisite reconstructions of the intracranial vasculature (Heiken et al, 1993). One way or another, CT can reveal malformations of some sort once they occurred, and although it provided the clinical community enormous help with the diagnosis and treatment of diseases, its inability to image function has excluded it from the functional imaging modality's group.

2.7.2 MRI

MRI revolutionised brain imaging by offering direct visualisation of brain structures with an accuracy similar to that of CT, but with better specificity to soft tissue and involving no radiation hazard. MR proton images provide information relating not only to proton density but also to the freedom of hydrogen-containing molecules to rotate and to the proportion of water contained in different body-fluid compartments. Furthermore, imaging of other biologically important nuclei is possible. For example sodium imaging can be used to reveal cerebral infarcts, neoplastic changes, and some kind of metabolism (Bamidis 1990).

Although one can claim that some measure of brain function could be obtained (e.g. with the use of paramagnetically labelled tracers and measurements of blood flow and/or water diffusion), it was not until recently (Belliveau et al 1991; Kwong et al 1992) that MRI was added to the armamentarium of non-invasive functional imaging modalities, transforming its name into the jargon functional MRI (fMRI). This was accomplished with the use of high-speed echo planar imaging techniques (EPI), which can efficiently sample the spatial information of the object (brain) after a single excitation of water molecules. In this way, all data needed for an image can be obtained in less than 100 ms, whereas a more conventional imaging sequence would take several tens of seconds (though images resulting from the latter process would have greater spatial detail). This type of fast sequence is particularly useful for sampling large portions of the brain many times at short intervals to monitor brain activity.

The most commonly used fMRI technique relies on a subtle increase in signal intensity in the regions activated during a carefully designed experiment (Turner and Jezzard 1994). The cause of this small increase in intensity is ascribed to a local change in blood oxygenation balance, which is in turn a result of neuronal activation. It has been known for many years that deoxyhaemoglobin is magnetically different from oxyhaemoglobin and that, in the case of blood passing through tissue, the presence of deoxyhaemoglobin creates point magnetic inhomogeneities within the blood vessels that result in

microscopic field distortions around the vessels. The coherence of the signal from hydrogen nuclei in the water content of the surrounding tissue is partially destroyed by those inhomogeneities, and, thus, the signal intensity is lower than it would be if they were absent. As a result, deoxygenated blood itself acts as an intravascular contrast agent, that can indeed be utilised instead of other labelled tracers (Kwong et al 1992).

During neuronal activity, local metabolism increases (Roy and Sherrington 1890) and local blood flow increases substantially, more than compensating for the demand for extra oxygen caused by the neuronal activity (Fox et al 1988). The local concentration of deoxyhaemoglobin, therefore decreases, and so the signal in those regions increases in intensity. Important new results have actually shown, that following photic stimulation, certain focal areas of grey matter display an initial negative change in signal intensity that reaches a maximum some 500 ms (Ernst et al 1994) or 2 s (Menon et al 1995) after the onset of the stimulus, while other local areas sustain a positive signal change.

In a typical fMRI experiment, statistical reliability is improved by collecting images at a few seconds intervals over a period of several minutes. By subtracting the control state image (resting condition) from the stimulated state, one can map regions of specific brain functions, like vision (Haxby 1995), hearing (Binder et al 1994), motor movement (Sadato 1995), or even language generation (Rueckert 1995) with and a temporal resolution of 3 seconds or less.

While an fMR image can be obtained rapidly enough (e.g. 50 msec) the much longer time constant for blood diffusion limits the overall temporal resolution and, therefore, the number of physiological questions that can be tackled. Another drawback is imposed inherently in the spatial resolution, as a consequence of the imprecise matching of cerebral blood flow changes to increased neural activity. To express it differently, it is neuronal activity that one is interested in examining, but it is blood flow that is triggered and subsequently measured, which in turn takes place in arterioles supplying wider cortical regions than those actually active, and so an inaccuracy of at least 2-3 mm should be anticipated, that is ameliorated even more when a large area of cortex (several cm^2) is activated (Turner 1995). However, there is much on-going research in this field, providing strong evidence that fMR images obtained under high magnetic fields (e.g. 4 T) might be sensitive to the state of capillary oxygenation (Menon et al 1995), thereby further decreasing the previous inherent limit.

Finally, we should mention recent developments on the analysis of the "functional MRI time-series" (Friston et al 1994; Worsley and Friston 1995), based on the concept of detecting significant and regionally specific correlations between sensory input and

measured physiological response. Such correlations are tested after convolving the sensory input with an estimate of the heamodynamic response function.

To conclude, the exciting prospect of combining functional information with exquisite anatomical imaging within the same modality has opened a hitherto fascinating prospects in the study of individual brain physiology. The "non-invasive" nature of fMRI that makes imaging repeatable over time within the same subject (allowing for intrasubject averaging) places fMRI into a really advantageous position over other radionuclide techniques (see below). It should finally be mentioned that there is real wealth of prospectives by injecting the physiological information (e.g. activated areas) obtained by fMRI as *a priori* knowledge into the MEG/EEG inverse problems (see Chapter 4).

2.7.3 MRS

Spectroscopic studies of functional activity-related changes in brain metabolism depend mainly upon the 1H nucleus, which is the most-sensitive to maximise signal strengths of the dilute metabolites that are in the millimolar range (Shulman et al 1993). While initial studies focused on the use of ^{31}P MRS for the detection of energy metabolites, increased interest has recently been observed in ^{1}H MRS, which extends the range of metabolites that can be studied, and provides improved spatial resolution. Anyhow, ^{1}H MRS metabolite measurements require sampling over voxels of > $1cm^3$ and acquisition times of several minutes. Usually, the spatial resolution is worse, involving many cubic centimetres depending on main magnetic field strength and specific task, although promises of studying voxels of mm^3 have been made (Posse 1995). Obviously, one cannot be satisfied with such records, however, MRS does indeed provide the opportunity to study brain chemistry in relation to anatomy when combined with MR imaging. In such cases, regions of interest (ROIs) can be determined on MR images and the changes of concentration in specific compounds can be monitored and associated to activities evoked by stimuli or to pathological conditions, e.g. neuronal loss resulting from hippocampal sclerosis (Gadian 1993).

2.7.4 Radionuclide Techniques: PET and SPECT

Functional imaging using radioactive tracer techniques has developed in the last 50 years to become a sophisticated highly sensitive (in the nanomole/picomole level) method of determining in vivo body tissue function. In the last decade, advances in detector technology and computing power led to a rapid increase in the use of emission tomographic techniques for research on normal and pathological brain function.

Single Photon Emission Computed Tomography (SPECT) is based on the use of tracers which emit γ-rays with an energy between 160-500 keV. Individual photons are detected

using either a rotating γ-camera or special purpose multidetector devices. The development of new radiopharmaceuticals for use in SPECT which can measure tissue function, together with advances in the collimating systems used, have improved the spatial resolution of SPECT which is now -in the brain studies- below 1 cm (Webb 1988).

Positron Emission Tomography (PET) uses radioactive tracers labelled with radionuclides emitting positrons during their radioactive decay; the latter then annihilate within a couple of millimetres giving rise to the production of two back-to-back 511 keV γ-rays which can be detected using a positron camera which records data only when two γ-rays are detected in fast-time coincidence. PET has therefore increased sensitivity and improved spatial resolution - 5-6 mm (Spinks et al 1988; Mintun et al 1989) with the potential of decreasing it further - over SPECT, enabling somebody to perform quantitative 3D dynamic PET studies.

PET has the ability to measure multiple parameters (blood flow, metabolism, receptor binding) in a single session, and to perform activation studies with accurate location of activated areas (Bartestein and Schober 1992). A number of such studies have been performed by research groups world-wide (Frith et al 1991; Corbetta et al 1991) and brain regions with increased or decreased activity (regional Cerebral Blood Flow, rCBF) -which correlates with neuronal synaptic firing- have been identified in association with specific tasks. However, the issue of mismatching between neuronal activity and blood flow as mentioned in the fMRI section holds here too, and together with the positron travel path inaccuracy pose inherent limits in PET's spatial resolution.

Moreover, in cases where small brain regions are activated, the spatial resolution of PET (SPECT) is not adequate to correlate to the underlying anatomy. Thus, the PET images have to be superimposed on MRIs, after some kind of registration procedure (see below), or fused with specific anatomical atlases (Mazziotta et al 1991). The key problem, though, of PET (which is even worse for SPECT) is its relatively poor temporal resolution (~10-40 sec). Although the transfer of activity between different brain regions is accomplished in a few milliseconds, it takes seconds for blood flow changes to lead to accumulation of enough data for statistically meaningful processing. This means that although the mainly activated areas can be identified, the duration and flow of activity from one brain region to another cannot be followed (Ioannides 1991). In fact, only the main nodes of activations will be highlighted, but little can be said about the spatio-temporal evolution of activity. Moreover, both PET and SPECT have the disadvantage of exposing the subject/patient to radiation, which means that experiments may not be repeated over time.

It should be mentioned here, that analysis of PET data has been vastly performed via the study of covariances across subjects undergoing the same experimental paradigm - presumably under exactly the same conditions. Ideas whose origins lie in the analysis of electrophysiological signals (i.e. EEG and MEG) have recently been incorporated in PET (and fMRI as well) to allow the study of covariances of activations across time and not across subjects (Friston et al 1994; Friston 1994).

Finally, it should again be emphasised that there can be exciting synergistic advances expected from the integration of these techniques with MEG/EEG, since the information obtained can be used to physiologically constrain the ambiguities in the MEG/EEG analysis (Wikswo et al 1993; Ioannides et al 1995c).

2.7.5 EIT

Electrical impedance tomography (EIT), applied potential tomography (APT), and impedance computer tomography (ICT) are synonyms for a technique that images the distribution of resistivity or conductivity of tissues within a body region . The method is comparatively new - it has only been developed during the past decade - and involves no known hazards (Jongschaap et al 1994). The electrical properties of tissue are imaged by injecting small currents and measuring the resultant voltages. These voltages are then converted into a tomographic image using a reconstruction algorithm. The spatial resolution of EIT is currently about 10% of the body diameter (Dijkstra et al 1993), and although this figure will improve as research continues, it is most unlikely that it will ever reach that of MRI or CT.

EIT can be applied to imaging brain function as follows: during the passage of an action potential, the resistance of the neuronal membrane drops to 1/40 of its resting value. However, attempts to record evoked electrical impedance responses using scalp electrodes and measurements at 50 kHz, concluded that the response was too small to yield reliable images. It was, therefore suggested that imaging neuronal discharge may be possible at lower frequencies (probably as low as DC) and cortical placement of electrodes (Holder 1993).

In practical terms, it is probably easiest to implement EIT imaging of the relatively large slow impedance changes which occur during stroke, cerebral ischemia or epilepsy, which are largely due to swelling, or during cortical spreading depression. The advantages of EIT over other techniques are only practical ones: it is safe (unlike PET/SPECT), inexpensive and portable, so that it can be used for continuous bedside monitoring or in developing countries (Boone and Holder 1995). However, much research is needed before EIT could be considered as a useful functional brain imaging modality.

2.7.6 NIRS

Near infrared spectroscopy/spectrophotometry (NIRS) measures tissue absorbance of light at several wavelengths in the spectral region from 670-1000 nm, thus enabling determination of concentration changes of oxygenated haemoglobin, deoxygenated haemoglobin, blood volume, and oxygenated cytochrome-oxidase (Villringer et al 1993). Since near infrared light penetrates biological tissue and even bone, such measurements can be performed through the intact skull. Although most of the so far employed studies have been performed in neonates, one can use such measurements in adult human brain, to record probably the same effects as those recorded by PET/fMRI but with higher time resolution (100 ms) (Hoshi and Tamura 1993). Although optical images of biological structure and function with a spatial resolution of better than 1 cm have been reported (Grease 1993), methodological difficulties associated with image reconstruction, render these images yet too crude for clinical use. In addition, the same as before inherent limitations in measuring neural activity through blood flow still apply. However, NIRS is a flexible and inexpensive technique, and in the future may become an alternative functional neuroimaging modality.

2.8 Overview: MEG versus others

We have described the most contemporary techniques for imaging brain structure and function. Limits on resolution of PET/SPECT/fMRI are becoming fairly clear. These are not instrumental limits, but arise from the as yet unknown relation between cerebral blood flow changes and increased neural activity. The temporal resolution of a few seconds arising from the time lag of haemodynamic response can be improved only by adoption of techniques based on direct detection of neural activity, such as EEG and MEG. On the other hand, EEG and MEG are not very accurate in imaging deep structures due to the problem of non-uniqueness as well as the conductivity uncertainties in the case of EEG.

Moreover, a proper comparison of MEG with the various imaging systems should include systematic criteria such as (apart from temporal/spatial resolution) sensitivity, reliability, specificity, and validity (Galen et al 1995). The specificity refers to the proportion of patients that a method deems are abnormal and who are in fact abnormal. The reliability of a test reflects its reproducibility. Validity refers to the accuracy of the information. In assessing clinical applications of functional imaging methods, it is important to examine all these parameters in the context of the populations of intended subjects and the nature of the target brain functions. MEG seems particularly promising along these lines, and one should expect it to "take over" once the above requirements are fulfilled.

It would have been unfair not to mention the costs involved too. PET and MEG seem to be the most costly techniques (order of million(s) of pounds), a fact originating from the need for an on-site cyclotron for the PET radionuclide production and the use of liquid Helium as a superconducting bath for MEG sensors. SPECT is relatively cheap and the most widespread in hospitals. The easiness of transforming a MRI unit into fMRI puts fMRI into an advantageous position over the others, despite its costs (which are high, but certainly less than those of PET/MEG). EEG is supposed to be the cheapest of all the modalities, although the costs of purchasing of modern EEG machine are not that modest (order of tens of thousands pounds). However, it is expected that the cost per MEG sensor will continue dropping with the advent of whole head systems, and it will be reduced dramatically when high temperature superconductors appear commercially - although it is argued that systems facilitated with the latter might not be appropriate for brain studies (due to high SQUID noise), but they will definitely be so for cardiac studies.

In an attempt to estimate the current effort on brain research, we may consider the presentations in the first International Conference on 'Functional Mapping of the Human Brain', taken place in Paris on June 1995. Figure 2-9 shows the relative proportion of the various techniques. As illustrated, PET scores the highest percentage, followed by fMRI. Although MEG is only fourth in the row, it would be useful to mention that the conference started with three invited lectures, one in each of PET, fMRI, and MEG, a fact that demonstrates the establishment of MEG in the functional neuroimaging community.

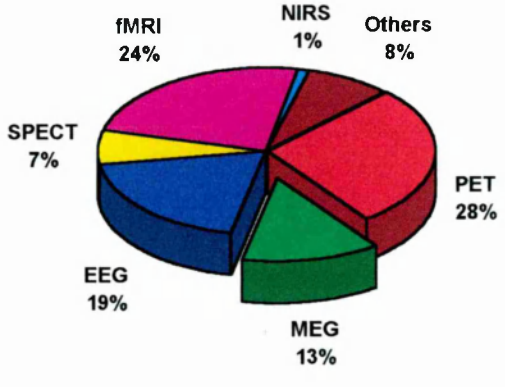

Figure 2-9: Relative proportion of research with the various functional brain imaging techniques, as judged from papers presented at the 1st International Conference on Functional Mapping of the Human Brain, held in Paris in June 1995.

Finally, we reiterate that synergistic advances can be expected from the integration of the EEG and MEG with the other modalities. Intercomparison of data obtained by EEG and MEG with complementary studies using invasive electrodes in patients, or PET, SPECT, and fMRI in patients and normal subjects will provide important validations across modalities. Animal models will provide additional validation.

3. Relating Structure and Function

In the previous section we described various brain imaging modalities. Some of these, can depict detailed brain anatomy (e.g. CT, MRI), while some others provide information regarding its function (e.g. PET, MEG). However, if functional information is to be meaningful, then the loci of activity must be clearly correlated to anatomical landmarks of the brain. The procedure of correlating two (or more) techniques is called coregistration or simply registration. The subject of this chapter is how structure (mainly MRI) and function (mainly MEG) can be integrated together, in other words, how the MRI/MEG registration can be accomplished.

3.1 In General

The need for registering two datasets (e.g. images) has come up in the last decade or so, in cases that is required to combine the information content of different modalities, since no single modality is capable of adequately imaging both anatomy and function or even providing all the anatomical data needed for a specific task (e.g. surgery, radiotherapy). For example, sometimes anatomical detail is more easily seen in MRI than in CT, differentiating tumour and oedema from grey and white matter in the brain. Bony structure is best visualised by CT whereas soft-tissue pathology and nervous tissue at the skull base is best seen by MRI. A need to combine these two modalities is therefore arising for the purpose of skull base surgery (Hill et al, 1991). In other situations understanding what a structure is responsible of doing, or diagnosis of a diseased state may be illuminated by functional imaging alongside with anatomical data (Mazziotta et al 1991; Bidaut 1991).

Matching different modalities is complicated because each may have its own geometrical description with different pixel sizes, slice thicknesses, data orientations, magnifications, and possibly non-aligned longitudinal axes (tilted transaxial planes). All these problems have to be addressed by image correlation methods (Webb 1993). Some of these problems are also met in the MEG/MRI registration. The importance of the final mismatch (registration error) will depend on the MEG model used and of course on the study itself. For instance, if a point descriptor (ECD) is used in a study of auditory evoked responses then 0.5-1.0 cm error may be acceptable. However, when the MEG study is used to guide radiosurgery procedures (Hellstrand et al 1993) accuracy becomes critical.

In the MFT* studies, the need to accurately correlate the estimates of activity with background structure is higher, since the shape as well as the position of the solutions becomes important (Bamidis and Ioannides 1993). Not only the shape of an activated structure (e.g. motor cortex) and the shape of the MFT solutions are highly correlated, but the definition of the source space requires accurate position and orientation of the subject's head/brain in the MEG system. This means that the brain outlines from MRIs have to be expressed in the MEG co-ordinate system so that MFT solutions can be obtained. Moreover, if a priori physiological knowledge is to be injected in the inversion procedure then the MEG locations of specific structures (extracted from MRIs) have to be precisely known.

3.2 Localisation in MEG

If one were to correlate the loci of activity, as identified by MEG, to anatomical brain landmarks, then a common co-ordinate system is required; such a system needs at least three fixed points for its definition, and can be used to specify both the sensor location and orientation and any landmarks or features of the brain as seen on a MR or CT image. One way of achieving such a coregistration, is by identifying common points on MRIs and MEG based locations. Points that have been used extensively, include the nasion (the deepest point of the nasal bone between eyes), the preauriculars (the points on the lateral face side just prior to the entrance into the ear canals), the inion (the protrusion of the occipital bone at the back of the head), and the front teeth (Hämäläinen et al 1993). An orthogonal system can be determined, for instance, by the two preauriculars and the nasion points.

The position and orientation of the Dewar (containing the SQUIDS, gradiometers etc.) with respect to the system already defined can then be accurately found by measuring

---

* *Magnetic Field Tomography (MFT) is examined in detail in the following Chapter*

the magnetic field produced by currents in small coils attached to the scalp (Ahlfors and Ilmoniemi 1989). Three such small coils can be mounted on a thin fibre-glass plate, which is then attached to the subject's head at a known point in the measurement area; the Dewar can then be positioned, the coils energised sequentially, and the resulting fields can be measured. The position of the coil set with respect to the head system defined previously can be determined with the help of a 3D digitiser. The position of the Dewar can be determined with an RMS error of about 1 mm (Hämäläinen et al 1993).

Another approach is based on an inductive magnetometer using three orthogonal coils in the receiver (attached to the subject's head) and in the transmitter (secured to the Dewar). The position and orientation of the magnetometer can be found from the measured mutual inductances. The locations of the head coils are obtained by a reference measurement: the 3D co-ordinates of chosen landmarks on the head are determined by touching them with a pointer, that has similar orthogonal coil transmitter, and energising the pointers coils (the process is usually referred to as "clicking"). The correlation of the head location (during the MEG measurement) with the subject's anatomical data (MR images) can then be accomplished by attaching pieces of oil-filled plastic tubes prior to the MRI acquisition to the same three or more landmarks chosen for the MEG experiment (Hämäläinen 1991).

3.3 Fundamental Principles of Registration

Let us assume that we are given two Cartesian co-ordinate systems, {Oxyz} and {O'x'y'z'}, and a single point, with **P** denoting its position vector in the first system, **P'** the position vector in the second one, and **b** the position vector of the origin O' with respect to the first system, as in Figure 3-1:

Representing the point by a 3-element column vector notation we have:

$$\mathbf{P} = \begin{pmatrix} x \\ y \\ z \end{pmatrix}, \quad \mathbf{P'} = \begin{pmatrix} x' \\ y' \\ z' \end{pmatrix}, \text{ and } \mathbf{b} = \begin{pmatrix} b_x \\ b_y \\ b_z \end{pmatrix} \tag{3-1}$$

Then

$$\mathbf{P'} = \mathbf{SRP} + \mathbf{b} \tag{3-2}$$

where R is a (3x3) rotation matrix, and S is a diagonal (3x3) scaling matrix. The rotation matrix R can be broken down as the product of three separate rotations. Let $R_x(\theta_x)$ be a rotation by θ_x about the x-axis, $R_y(\theta_y)$ be a rotation by θ_y about the y-axis, and $R_z(\theta_z)$ be a rotation by θ_x about the z-axis (Foley and Van Dam 1989).

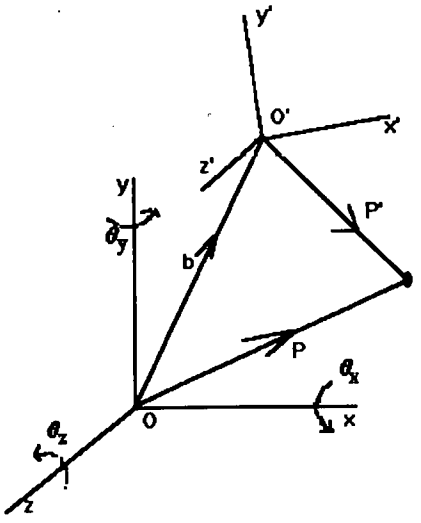

Figure 3-1: Representation of a point in two different co-ordinate systems.

Then (and implicitly defining a specific order of sequential rotations):

$$\mathbf{R} = \mathbf{R}_z(\theta_z)\mathbf{R}_x(\theta_x)\mathbf{R}_y(\theta_y) \tag{3-3}$$

where

$$\mathbf{R}_x(\theta_x) = \begin{pmatrix} 1 & 0 & 0 \\ 0 & \cos\theta_x & \sin\theta_x \\ 0 & -\sin\theta_x & \cos\theta_x \end{pmatrix}$$

$$\mathbf{R}_y(\theta_y) = \begin{pmatrix} \cos\theta_y & 0 & \sin\theta_y \\ 0 & 1 & 0 \\ -\sin\theta_y & 0 & \cos\theta_y \end{pmatrix} \tag{3-4}$$

$$\mathbf{R}_z(\theta_z) = \begin{pmatrix} \cos\theta_z & \sin\theta_z & 0 \\ -\sin\theta_z & \cos\theta_z & 0 \\ 0 & 0 & 1 \end{pmatrix}$$

The scale matrix in general may be written:

$$\mathbf{S} = \begin{pmatrix} s_x & 0 & 0 \\ 0 & s_y & 0 \\ 0 & 0 & s_z \end{pmatrix} \tag{3-5}$$

where s_x, s_y, , s_z are the scaling factors in the x,y,z directions. If the scaling is assumed to be isotropic then **S** collapses to s**I**, where **I** is the identity matrix and s is a scalar constant. Combining Equation 3-2, Equation 3-3, Equation 3-4, Equation 3-5 we get:

$$\mathbf{P}' = \begin{pmatrix} x' \\ y' \\ z' \end{pmatrix} = \begin{pmatrix} s_x C_z C_y + s_x S_z S_x S_y & s_x S_z C_x & -s_x C_z S_y + s_x S_z S_x C_y \\ -s_y S_z C_y + s_y C_z S_x S_y & s_y C_z C_x & s_y S_z S_y + s_y C_z S_x C_y \\ s_z C_x S_y & -s_z S_x & s_z C_x C_y \end{pmatrix} \begin{pmatrix} x \\ y \\ z \end{pmatrix} + \begin{pmatrix} b_x \\ b_y \\ b_z \end{pmatrix} \quad (3\text{-}6)$$

where $S_{x,y,z}=\sin\theta_{x,y,z}$ and $C_{x,y,z}=\cos\theta_{x,y,z}$. Note that the rotations and scaling are not commutative; they must be performed in the order written. The centre of the rotation (scaling) has been silently kept to be the origin O of the first system. If rotations about an arbitrary point $\mathbf{P}_1$ are desired, then a sequence of three fundamental transformations is necessary:

- Translation so that $\mathbf{P}_1$ is at the origin.
- Rotation (scaling).
- Translation so that the point at the origin returns to $\mathbf{P}_1$. These operations can be described by:

$$\mathbf{P}_i' = \mathbf{SR}(\mathbf{P}_i - \mathbf{P}_1) + \mathbf{P}_1 + \mathbf{b} \quad (3\text{-}7)$$

In the presence of noise which arises as a result of errors in locating equivalent 3D points in the two systems, a noise vector $\{N_i\}$ has to be input in Equation 3-7 leading to:

$$\mathbf{P}_i' = \mathbf{SR}(\mathbf{P}_i - \mathbf{P}_1) + \mathbf{P}_1 + \mathbf{b} + \mathbf{N}_i \quad (3\text{-}8)$$

Finding the registration transformation that relates $\{P_i\}$ and $\{P_i'\}$ involves determining the S,R,b, which minimise noise errors (cost function, F):

$$\mathbf{F} = \sum_{i=1}^{n} \{\mathbf{N}_i\}^2 = \sum_{i=1}^{n} \left|\mathbf{P}_i' - \mathbf{P}_i\right|^2 \quad (3\text{-}9)$$

3.4 A Review of the Registration Techniques used in Medical Imaging

There is no universally acceptable method for solving the registration problem. The available techniques have been classified by Kessler (1989) into four individual groups. These are point-matching, line-matching, surface-based matching, and interactive matching. The first three of these involve minimising some merit or cost function (representing the mismatch error) in order to align one dataset with another. The last group, however, relies on a user attempting to register anatomical landmarks interactively, in a trial-and-error mode.

3.4.1 Point/Line-Matching

The point-matching method makes use of either external fiducials placed on the subject's head (e.g. small spots of oil for MRI, or solder for CT, or $^{99}Tc^{m}$ for SPECT, or ^{68}Ga for PET, or coils for MEG) or observer-determined anatomical point landmarks (e.g. the apical turn of cochlea, a blood vessel, an identifiable part of a sulcus or gyrus (Hill et al 1991)). It has been used in a number of cases to register MR and CT images (Hill et al 1991), PET images with MR images (Kessler 1989; Evans et al 1989), and PET/SPECT with MR/CT (Rizzo et al 1990). The registration task is to, first, identify corresponding landmark points in each set of images, and then determine the transformation among these corresponding points. Usually the scaling is regarded as being isotropic or even known, so the system in Equation 3-9 is solved for the translation and the three rotation angles only. The cost function can be formed by summing the squares of the distances between corresponding points. Kessler (Kessler 1989) mentions that four points are required to find all the parameters*, however, he is often using 5-12 points to reduce sensitivity to localisation errors. Similar techniques have been applied to correlate EEG measurements with MRIs (Lagerlund et al 1993), by gluing vaseline filled capsules on the scalp to produce delineated regions of increased signal on MRI scans in order to mark the 33-EEG scalp-electrode positions.

The line-matching methods are used under circumstances where it is difficult to ensure that single points are in the field of view. In such cases a custom mask for the head (Kessler 1989) or a stereotactic frame (Peters et al 1986; Wilson and Mountz 1989), that employs rods filled with the same materials as for point-matching are used. The orientations of the rods are chosen to maximise the sensitivity of the method. A merit function involving the centres of the rods can then be minimised (Kessler 1989; Webb 1993).

3.4.2 Surface-based Methods

This is probably the most difficult to engineer but also the most reliable method. It requires that the same surface can be described by the two modalities of interest. Different points are usually involved in the definition of each surface. The jargon "head-hat" fitting has come into use to name this technique (Pelizzari et al 1989). The rotated "hat" (usually the surface from the less accurate modality) have to be transformed in order to fit the "head". Neiw et al (1991) further classify these methods into the principal axes matching technique, and the surface matching technique.

---

* *Only three points are needed though, if scaling is known.*

The principal axes method computes the centroids and principal axes (of symmetry) from the two sets of 3-D surface model built by stacking up a series of surface contours identified in the tomographic slices. The translational difference between the two models is estimated from the difference vector between the two centroids. After the centroids are aligned by applying the appropriate translation, the rotational correction is obtained by aligning the principal axes of the two models.

The surface matching technique works as follows: we are seeking the geometric transformation (relating the "hat" to the "head") that minimises the cost function which is formed by summing up the squares of the distances of each "hat" point to the surface of the "head". Usually a point "below" the "head", like the centroid of the "head" points, is given and a ray pointing from each "hat" point to the above point intersects the "head" surface at $\mathbf{P}_{int}$. The squared distance of the "hat" point to this intersection point is then entered in the cost function (Pelizzari et al 1989).

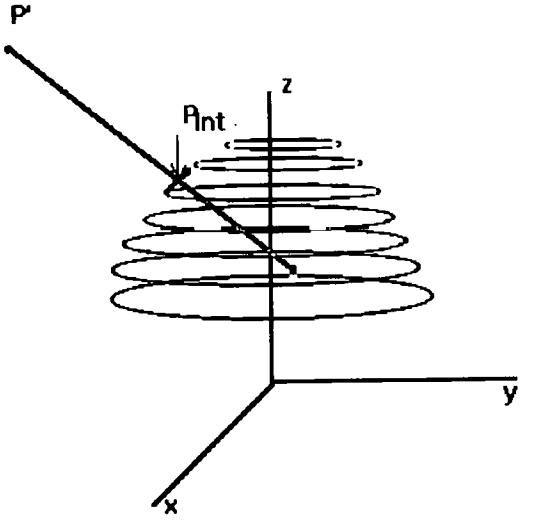

Figure 3-2: The ray from the "hat" point $\mathbf{P}'$ to a point below the "head" (circular disks) intersects the "head" at point $\mathbf{P}_{int}$. The distance of $\mathbf{P}'$ to $\mathbf{P}_{int}$ is contributing to the cost function.

A number of tricks have been employed in the last few years to further optimise this technique. For example, tiled surfaces are constructed for each dataset (e.g. Fuchs et al 1990, cited in Webb 1993), so that the surface of the head and therefore the intersection of the mentioned ray (from the "hat" point to the "head" centroid) can be more accurately determined. Moreover, the extraction of the surface (i.e. the contours from individual tomographic slices) has been automated (Neiw et al 1991) to overcome the difficulties and

the possible errors arising from the human interaction. Neiw et al (1991) have also devised a stepwise process to fine-tune the fitting. In the initial matching phase, the cost function involves interpolations that only produce an approximate result. With a rough matching estimate resulting from the first phase as an input, a final matching step then fine-tunes the solution.

More recently a new technique was developed to register surface data (Woods et al 1992) from PET on a voxel-by-voxel basis. To align two image datasets, the algorithm is calculating the ratio of one image to the other for each voxel and then iteratively moves the images relative to each other to minimise the variance of this ratio. It is based on the assumption that if two image sets are accurately aligned then the value of any voxel in one image set is related to the value of the corresponding voxel in the other image set by a single multiplicative factor, R. If the sets are misaligned, R is no longer constant, but varies from voxel to voxel throughout the image. The alignment algorithm is, therefore, attempting to minimise this voxel-to-voxel variation. Modifications to this algorithm (like binarising the images, extracting the MRI brain contours etc.) can be implemented to transform this technique into an inter-modality (e.g. PET to MRI) alignment procedure. However, the technique requires that exactly the same volumes can be imaged adequately so that the alignment is successful.

3.4.3 Accuracy achieved by various methods.

Most of the simulated studies (e.g. phantom studies, or model data) claim that an accuracy comparable to the spatial resolution of the imaging device with the lowest spatial resolution can be achieved. Some researchers have even measured the geometric distortions of their scanning systems (e.g. MRI) in an effort to determine the inherent registration limits (Hill et al 1991; Van den Elsen and Viergever 1991). For MRI images, which are the ones with the best resolution, a maximum voxel displacement of 2.3 mm for transverse slices at the periphery of the head coils of view, with an average integral non-linearity of less than 0.8 mm were reported (Hill et al 1991). Keeping this in mind, the residual misfit between models of the external surface from MRI and PET phantom measurements, which was reported to be of the order of 1.5-2.0 mm (averaged over the surface) seems very reasonable (Mazziotta et al 1991; Pelizzari et al 1989). In the same reports an accuracy of $\leq 3°$ for rotation, 1 pixel (~1 mm) for translation and <1 pixel for scaling, was resulted when two copies of an identical image contour set were displaced by known amounts of rotation, translation and scaling. The same accuracy (~1.43 mm misfit/point, (Hill et al 1991)) was demonstrated by point matching techniques, but it was commented that "the registration accuracy will be better than this since a least square technique is used to derive the transformation matrix and, as more points are identified than the necessary to solve the transformation, there will be some averaging of

errors". Finally, mean misregistration error of 0.6-0.7 mm, which is less than the used pixel size (1.745 mm) was achieved by the voxel-to-voxel method (Woods et al 1992) in PET studies.

3.5 Registration studies at the OU*

3.5.1 Motivation

As the point-matching technique was the easiest one to engineer and solve, this was universally used by most MEG groups world-wide. It was noticed, however, that the 0.5-1.0 cm accuracy achieved by the use of three markers (nasion, preauriculars) (George et al 1989) could be reduced down to millimetres by procedures incorporating surface alignment techniques, so that the MEG/MRI matching accuracy can approach that of MRI/PET, allowing for more reliable multimodal imaging and/or intermodal comparisons (Walter et al 1992).

There was, therefore, recently a movement towards the use of the surface matching technique in MEG and EEG studies. Abraham-Fuchs et al (1991) and Towle et al (1993) used this technique as described previously (Pelizzari et al 1989) to register digitised points on the scalp obtained for MEG and EEG measurements respectively, with MRI images. Gevins et al (1990) also digitised the EEG electrode positions and minimised the mean distance for all electrodes (to the closest point on the scalp surface MRI contours) to align the EEG and MRI systems. An accuracy in the order of 2-3 mm was reported in all cases.

For all the reasons explained in paragraph 3.1 an accuracy on the 1.0 cm level would not be adequate in our studies. The accuracy described in the latter cases instead is desirable. Moreover, there were a couple of occasions where the use of three fiducials resulted in inconsistency. Figure 3-3 displays the situation where the fit of the pre-auricular and the nasion points (marked with arrows in (a)) is excellent (crosses in (b) but the description of the digitised scalp in the MEG system (red dots in (b) does not fit with the outlines as extracted from the presumably aligned MRIs (green contours in (b). This was probably due to the inconsistent definition of the fiduciary skull landmarks in each acquisition (MEG and MRI). Notice that the same kind of discrepancy is resulted in two individual cases (subjects).

The need to move to a less subjective alignment procedure is, therefore, obvious. However, a point matching technique is always useful as an initial matching step, and

---

* *Open University*

sometimes is the only one available. Thus, we developed two systems: one that uses a point-matching algorithm, and another based on the surface matching technique. In the following, we are going to describe the implementation of each method in detail.

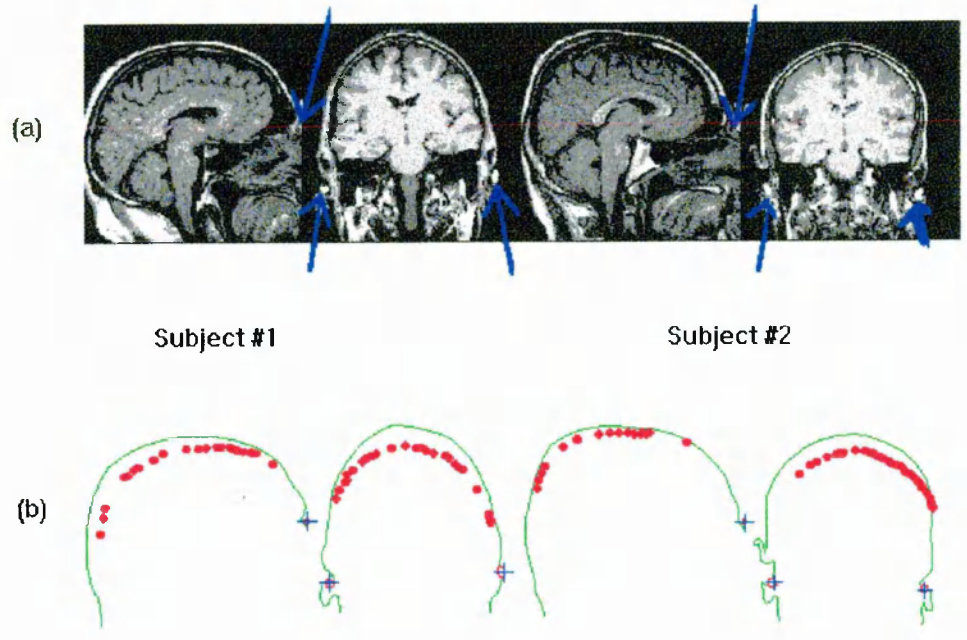

Figure 3-3: The arrows in (a) show the vitamin pills used to perform the point-matching. The fit of the MEG co-ordinates of the pills (blue crosses in (b)) with their MRI ones (marked as little red circles in (b)) is perfect. However, the head shape outlines in the system (red dots) do not match the MRI scalp outlines (green contours).

3.5.2 Point Matching

Two separate subsystems, namely "PM-ALL" and "PM" (basically acronyms of Point Matching), used under different situations, were developed to perform the point matching task. This is not due to the different nature of the problem in each case, but it was only implemented to satisfy the ways information was sent from other labs world-wide, into our lab. The first subsystem, "PM-ALL", needs points with known pixel co-ordinates (MRI) and their corresponding MEG co-ordinates to be given. No initial estimate is required, and the scaling parameters are unknown. On the other hand, scaling is assumed to be known for the second subsystem, "PM", which also requires an initial estimate for the transformation parameters. The MEG co-ordinates of at least 3 points that can also be identified on the MRIs are the inputs to "PM". In the following, we describe the principles and the performance of each system separately.

3.5.2.1 "PM-ALL"

3.5.2.1.1 The formulation

As already mentioned above, "PM-ALL" assumes that corresponding points are given in the MRI system (pixels) and the specific MEG system (in meters). The MRI slices are assumed to contain $(2xN_c)x(2xN_c)$ pixels with the (N_c, N_c) pixel being the centre of each MRI slice. Then a pixel, P^i, in the nth MRI slice (Figure 3-4) will be

$$\mathbf{r}_{ni} = \mathbf{r}_n(P_1^i, P_2^i) = \mathbf{r}_o + s_3(n - n_o)\hat{\mathbf{e}}_3 + s_1(P_1^i - N_c)\hat{\mathbf{e}}_1 + s_2(P_2^i - N_c)\hat{\mathbf{e}}_2 \qquad (3\text{-}10)$$

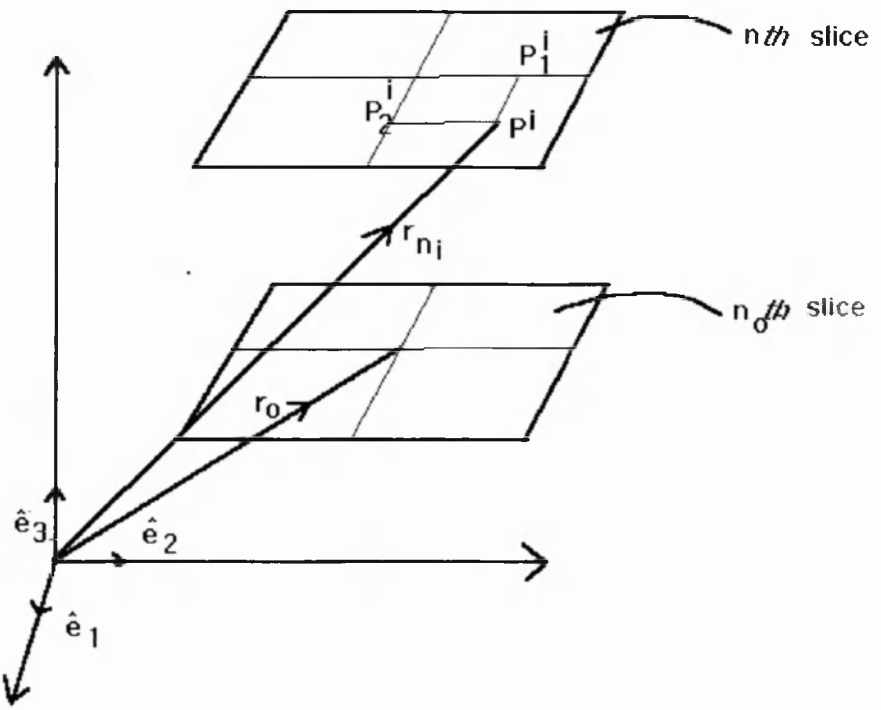

Figure 3-4: A point P^i in the nth MRI slice and its representation in the MEG system.

where $\hat{\mathbf{e}}_1, \hat{\mathbf{e}}_2, \hat{\mathbf{e}}_3$ the unit vectors that compose an orthogonal Cartesian system (the MEG system) and so $|\hat{\mathbf{e}}_1|=|\hat{\mathbf{e}}_2|=|\hat{\mathbf{e}}_3|=1$ and $\hat{\mathbf{e}}_1\cdot\hat{\mathbf{e}}_2 = \hat{\mathbf{e}}_1\cdot\hat{\mathbf{e}}_3 = \hat{\mathbf{e}}_2\cdot\hat{\mathbf{e}}_3 = 0$, $\mathbf{r}_{ni}$ the MEG vector of P^i, $\mathbf{r}_o$ is the origin vector of slice n_o (in other words the pixel (N_c, N_c) of slice n_o in the MEG system), s_1, s_2, s_3 are the scale parameters along the three axes, and P_1^i, P_2^i the pixel co-ordinates of P^i. Then if a second point P^j is given on the nth MRI slice, Equation 3-10 can give:

$$\mathbf{r}_{ni} - \mathbf{r}_{nj} = s_1(P_1^i - P_1^j)\hat{\mathbf{e}}_1 + s_2(P_2^i - P_2^j)\hat{\mathbf{e}}_2 \qquad (3\text{-}11)$$

or

$$R_{ij} = |\mathbf{r}_{ni} - \mathbf{r}_{nj}|^2 = s_1^2(P_1^i - P_1^j)^2 + s_2^2(P_2^i - P_2^j)^2 \quad (3\text{-}12)$$

A minimum of 2 points can give s_1, s_2, however, a greater number of points (e.g. N_1) given in slice n, can be used to solve for s_1, s_2 in the least square sense i.e. minimising the error E:

$$E = \sum_{i=1}^{N_1-1} \sum_{\substack{j=i+1 \\ i<N_1}}^{N_1} [R_{ij} - s_1^2(P_1^i - P_1^j)^2 - s_2^2(P_2^i - P_2^j)^2]^2 \quad (3\text{-}13)$$

by taking $\frac{\partial E}{\partial s_1^2} = \frac{\partial E}{\partial s_2^2} = 0$ and solving a 2x2 linear system of equations. If a number of points are given in other slices (e.g. N_2 points in slice n_2), the process can be repeated by getting s_1', s_2', and then averaging s_1, s_2. Usually s_1 can be taken to be equal to s_2 (or both equal to their average) if we know that the MRI slices are isotropic.

We can further use s_1, s_2 and Equation 3-11 to find the component of each unit vector (e_{1x},e_{1y},e_{1z}, etc.). This can be done by reformatting Equation 3-11 into:

$$r_{x_{ij}} = s_1(P_1^i - P_1^j)e_{1x} + s_2(P_2^i - P_2^j)e_{2x} \quad (3\text{-}14i)$$

$$r_{y_{ij}} = s_1(P_1^i - P_1^j)e_{1y} + s_2(P_2^i - P_2^j)e_{2y} \quad (3\text{-}14ii)$$

$$r_{z_{ij}} = s_1(P_1^i - P_1^j)e_{1z} + s_2(P_2^i - P_2^j)e_{2z} \quad (3\text{-}14iii)$$

where $r_{x_{ij}}, r_{y_{ij}}, r_{z_{ij}}$, the x,y,z components of $(\mathbf{r}_{ni} - \mathbf{r}_{nj})$ in the MEG system. Again forming the errors (e.g. for Equations 3-14i)):

$$E_x = \sum_{i=1}^{N_1-1} \sum_{\substack{j=i+1 \\ i<N_1}}^{N_1} [r_{x_{ij}} - s_1(P_1^i - P_1^j)e_{1x} - s_2(P_2^i - P_2^j)e_{2x}]^2 \quad (3\text{-}15)$$

and letting $\frac{\partial E_x}{\partial e_{1x}} = \frac{\partial E_x}{\partial e_{2x}} = 0$ we can solve a 2x2 linear system to get e_{1x}, e_{2x}. Similarly we get (e_{1y}, e_{2y}) and (e_{1z}, e_{2z}) and we can, therefore, form the unit vectors $\hat{\mathbf{e}}_1$, and $\hat{\mathbf{e}}_2$. The third vector can then be formed by using:

$$\hat{\mathbf{e}}_3 = \hat{\mathbf{e}}_1 \times \hat{\mathbf{e}}_2 \quad (3\text{-}16)$$

So far we have found (s_1, s_2, $\hat{\mathbf{e}}_1$, $\hat{\mathbf{e}}_2$, $\hat{\mathbf{e}}_3$), and the remaining unknowns are (s_3,$\mathbf{r}_o$). If we consider point P^i to be in slice n_i and point P^j to be in slice n_j, then Equation 3-10 gives:

$$\delta\mathbf{r}_{ij} = \mathbf{r}_i - \mathbf{r}_j = s_3(n_i - n_j)\hat{\mathbf{e}}_3 + s_1(P_1^i - P_1^j)\hat{\mathbf{e}}_1 + s_2(P_2^i - P_2^j)\hat{\mathbf{e}}_2 \quad (3\text{-}17)$$

or

$$\left|\delta \mathbf{r}_{ij}\right|^2 = s_3{}^2(n_i - n_j)^2 + s_1{}^2(P_1^i - P_1^j)^2 + s_2{}^2(P_2^i - P_2^j)^2 \tag{3-18}$$

where only s_3 is unknown. Thus we get:

$$s_3 = \sqrt{\frac{|\delta \mathbf{r}_{ij}|^2 - s_1{}^2(P_1^i - P_1^j)^2 - s_2{}^2(P_2^i - P_2^j)^2}{(n_i - n_j)^2}} \tag{3-19}$$

Again the value of s_3 is optimised by taking the average of all the possible combinations of points. This is in fact what "PMALL" does.

Finally, the origin vector $\mathbf{r}_o$ for slice n_o (arbitrarily defined to be a slice with N known points on it) can be obtained from Equation 3-10 by letting $n=n_o$, and then averaging for all points. That is,

$$\mathbf{r}_o = \frac{\sum_{i=1}^{N} [\mathbf{r}_{ni} - s_1(P_1^i - N_c)\hat{\mathbf{e}}_1 - s_2(P_2^i - N_c)\hat{\mathbf{e}}_2]}{N} \tag{3-20}$$

We then have defined all the necessary parameters. Lastly, the origin centre $\mathbf{r}_{o,n}$ of the nth MRI slice, which is another necessary input into our display system (i.e. IMAGE*), will be (see Figure 3-5):

$$\mathbf{r}_{o,n} = \mathbf{r}_o + (n - n_o)\underline{\delta} = \mathbf{r}_o + (n - n_o)s_3\hat{\mathbf{e}}_3 \tag{3-21}$$

---

* *IMAGE is a graphics enviroment developed at the OU (Singh et al 1992); it is desinged to offer the user a set of appropriate graphical representations of MEG data, like, for example, MFT solutions (or dipoles) with background MRI. The transformation matrix associating the MEG and MRI systems needs to be obtained externally (e.g. by one of the methods described here) and then ported into the system.*

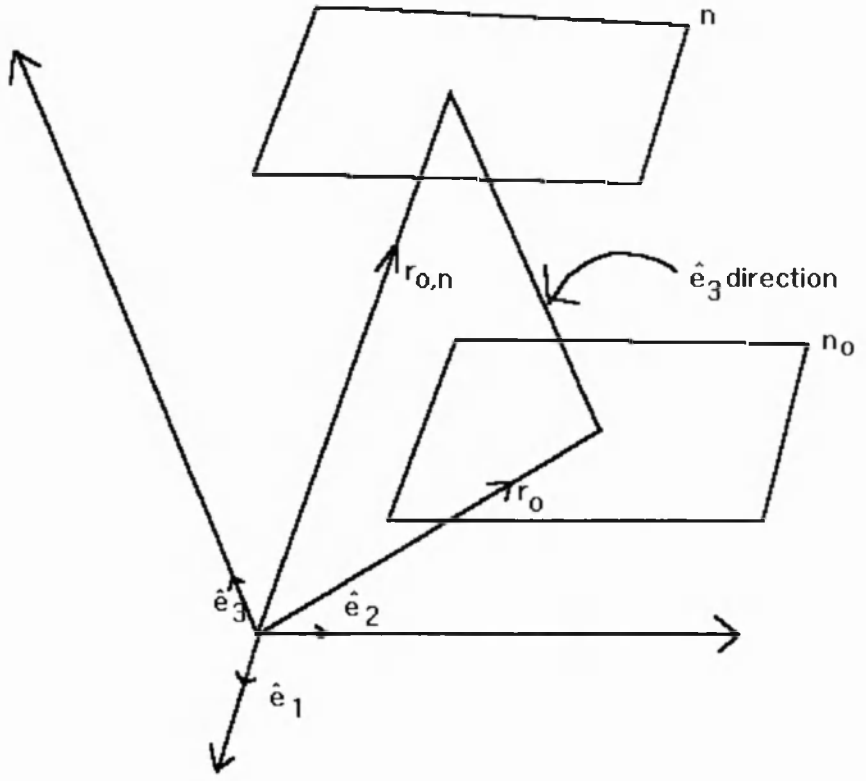

Figure 3-5: The centre of the nth slice is defined according to slice no and the third directional unit vector.

3.5.2.1.2 Results

We shall demonstrate how the above formulation works in a situation where 18 corresponding points were given. These were identified as watermarks (high MRI signal) in 3 MRI slices; each slice contained 6 such given points, marked by arrows in Figure 3-6(a). Care was taken, so that the MRIs were displayed in consistency with what the transformation matrix found ($\hat{\mathbf{e}}_1$, $\hat{\mathbf{e}}_2$, $\hat{\mathbf{e}}_3$) meant when used by IMAGE.

Figure 3-6(b) shows the results obtained when $s_1 \neq s_2$, while in Figure 3-6(c), s_1 and s_2 were taken equal to their average in all the formulae of the previous paragraph. The coloured dots are the points as given in the MEG system (red shows points on the right side of the head, green shows points on the left). The fit in Figure 3-6(c) is perfect, while in Figure 3-6(b) a small discrepancy appears in two of the slices. Notice that the most left slice was taken to be slice n_o (see previous paragraph).

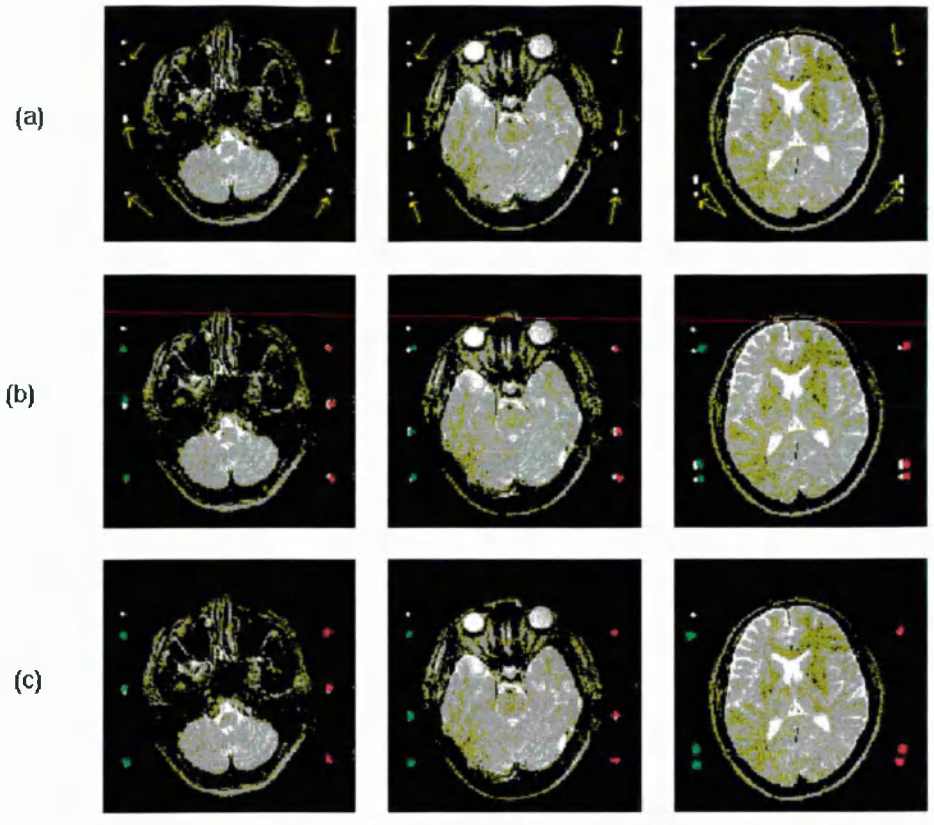

Figure 3-6: The fit of the MEG points to their points defined in the MRI system (shown by the arrows in (a)). The x,y scaling factors were assumed to be different in (b), while they were taken to be equal in (c).

3.5.2.2 "PM"

3.5.2.2.1 In General

In this case the x-y scaling factors and the interslice distance of the MRIs are supposed to be known. An initial estimate, $\mathbf{R}_o$, for the rotation matrix, and, $\mathbf{b}_o$, for the translation are needed. It should be mentioned that this is not very crucial for finding the solution to the problem, but it is necessary to define these parameters so that the new transformation is correctly defined. In other words, the system will try to find the best $\theta_x,\theta_y,\theta_z$, that compose **R** (see **Error! Switch argument not specified.**, Equation 3-4) and the best $\Delta\mathbf{b}$, so that the new rotation matrix, **R'**, and the new translation **b'** are given by:

$$\mathbf{R}' = \mathbf{R}\mathbf{R}_o \,, \qquad \mathbf{b}' = \mathbf{b}_o + \Delta\mathbf{b} \tag{3-22}$$

The system is using the transformation of points as defined by Equation 3-7, but with **S=I**=identity matrix, and $\mathbf{P}_1=\mathbf{b}_o$. That is,

$$\mathbf{P'} = \mathbf{R}(\mathbf{P} - \mathbf{b}_0) + \mathbf{b}_0 + \Delta\mathbf{b} \tag{3-23}$$

For each MEG point its corresponding MRI point is the one closest to it. So the cost function, F (see Equation 3-9), is formed by summing the squares of the distances between such corresponding points. Finding the parameters $\theta_x,\theta_y,\theta_z$, and $\Delta\mathbf{b}$, involves minimising F with respect to these parameters.

3.5.2.2.2 *Minimisation*

The way that we initially tried to solve this minimisation problem involved numerical estimates of the derivatives of F with respect to each parameter. For example, consider the 2-dimensional case where only rotations around the z-axis (θ_z) and translations by D_x, D_y in the x,y directions respectively are allowed. Then if S_{oj} is the initial distance of the jth MEG point to its corresponding MRI point, and S_j the distance when the MRI points were transformed according to Equation 3-23 by small amounts $\Delta\theta_z$, ΔD_x, ΔD_y then F could be approximated by:

$$F = \sum_{j=1}^{\#MEG\ points} [S_{oj} + D_x(\frac{\partial S}{\partial D_x}) + D_y(\frac{\partial S}{\partial D_y}) + \theta_z(\frac{\partial S}{\partial \theta_z})]^2 \tag{3-24}$$

where

$$(\frac{\partial S}{\partial D_x})_j \approx \frac{S_j - S_{oj}}{\Delta D_x}, \quad (\frac{\partial S}{\partial D_y})_j \approx \frac{S_j - S_{oj}}{\Delta D_y}, \quad (\frac{\partial S}{\partial \theta_z})_j \approx \frac{S_j - S_{oj}}{\Delta \theta_z} \tag{3-25}$$

Then a system of linear equations can be formed by taking:

$$(\frac{\partial F}{\partial D_x}) = (\frac{\partial F}{\partial D_y}) = (\frac{\partial F}{\partial \theta_z}) = 0 \tag{3-26}$$

In the real 3-d case of course we have a 6x6 system which can be solved to give θ_x, θ_y, θ_z, D_x, D_y, D_z. Although such a methodology worked perfectly well when "ideal" data were tried, the system often failed in the presence of noise. Forming the singular values of such a system did not give any indication that the problem could be resolved by a "Singular Value Decomposition" method (Press et al 1988). This is probably due to the approximation of the derivatives in Equation 3-25. A possible way to avoid this could be to calculate the derivatives from an analytical form (i.e. to get true derivatives) and not just to approximate them with numerical differences. This is in fact what Woods et al (1992) use in their algorithm. In order to avoid the computation of derivatives we used an algorithm developed by Powell in 1964, but as it was implemented more recently (Press et al 1988).

3.5.2.2.3 *Results*

The above method works well and has been successfully used in a number of cases, since 1993. We wish to present herein the results of some tests demonstrating the usefulness of "PM". A set of MR images was rotated and translated by known amounts of θ_x, θ_y, θ_z, b_x, b_y ,b_z and points obtained from the new set were supposed to be the MEG points according to which the initial set should be registered. It has to be stated that these points were obtained by a "mouse clicking" procedure in "IMAGE" and so contain a little amount of noise, that would not be present if they were just mathematically obtained using Equation 3-23. Table 3-1 demonstrates the results. The RMS misfit per point values were determined by taking the square root of the cost function after the latter was divided by the number of points, which was equal to three in all these cases.

Table 3-1: Results from "PM" (Point-Matching). Three points were rotated and translated away from the true positions (initial errors). PM tried to "bring them back" to their proper positions. At the end of the process the "final errors" were evaluated. Note the small final RMS misfit/point values.

Errors	b_x (mm)	b_y (mm)	b_z (mm)	θ_x (deg)	θ_y (deg)	θ_z (deg)	RMS misfit/point (mm)
initial	-15.0	+10.0	+15.0	+8.0	+4.0	-10.0	28.68
final	-0.2	+0.3	+0.4	+0.1	+0.1	-0.1	0.30
initial	+20.0	-10.0	+10.0	+6.0	-3.0	+8.0	29.60
final	+0.2	+0.3	+0.4	+0.1	+0.1	-0.1	0.56
initial	+5.0	+5.0	+5.0	-2.0	-2.0	-2.0	10.40
final	+0.4	-0.4	+0.7	-0.1	-0.2	+0.2	0.42

Observing from Table 3-1 the high accuracy that PM can provide, one may be guided to the wrong impression that all the reasoning about implementing a surface matching technique as discussed in paragraph 3.1 was false. However, it has to be emphasised that PM works as neatly as the above example indicates, if the points identified in the two sets correspond to exactly the same landmarks. In many cases it is simply impossible to do so. For example, in an auditory MEG experiment, one or both preauriculars may not be

accessible as the Dewar is placed directly above the temporal area. Even if the same point is used, often this is done by different people, often at different days and sometimes in different laboratories. If an erroneous identification of points is given then inconsistencies like the one presented in Figure 3-3 may arise. Thus, we do not suggest point-matching as a method of choice in registering MEG recordings with MR images. However, we do recommend it as a useful tool towards a good registration. This is, firstly, because it can provide a reasonably good (sometimes very accurate as well) initial estimate of the parameters to be input in a surface matching technique. Secondly, it is a quick and accurate technique in simple tasks; for example, when different MRI incidences (e.g. sections) of the same subject need to be registered. This is demonstrated in Figure 3-7, where sagittal and coronal sections of the same subject are involved. Vitamin pills marking the nasion, the left and right pre-auricular points were easily identified in both sets. The coronal set was rotated and translated arbitrarily. After "PM" registers the two sets, points taken on the mid-sagittal line on the coronal slices, are joined and superimposed on the mid-sagittal slice. The points from the coronals fit the mid-sagittal scalp outline perfectly.

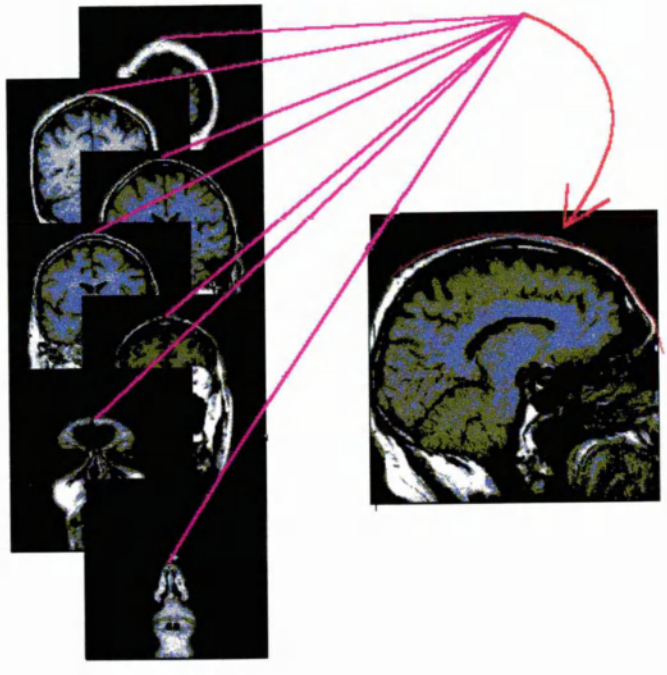

Figure 3-7: The rotated coronal slices were registered with the sagittal ones. Then points on the mid-sagittal line on the coronal slices were joined (red line) and superimposed onto the mid-sagittal slice. The contour defined by the "coronal" points fits perfectly with the scalp outline in the mid-sagittal slice.

3.5.3 MEG-MRI Surface-Matching

In devising a surface-matching method to register the MEG data with MRI images, we follow similar ideas to those already presented in previous paragraphs. First of all, we assume that the head of the subject can be described as a 3D-object by both modalities. The latter means that the head shape outlines have to be taken from each MRI slice, so that a stack of such outlines can represent the head surface. The head must also be digitised in the MEG experiments. Obviously, the better the head surface is described by each method the easier will be to register them; we shall come back to this point later. It is also clear that the head can be better described by the MRI contours than by the MEG points, so in the "head-hat" analogy, the MRI points represent the "head", while the MEG points represent the "hat". However, since the MEG co-ordinate system is the one which we always want to use after registration, it seemed to us more reasonable to refer to this system. In other words we attempt to fit the "head" (MRIs) into the "hat" (MEG).

We make use of Equation 3-7 again (with $\mathbf{S}=\mathbf{I}$) to transform the MRI points $\{\mathbf{P}_i\}$ into the MEG system ($\{\mathbf{P}_i'\}$ points). An initial estimate for the rotation matrix*, $\mathbf{R}=\mathbf{R}_o$, and the translation vector, $\mathbf{b}=\mathbf{b}_o$, has to be provided, while scaling is assumed to be known. Then $\mathbf{P}_1=\mathbf{b}_o$ in Equation 3-7, so we end up with Equation 3-23 again. We also use Powell's method (the same as in point-matching) to minimise the cost function, F, as given by Equation 3-9, where the sum extends to the total number of MEG points.

The contribution to F for each MEG point is found as follows: a line connecting the specific MEG point, $\mathbf{P}_i$, with the centre of gravity, **CG**, of the MRI points, (in the current position) is formed and the distances of the MRI points that lie in the subspace between $\mathbf{P}_i$ and **CG** are calculated. If no MRI point with a distance smaller than 3 cm is found $\mathbf{P}_i$ is discarded from the calculation of F. If no distance is smaller than 1 cm, but for some distances, d, the relation 3 cm<d<1 cm is true, then the squared distance of $\mathbf{P}_i$ to the MRI point lying closest to the $\mathbf{P}_i \rightarrow$**CG** line is entered in F. If, however, there are MRI points that lie within 1 cm distance from the $\mathbf{P}_i \rightarrow$**CG** line, then a patch of all these points is formed (Figure 3-8) and their average point is taken as the intersection of the above line with the head. The squared distance of $\mathbf{P}_i$ to this intersection point is then input in F.

It is obvious, however, that such a cost function will be a good minimisation criterion close to the true solution, but may not describe the problem very well in positions far away from it. This was noticed in our early attempts to minimise a 6-dimensional

---

* *Successive rotations of* $\mathbf{R}_o$ *are performed using the axis-specific rotations of* ***Error! Switch argument not specified.****. At each step,* $\mathbf{R}=\mathbf{R}'\mathbf{R}_o$ *, where* $\mathbf{R}'$ *is given by Error! Switch argument not specified. with the proper step parameters.*

function using Powell's method, as it was employed in "PM". So the following tricks are implemented. First, we are trying to fix the translation as much as possible. To do this, the corresponding MRI point for each MEG one is found (as described above) and the centres of gravity of the MEG points (**G1**) and their corresponding MRI points (**G2**) are calculated. The translation shift ($\Delta b_x, \Delta b_y, \Delta b_z$) is then evaluated by attempting to make **G2** coincide with **G1**. The procedure is repeated and it only stops if the shift is small enough (e.g. its module is less than 1 mm).

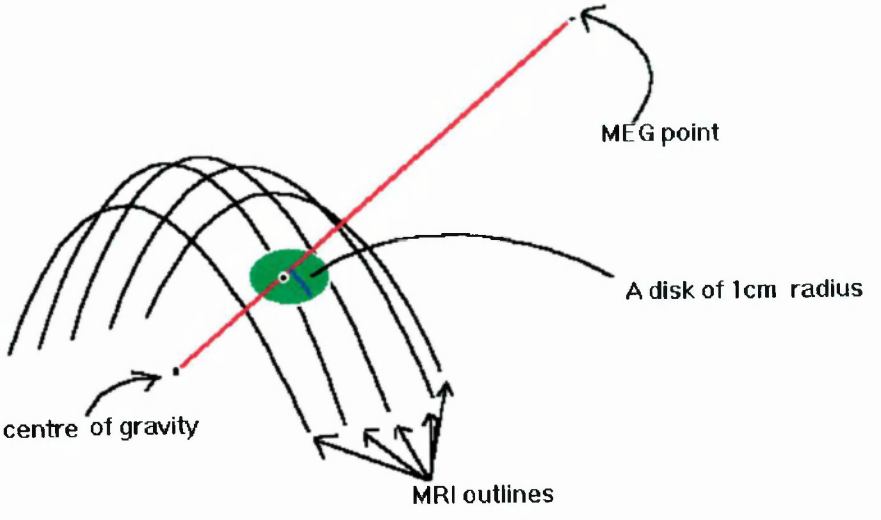

Figure 3-8: For each MEG point a "head" patch that corresponds to it is formed. Then the squared distance from the MEG point to the patch is contributing to the cost function.

Having roughly fixed the translation, a 3-dimensional minimisation of F with respect to the three rotation angles is attempted. Once F stops decreasing (in successive iterations) further than a specified limit, a 6-dimensional minimisation is finally tried starting at the point (e.g. $b_x, b_y, b_z, \theta_x, \theta_y, \theta_z$), that is so far obtained. The iterations are terminated when F stops decreasing again further than a limit lower than the one previously set. The final answer is accepted if the RMS misfit per MEG point is less than 3 mm.

In order to evaluate the method we used again simulated data. That is, a set of MRI slices was rotated and translated by known amounts of $\mathbf{b}_o, \theta_x, \theta_y, \theta_z$, and various points on the scalp were taken; these assumed to be the "MEG" points. In addition, the head contours of the original slices were obtained. Then the system was asked to fit the two datasets. Table 2 summarises the results.

Table 3-2: Results from MEG/MRI Surface-Matching. A set of points was rotated and translated away from their true positions (initial errors). The Surface-Matching program was then asked to return them back to their original positions. At the end of the process the "final errors" were evaluated. Note that the values for the final RMS misfit/point are less than 3 mm in all cases.

Errors	b_x (mm)	b_y (mm)	b_z (mm)	θ_x (deg)	θ_y (deg)	θ_z (deg)	RMS misfit/point mm)
initial	+10.0	-10.0	+10.0	-5.0	+2.0	+6.0	14.18
final	-0.14	-0.78	-0.10	-1.4	-0.1	-0.4	2.46
initial	-15.0	+10.0	+15.0	+8.0	+4.0	-10.0	12.7
final	-1.23	+0.08	+1.76	+1.02	+2.1	-0.18	3.0
initial	+5.0	+5.0	+5.0	-2.0	-2.0	-2.0	6.40
final	-0.1	+0.66	-0.1	-1.3	-0.05	+1.0	1.40

Before criticising Table 3-2, it has to be stressed that the MRI interslice distance was 6 mm in all the cases. This is probably a severe limitation, since it drastically affects the calculation of the cost function, due to the formation of the patches (Figure 3-8). The number of MEG points used varied between 120 to 450. We did not observe a very significant role of this number of points, although as mentioned earlier, if the head could be described *perfectly* in the MEG system we could claim that a perfect fit (down to 1 MRI pixel accuracy) may be found. Since for a highly symmetric object, such as a sphere or cylinder, clearly a unique transformation cannot be found based only on matching surfaces, points on the head that sufficiently highlight the lacking of such a perfect symmetry (of the head) are very important in such a methodology. Additionally, points that lie in perpendicular directions and describe the head surface in a special manner could also be very useful. This is proved by the following example.

A set of MRI slices was rotated and translated and 69 points lying on the MRI scalp were taken to represent the MEG points. No special attention was paid in the selection of these points. The registration results are given in Table 3-3 ("final1" row). An RMS misfit of 3.4 mm was obtained. Getting additional points, which were lying on the midsagittal line or/and the midcoronal slice (since the coronal slices were used throughout) improved the

fit quite substantially (final2 row). One should note that although the initial RMS misfits/point were different (due to the different number of points used), the starting errors were the same in both cases, as seen in Table 3-3 (init1, init2). The results become more obvious in Figure 3-9 where "MEG" points (red dots) on two MRI slices are given in the correctly transformed set (Figure 3-9a). Figure 3-9(b) describes the results achieved by fitting the 69 points, while (Figure 3-9(c)) those achieved by fitting the 129 points. The correspondence of points in (Figure 3-9(a)) and (Figure 3-9(c)) is almost perfect while (Figure 3-9(b)) is obviously not a very accurate result.

Table 3-3: The significance of the "quality" of points; Correction of the same initial error is attempted using different number of points. In the first case (69 points), no care was taken in the selection of the points. In the second (129 points), 60 additional points in two perpendicular directions (midsagittal line, midcoronal line) were added to the original 69. The fit in the second case is significantly improved (compare rows final1 and final2) of the last column.

Errors	#points used	b_x (mm)	b_y (mm)	b_z (mm)	θ_x (deg)	θ_y (deg)	θ_z (deg)	RMS misfit/ point (mm)
init1	69	+10.0	-10.0	+10.0	-5.0	+2.0	+6.0	5.0
final1	69	-1.19	-1.0	+2.7	-2.4	+2.4	-0.1	3.4
init2	129	+10.0	-10.0	+10.0	-5.0	+2.0	+6.0	14.18
final2	129	-0.14	-0.78	-0.10	-1.4	+0.1	-0.4	2.46

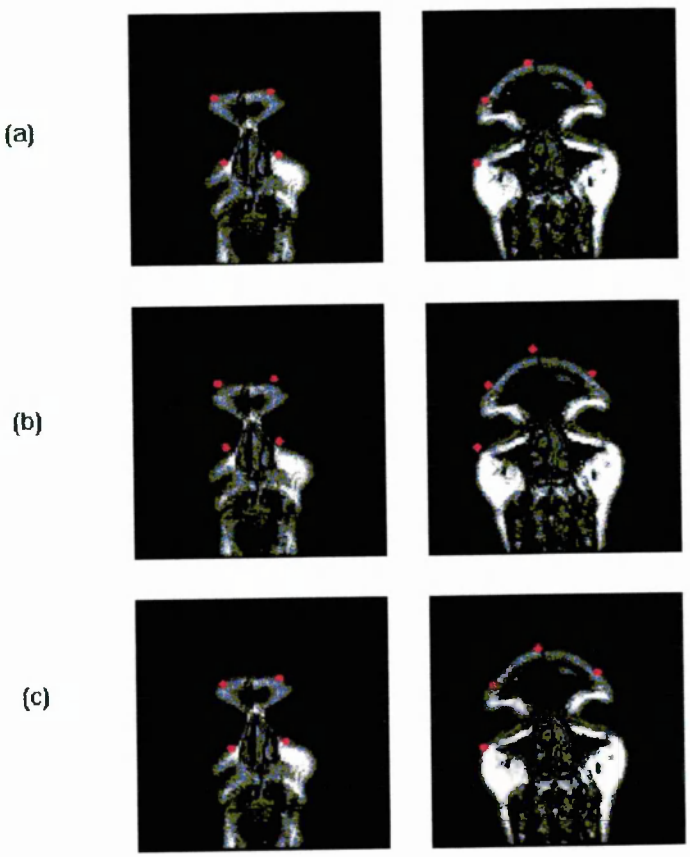

Figure 3-9: Visualisation of the registration result. Points identified on (a) are superimposed on (b), and (c). In (b) 69 points were used to perform the registration (final1 row in table 3), while 60 additional points (total of 129 points) lying on the midsagittal and midcoronal slices were used in (c) (final2 row in Table 3-3).

3.5.3.1 Examples

In this section we shall try to visualise further the accuracy we have achieved with surface matching. In attempting to do so, we deliberately start with the case that motivated us to employ such a strategy, that is the inconsistency of Figure 3-3. Figure 3-10 shows how the problem was resolved using the surface matching utility. In the bottom plate of Figure 3-10 the MEG headshape points fit well with the MRI skull contours. However, the fiduciary points fall off the range of the vitamin pills as marked with circles in the MRIs.

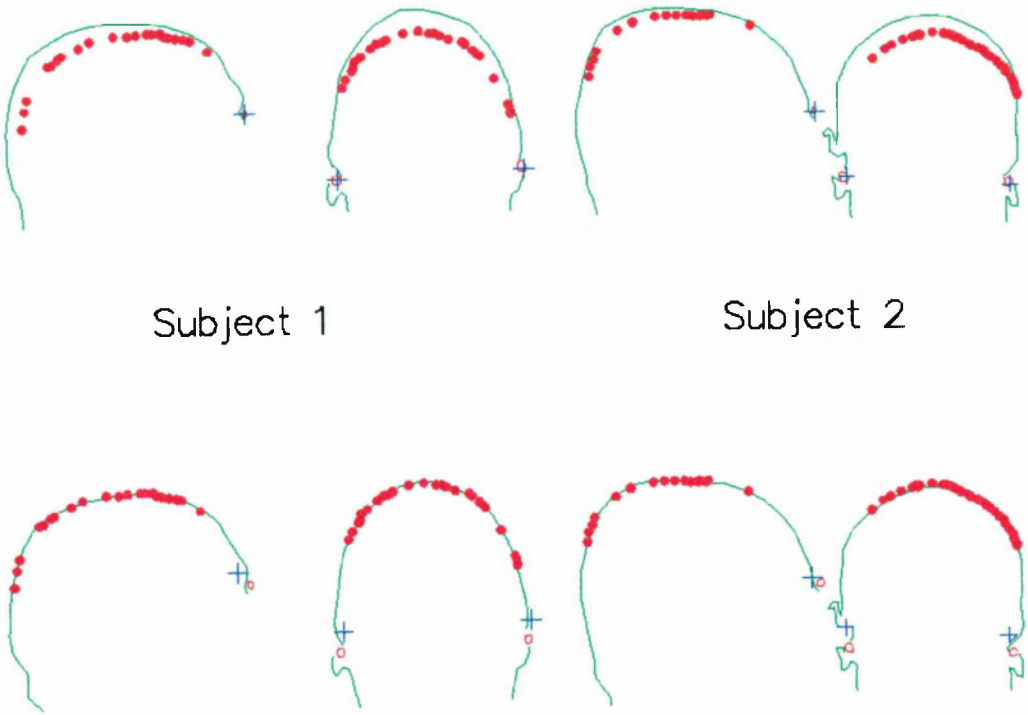

Figure 3-10: In the top plate, the headshape MEG points (dots) do not fit with the MRI skull outlines, despite the matching of the MEG fiduciary points (crosses) with the MRI fiduciary points (circles). In the bottom plate, surface matching was performed to resolve the problem. Note the good fitting of the dots on the skull MRI outlines. The mismatch between the crosses and the little circles reveals the origin of the inconsistency.

The availability of a big number of MEG headshape points, not only offers redundancy, thereby permitting surface matching to be performed, but also helps in the visualisation of the result. The latter is necessary since the figure of RMS mismatch per point might not represent the situation sufficiently well, since a relatively high value (e.g. 6 mm per point) might be the consequence of the high contribution of only a few "bad" points - like

for example points lying in a small hair patch. Viewing the fit in consecutive MRI slices or in different pseudo-3D perspectives gives a much better impression of the final result.

Figure 3-11 further illustrates the fit in the case of subject 2 in Figure 3-3 (or Figure 3-10) after surface matching. Once such a registration was performed (using a single set of MRI sections, e.g. coronal) the MEG data points can be selected and displayed on appropriate MRI slices. Figure 3-11a shows four coronal slices of one subject after surface matching was attempted. The MEG points that lie within 2 mm distance from each slice are displayed as red dots. The green lines are just connecting the nasion, left and right pre-auricular points. The fit of the MEG head shape points to the MRI scalp, from anterior (left) to posterior (right) is very satisfactory.

Performing point matching ("PM") we then registered the sagittal (Figure 3-11b) and the axial (Figure 3-11c) MRI sections with the coronal ones (the nasion, and the two pre-auricular points were used). The fit of the MEG points on the head edges is very satisfactory in all cases.

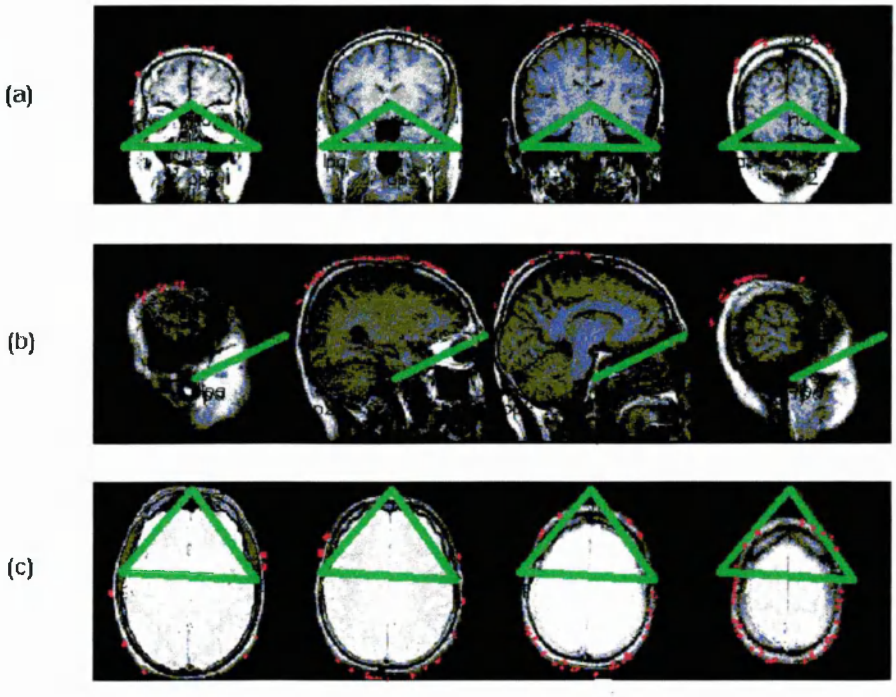

Figure 3-11: The MEG head shape points (red dots) were registered with the MRI scalp outlines, as the latter were extracted from the coronal MRI slices. Then a point-matching was employed to register the coronal with the sagittal (in (b)) and axial (in (c)) sections. In all cases, the MEG points that lie 2 mm from the displayed MRI slices are drawn. Their fit with the MRI scalp is very satisfactory in all three cases.

In Figure 3-12 we show another example of registered MEG and MRI datasets. In this case, only axial MRIs were available (3 mm interslice distance), and, therefore, the top of the head was not described by MRI. A big number of MEG points was, however, collected. The latter allowed for a very challenging visualisation of the actual result. Not all MEG points were used in the matching process; only a smaller, but sufficiently distributed MEG set was used. The final mismatch per point was 4.5 mm. As seen in Figure 3-12 the fit between MEG and MRI appears excellent in all different perspective views. One nearly axial view (last plot), however, reveals that the nominal value of the obtained mismatch was correct, since there might be a small error (some 2-3 degrees probably) in one of the rotation angles. Such an error may well be regarded as acceptable given the reasons we address in the following section.

Finally, Figure 3-13 shows an example where surface matching provided an excellent fitting, and confidence was maintained throughout the visualisation procedure. In this case, the actual value of the RMS mismatch per point was again 4 mm, and a total of some 2,500 MEG points were used. However, one can note a small patch of MEG points, which were obviously lying off the head surface, thereby explaining the relatively "high" figure of 4 mm mismatch per point.

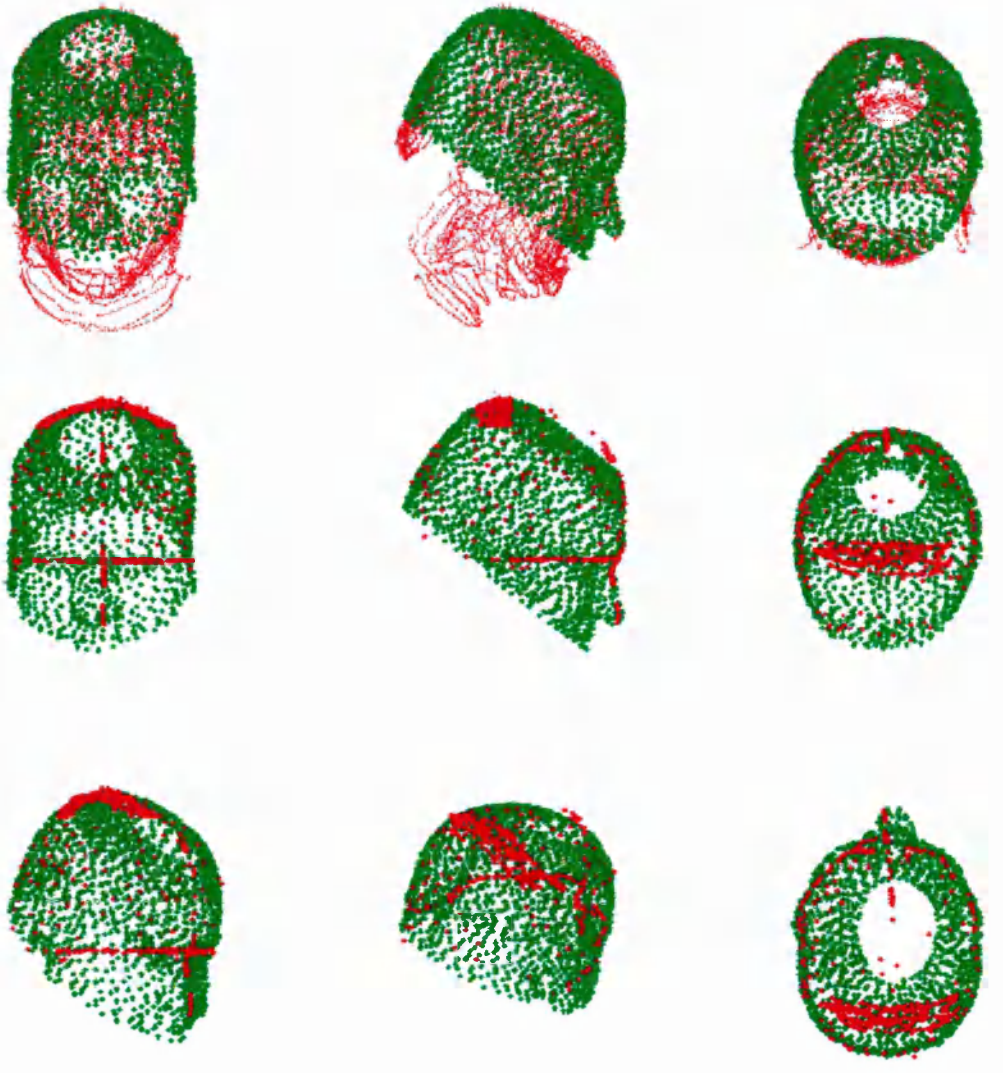

Figure 3-12: Visualisation of the registration result in different perspective angles. In the top, all the MRI outlines (green) are superimposed on the overall MEG headshape (red) built from over 12,000 points. In the middle and bottom plates, the MEG points used in the surface matching process are shown as big red dots superimposed on the MRI skull outline points (green as before). Note the lack of MRI points at the top of the head (due to lack of data during MRI acquisition). The fit between MEG and MRI appears excellent in all views; however, the last figurine in the series, reveals that there might be an error of some 2-3 degrees in one angle (i.e. a mismatch of some 4-5 mm).

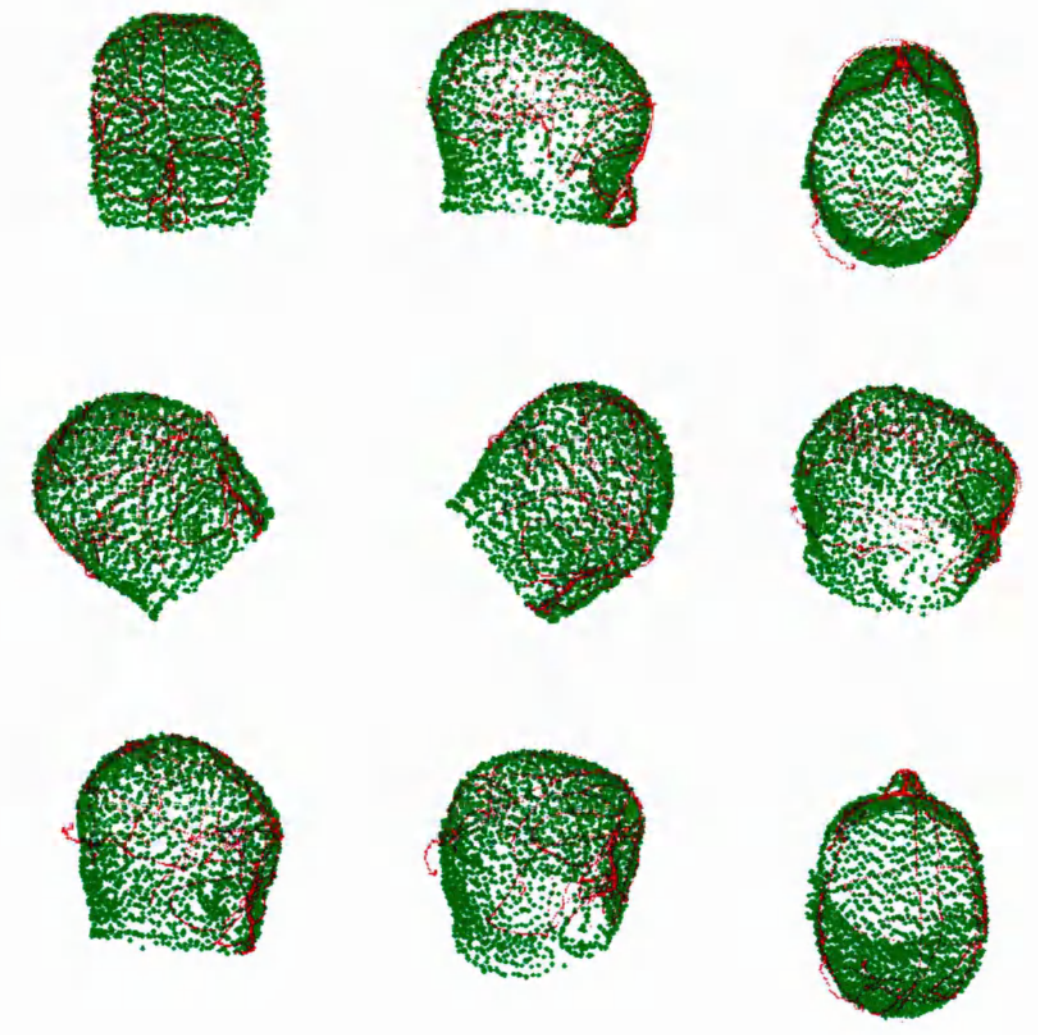

Figure 3-13: Another example of visualising the registration result in different perspective angles. MEG headshape (red) points are superimposed on MRI outlines (green). The fit between MEG and MRI appears excellent throughout. The RMS mismatch per point was 4 mm. See main text.

3.6 Discussions

3.6.1 In General

The accuracy we achieved in the simulations was in the 1.4-3.0 mm range; such an accuracy is very satisfactory if compared with the interslice MRI distances used (6 mm; 30-32 MRI slices used in total) and the simple way of determining the distance of the MEG points to the surface of the MRIs. The numbers of MEG points used are comparable with those that other MEG/EEG groups use in similar techniques. For example, Towle et al (1993) used 150 digitised points on the scalp and 64 MRI slices to get an accuracy of 2-3 mm; Gevins et al (1990) claim a 2 mm mean error distance resulted in EEG experiments when MR images with a 3 mm interslice spacing were used; Kober et al (1995) also claim a 2 mm accuracy achieved after fitting 300-2000 MEG points into 128 slices. Finally, Wang et al (1994) a total inaccuracy 3-6 mm when dealing with real data.

Despite the good simulation indications, however, the actual registration figures we have obtained in the last 2 years in the analysis of "real" MEG data, are usually in the range between 3-5.5 mm[+]. These values are greater than the previously quoted ones, however, as Wang et al (1994) note, they do seem adequate due to intrinsic resolution of the data and images. In MR images, misalignments are caused by sagging of soft tissue on the face and difficulties in reliably identifying scalp surfaces in the most lateral and most superior MR slices. In the MEG headshape acquisition, soft tissue (i.e. face) also causes a small error, since one cannot guarantee the immobility of flesh when the digitiser is in touch with it[*]. Very "hairy heads" might also cause additional problems, which can give rise to a few millimetres errors.

The latent assumption of the correctness of the MEG points should also be addressed here. Usually, the headshape is acquired prior to the actual MEG measurement: 3-5 "fiduciary" points are clicked in order to determine the MEG co-ordinate system. Then, the whole or parts of the head are digitised, assuming the subject kept his/her head still thoughout the duration of the digitisation process. However, the whole process might last a few to several minutes depending on the number of the acquired points. At the

---

[+] *However, the "real datasets" we have been using were always part of an actual MEG experiment (e.g. auditory odd-ball, CNV etc). In other words, we have never attempted any model experiments as such, in which all the individual steps would have been carefully followed to allow for a proper registration accuracy evaluation.*

[*] *One may need to consider the involuntary, tick movement of a subject too, when the digitizer touches the most sensitive points of the face, like for example those in the vicinity of the eyes, upper lips etc.*

end, the same fiduciary points are re-clicked, and the error is estimated. Such an error, might be as little as 0.1 mm but might be as much as 1.5 mm. If it is bigger than 2-3 mm the process should definitely be repeated, if the MEG data are considered to be accurate. After the subject is placed in the under the probe(s), the same as before fiduciary points have to be clicked again in order to obtain the sensor locations in the previously defined system. Usually, however, some of the points are not accessible, since they are covered by the probe(s). For instance, in an auditory experiment, one or both preauricular points are covered. The transformation of the sensor locations into the headshape system, might then be dependent on points along a 2D curve, like the midsagittal line, containing the nasion, C_z, and inion. This might cause problems, if the points clicked are not exactly the same ones. Redundancy is necessary in this case, and therefore a very detailed procedure is established now (Dammers et al 1995), which is trying to avoid such drawbacks optimising the overall process. A subject-specific mask is, therefore, used, and the fiduciary points are measured (using a flexible ruler) and marked with a pen. Extra points on the face, which will not be covered by the probe, are also marked, with the prospective that the sensor transformations will be based on more than 3 points and points more widely distributed. This procedure is doable, also even if a helmet like system is used, where the whole head (but not the face) is inaccessible. Finally, the forthcoming release of the BTi helmet system is supposed to be having a number of coils placed on the head facilitating dynamic head shape definition. It yet remains to be seen how much improvement in accuracy will this process add.

We have demonstrated in the previous sections that the RMS misfit per point is not an absolute criterion:

- point matching can give very good figures of RMS mismatch which may be completely wrong (see Figure 3-3).
- its value is averaged over the whole head surface; that is, it can have a significantly large value (e.g. 5 mm) due to some points only, while all the other points may fit the MRIs perfectly (e.g. Figure 3-13). Thus, pictures like those of Figure 3-11, Figure 3-12, and Figure 3-13 are very useful in judging the quality of registration results.

Optimising the way the distance to the MRIs for each MEG point is defined, for instance constructing a triangulated surface for the MRIs and then finding the intersection of the ray in Figure 3-8 with an appropriate triangle or its projection on a spherical surface (Kessler 1989), together with decreasing the MRI interslice distance (while increasing the total number of slices used), will further improve the resolution achievable. Such an approach may resolve problems like the slight nose mismatch in Figure 3-12, since obtaining the average point over a small radius might be inappropriate in rough

anatomical regions. Furthermore, automatic techniques for outlining the head contour on the MRIs, which is currently performed manually, will save time and also eliminate the possible errors from human interaction (although imposing computer generated errors).

It should be mentioned here that, so far, no consideration was taken on reducing the registration computing time. All the coding (including "PM", "PMALL") was implemented in FORTRAN 77, but in the most standard way, so that it can run under different computer platforms (compilers)/operating systems, like VAX/VMS, I860s, and DEC Alpha Workstations/Unix. Typical times[+] elapsed for registering a "head" model of ~2500 points, using ~100-200 MEG points are between 5-10 minutes on an Alpha Workstation, 10-20 minutes on an I860, and hours on a VAX/VMS (although timing on the latter cannot be accurately monitored, since it is a multi-user framework system at all times). Moreover, trying to fit the MEG points into the MRIs (i.e. keeping the MRIs solid, and transforming the MEG points) will decrease the computing time further, especially if a tiling procedure is attempted.

We finally wish to emphasise that the method of choice for registering MEG and MRI would be a combination of a point matching technique with a surface matching. Starting with point matching will provide a first quick estimate of the solution[†], and such an estimate can be used as a starting point in the stepwise surface matching we described. In addition, the locations of specific *a priori* known landmarks (e.g. nasion, nose, inion, preauriculars) together with the availability of a big number of MEG headshape points will ultimately provide a clue for the goodness of fit, which is not always absolutely obvious from the RMS misfit values. Figure 3-14 demonstrates the above points with adequate clarity. Initially, we have unregistered datasets (Figure 3-14 left), a very good estimate is provided by point matching (Figure 3-14 middle), and the fit is further improved using surface matching (Figure 3-14 right). In our experience, whenever point registration was considered as unreliable, surface matching improved the accuracy by 1-2 cm, while in the general case, an improvement of 1-4 mm was achieved.

Finally, the usefulness of point-matching in simple cases where different MRI sections need to be registered (e.g. see Figure 3-11) should also be appreciated, since it is very quick and can be accurate when corresponding points on the images are identified. We found it especially useful when registering different sections of MR images (e.g. coronals, sagittals etc.). We are going to show this with a last example, which possesses a clinical significance. It is drawn from the MFT analysis of an auditory evoked odd-ball

---

[+] *these are times of interaction and not CPU times*

[†] *in fact sometimes, can be as good and accurate as any other method*

experiment (Ioannides et al 1995b). In this experiment, three normal subjects and one patient were studied. The patient suffered from intractable epilepsy and had undergone surgery to remove part of the right medial temporal lobe. For all subjects, MEGs were recorded using a BTi Neuromagnetometer consisting of seven, second order gradiometers contained in a cryogenic Dewar. The stimuli were 50 ms tone bursts at 95 dB, delivered to the subjects' left ear through a long, plastic tube. The stimuli, a 1 kHz frequent tone appearing with a probability of 0.8 and a 2 kHz infrequent tone (odd) appearing with a probability of 0.2, were delivered at a rate of one per second. The subjects' task was to count and report at the end of each recording session the number of infrequent stimuli.

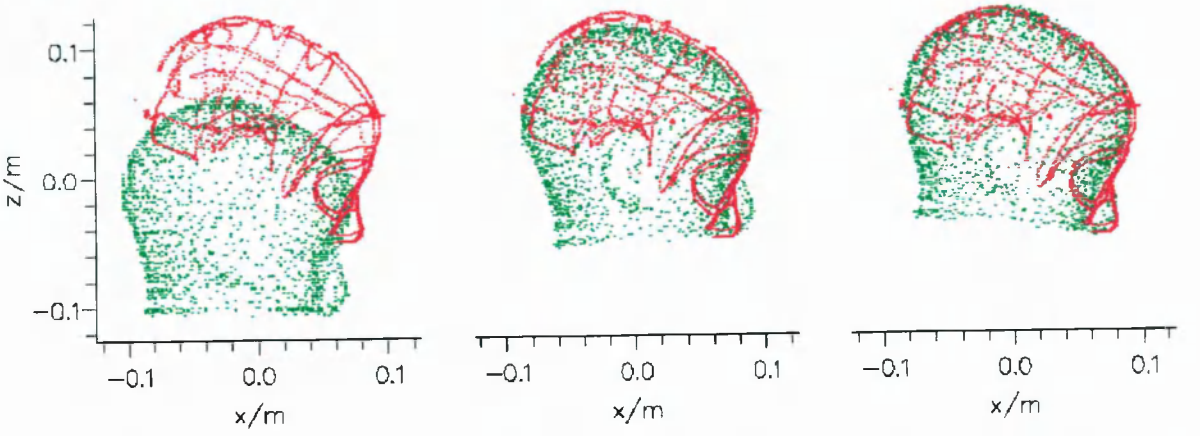

Figure 3-14: Skull outlines in MRI (green) and MEG (red) co-ordinate systems: before registration (left), after point matching (centre), and after surface matching (right). Surface matching improved the fit for some 3.5 mm.

The MEG signal for each subject was analysed using MFT. The resulting estimates of activity, at each time-slice, or integrated over fixed time intervals, were projected onto co-registered MRI slices of each subject. For the patient MRIs were taken both before and after surgery; he had participated in the odd-ball experiment only after surgery. However, only axial post-surgery MRIs were available. These and the pre-surgery axial sections were coregistered (using the combination of point and surface matching) with the MEG system and hence with each other; the presurgical coronal and sagittal sections were then registered to the MEG system using 3 points (nasion and 2 preauriculars). It is therefore, preferable to show the MFT estimates superimposed onto the early, and more complete set of MRIs, so that the amygdala-hippocampus complex is seen (which had been removed by the time of the experiment). The area affected by surgery is seen in Figure 3-15 (a) in one axial slice from the MRI set after surgery, and is also marked on three slices from the better set of MRIs obtained before surgery (Figure 3-15 (b,c,d)).

Figure 3-16 shows early responses: the MFT displays show instantaneous activity along a sagittal plane at the level of the right hippocampus. For all normal subjects examined, TB, KS (2 out of 3 shown), MFT analysis provides support for a very early activation in the depth of the temporal lobe; the precise timing of activation and the details of the distribution are different for each subject. Note the similarity for the responses to the frequent and infrequent stimuli. For the patient no activation is seen in the (removed) amygdala and hippocampal region (pink points outline the excision), but by 50 ms after stimulus onset a strong activity is established on the right side of the midline precentral area, which is usually associated with motor control. This area is the most prominent area of activity for the patient for both conditions. Unfortunately, similar data before surgery were not available, so it is unclear whether the activity has shifted after surgery or it was displaced earlier by the original pathology.

In Figure 3-17 instantaneous MFT displays of the intensity are shown, for the response to the infrequent stimulus just after the P2 peak, at three instances 190, 200 and 210 ms after the onset at the ear of the infrequent stimulus. Near medial sagittal slices containing the hippocampal amygdala complex are displayed, for subject KS and the patient JH. For KS the activity follows anatomical structures as it does for the patient; for the patient, however, the activity stops where the structure is absent.

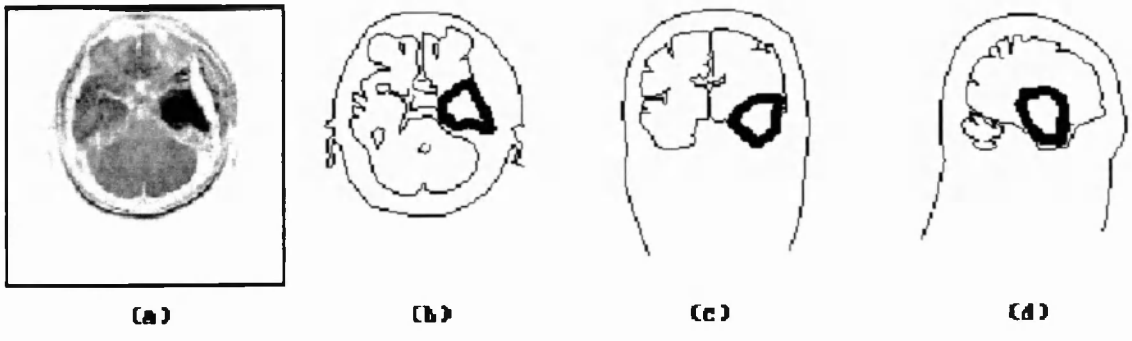

Figure 3-15: (a) Axial MRI slice of patient JH after surgery; (b, c, d) Skull and brain tracings for axial, coronal and sagittal MRI sections of the same subject before surgery. After aligning all sections with the MEG system, the part removed at surgery is outlined in the 1 cm thick slice (a), and its co-ordinates are transferred across into the 0.6 cm thick complete set of MRIs (thick line drawings).

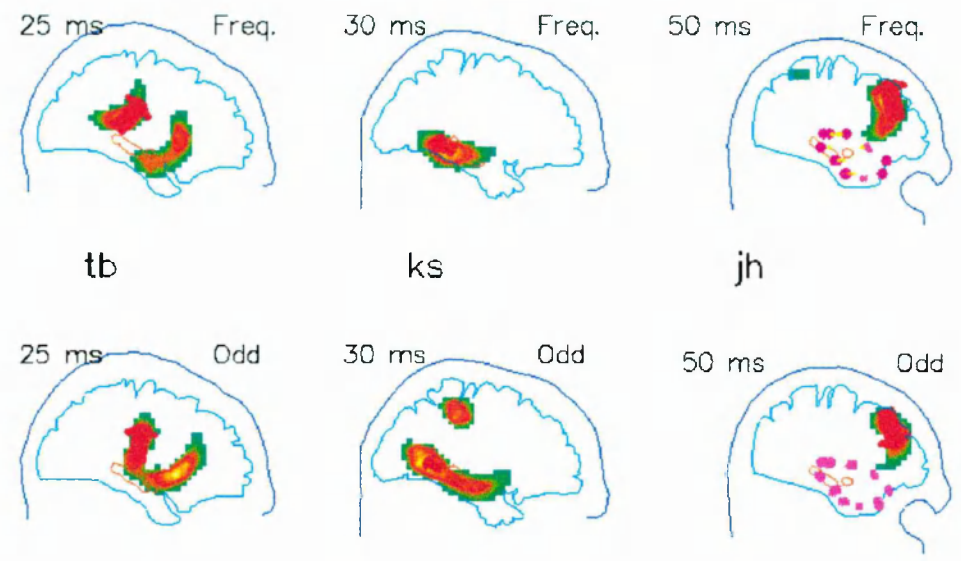

Figure 3-16: Instantaneous MFT displays for two normal subjects, TB at 25 ms and KS 30 ms after stimulus onset, and for the patient JH at 50 ms. A sagittal plane is shown, through the amygdala and hippocampus which are shown in outline. The level of activity at each time-slice is shown as colour coded contour plot of the modulus of the MFT estimate for the primary current density $|J(r,t)|$ (yellow > red > green); at the point of maximal strength an arrow is printed showing the projection of J along the plane of the display. For the patient, the tracing of the brain outline and amygdala and hippocampus were obtained from MRI slices acquired before the surgery. The pink dots mark the co-ordinates of the excised part that lie within 4 mm from the displayed MRI slice.

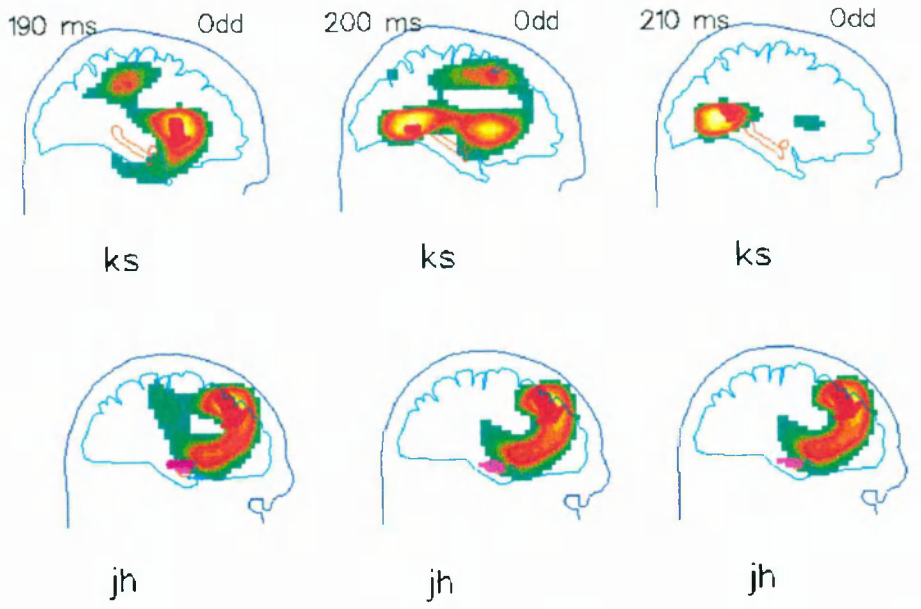

Figure 3-17: Instantaneous MFT displays similar to those in Figure 3-16, but for the period just after the P2 peak. In the top row the activity in response to the odd stimulus for subject KS appears to hover in the amygdala region before funnelling through the hippocampus at a latency of 200 ms. In contrast for the patient the activity arches towards the amygdala region without making progress, since the area was removed as indicated by the pink region.

3.6.2 The basis for future developments

The result of a registration accuracy in the millimetre range can serve as the basis for improving the "quality" of the MFT solutions, by bringing in complementary anatomical information to restrict the set of possible source configurations. For example, the source space could be restricted to be the volume occupied by the cortex as this is delineated in the MRIs of the subject. As techniques capable of reliably handling regions close to the centre of the head are developed, the source space can be made specific to deep brain nuclei like the thalamus or hippocampus. Under such improvements, the MFT analysis could be reformed to tackle physiologically interesting questions such as "what brain structures have become activated at a specific instant" and "what is the sequence of the activated structures over a time window in a specific experiment".

Moreover, the use of a standardised brain model for understanding the activation of the underlying anatomy seems now a realistic prospect. This would of course require further processing (registration) in order to register the subject-specific MRIs with a common average or an idealised brain model (atlas). This could be accomplished by finding specific landmarks on the MRIs (e.g. the bi-commissural line, the brain extrema) with

known co-ordinates on an atlas system (e.g. Talairach and Tournoux 1988). The latter would of course require to use points from different MRI sections. As the MRI data that we have been using so far have been acquired from multiple incidences (e.g. axial, coronal, sagittal sections) the registration of these is an important prerequisite, for which we are now confident to claim that is done with high accuracy. However, this problem needs special attention, since the formulation for a rigid body transformation we applied so far, must be extended to include a "plastic" transformation of the brain. In this case, the brain is scaled (stretched) along various directions in order to fit the standarised, general brain.

The development of a standardised atlas will allow for intersubject comparisons in a specific experiment. Furthermore, data from different modalities (e.g. PET) can be fused under the same reference frame allowing for an intermodality comparison and exchange of information. Transforming the individual datasets into a standardised anatomical platform (brain atlas) would mean that all brains will have the same anatomic appearance (Greitz et al 1991). Hence, all differences between individuals observed in MEG studies will be functional. This can be further extended to accommodate studies from different modalities such as PET, SPECT, fMRI. Ambitious world-wide projects envisaging the merging of diverse functional imaging modalities with neuroanatomical and neurochemical data into a common electronic database, are already on the way (Fox et al 1995; Mazziotta 1995).

The relatively high precision the implemented methods could offer is also very important in neurosurgical studies. MEG can be used to clarify situations where the anatomy of a patient (as appeared in MRI) is altered due to specific pathology (e.g. a lesion or tumour). Presurgical planning can be substantially improved if the MEG obtained information is utilised to reveal the function of the pathologically distorted brain areas. Kamada et al (1993) used somatosensory evoked MEG studies to guide neurosurgery operations of pathological somatosensory cortical regions. Consequently, the higher the accuracy of such a multimodal study is, the less hazardous the operations are.

In studies where epileptic patients are involved, a highly accurate localisation of the spread of epileptic discharges within the brain, as obtained by MEG, can aid stereotactic radiosurgery. Stereotactic radiation devices such as the *gamma knife* can be used to destroy sharply circumscribed volumes of pathological brain tissue as small as 50 mm^3 in a single session of radiation (Leksell 1971). Hellstrand et al (1993, 1995) studied the centres of focal epilepsy with MEG and successfully used the above device to treat epileptics.

3.6.3 Synopsis

The methods presented in this chapter represent a set of tools which allow the quantitative integration of 3-dimensional imaging datasets acquired with different modalities. Although the environment in which these methods were developed and tested was for the purpose of MEG/MRI fusion, no assumptions were made so as to exclude the application of the techniques in other studies (e.g. EEG/CT).

The precision achieved is comparable to that achieved in registering other modalities (e.g. PET/MRI). Such an accuracy is required to improve the quality of the MEG (MFT) studies, to allow for multimodal comparisons, and finally to expand the MEG application range into clinically useful circumstances.

4. Inverse Problem

In the previous chapter, we have explored ways of combining the MEG results with images of anatomy. The term MEG results actually refers to MEG solutions. In order to obtain the MEG solutions though, one has to solve the so-called biomagnetic inverse problem. This is in fact the topic of the present chapter. We first state the nature of the problem, and also describe important associated concepts. We then review the various methodologies employed worldwide only to place Magnetic Field Tomography (MFT) - the method we use throughout this thesis - in the general context of the biomagnetic field. MFT is finally described in greater detail at the end of the chapter.

4.1 In General

In the neuromagnetic inverse problem, the goal is to infer (or estimate) the distribution of cerebral currents from measurements of the magnetic field (and/or its spatial gradients). In most practical cases, the inverse problem entails a comparison between the actual measurements and those predicted by a theoretical model, leading to the determination of an optimal set of (model) parameters. The optical parameter set is chosen so that the data and associated constraints are "best satisfied". The expression "best satisfied" usually contains as a measure that the difference between theory and measurement is minimal. If the source configuration has a fixed geometry, the relative strength and orientation of the primary current density at each point in space is constant, and only the overall strenght is allowed to vary, then a single MEG (EEG) sensor would suffice to provide a precise description of the temporal variation of source strength, irrespective of how complex the generator and the conducting medium might be. In other words, the

bioelectromagnetic inverse problem can be uniquely solved (within a normalisation constant) for fixed sources (Ioannides 1994).

However, the situation is much more complex if spatial variations in source activity are allowed. As Helmholtz showed in 1853, it is impossible to uniquely determine the spatial distribution of activity within a confined volume from measurements of the surface potential and/or the magnetic field outside the body. To put it simply, there is an infinite set of different current distributions that could give rise to the same observed signals. The above statement expresses the "non-uniqueness" hurdle of the bioelectromagnetic inverse problem*

There are several reasons for this non-uniqueness. Firstly, there are primary current distributions that are either magnetically silent (**B**=0 outside the conductor, G), electrically silent (**E**=0 outside G), or both. A magnetically silent source that produces an electric field is a radial dipole in a spherically symmetric conductor (Figure 4-1a) as we saw in the second chapter. An example of an electrically silent source that does produce a magnetic field is a current loop (Figure 4-1b). A uniform distribution of primary current perpendicular to a closed surface generates neither electric nor magnetic field outside (Figure 4-1c).

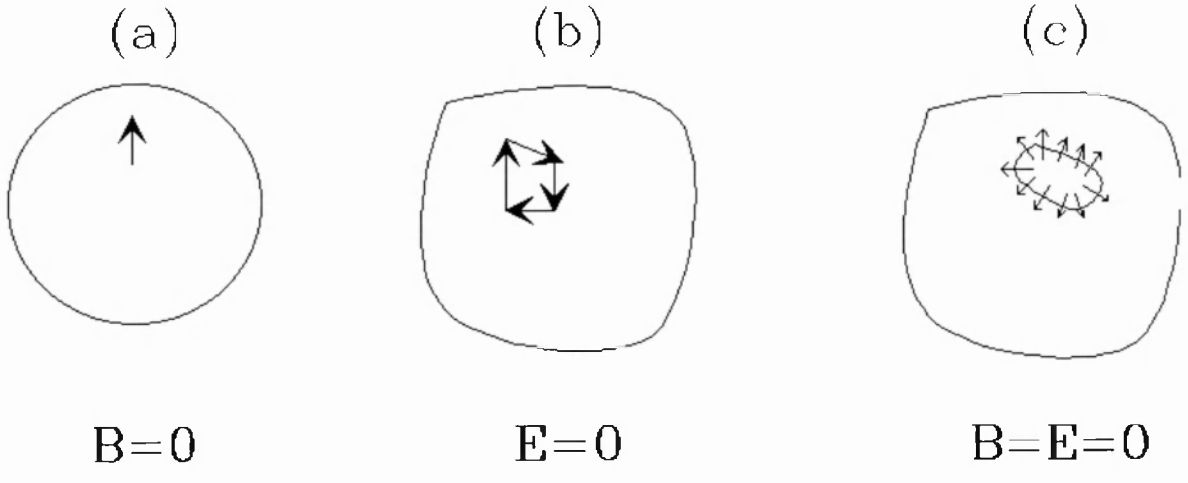

Figure 4-1: Examples of silent sources. (a) a radial current dipole is magnetically silent; (b) a closed loop of current is electrically current; (c) a uniform distribution of current perpendicular to a closed surface is both magnetically and electrically silent.

* *Another way of describing this, is by saying that the bioelectromagnetic inverse problem is "ill-posed".*

Secondly, any one magnetic detector (e.g. gradiometer, magnetometer) will only be sensitive to two out of three components of the current density, so some sources are "silent" for particular detector geometries. Of course, by using many different detectors it is possible to reduce this effect, but in each and every measurement system the problem of silent sources will remain.

Furthermore, it is possible for a complicated combination of currents to mimic the fields generated from a simple primary source. This is a cosequence of the superposition principle: if two or more sources are simultaneously active, then the overall field is the vector sum of the individual fields. For instance, if two dipoles are close together relative to the distance at which the field is measured, the resulting field is indistinguishable from that of a single different dipole. Moreover, the same field pattern may be reproduced by some current distribution too.

Because of the non-uniqueness, we must restrict ourselves to searching for a solution among a limited class of source configurations. Confining the family of possible solutions, usually involves the injection of *a priori* information into the inverse problem, which avoids non-uniqueness. Methods for handling this restricted inverse problem are the main topic of this chapter. We divide such methods into two general categories: first, those modeling the data by assuming a single or a small number of point sources being active at anyone time, and secondly those allowing for more realistic distributions of currents. It is not our intention to extensively describe every single method used worldwide. We rather describe the most important ones in a short but succint manner, and we then focus on the charcteristics of Magnetic Filed Tomography, which is the method we are going to utilise in this thesis. Before doing so though, we have to discuss an important physical concept that provides the connection between the measurements and the sensitivity of the sensors to model the various sources. That is, the concept of the *Lead Fields*.

4.2 Lead Fields

A magnetic (or electric) measurement can expressed as a linear function of the primary current density $\mathbf{J}^p$. Thus, if $m_i(\mathbf{r})$ is the output of the ith magnetometer located at $\mathbf{r}$, then there is a vector field $\mathbf{\Phi}_i(\mathbf{r},\mathbf{r}')$ satisfying:

$$m_i(\mathbf{r}) = \int_Q \mathbf{\Phi}_i(\mathbf{r},\mathbf{r}') \cdot \mathbf{J}^p(\mathbf{r}')du \tag{4-1}$$

$\Phi_i(\mathbf{r},\mathbf{r}')$ is called the lead field; it describes the sensitivity distribution of the *i*th magnetometer (Tripp 1983) and depends on the conductivity $\sigma=\sigma(\mathbf{r})$ and on the coil configuration of the magnetometer* . The integral extends over the volume Q, which is usually termed as the source space, i.e. the space where the primary current distributions are believed to by lying in. The output of the magnetometer is given of course by

$$m_i(\mathbf{r}) = \frac{1}{A}\int_{coil} \mathbf{B}(\mathbf{r})\cdot d\mathbf{S} \tag{4-2}$$

denoting the magnetic flux threading the detection coil of the ith magnetometer, divided by the area *A* of the pickup loop. The integration extends over the whole area of the detection coil.

The lead field as defined by Equation 4-1, is readily obtained if one computes the magnetic field $\mathbf{B}=\mathbf{B}(\mathbf{Q},\mathbf{r}')$, resulting from any dipole $\mathbf{Q}$ at any location $\mathbf{r}_Q$. However, knowledge of the conductivity profile $\sigma(\mathbf{r})$ is required so that the effect of volume currents can be properly taken into account. For $\mathbf{Q}$ located at $\mathbf{r}_Q$, $\mathbf{J}(\mathbf{r}) = \mathbf{Q}\delta(\mathbf{r}-\mathbf{r}_Q)$ and so Equation 4-1 becomes:

$$B_i(\mathbf{Q},\mathbf{r}_Q) = \Phi_i(\mathbf{r}_Q)\cdot\mathbf{Q} \tag{4-3}$$

Using Equation 4-3, all three components of the lead field can be obtained for any $\mathbf{r}_Q$. Furthermore, if the sensor consists of a set of planar coils with normals $\mathbf{n}_j$, j=1,...,m, we have:

$$B_i(\mathbf{Q},\mathbf{r}_Q) = \sum_{j=1}^{m}\int_{S_j}\mathbf{B}(\mathbf{Q},\mathbf{r}_Q)\cdot\mathbf{n}_j dS_j \tag{4-4}$$

where the directions of the normals nj have been chosen to take into account the winding sense of the coils, so that a field satisfying $\mathbf{B}\cdot\mathbf{n}_j > 0$ yields a positive signal at the output and vice versa.

When the conducting medium is modelled by a sphere, then the formulae of Equations 2-16 to 2-18 (Sarvas, 1987) can be used in association with the above two formulae to yield the expressions for the lead fields for specific sensor designs over a spherical conductor.

---

* *The lead fields* $\Phi_j^E(\mathbf{r},\mathbf{r}')$ *of an electric measurement* V_j *are given by* $V_j(\mathbf{r}) = \int_Q \Phi_j^E(\mathbf{r},\mathbf{r}')\cdot\mathbf{J}^p(\mathbf{r}')du$

where $V_j = \int_1^2 \mathbf{E}\cdot d\mathbf{l}$ *is the voltage between electrodes 1 and 2.*

$$\Phi_i(\mathbf{r},\mathbf{r}_Q)=\frac{\mu_o}{4\pi F^2}\left[F\mathbf{r}_Q\times\hat{e}_{coil}+(\hat{e}_{coil}\cdot\nabla F)\mathbf{r}\times\mathbf{r}_Q\right] \quad (4\text{-}5)$$

with F and ∇F given by Equations 2-17, and 2-18 respectively. By integrating over the gradiometer coils one can get a value for the lead field of an arbitrary gradiometer. If the conducting medium is modelled differently, then the magnetic field expression is different and so is Equation 4-5. For instance, Fieseler et al (1995) have calculated the analytic lead expressions for a homogeneous conducting spheroid, which is the simplest model with a more complicated geometry and reduced symmetry than the sphere.

In summary, lead fields are vector quantities affected firstly, by the relative location of source space and the detection coils (together with the coil orientation); secondly, since integration over the sensors is needed, the coil shape is of importance on the lead field pattern; and finally lead fields depend on the conductivity profiles, and hence different medium models have different effects on the lead field pattern.

4.3 Current dipoles

As already mentioned in chapter 2, when a small region of the brain is active, the resulting electromagnetic field is usually very close to that of a current dipole. The reason is that the dipole is the leading term in the current-multipole expansion and the field strength from higher terms dies off with distance more rapidly than that from the dipole (Katila 1983). Therefore, from a distance that is large compared to the extent of the source(s), any source configuration looks like a dipole, usually referred to as the equivalent current dipole (ECD).

Brenner et al (1978) were the first to reveal the dipolar appearance of the magnetic-field pattern due to a localised cortical current source underlying somatosensory evoked responses (fields). Since then, the analysis of MEG data has been largely dependent on models incorporating a single or more dipoles. Even today, the majority of MEG researchers still use such a simplistic model, although one can note a recently general movement towards more realistic models allowing for distributions of current. Although dipoles as such are not used as methods of study in this thesis, we shall briefly describe the dipole model analysis, mainly for historical reasons.

4.3.1 Single Current Dipole

In the early days of MEG, the estimates of the location, amplitude, and orientation of the dipole were based on a simple geometrical construction utilising the shape of the field map. Assuming that one measures B_z on the plane $z=z_0$ above a horizontally layered conductor, then the dipole parameters can be found from the pattern directly. The tangential location is midway between the field extrema, while its direction is

perpendicular to the plane passing through the minimum and the maximum and parallel to the z-axis. The depth, d, of the dipole is related to the distance Δ between the extrema, with the formula $d = \Delta/\sqrt{2}$. In other words, the depth is about 71% of the measured span of the extrema (Williamson and Kaufman, 1981). A similar approach can be followed in the case of a dipole embedded in a spherical conductor.

Since a radial dipole in a conducting sphere (or a dipole normal to the flat surface of a conducting slab) produces no external magnetic field, one should note, that any arbitrary radial dipole may be added to any derived tangential dipole (as estimated from the measurements) without distorting the field pattern observed*. Furthermore, the above treatment, assumed that only the radial component of the magnetic field is measured. The geometry of the skull in certain brain regions and the placement of the sensor make it unlikely that only this component is measured, in which case one has to take into account tangential components of the magnetic field as well. The latter means incorporating volume current effects, for which Ilmoniemi et al (1985) have derived expression allowing for an easy solution of the forward problem; the inverse problem then reduces to a search of parameters that produce results in best agreement with the measured data.

The most standard method of estimating the location and the direction of the current dipole (or even generally the configuration of any source) is by performing a nonlinear least-squares search. The dipole is assumed to be dynamic so that its location, orientation and strength are allowed to change with time; no temporal correlations are presumed, that is, each time instant (timeslice) is treated separately. This model is usually referred to as the moving-dipole model.

If m is the number of measurement locations (i.e. number of sensors), then assuming a conducting medium (e.g. sphere) and a dipole placed somewhere in a source space, one can calculate the theoretical values, b_i (i=1,m), predicted by the specific dipole using analytic expressions (e.g. those of Equations 2-16, to 2-18) for each measurement location. Determining the correct dipole in the least-squares sense then involves minimisation of the function G, with respect to the dipole parameters:

$$G = \sum_{i=1}^{m} (B_i - b_i)^2 \qquad (4\text{-}6)$$

---

* *Such a radial dipole will contribute a strong signal to the EEG measurement, thereby highlighting the complementarity between electric and magnetic measurements.*

The goodness-of-fit, g, is usually given by:

$$g = 1 - G \Big/ \sum_{i=1}^{m} B_i^2 \tag{4-7}$$

If g=1, the model agrees completely with the data. If g=0, the model is irrelevant and does not describe the measurements any better than any other random model would. Deviations of g from 1 are caused by measurement noise, but also by the inadequacy of the source model. A value of g greater than 0.9 is commonly assumed to be good enough, and ususally values of 0.96 or higher characterise ìgood solutions".

The problem of determining suitable and adequate confidence limits for the single dipole model has been the topic of discussion by several researchers. A fairly recent review by Hämäläinen et al (1993) highlights the most important aspects of the problem and contains full references. It is worthy to mention herein, the stringest selection criteria followed by various researchers in order to produce ECD solutions of clinical usefulness. For example, Vieth et al (1992) developed a method called Dipole-Density-Plot (DDP) capable of extracting concentrations of ECDs across time in a quantified way, by accepting only dipole localisations beyond a minimal singal-to-noise ratio (SNR) and beyond a minimal dipole density in a discrete spatial unit. Galen et al (1992) used signals filtered in the delta region (0-4 Hz) and correlation coefficients above 0.95 to study the slow wave ECD locations in patients.

We would finally like to emphasize a few more points of concern here. First, the uncertainties in the longitudinal direction (i.e. along the direction of the ECD) and in depth are higher than - usually double - those in the transverse directions (i.e. perpendicular to the dipole and its location vector). Second, since the modeling error is only weakly reflected in the goodness-of-fit measures, one always has to bear in mind that even if the fit is good the model itself might be misleading. The latter can be easily understood considering the resemblance between the field distributions produced by a single dipole, a side-by-side pair, and a dipole distribution along a line.

4.3.2 Multi-dipole models

The instantaneous state dipole, for which just a single timeslice of data is considered (typically at the peak of the observed MEG response), is the simplest of the dipole models. The obvious extension to the full temporal information is simply to treat each timeslice with a separate static model. At each timeslice the locations and moments are calculated for each dipole, independently of all other timeslices (moving and rotating dipole). The next generalisation can be accomplished by assuming multiple, spatially

separated dipolar sources. If the distance between the individual dipoles is sufficiently large (usually more than 4 cm) and their orientations are favourable, or if the temporal behaviours of the sources differ, the field patterns may show only minor overlap and they can be fitted individually using the single-dipole model. This approach has been successfully pursued to separate out activities from the first and second somatosensory cortices (Hari et al 1984).

However, if there is a temporal overlap, or the sources are close together in space, then one needs to resort to a multidipole model. In this case, the separate treatment of each timeslice has to be abondoned and the spatiotemporal course of the signals as a whole has to be effectively taken into account.

Three kinds of such models can be found. Since some researchers believe it is more realistic to assume that different parts of the cortex with different cortical function are activated electrically under specific tasks (George et al 1989), one could model the dipoles to have fixed locations and but allowing their orientations to vary with time (fixed location, unconstrained orientation). In the second model, the dipoles are not only at fixed locations, but they also have fixed unit orientation of their moments; the magnitude and the polarity of each moment are allowed to vary though (fixed location and orientation). This comes from the argument that, physiologically a dipole orientation should not rotate, because the dipole model represents a fixed neuroanatomical structure (Scherg and von Cramon 1985). Finally, the most general model contains both rotating and fixed dipoles.

Denoting the measured and predicted data matrices by M_{jk} and B_{jk} respectively, where j=1,...,n counts the meaurement points and k=1,...,m indexes the time instants under consideration, one has to minimise the (least-squares) cost function:

$$C = \left\| \mathbf{M} - \mathbf{B}(x_1, \ldots, x_q) \right\|_F^2 \tag{4-8}$$

where $x_1,...,x_q$ are the unknown model parameters and $\|\cdot\|_F^2$ denotes the square of the Frobenious norm (*Tr* indicates the "trace" of a matrix i.e. the sum of the diagonal elements):

$$\|\mathbf{R}\|_F^2 = \sum_{i=1}^{n} \sum_{j=1}^{m} \mathbf{R}_{ij}^2 = Tr(\mathbf{R}^T \mathbf{R}) \tag{4-9}$$

Perhaps one of the greatest problems in this sort of analysis is determining the number of dipoles. If too few are assumed, then the calculated dipoles are biased by the missing ones; if too many dipoles are specified, then spurious dipoles are introduced, which may

be indiscernible from the true dipoles. Since the computational cost and numerical sensitivity of most iterative minimisations increases dramatically with the number of parameters, then the choice of too many dipoles adds unnecessary computational burden.

Assuming p dipoles located at r_d, (d=1,...,p), and neglecting the radial component of each dipole (i.e. dipoles embeded in a spherical conductor, and measurements being insensitive to radial components), one can allow p_1 constrained orientation dipoles, and p_2 of unconstrained orientation ($p=p_1+p_2$). We are, therefore, seeking for $r=p_1+2p_2$ dipole source components - one for each constrained-orientation and two for each unconstrained-orientation dipole.

Under such conditions, the predicted data can be expressed as:

$$\mathbf{B} = \mathbf{GRQ} \tag{4-10}$$

where **G** is an nx2p gain matrix composed of the unit dipole signals, **R** is a 2pxr matrix differentiating between constrained- and unconstrained-orientation dipoles (which becomes the identity matrix if only rotating dipoles are assumed), and finally, **Q** is an rxm matrix containing the amplitude time series of the dipoles at each time instant.

But how is the correct choice for p_1 and p_2 accomplished prior to the minimisation stage? De Munck et al (1990) suggested a method based on an analysis of the singular value decomposition (SVD) of the measured data to perform this task. However, even if one selects the proper number of dipoles, r, needed to fit the data, there is still the remaining problem of dividing this number into p_1 and p_2 components so that $r=p_1+2p_2$ (Mosher et al 1990).

In order to deal with this problem efficiently, but also solve the least-squares system (Equation 4-8), the so-called MUSIC algorithm (MUltiple SIgnal Characterisation, Schmidt 1986) was introduced into the MEG analysis (Mosher at al 1992; Mosher 1993). This algorithm can be summarised by the following steps.

- Perform a SVD on the spatio-temporal data matrix $\mathbf{M} = \mathbf{U\Sigma V}^T$ and identify the rank, r, of the signal subspace from the break in the singular value spectrum $\mathbf{\Sigma}$. Partition the left singular vectors, $\mathbf{U} = [\mathbf{U}_s \mathbf{U}_n]$, into bases for the signal $\mathbf{U}_s$ and non-signal or noise $\mathbf{U}_n$ subspaces.

- Over a grid of 3d-locations, calculate at each location the corresponding forward gain matrix of a "regional" dipole source located at the point, and compute its SVD, $\mathbf{G} = \mathbf{U}_G \mathbf{\Sigma}_G \mathbf{V}_G^T$. For each location, evaluate the "MUSIC metric" for a fixed-orientation

dipole, $J_h = \lambda_{max}\left\{\mathbf{U}_G^T\mathbf{U}_s\mathbf{U}_s^T\mathbf{U}_G\right\}$, that is, the maximum eigenvalue of the expression in brackets. Then, form 2d slices through the 3d space and plot the quantities J_h seeking for their maxima (peaks).

- At each peak, check to see if there are multiple closely spaced sources by computing the "rotating" or "regional dipole metric" $J_r = \left\|\mathbf{U}_s^T\mathbf{U}_G\boldsymbol{\Sigma}_G\right\|_F^2 \Big/ \left\|\boldsymbol{\Sigma}_G\right\|_F^2 = \left\|\mathbf{U}_s^T\mathbf{G}\tilde{\mathbf{G}}\right\|_F^2$ with $\tilde{\mathbf{G}}$ being the normalised gain matrix. Sources where $J_r \approx J_h \approx 1$ must be represented by a dipole with varying orientation. For fixed-dipoles (only), estimate dipole orientation by calculating the eigenvector associated with λ_{max}. Repeat this analysis until p_1 fixed dipoles and p_2 rotating dipoles are found, so that $r=p_1+2p_2$.

The appeal of this method is that "scanning" is performed quickly with a one dipole search, rather than the r-dipole search necessary in a complete fit. The method seems to produce reasonable results with both real and simulated data. However, if there are strongly correlating sources with overlapping field patterns, the predictions might be misleading. Thus, Mosher et al (1995), have also incorporated a Monte Carlo approach to testing the "goodness" of the various MUSIC peaks, after the data have been initially scanned. One should always recall though, that if the head (conductivity profile) and more importantly the source (i.e. dipole) models are incorrect, then the algorithmn would fail to explain the data - a statement which also applies, of course, to all other source models as well.

4.4 Current distribution models

Instead of working with point like source models as those described above, more general and realistic solutions of the inverse problem can be attempted. In order to avoid the non-uniqueness ambiguity though, one has to make some restrictions by including some kind of *a priori* information. In this case, however, the restrictions will not be associated with the model itself, but they might for instance limit the volume or generally the space where one should seek for sources. The first ever such attempt, was the minimum-norm estimates attributed to Hämäläinen and Ilmoniemi (1984). However, the first three dimensional current distribution reconstructions (MFT) were developed here at the Open University by Ioannides and collegues in late 80's to early 90's. Other methods started appearing fairly recently, but no other method has been tested that extensively with real data as has MFT been.

In the following, we will review the current literature on distributed source modeling. Apart from the Fourier-space method, all the others make use of the lead field definition of section 4.2. Under this concept, the non-uniqueness of the inverse problem can be

framed as follows: only current distributions that yield $m_i \neq 0$ for at least one i in Equation 4-1 can be detected.

4.4.1 Fourier Imaging

This imaging method is a matrix inversion reconstruction based on the Fourier transformed Maxwell equations in combination with sampling theorems (e.g. the Whittaker-Shannon sampling theorem). It was proposed by Dallas (1985), who took the Fourier transforms of Maxwell equations (Equations 2-4 iii,iv) to obtain a set of linear equations relating the current and magnetic fields. By sampling the Fourier transform of the two fields and decomposing the magnetic field into two regions, the measurement region and a "forbidden region" over which the field cannot be measured (the forbidden region characterises the biological object, wherein the currents are located, i.e. head), a large set of linear equations can be formed. The unknowns in the equations are the samples of the Fourier transforms of the magnetic field in the forbidden region, and of the current field in a reconstruction region. The reconstruction space, is the region of interest, where the current density distribution is reconstructed - it is enclosed by the forbidden region (Kullmann and Dallas 1987).

In the algorithm, the reconstruction and the regions are discretised into sample cells; for instance, a whole simulation space could be composed of 32x32x32 equidistant pixels, divided into three parts consisting the three mentioned regions. The density of the sampling points is determined by the sampling theorem.

Such a formulation has the advantage that it provides simultaneous reconstruction of the internal current and magnetic fields It does not, however, eliminate the ill-posed nature of the problem or reduce the null space of the system matrix which leads to the infinite set of possible solutions. Early computer simulations reconstructed complex, but planar only, current distributions; they seemed to be quite robust, independent of any special generator model, and rather stable against external noise of the magnetic field (Kullmann and Dallas 1987). At a later stage, the method was successfully applied in three dimensions given *a priori* information about the depth of the sources. However, in the lack of such information, the determination of the depth, and therefore the correct current reconstruction, was based on a rather empirical, and inefficient rule of discontinuity in the imaged current density occurring just above the right location of the source (Kullmann et al 1989).

More recently, the method was extended to incorporate the calculation of volume currents for arbitrary conductivity distributions, but also to allow for injecting more general *a priori* information that would resolve the undetermination of the equations set

(e.g. one such assumption could be that the z-component of the current density is zero in the entire reconstruction region). The simulations though, were severely dependent on the different assumptions and approximations made (Dallas et al 1992). Moreover, the method has not been used with real data yet.

4.4.2 Lead Field Synthesis or Spatial Filter Imaging

Spatial filtering is a signal processing technique developed to enhance the SNR of spontaneous MEG measurements, and generally allow for the analysis of unaveraged MEG data (Robinson 1989; Robinson and Rose 1992). The spatial filter used by this method is a linear projection operation in which the target parameters (e.g. the co-ordinates and the current vector), spatial selectivity, and SNR are determined for each voxel of the source space (i.e. 3d brain volume) by an array of coefficients w_i (i=1,...,M; M is the number of physical sensors).

Given Equation 4-1, the filter output or "virtual sensor" for position and orientation parameters is then:

$$m_v = \sum_{i=1}^{M} m_i w_i^v \tag{4-11}$$

implying that the synthesized lead field (or spatial response of the virtual sensor) is

$$\Phi_v(\mathbf{r}) = \sum_{i=1}^{M} \Phi_i(\mathbf{r}) w_i^v \tag{4-12}$$

The filter coeeficients are then computed through a minimisation of the difference between the synthesized lead field and an ideally selective delta function, defined as unity at target v:

$$C = \int_{Q} \left[\Phi_v(\mathbf{r}) - \underline{\delta}^v(\mathbf{r}) \right]^2 dr^3 \tag{4-13}$$

However, Robinson and Rose (1992) suggested alternative and more useful ways of obtaining the array of spatial filter coefficients, though the use of a covariance matrix of the measured data and the fowrard solution for the physical sensors due to target dipoles at v, so that the interfering signal portion unrelated to the target parameters is minimised. At the final stage, an image of either the time-integral or instantaneous source activity is created by projecting the measurements through an array of regularly spaced spatial filters, representing each voxel in the image.

Dipolar sources are identified by scanning the image for local peaks of signal intensity, and it has been shown with simulations that a localisation with 1 mm accuracy can be

achieved. The method was also applied to real auditory data suggesting the existence of distributed rather than point-like sources for middle to late N100 and P200 components.

Based on this methodology, Grummich et al (1992) developed an algorithm which they named Current Localisation using Spatial Filtering (CLSF). They used MEG measurements of a patient with a cerebral cyst to validate CLSF by showing the constant - in time - activation of a region close to the cyst.

More recently, Spatial Filtering was expanded and was given the acronym SAM (Synthetic Aperture Magnetometry) (Robinson 1995). In the SAM approach, one stipulates a source location (the "target") relative to an array of sensors. A set of linear beamsteering coefficients are computed using the measurement statistics (in the form of the covariance matrix) together with the forward solutions for each individual sensor. The measurements are then projected through the beamsteering coefficients. The result is a time-series estimating source activity at the target. In practice, one can easily (in real time) see single trial auditory evoked response, with no signal averaging or bandpass filtering. The constraint is provided by the MEG measurement, itself (Robinson 1995).

The same measurements can also be projected through coefficients specific to other targets. The result can also be displayed as a time-evolving source intensity map. The processing power needed is rather minor making SAM very promising. However, real, successful applications of this technique are yet to be seen.

4.4.3 Minimum norm estimates

When refering to current distributions as elements of a current space G - the source space Q into which J^p is confined could then be a curve, a surface, a volume, or a combination of discrete points - the inner product of two such elements $\mathbf{J}_1^p$ and $\mathbf{J}_2^p$ is defined by:

$$\left\langle \mathbf{J}_1^p, \mathbf{J}_2^p \right\rangle = \int_Q \mathbf{J}_1^p(\mathbf{r}) \cdot \mathbf{J}_1^p(\mathbf{r}) dV \tag{4-14}$$

The amplitude of a current distribution is defined by its norm:

$$\left\| \mathbf{J}^p \right\| = \sqrt{\left\langle \mathbf{J}^p, \mathbf{J}^p \right\rangle} = \left[\int_Q \left| \mathbf{J}^p(\mathbf{r}) \right|^2 dV \right]^{1/2} \tag{4-15}$$

The minimum-norm estimate (MNE) (Hämäläinen and Ilmoniemi 1984, 1994) is a current distribution with the smallest possible norm that explains the measurements. It is the best estimate for $\mathbf{J}^p$ provided that all prior knowledge about the primary current is

limited to specification of the source region Q only, and if "best" is taken to mean that the expectation value of the integrated error $\int_Q \left(\mathbf{J}^p_{est} - \mathbf{J}^p\right)^2 dV$ is minimised.

Given a set of M measurements m_i, one can only obtain information about primary currents lying in the subspace of G that is spanned by the lead fields. Using Equation 4-1 and Equation 4-14, we can now express m_i as $m_i = \langle \Phi_i, \mathbf{J}^p \rangle, \quad i = 1,\ldots,M$. In other words, a magnetic field measurement is seen to constitute a projection of a current vector on the lead field. The current components that lie in the space not spanned by the lead fields (i.e. in the complement space of Q) are assumed to be zero (e.g. silent components). The current density estimate can then be expressed as a linear combination of the lead fields:

$$\mathbf{J}^p_{est} = \sum_{i=1}^{M} w_i \Phi_i \tag{4-16}$$

where w_i are the weights depending on m_i. Forcing $\mathbf{J}^p_{est}$ to reproduce the measurements, we obtain a set of linear equations $\mathbf{M} = \Gamma \mathbf{w}$, with $\mathbf{M} = (m_1, m_2, \ldots, m_M)^T$, $\mathbf{w} = (w_1, w_2, \ldots, w_M)^T$, and $\Gamma_{ij} = \langle \Phi_i, \Phi_j \rangle$ is an MxM matrix. In this notation Equation 4-16 can be written as

$$\mathbf{J}^p_{est} = \mathbf{w}^T \Phi \tag{4-17}$$

where $\Phi = (\Phi_1, \Phi_2, \ldots, \Phi_M)^T$. The formal solution for the weights is $\mathbf{w} = \Gamma^{-1}\mathbf{M}$. The current distribution with the smallest norm* among those producing the measured signals is given by

$$\mathbf{J}^p_{est} = \mathbf{w}^T \Phi \tag{4-18}$$

This kind of solution though, has the disadvantage of usually being very unstable, and the result being highly dependent even on small amounts of noise or numerical errors. It is therefore necessary to regularise the solution by suppressing those components of $\mathbf{J}^p_{est}$ that are "poorly coupled to the sensors". A widely used approach, is to truncate the sum of the components, so that those dominated by noise are zeroed. Another way, is to deliver weights to the different components according to their SNRs (Ilmoniemi and Numminen 1992). The regularised solution is then:

---

* *This is also known as the Moore-Penrose inverse.*

$$\mathbf{J}_{est}^{P} = \left(\tilde{\Gamma^{-1}} \mathbf{M} \right)^{T} \Phi \tag{4-19}$$

where $\tilde{\Gamma^{-1}}$ is the regularised inverse of Γ.

It should be emphasized that this estimate is optimal only when the assumption about the source space is valid and no additional prior information is available. Therefore, the MNE is useful for routine displays and as a starting point for further analysis (Ilmoniemi 1994).

In fact, this is exactly what Wang et al (1992, 1993) have recognised. They used the minimum-norm method, but assumed that the source space could be restricted to the cortical surface, represented as an L-shaped wall consisted of two vertical planes (Wang 1993) and also by a two-sheeted hyperbolic cylinder modeling a sulcus (Wang et al 1995c) or even more such sulci and gyri together (Wang et al 1995b). They also made the additional assumption that the current should always be directed normal to the cortical sheet (i.e. source space) for all the reasons presented in Chapter 2. In practice, they computed the inverse from a set of a big number of nodes distributed across the cortical surface and representing the locations of current dipoles that comprised the current image (e.g. 750 such dipoles, Wang et al 1995b)

This method was given the name Minimum-Norm Least-Squares inverse (MNLS) but is also known as "constrained minimum-norm estimates". It was later expanded to include the time-dependent solution in a spatio-temporal model (Wang et al 1995a), where the temporal dimension was incorporated in the previous notation tranforming the column vectors of the measurements and solutions into matrices. This also allowed the calculation of time-averaged solutions and field powers in order to image "significant regional changes" in the spontaneous brain activity elicited in specific cognitive tasks (Wang et al 1993).

Although this technique seemed to produce robust images of current distributions, it has only been employed so far for the cortical mantle, thereby excluding the study of subcortical nuclei. Moreover, the representation of the source space as a subject-specific cortical surface contains obvious hazards for all the reasons mentioned in Chapter 3. That is, the model will be expected to perform well, only and only if the coregistration of the MRI and MEG systems is very accurate, and if the subject was completely immobile during the MEG recordings.

Another interesting approach based on minimum-norm and regularisation methods and using morphologically constrained current density distributions, where the

reconstruction space is limited to physiologically relevant structures, is the so-called Cortical Current Imaging (CCI, Fuchs et al 1995). This method also makes use of the whole temporal range instead of signle time-instants (Wischmann et al 1995). The cortex is segmented from individual anatomical data (i.e. 3d MR images - and so the previously mentioned precautions on coregistration errors hold true here too); the volume of interest is given by the sensitivity range of the MEG measuring device - usually a cylindrical volume attached to the cryostat. Subsequently, the points representing the segmented cortex are subsampled into patches arranged as closely as possible on the manifold (Wagner et al 1995).

The computation of the CCI, which is a discrete approximation of the current density in the cortex, ivolves "design-dipoles" located at the cortical points with an orientation again normal to the calculated local surface are used to set up the lead field matrix. A depth normalisation is carried out by assigning each design-dipole a strength proportional to the second power of its mean distance from the measuring coils. Therefore, only one linear parameter per reconstructed dipole is aimed, which is the strength relative to that of the design-dipole. An iterative scheme is also employed, where after each step, the points holding the smallest currents are discarded in the subsequent iterations. Each iteration uses a bigger number of points in consideration and a smaller number of currents. The stopping-criterion is usually the deviation between the reconstructed and the measured magnetic field. This method also seems robust and promising[+], but only cortical reconstructions have been obtained so far, with only a limited number of physiologically interesting results.

Finally, another interesting and indeed very promising inverse algorithm called FOCUSS (FOCal Undetermined System Solution) has recently become available (Gorodnitsky et al 1992; Gorodnitsky 1995), claiming that it can accurately resolve the depth and extent of sources, including point sources. The essense of the algorithm is the iterative application of weights derived from the previous reconstruction. Here again, the minimum-norm solution consists the initial step of the process; it is restricted, however, in an one-voxel-thick region along the surface of the model volume (the volumetric model may contain 32x32x32 or 16x16x8 voxels determining a sphere sometimes grooving in the surface to represent the cortical sulci). A procedure is then employed in which the weight vector is

---

[+] *The method has been recently renamed into the prosonym "CURRY" (current reconstruction and imaging) and comprises a software package (developed in the Phillips GmbH research laboratory) and commercially distributed world-wide by Neuro Scan Inc (Neuro Scan News, 1995).*

replaced by the new solution, or multiplied by the new solution, or the normalised basis matrix* is multiplied by the new solution. This can be thought of as concentrating the solution around the true sources untill they are resolved sufficiently well. The reconstructions are performed in an hierarchical manner, where a coarse reconstruction grid in the beginning is systematically increased in resolution if there is an indication of a source in this region.

The algorithm was tested against simulated data, and it only failed on certain "difficult" source distributions. The problems under current consideration include the initialisation step, and the iteration stoppping-criterion. Improvements of the algorithm based on "genetic schemes" combined with stochastic processes are also under development (George et al 1995a).

4.4.4 Magnetic Field Tomography (MFT)

MFT was the first technique capable of recovering reliable estimates for the full three dimensional for the primary current density distribution. It was developed and implemented at the Open University, UK (Ioannides et al 1990a) and a review describing the logical and algorithmic steps of MFT has been published recently (Ioannides 1995b), together with a longer description highlighting the historical links with EEG which slowed down the development of MEG analysis (Ioannides 1994).

MFT is based on a probabilistic treatment of the inverse problem (Clarke and Janday 1989; Clarke 1989), where the expected current density $\mathbf{J}^n_{est}$ is expressed as a linear combination of expansion functions:

$$\mathbf{J}^p_{est}(\mathbf{r}) = \sum_{i=1}^{M} A_i \Phi_i(\mathbf{r}) w(\mathbf{r}) \tag{4-20}$$

where M is the total number of sensors, $w(\mathbf{r})$ is the a priori probability weighting function defined throughout the source space Q and incorporating any prior information about source location, and A_i are coefficients of the expansion functions. The latter can be determined using Equation 4-1 and Equation 4-20 through a set of linear equations:

$$m_i = \sum_{j=1}^{M} \mathbf{P}_{ij} A_j \tag{4-21}$$

where the matrix **P** is described using the definition of Equation 4-14:

---

* *Each column of this matrix receives a source-voxel normalisation, based on the average distance from the particular voxel to all sensors.*

$$\mathbf{P}_{ij} = \left\langle \Phi_i, \Phi_j w(\mathbf{r}) \right\rangle = \int_{\Omega} \Phi_i(\mathbf{r}) \cdot \Phi_j(\mathbf{r}) w(\mathbf{r}) dV \tag{4-22}$$

If **P** is suffieciently non-singular, it is obviously possible to invert Equation 4-21 and obtain the coefficient values A_i, and subsequently from Equation 4-20 the estimate for the current density.

However, some of the lead fields may inevitably be linear combinations of others, rendering **P** singular or almost singular. An SVD technique can be used at this point to turn **P** into non-singular; another alternative was initially followed, where a smaller subset of expansion functions is used, so that

$$\mathbf{J}^p_{est}(\mathbf{r}) = \sum_{i=1}^{t} A_i \Phi_i(\mathbf{r}) w(\mathbf{r}), \quad t \le M \tag{4-23}$$

The choice of t and the selection of sensors is of importance though: one wants to avoid singularity, and, therefore, t could be chosen to be as small as possible, and sensors farther away from one another could be selected so that their individual lead fields are independent; if t is too small though, then spatial resolution is reduced, although the solutions become significantly stable. The choice of eliminating sensors was useful for carrying out tests investigating how resolution improved with increasing the number of sensors.

A way of controlling the resolution versus noise sensitivity is through regularisation; a regularisation parameter, ζ, is introduced so that,

$$\tilde{\mathbf{P}}_{ij} = \sum_{k=1}^{M} \left[\mathbf{P}_{ik} \mathbf{P}_{kj} + \zeta \mathbf{P}_{ij} \right] \tag{4-24}$$

Equation 4-21 is then replaced by the square system

$$\tilde{m}_i = \sum_{j=1}^{t} \tilde{\mathbf{P}}_{ij} A_j \tag{4-25}$$

where

$$\tilde{m}_i = \sum_{j=1}^{M} \mathbf{P}_{ij} m_j \tag{4-26}$$

For convenience, the dimensionless quantity $\tilde{\zeta} = \zeta M / Tr(\mathbf{P})$ is introduced in such a way that unity marks a rough divide between large and small values of currents. In practice, $\tilde{\zeta}$ is progressively decreased until the characteristic transition to large sensitivity to noise

is reached; a value at least twice the critical value is then chosen*. For such a choice, $\tilde{\mathbf{P}}$ is positive definite and numerical problems are eliminated.

In the limit where $\tilde{\zeta} \to 0$, and $w(\mathbf{r})$ is constant throughout the space, the method reduces to the minimum-norm approach (Hämäläinen and Ilmoniemi 1984) described previously. The effect of the regularisation process is achieved through the elimination of huge and physiologically meaningless currents. This becomes obvious considering the system with M=t=1 (we ignore for this purpose the relation $\tilde{\zeta} = \zeta M/Tr(\mathbf{P})$, since we want to let P11 tend to zero but retain a non-zero value for $\tilde{m}_1$). From substitutions into previous equations we get:

$$A_1 = \frac{m_1}{P_{11} + \zeta} \tag{4-27}$$

which leads to

$$\mathbf{J}^p_{est}(\mathbf{r}) = \frac{m_1}{\mathbf{P}_{11} + \zeta} \Phi_1(\mathbf{r}) w(\mathbf{r}) \tag{4-28}$$

Given that $\mathbf{P}_{11}$ cannot be negative - **P** is positive definite - the smallest value it can get is zero. In that case $\mathbf{J}^p_{est}$ will only have a maximum value rather than infinity, thereby restricting the likelihood of huge current densities.

The first solution obtained $\mathbf{J}^p_{est,0}$, is subsequently iterated by repeating the inversion, with a new probability weight, which is the product $\mathbf{J}^p_{est,0} w(\mathbf{r})$. This weighting factor is applied to sharpen up the image. In fact, Ioannides et al (1990a) also carried out extensive tests in which the square or the square root of the first current density estimate was multiplied by the probability weight in order to form the product used as the weighting factor in the second iteration. It was empirically shown, that using the square lead to elimination of small but significant source elements, while using the square root provided too slow a convergence. With a weighting function proportional to the magnitude of the current density the iterative scheme converged within one iteration, leading to distributed solutions with fine detail. The major disadvantage of this scheme though, is that it imposes heavy computational demands, because for each timeslice a

---

* *In the current software implementation, the user varies* $\tilde{\zeta}$ *through the use of a "smothing parameter", s, which is defined by* $\tilde{\zeta} = 10^{-s}$.

new matrix must be computed; these have been satisfied in the OU implementation by a 30-node transputer array (Liu et al 1993) and very recently by fast UNIX workstations.

The source space used with the above described algorithm can be extended up to regions from which physiologically reasonable activity produces signals just above the noise level; the depth is chosen so that sources throughout the source space can be correctly localised with a simple form for $w(\mathbf{r})$. The definition of the source space Q is very flexible and can be a cylinder, a (part of a) hemisphere with its curvature adjusted to follow the subject's brain or even any other shape that one may desire for specific analyses* (Liu MJ and Ioannides 1995). Although Q is a real 3d volume and the solutions continuous functions, Q is usually cut in 9 levels (each level is comprised by 17x17 pixels) and the solutions displayed along these cuts (tomes) often parallel to the plane or surface of sensors, so that the relative sensitivity within each slice is constant. Such displays are referred to as MFT images and they can then be fused with the subject's/patient's MRIs, provided the success of the registration procedures described in the previous chapter.

A Gaussian shaped weighting function that increases monotonically with depth has been used so far, with the only adjustable parameter being the rate of decay, chosen through tests with computer generated points sources+. All this function is doing, is that it stretches the lead fields towards depth, thereby redistributing the sensitivity - which is otherwise "wasted" in the area just below the sensors; it also improves the resolution in Q, and it is necessary for the recovery of deep activity.

The enhancement of deep generators though, is not complete, since the strength of a deep source is considerably reduced compared to the strength of a similar superficial source. In other words, we can "see" something deep, only if it is strong enough, and not simultaneously active with a superficial generator of similar strength. This should not lead to confusion, that MFT can recover either superficial or deep activity but not both. Provided that the superficial source is considerably less strong than the deep one, MFT can recover both even if they are simultaneously activated. Moreover, the overall uncertainty in relative strength at different depths does not change with time, and the time dependence of the solutions provides a reliable estimate of how the relative power between superficial and deep activity varies with time (Ioannides 1995b).

---

* *For example, one could use MRI slices to restrict the source space within the gray matter. However, such an approach has not been pursued so far.*

\+ *The other adjustable parameter is the previously mentioned smoothing that controls the regularisation. Routine tests for both of these parameters are presented in the following chapter.*

Although an algorithm incorporating temporal constraints has been presented (Alavi et al 1993) it has not been fully tested yet, and no such constraints have been used with MFT so far. This is similar to the instantaneous dipole modeling with one major difference though: although the current density estimate is obtained separately at each time instant activity seems to be varying smoothly with time. To put it differently, activity does not "jump" abruptly from region to region, but as one region becomes less active another one appears and gains strength progressively, to finally become the most strongly activated area and so forth. This is in agreement with the common sense in one's understanding of brain function.

Finally, in the MFT analysis, one usually displays the intensity $P(\mathbf{r},t)=\left|J^{p}_{est}(\mathbf{r},t)\right|^{2}$, with the practical advantage of dealing with a (positive) scalar than a vector. Post-inversion processing can be applied to $P(\mathbf{r},t)$ as a consequence of the fact that the intensity is always positive. Integrals of intensity in space and time can be employed by MFT leading to i) measures of activations in time, $A(t)$, in a region of interest (ROI)# :

$$A(t)=\int_{t-\frac{\delta t}{2}}^{t+\frac{\delta t}{2}} dt' \int_{ROI} P(\mathbf{r},t')dS \tag{4-29}$$

or ii) displays of temporal integrals of intensity $I(\mathbf{r},t)$

$$I(\mathbf{r},t)=\int_{t-\frac{\delta t}{2}}^{t+\frac{\delta t}{2}} P(\mathbf{r},t')\mathrm{d}t' \tag{4-30}$$

By selecting certain ROIs and/or time intervals δt the dynamic aspects of brain activity will appear at different spatio-temporal scales.

In conclusion, MFT offers a powerful tool for solving the inverse problem. It can reveal the number and locations of activated areas, under the prior assumption that there exist only a small number of localised sources at any one time. Moreover, it offers the capability of studying both superficial and deep activity. A number of new techniques have recently been proposed and many of them follow identical or similar steps as MFT

By ROI we imply a square subregion of a source space level, but there is generally no limitation in this, so that 3-dimensional ROIs could be implemented in the future, provided that integration in the follwoing formula is curried out through volumes rather than planar regions dS.

(e.g. the FOCUSS algorithm+). However, the way the source space definition is coupled to the sensitivity profile of the sensors and the brain outline, the tests undertaken for the selection of the smoothing parameter and the probability weight - and in particular the way the latter is incorporated in the iterative process - together with the concept of using the intensity (or its spatio-temporal integrals) are original and unique to the OU algorithm. Up to date, MFT has been tested not only with computer simulated data, but also with evoked MEG responses (Ioannides et al 1993a), and with MEG signals generated by dipoles implanted in the head of an epileptic patient (Ioannides et al 1993b). In all these early studies MFT's localisation capability was compared with that of ECD models and it was found to be suprisingly good. It was also shown, that MFT could cope with activity spread over different regions, a situation where the ECD failed. More recent MFT studies have shifted towards more realistic studies of normal brain function (Ioannides et al 1994), brain pathophysiology (Ioannides et al 1993c, Ioannides et al 1995a), and especially studies of single epochs signals instead of signals averaged across epochs (Ioannides et al 1995b). In fact, one of the main goals of this thesis, is to apply the single epoch MFT studies into pathophysiology (i.e. epilepsy) and extract any physiological significance. Before doing this though, we will present some MFT tests and simulations that demonstrate how the method is applied and what its strengths and likely limitations are.

+ *Another recent method - not mentioned in our treatment before, is the so-called LORETA, standing for Low Resolution Electromagnetic Tomography (Pascual-Marqui et al 1994), originally LORETA developed for use with EEG data, but readily available for MEG as well. LORETA also makes use of regularisation in order to produce "smooth 3d images with a relatively low spatial resolution". LORETA's implementation also uses MFT's original representation ideas on cutting the source space into equidistant levels along its depth and dividing each level into grid points. Similar ideas are also used in a similar method called PROMPs, which was presented by Greenblatt in the recent Biomagnetism Conference (Greenblatt 1996).*

5. MFT tests and simulations

In this chapter we present some MFT tests and simulations in order to demonstrate the potential of MFT and identify its limitations at least as far as the implementation that is going to follow in the next few chapters is concerned. These tests cannot, of course, be exhaustive; they are performed in of support the MFT analysis of real data that follows. Both the spatial and temporal aspects of MFT are discussed. The first section describes "routine" tests which should be carried out by every "MFT practitioner". Attention is then paid on the effect the number of sensors has in the spatial resolution. We subsequently focus on the recovery of deep activity from both unilateral and (simultaneous) bilateral measurements. Finally the spatio-temporal aspects of the MFT analysis are investigated through a set of dynamic simulations with a gradually increasing physiological significance.

5.1 "Training" the system

The first part of the MFT analysis involves extensive use of computer generated data. The task is to define the correct values for the "free MFT parameters", these are the decay of the Gaussian probability weight (or generally any other probability function) and the appropriate regularisation parameter (or smoothing as mentioned before). To accomplish this, a number of model inversions are carried out with different decay factors and different smoothing; the set of parameters that leads to the best reconstruction of known sources which are uniformly spread throughout the source space volume, is thereafter selected. This stage is a rudimentary analogue of the training session in neural network

studies (Ioannides 1994). After both parameters are fixed, no further modifications are allowed: they are kept constant in any subsequent inversions of real data.

These tests are compulsory in the MFT analysis, and are carried out in a routine basis every time a user needs to analyse a new experiment. We do feel, however, that their presentation here is necessary for two reasons: first to provide support for the validity of our results, and secondly, because they have never been demonstrated before in a compact and detailed manner utilising visual examples.

5.1.1 Source space configuration and display definitions

The source space definition and the probability weight can be considered as a means of introducing large scale anatomical or physiological constraints. In addition, the source space, where the primary currents are confined, should be consistent with the overall sensitivity profile of the sensor arrangement. In the early days of MFT, the source space consisted of a 2-dimensional disk, or part of the surface of a sphere, or a 3-dimensional cylinder. In more recent applications, a part of a 3-dimensional hemispherical volume with its boundary outlining as well as possible the cortical surface below the sensors is commonly used (Liu MJ and Ioannides 1995). The depth or extent of the source space is determined by the sensor characteristics, their geometrical configuration, and the noise level in the measurements.

The thickness of the Dewar is typically some 1.5 cm while the thickness of the scalp, the skull, and the cerebrospinal fluid layer is approximately 1.5-2.0 cm. Assuming that detection of neural activity 9-10 cm away from a sensor is too weak with present technology, the depth of a source space should not exceed the value of 6.0-7.0 cm, if one wants to maintain good localisation accuracy at the superficial levels as well as acceptable reconstructions of deep generators. From the practical point of view, it is difficult to maintain resolution throughout the volume if the depth is greater than say 6 cm for a 37 channel system.

Such an example is shown in Figure 5-1 where the horizontal bars on the left represent the planar arrangement of the 37-channels of the Siemens KRENIKON system. The source space is designed to cover the left hemisphere of the subject, but also follow as closely as possible the cortical surface below the sensors*. For display purposes, the hemispherical volume is cut at regular intervals, and activity is computed and displayed

---

* *A sphere is usually fitted to the subject's brain (on the side of the sensor array) from multislice MRIs and the source space depth is then extended according to the sensor coverage and noise level in the measurements.*

as a contour plot. Each cut is rotated so that it is flat on the page and displays at successive depths are placed in order, with the most superficial (level 9) at the top and the deepest (level 1) at the bottom. In this specific case, the distance between the most distant levels is 5.4 cm, making the overall thickness of the source space to be 6.1 cm. All contour plots used in this thesis, represent the square of the estimated current density. The colour scale displayed at the utmost right is also universal for all the thesis results: yellow corresponds to strong activity, while blue to low activity.

One should note, that although the different levels correspond to different radii, they are all represented by the same cross section in such a display due to our software's inheritance of dealing with constant cross section cylinders. Furthermore, a cross will be taken to mark the position of a "test current dipole" at a specific depth. By placing MFT solutions at successive time instants next to each other, we obtain a spatio-temporal display. We shall use such displays in the following sections to indicate the various test dipoles as different time-instants.

We finally highlight the conducting medium modelling: a sphere fitted to the local (to the sensors) curvature of the inner skull surface is taken as the conductor for all the reasons explained in the second chapter. A projection of the sphere onto the plane of the specific MRI outline is depicted by a circle in Figure 5-1, while a small dot represents its centre.

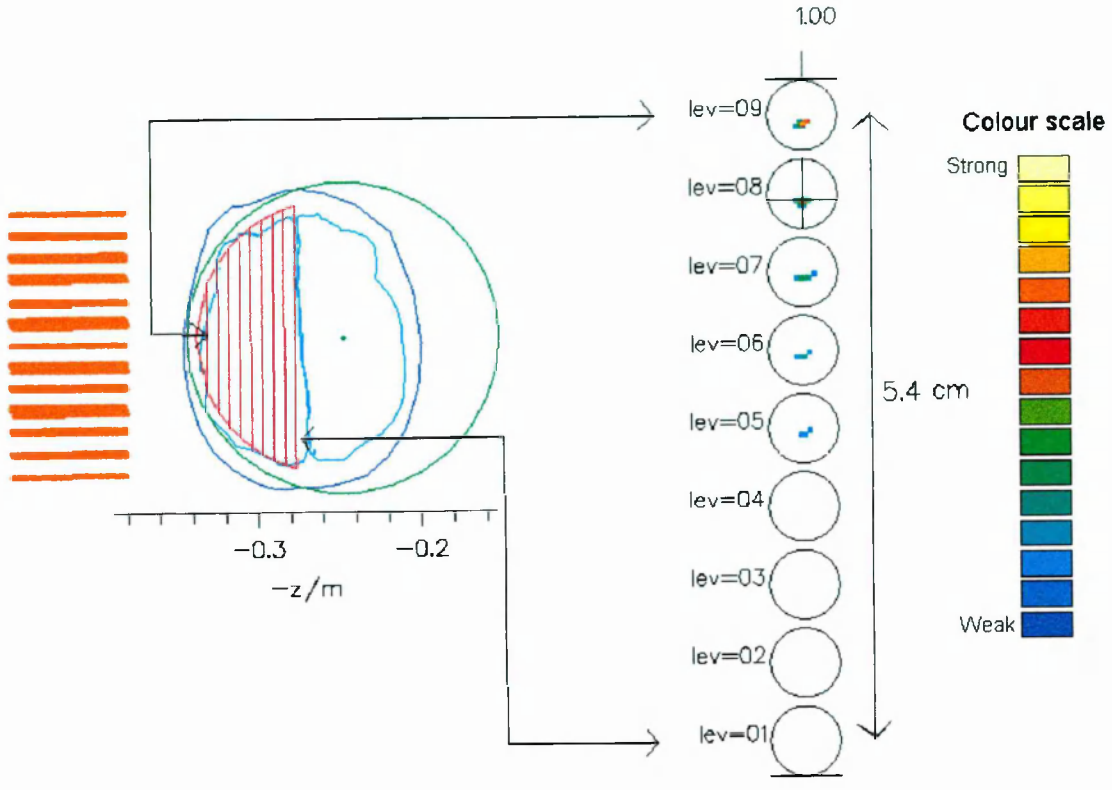

Figure 5-1: An example of MFT modelling and display. Left: the source space is part of a 3-dimensional hemispherical volume, represented as 9 sectional cuts. The distance between the most superficial level (9) and the deepest level (1) is 5.42 cm; the overall thickness of the source space is 6.1 cm. Horizontal bars indicate sensor positions. The circle depicts the projection of the conducting sphere on the specific MRI outline plane, while the small dot the conducting sphere centre. Right: each level is rotated so that it is flat on the page; displays at successive depths are placed below each other. Activity is shown as a contour plot. A cross indicates the position of a test current dipole (see next section). Far right: the colour scale convention used throughout this thesis: strong activity is plotted in yellow, weak in blue.

5.1.2 Selecting the proper parameters

Having defined a reasonable source space for a specific experimental set-up, the next step is to adjust the decay of the probability weight and the smoothing parameter. These are undertaken one at a time. The process is initialised by generating a set of current dipoles distributed throughout the entire source space. The forward problem is then solved for this set, so that a simulated signal is generated for the particular experimental set-up. Given such a signal, the problem is to reconstruct the current sources that gave origin to the specific signal. To simulate real experimental conditions, a 10% random noise is added in the values of this signal file. In the following examples, a "standard" set of dipolar sources will be used, containing 18 single dipoles and 9 two-dipole-combinations. Care is also taken so that none of the dipoles possesses a radial component.

We use a zero smoothing value to start with ($s = 0 \Rightarrow \tilde{\zeta} = 1.0$). If a uniform probability weight is used, then as mentioned before, the sensitivity is "wasted" in the region directly underneath the detector array. This means that very superficial sources will be correctly recovered, but little or nothing can be said about even slightly deeper ones* . In this case, MFT shares a great deal of similarity with the minimum-norm estimates method, but is still more robust due to the regularisation and iteration procedures. Figure 5-2 displays reconstructions of the standard current dipole set, that demonstrate exactly the above statement.

The picture is changed dramatically if a probability weight that increases monotonically with depth is used. We have only been using simple Gaussian forms for the probability function. The formula used for a Gaussian function is:

$$g(\mathbf{r}) = e^{-\left[\frac{|\mathbf{r}-\mathbf{r}_0|^2}{\lambda}\right]} \tag{5-1}$$

For $\mathbf{r}_0$ we usually (always in this thesis's material) choose the centre of the conducting sphere. It is also possible to vary the probability weight with emphasis in different directions. That is, a probability weight is chosen for reconstructing sources in depth (e.g. in the $\hat{e}_3$ direction, or z-direction in Figure 5-1), while another different probability weight can be selected for reconstruction of sources in a plane (e.g. $\hat{e}_1$, $\hat{e}_2$, or xy-plane). So, a probability biasing only along the third direction (depth) will be:

---

* *One should note that deep means away from the sensors (or deep source space levels); so deep generators may in fact be cortical, depending on the source space orientation.*

$$g(r_3) = e^{-\left[\frac{(r_3 - r_{03})^2}{\lambda_3}\right]} \tag{5-2}$$

while that along a plane will be:

$$g(r_1, r_2) = e^{-\left[\frac{(r_1 - r_{01})^2 + (r_2 - r_{02})^2}{\lambda_{1,2}}\right]} \tag{5-3}$$

One can use either Equation 5-1 or a combination of probabilities according to Equation 5-2 and Equation 5-3. We have observed that for a probe with a flat surface (i.e. planar arrangement of sensors, like that of the KRENIKON system) the simple form of Equation 5-1 is sufficient, and there exists no special need to use the combination of Equation 5-2 and Equation 5-3. For a curved system though (i.e. like the BTi MAGNES probe(s)), the latter choice produces a better reconstruction quality. In the following, despite the use of the KRENIKON set-up of Figure 5-1, we shall make use of the combination of probabilities, but $\lambda_{1,2}$ will be kept constant at the value of 5 cm. Varying λ_3 we get a series of pictures with different depth enhancements. In Figure 5-3 depth enhancement is too strong, while in Figure 5-4 is a bit weak. The solution with the best choice is shown in Figure 5-5.

Keeping the decay factors constant, we then try inversions with variable smoothing parameter. For the sake of simplicity we shall only show reconstructions of the second half of the dipole set. Three different choices are shown: in Figure 5-6, the choice of smoothing results in reasonably good reconstructions; in Figure 5-7, one is aiming for finer details; trying to obtain too much detail in the presence of noise, results in artefacts, as Figure 5-8 demonstrates. Although regularisation seems correct even in Figure 5-7, we usually double the limiting value of the regularisation parameter, $\tilde{\zeta}$, so as to avoid amplification of noise in more noisy situations than the simulated one (10%). Doubling $\tilde{\zeta}$, gives the smoothing the value used in Figure 5-6.

Having obtained the correct regularisation, one can fine-tune the probability weight, by trying inversions with smaller steps of decay factors, but using the proper smoothing. The final result is shown in Figure 5-9, assuring that the system is virtually "trained". The values for the two free parameters (decay and regularisation) are now fixed, and are the ones to be used in any subsequent inversions of real data corresponding to the same experimental set-up. Alteration in the sensor/patient positions (even if one selects the same source space), requires repetition of the "training" procedure.

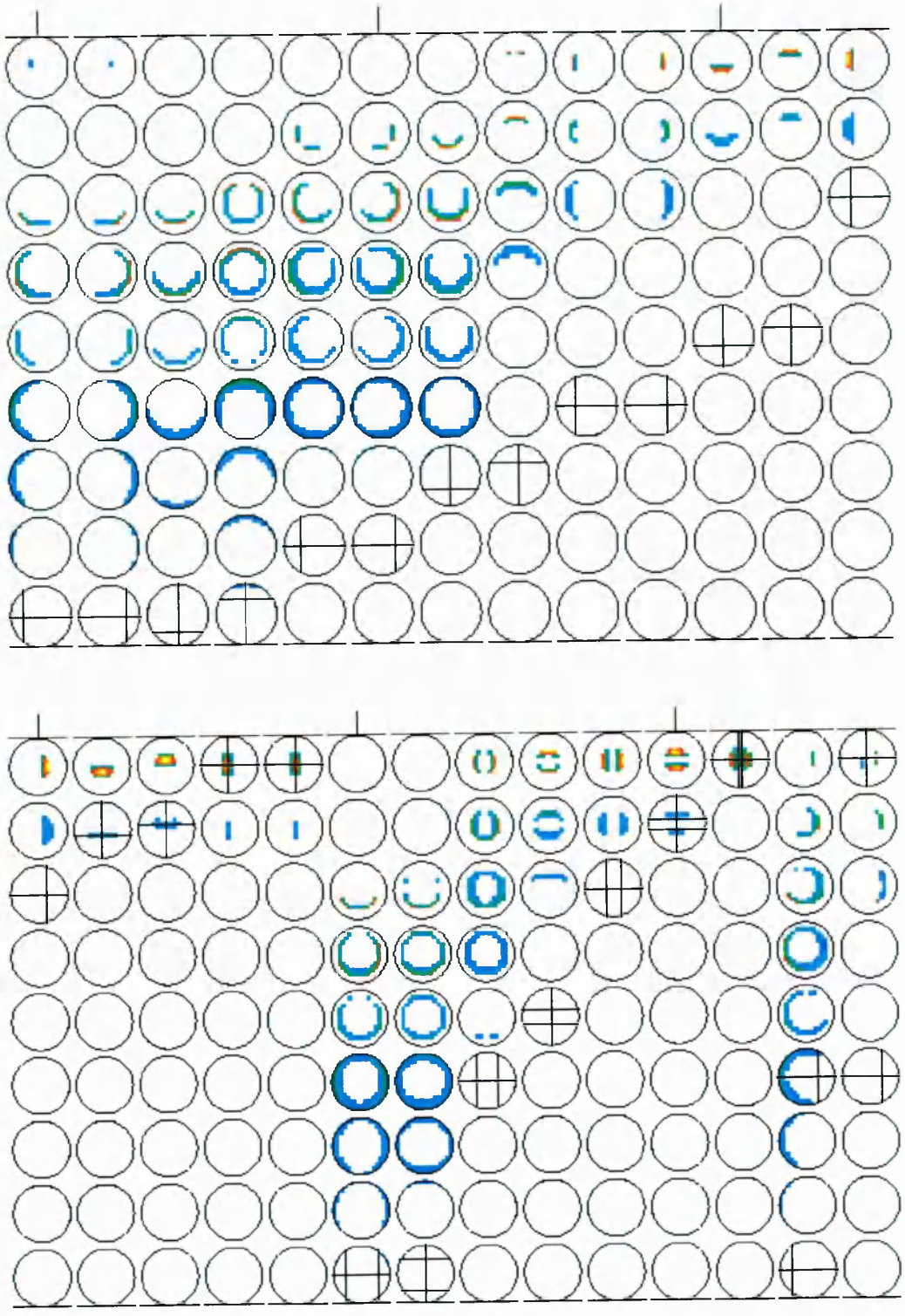

Figure 5-2: Reconstructions of the standard current dipole set using unitary regularisation and uniform probability weight. Note that although very superficial dipoles are correctly reconstructed, sensitivity is wasted in the region underneath the sensor array, and as result nothing can be said about non-superficial sources.

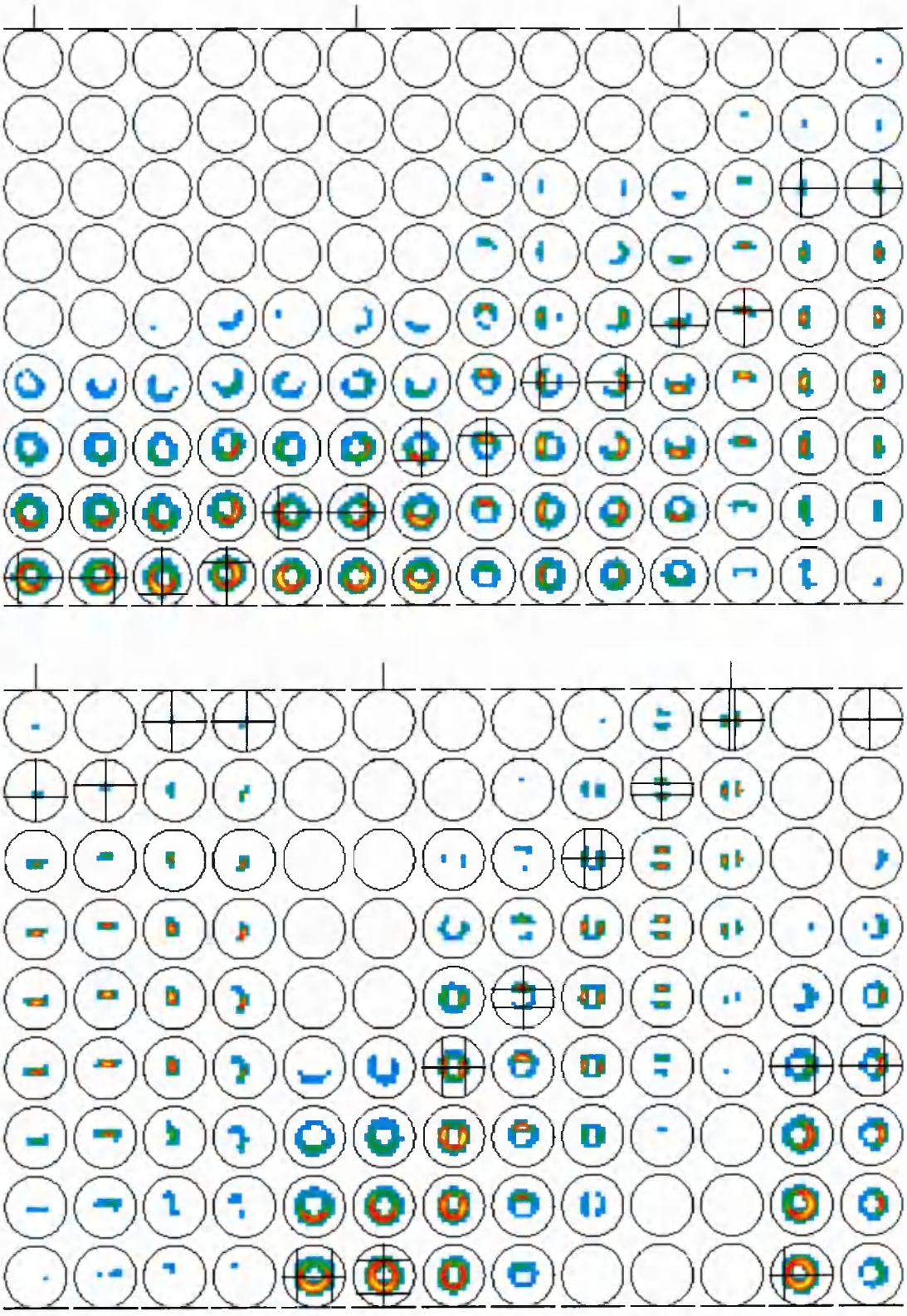

Figure 5-3: In these reconstructions $\lambda_3 = 4.5\ cm$, and deep sources are correctly recovered, but superficial and middle-depth ones are "pushed" deeper. The depth-enhancement is too strong, and λ_3, the probability decay parameter, needs to be higher.

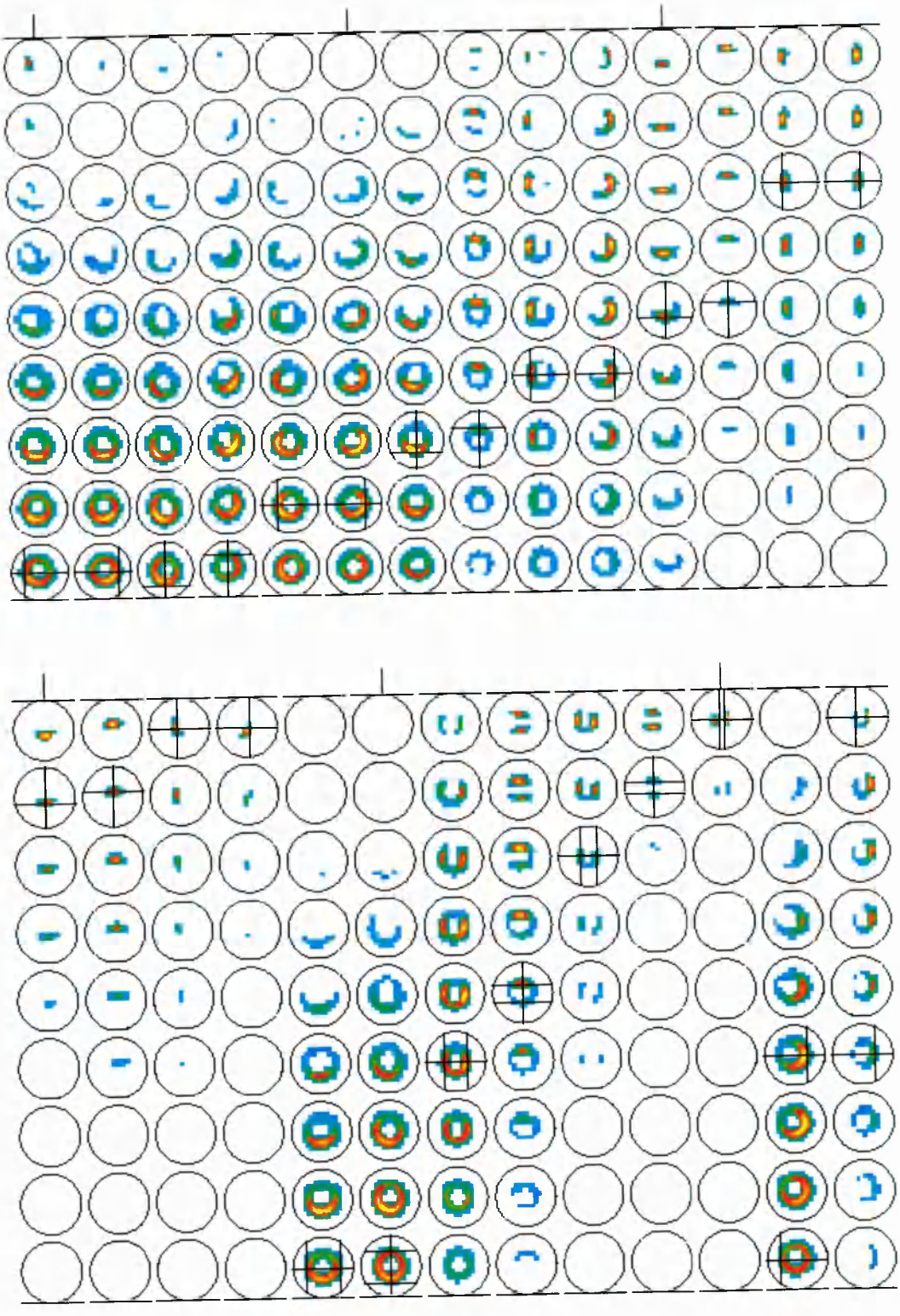

Figure 5-4: Reconstructions where deep and fairly deep sources are not correctly recovered (the effect is more obvious in middle levels), while very superficial ones are fully benefited. The depth-enhancement is weak $\lambda_3 = 6.0\ cm$, and the decay needs to be decreased.

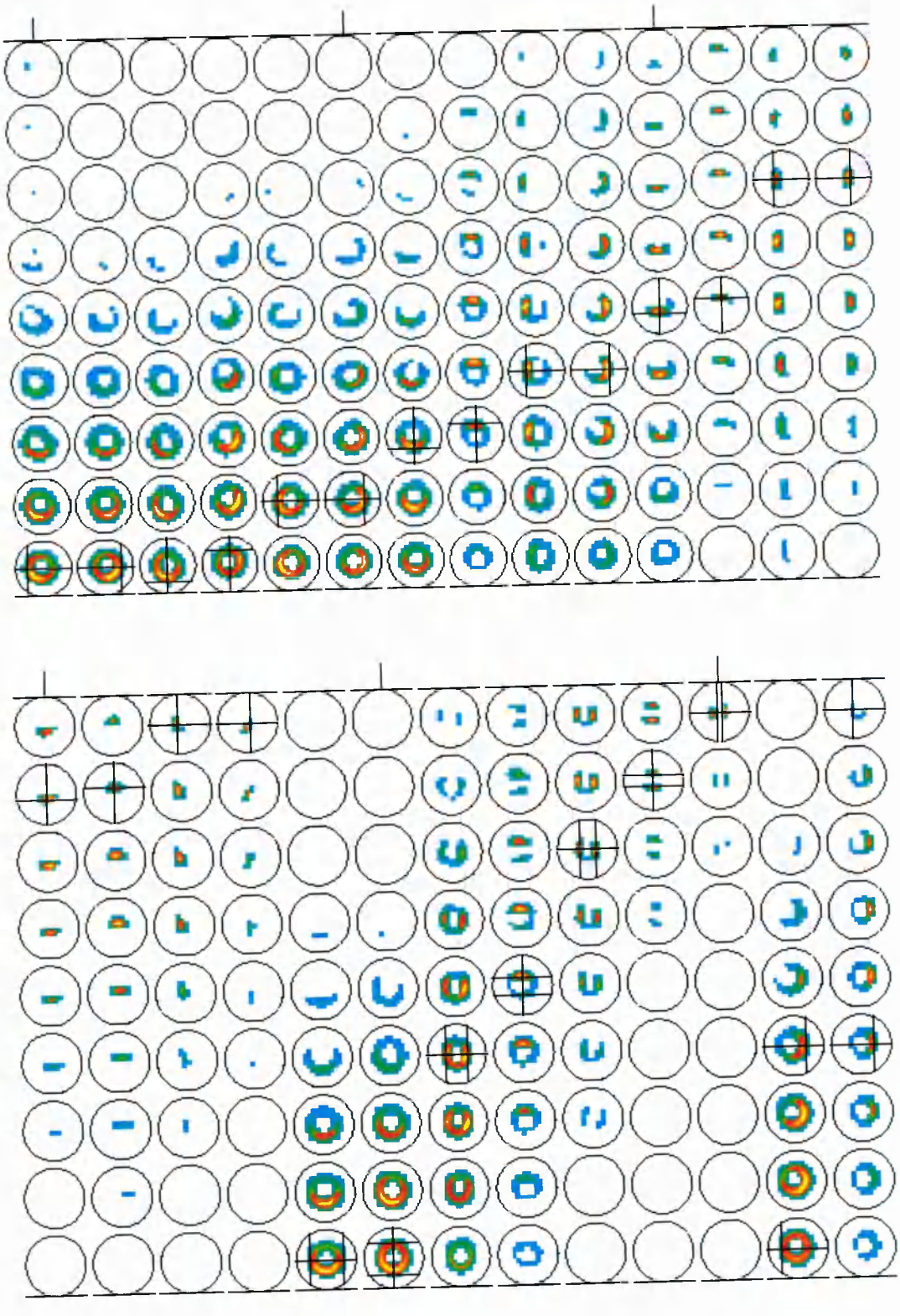

Figure 5-5: Reconstructions where the depths of most sources are correctly recovered; In this case $\lambda_3 = 5.3\ cm$, and it is the appropriate choice.

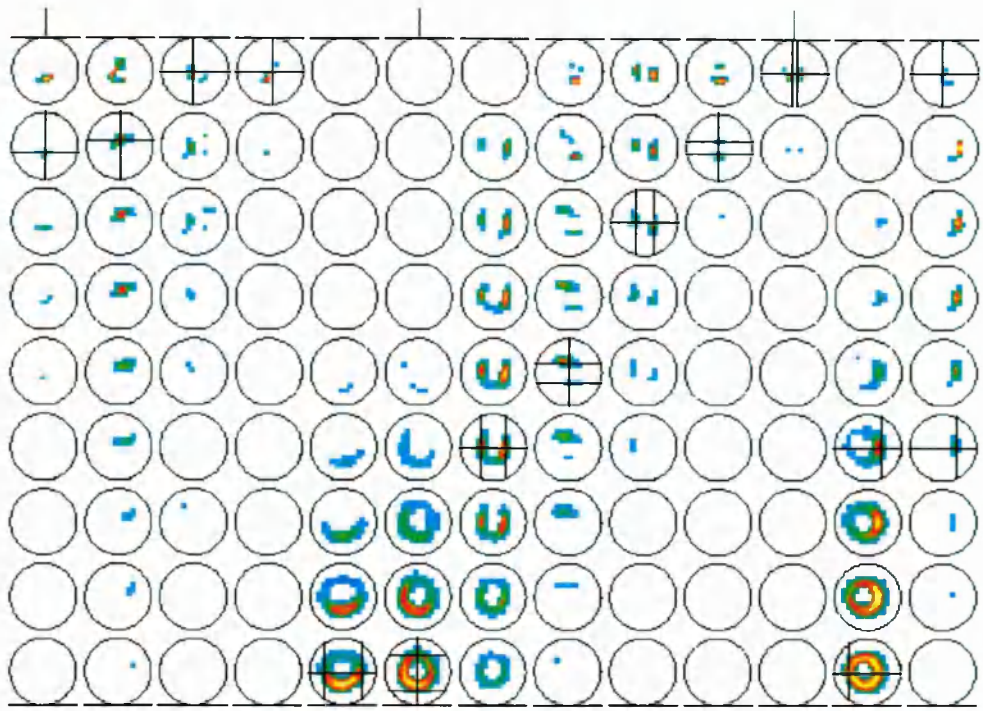

Figure 5-6: Inversions with the selected probability decay factors, but for smoothing s=1.0. The reconstructions seem reasonably correct.

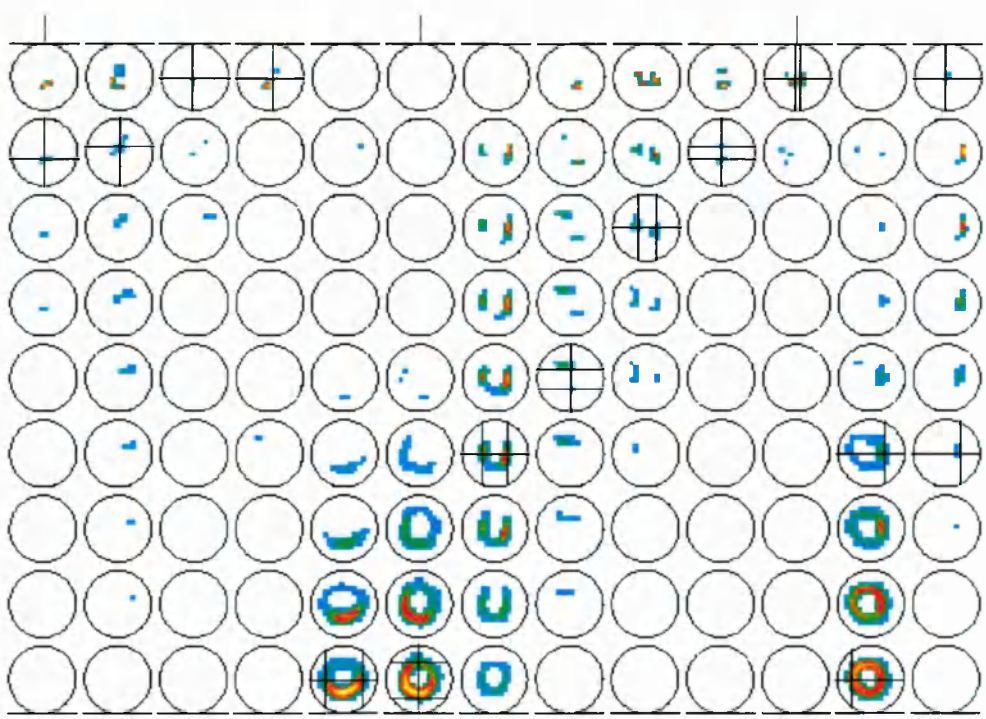

Figure 5-7: Inversions with the same probability, but for smoothing s=1.3.

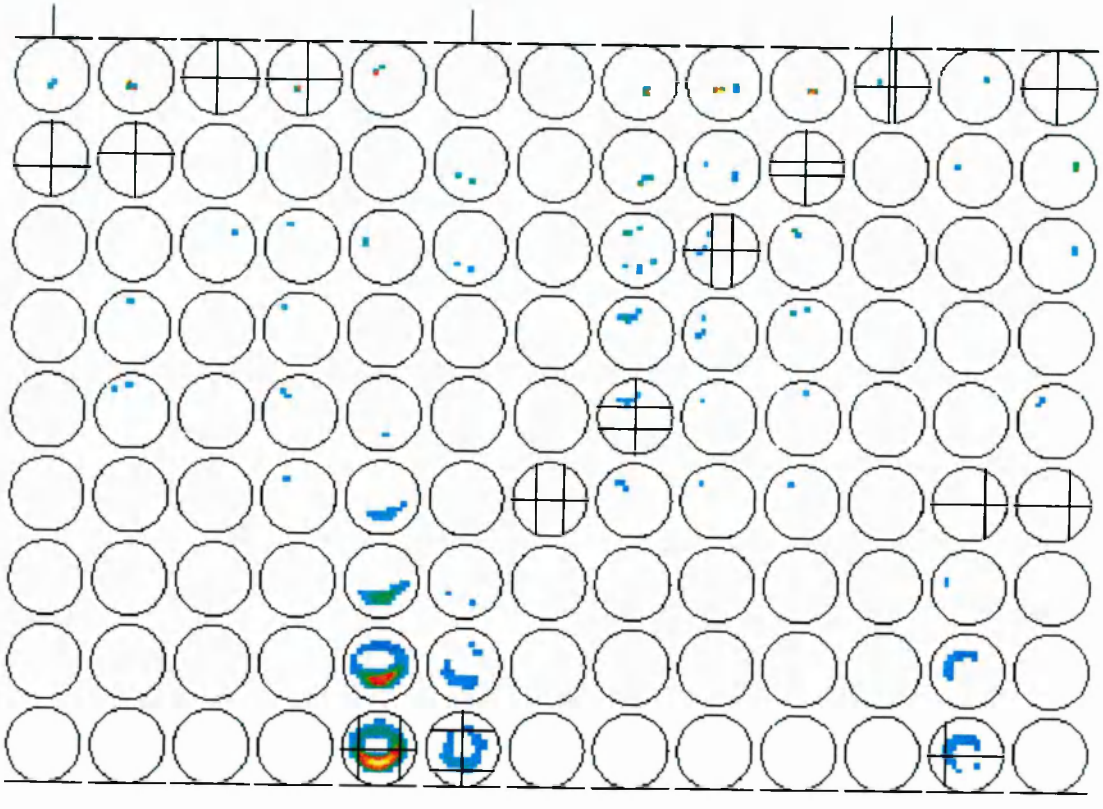

Figure 5-8: The same probability is used, but smoothing s=2.0. Trying to make too fine reconstructions in the presence of noise results in eventual loss of detail. This smoothing value is definitely unacceptable.

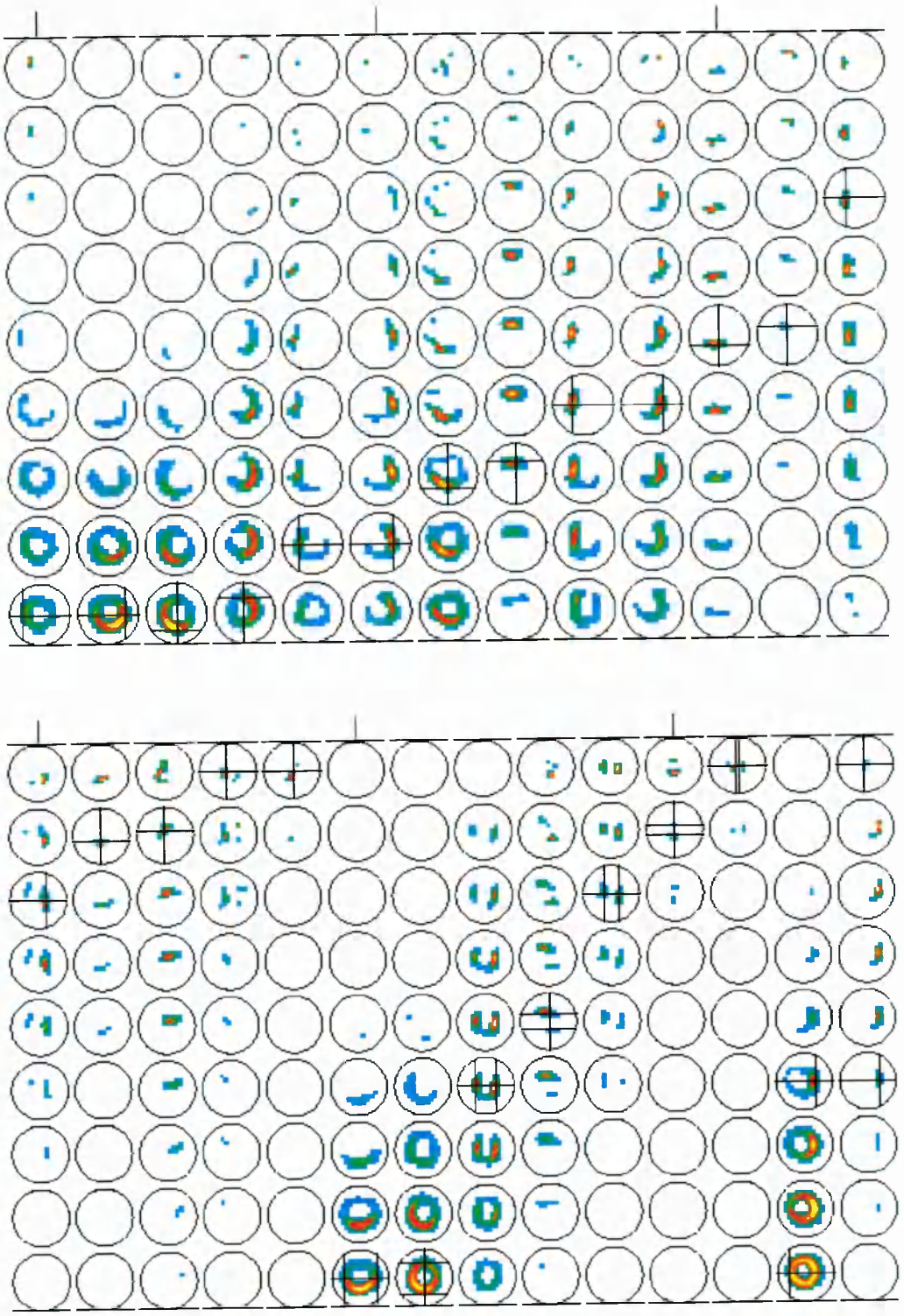

Figure 5-9: The final result with properly defined probability decay and smoothing parameters. These are, $\lambda_3 = 5.2\ cm$, and $s = 1.0 \Rightarrow \tilde{\zeta} = 0.1$. These values are now fixed, and are the ones to be used with any real data of the same experimental set-up.

5.2 Sensor number effects in MFT estimates

In this section we attempt to understand how the MFT estimates of activity are affected when the number of channels of a given probe used in the analysis is reduced. The main reasons we wish to do so are twofold. First, because some of the MFT analysis presented in this thesis is based on recordings where a few MEG channels (i.e. 7 out of 37) were not functioning properly, and as a consequence are not included in the analysis. Furthermore, we believe it is one of the ways to demonstrate the robustness of MFT as a method of MEG analysis, especially when unaveraged or single epoch ("noisy") data are concerned. The endurance of the MFT estimates in the presence of noise and in relation to the number of sensors was also discussed in the early publications of the method (Ioannides et al 1990a). However, those estimates were relied on the source being a circular disk, that is only the 2-dimensional case was considered. Herein, we expand some of those conclusions in the case of the 3-dimensional MFT reconstructions.

In order to achieve this, we make use of the experimental set-up already used in the previous paragraph (set-up 1), in which some of the 37-sensors are omitted on purpose. This leads to two distinct set-ups: set-up 2, with 19 sensors, and set-up 3 with 13 sensors only. The specific arrangements are displayed in Figure 5-10. Although different sensor configurations would, in general, demand different choices for the probability weight, we have observed that the same choice works reasonably well for all three configurations.

A proper treatment of this issue would require formal analysis using the sampling theorem (e.g. Nyquist 1928; Shannon 1949). Such analyses have been widely used in the MEG literature to obtain optimal sensor configurations (i.e. channel separation and geometrical arrangement) for various probes, so that neuromagnetic field sampling is maximised and aliasing is eliminated (see for example Hoenig et al 1991; Ahonen et al 1993). Our approach will be different, simpler but more focused on the specific MEG examples we wish to study. We once more use the standard dipole set and the displays as defined before.

For the sake of clarity, we start with reconstructions of noiseless data. The full probe (i.e. set-up 1) was used in Figure 5-11, while set-ups 2 and 3 were used in the production of Figure 5-12 and Figure 5-13 respectively. The message in these figures is that, MFT performs quite well even when the sensor number is significantly reduced. The main effect as this reduction occurs is some kind of "blurring" in depth[+]. In other words, the obtained solutions cannot be very focal; they are instead distributed in more levels of the source space, despite the fact that the point of maximum activity might still be recovered

---

[+] *Although one could argue that blurring is generally present in all set-ups anyway.*

successfully. This "blurring" is almost absent in the case of deep generators, but becomes obvious for middle-depth and even more prominent for superficial dipoles. In addition, one would expect the set-ups with fewer sensors to be less accurate in the localisation of superficial, in particular, sources, but such an effect cannot be clearly seen in these displays.

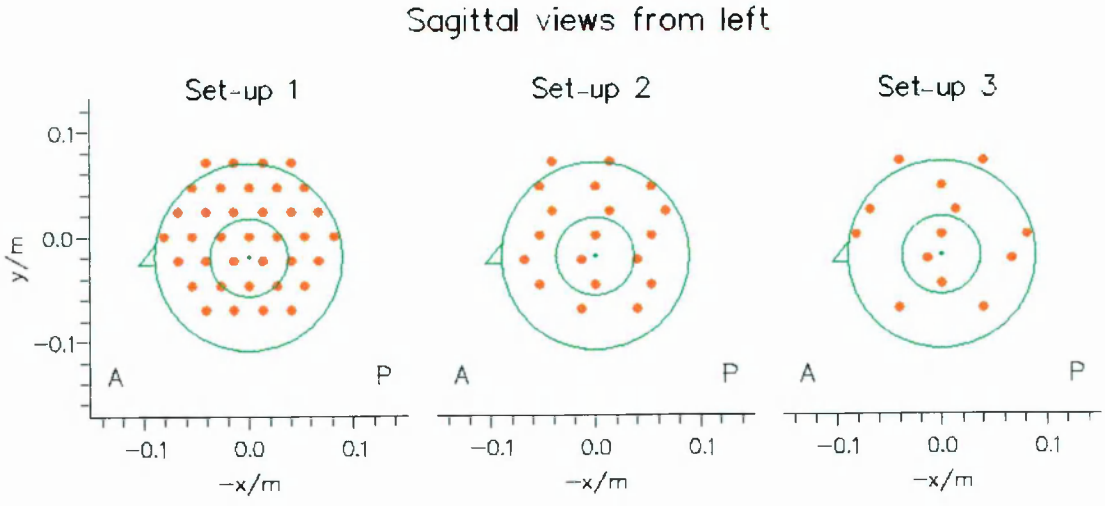

Figure 5-10: The number of sensors in set-up 1 (37) is progressively lowered to obtain set-ups 2 and 3 with 19 and 13 sensors respectively. Big dots represent projections of the sensor positions on the source space display. The big circle corresponds to the bottom source space level, while the small to the top (superficial) one - the small dot is the centre of bottom level. A miniature triangle depicting the note helps in the definition of posterior (P) and anterior (A) directions.

An important question then naturally arises: why should one bother building expensive multichannel channel systems, when even oligochannel probes (of the same head-coverage) are capable of providing satisfactory solutions? The answer relates to the role played by noise and is shown in the following two Figures, where 20% random noise was added in the signals*. We show the results for deep dipoles where the effect is more obvious. As the noise level increases, set-ups with less sensors become more vulnerable to noise. So, for instance, the MFT estimates are very satisfactory when all channels are used (Figure 5-14) but become less satisfying when only one half of the sensors is used (Figure 5-15 top) and even less when one third of the sensors is in use (Figure 5-15 bottom). This can be easily seen in the 7th and 10th dipoles (columns) of set-up 3 (Figure 5-15 bottom), where the shape of the actual solutions is distorted. This is a serious effect,

* *Reconstructions with 10% added noise did not show prominently the differences described next.*

since a focal solution might appear as distributed in more then one distinct regions. One should, however, appreciate the fact the MFT is still able to localise most of the dipoles - which are themselves an inherently stringent test for MFT, since the method is optimal for distributions of current rather than point sources - in the presence of 20% noise and with two thirds of sensors not functioning.

In support of the latter statement, we also include in Figure 5-16 the displays for the most superficial dipoles for set-up 3. Although again some distortions can be seen in some dipoles (a fact that accounts for the "few" widely distributed sensors, in a very noisy environment), MFT proves to be quite robust by being capable to recover quite well even some of the doublets. This robustness against noise (in addition to the test presented in the original versions of the method, cf Ioannides et al 1990a), together with the obvious fact that a small number of missing channels does not affect the MFT estimates dramatically, are contributing to our confidence in successfully using MFT in single epoch data analysis.

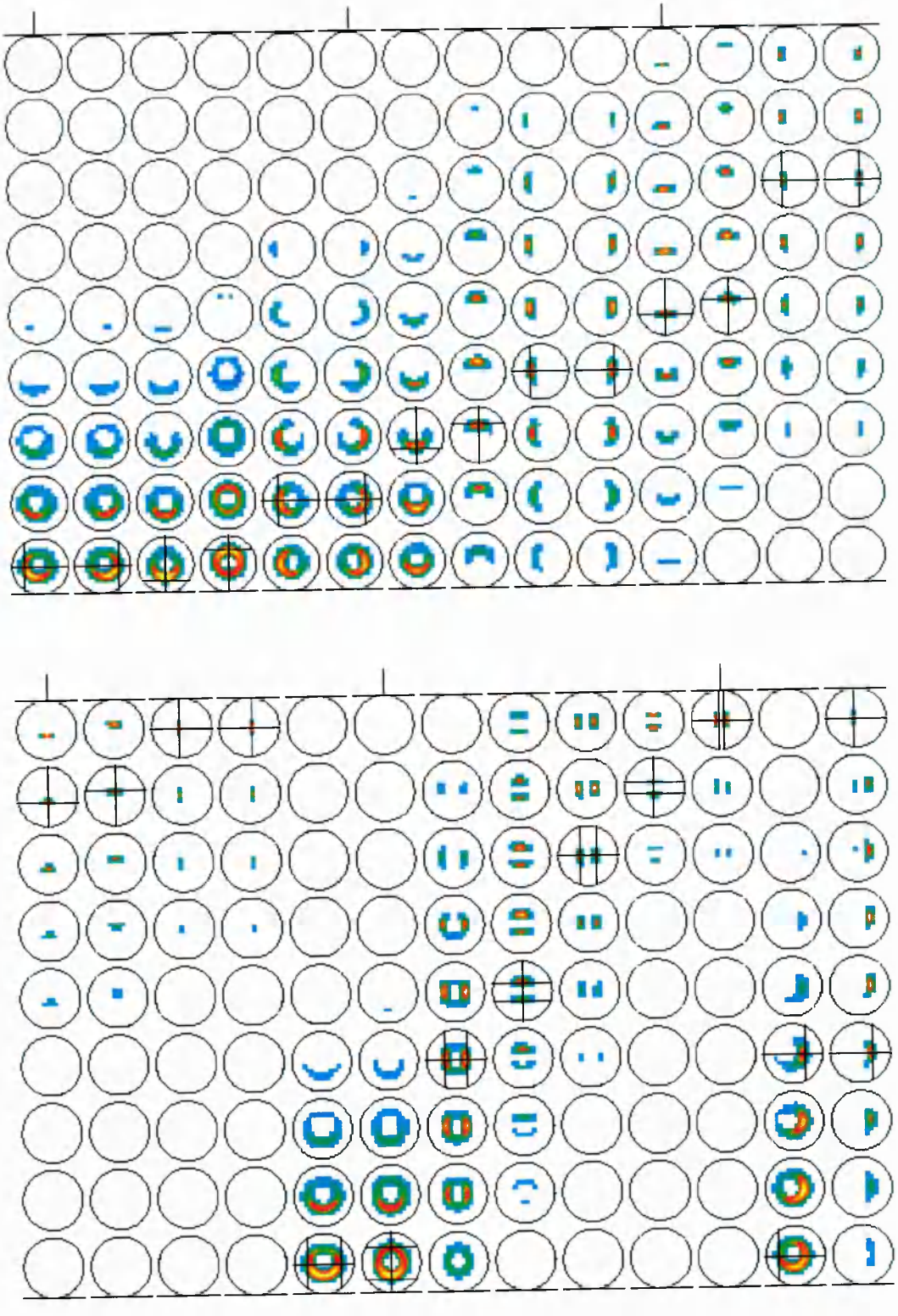

Figure 5-11: Reconstructions of the standard dipole set for set-up 1 (noiseless data).

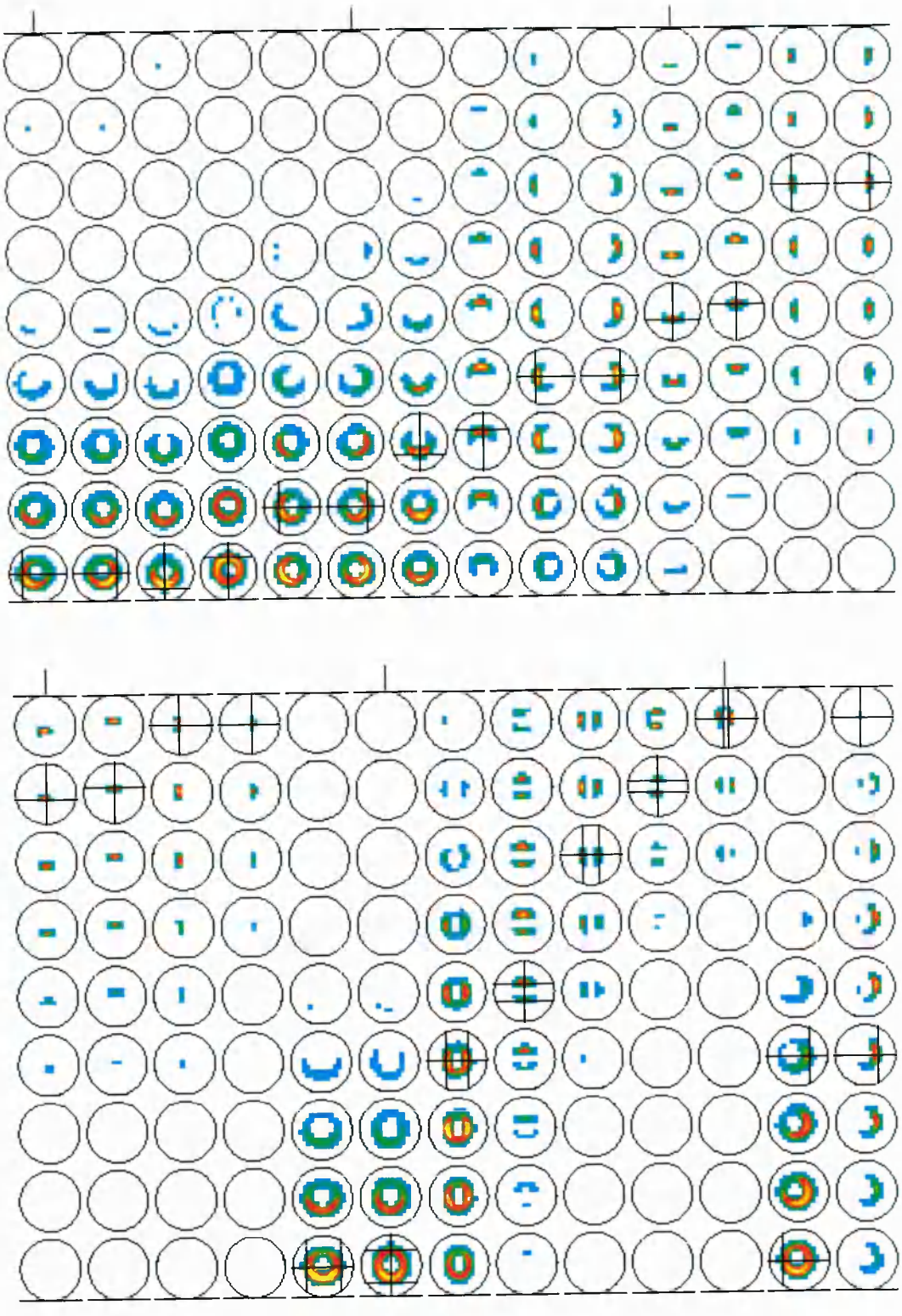

Figure 5-12: Reconstructions of the standard dipole set for set-up 2 (noiseless data).

Figure 5-13: Reconstructions of the standard dipole set (no noise) for set-up 3.

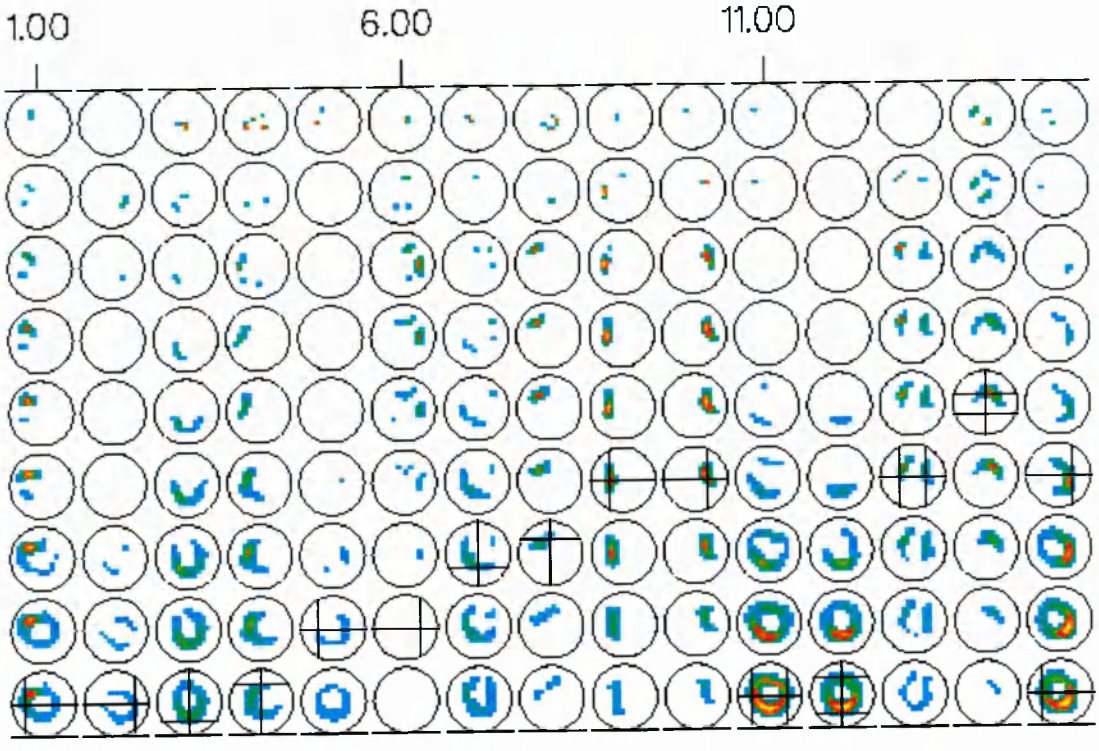

Figure 5-14: Reconstructions of "deep" dipoles in the presence of 20% random noise for set-up 1.

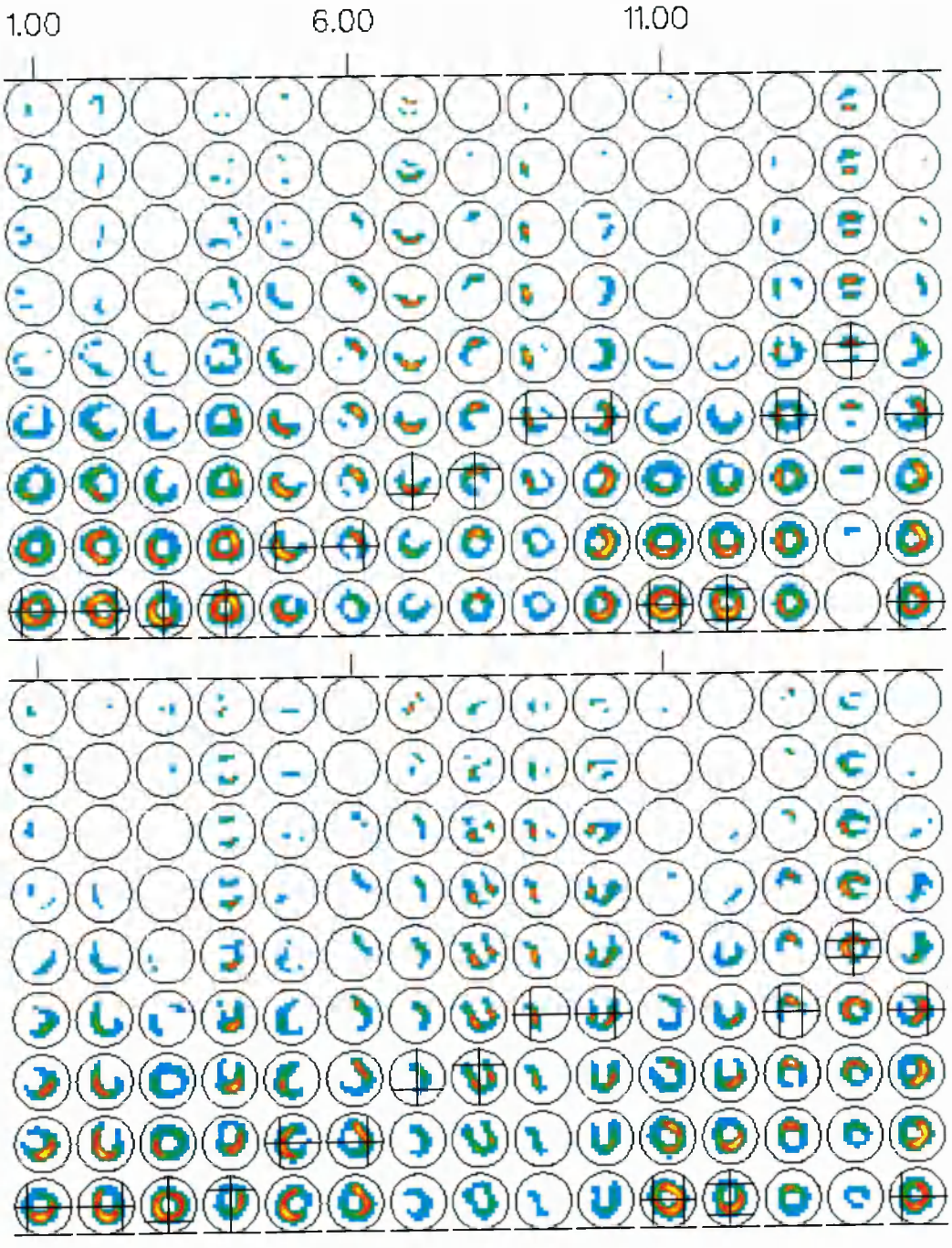

Figure 5-15: Reconstructions of the "deep" dipoles in the presence of 20% random noise for set-ups 2 (top) and 3 (bottom).

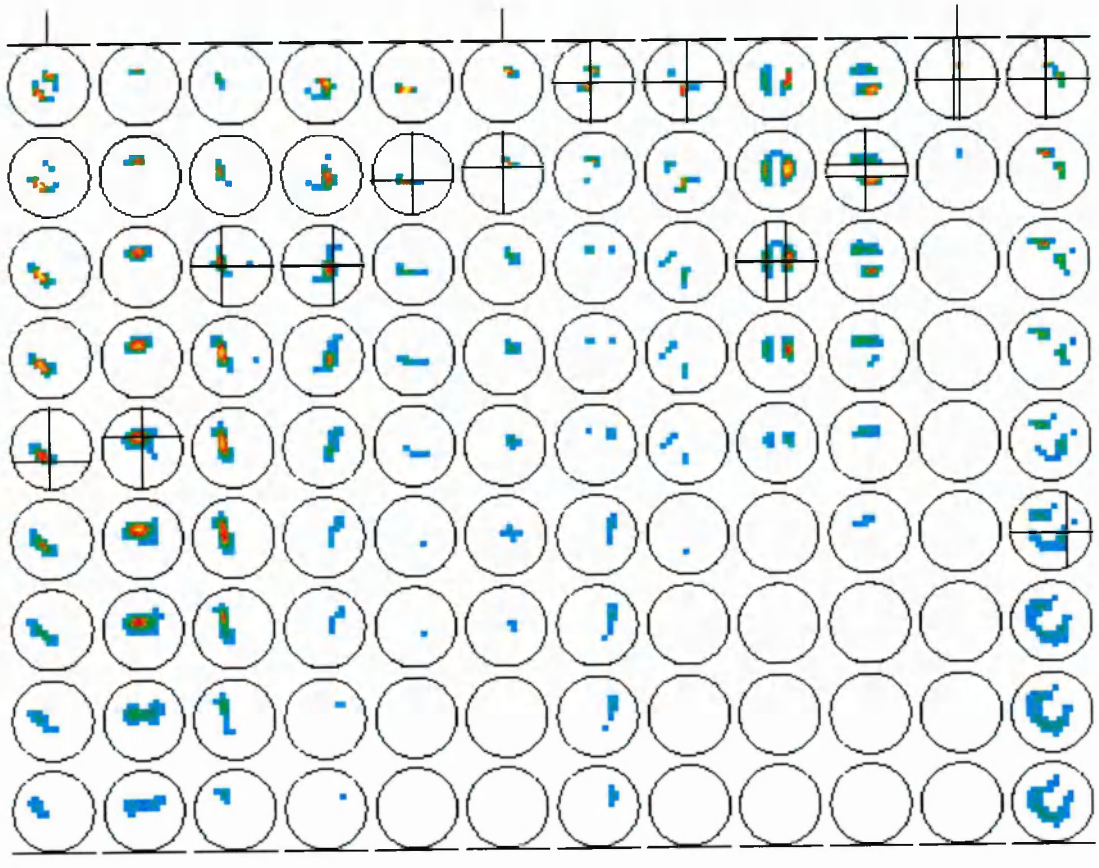

Figure 5-16: Reconstructions of the superficial dipoles in the presence of 20% random noise for set-up 3.

5.3 Recovering deep activity

In this paragraph we present some simulations to test MFT's capability to reveal deep activity. Section 5.1.1 discussed points one should bear in mind when designing a "proper" source space. This design, however, does not in any way exclude the possibility of sources being outside the presumed source space. So, an interesting question could be framed as follows: how are the MFT solutions affected when strong deep sources outside the assumed source space are present? In other words, what would happen if some strong generators were active in the right cerebral hemisphere and the source space covered only the left one? We attempt to approach this issue under two distinct cases: first, assuming unilateral measurements (i.e. measurements from only one side of the head), and secondly, considering bilateral (simultaneous) recordings.

5.3.1 Unilateral case

We start with a simulated experimental set-up of the KRENIKON system placed over the subject's left temporal area (we shall assume noiseless data in the following). Figure 5-17 shows the positioning of the subject with respect to the probe, the source space used, and also outlines of some anatomical structures. Dipoles (marked by thick arrows) are placed in various regions, mainly deep ones. Use of one cortical dipole is only included to help in the discussion to follow. In the top plate, the dipole is placed progressively deeper: at left hippocampus (LHi, corresponding source space position is between levels 3 and 4), at brain stem (level 1), and at right hippocampus (RHi, outside source space). The two thalami are also involved. Some two dipole combinations are allowed, as explained in the caption. Conductivity is modelled by a sphere fitted to the curvature of the left inner skull surface.

In Figure 5-18 we display the solutions for the assumed dipoles. As it can be seen, sources within the source space are satisfactorily recovered*. One should note the difference in the shape of the solutions, when a single generator is present as opposed to the case where a pair of generators is active (see, for instance, the difference between the first and the last plot, but also that of the left most middle and the centre bottom figurines). When strong generators are present beyond the bottom source space level, solutions appear as "focal" (in the coronal perspective) deep activity, that could be attributed to the cerebellum for example. Would it be possible to distinguish between

---

* *It should be recalled that we are dealing with the "most favoured" MEG case, assuming non-radial sources only.*

activity that originates from the actual source space volume and activity that is generated further beyond it? To tackle this question, we devised a novel way of applying MFT.

Given that such deep activity is identified in the original source space, we then design a new source space that accommodates all the deep anatomical structures of interest. Given that this source space involves larger distances from the sensors, enlarging the current source space a bit deeper would not be a reasonable suggestion, since the latter would affect the localisation accuracy in superficial levels. We, therefore, choose a small cylinder, occupying a volume just about enough to cover the regions of concern. Routine tests are, of course, performed from the beginning, so that the probability decay factors are properly readjusted to correctly recover activity in this region.

A planar projection of this new source space can be viewed in Figure 5-19, together with the "new" estimates of activity. Using the cylindrical source space, we can distinguish both left and right hippocampi and thalami. More importantly we can now see where the "focal deep" activity appearing in the previous plots is coming from. This procedure can be imagined as a "focusing process": we have indications that something is activated in the depth of the original source space, and we "re-focus our lens" (the lead fields multiplied by the new probability weight) over that deep region, in order to make sense of the on-going reality. Image "blurring" due to the large area occupied by the deepest level(s) of the hemispherical source space can also be resolved in this way.

We can only "see" such a deep activation though, only if the current generator were strong enough, and more importantly if no other more superficial generator were present. If RHi is activated simultaneously with LC or LHi then we cannot recover RHi using information from one side of the head only. So, for instance, if both hippocampi are present, the solution is very similar to that of the activated brain stem.

Another obvious disadvantage manifests itself when superficial cortical activity is present. In such a case, activity is just projected on the top cylindrical level (cf most central plot in the bottom plate of Figure 5-19). However, this process will only be used during the time instances that deep activity is identified in the original source space. In other words, when information from the original source space is sufficient, the cylinder is neglected. Extensions to deal with simultaneously activated sources are under consideration, but will not be discussed further.

One should of course realise the inherent limitations of such a process. Although, from Figure 5-19 it appears that one can distinguish between RHi and RTh activations, much more work is needed for defining the influence of small perturbations to either noise or modelling (e.g. wrong conductivity profiles). To put it differently, we shall only trust the level of activation in the bottom levels of the cylinder, but not the actual localisations. The

cylindrical estimates were obtained using the same as before conducting model (i.e. a sphere fitted to the left side). Attention must be, therefore, paid since we are dealing with very "central" head regions where one is not certain what the correct conductivity profile might be. Realistic head modelling and/or conducting ellipsoid approaches (Fieseler et al 1995) might be more appropriate but will not be pursued herein. To simulate, though, the kind of error that one could expect, we shall attempt another simplified test, assuming that the conducting sphere model is always valid, but the centre of the sphere is unknown.

The "old" conducting sphere centre is, therefore, shifted by (-1 cm, +1 cm, -1 cm) in all three directions (x,y,z). The forward problem is then solved for the previous sources, but with the new conducting centre, in order to generate a signal. Inversions are then attempted for the latter, but using the old conducting centre. We have carried out the inversions for both source spaces, but we only show here the deep-cylinder estimates, where the situation is a bit easier to view.

The cylinder plots in Figure 5-20 show the solutions where the same conducting model was used in both the forward and inverse problems (in fact the solutions are the same with those used in Figure 5-19). Figure 5-21 demonstrates the case where the inconsistent definition of the conducting centre was intentionally introduced, as mentioned above. Only minor effects are indeed observed, with the most obvious one being that of the 6th "time-slice" (i.e. RTh activation). So, an error of some 1.73 cm in the conducting centre involves very small distortions. The unanswered question, of course, is what happens when the conducting medium is not a sphere.

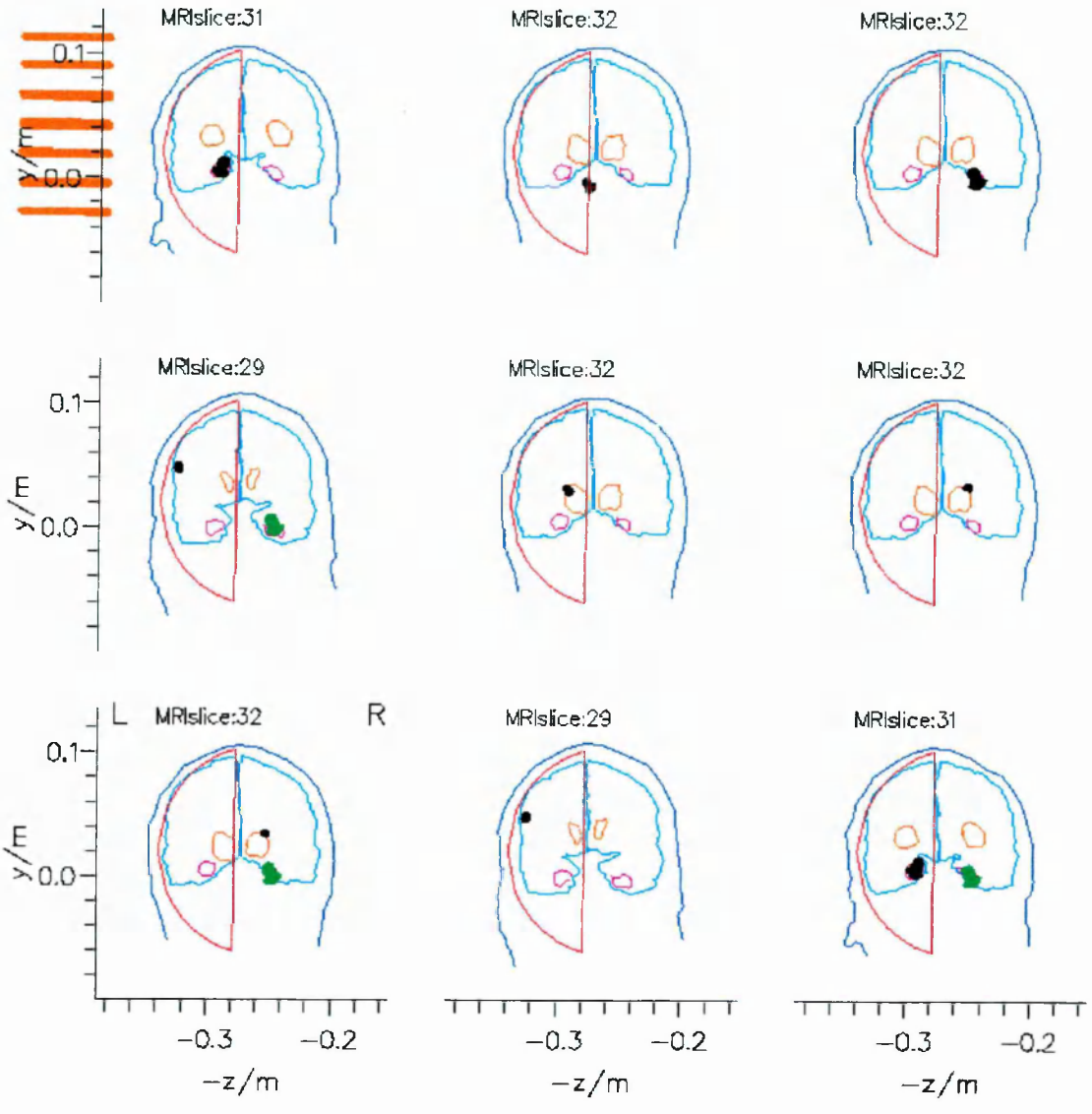

Figure 5-17: Simulation of unilateral recordings with the KRENIKON system. Skull and brain MRI outlines of a subject are shown together with approximate MRI outlines of the thalami and hippocampi. The original source space is part of a hemisphere, and covers the left hemisphere. Dipoles are shown as thick arrows and are placed in various anatomical regions (from top left to bottom right): left hippocampus (LHi); brain stem; right hippocampus (RHi); left cortex (LC) and RHi together; left superior thalamus (LTh); right superior thalamus (RTh); RHi and RTh together; LC; LHi and RHi.

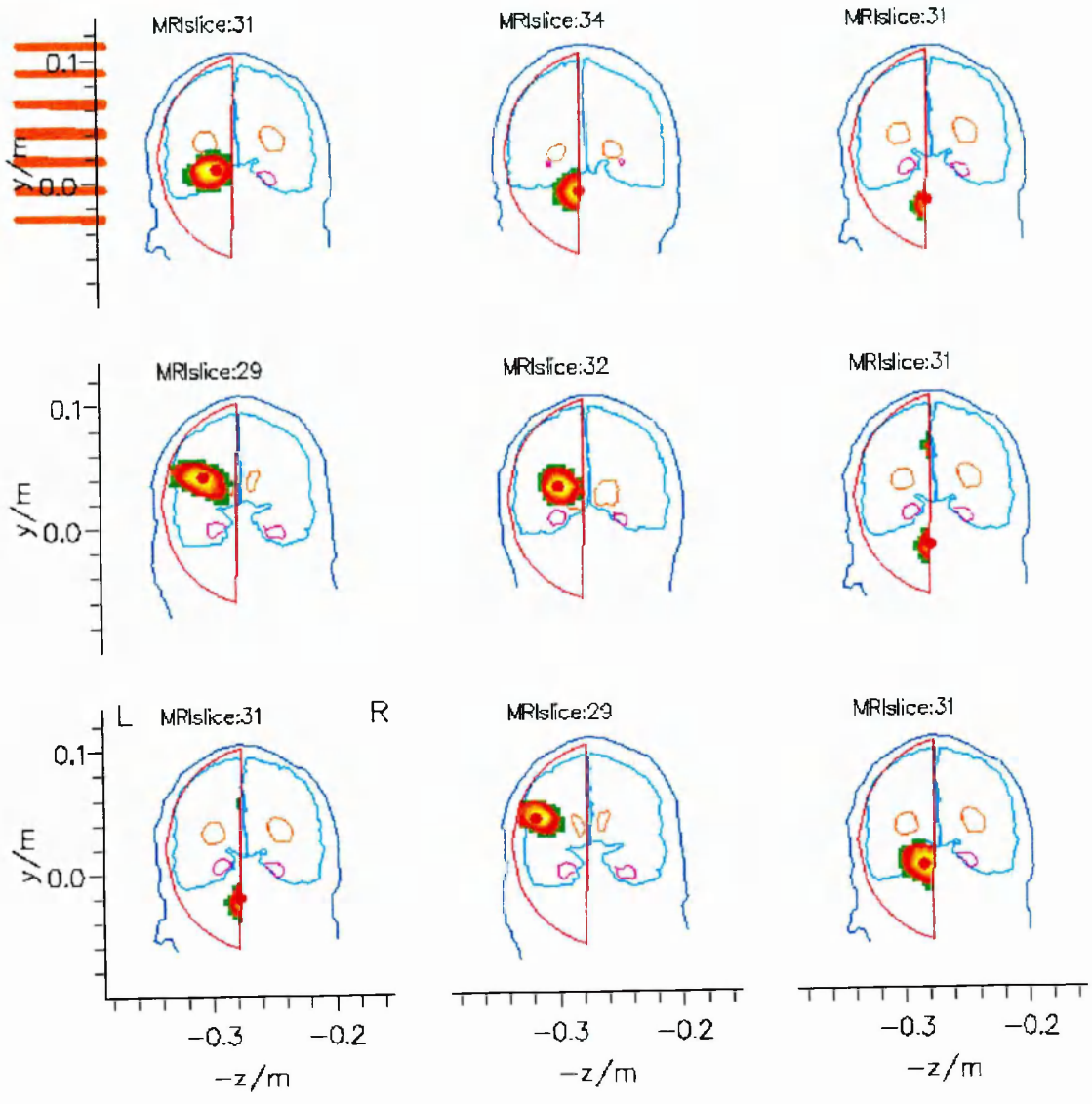

Figure 5-18: Contour plots of the squared current density estimates of the previous sources using the hemispherical source space. Successive MRI slices differ by 6 mm, and are selected according to the position of the maximum activity (marked by a dot). Sources within the source space are satisfactorily recovered; when strong generators are present beyond the bottom source space level, solutions appear as "focal" (in this coronal perspective) deep activity.

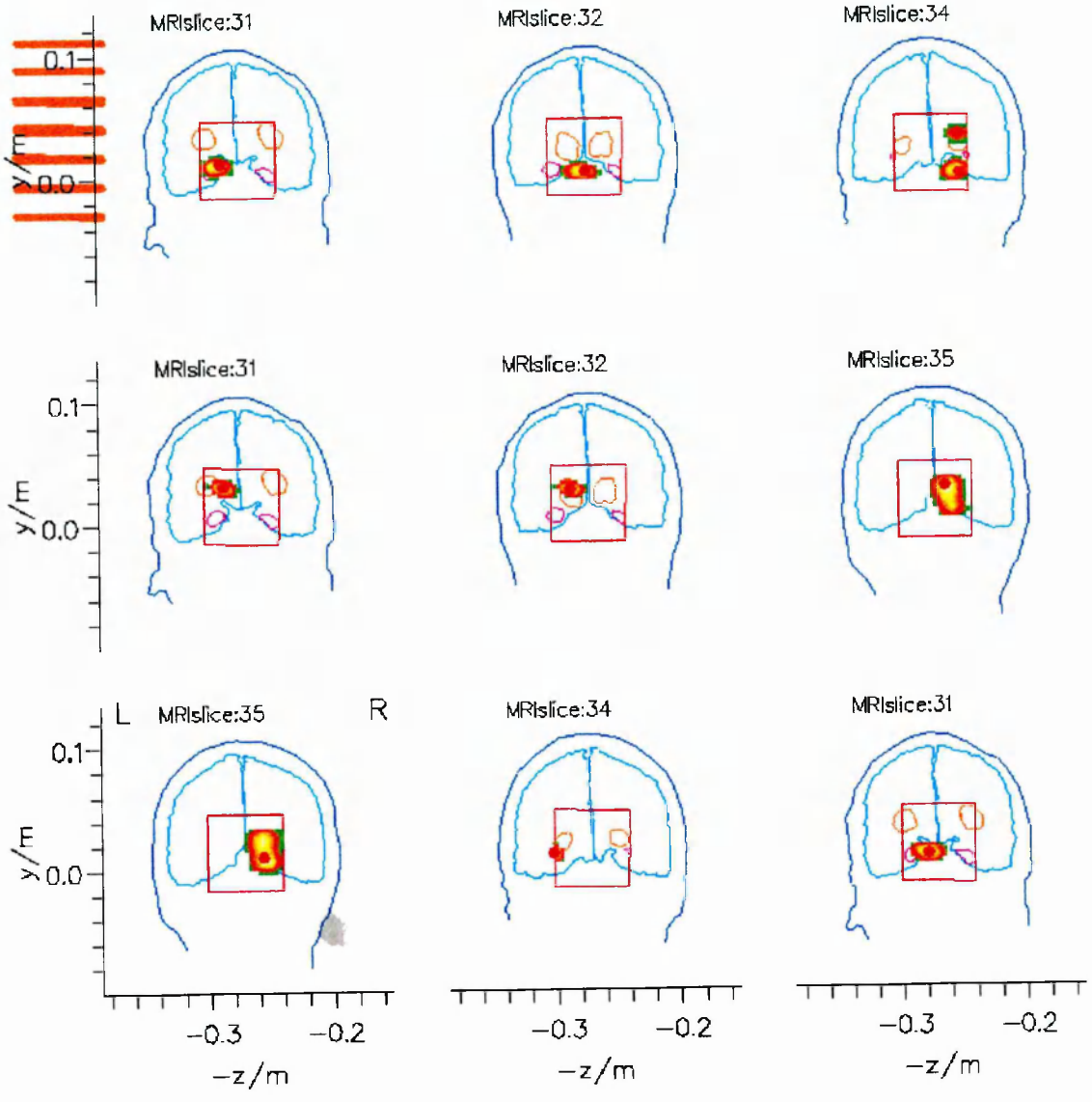

Figure 5-19: Plots where the current density estimates are obtained within a centrally - to the head - placed small cylinder after the probability decay factors were properly readjusted. Provided that conductivity modelling is correct, we can now see where the "focal deep" activity appearing in the previous plots is coming from.

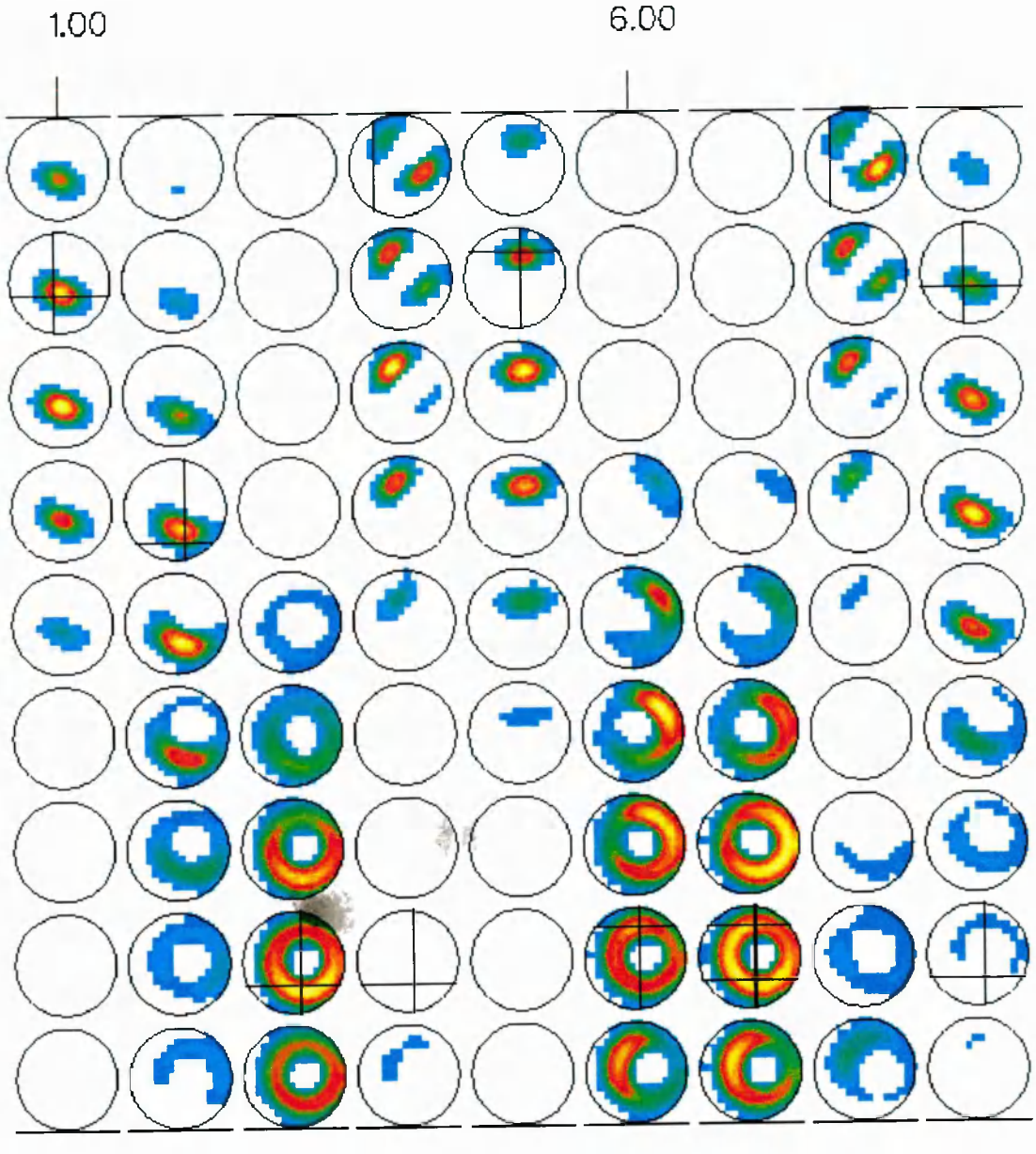

Figure 5-20: Recontructions of the previous sources within the small central cylinder using the same conducting centre for both the forward and inverse problems.

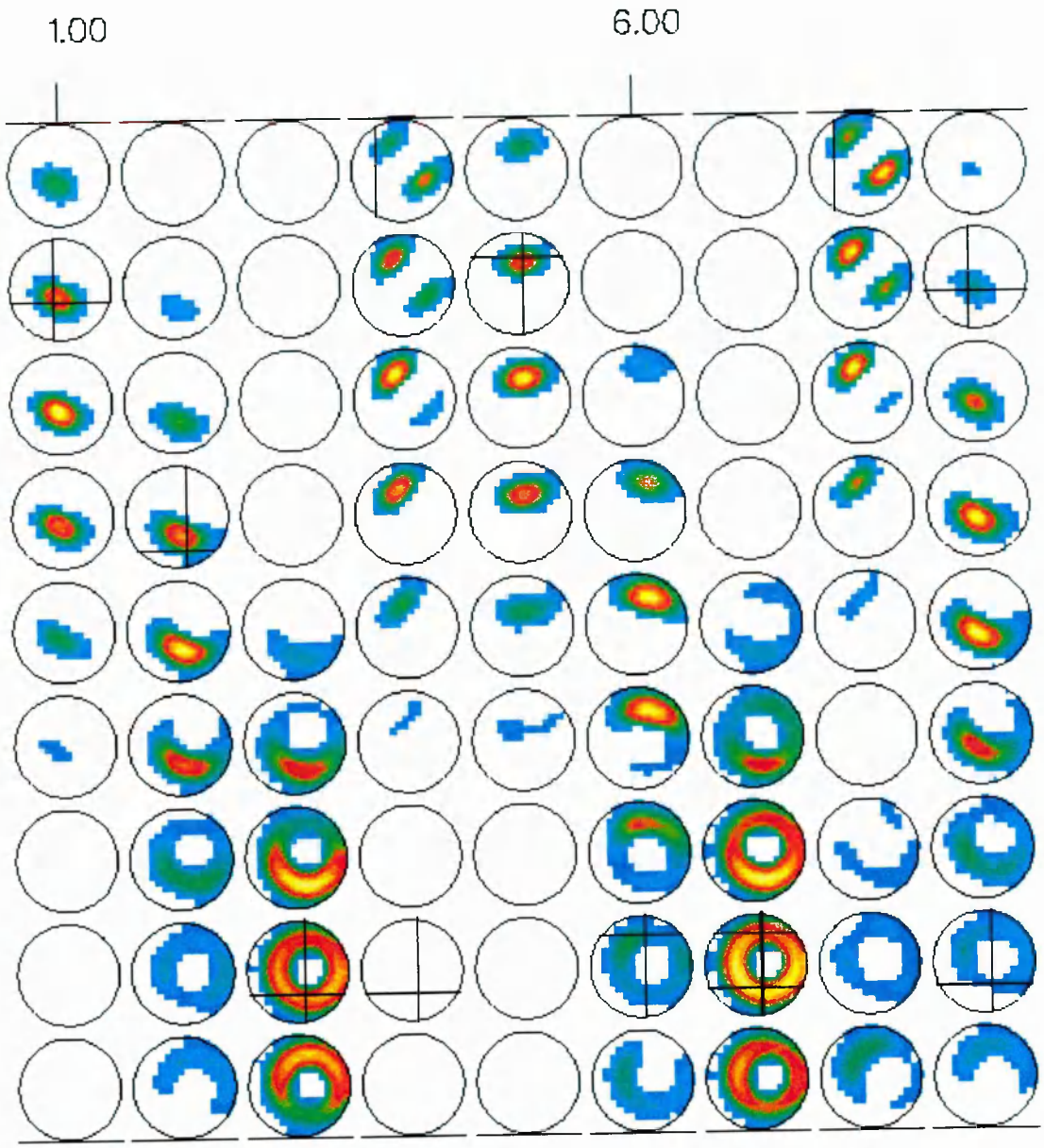

Figure 5-21: Small central cylinder recontructions of the previous sources where the conducting sphere centre for the forward problem had a difference of (-1 cm, +1 cm, -1 cm) from the one used in the inverse procedure.

5.3.2 Bilateral Measurements

In this section we assume that the KRENIKON system is a "twin probe system" (2x37 channels), that is, it consists of two identical Dewars that can be placed over each side of the head, so that both lateral aspects of the head are covered. We will now examine how the previous generators are recovered with MFT when recordings from the right probe only are available - as compared to the case of the left probe reconstructions, and what can be done when both probes are simultaneously used. We emphasise here, that similar tests have been performed with the BTi twin MAGNES system (2x37 channels), where a real experimental set-up was utilised, and the results were very similar indeed with the ones presented below. The decision to demonstrate the results from the hypothetical "twin KRENIKON" system rather than the more realistic twin MAGNES case, was taken so that continuity and coherence with the previous section is maintained.

For the purpose of the simulated twin KRENIKON system, the right probe, as mentioned, was "designed" identical to the left one, and was the mirror image - relative to the subject - of the left side. The familiar "small" cylindrical source space was used again in all conditions. The conductivity profile, as "seen" from the right probe, was modelled with a conducting sphere fitted to the inner skull surface of the right side; in the case of simultaneous bilateral recordings, the sphere was fitted to both sides together - however, we shall discuss the importance of this point later on.

In order to display all the details of the MFT solutions, we use the familiar cylinder plots, but rotated in such a manner, so that each row corresponds to a given timeslice (e.g. either a single or a double dipole source). In this way, the left and right sides of the source space become easier to view; in addition, it is more obvious which level of the source is regarded superficial relative to the sensors. For completeness, we show in Figure 5-22 the reconstructions in the small cylindrical source space of the former dipole set in the case of the unilateral measurements from the left.

If the same sources are measured from the other side of the head only, the scene changes to that of Figure 5-23. In this case, right cerebral hemisphere sources are localised successfully, and the level of activation in the left side is also correctly recovered. RHi (rows 3 and 7 in Figure 5-23) and RTh (rows 4 and 7 in Figure 5-23) activations can now be easily discriminated. On the other hand, when both RHi and LHi are simultaneously active (last row of Figure 5-23) only RHi can be seen this time (accordingly, the same effect was noticed in the recordings from the left side, where only LHi could be recovered). It should be emphasised here, that activation of left cortex (LC) does not affect the solutions - especially when a right side generator is present (row 4 in Figure 5-23); when LC is solely active the solutions appear as low magnitude patterns which

would be lost in the presence of any noise level (this is not clear though in row 8, because each row is individually normalised).

We now assume that the two probes record simultaneously and are both utilised in the MFT reconstructions. The conducting medium was modelled by a sphere fitted to both sides of the head. The centre of this very sphere was used in both forward and inverse problems. The smoothing parameter used was the same as in the previous reconstructions (i.e. s=1.0) and the decay parameter for the Gaussian probability weight was $\lambda_3 = 3.2cm$. Figure 5-24 shows the set-up conventions used together with the solutions. In this case, both sides are recovered in one go even if there are simultaneously activated sources in each side. The only problem is that the solutions are a bit distorted, due to the proximity of the conducting sphere centre. That is, the conducting sphere centre is almost at the centre of the head since it is fitted to both sides. Therefore, its distance from the left hippocampus (or thalamus), for example, is less than what it would have been if the sphere was fitted to the left side only (the difference in this specific case is approximately 2.5 cm). This effect appears in the MFT solutions as some sort of "edge distortions". These distortions are neither dependent on the size of the source space, nor on the number of the sensors used*.

Although it can be claimed that in the combined probe case information about both sides is recovered in one go, there is no substantial benefit, since more accurate information for each side can be available by separate inversions (compare, for instance, the "timeslices" containing the left (or right) hippocampal dipole in all three reconstructions, i.e. Figure 5-22, Figure 5-23, and Figure 5-24). The advantage of using both probes together in association with a small cylindrical source space in the centre of the head, could be revealed if two distinct conducting centres are used: one for the left, and one for the right. In the latter situation, each side would be correctly reconstructed without any distortion, and conductivity modelling would probably be closer to reality. Such reconstructions would be expected to be more powerful, since two different probability weights could be used, one for each conducting centre. It is through this kind of modelling that more reliable information about deep sources can be recovered. Unfortunately, however, this option is currently not available in our lab, and is, therefore, not pursued.

---

* *Simulations were repeated with a bigger central cylindrical source space covering a larger volume in the centre of the head. This is now more reasonable, since information is available from both sides. The number of sensors was also varied; a hexagonal array of 2x19 sensors was selected, so that only sensors that are projected within the cylindrical cross-section are used. Omission of a few channels did not affect the solutions. In all cases the results were the same.*

Furthermore, combinations of signals or signal transformations would probably boost such a methodology. For example, summations of readings for nearby sensors would eliminate any "superficial components", while enhancing deep sources. Clearly, more work along these lines is necessary. A number of changes are envisaged with the use of bilateral measurements and the helmet systems; but since in the major part of this thesis is concerned with real data from one side (in fact, bilateral recordings are only used in Chapter 8), these changes will not be discussed further.

Finally we emphasise that our strategy in localising deep activity is summarised by the following methodology: if the hemispherical source spaces from both sides (left and right) identify/indicate the same localisation(s) for "deep" activation and the localisation(s)/levels using a small, central cylinder (with one conducting centre into account) are in consensus, then something has to be definitely active down in that depth!

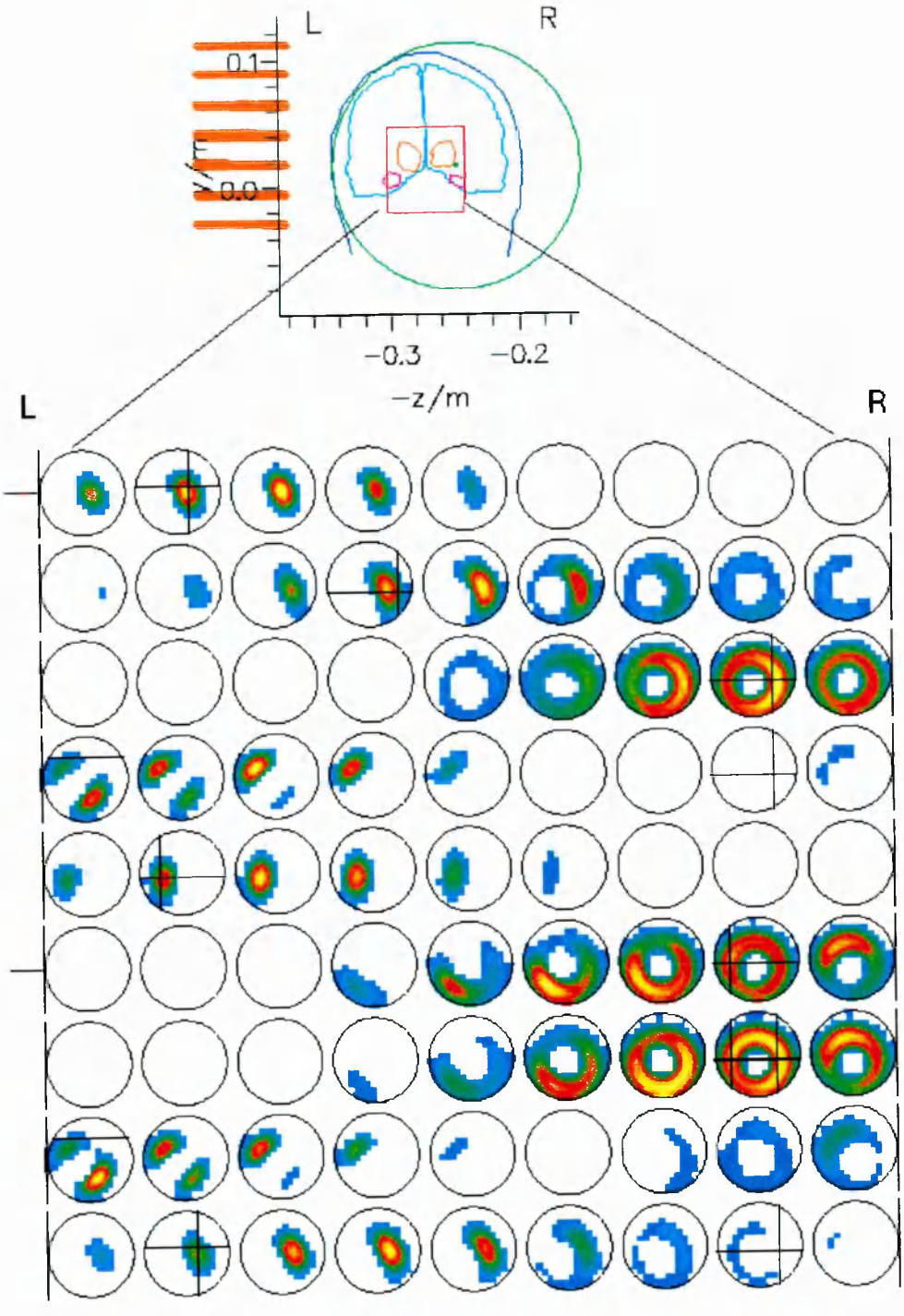

Figure 5-22: Reconstructions of the dipole set defined in Figure 5-17 using the left probe only. Each horizontal row represents one timeslice (i.e. a single or double dipole). In this perspective is easy to visualise which cylinder level is proximal to the sensors side.

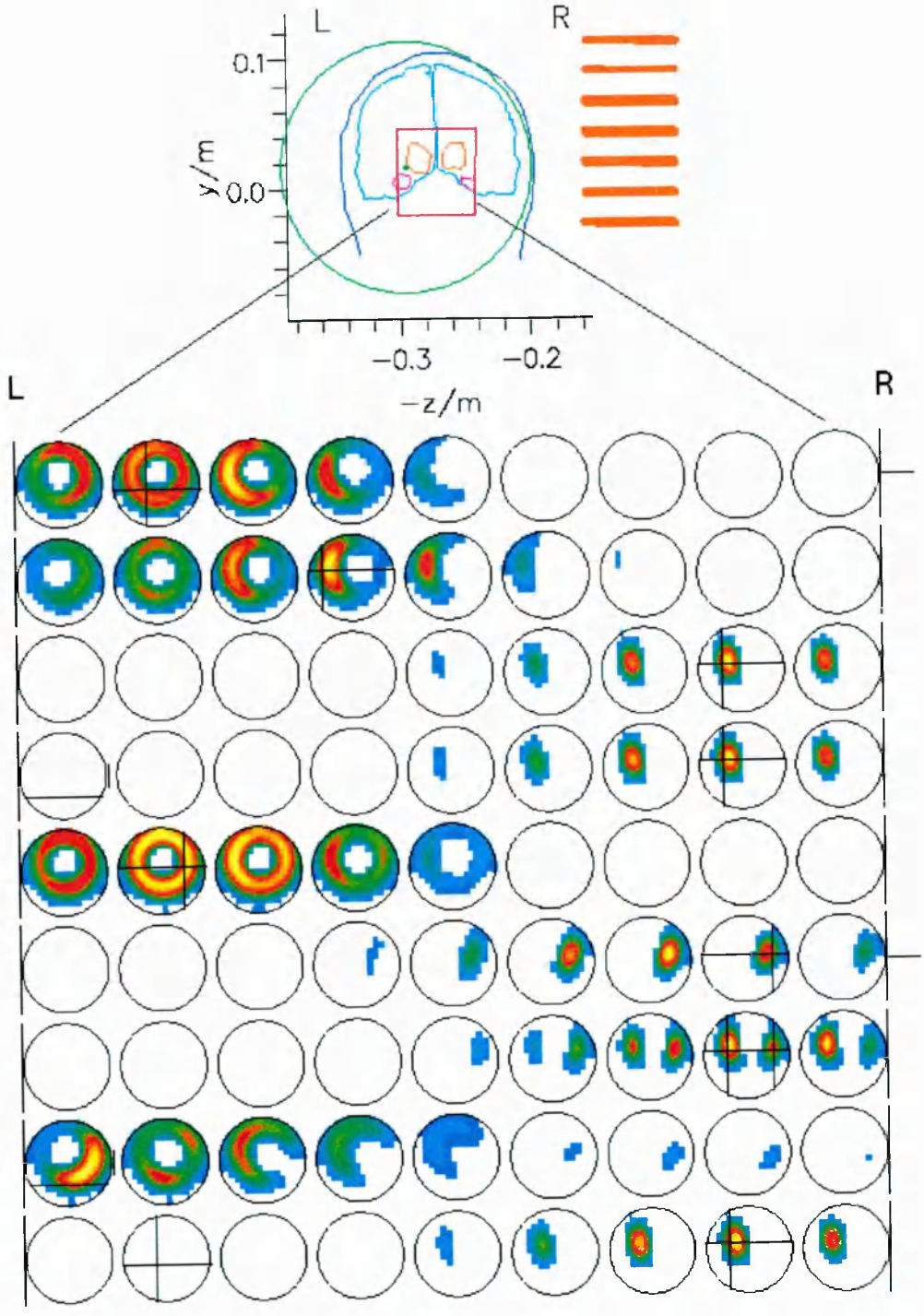

Figure 5-23: Same as before, but using the right probe only. The conducting sphere is fitted to the right side only. All the right side generators are recovered successfully; when left side generators are active, the level of activation is correctly recovered. However, when both LHi and RHi are simultaneously activated (last row), only RHi is "seen". This inversion complements the information obtained from using the left probe alone.

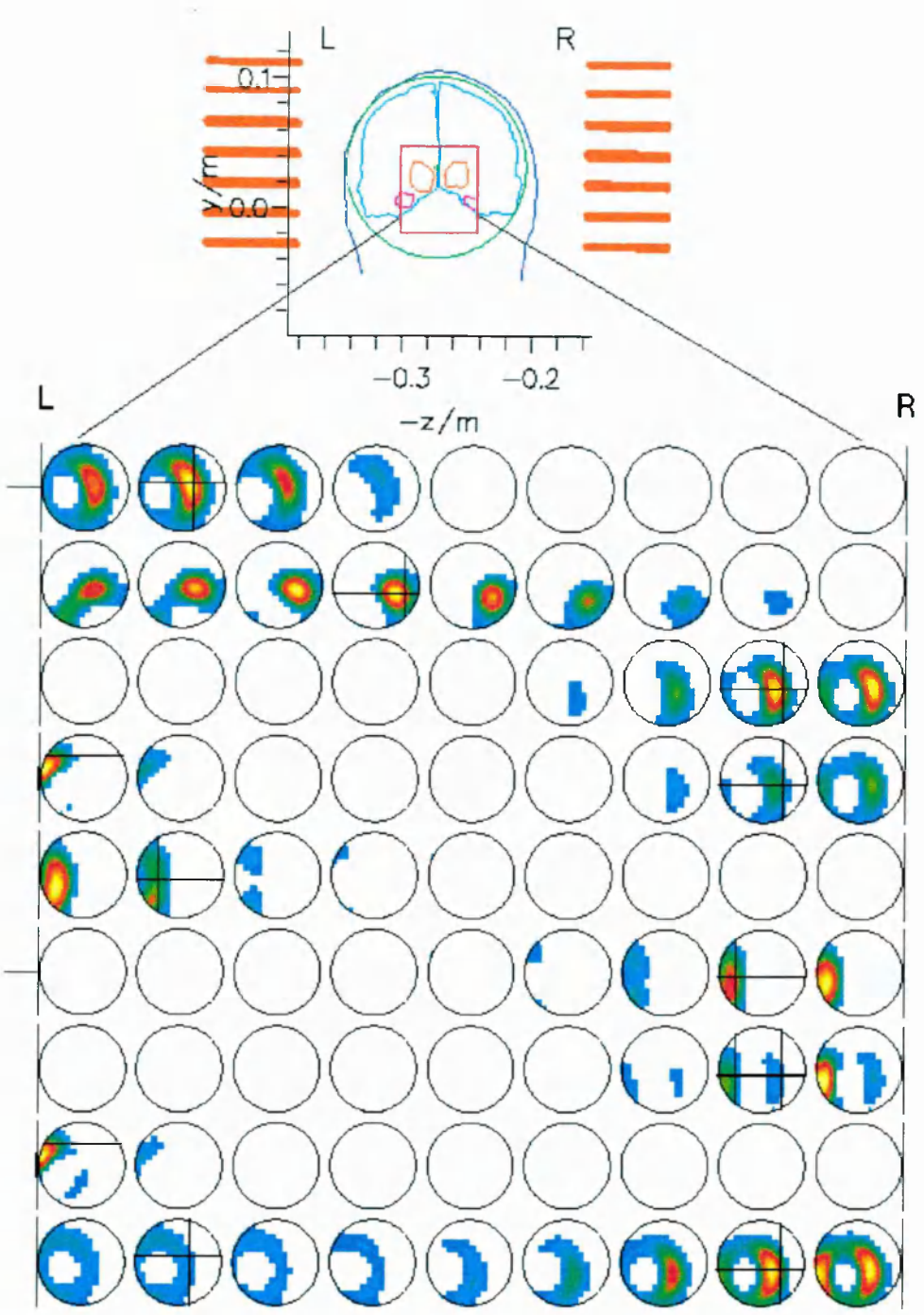

Figure 5-24: Same as before, but using both probes together in the MFT process. The conducting sphere is fitted to both sides. Both side generators are recovered; however, the images are distorted a bit, due to the proximity of the conducting sphere centre. The advantage of using such a combination is that one can obtain information about both sides in one inversion, rather than combining elements from two separate (left and right side) inversions.

5.4 Dynamic simulations

We have already mentioned in the previous chapters that timeslices are computed completely independently from each other in the current MFT implementation. In the sort of examples we have used in this chapter, there was no syllogism concerning the evolution of time. To put it more simply, we have used physiologically meaningless cases, where the left hippocampus could be active for just one moment, but completely "switched off" in the next timeslice during which all the activity were transferred to the right hippocampus. This was a consequence of the fact that we have, so far, dealt only with the spatial aspects of the MFT analysis relevant to our work. We now extend the simulations further to include the time characteristics of the various activated sources, thereby testing the temporal elements of our analysis. We follow the route of going from the more simple to the more complicated and at the same time more realistic cases. In all the simulations presented below, it is assumed that the sampling frequency of the instruments is 1000 Hz, that is, the time step is 1 ms.

In order to perform such simulations, a software suite was developed, that allows the user to design his/her own "dynamic brain". The user decides how many regions can be of interest (ROIs) in a specific experimental set-up. A set of fixed-orientation dipoles are then placed in the various ROIs (usually one dipole per ROI). The strength of each dipolar source (Q_k^*) is allowed to change with time. For the purpose of the present simulations, we have implemented a Gaussian-shaped temporal variation, where the user is free to choose the decay factors (λ_k) of each activation, as well as the exact timings for the maxima of each activation (t_k). Each dipole can be chosen to be activated once or several times, t_{ki} $(i = 1,\ldots,n)$, with same or different decay factors, λ_{ki} $(i = 1,\ldots,n)$, (the decay factor determines how sharp/smooth an activation can be). At each time instant, the overall strength of each dipolar source, $Q_k(t)$, is then given by:

$$Q_k(t) = \sum_{i=1}^{n} Q_k^* e^{\left(\frac{t-t_{ki}}{\lambda_{ki}}\right)^2} \tag{5-4}$$

Given that N such dipoles are active at each timeslice $(k = 1,\ldots,N)$, the forward problem is solved for a given sensor set-up and a given conductivity profile. MFT is then asked to reveal not only the position of each source, but also their temporal characteristics.

Since the actual power of MEG as a functional brain imaging technique is the combination of its (fair) spatial and (excellent) temporal resolution, we consider these tests of importance in the MEG analysis, since they are going to indicate whether or not a technique of analysis (MFT in our case) is capable of divulging the detailed temporal behaviour of diverse anatomical regions.

5.4.1 Recovering the temporal aspects of a single source

We start with the simplest case, where a single source is present at any time instant. In particular, we will assume that unilateral measurements are performed, with the 37 channel BTi MAGNES system, placed over the temporal area of a subject, and the source being active is the hippocampus (located some 4 cm deep in the right hemisphere). We further suppose that the hippocampal dipole obtains its maximum activity at 10, 33, and 65 ms, with decays of 5, 10, and 20 ms respectively. To demonstrate the MFT results, we make use of two concepts described in chapter 4, in addition to the familiar cylinder plots. These are, the measures of activations in time (Equation 4-29) and the displays of temporal integrals of intensity (Equation 4-30). Figure 5-25 shows the MFT results in such a fashion.

The "experimental" time runs for some 83 ms, and displays of the intensity integrated throughout the whole period are shown in association with the subject's anatomy (Figure 5-25 left). The ROI - indicated by a rectangular - covers the hippocampus and the evolution of activity within this ROI is illustrated on the right. Two cases are examined: first reconstructions from noiseless signals (Figure 5-25 bottom), and second, reconstructions when 20% random noise is added to the signals (Figure 5-25 middle and top). In each case, the green curve shows the actual activation profile of the dipole (drawn using Equation 5-4), while the blue one, is the MFT activation curve. The cylinder plot at the top part of Figure 5-25 corresponds to the 20% noise case. The dipole is always located between levels 4 and 5 (but is projected onto level 4 since is more closer to it), and the ROI is obtained from level 4.

One can note the minor effect the significantly high noise content has on the MFT results. Moreover, the MFT activation curves, seem to describe the dipole profile quite well in both cases. The only difference between the actual dipole profile and the MFT activations is that the former is, in general, "wider" than the latter, an effect that is probably associated with the intrinsic difference between a dipole and an MFT distributed solution.

Finally, as can be noticed in the cylinder plot (Figure 5-25, top), the solutions are a bit spread over different levels. Provided that the "routine tests" were properly performed, the maximum of the current density would occur in the correct level (between levels 4 and 5 in this particular case). So in fact, one can first identify this level and then study it in detail: outline the region of interest, and recover its underlying dynamics throughout the whole time period.

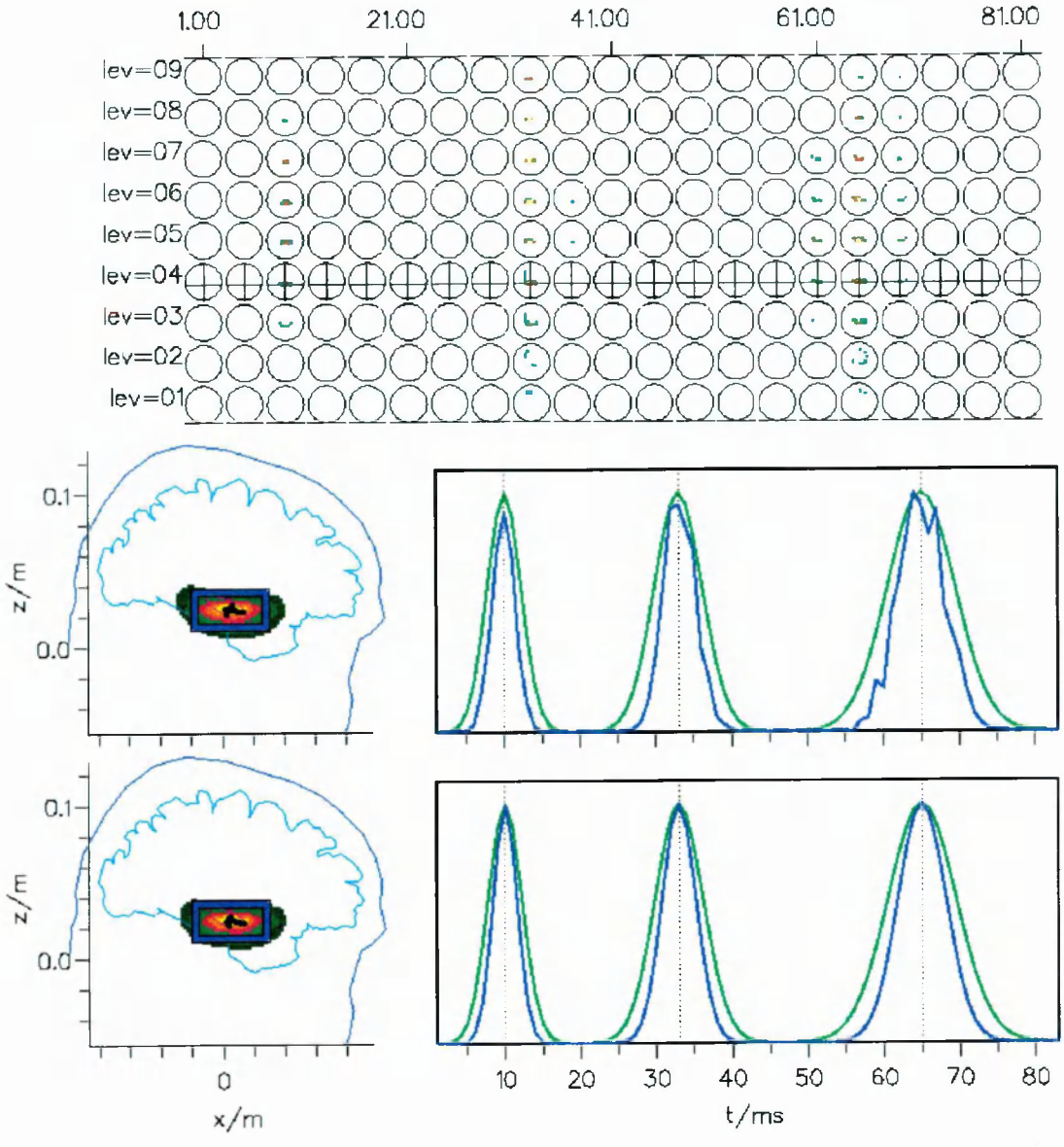

Figure 5-25: A dipole, located at the hippocampus of a subject, is activated at 10, 33, and 65 ms with activation decays of 5, 10, and 20 ms respectively. The dipole strength profile is illustrated by the green curve. Top: the 9-level MFT solutions for the whole period (every fourth timeslice is shown) when 20% noise is added to the signals produced by the dipole. Middle and bottom: on the left, integrals of intensity throughout the whole period are superimposed on the subject's MRI outline (bottom for the noiseless case, middle for the 20% added noise case); the MFT measures of activation within the rectangular ROI are displayed on the right (blue curves). The dipole is marked by crosses in the cylinder plots and by arrows in the intensity displays.

5.4.2 A superficial and a fairly deep source

In this section we test MFT's performance in the case where the previous hippocampal dipole, is activated in the presence of another, more superficial source. In particular, we assume that the second source is located at the subject's parietal cortical area* (in the same cerebral hemisphere with the hippocampus). The two regions are now allowed to be activated distinctly - with various activation decays - as well as in concert, and the same as before experimental set-up is used.

Figure 5-26 shows the MFT results in the presence of 10% added noise. On the right, the reconstructed activation curves for the parietal (orange) and hippocampal (blue) regions are in turn compared with the actual dipolar profiles; the top figurine combines the two activation curves for a better comparison. The ROIs together with the integrals of intensity over the periods marked by dashed vertical lines (during which each source is solely active) are given on the left part of the figure.

A number of facts become obvious from Figure 5-26. First, as expected, MFT can recover each source when it is solely active. Secondly, when the sources are activated simultaneously, the two MFT activations curves are peaked together. Furthermore, one can observe the smooth transitions from one region to the other. Sequential shifts of activity are depicted quite nicely in the MFT activation curves: as activity in one region starts declining and reappears in another region - e.g. 5 ms later - one activation curve is depressed while the other is peaking. The most difficult case is presented in the period from 55-80 ms when the parietal dipole obtains two sequential maxima at 65 and 75 ms, with decays of 20 and 10 ms respectively; in the meantime the hippocampal area is subjected to a sharp (5 ms decay) activation at 70 ms. Even in this case, one can note the peak of the hippocampal activation in between the two broader parietal activations.

A slight MFT defect that is also revealed when Figure 5-26 is examined carefully is that there are minor contributions from one region to the other, associated with the spread of the MFT reconstructions over different levels noticed before. In this particular case, one can note small peaks in the hippocampal activation when the hippocampal dipole is silent, but the parietal one is activated. These peaks are much smaller in magnitude though, from those representing an actual hippocampal activation. The "reflection" of one region into the other, is dependent on the relative strength (and distance from the

---

* *Given that the 9th level of our source space is the most superficial one, this area is taken to be at level 8. That is, we now have dipoles at the 4th and the 8th source space levels. The parietal dipole is at location (0.02,-0.056,0.06), while the hippocampal at (0.004,-0.027,0.018); all co-ordinates are with respect to the BTi head based MEG system - units in meters. The resulting distance between the two sources is 5.3 cm.*

sensors of course) of the various sources. In this example, the strength ratio follows the relation $Q_{Hippo}/Q_{parietal} = 10/3$ and minor reflections of the parietal activation are seen on the hippocampal one. If the relationship were $Q_{Hippo}/Q_{parietal} = 100/3$, then the reverse would have been observed.

Before we proceed into more complicated examples, we mention here that the vertical axes in the activation curves are defined in arbitrary units - this is a consequence of the fact that the physically meaningful magnitude of the actual current density is lost during the MFT iteration process. Therefore, only relative magnitudes are of importance and not the absolute values. A further MFT deficiency is apparent here, since not all the peak maxima are fully recovered - especially for the deep source. However, one should recall that in the presence of noise (e.g. 10% here) all the peaks would not necessarily be equal anyway.

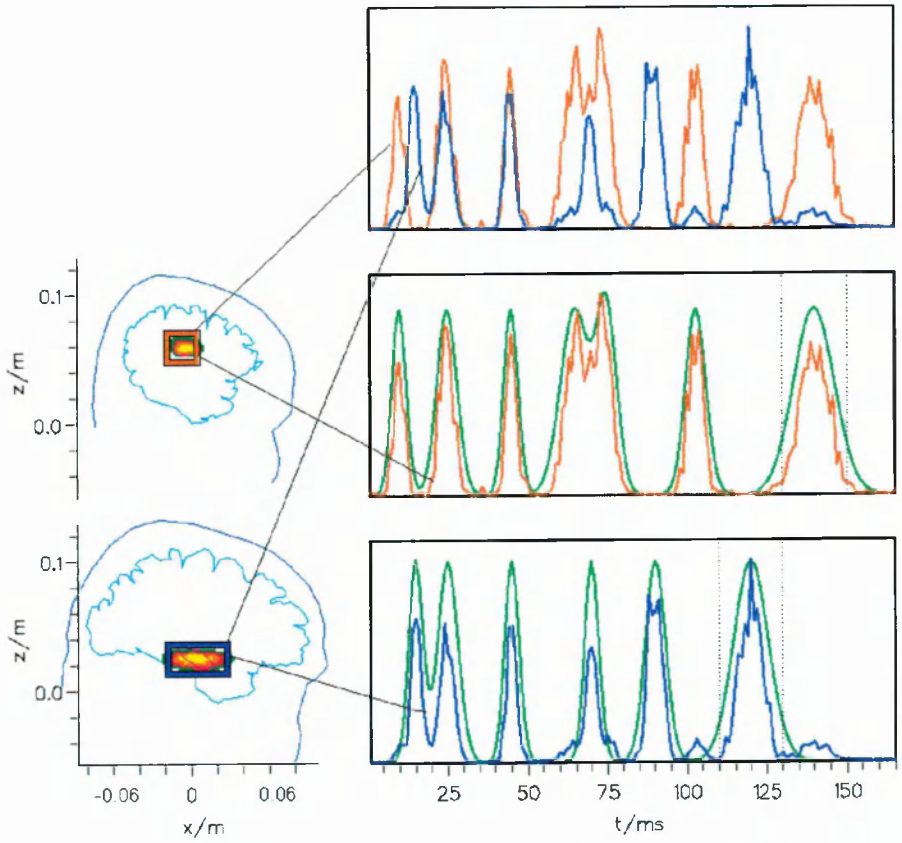

Figure 5-26: MFT results in the presence of 10% added noise. Right: the reconstructed activation curves for the parietal (orange) and hippocampal (blue) regions are in turn compared with the actual dipolar profiles; in the top graph the two reconstructed activation curves are themselves compared. Left: the two ROIs together with the integrals of intensity over the periods marked by dashed vertical lines.

5.4.3 Three nearby, fairly deep sources

Let us suppose that there are three nearby sources at the depth of the temporal lobe, placed along the subject's main hippocampal axis. In particular, we assume that the first dipole is just anterior to the hippocampus and more specifically in the amygdaloid region, the second one is right at the middle of the hippocampus, and finally the third is at its posterior end. We start with the simplest case where the dipoles are separately activated at a given time instance*; their strengths were taken to be equal.

Simulations were performed with the three dipoles having the same orientation, but also with the middle one having a slightly different one. In both cases the results were similar, but we only show in Figure 5-27 the results from the latter case. The task in question is whether one can distinguish the three sources or not by using the MFT activation curves within small ROIs centred over each dipole+.

As can be inferred from the MFT activation curves at the bottom right of Figure 5-27, each area is liable to contributions from the other nearby sources. However, the overall maximum of each activation occurs at the time that the specific source possesses its maximum strength. This is not true though for the middle source; so it seems that it is not probably very safe to attempt to distinguish between the middle and the posterior/anterior sources. On the contrary, one can discriminate reasonably well between activity in the anterior and posterior hippocampal ends, since the activation maxima of each of these two regions are correctly recovered and the contribution of one region on the other is considerably low when compared with the real maximum of the actual region. This provides the background for the observation of transitions from the anterior (e.g. amygdala) to the posterior of the hippocampus, when real data are analysed (see Chapter 7).

In each case, the integral over a finite time of the MFT intensity (and the same applies for the instantaneous MFT displays) is spread over a region, which covers much of the

---

* *Measurements are performed unilaterally over the temporal area of the subject, using the KRENIKON 37 channel system, and 10% random noise is added on the signals.*

+ *A subtle remark, which also applies to the rest of the results in this thesis, is that the number of grid points in each source space level is fixed (i.e. 17x17). However, when a hemispherically shaped source space is used, the superficial levels are inevitably smaller than the deeper ones. As a consequence, there are a lot of "zero-valued" pixels in the first few levels; these are not yet eliminated from our software, so as to increase the resolution in the top levels. In other words, one can use the full grid (17x17) to cover each superficial level, rather than basically having a 17x17 grid at the bottom and an effective 10x10 grid at the surface. This may prove to be very important in the future.*

hippocampal structure. However, the point with the maximum intensity (yellow coloured) is in good agreement with the position of each dipole (black arrow) as can be noticed in the top part of Figure 5-27 (despite a small deflection in the first one), a point which we shall come back into at the end of the section.

But what would happen in more complicated situation where the previous sources would be active separately but with overlapping activation profiles, or even simultaneously active, and furthermore, sequential shifts of activation (e.g. anterior-posterior-anterior) would occur? To tackle this question we devised a model that facilitates all the above and can be seen in Figure 5-28. The same as before sources and ROIs are used, but the temporal evolution of each source is now different (see middle row of Figure 5-28). The overall activation patterns obtained can be viewed in the bottom right of the figure. Since we declared confidence in discriminating the posterior and anterior areas using the MFT activation curves, we would like to concentrate on these two areas only.

In Figure 5-29, we display the model strength profiles for the previous two regions (left) together with their corresponding MFT activation curves (right), in smaller time intervals, so that temporal differences become clear. When the two areas are simultaneously activated (dashed profile parts), the MFT activation curves are peaked together and there is no time lag in their ascending or descending valleys. This is true for diverse decay factors (activation time widths). However, when a sequential activation occurs in the two regions, it is nicely reflected in the MFT curves, which show a distinct time lag in the rising or falling of the two peaks. It is worthy to mention, that given the presence of 10% noise, one should not anticipate to recover the temporal evolutions exactly. In such cases, signal filtering improves the whole image and the peaks of each source become more clear.

Having discussed all the above, one may be under the impression that the temporal resolution of MFT might be very good, however, nothing much can be claimed about its spatial capabilities, since the "spread" of the solutions in that depth (nearly 4.5 cm deep in the cerebrum) is extended over the whole hippocampal structure. That is, very little could be said regarding the spatial propagation of activity in that fairly deep level. Nonetheless, a complementary concept proves to be useful in this situation. That is, as already mentioned a while ago, the transitions of the point with the maximum integrated or instantaneous intensity itself. To demonstrate this we shall use two time intervals in the previous model: the period between 10-30 ms, and also the period between 30-50 ms.

The changes in the magnitude of the instantaneous intensity within a given image can be displayed by connecting areas of strong activity with arrows. This translates into an

image of the sequential shifts of strong activation, thereby providing hints of how the various anatomical regions of the brain might be connected. Such an illustration is given in Figure 5-30. In the first epoch (10-30 ms) activity is supposed to be propagating from the anterior, through the middle, to the posterior parts of the hippocampus, while in the second one (30-50 ms), we expect a shift from posterior to anterior and back to posterior, as can be inferred from Figure 5-29. This is indeed what is observed in top row of Figure 5-30, where these "connectivity images" are displayed (left and right for the first and second epochs respectively). The previous expectations are confirmed with minor deflections due to the presence of random noise[#] . For completeness, the integrals of intensity over the specific epochs are also included in the bottom of Figure 5-30 which do not seem to be that informative, but one should appreciate that their slightly different shape/orientation indicates the overall trend in the sequence of transitions over the particular periods.

[#] *We anticipate that if integrals of intensity over some 3-5 ms are used to obtain these shifts, the picture will become much clearer.*

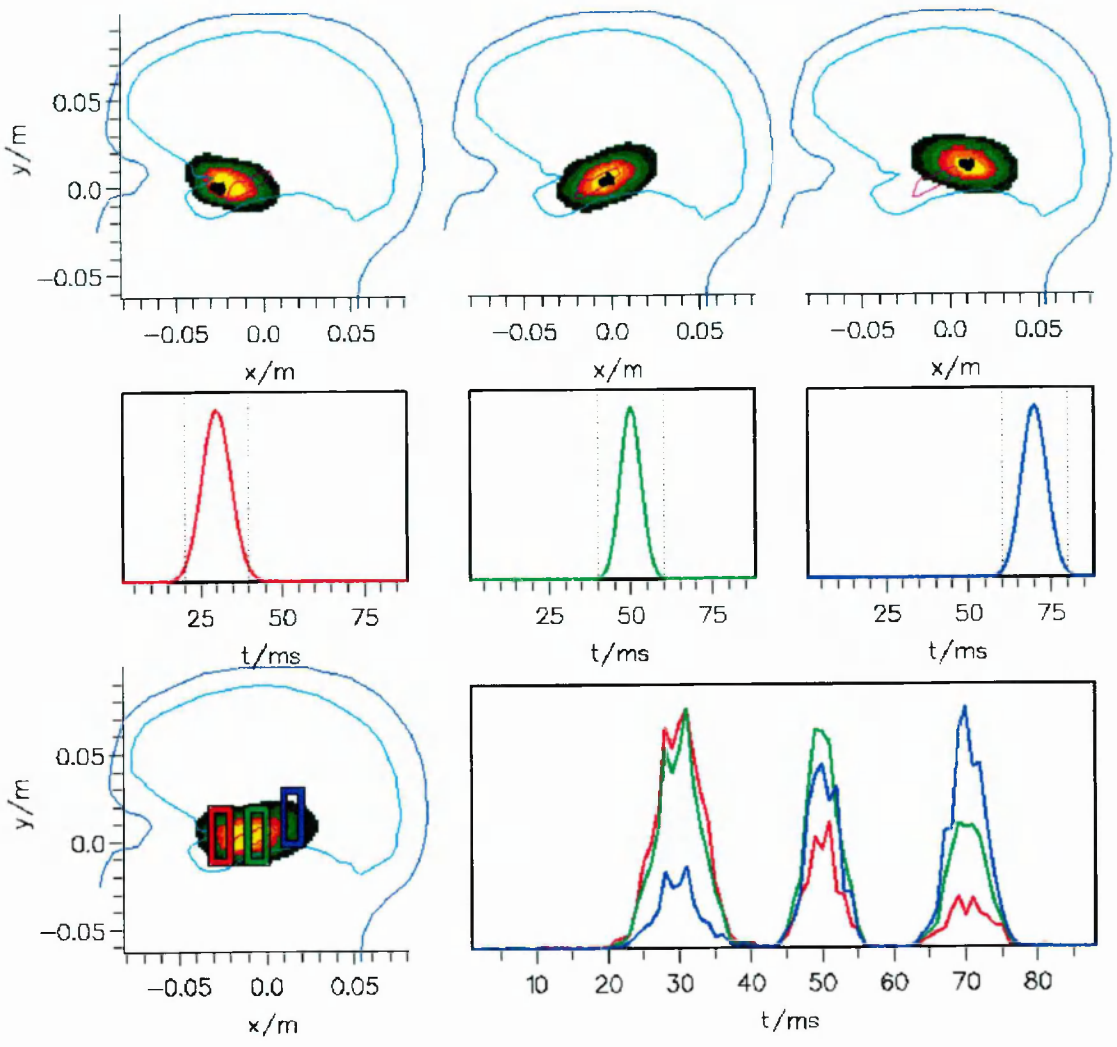

Figure 5-27: Top: dipoles (arrows) along the hippocampal axis and integrals of intensity over the periods that each source is distinctly active - marked by vertical dashed lines below, are superimposed on MRI outlines. Middle: model profiles for each dipole. Bottom: ROIs and intensity integrated over the whole period (left) and MFT activation curves (right).

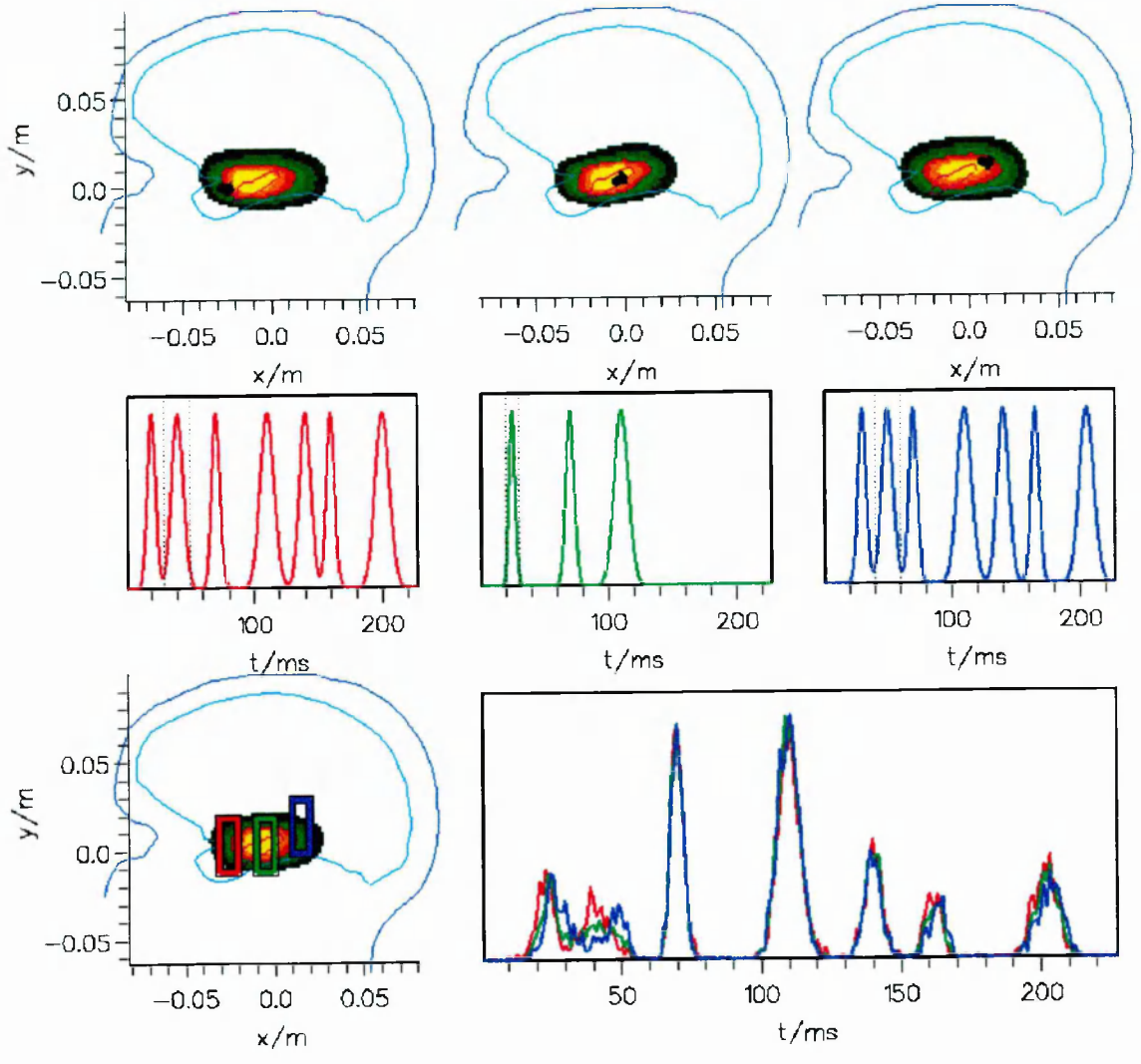

Figure 5-28: The same display as in Figure 5-27 but for a more complicated temporal evolution of the three sources.

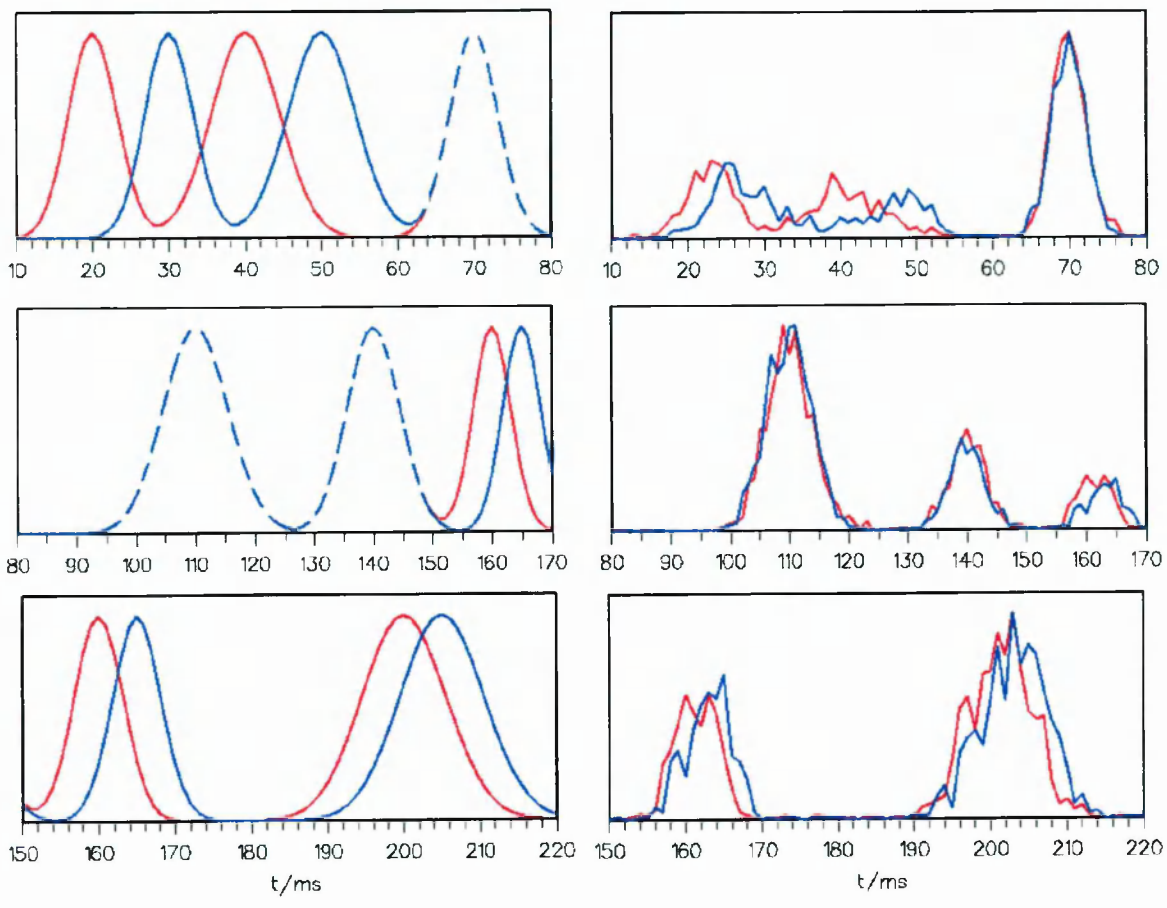

Figure 5-29: Model strength profiles for the anterior and posterior dipoles (left) together with their corresponding MFT activation curves (right), in smaller time intervals, so that temporal differences become clear. When there is a simultaneous activation (dashed parts), the MFT activation curves are peaked together. When there is a sequential transition in the activation there is a time lag in the ascending or descending valleys of the MFT curves.

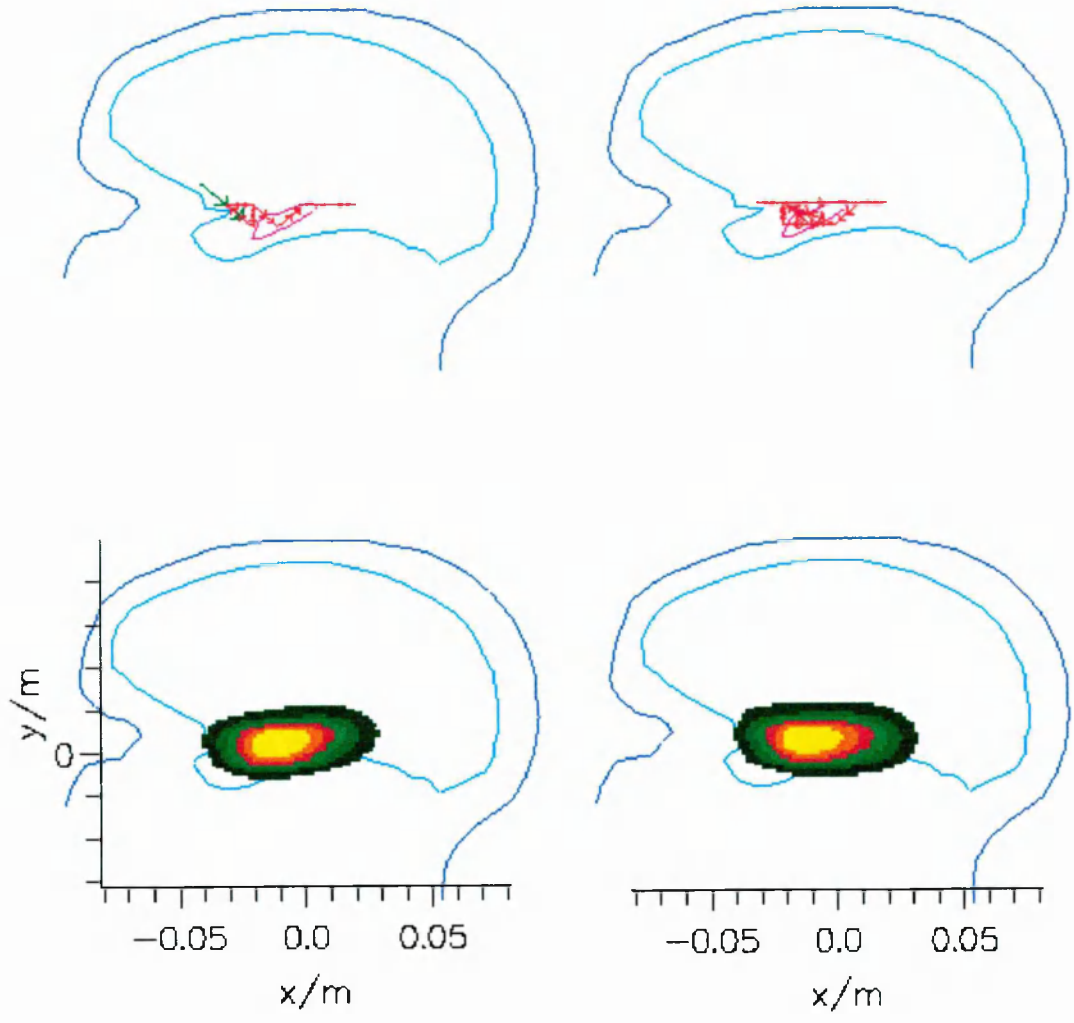

Figure 5-30: Top: the changes in the magnitude of the instantaneous intensity are displayed by connecting areas of strong activity with arrows. This translates into an image of the sequential shifts of strong activation, thereby providing hints of how the various anatomical regions of the brain might be connected. On the left, the interval 10-30 ms of the model in Figure 5-28 is illustrated where activity propagates from the anterior, through the middle, to the posterior parts of the hippocampus. On the right, the interval 30-50 ms of the same model is given with sequential shifts of activity from posterior→anterior→posterior. Bottom: integrals of intensity over the specific epochs. Note their slightly different shape/orientation which indicates the overall trend in the sequence of transitions over the particular periods.

5.4.4 Bilateral hippocampal activation

We finally examine in this section the case where both hippocampi are activated during the same "recording"; we allow for separate as well as simultaneous activations with different time constants (decays). Simultaneous bilateral measurements with the twin BTi MAGNES system are assumed. MFT is performed within a central cylindrical source space (both probes - 2x37 channels - are used in one go) and conductivity, as mentioned before, is modelled by a single sphere fitted to both head sides*.

The results are shown in Figure 5-31. In the two bottom rows of the figure, each MFT activation curve is compared with its corresponding model dipole profile, as usual, while in the top row the two activation curves are plotted together in order for the temporal differences to be highlighted. It can be noted that each activation curve describes its model very well; the different decay constants of the two activations are also reflected in the solutions. No contributions from one hippocampal region are observed in the other, and both sources can be recovered simultaneously. Furthermore, the temporal features of each region are reflected in the MFT activations regardless of the specific characteristics of its homologous contralateral region. Notice, for example, the behaviour of the activation curves around 150 ms as compared with that around 260 ms. In the former case, a sharp (5 ms time constant) left hippocampal activation occurs together with the much broader (30 ms time constant) activation of the right hippocampus, while in the latter, both hippocampal regions undergo a broad activation (30 ms time constant).

In addition, sequential activation shifts are also nicely depicted in these curves, when activity is interplayed between the two regions over a few milliseconds time (see the first 50 ms, for instance). Such interplays of activation are better viewed in Figure 5-32, where the left (bottom) and right (top) hippocampal MFT/model activations are plotted together with a "depth-time-plot" (middle). In the latter, the activity is integrated across the cylinder levels and the integrals are displayed as contour plots of average intensity (across depth and time); this comprises a convenient way of summarising the changes in the levels of activation over long time intervals. All the above points become clear in Figure 5-32: whenever a broad activation occurs, the contour plot occupies a wide area; shifts of activation from the left (bottom-side) to the right (top-side) now become more obvious.

In conclusion, MFT's performance is quite satisfactory in this particular case, recovering well much of the underlying spatio-temporal information. However, one should always

---

* *The same conducting centre was used for both the forward and inverse problems.*

be aware of the intrinsic limitations associated with this kind of modelling as discussed previously in section 5.3.2.

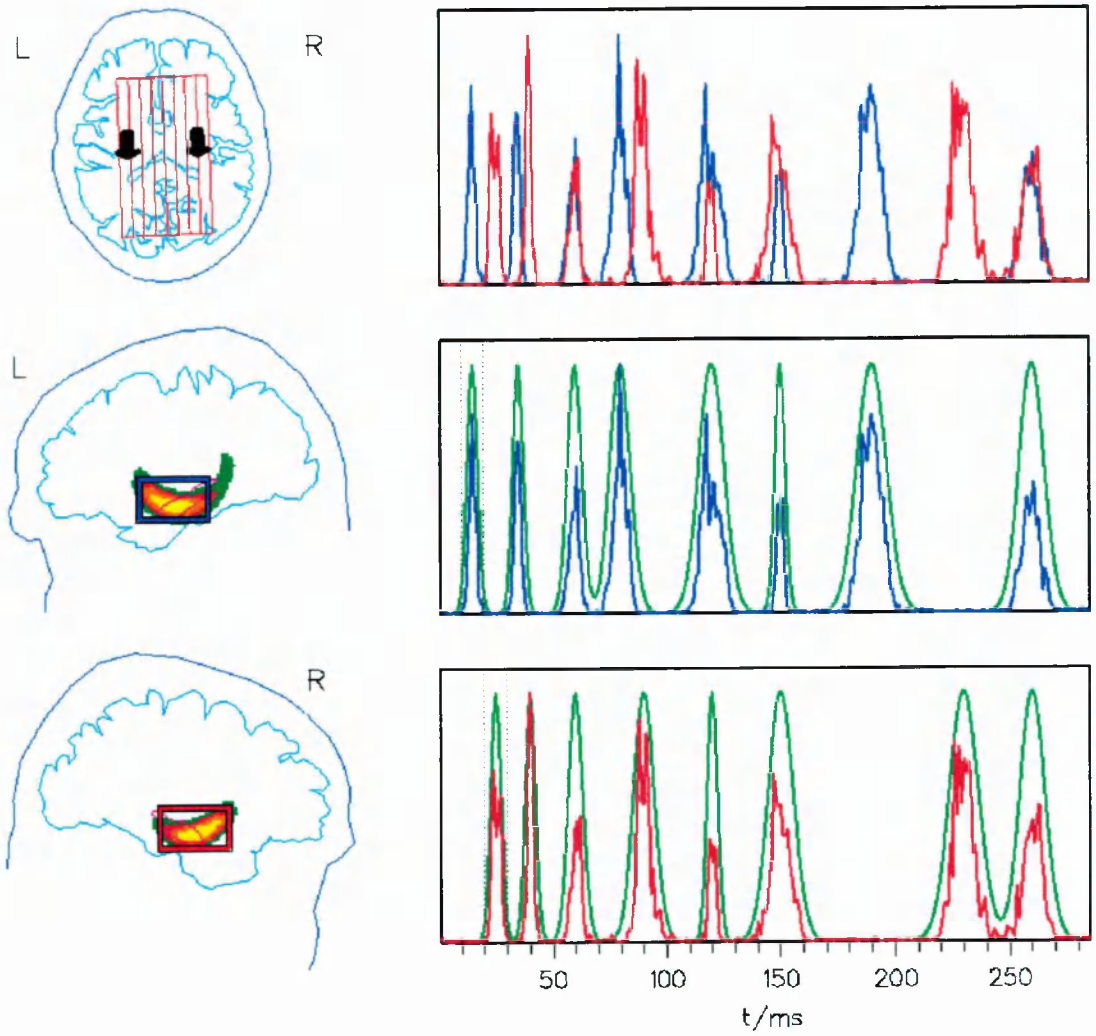

Figure 5-31: Results from modelling bi-hippocampal activation. The MFT activation curves (red) are compared with their corresponding model dipole profiles of the right (bottom) and left (middle) hippocampus (green). Integrals of intensity over 10 ms (marked by vertical dashed lines) and ROIs are presented on the left parts. The top row shows the dipole positions inside the cylindrical source space (left), but also the two hippocampal MFT curves for effortless comparison.

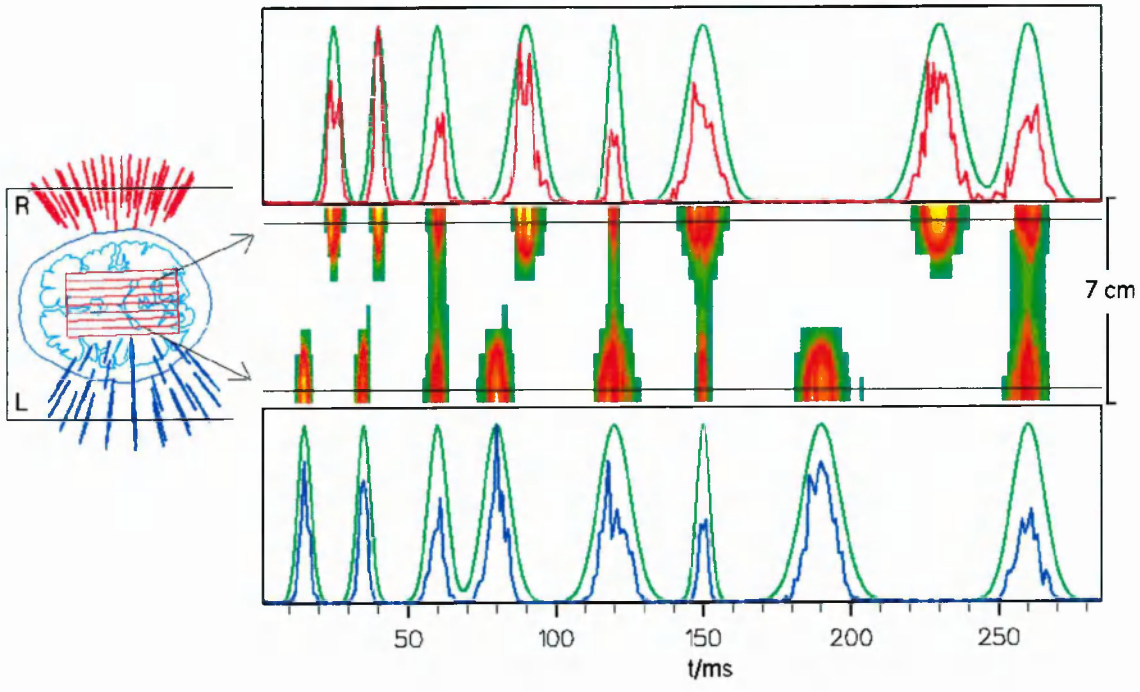

Figure 5-32: Left: cylindrical source space and sensor positions for the two the twin MAGNES BTi system. Right: MFT activation curves (red/blue) and model dipole profiles (green) for the left (bottom) and right (top) hippocampus. In the middle a depth-time-plot illustrates contour plots of average intensity across depth and time (as integrated across the cylinder levels). The changes in the levels of activation over the whole time interval are summarised in this way. Interplays of activation between the two regions (left and right) are easily observed, as well as the length (time constant) of each activation. The two horizontal lines mark the approximate level of the two dipoles in the 7 cm high cylinder.

6. MFT study of Unaveraged Interictal Epileptic events

6.1 Introduction and Historical Remarks

Epilepsy is a Greek word formed form two components: *"epi"*, which means upon, and *"lepsy"*, which comes from the root *"lamvano"*, meaning *to seize*. Medically, a person with epilepsy is someone who is subject to recurrent interruptions of brain function (seizures or fits), due to sudden disorderly nerve discharges. Epilepsy is not, however, a "nervous" condition in the generally accepted sense of the word (McGovern 1982). To put it differently, "there is no disease named epilepsy" as Niedermeyer (1993c) authoritatively states. Rather, epileptic seizures are abnormal reactions of the brain caused by numerous and diverse diseases, in which the entire brain or parts of it may be involved. The type of seizure is largely determined by the actual extent of brain involvement. The basic disorder is most commonly localised in the brain, however, functional failure of other important organs outside it and associated metabolic-toxic changes may also lead to encephalopathies and, therefore, epileptic seizures (Niedermeyer 1993c).

The very first descriptions of epileptic phenomena are traced back to the ancient Greek times. In fact, the first attempts to disconnect such phenomena from any kind of superstitious beliefs, but also to associate and explain them in terms of natural causes are found in the Hippocratic collections around 400 BC (Translated by Jones, 1981):

> *"I am about to discuss the disease called 'sacred'. It is not, in my opinion, any more divine or more sacred than other diseases, but has a natural cause, and its supposed divine origin is due to men's inexperience, and to their wonder at its peculiar character..."*

Modern epilepsy research was initiated by Jackson and Gowers, who described and distinguished different types of epileptic fits. However, the breakthrough was certainly accomplished by Berger, whose endless efforts made possible the measurement of brain's electrical activity under both physiological and pathophysiological conditions. The role of the EEG in clinical epilepsy was first discussed by Gibbs, Davis and Lennox (Gibbs et al 1935), but Kaufmann (or else Rostovtsev), a pioneer in experimental epilepsy, was the first to postulate that "abnormal discharges indicate abnormal neurons" (Brazier 1973). Their work, together with the stimulation observations during brain surgery by Penfield and Jasper and many others established a firm basis for the scientific diagnosis and classification of epileptic seizures (Pockberger, 1995).

Recent investigations suggest that about 1% of the general population suffer chronically from epileptic seizures (Speckmann et al 1992), making it more than two million people of all age groups in the US alone (Shin and McNamara, 1994). Current medical therapy is largely symptomatic and not always satisfactory. Antiepileptic drugs can control seizures in many patients, but they may be ineffective in more than half of the patients in certain kinds of epilepsies. Removal of epileptic tissue can cure a select population, and new drugs are forthcoming, but for many epilepsies there are no prophylactic regimen or easy cure (Shin and McNamara, 1994).

6.2 Terminology

6.2.1 Seizure types and electric patterns[+]

Epilepsy is a syndrome of episodic brain dysfunction characterised by recurrent unpredictable spontaneous seizures. *Partial seizures* begin in a localised brain region, whereas *generalised seizures* show widespread involvement of both hemispheres from the outset. Although the symptoms based classification of seizures is a "thankless job" (Niedermeyer, 1993c), a general classification list does exist, as it was compiled by the

---

[+] *"...they devise many fictions of all sorts, about this disease among other things, putting the blame, for each form of the affection, upon a particular god. If the patient imitate a goat, if he roar, or suffer convulsions In the right side, they say that the Mother of Gods is to blame. If he utter a piercing and loud cry, they liken him to a horse and blame Poseidon...If he foam at the mouth and kick, Ares has the blame..." (From the Hippocratic Collections,'The Sacred Disease'; translated by Jones, 1981).*

"Commission on Classification and Terminology" of the "International League against Epilepsy" back in 1981, and more recently revised to incorporate new features such as aetiology and age of onset in addition to the different combinations of seizures (1989). There is no point in describing such a list in great detail but it is worthy to mention herein some of the most frequently met examples of generalised seizures, which are *absence (petit mal)*, *myoclonic* (see chapter 8), and *tonic-clonic (grand mal)* seizures.

Depending on whether or not the level of consciousness is affected, partial seizures are divided into *complex*, *simple* and also *partial seizures evolving to secondarily generalised seizures*. Most *complex partial seizures (CPS)* are believed to originate from the temporal lobe and hence are called *temporal lobe seizures*. Patients frequently have more than one kind of seizure. For instance, when simple partial seizure precedes a complex partial seizure, it is referred to as an *aura*. Complex partial seizures constitute a major percentage of epilepsies and are rather disabling as a consequence of impaired consciousness. They are often medically intractable in that doses of medications with tolerable side effects will not satisfactorily control the seizures.

The time period of a seizure is referred to as *ictal*, while that between seizures as *interictal*. During the latter interval, epileptic discharges are continued, but they may be very short-lasting and, therefore, not lead to any kinds of typical symptoms. Other commonly used terms include *convulsion*, implying ictal behaviour with vigorous motor activities, and *status epilepticus*, denoting a very prolonged seizure or seizures occurring so frequently that full recovery of brain function is not retrieved interictally.

EEG has revolutionised the entire field of epileptology, and is still today the main tool used in the diagnosis and investigation of epileptic cases. Epileptic discharges, manifest themselves through "special" electric patterns that give rise to certain EEG signals. Some terminology has naturally accompanied such epileptic signatures and the same kind of "language" has inevitably been followed in the MEG epilepsy research. It is important to give here some of these definitions, since we shall be using them extensively in this and the following few chapters. We only, however, deal with the most basic definitions concerning the interictal period - the period studied in this thesis*.

- A *spike* is a transient, clearly distinguished from the background activity, with pointed peak (of variable amplitude) and a duration from 20 to under 70 msec (IFSECN, 1974). Discrimination against background is aided by their high peaks or faster character (i.e. the shorter duration) (Niedermeyer, 1993b). Spikes have many characteristics in common and yet there are also remarkable inter- and intra-individual variations.

---

* *Actual plots of the various patterns as recorded by MEG will be given at later stages.*

- A *sharp wave* is similarly a transient, clearly distinguished from the background activity, with pointed peak (of variable amplitude) but with a duration of 70-200 msec, i.e. more than approximately $1/14^{th}$ to $1/5^{th}$ of a second (IFSECN, 1974). Some sharp waves though may exceed the maximum length of 200 ms and others may become more complex. Spikes and sharp waves are epileptically/neurophysiologically closely related phenomena (Hellstrand 1995); both of them are typical paroxysmal discharges and highly suggestive of an epileptic seizure disorder, although both phenomena may occur in patients without a history of seizure disorder (Niedermeyer 1993b). Sharp waves are usually found as random focal discharges; most anterior temporal spikes are, in strict sense, sharp waves. This is also true for most benign Rolandic spikes of childhood.
- A *spike and wave complex* is a pattern consisting of a spike followed by a slow wave. There has been evidence that such a complex is not just simply an association of a spike and slow wave, but it represents an alternating succession of excitation and inhibition. Depending on the frequency of their appearance, there is a distinction between classical (3/sec), slow (1-2.5/sec) and fast (4-5/sec) spike wave complexes and also the smaller 6/sec spike wave discharge, justified on the basis of different clinical-epileptological correlates of each type (Niedermeyer 1993b).

6.2.2 Epileptic zones and relevance of interictal recordings

An *epileptic focus* is simply an area of the cerebral cortex where a considerable number of neurons are involved in the epileptic process. This theoretical definition though might not be adequate as a basis for successful epilepsy surgery, since pathologically discharging neurons might be widespread and the complete removal of the affected area would lead to considerable neurological and neuropsychological deficits in the patient, certainly unjustifying the need for quality life improvement (Elger 1992). Furthermore, the term *focus* might be misleading having different meanings for different investigators. For example, although an EEG spike focus represents *the maximum of an extensive area* of cortex involved in the generation of the epileptiform discharge, some have used the term in a more literal fashion implying a focal point of epileptogenicity (Lüders et al 1993). In the light of the considerable controversy concerning the definition of the epileptic focus a different approach has been proposed based on the identification of different zones and lesion in the epileptic cortex (Lüders and Awad, 1992).

According to that approach, a prerequisite for a successful epilepsy surgery is the *epileptogenic zone*, which the brain area to be removed in order to cure epilepsy, thereby granting seizure freedom. Unfortunately, this zone cannot be adequately defined by any current methodology, and therefore its boundaries have to be outlined in hypothetical

terms as punctually as possible, in order to have the maximum benefit for the surgical candidate while reducing the possible functional deficits to the minimum (Elger 1992).

The *irritative zone* is defined as the area which generates the interictal activity. It is usually larger than the epileptogenic zone, since it is believed that interictal epileptiform discharges are mostly arising from a rather extensive cortical area. This area is associated with the recordings of the sharp transient signals defined in the previous section. However, there has been evidence suggesting that some epileptogenic zones may extend beyond irritative zones or even exist in the absence of any detectable irritative zone (Lüders et al 1993).

The *pacemaker or ictal onset zone*, on the other hand, is the brain region which the actual seizure originates from. Visual inspection of the clinical semiology of a seizure is the only way to define the beginning of a seizure by other means than electrophysiological techniques. The relation between the irritative and pacemaker zones is difficult to determine. It seems that the latter is within the former; appropriate placement of invasive electrodes may, therefore, detect the actual location* . It is also possible that this zone represents the area of cortex with the lowest threshold for seizure generation, but after its resection other cortical areas of relatively higher threshold for seizure generation (but still at an abnormally low level) could become ictal onset zones (Lüders et al 1993).

The *epileptogenic lesion* is defined as the anatomical lesion which is responsible for causing the seizure disorder originally. Neuroimaging techniques prove to be invaluable in determining such lesions. As a rule of thumb, the epileptogenic zone may be adjacent to or covering an area in which the lesion is located; resection of the lesion itself may successfully eliminate seizures, but in other cases, a lesion might not even be related to the epileptic disorder.

The *ictal symptomatogenic zone* is the part of the brain which, when activated, initiates the epileptiform symptoms characterising the patient's seizure onset. The clear definition of this area can be again as problematic as the pacemaker zone itself, and experience shows that only rarely there exists a good overlap between the two zones. Finally, the *functional deficit zone*, is the brain area which interictally shows an abnormal functioning determined by neurological and/or neuropsychological examination or functional neuroimaging. This zone can be the result of an anatomical destruction of the underlying

---

* *However, the clear cut definition of the very first beginning of the seizure and, therefore, the smallest brain region involved in seizure activity, is difficult to obtain and can lead to a misjudgment due to the limited number (spatial sampling) of invasive electrodes (Elger 1992).*

brain tissue or it may be a consequence of the interictal discharges themselves. However, its determination is of considerable value for the definition of the epileptogenic zone.

As mentioned before, the epileptogenic zone is the area whose removal would be necessary for complete abolition of seizures and, therefore, should be the target area for a successful surgery/radiosurgery. All the other zones defined above give information about the approximate location and/or lateralisation of abnormal cortex that could become an ictal onset zone, but there is no clear evidence as yet to suggest that any of them can be consistently used to delineate the boundaries of the epileptogenic zone. So, how is the area of cortex to be removed actually defined? The following principles are used as general guidelines by most centres world-wide for the definition of the cortex to be removed (Lüders et al 1993):

- The ictal onset zone is always removed, with some exceptions in cases of clear structural lesions. Invasive recordings are performed for the definition of the ictal onset zone.
- Epileptogenic lesions are always removed.
- In neocortical cases with no clear lesion on neuroimaging, it is common practice to obtain invasive recordings and to remove the ictal onset zone including areas of early propagation, and also adjacent cortex that shows frequent and high-amplitude, long-duration spiking (provided is not located over a normally functioning cortex). Removal of the entire irritative zone is usually inappropriate; the symptomatogenic and functional deficit zones are useful for guiding the invasive monitoring strategy, but not good indices of the epileptogenic zone boundaries as such.

How does MEG fit in all these? As mentioned in the previous chapters, movement in general is a problem in MEG, so one faces the particularly difficult problem in epilepsy studies because, as discussed above, the most important data for localising epileptogenic regions are ictal events that are generally associated with movement to one or another degree. Furthermore, the logistics concerned with MEG recording over considerably long time periods - usually involving outpatients on therapeutic levels of anti-epileptic drugs (Ebersole et al 1995) - make it even more complicated to capture seizure activity. As a consequence, most studies have to be performed interictally. However, there have been a few studies from purely electrographic seizures and seizure onset just prior to movement.

The first study of the latter kind was performed with a single channel MEG system conducted for a patient with frequent seizures and it was shown that the magnetic field patterns associated with those seizures agreed well with the intracranial localisations (Sutherling et al 1988). Ebersole and co-workers (1995) recently reported on multichannel

seizure recordings of five patients with intractable complex partial epilepsy and confirmed that the MEG localisations of initial ictal onsets of complex partial seizures were in agreement with invasive EEG recordings, but, most importantly, were within the irritative zones defined by interictal data.

But, how relevant are interictal MEG recordings? Since the localising validity of temporal interictal epileptiform abnormalities in general has been the subject of much debate (Quesney et al 1993), it is important to review here the latest interictal MEG findings. Stefan et al (1994) recently reported a MEG study (Siemens 37 channel system) of 22 patients with definite temporal lobe epilepsy, as defined by invasive and non-invasive EEG, MRI volumetry (see next section), ECoG and surgical outcome. They found a satisfactory correlation (less than 1 cm) between the MEG localisations and lesion margins (7/8 patients with tumours and good surgical outcome) or atrophic hippocampi (8/9 patients with temporal or hippocampal atrophy). Similar results were obtained by Ebersole and colleagues (1995) using the bihemispheric BTi probe system (2x74 channels) and detecting and localising focal areas of MEG epileptiform activity when structural neuroimaging (MRI/CT) were without focal abnormalities. Another recent report based on 50 seizure surgery candidates (Smith et al 1994) suggested that interictal MEG was in good agreement with video EEG monitoring with surface electrodes both ictally and interictally and Electrocorticographic (ECoG) recordings during surgery; in addition MEG has been very helpful in avoiding invasive - and expensive - EEG studies typically used in presurgical evaluation.

Ebersole and Smith (1994) compared interictal spike MEG patterns of 13 temporal lobe epileptics with seizure onset results from intracranial monitoring; a good correlation between MEG localisation and seizure onset was found when the latter was localised, but also a correspondence between certain MEG patterns with non-localised onsets. Studies by Eliashiv et al (1994) have also indicated that interictal MEG spike lateralisation and localisation were in concordance with depth-electrode irritative and ictal onset zones in extra-temporal lobe patients, and may additionally aid in targeting previously unsuspected brain regions for further investigations. Furthermore, Stefan et al (1992) in the first ever conducted combined multi-channel (37) and surface EEG seizure recordings in correlation with intraoperative ECoG and MRI, SPECT, and PET, localised the interictal activity in the same region as the ictal seizure onset, with later spread to other regions, in three patients which were all seizure free following surgery. Finally, Hellstrand et al (1993) were the first to apply the stereotactic gamma irradiation technique for treating "focal epilepsy". Their approach was based on the assumption that stereotactic interictal MEG truly mirrored spatially and temporally the onset and spread of focal epileptic activity. Their successful treatment results suggested that the above

concept was valid: since the seizures were abolished when the interictal MEG centres of epileptic activity were irradiated, it seemed that the interictal MEG recordings carried information about the sites important for developing the ictal onsets sites, too.

In conclusion, presurgical MEG investigations could be applied in reducing invasive recordings in tumoral focal epilepsies and mesial temporal atrophy/sclerosis, but also guiding the actual invasive procedures and providing information concerning the spatial relation of the epileptogenic region, lesion or functionally important zones (e.g. by presurgical MEG mapping of somatosensory and auditory cortices and language centres) (Stefan et al 1994) but also ruling out multifocal subjects or subjects with sources localised unacceptably close to functional cortex and to guide electrodes (Galen et al 1995).

6.3 Epilepsy Neuroimaging and MEG

A number of neuroimaging techniques are available to complement electrophysiological findings/methods when evaluating patients with intractable localisation-related epilepsies and epileptic syndromes prior to possible surgical treatment; such techniques assess both structural and functional abnormalities. CT has been used as the main tool for such purposes for long time, but MRI has been proven to be better in the detection of small epileptogenic lesions, and especially in the determination of the already mentioned hippocampal atrophy. MRI-conducted hippocampal volumetric assessment has also made significant inroads in the preoperative investigation of temporal epileptics: normal subjects show a bilateral symmetry of these structures, while - sometimes very small - asymmetries are demonstrable in patients with previously cryptogenic temporal lobe epilepsy (Boon 1994). In addition, proton (^{1}H) MRS may also be used in these cases showing significant reductions in signals (or ratios) of specific metabolites (e.g. N-acetylaspartate, NAA) characteristic for epileptic groups as opposed to normals (Gadian et al 1994).

Functional brain imaging methods such as PET and SPECT have been playing a useful role in the presurgical assessment. Since seizures are associated with pronounced changes in the cerebral blood flow (CBF), there is a global increase in CBF during generalised seizures; with partial seizures increases are more localised, and may correspond to the epileptogenic "focus" as defined by electrophysiology. Interictally, areas of reduced regional cerebral blood flow (rCBF) may be seen, often corresponding to the main focal EEG abnormality (Lancet 1989). SPECT findings have been more consistent in cases of intractable complex partial seizures. In the latter cases, Duncan et al (1993) report hyperperfusion of the whole temporal lobe during the seizure, followed by hyperperfusion of the hippocampus and simultaneous hypoperfusion of the lateral temporal structures up to 2 min postictally; from 2-15 min postictally hypoperfusion of

the whole temporal lobe was noticed. Quantification analysis - in addition to the visual image inspection - may improve the assessment quality (Friberg and Lonborg-Jensen, 1994). PET results broadly parallel the SPECT studies but they add information about hyper/hypo-metabolism (Franck et al 1986; Theodore 1995), which is of course closely linked to changes in rCBF. In ictal studies, however, PET often shows complex multifocal patterns of altered metabolism reflecting both the site of onset and the subsequent spread within the hemisphere, in contrast with SPECT findings that most commonly show a single focal area of hyperperfusion (representing the zone of maximum rCBF increase) (Lancet 1989). Finally, the use of PET-radionuclides that selectively bind to benzodiazepine receptors, that are localised to neurons, might prove very useful in differentiating between various categories of patients with partial seizures (Savic 1995).

Finally, fMRI can also be used to depict signal increases in cortical regions and in the major draining vessels during seizures (Jackson et al 1994). Moreover, it permits more complex functional presurgical brain mapping, supplementing invasive techniques such as operative cortical stimulation and intracarotid amobarbital tests (Morris et al 1994). However, fMRI has not been shown to be any useful yet in the detection of subclinical/interictal activity in order to gain much wider application in epilepsy investigations.

Despite the considerable interest in the previous modalities and the wide availability of some of them (i.e. SPECT), these techniques lack the temporal resolution to capture fast neuronal activity changes. Although seizures of hippocampal origin can remain localised long enough for the above modalities to be accurate, neocortical temporal and extra-temporal lobe seizures may routinely propagate rapidly and perhaps too rapidly for such techniques to provide a clear picture; moreover, interictal activity may propagate over considerable distances in tens of milliseconds making its traces undetectable with "slow" modalities (Ebersole et al 1995). Only EEG and MEG offer sufficient temporal resolution to accurately follow epileptic activity.

The first ever epileptic MEG recording, conducted by Cohen 24 years ago, demonstrated that hyperventilation-induced slow waves could be detected in a patient with psychomotor seizures using a single channel magnetometer in a magnetically shielded room (Cohen 1972). Since then, a number of other cases have been studied in several laboratories. MEG has been used to locate both single sources and multiple irritative areas (Barth et al, 1982, 1984).

Those early MEG measurements relied on repositioning the single channel probe around the head. Under such conditions, averaging single events of interest, e.g. spikes, spike-wave complexes, was necessary: the signals were collected over long time periods, often

hours, to generate an extensive coverage sufficient for localisation. Typically electroencephalographic (EEG) recordings produced the triggering events for the averaging procedures. However, the possibilities of analysing the propagation of activity over time were very limited.

Today's multichannel MEG systems have opened new avenues to study the spatio-temporal evolution of epileptic activity more faithfully and, therefore, during the last few years, MEG has become a tool for localising zones of epileptic activity in different regions of the human brain (Hellstrand et al 1995; Paetau et al 1992; Sutherling et al 1991). Despite the numerous MEG successes in epilepsy[+] , one of the most serious limitations has been the source model used in virtually all clinical studies to date, namely, the single-equivalent current dipole (ECD). This fact has now been realised in the biomagnetic community (see for instance e-mail messages in BioMagList, summer 1995), and, therefore, in parallel with the advances in SQUID technology, elaborate methods have been and are currently being developed to identify the generators of the epileptiform signals.

6.4 Studying interictal epileptic events with MFT

As mentioned before, a number of investigators (Sato 1992; Baumgartner et al 1992) have underlined the potential in modern multichannel MEG systems to directly analyse interictal epileptic data without any signal averaging. However, the equivalent current dipole (ECD) approach has usually been employed to pursue such studies (Hellstrand et al 1993, 1995; Stefan et al 1995). The description of on-going activity that the ECD model provides is crude. It is too sensitive to noise, and only gives a reasonable source localisation through short segments of the period studied. This leaves most of the event unexplained. Since there is ample evidence that a single event of epileptiform activity extends to more than one area of the brain, corresponding to more than one zone of epileptic activity (Graf et al. 1984; Sutherling and Barth 1984; Baumgartner et al. 1992; Laxer et al. 1993) any single-ECD model is liable to give rise to misleading localisations, especially when used in association with unaveraged events where the signal-to-noise ratio (SNR) is not particularly high.

Even in the early days of MEG, results obtained with single channel probes based on EEG triggered averaging were indicating involvement of distinct brain areas interictally. In an interesting study, both scalp and sphenoidal EEG spikes were used as triggers for

---

[+] *These were the fortunate consequence that ECD modeling of many epileptic events was "sufficient" if appropriate acceptance criteria were applied to the resulting solutions.*

averaging the magnetic spikes (Sutherling and Barth 1989). Different latencies were observed for the two triggers suggesting propagation of the discharge between different parts of the temporal lobe. Given the requirement for studying the unaveraged epileptic data, in addition to the usual involvement of extended brain areas in the generation of epileptiform activity, it is sensible to expect that robust distributed source model methodologies such as MFT should perform better.

Furthermore, MFT is an ideal tool for separating deep and superficial activity as we showed in the previous chapter. As we also demonstrated there, small, but physiologically significant, temporal differences in the activation of diverse brain regions of interest (ROIs) can indeed be studied with MFT. Both the above points are believed to be of great importance in epilepsy, as inferred from earlier sections of this chapter, rendering MFT a novel way for the study of epileptogenesis.

In the following, we first describe the material and methods used in our analysis; we then establish the links with previous epilepsy MFT work referring to a comparison between the ECD and MFT solutions, and comparing solutions obtained with two different source space models, namely the partial hemispherical and cylindrical volumes, for the same datasets. We then indulge in the analysis of unaveraged epileptiform events demonstrating spatio-temporally coherent results, thereby proving the feasibility of studying unaveraged pathophysiological datasets with MFT.

6.4.1 Materials and Measurements

6.4.1.1 Case history (Pat1)

Our first case (Pat1) was a 35-year-old male patient with a history of pharmacoresistant epilepsy of a complex partial type (CPE) since the age of 20. Clinically, he suffered from daily seizures with absence periods of 5-10 minutes. His MEG sessions (5 min on either side of the head while he was resting with eyes closed) were stereotactically performed to make concomitant radiotherapy (gamma irradiation) possible (cf Hellstrand et al 1993). However, only the left-sided data were available to us, and consequently this is the dataset to be used in the following analysis.

6.4.1.2- Recordings and Methodology

MEG signals were recorded over the left temporal lobe of the patient. EEG recordings with surface electrodes covering the frontal, temporal, central and parietal aspects of the brain were additionally performed, as were measurements of the ECG (extremity leads). The 37-channel Siemens KRENIKON system was used to record the MEG signal with an acquisition rate of 400 Hz and on-line band-pass filtering 0.5–70 Hz. Only 29 of the MEG

channels were valid though, and our analysis is, therefore, based on the signals of those* . Figure 6-1 shows the probe arrangement in relation to the patient together with the geometry of the sensors in a plane parallel to the left temporal region of the patient. The positions of the missing channels are easily inferred.

An MRI investigation was also performed using the same with the MEG stereotactic frame. This allowed the registration of MRI and MEG (using the techniques described in section 3.5.2.1) and the later fusion of information from the two modalities under the same co-ordinate system, that is MEG-probe system (see Appendix A for some details of the Siemens co-ordinate system).

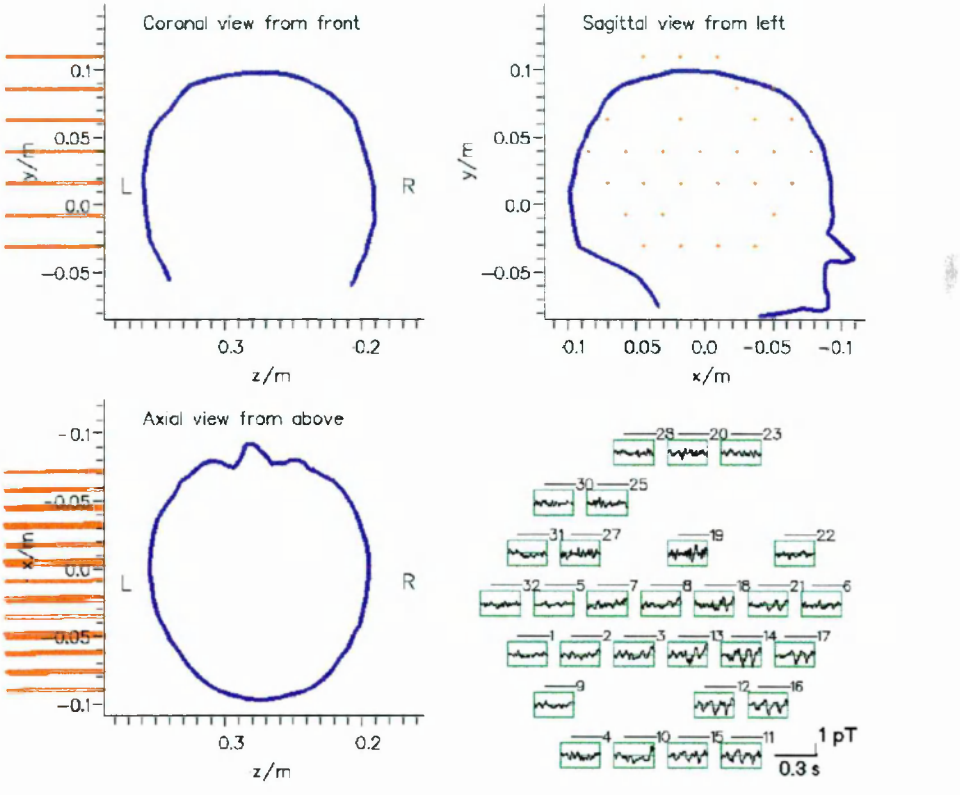

Figure 6-1: The sensor set-up (central, left temporal) relative to the patient in a coronal, sagittal and axial aspect. Horizontal bars (coronal and axial sections) and dots (sagittal section) are used to mark the channel positions in the MEG co-ordinate system. Bottom right: an interictal sharp wave event is displayed in a planar-channel layout. Only 29 out of the 37 channels are used; the rest are left out as invalid.

---

* *As shown in the previous chapter, the degradation of the MFT "images" due to the lack of some channels is small.*

In the following, we make use of three different sets of data: the *raw* set (no other filtering apart from the on line band-pass 0.5-70 Hz); the *filtered* signals, yielded after additional digital band-pass filtering from 1.5–47.5 Hz, and application of a Magnetocardiogram artefact correction algorithm (Abraham-Fuchs et al 1992); and finally the *averaged* set, obtained by averaging several "similar" (filtered) epileptiform events as identified by a spatio-temporal matching technique (Abraham-Fuchs et al 1990).

The spatio-temporal matching technique (as applied in the commercial Siemens software) is based on the idea that identical shapes of spikes/spike-wave complexes temporally, as well as spatially (with respect to MEG channel distribution), represent activities of nearly identical generators with "comparable propagation paths". Thus, averaging events with a high grade of temporal and spatial correlation should not, in principle, result in a mixture of different events, but rather revelation of the relevant centres of epileptic activity (Stefan et al 1992).

"Similar" epileptiform events are compared by a combined correlation of temporal and spatial electric and magnetic patterns. First, a set of successive magnetic field maps is selected (by an expert) as representing an epileptiform event of interest (e.g. spike or sharp wave); this is named as a *template event*. Then the spatial and temporal information in this time window is combined into one "template vector" of dimension N (number of active MEG channels, e.g. 29) by M (number of timeslices in the interval of interest, e.g. M=40-200, corresponding to 100-500 ms). Subsequently, this template window is moved in time over the entire range of measurement data, and the correlation coefficient of the template vector with the corresponding vector in each time instant is calculated. Deviations from the random (uncorrelated) Gaussian distribution of the correlation coefficient values are indicated as peaks, representing similar events. Such events (above a significantly high, but arbitrary, correlation coefficient threshold) are then aligned and averaged to obtain the average signal (for a more detailed description see Abraham-Fuchs et al. 1990). The process is visually summarised in Figure 6-2.

6.4.1.3 MFT analysis

MFT was first applied for Pat1 by Ioannides et al (1993c) in order to study the average of 39 sharp waves lasting 275 ms. Solutions were obtained within a 3-dimensional cylindrical source space with its third axis (depth symmetry axis) along the direction of the most central sensor (i.e. sensor number 8 in Figure 6-1). The cylinder was 5.5 cm deep and had a cross section with a radius of 4 cm . Conductivity was modelled with a sphere "fitted" globally to the brain volume (i.e. both sides); the probability weight was of a simple Gaussian form (along the z-direction only) with a decay factor, $\lambda_3 = 0.04m$; the

regularisation parameter was chosen to be $\tilde{\zeta} = 0.05$. The purpose of that study was to compare the MFT solutions of the average sharp wave with those obtained with the ECD model using identical conducting centres. A more recent study (Ioannides et al 1995a) extended the earlier MFT results by analysing the corresponding raw and filtered sharp wave signal, for a single event.

Since then, the MFT analysis in our lab has been improved with the introduction of partial hemispherical volumes for use as source spaces (Liu MJ and Ioannides 1995). We, therefore, repeated the analysis for a partial hemispherical volume fitted to the patient's left cerebral hemisphere[+]. In so doing, apart from reconfirming previously obtained results - and, thereby, building up confidence for the correctness of our analysis - we also had the chance to test the stability of the MFT solutions for the same (three) datasets under different source volumes, probability weights and regularisation parameters. Furthermore, we also used a different conductivity profile: the conducting sphere fitted to the curvature of the inner skull surface of the left (ipsilateral to the measurements) side only.

In the following, we present the comparison of the ECD solutions with the MFT results in the case of the hemispherical volume, followed by the comparison of the MFT solutions for the cylindrical and hemispherical volumes. The same conducting centre (that of the globally fitted sphere) was used in both cases in order to avoid complications. Apart from these two sections, however, the rest of the MFT results presented in this chapter were obtained with the left-fitted sphere, as described above, since this is believed to be a better model, for the reasons outlined in the second chapter of this thesis.

So, in summary, we have three distinct analysis models as shown in Figure 6-3. The one in (a), as described above and used by Ioannides et al (1993c), that in (b) facilitating a direct comparison between ECD and MFT, but also between (a) and (b), and finally the one in (c), which is believed to represent the underlying reality more faithfully and is used in presenting the rest of the MFT analysis. In both (b) and (c) the regularisation parameter was chosen to be $\tilde{\zeta} = 0.1$; the same as in (a) simple Gaussian probability weight was also used with a decay factor, $\lambda_3 = 0.0425m$ in (b) and $\lambda_3 = 0.05m$ in (c).

[+] *A number of other events - apart from the originally used one - were also studied in an attempt to home into the spatio-temporal details of the time course of each event and obtain any "cross-event" systematics.*

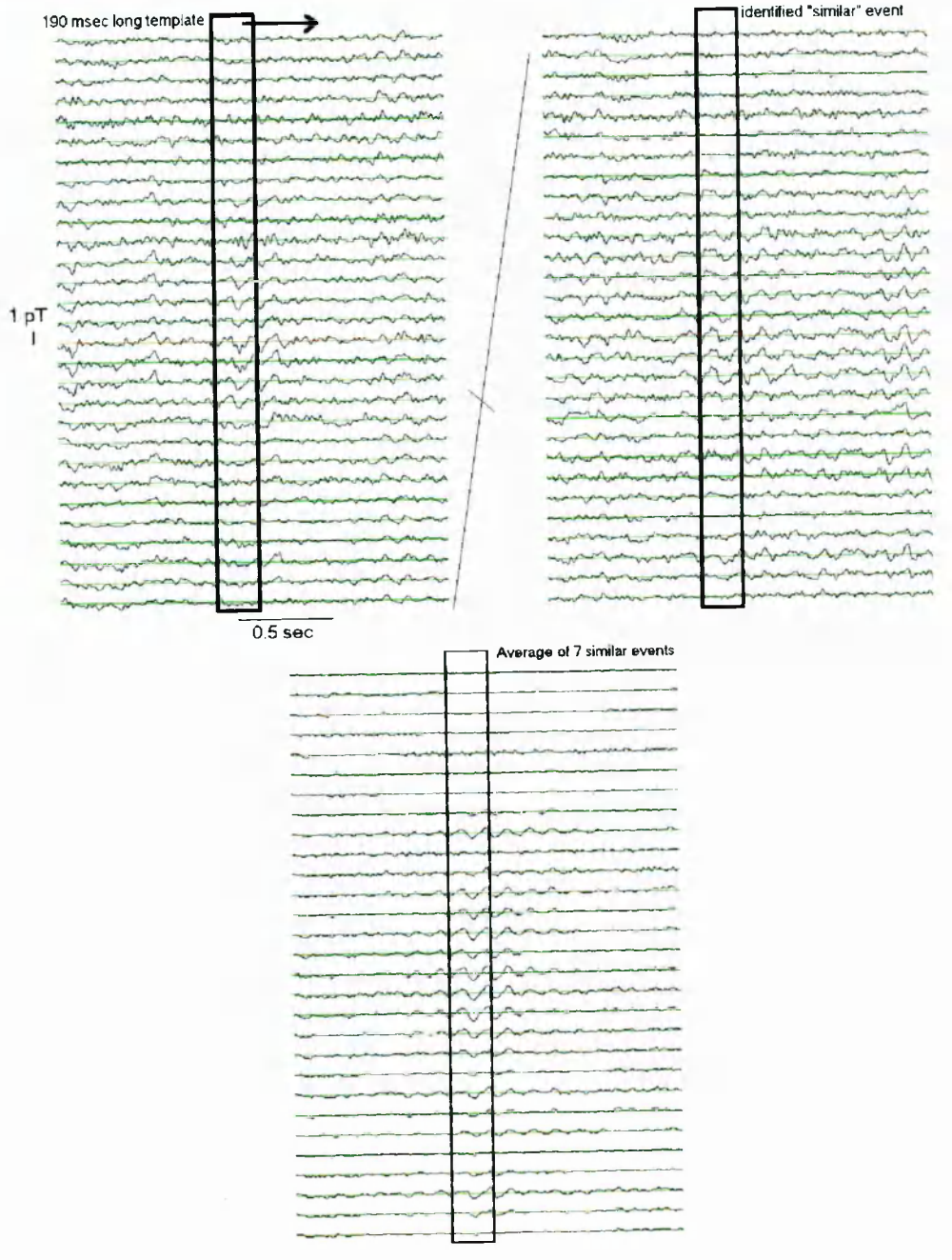

Figure 6-2: Summary of the spatio-temporal correlation technique: an epileptiform event of interest (*template event*) - a sharp wave in this example - is selected. This template window is subsequently moved in time over the entire measurement set, to identify any *similar* events. Such events are then aligned and averaged to obtain the *averaged* signal, like the one shown on the bottom. Note the improvement in the signal-to-noise ratio for the averaged signal, even after use of only 7 events.

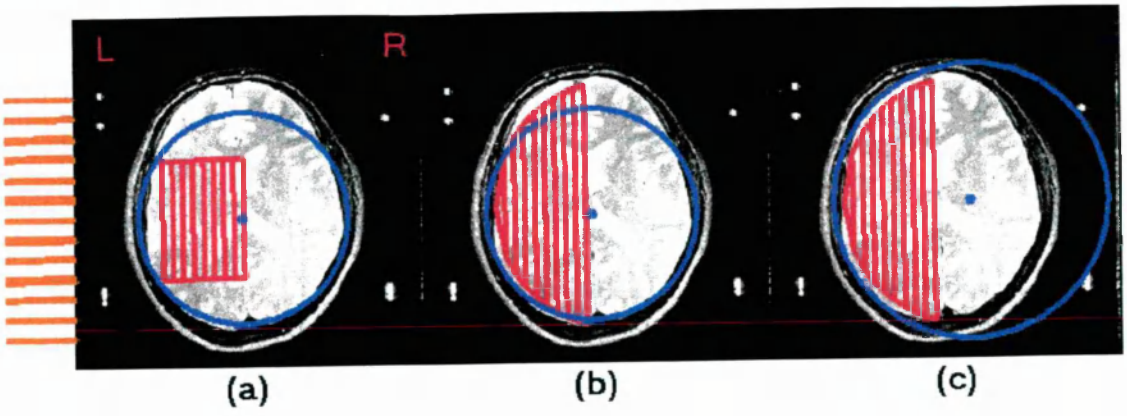

Figure 6-3: The three distinct analysis models. In (a), the source space is a cylinder and the conducting sphere is "fitted" to both brain sides (analysis as presented in Ioannides et al 1993c). In (b) a partial hemispherical volume is used as source space, while the conducting model is identical to that in (a). In (c), the source space is identical to that in (b), but the conducting sphere is fitted to the inner skull surface of the left side only. The projection of the source spaces onto a patient's MRI slice are outlined in red (all 9 levels shown), while those of the conducting spheres in blue. A blue dot denotes the conducting centre; bars on far left mark the sensor positions. Note the water markers outside the skull which compose part of the stereotactic system and were also used in the MRI/MEG registration.

6.4.2 MFT - ECD comparison

As we already mentioned, earlier MFT studies of interictal epileptic activity compared ECD* and MFT results for a 275 ms long sharp wave event composed by averaging - as explained above - by 39 similar sharp waves. The full epochs were extended for about 1 sec on either side of the middle point of each (aligned) event. We complete the comparison here by displaying the results in association with the patient's MRIs - earlier studies used only cylinder plots - using set-up (b) in Figure 6-3; a comparison in the case of the unaveraged (filtered) sharp wave is also included to probe the discussion concerning the disagreement of the two methods and also "prepare the grounds" for the single epoch analysis that follows.

The average sharp wave is shown in Figure 6-4 (all channels are superimposed). The short periods marked by two light vertical lines contain the timeslices to be used for the comparison: the early period (most left vertical lines) is studied in the middle row, while

---

* *A standard iterative inverse solution scheme, the moving dipole algorithm (Cuffin 1985), was used to calculate the ECD results. This algorithm consists a standard utility of the Siemens software suite.*

the period containing the signal maximum of the sharp wave (two most right lines) is given in the bottom. The MRI slices for display are selected according to the 3D co-ordinates of the position with the maximum current density value, which is also marked by a red dot (the actual value of the current density modulus is printed below each display). The solutions from all 9 levels of the source space (the extremes of which are outlined in red) lying within 4 mm on either side of the defined plane are then superimposed on the MRI slice. The position of the ECD solution is also projected on the same slice as a blue dot, and its goodness of fit, the correlation coefficient value, is given on bottom right corner of each display. More numerical details are given in Table 6-1 and Table 6-2.

As inferred, the agreement between ECD and MFT solutions is quite satisfactory: the MFT distribution always includes the ECD localisation within its "boundaries" and the current density maximum almost coincides with the ECD point whenever the ECD solution describes the data well (i.e. when the correlation coefficient is greater than 0.96 e.g. at t=995 ms). Even in the depth, where the MFT solutions are blurred, and, therefore, the position of the current density maximum should be interpreted with caution, we still have a good agreement in the displays (although there is some 2 cm difference in the y-co-ordinate, that is, in the direction perpendicular to the MRI plane). We have to emphasise, however, that comparing the actual position of the maximum MFT solution with the current dipole is not a "fair deal" for MFT, since it is biased against the distributed source, collapsing all information to a point. However, the agreement we obtain is worth showing, and thus, we tabulated the results in the corresponding Tables.

Disagreement between ECD and MFT is expected when the activities involved are more widespread, or when multiple areas are coactivated simultaneously. The latter is what actually happens around t=1000 ms and up to t=1010 ms: a second, more superior cortical area is becoming active, but is less strong than the first area. This explains why the ECD fit to the data is progressively dropped down to 0.931 from 0.97. This area is not seen, however, in the MFT solutions on the displayed MRI slice since it is located in a much more superior slice; it is, however, indeed observed when the familiar cylinder plots are reviewed (these are not display here, but this point is going to be discussed further while explaining Figure 6-6).

But how would the two methods perform when considering unaveraged data? When the filtered (but unaveraged) template sharp wave event is studied the fits to the data provided by ECD are lower in general. This is partially arising from the noise content of the data (in addition to the above reasoning). In Figure 6-5, we have selected for display two time segments where an ECD solution with sufficiently high fit (better than 0.9) is obtained. Note the poorer values for the correlation coefficient of the ECD fit and that the

same trends with the case of the average signal are observed (middle row). At the bottom row, however, the disagreement between the two methods is gradually worsening, due to the simultaneous activation of more than one centre. Note that this disagreement is worse than the average signal case, since the noise content of the data together with the co-existence of another active centre make the ECD to be completely out of the "distributed source boundaries".

The latter point becomes more prominent in Figure 6-6, where another time interval of the same filtered signal is selected. In this case, MFT reveals a deep area becoming active in the presence of a superficial centre of activation. The MFT solution varies smoothly as activity in the deep area becomes apparent and eventually dies off. The ECD localisation in this case is completely out of place overall, with a very low fit to the data (middle row) or no fit at all (bottom row). One should also note the generally expected trend (Ioannides et al 1993c) that, with the activity becoming distributed, the depth of the ECD localisation is increased (see both Figure 6-5 and Figure 6-6).

When the completely unfiltered and unaveraged sharp wave event is taken into account (raw signal) the ECD failed to provide sensible solutions to the measurements. MFT, however, performed similarly well even in this case as will be discussed in detail in section 0. Before we do that, we compare the results obtained with this hemispherical source space with those obtained from the cylinder (i.e. set-ups.(a) and (b) respectively in Figure 6-3).

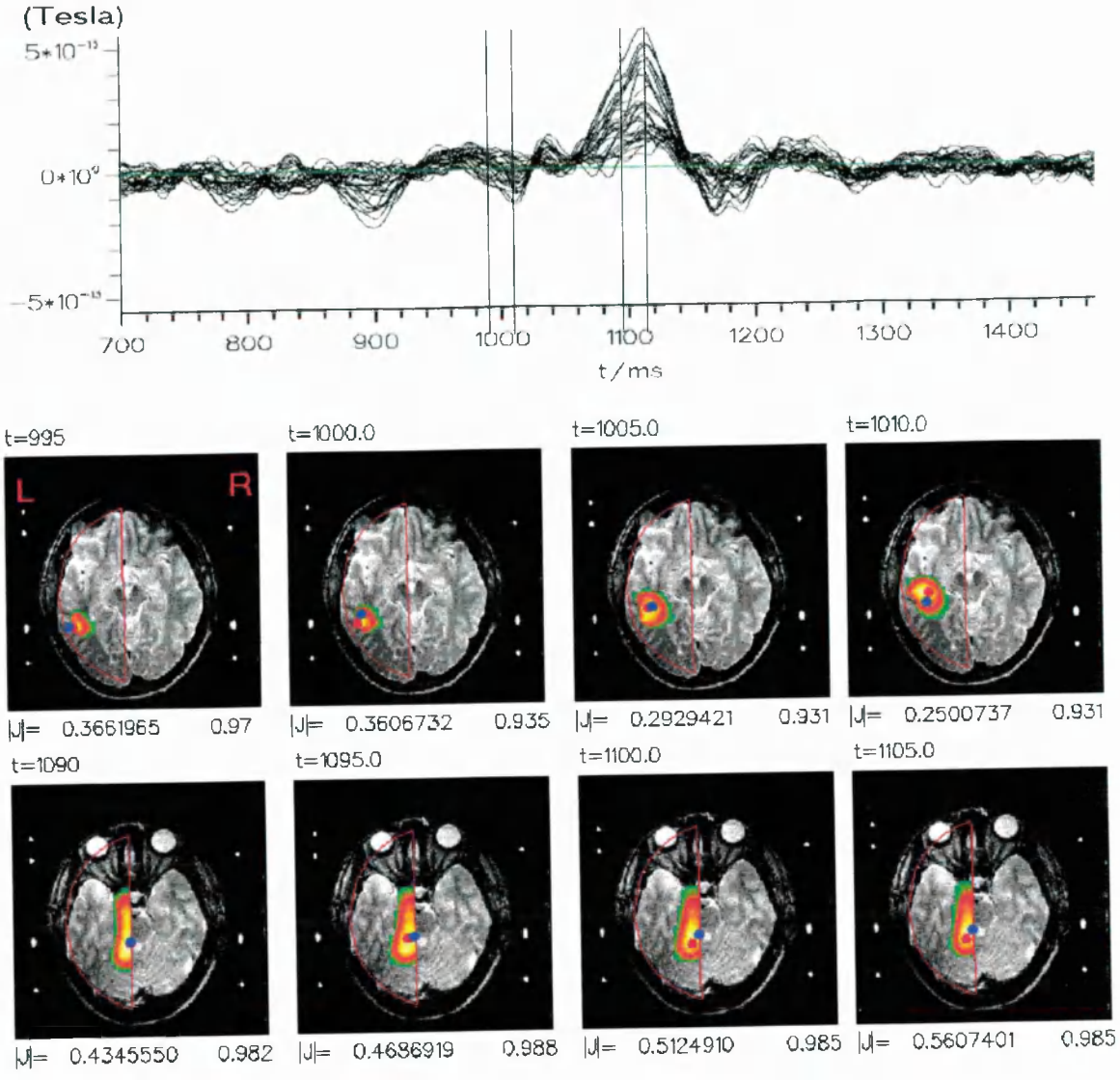

Figure 6-4: Top: the average of 39 similar sharp waves (all channels are superimposed). Light vertical lines mark the short periods used for the MFT-ECD comparison: the early period (most left vertical lines) is studied in the middle row, while the period where the signal maximum of the sharp wave occurs (two most right lines) is given in the bottom. The MRI slices are selected according to the position of the maximum current density (red dot, actual value of its modulus is printed below each display). Each display is normalised separately (as far as colour scale is concerned). The source space extremes are outlined in red. MFT solutions lying within 4 mm on either side of the MRI slice are displayed. The ECD localisation is also projected on the same slice as a blue dot; the corresponding correlation coefficient value, is given on bottom right corner of each display. For details see also Table 6-1 and Table 6-2.

Table 6-1: Localisation details for ECD and MFT for 4 timeslices of the average sharp wave shown in the top row of Figure 6-4 (time period is marked by the two light vertical lines on the left). The corresponding solutions can be seen in the middle row of Figure 6-4. The MFT localisation details have been obtained from the position of the maximum modulus of the current density. Note the generally good agreement between MFT and ECD.

method	*latency (ms)*	*x (m)*	*y (m)*	*z (m)*
ECD	995.0	0.289E-01	0.48E-02	0.330
MFT	995.0	0.297E-01	0.49E-02	0.327
ECD	1000.0	0.210E-01	0.49E-02	0.323
MFT	1000.0	0.297E-01	0.49E-02	0.327
ECD	1005.0	0.186E-01	-0.2E-03	0.316
MFT	1005.0	0.197E-01	0.49E-02	0.320
ECD	1010.0	0.104E-01	0.27E-02	0.304
MFT	1010.0	0.964E-02	0.49E-02	0.307

Table 6-2: Same as in Table 6-1, but for another period when deep activity is identified from both methods (time period marked by the two right most vertical lines). The corresponding solutions can be seen in the bottom row of Figure 6-4. Note the generally good agreement between MFT and ECD, despite the expected blurring of the MFT solutions in depth.

method	*latency (ms)*	*x (m)*	*y (m)*	*z (m)*
ECD	1090.0	0.186E-01	0.165E-01	0.280
MFT	1090.0	0.197E-01	-0.51E-02	0.280
ECD	1095.0	0.180E-01	0.75E-02	0.281
MFT	1095.0	0.197E-01	-0.51E-02	0.286
ECD	1100.0	0.208E-01	0.112E-01	0.280
MFT	1100.0	0.297E-01	-0.51E-02	0.286
ECD	1105.0	0.208E-01	0.210E-01	0.279
MFT	1105.0	0.297E-01	-0.51E-02	0.286

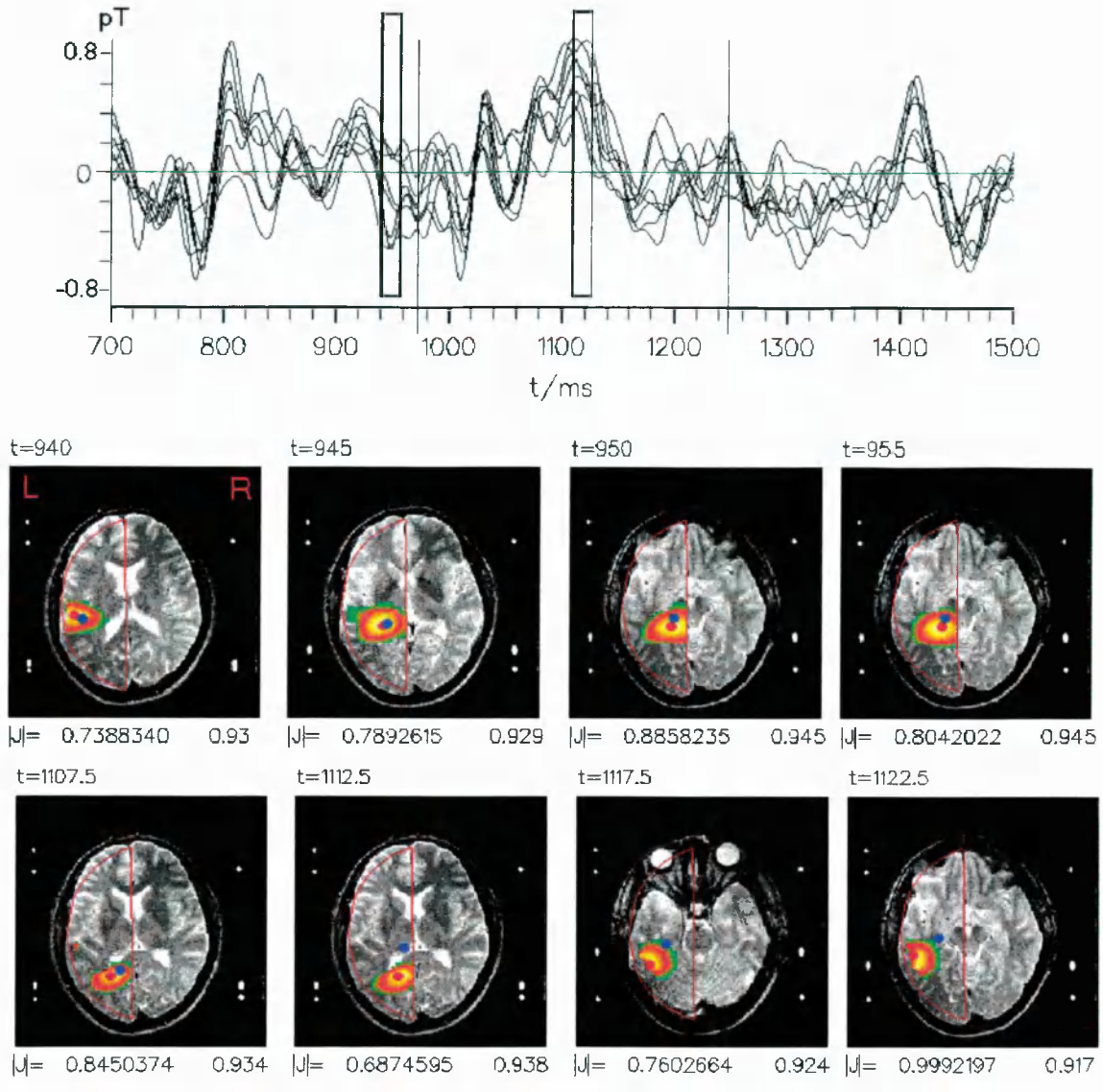

Figure 6-5: Top: the unaveraged filtered signal with the template sharp wave event shown between the two light vertical lines (signals from the strongest channels only are shown for better clarity). The two rectangles mark the short periods used for the MFT-ECD comparison: just prior to the template event and around the peak. The early period (left rectangle) is studied in the middle row, while the period around the peak (right rectangle) is given in the bottom. Rest of annotations follow the conventions in Figure 6-4. Note the generally lower ECD correlation coefficients than those obtained in the average signal (SNR was better there), and the disagreement between MFT and ECD in the bottom row, indicating another centre of activity in another location (not revealed here though). Also note the "deeper" ECD localisations in the bottom row.

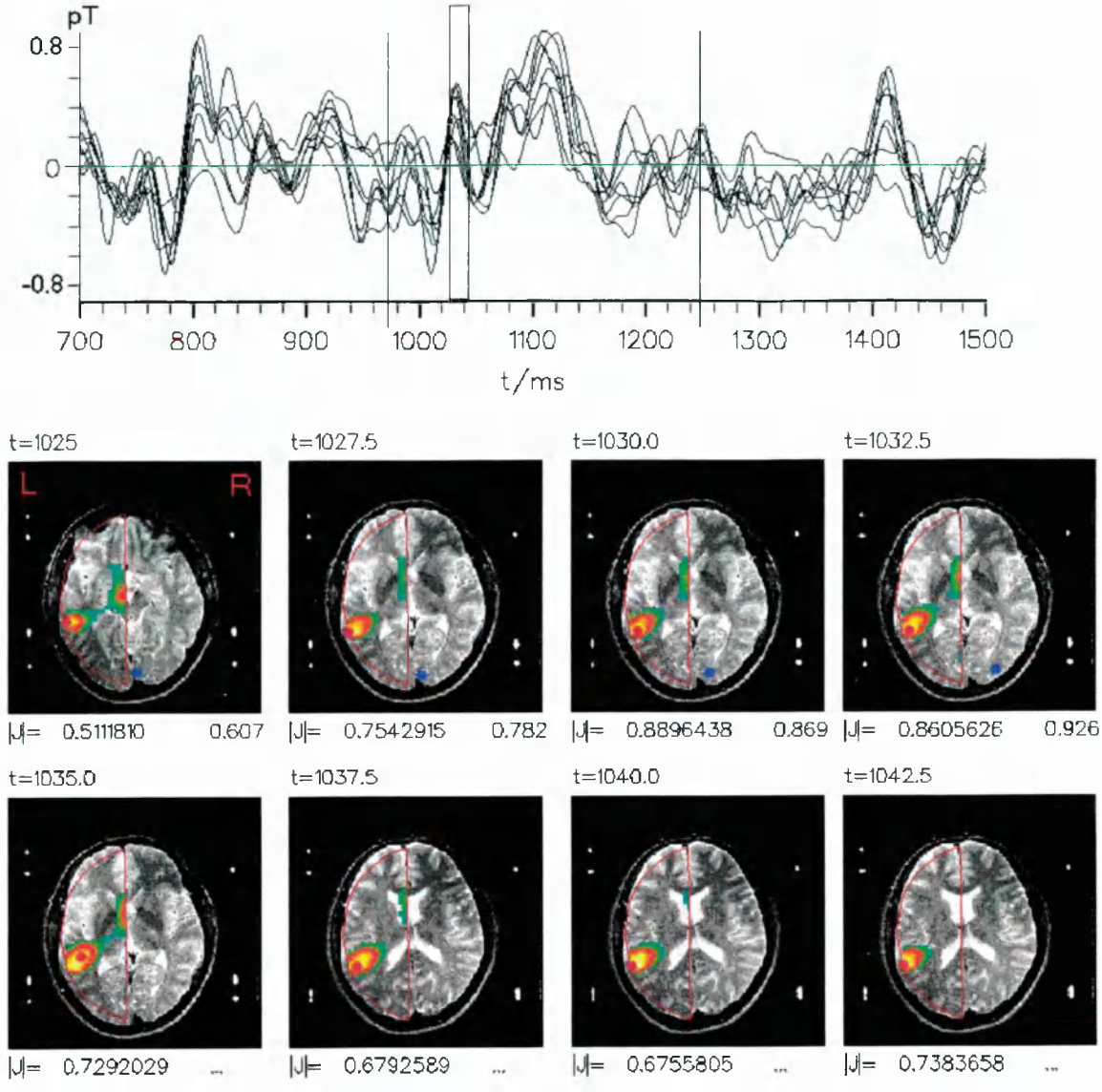

Figure 6-6: Same as in Figure 6-5, but for another interval (see rectangle) during the filtered signal (template sharp wave event), during which a deep area is becoming active at the presence of a superficial source. The ECD localisation is completely out of place, fitting the data more and poorly until it fails to provide a sensible solution (three dots in the place of the correlation coefficient). The MFT solutions, on the contrary, vary smoothly as activation of the deep area appears and gradually dies off.

6.4.3 MFT source-space comparison: cylinder versus partial hemisphere

The issue of comparing different three dimensional volumes for use as source spaces in MFT, together with the introduction of the partial-(hemi)sphere-shaped volumes was originally discussed by Liu MJ and Ioannides (1995). They compared three source space volumes: a small cylinder, which was completely "inside" the brain but leaving a considerable part of the more superficial cortex uncovered, a large cylinder, covering the superficial parts well, but also inevitably including some non-brain regions, and finally a hemisphere. Moreover, that study used computer generated data as well as real averaged MEG data from a simple auditory experiment conducted with numerous probe placements of a 7-channel system. Our attempt here is to confirm those results by studying the case of the small cylinder with the partial hemisphere (i.e. (a) and (b) in Figure 6-3) and complement the old conclusions by employing analysis of real multichannel and unaveraged data.

We have implemented the comparison using all three mentioned sets of data and the same conclusions apply to all of them, but for the purpose of this section, we have chosen to concentrate on the filtered set only. Generally speaking, the solutions obtained with the two source spaces look very similar indeed, despite the different probability weights, regularisation parameters - as mentioned in section 6.4.1.3 - and reconstruction volumes[+]. Their projections on the patient's MRI slices have the same form/shape both in superficial and deep levels; their MRI localisations are either the same, or nearly the same, but in any case they only differ at the most by one MRI slice or less than 6 mm (interslice MRI distance is 6 mm in this case, but the actual result would have been better given images with smaller interslice distance). A typical example is shown in Figure 6-7 and Figure 6-8 comparing three timeslices 10 ms apart for the superficial and deep levels respectively, in an interval during which activity appears in both superficial cortex and deep structures simultaneously.

However, the above statements hold true with one assumption. That is, activity as revealed with the use of the small cylindrical source space, is well within the boundaries of the cylinder. If activity is outside the cylinder or very close to its edges, then, as it was noticed originally (see Liu MJ and Ioannides 1995), we are led to fuzzy solutions which usually give artefacts at the near (to the sensors) side levels.

We demonstrate this effect in Figure 6-9 and Figure 6-10. In the former a full set of 5 ms apart timeslices is shown (marked with a rectangle within the template signal) for the

---

[+] *This finding, although expected, is important, as it demonstrates the applicability of the logic of "training the MFT process in the early session".*

cylinder (middle) and partial hemisphere (bottom), while in the latter we focus on three of the timeslices and observe the differences on the MRI projected solutions. It is easy to see from Figure 6-9 that the hemisphere solutions are, in general, less fuzzy and lead to a better localisation* . In addition, ambiguities encountered in cases of close-to-cylinder-edge activities are resolved (e.g. see solutions at latencies 1055-1060 ms and 1105-1110 ms). Moreover, the superficial artefacts mentioned before, are eliminated by the wider coverage the hemispherical source space affords. The latter is better visualised with the use of the MRI projected solutions in Figure 6-10. Note the smooth development of an activation just at the posterior boundaries of the cylinder - but well within the hemisphere - which leads to superficial artefact in the cylinder case (see the middle timeslice) which is absent, of course, in the hemisphere solutions.

The results we have shown in this (and the previous) paragraph confirm previously drawn conclusions, extend some of the early observations in real, unaveraged, multichannel MEG data, and more importantly, provide confidence for the correctness of our results. We are now going to concentrate on the analysis of unaveraged (raw) data for the template we examined so far, but also for a number of other template events (and associated similar events), always for Pat1, and from now and on using set-up (c) in Figure 6-3.

---

* *One should note that the level appearance is not the same in the two source spaces. In other words, the 9th level of the cylinder does not correspond exactly to the 9th level of the hemispherical space; it is actually between levels 8 and 9 as one may have carefully noticed in Figure 6-3.*

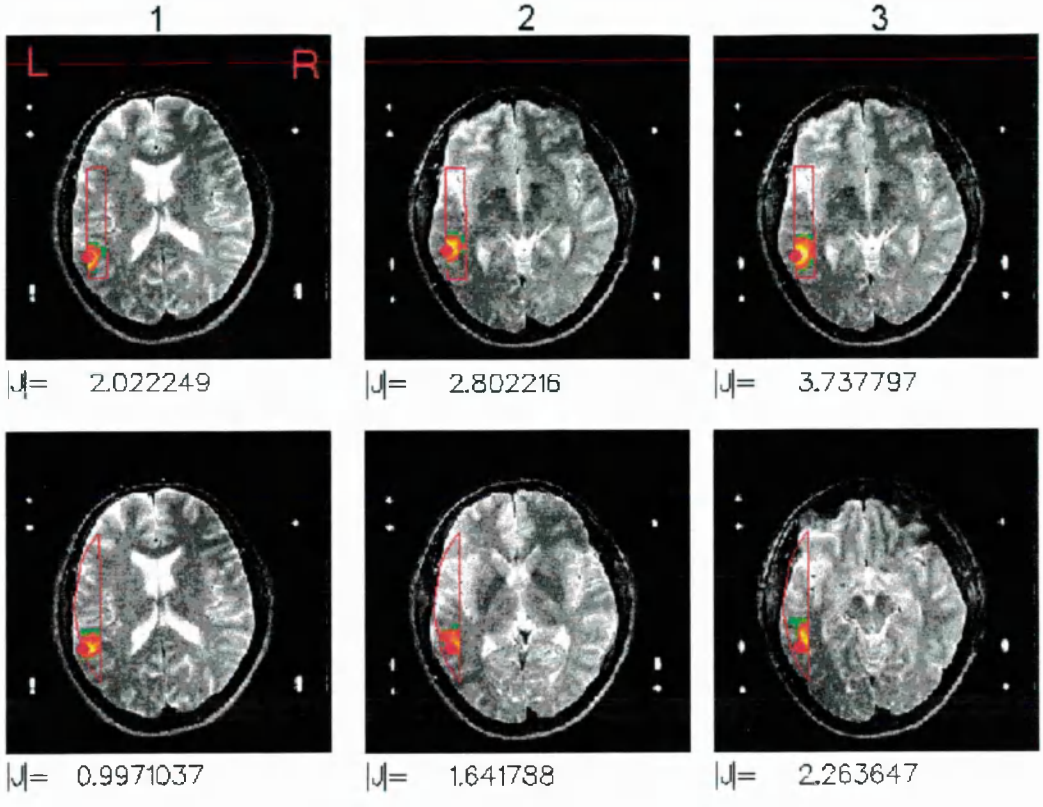

Figure 6-7: Comparison of the solution obtained from the cylindrical and partial hemispherical source spaces. The filtered template signal is used throughout. Solutions are projected on the patient's MRI slices in the way used so far, but considering only the top 3 levels of the each source space (levels 7-9). Note the similarity of the corresponding solutions and the nearly same MRI localisations (there is one MRI slice difference in the second and third column, see text). The three timeslices are 10 ms apart during an interval at which activity appears in both superficial cortex and deep structures simultaneously (1: t=1040 ms; 2: t=1050 ms; 3: t=1060 ms).

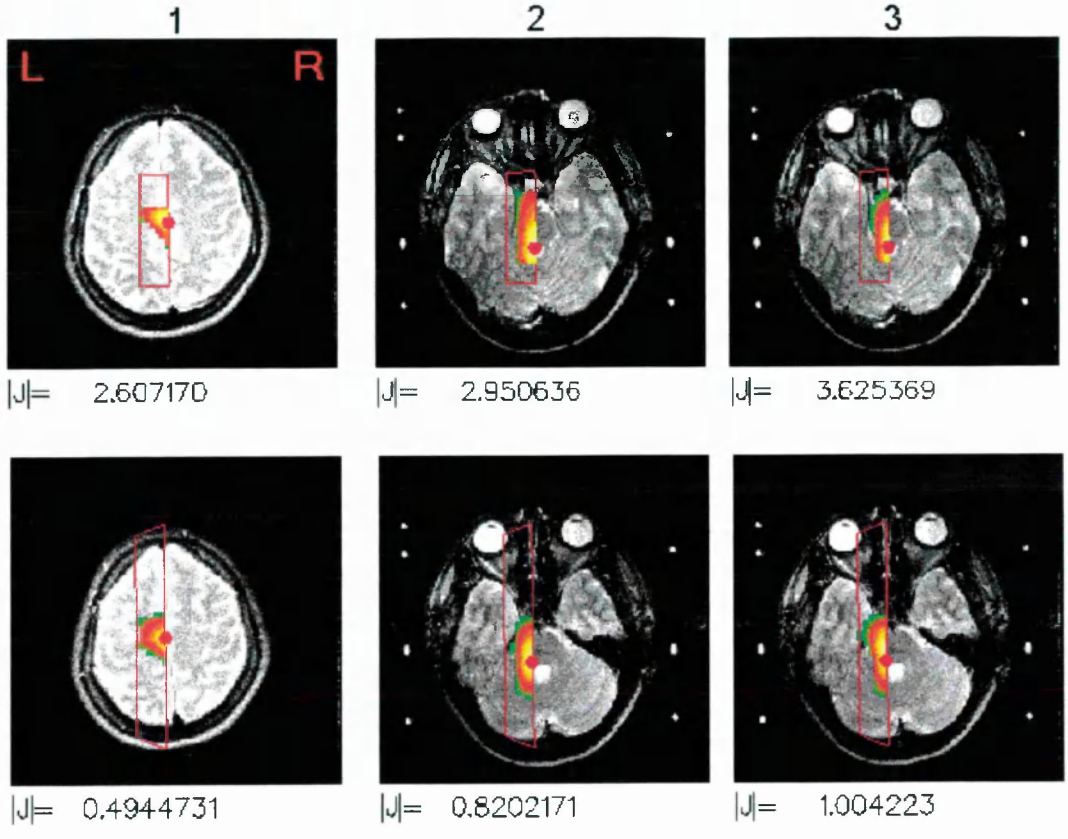

Figure 6-8: The same as in Figure 6-7 but considering the deep levels only, that is, levels 1-4 for both source spaces. Note the similar shape and localisation obtained with the two source spaces and also the different current density values due to the use of completely different sets of reconstruction parameters (the same holds true for Figure 6-7 as well). Instances shown: 1: t=1040 ms; 2: t=1050 ms; 3: t=1060 ms)

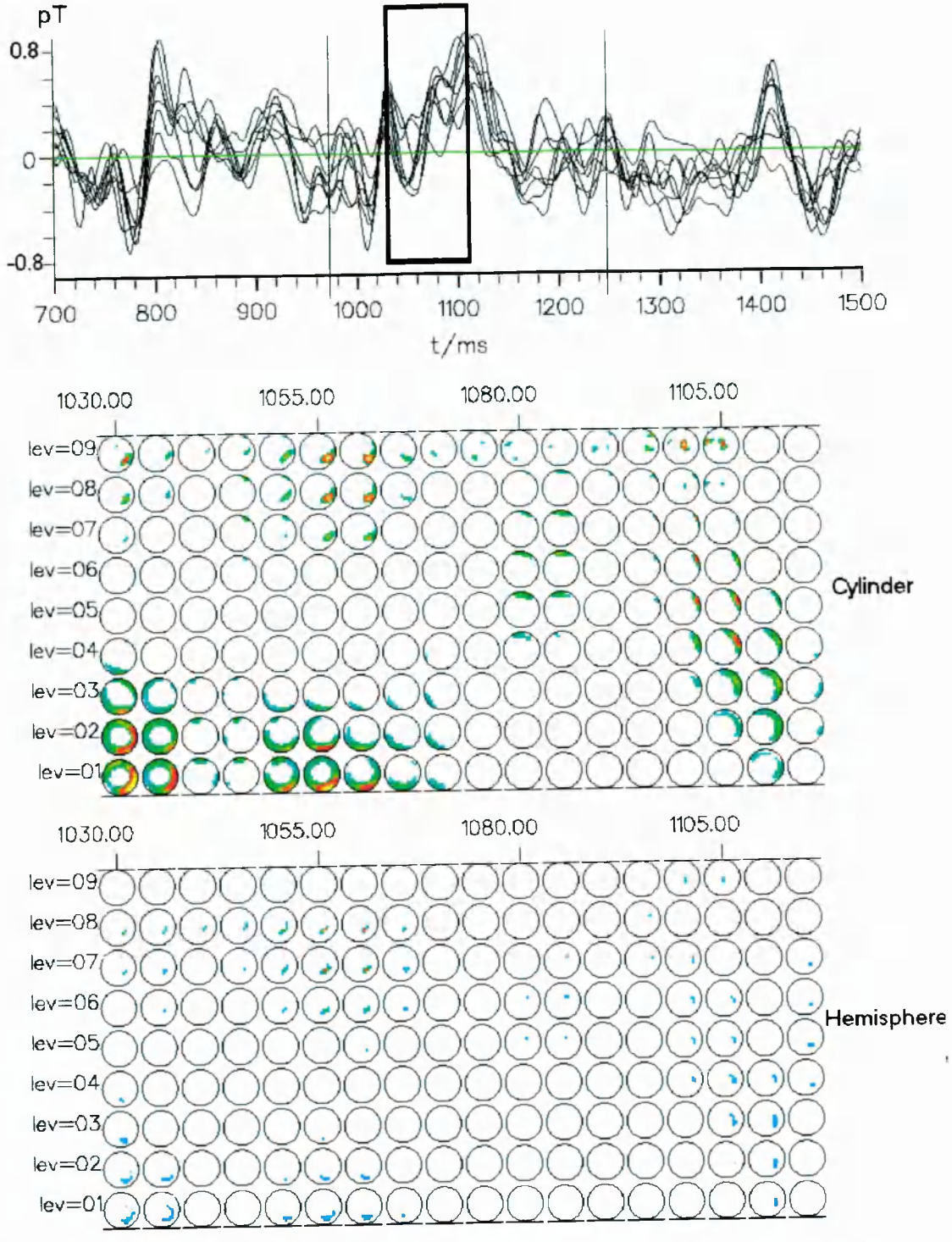

Figure 6-9: Top: filtered template signal (superimposed are the strongest channels). A rectangle marks the time interval used below (sharp wave within light vertical lines). Middle and bottom: 5 ms apart plots for the cylinder (middle) and hemisphere (bottom). It is easy to see that the latter are less fuzzy and better localised. Ambiguities encountered when activity is close to the cylinder-edges together with "the superficial artefacts" in the cylinder case are eliminated by the wider coverage the hemisphere provides (see text).

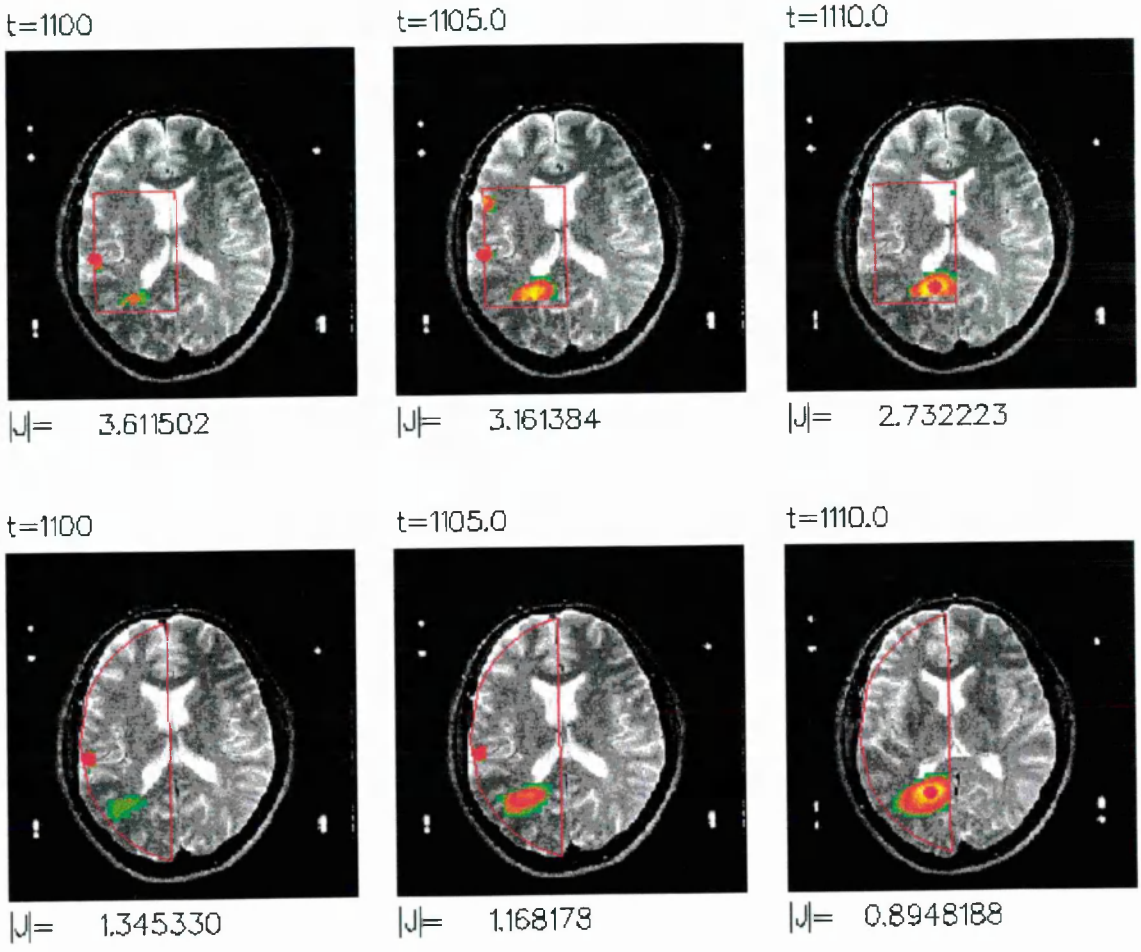

Figure 6-10: Elimination of the superficial artefacts by the wider coverage afforded by the hemispherical source space. Note the smooth development of an activation just at the posterior boundaries of the cylinder - but well within the hemisphere - which leads to superficial artefact in the cylinder case (see the anterior end of the middle column) which is absent in the hemisphere solutions.

6.4.4 The study of unaveraged interictal events

As we have already mentioned before, the ECD solutions for the filtered and raw signals fitted the measurements poorly, and were different to the dipole solutions extracted from the averaged data. The MFT solutions for the unaveraged data maintain the form displayed in the MFT solutions for the averaged data. This similarity, however, is not maintained at each and every timeslice as activity from other areas is also present (Ioannides et al 1995a). But as the intensity is integrated over fairly long time intervals the solutions extracted from the filtered and raw signal begin to resemble each other and also those extracted from the average signal. In order to demonstrate this effect, we shall examine the deep and superficial levels of our source space separately.

The following two figures show integrals of intensity over 20 ms for the first 80 ms of the sharp wave event we have examined so far: in each figure, the top row corresponds to the solutions for the averaged signal, while the middle and bottom rows to those of the filtered and raw signals respectively. In Figure 6-11 we display the solutions for the superficial levels (levels 7 to 9) of the source space while in Figure 6-12 those for the deep ones (levels 1 to 4). One can note the similarities in the three sets of solutions but also the differences which become more evident if we take into account the MRI slice numbers. As the integration interval becomes longer and longer some of the differences at individual timeslices disappear and the solutions of the three sets look more and more alike, as can be seen in the next three figures. In particular, Figure 6-13 and Figure 6-14 deal with integrals over 50 ms (we use the same format with the previous two figures), while in Figure 6-15 we show solutions integrated over 100 ms - both superficial (top) and deep (bottom) levels are included in the same plot in this case: averaged on the left, filtered in the middle, raw on the right columns. The agreement between the three sets of data in the latter figure is remarkable.

How long integration intervals one should use to observe such similarities though is a question without a clear answer. We believe that this is very much dependent on the specific characteristics of the signal under consideration, in other words how fast or slowly the activation patterns change. Moreover, it is not guaranteed that the integration interval of choice (i.e. the one showing the similarities) in a certain template event will be the "gold-standard" for the rest of events, since differences in the individual signal signatures are expected.

To extend the discussion in the temporal domain we shall involve the familiar activation curves. In order to do this, we shall display the 100 ms integrated solutions in sagittal views and by "outlining" the two strongest areas of activation (one superficial and one deep) we shall examine their temporal behaviour, as it appears in the averaged and raw

solutions. The left part of Figure 6-16 shows the integrated solutions for the superficial (level 9, top) and deep (level 1, bottom) level, and for the solutions extracted from the average (left) and raw (right) signals. The two sets of rectangles denote the ROIs for the areas of activation. The right half of the figure displays the activation curves in the two ROIs: the superficial on the top, and the deep on the bottom (averaged in blue, raw in red).

Comparing the two activation curves of the deep region, it appears that the average does not reflect the underlying reality faithfully. For example, the activity leading to the sharp wave maximum in the average signal exhibits an explosive build up at the deep level. This is absent in the corresponding activation curve from the unaveraged signal. Instead, the subcortical activation, at the time of peak activity in the average signal (i.e. around 1110 ms), coincides with the last subcortical burst of activity before an interval of low activation. The latter was characterised as "a period of almost complete inactivity" when the activation of the filtered signal was taken into consideration (cf Ioannides et al 1995a) and it was speculated that it was probably this period of silence following a (focal) deep activation that it was picked up by the spatio-temporal template.

In order to tackle this issue properly we have examined a number of other template sharp wave events (raw and averaged) together with their corresponding similar events (raw)*; analysis for two series of them will be presented herein. In so doing and by showing elements of spatio-temporal consistency, we will prove that the analysis of unaveraged epileptic events is indeed feasible, thereby extending the conclusions of previous single epoch analysis of auditory responses in healthy subjects (Liu 1995) to pathophysiology. At the same time we shall provide hints about the potential of the spatio-temporal template technique (Abraham-Fuchs et al 1990).

The two template events we are going to present here were 172.5 ms and 187.5 ms long respectively. For the first one, 10 similar events were aligned and averaged to obtain the averaged template epoch+ (template period between 912.5 ms-1085 ms), while only 7 for the second one (template period between 907.5 ms-1095 ms). MFT analysis was performed on 6 similar epochs for each set in addition to the raw and averaged epoch of each one.

---

* *Ideally, we should examine each of the similar epochs comprising the specific template event we have examined so far; however, such data were not available to us. On the contrary, such details were available for other template shrp wave events, and so our analysis will be based on those.*

\+ *Each epoch was 2 sec long: the middle point of the events were used as "centres", and the epochs were extended for 1 sec on either side of their "centres".*

We noticed that the same regions with those of the previous template were also appearing to be active in these sets too (other areas were also seen active, especially in the solutions of the unavereraged signals). We therefore kept the same ROIs as in Figure 6-16 for the MFT activation curves. For the first set, we observed the same kind of disagreement in the temporal evolution of activity between the raw and averaged epoch. That is, the time of the peak activation of the deep region as appearing in the averaged record did not correspond to significant activation of the region when the raw (unaveraged) record was considered. However, when the results of the 6 similar epochs were also reviewed cause of this effect became much more clear. In Figure 6-17 we present these results using both activation curves of the deep region (middle column) and time-depthplots (right column) along with signals of one MEG channel (left column).

The top two rows in Figure 6-17 correspond to the averaged (blue signal and activation traces) and raw (red traces) template epochs respectively, while the following 6 rows to the 6 similar epochs. The activation of this deep region is peaked during the time interval denoted by the pink rectangle. During this period and despite the apparent "silence" of the same region seen in the raw template, some of the epochs reveal a consistent activation of the region within this specific time window. This is also seen in the column with the depthplots: some of the epochs are well correlated (and aligned) with the averaged one, like for example epochs 2, 3, 4, 6 (rows 4, 5, 6, 8 from the top), while some others, like 5 (row 7) are not. The same effect can be observed during another smaller interval containing the second major peak of the averaged activation (marked with brown). Some of the epochs "agree" well with the behaviour of the averaged record in both intervals (i.e. epoch 3), others better in one interval than the other (i.e. epoch 2), while some only in one (i.e. epoch 5). So, it seems that the peaks appearing in the activation of the averaged record can be explained by the cumulative effect of activations at each individual epoch (with varying amplitudes) during short time windows. In other words, the spatio-temporal matching technique might be correctly identifying and aligning correlated epochs. Furthermore, it seems that actual deep activity is "picked up" by the spatio-temporal technique rather than the silence-periods following focal deep activations as speculated initially.

Verification of these conclusions was obtained with the second set of epochs as displayed in Figure 6-18. In this case, averaged and raw templates were in consensus regarding the activation of the same deep region. All of the studied similar epochs appeared to be also in agreement during the short time interval of the main peak (pink rectangle), suggesting again *a cumulative effect of activations at individual epochs giving rise to the appearance of the*

*averaged peak**. In order for the spatial (anatomical) coherence among the averaged/raw template and the different similar epochs to be better demonstrated, we present in Figure 6-19 integrals of intensity for the deep levels over some 20 ms - 10 ms on either side of the latency t=1020 ms, that is nearly the peak time of the activation for the averaged template. The agreement is generally very good, although some epoch variability is clearly evident (see epochs 2, 3, 4). The latter, however, can be partly explained by the effect the central point of the intensity integration induces, since the latency 1020 ms is not exactly "central" in our time window for all epochs.

Similar results can be obtained for the superficial levels and ROI. The time-depthplots in this case, however, are not very helpful and are going to be omitted. Figure 6-20 shows the activations of the previously selected superficial ROI during the various events of the first set of epochs (their corresponding deep activations were given in Figure 6-17). As can be noticed, the temporal evolution of the superficial activity is more capricious than the deep one, but again the built up of the peaks in the averaged record (the two main ones are marked) can be explained along the lines of the mentioned framework, i.e. resulting from variable amplitude activations of the ROI throughout the various similar epochs. Longer integrals of intensity result in more useful displays in this case; such integrals over the first 80 ms of each event are given in Figure 6-21 for the superficial levels of the source space. The concordance among the various events is clear (note also the MRI slice number which with only one exception ranges from 10 to 13, i.e. giving an overall range of less than 1.8 cm slice range).

All the above results, provide hints that the spatio-temporal matching technique accomplishes a useful operation in the identification and alignment (for averaging purposes) of single interictal events. Our initial goal was to fully test this algorithm through the use of data from other patients as well. However, some commercial (Siemens) software changes made it unclear whether the results for other patients would be exactly under the same framework or not (Hellstrand 1995). This and the given limitation of not having access to the software (and/or source code) ourselves deterred us from our original intentions. However, we shall use information from the Siemens program to roughly obtain the "temporal whereabouts" of the various interictal events, but we shall not assume that the individual events are properly aligned.

To conclude, we have used MFT to identify aspects of spatio-temporal coherence among the various "similar" epochs, and hence explain at fundamental level how the

---

* *The two smaller peaks of the average could also be explained under the same scheme but with weaker effects.*

unaveraged interictal events built up the average. As we have demonstrated, MFT (MEG) allows single epoch processing which provides a direct way of studying consistency and variability of pathological brain function. Moreover, as in the case for normal auditory processing, a consistent picture seems to emerge: the average is made up of contributions which occur intermittently and at variable latencies. Features in the average appear to be the outcome of higher aggregation of similar events in some epochs; each feature arises from contributions of different epochs. Nevertheless, as we have shown, the average portrays a valid summary in two ways (Ioannides et al 1995b):

- if the activity in an area is integrated over a period of time, then the averaged and single epoch integrals agree more and more as the interval of integration increases, despite huge variability from moment to moment in single events.
- Dominant features in the MFT solutions extracted from the averaged event are seen in the MFT solutions of single, unaveraged events, although in the latter are usually buried in a stronger more variable background. This is seen both in superficial and deep activity.

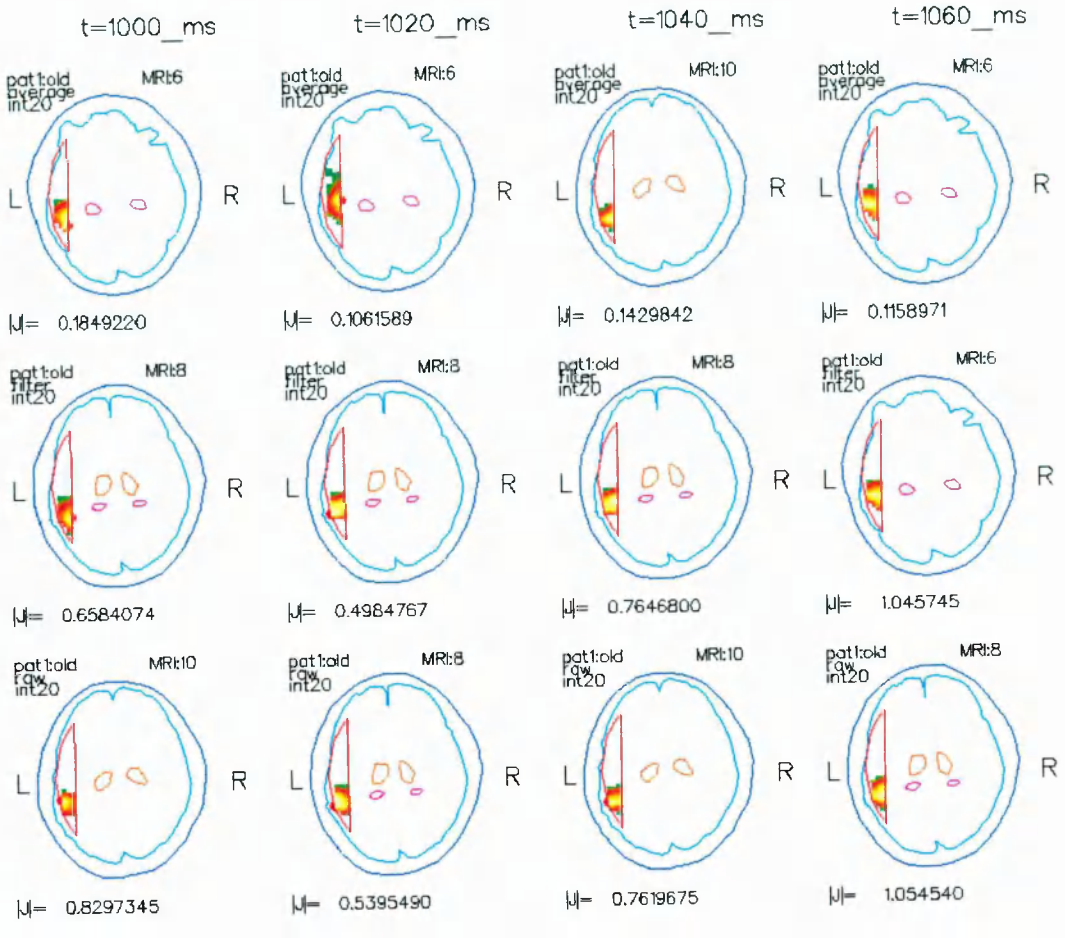

Figure 6-11: integrals of intensity over 20 ms for the first 80 ms of the sharp wave event we have examined so far corresponding to the solutions extracted from the averaged (top row), filtered (middle row) and raw signals (bottom row). Only the superficial levels of the source space (levels 7-9) are displayed. The solutions are superimposed on the patient's MRI outlines of the skull (blue), brain (light blue), thalami (orange), and hippocampi (pink). One can see that the three records show similarities in general, but these are not maintained at each time step (see the MRI slice number printed within each plot; interslice MRI distance is 6 mm). The situation would be worse if the single timeslices are considered at steps of 2.5 ms rather than integrated solutions over 20 ms.

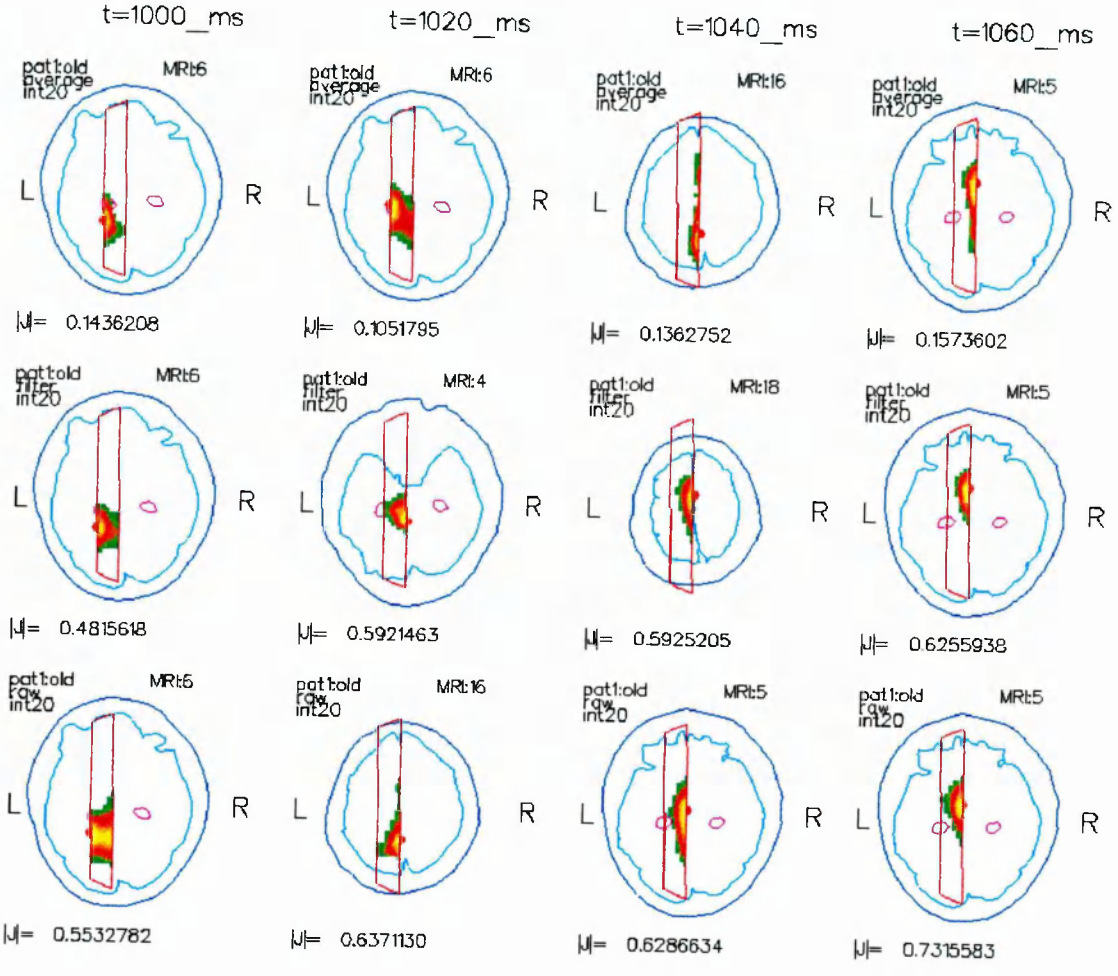

Figure 6-12: same as in Figure 6-11 but for the deep levels of the source space (levels 1-4). Same comments apply.

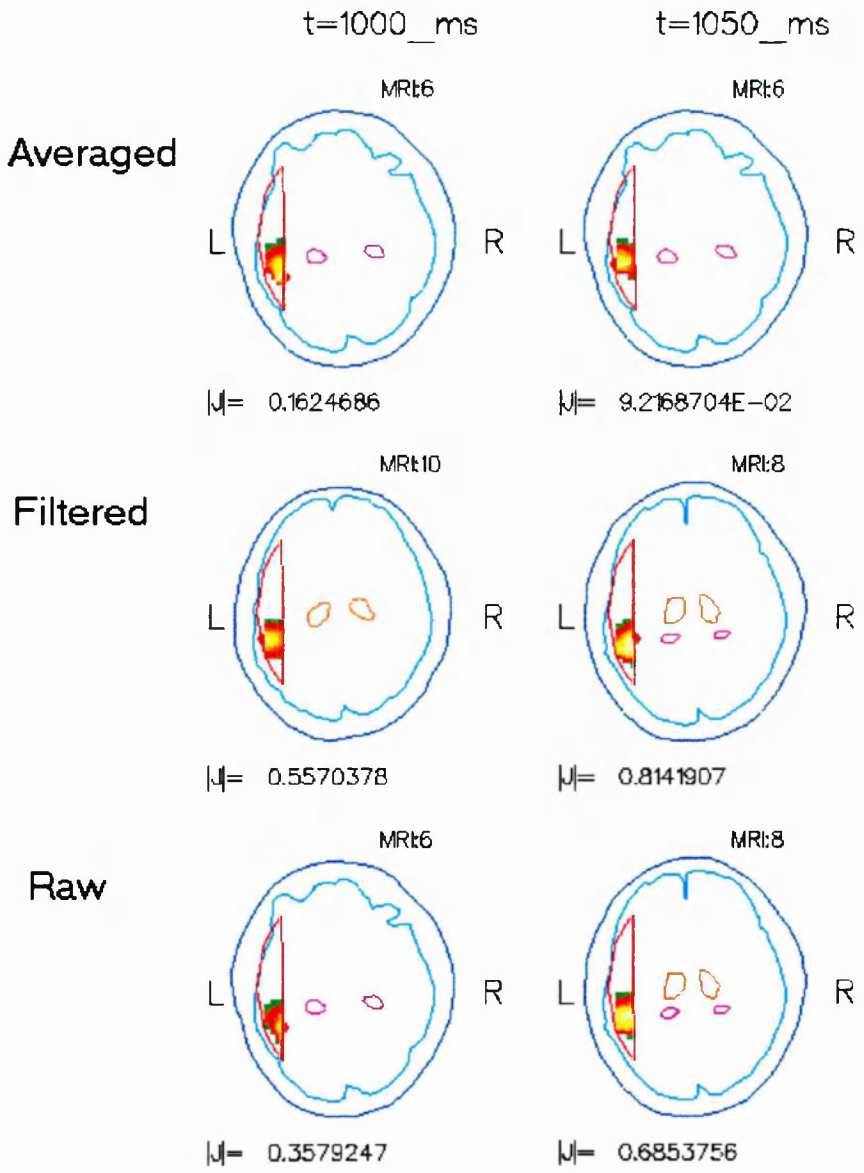

Figure 6-13: same as in Figure 6-11 but with the intensity integrated over 50 ms. The solutions for the three datasets begin to look more similar to each other. Only superficial levels are considered.

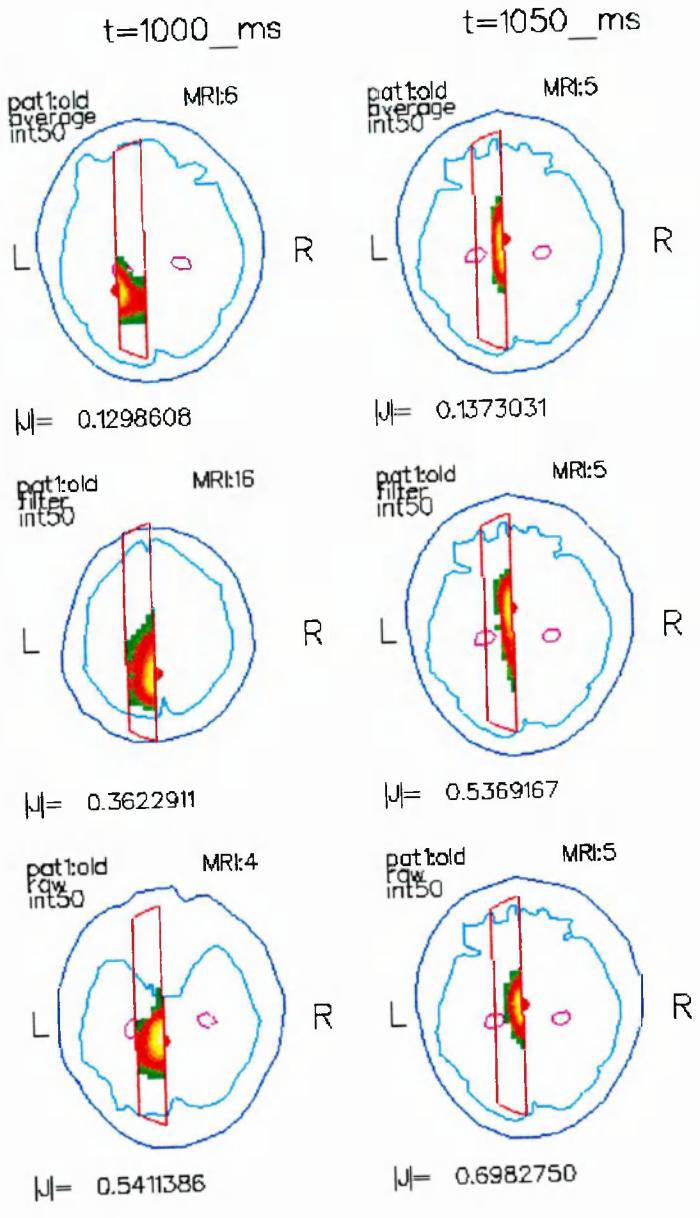

Figure 6-14: same as in Figure 6-13 but for the deep levels.

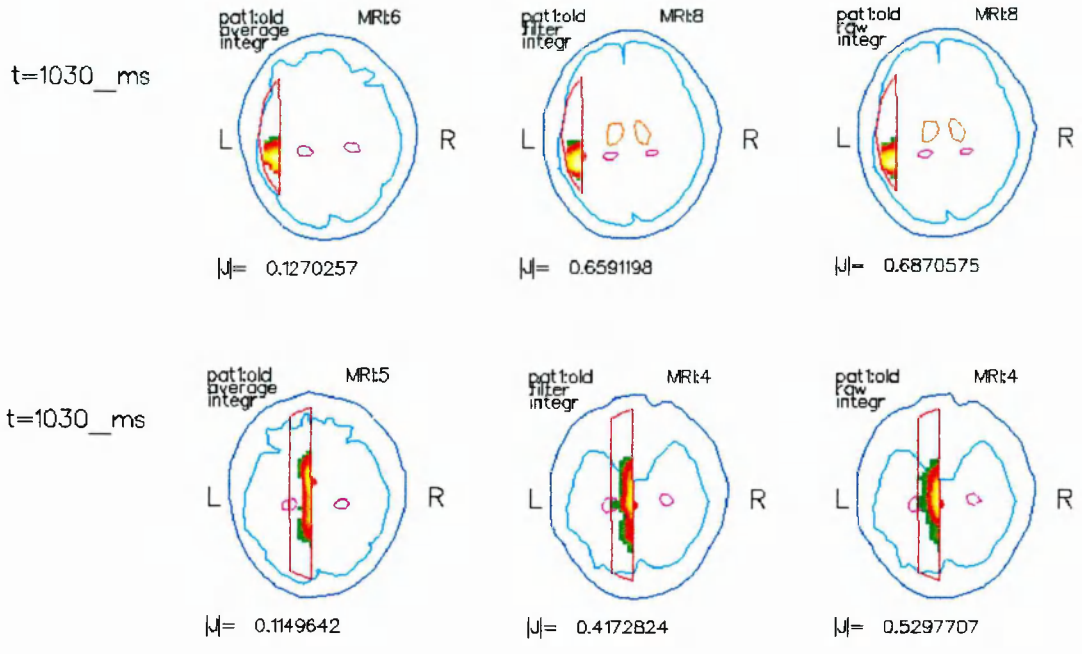

Figure 6-15: integrals of intensity over 100 ms for the averaged (left column), filtered (middle column) and raw datasets (right column). Superficial levels are considered at the top, deep ones at the bottom. Note the more "similar appearance" of the three sets of solutions.

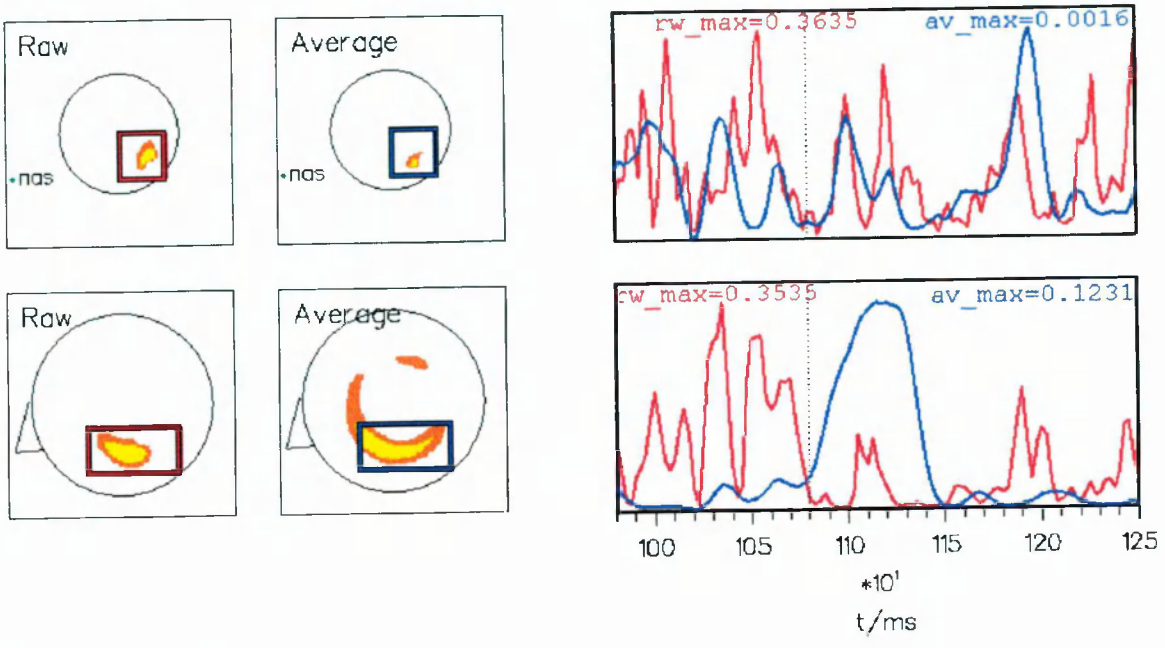

Figure 6-16: Left half: 100 ms integrated MFT solutions for the superficial (level 9, top) and deep (level 1, bottom) level, and for the solutions extracted from the average (left) and raw (right) signals. A small triangle in the deep level denotes the nose, while a small dot indicates the nasion (nas) in the superficial. The same ROIs are used in both raw and averaged cases, seen as two rectangles (one superficial and one deep) in red and blue colours respectively. Right half: activation curves for the same two ROIs (raw in red, averaged in blue) for the period of the sharp wave event. The maxima of each curve are printed with suitable colours in arbitrary units, while dashed vertical lines indicate the time interval (from the beginning of period shown) used for the integration. Note that the raw and averaged records show some disagreement in evolution of the activity, especially the deep one: around the time of the sharp wave maximum (1110 ms) the average record exhibits an explosive build up at the deep level which is absent in the corresponding activation curve from the raw signal.

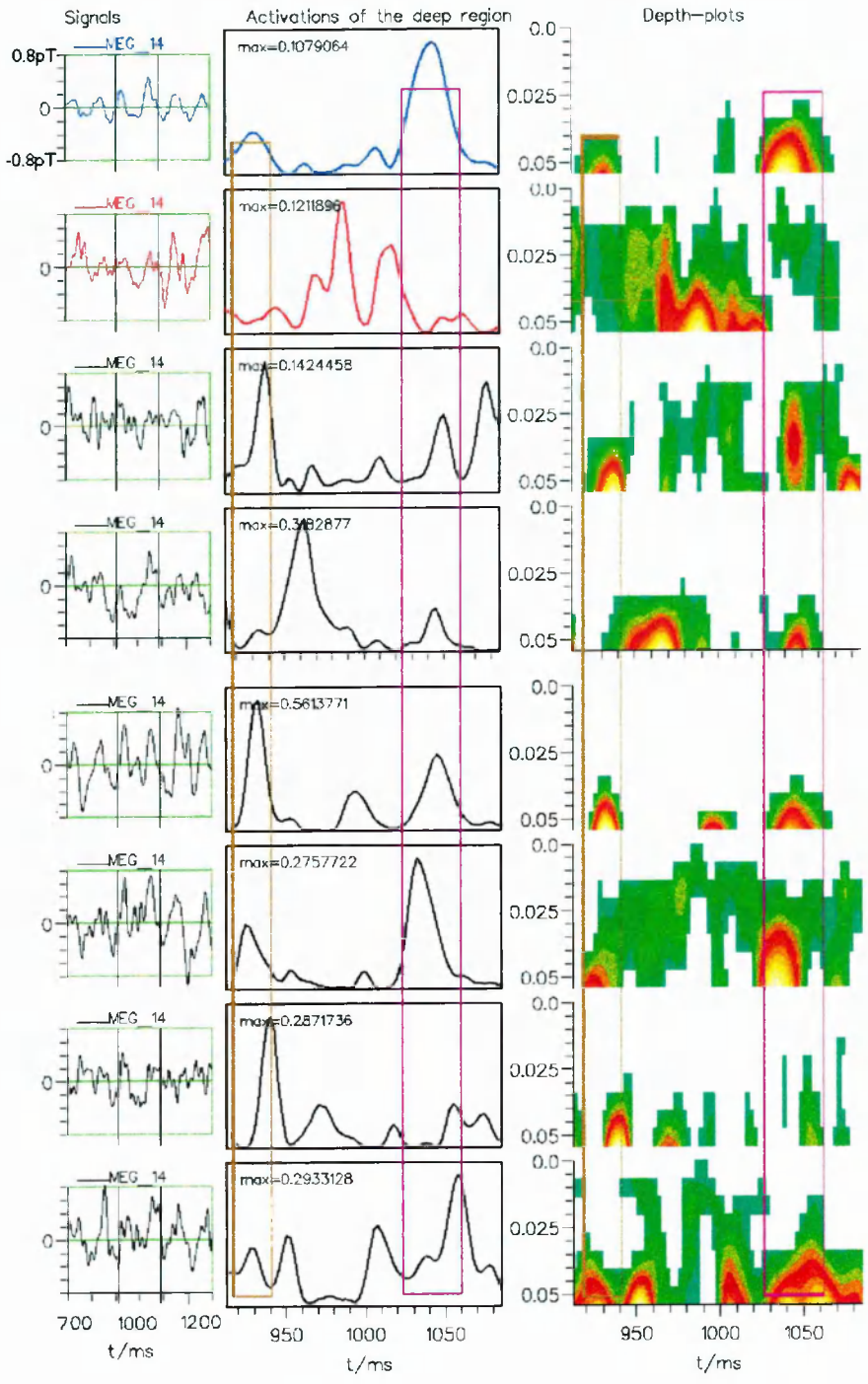

Figure 6-17: Epoch set 1. *Top two rows*: averaged (blue) and raw (red) template; *rest*: 6 similar epochs. Left: signals from one MEG channel. *Middle*: activation curves of the deep region. Right: time-depthplots. At the interval of peak averaged activation (pink), epochs reveal a consistent activation, also seen in depthplots: some of the epochs are well correlated with the averaged (rows 4, 5, 6, 8 from top), while some others (row 7) are not. Similar effects can be seen during another interval containing the second major peak of the averaged activation (brown).

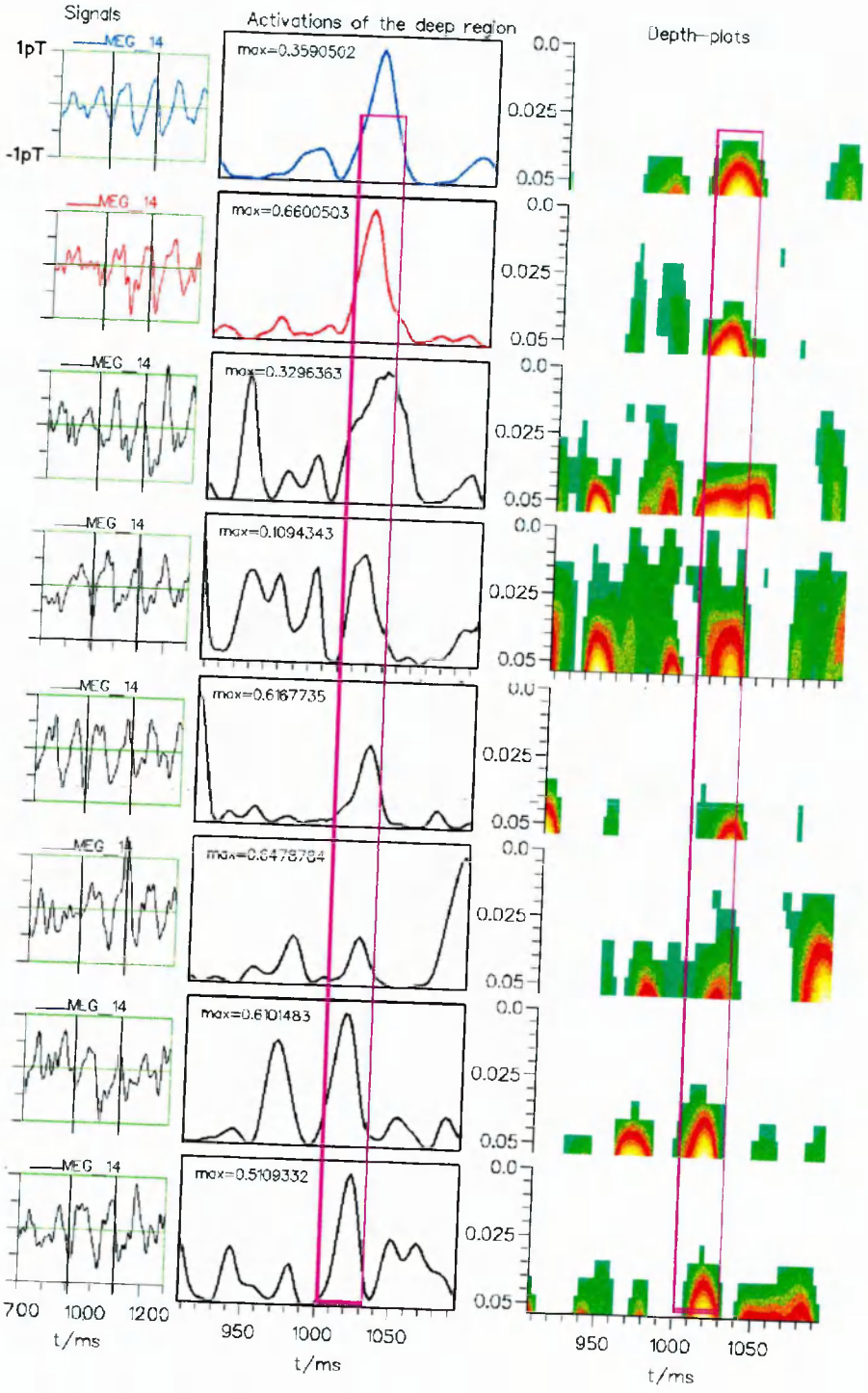

Figure 6-18: same as in Figure 6-17 but for epoch set 2. The cumulative effect of activations at individual epochs seems again to give rise to the appearance of the averaged peak (pink time window).

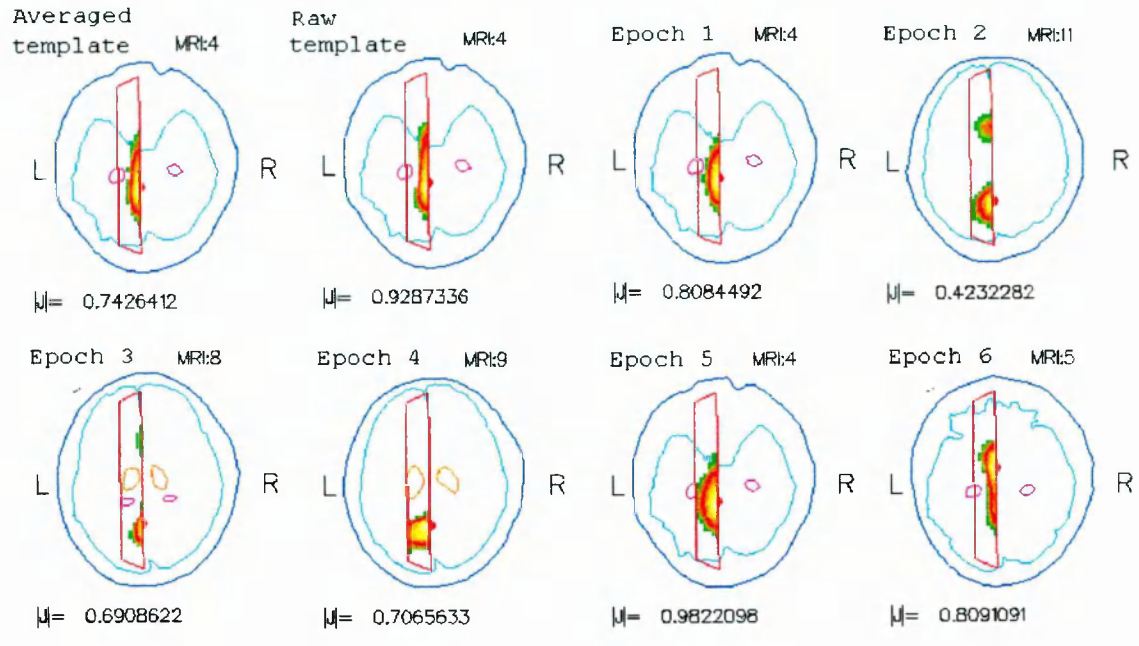

Figure 6-19: Epoch set 2: integrals of intensity (for the deep levels) over t=1010-1030 ms, that is 10 ms on either side of the activation peak time for the averaged template, superimposed on proper MRI outlines. Note the generally good agreement between averaged (top left) and raw (top, second from left) templates extended in the similar epochs despite some epoch variability (see epochs 2, 3, 4). The latter, however, can be partly explained by the effect the central point of the intensity integration induces, since the latency 1020 ms is not exactly "central" in our time window for all epochs.

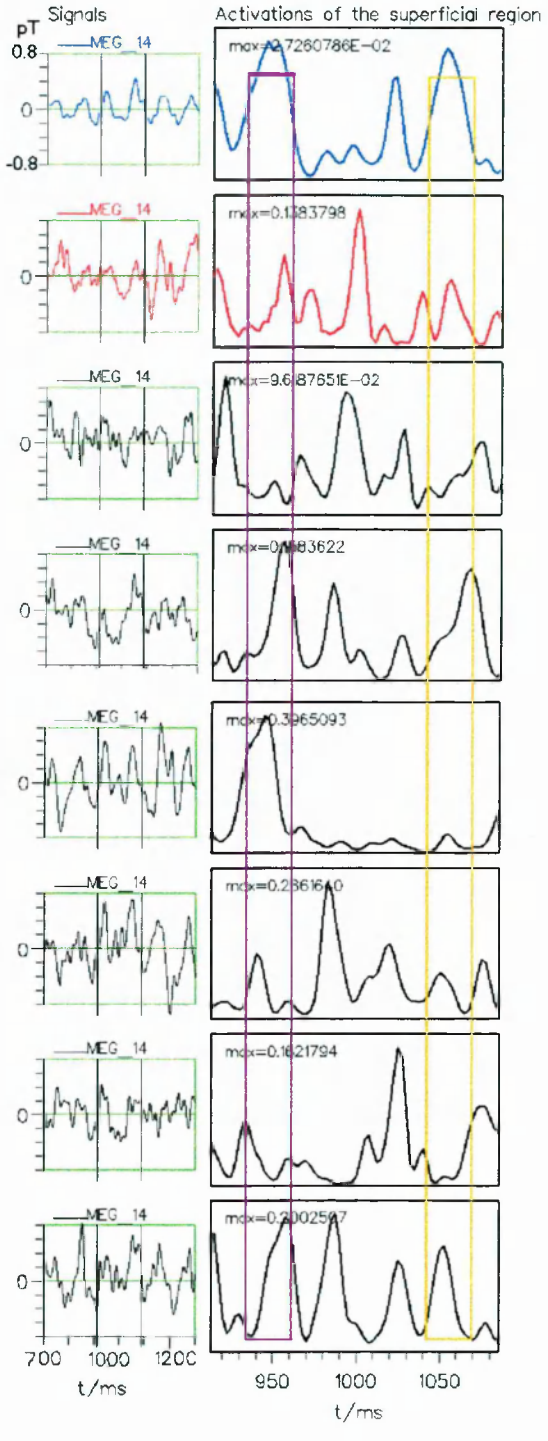

Figure 6-20: Epoch set 1; top row corresponds to the averaged template, second from top to the raw template, while rest to the similar epochs. Left: signals from one MEG channel. Right: activations of the superficial ROI (seen in Figure 6-16). The built up of the peaks in the averaged record - the two main peaks are marked - can again be explained as resulting from the variable amplitude activations of the ROI throughout the individual epochs It is also worth noting the generally lowered magnitudes involved, especially in the activation for the averaged epoch.

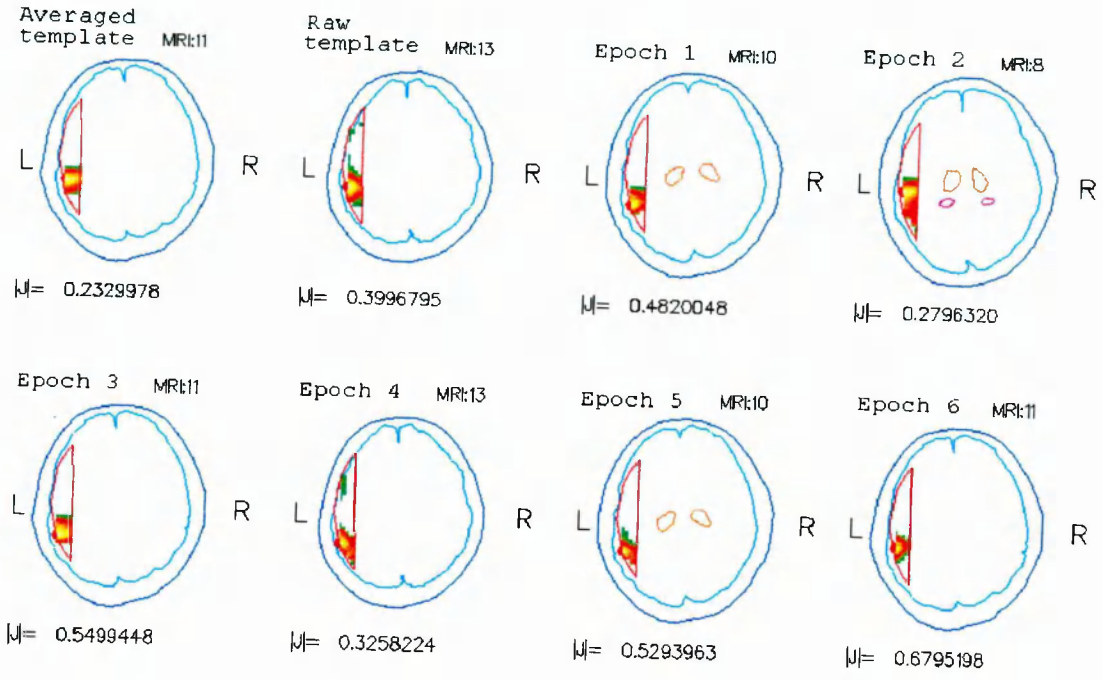

Figure 6-21: Epoch set 1. Integrals of intensity (for the superficial levels only) over the first 80 ms of the interictal events superimposed on co-registered MRIs of the patient. The first display refers to the averaged epoch, the second one to the raw template, while the rest 6 to the similar raw epochs respectively. The concordance among the various events is clear (note also the MRI slice number which with only one exception ranges from 10 to 13, i.e. giving an overall range of less than 1.8 cm slice range).

7. Spatio-temporal Evolution of Epileptic Activity during Unaveraged Interictal Events

7.1 Introduction and rationale

In the previous chapter we have used MFT analysis to study unaveraged interictal events from a single epileptic patient who exhibited pathological activity in temporal areas. In the current chapter, we examine further the spatio-temporal evolution of activity derived from MFT analysis of unaveraged interictal signals in another two epileptic patients. In common with earlier results, we find activations which are highly variable from one interictal event to the next; nevertheless, closer comparison reveals physiologically plausible activation sequences.

We mentioned before that many MEG investigators underlined the potential in multichannel MEG systems to analyse interictal epileptic data directly, without signal averaging (e.g. Sato 1992). But why should one put effort on the analysis of such datasets? A simple answer to this question could be given on the neurophysiological grounds of epilepsy. Witte et al (1992) state that analysis of individual spikes would be preferable to that of an "averaged spike", since spikes of similar shapes may arise from different cortical areas. Moreover, an averaging technique might give good localisation results at the maximum of the spike (in consensus with some unaveraged spikes), but one cannot guarantee that the propagation of epileptic activity as appearing in the averaged record would represent the actual epileptic propagation. However, the study of unaveraged epileptic events, necessitates a *robust analysis method* that: (i) does not include

any preconceptions on the number and position of sources; (ii) allows for distributed sources, since extended and/or multiple brain areas may be involved in the generation of epileptiform activity (Barth et al 1984; Graf et al 1984). Magnetic Field Tomography (MFT) meets these requirements as explained in Chapter 4, and, therefore, comprises an ideal tool to study epileptic propagation without averaging. So, in the following, our emphasis is drawn on the propagation characteristics of the interictal activity: we study the interactions between neocortex and middle temporal structures, as well as the spatio-temporal signatures of the activity in the depth of the temporal lobe. Indications for involvement of the contralateral (to the measurements) hemisphere are also studied for one of the patients (Pat2; see following section). At the end of the chapter, we contrast our findings with what has been so far reported in studies with intracranial recordings on epileptic patients, and comment on the physiological plausibility of our results.

7.2 Materials and Methods

7.2.1 Patients

As mentioned already, two temporal lobe patients are used in this study. The major part of our analysis was conducted for one of the patients (Pat2), with small but supporting analysis of data from the other patient (Pat3).

7.2.1.1 Case history (Pat2)

The data were obtained from an 18-year old girl with a history of complex partial epilepsy since the age of 14, with daily seizures of dizziness and impaired consciousness. Anti-epileptic treatment (monotherapies as well as different drug combinations) had no effect. Numerous routine EEGs were conducted, initially without showing any abnormality. At the age of 16, one recording showed fronto-temporal spike-wave activity in the left hemisphere. Two years later, a 24-hour-recording with surface and sphenoidal electrodes (ambulatory cassette EEG) recorded seizures, starting usually in the vicinity of the left sphenoidal electrode, but also over more centro-temporally placed surface electrodes on the left side.

CT scans were negative, but MRI revealed a small amount of possibly pathological tissue in the anterior pole of the left temporal lobe, and with a contrast injection a small lesion of the blood-brain-barrier was demonstrated. However, a concomitant stereotactic biopsy of the region contained only cells from an unspecific, inflammatory reaction in the tissue. A C-11-methionine PET scan revealed no increased uptake of the tracer, i.e. did not

indicate a malignant tumour. The patient underwent several stereotactic MEG measurements* - some of these have been used in this study - and was later referred to functional stereotactic radiosurgery, using the Leksell Gamma Knife®. The target volume for this surgery was based on the presurgical MEG localisations of the interictal epileptic activity together with conventional intracranial recordings of seizure start. After the radiosurgery, she was seizure free for three years, but later developed signs and symptoms of a glioma in the actual region. A resection of the anterior part of the left temporal lobe was then performed and the patient is now seizure free.

7.2.1.2 Case history (Pat3)

The patient, 42-year-old male, has suffered from partial complex seizures since the age of 13. No known aetiology to this, but the patient's twin sister had epilepsy of a generalised type since her birth. Clinically his seizures began with visual symptoms: the patient was seeing an old woman with a baby. Later, more acoustic sensations, like "noise", dominated. Generalisations of the seizures occurred frequently.

EEG recordings were normal, initially. However, after one year of anti-epileptic medication with phenyloine and barbiturate the patient sometimes showed right-sided occipital-temporal delta-theta activity in the EEG, although most of the recordings were non-pathological. Later on, the patient developed bilateral EEG-abnormality of similar kind, sometimes with sharp wave-like discharges, bilateral over the fronto-temporal regions.

MEG measurements performed under controlled stereotactic conditions were recorded. Their analysis with ECD showed localised bilateral temporal epileptic activity, mainly in the mesial part of the temporal lobes, in the right lobe extended to its lateral and posterior regions as well. Epileptic activity was also found in the right frontal and right and left parietal lobes, but to a much lesser extent.

Bilateral intracranial electrodes (subdural strips) were used to study the regions of seizure onsets. 11 seizures were detected, all of the complex partial type, one with secondary generalisation. The onsets were always limited to the mesial area of the right temporal lobe, with further spread within this lobe. Clinically, nothing at all or very small

---

* *In such measurements, a non-invasive and non-magnetic head fixation frame is employed to "lock" the patient's head to the couch on which he/she is lying during the MEG sessions. The same stereotactic frame can also be used in MRI acquisitions and/or radiosurgical procedures to facilitate fusion of MEG data with MR images and/or radiation treatment plans (see Hellstrand et al 1993).*

movements of the left leg could be observed, the latter only when the spread was established over the entire right temporal lobe.

A resection of the right temporal lobe was performed, based on the results of the MEG and the intracranial EEG findings, after a bilateral Wada test. Since then (2 years post-surgery follow-up) the patient has been seizure free and is working full-time. EEG checks have been negative.

7.2.2 Measurements and analysis

The MEG recordings used in this study were the presurgically performed ones, made with the 37-channel KRENIKON® system (Siemens, Erlangen, Germany for Pat2; Karolinska Hospital, Stockholm, Sweden for Pat3). All measurements were made within a magnetically shielded room (Vacuumschmeltze®, Germany). Only 30 channels were valid for Pat2, while full sensor capacity (37 channels) was utilised in the Pat3 case. The patients lay comfortably on a couch, with their heads locked into a stereotactic frame, *ad modum* Leksel®, using a plastic helmet fixed to the couch and provided with water marks visible in MR images. The plane of sensors was centred over, and parallel to, the left (Pat2) or right (Pat3) temporal area of the brain during the recordings. In addition to the MEG, EEG recordings were taken using surface electrodes covering the frontal, temporal, central and parietal aspects of the brain, together with recordings of the ECG (extremity leads).

The data were band-pass filtered on-line through 0.5–70.0 Hz, digitised at 0.4 kHz (Pat2) or 0.5 kHz (Pat3). Stereotactic MRI studies followed the MEG sessions, and the images were transferred to the MEG system, and later fused with their stereotactically pre-defined model volumes. The homogeneous conducting sphere was used to model the conductivity; the sphere was fitted to the local curvature of the inner skull surface as identified from multisliced MRIs. Three dimensional MFT estimates for the primary current density, $\mathbf{J}^p$, were obtained within partial hemispherical volumes encompassing the left (Pat2) or right (Pat3) hemispheres; the distance from the cortical surface to the centre of the brain measured 61 mm (Pat2) and 71 mm (Pat3) respectively. The smoothing parameter was 1.0 in all cases. A Gaussian *a priori* probability weight was used, centred at the midpoint of the conducting sphere; the decay factors were, $\lambda_3 = 0.05m$ (Pat2) and $\lambda_{1,2} = 0.05m$, $\lambda_3 = 0.052m$ (Pat3) - adjusted to correctly recover point sources generated by the computer (see Chapter 5).

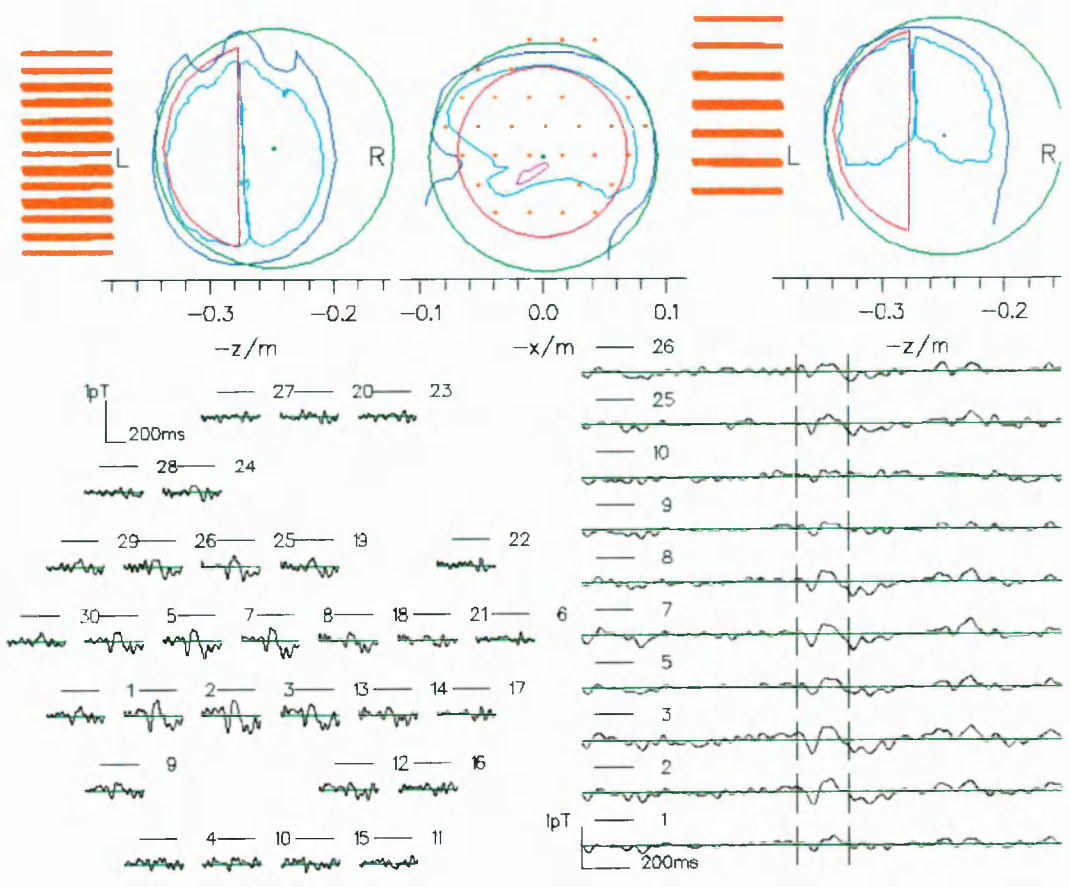

Figure 7-1: Experimental set up for Pat2. Top: the sensor positions relative to patient anatomy. In the axial and coronal sections, a bar represents each gradiometer sensor, while in the sagittal a dot shows the projection of the gradiometer onto the displayed slice. The conducting sphere used to model the conductivity of the brain, and the source space are also marked. Bottom: an interictal epileptic spike event is shown in two different views. On the left signals from all channels are displayed according to channel location, while on the right, only the strongest ones are successively illustrated.

The MFT analysis included epochs of various templates (as explained in Chapter 6), totalling in all about 30 seconds extracted from an MEG session of 5 minutes (Pat2)* . For Pat2, the following types of datasets were analysed: the digitally unfiltered data (raw data, 0.5–70 Hz filtering only), and unaveraged, digitally band-pass filtered signals of the

* *For Pat3, we only analysed some 8 secs out of a total 5.5 min.*

ranges 1-40 Hz, 1-20 Hz, 1-12 Hz, 1-6 Hz, and 4-8 Hz (i.e. theta range)[+]. Although all the details of the temporal sequence of the activity did not match precisely, no significant differences in the localisations given by MFT solutions resulted from filtering the signals. Such an example is shown in Figure 7-2, which is divided in 3 parts. The top part displays raw data (i.e. 0.5-70 Hz), the middle one, data filtered between 1-20 Hz, while the bottom one, data in the theta range. For each part, the right half contains superimposed signals from all channels (top) together with their corresponding Fourier Transforms (FTs, bottom). On the left of each part, instantaneous estimates of the intensity for the times indicated by the light vertical pointers are superimposed on drawings from the closest axial slice (top) and on a fixed sagittal outline through the hippocampus (bottom). One can see that despite slight differences in the localisations, all three datasets reveal activation of the hippocampal complex.

Thus, in order to avoid complexity, to maintain as much of the information as possible, and to circumvent the 50 Hz signal-contamination (see the small 50 Hz-blip on the FT spectrum of the raw data), the analysis presented here has been limited to those datasets filtered in the 1-20 Hz range for both patients.

7.2.3 MFT analysis

Similarly as before, the instantaneous MFT estimates were studied, as well as the temporal integrals of the intensity, $|\mathbf{J}^p|^2$. We used integrals of intensity in space (activation curves) to study the temporal evolution of activity within certain ROIs, as well as displays of temporal integrals of intensity to obtain summaries of activations within a given time window. Whenever activation curves within specific ROIs or levels of the source space (e.g. at the depth of the temporal lobe - hippocampal level) indicate strong activation, the spatial changes in the maximum activity are studied; such changes within a given image/level are displayed by connecting areas of strong activity with arrows. This provides an image of the various anatomical regions of the brain which are directly or indirectly functionally connected, allowing for propagations and/or sequential shifts of activity to be studied (see Chapter 5).

As mentioned in the introductory section of this Chapter, it is common for MEG researchers to localise a dipole at the peaks of the epileptic signals (e.g. Nakasato et al

---

[+] *The filtering as well as the Fourier Transform (see below) procedures were performed on 2 sec long signal segments. In other words, we did not obtain the 2 sec epoch-segments after filtering the whole signal set (i.e. 5 min long).*

1994). However, we have selected the spatio-temporal sequence of the rising time period of the spikes to study the build-up of the epileptogenic spread of activity.

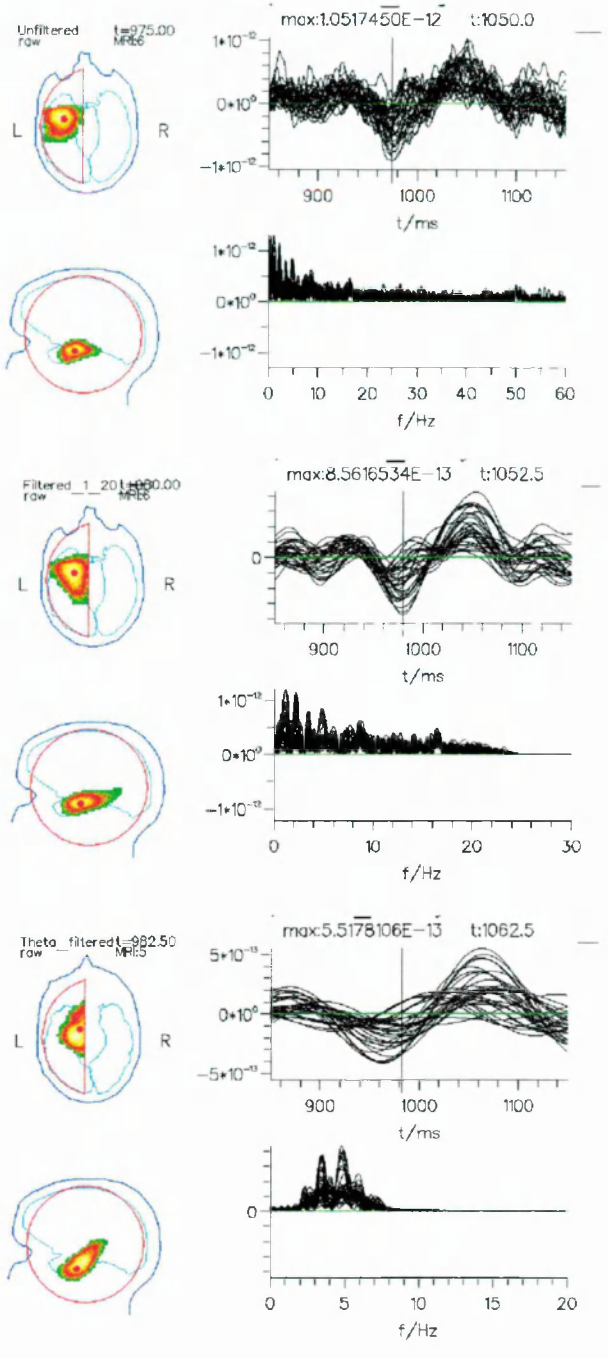

Figure 7-2: MFT of different filtering regimes (Pat2). Top: raw data; right half: superimposed signals from all channels (top) and corresponding FTs (bottom); left half: instantaneous estimates of intensity superimposed on axial and sagittal MRI drawings (see text). Middle: same but, 1-20 Hz filtered data. Bottom: data in the theta range. All three datasets reveal activation of the hippocampal complex.

7.3 Results

7.3.1 Neocortical and deep temporal interactions

We start our analysis by studying spatio-temporal activation sequences for Pat2. A typical interictal spike used in the analysis is shown in Figure 7-3 together with its MFT displays of intensity presented in a cinematic mode. Integrals of intensity over 20 ms were analysed in successive steps: the first rising phase of the spike to the negative peak; the rise to the main maximum to the end of the positive slope. During the initial, rising phase of the event, the activity appeared in the superficial, cortical area of the left temporal lobe, then in its deep, fronto-mesial regions, to be found at the negative peak of the signal, in the amygdala-hippocampal complex (cf the axial-coronal projections). From there it spread back to the cortex.

In the bottom row of Figure 7-3, the propagation of activity is displayed in a fixed sagittal plane through the hippocampus. The temporal evolution of the activity analysed moved from the anterior parts of the temporal lobe, through the amygdala and hippocampus, to the posterior regions (we shall return into this observation later on). Note the shape of the MFT solution at the time of the negative peak (third column), which seems to replicate the shape of the hippocampus.

The oscillations between the hippocampal area and the cortical part as delineated in the top right corner of Figure 7-3 are clearly demonstrated in the top middle box. Note the appearance of cortical activation before and after hippocampal activations. The time differences of the activations from cortical to deep or deep to cortical areas varied between 10 to 60 ms. Similar patterns of activation were observed in all the events studied.

MFT indications of cortical activation before and after deep temporal activation were also hinted in earlier studies involving the case of Pat1 (see for instance Figure 6-16 and Ioannides et al 1995a). In our next set of MFT analysis we have examined a series of (right side) cortical and hippocampal activation curves for Pat3. Interplays between deep and cortical activation occurring with various delays (also between 10 to 60 ms) were revealed once more. An example that combines data from both Pat2 (a different spike from the one used in Figure 7-3) and Pat3 is shown in Figure 7-4. The previous trend is again evident: during the initial phase of the spike, the activity appears in superficial, cortical areas of the temporal lobes (a); around the peak of the spike (b) in the amygdala-hippocampal complex, and then back to the cortex (c).

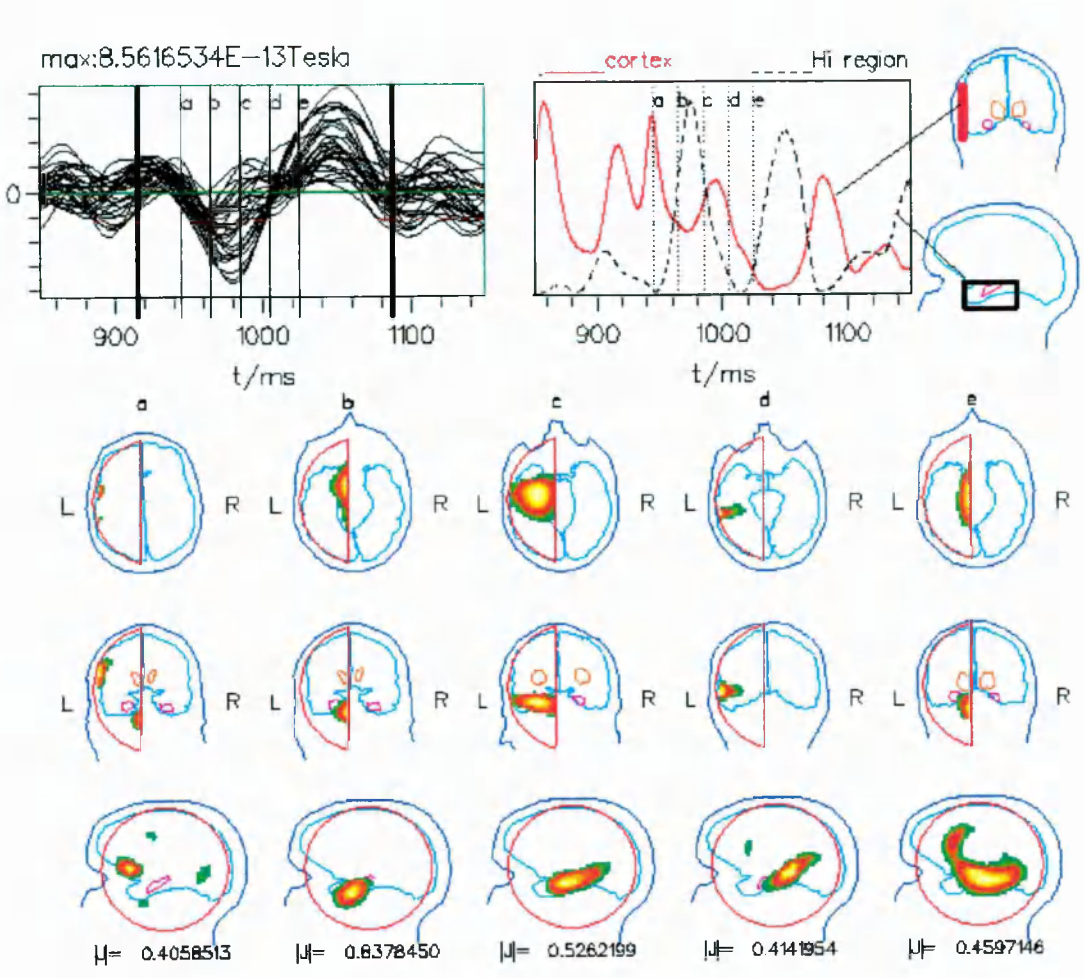

Figure 7-3: Top left: interictal event with superimposed signals of 30 channels; template interval within heavy lines; lettered vertical lines mark the times used for the MFT estimates of intensity displayed in the bottom part of the figure. Top middle: the temporal evolution of activity in the left hippocampal region (black) and in the temporal cortex (red). Top right: the hippocampal and cortical regions of interest. Bottom: MFT estimates of intensity integrated over 20 ms (i.e. 10 ms on either side of each lettered line). *Axial and coronal displays*: the solutions are superimposed on drawings of the closest MR image; *sagittal display*: solutions on a fixed MRI slice at the hippocampal level. Note L-left side, R-right side, projections of the hemispherical source, and modulus of $\mathbf{J}^p$ (in arbitrary units, beneath each sagittal section).

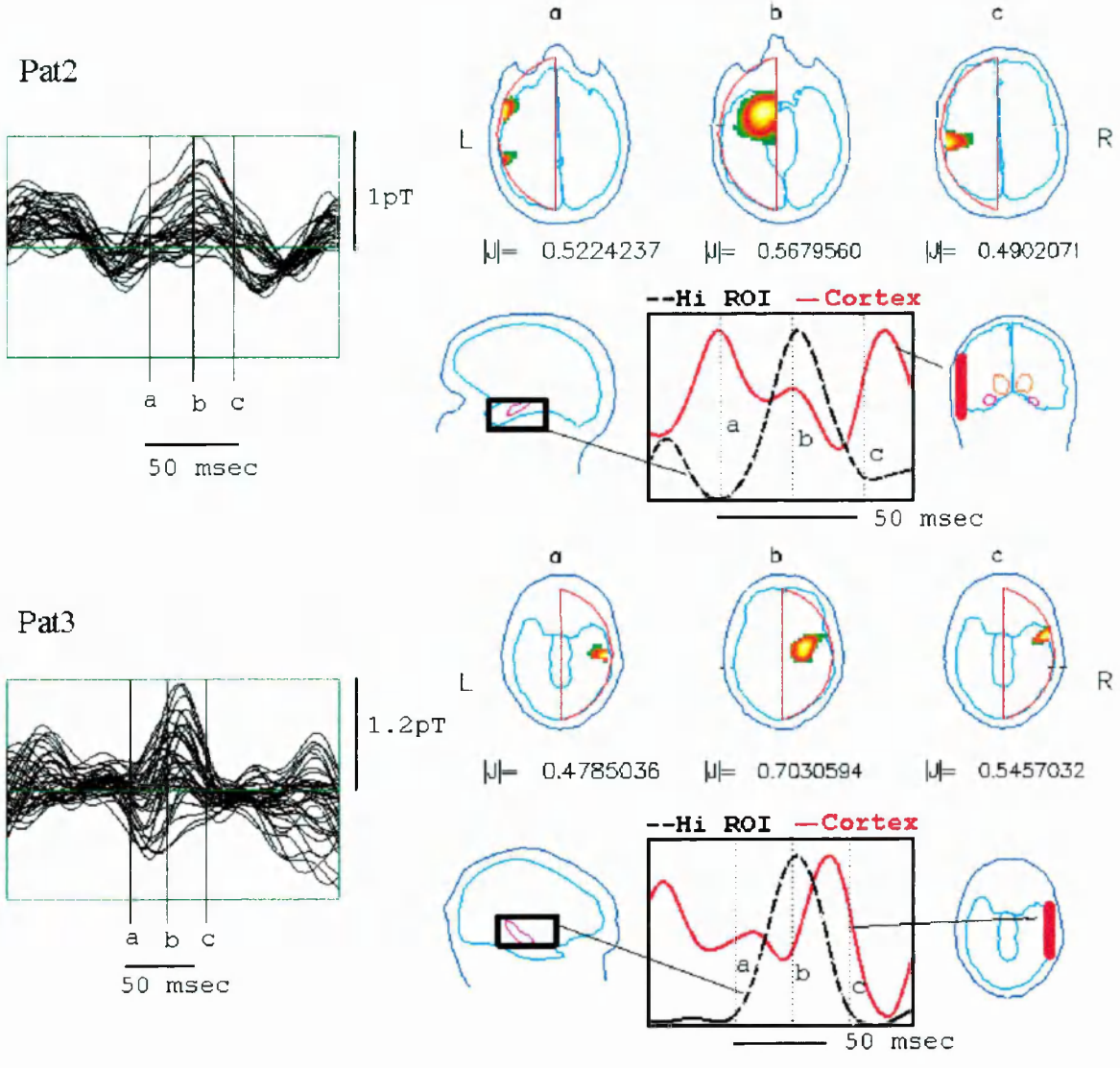

Figure 7-4: Top half; Pat2; Left: left-hemisphere interictal spike with superimposed signals of all channels (note time bars a-c). Right; *top row:* instantaneous MFT estimates of intensity on axial MR images (note time instants a-c and $|\mathbf{J}^P|$ values in arbitrary units); *bottom row; middle:* graph of temporal evolution of activity in the left hippocampal area (dotted line) and temporal cortex (full line) (note time bars a-c); *bottom row; left and right:* MR images of ROIs at the level of hippocampus (sagittal view) and temporal cortex (coronal view). Bottom half: similar, but for the right hemisphere of Pat3.

Different cortical areas are involved in the pre- and post-deep activation, which might, therefore, be thought to be of no physiological significance. We back-averaged the 3d MFT solutions from a number of single epoch events, time-locked to the peaks of strong hippocampal activations. This procedure selectively amplifies activations from areas which maintain a consistent time relation with the activation in the hippocampus. An arbitrary threshold - with slightly different values for either patient - was used to select the time intervals of "strong" hippocampal activation. Such a selection indicated some 18 time segments for Pat2 (out of the 30 sec studied) while some 19 for Pat3 (out of an 8 sec study). Back-averaging of these single event solutions was then performed for each patient separately. Some 50 ms intervals before and after the time instants of the selected hippocampal events were used in the back-averaging procedure. As a result, the back-averaged solutions were some 100 ms long (time run from 0-100 ms), with "expected" hippocampal activation centred around the latency of 50 ms.

In so doing, two main cortical ROIs were revealed for each patient: one fronto-infero-temporal and one more posterior in the temporo-parietal region (especially in the case of Pat2). The previously observed sequences of neocortical and deep temporal activations became much clearer after this procedure. The results are summarised in Figure 7-5.

One can easily note that the cortical ROIs involved remain "silent" during the interval of hippocampal activation, but, they do fire before and after this interval. This is clearly shown in the cortical activation curves, which reveal distinct peaks above the noise level before and after the hippocampal firing. Similar patterns occur for both patients. Note also that the cortical areas do not seem particularly "focal", but they appear rather extended. Furthermore, and as the schematics at the far right of Figure 7-5 demonstrate, there seems to be an interplay of activation between the different regions of the cortex followed by a "drop" of activity at deeper levels. This drop, however, appears to be responsible for the high amplitude observed signals (i.e. spike peaks; see Figure 7-3 and Figure 7-4).

The hippocampal area in turn, appears to be interacting mostly with the anterior cortical ROI, in both patients. The image revealed from the back-averaged solution (cf. schematics in Figure 7-5) may not necessarily represent the actual sequence of activations in each individual event, but it does mean that it occurs frequently (more than half of the events studied for each patient), and certainly above chance.

It is finally worthy of note, that the time delay from the cortical (the pre-hippocampal one) to hippocampal activation as given by the back-averaged record is some 30 ms for Pat2 and some 20 ms for Pat3. This again represents the "mean" - and probably the most

frequently observed - time delay value from the range of 10-60 ms observed in individual solutions.

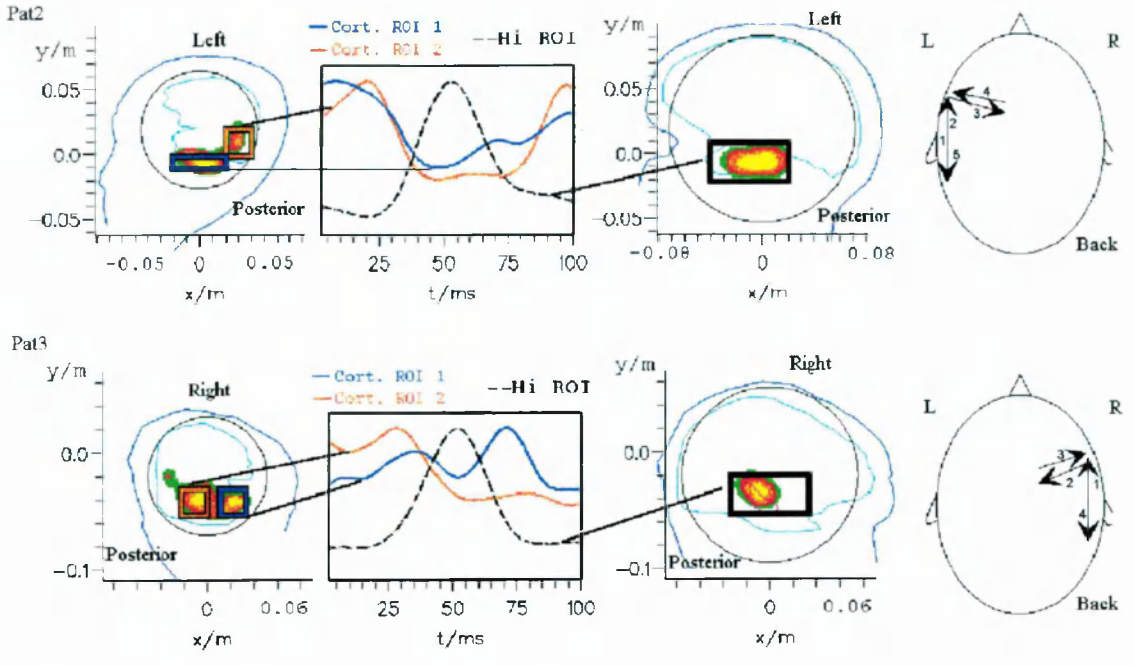

Figure 7-5: Top row: (Pat2); *Left*: superficial integrals of intensity over 100 ms, after back-averaging 18 single event solutions of strong hippocampal activation. Two main ROIs are revealed in the sagittal view: one fronto-infero-temporal and one more posterior in the temporo-parietal region. *Middle*: graph of activations of the cortical and hippocampal ROIs. Note the pre- and post-hippocampal activation of the cortex. *Right*: sagittal view of deep intensity integrals after back-averaging. Hippocampal activation is clearly shown. *Extreme Right*: schematic axial view of the neocortico-mesiobasal interactions emerging from the back-averaged solutions; the sequence appears as: anterior-cortex→posterior-cortex→anterior-cortex→Hippocampus→anteriro-cortex→posterior-cortex. Bottom: Similar, but after back-averaging 19 solutions for Pat3. Activation sequence appearing from the back-averaged solutions (extreme right schematic) involves: post.-cort.→ant-cort.→Hi→ant-cort.→post-cort. The circles in the sagittal views illustrate a projection of the appropriate source spaces.

7.3.2 Propagation patterns at the depth of the temporal lobe

For both patients, the MFT estimates at the peaks of the spikes indicated activation at the depth of the temporal lobe. The shapes of the solutions were consistent with activation of the hippocampal areas. Studying the spatial changes in the maximum activity in a sagittal section through the amygdala and hippocampus complex, we noticed that for

most of the events studied for each patient, activity seemed to be propagating mostly in the anterior-posterior direction, suggesting spread from amygdala to hippocampus. This effect was more prominent for Pat2, for whom the shapes of the integrated intensity during such intervals clearly portray such a trend.

The above are illustrated in Figure 7-6 which depicts summaries of the activity in 60 ms intervals during the positive peaks of various spikes for Pat2. The integrals of intensity over these intervals are displayed in the third row. The changes in the maximum activity (computed every 2.5 ms) are marked by arrows in the middle row. As mentioned already, a trend seems to emerge: activity is initiated away from the hippocampus, either in the cortex or (in some signals) in an area posterior to the hippocampal region, then propagates to the anterior part of the hippocampus-amygdala complex. A similar trend can be inferred from the shape of the integrated intensity which usually appears along an arch indicating propagation from structures anterior to the hippocampus along its main axis to its posterior end. This was the case in 12 out of the 26 events studied. In 4/26 events (one is shown in the second column of Figure 7-6) we observed activity propagating from the posterior area of hippocampus to its anterior region. In 6/26 events there was a sequential shift in the peaks of activity: anterior hippocampus → posterior hippocampus → anterior of hippocampus, while the pattern with the reverse order (i.e. posterior→anterior→posterior) was seen in 2/26 events. In only 2/26 events was no such shift observed: instead the activity stayed rather stationary in the posterior parts of the hippocampus (cf the start position of activity in the second column of Figure 7-6).

Such propagations and/or sequential shifts of activity were also visualised using activation curves within small ROIs in the anterior and posterior hippocampal area. The validity of such modelling was demonstrated and discussed in Chapter 5 (see section 5.4.3). An example illustrating the two main patterns of "deep propagation" for Pat2 (i.e. anterior→posterior propagation and anterior→posterior→anterior sequential shifts) is given in Figure 7-7.

Having conducted such observations for Pat2, we questioned whether similar statements could be made for Pat3. So, by studying the spatial changes in the maximum activity in a sagittal section through the hippocampal complex (level 5 of the source space used for Pat3) during the periods that activation at this level occurred, we were able to identify patterns similar to those of Pat2. In specific, we noticed again that activity seemed to be mostly propagating from anterior to posterior (7 out of 15 events studied), as illustrated in the first two display columns of Figure 7-8. Propagations from posterior to anterior (third display column of Figure 7-8) were less frequent here too (4/15 events), but they were a bit more frequent than in the case of Pat2 (the specific figure there was 4/26; see

above). Shifts of activity from posterior to anterior and back to posterior were more consistently observed in this case (4/15) and a typical example is given in Figure 7-8 (last column).

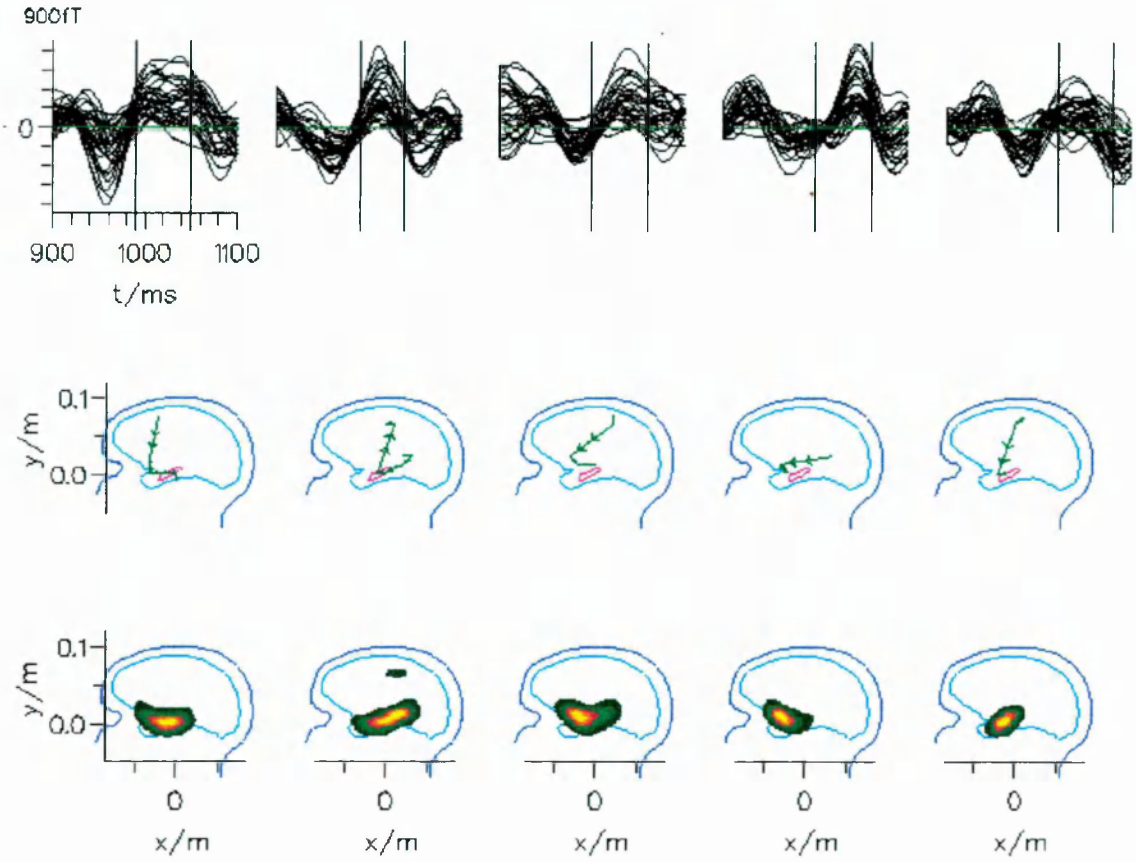

Figure 7-6: Sequences of events of the various interictal spikes at the depth of the left temporal lobe of Pat2. Top: superimposed signals of five individual interictal spikes; a pair of vertical bars mark the 60 ms period used in the next two rows for each spike. Middle: Shifts of the instantaneous activity (arrows) during the 60 ms periods. Bottom: MFT solutions integrated over the 60 ms period. Sagittal plane as in Figure 7-3 (see text).

As already mentioned in the beginning of this section, the shapes of the intensity integrated over some 60-70 ms within the course of the various spikes does not reveal the same "arc" as prominently as in the Pat2 case. However, the connectivity plots (second row of Figure 7-8) do show involvement of structures anterior to the hippocampus. Furthermore, some of the intensity integrals show activity extended further anterior to the hippocampus, making the suggestion for a spread from amygdala to hippocampus (and vice versa) valid here too. The latter effect can be seen in the first, third, and fourth displays of the last row in Figure 7-8.

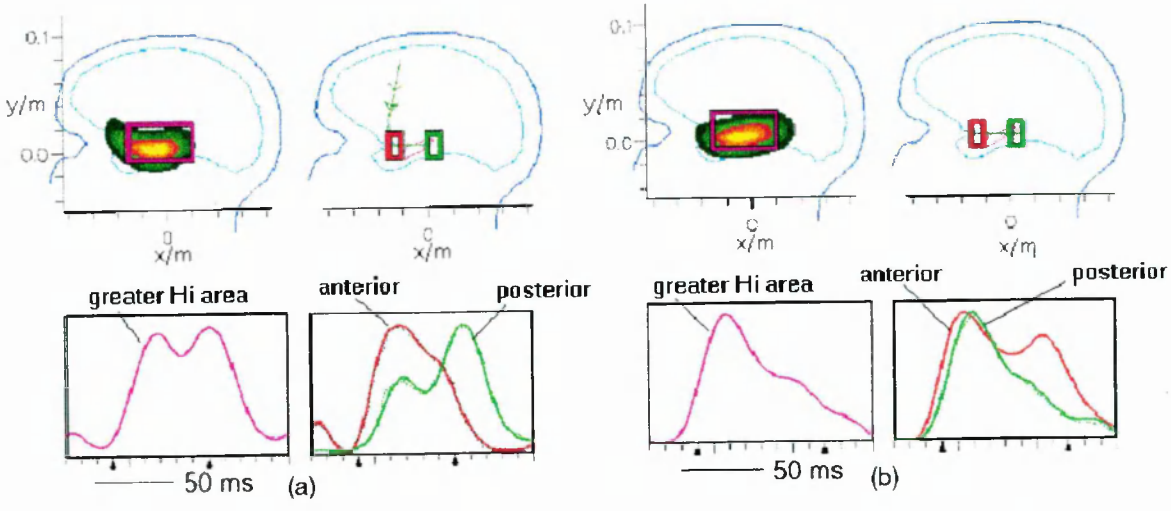

Figure 7-7: Pat2. (a) Integrated intensity over 60 ms in a sagittal level through hippocampus (left). Instantaneous shifts of maximum activity computed every 2.5 ms (right). Propagation from anterior to posterior hippocampus is observed. Note the shape of the integrated intensity and the activation curves for the two indicated ROIs (bottom right). Activation of the greater hippocampal area is given in bottom left. (b) Similar but with anterior-posterior-anterior sequential shifts.

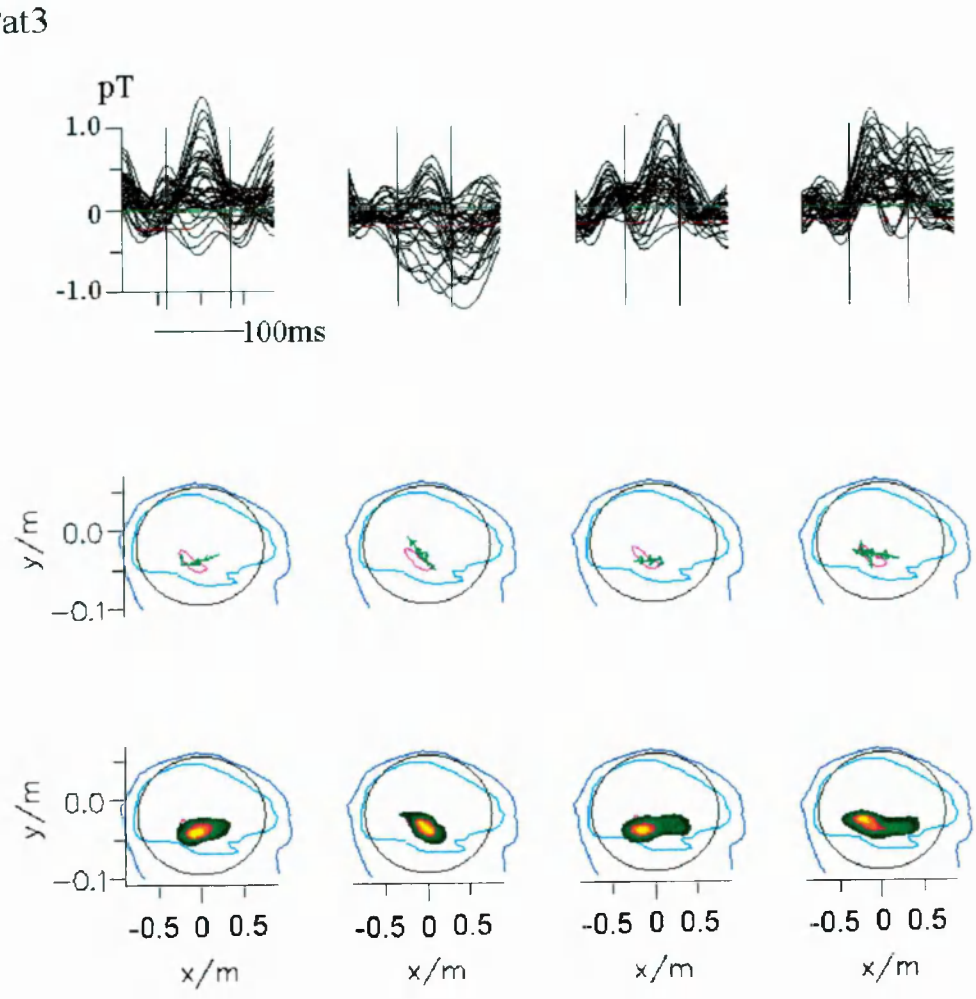

Figure 7-8: Sequences of events during the course of various interictal spikes at the depth of the right temporal lobe of Pat3. Top: superimposed signals of four individual interictal spikes; as in Figure 7-6, a pair of vertical bars mark the period used in the next two rows for each spike (some 56-74 ms in each case). Middle: Shifts of the instantaneous activity (arrows) during the indicated periods. The first two displays show anterior→posterior propagations; third display corresponds to a posterior→anterior propagation; finally, the fourth display demonstrates posterior→anterior→posterior sequential shifts. Bottom: MFT solutions integrated over the above periods. A fixed sagittal MRI slice at the level of the hippocampus is used throughout. Circles illustrate a projection of the appropriate source space level.

7.3.3 Separate tests for bilateral activity

In the case of Pat2, we found activity in the very bottom of the source space, which could have been generated from the contralateral hemisphere. It is well known that anatomically homologous sites (mirror foci) are often simultaneously active in epileptic discharges. Thus, the question arose whether the hippocampus of the right hemisphere was responsible for the deep activity observed. Computer simulations with dipole sources appearing in the right hippocampal region were compared to actual data of the very deep activity. The results are summarised in Figure 7-9a. The two solutions show a striking similarity.

Further tests were performed using a "deep and small" cylindrical source space, designed to cover the hippocampi and thalami of the two hemispheres. The inversion parameters were adjusted* to recover activity within this volume, as explained in Chapter 5. The same uniform conducting sphere model was used as before (i.e. the one fitted to the left side only; this is, of course, a(n) (unavoidable) problem).

Figure 7-9b summarises the results of the computer simulations. It appears that satisfactory MFT estimates are found when dipoles are placed within the volume of either hippocampus. We, therefore, used the cylindrical source space for the periods where strong deep activity was evident in the MFT estimates of our original hemispherical source space.

In Figure 7-9c the two models are combined to recover activity from the two hippocampi. At the bottom of Figure 7-9c we show the activations of the two hippocampi as extracted from the template signal displayed in Figure 7-3. Note the temporal development of activity in the two hippocampi - a point we shall return into shortly.

Of course modelling such deep activity always embraces the danger for interference of noise artefacts, therefore, calls for a careful interpretation of these results. However, the fact that such activity was consistently observed in all epochs studied, and amplified when the stable integrals of intensity were considered, rules out the possibility of noise artefacts as primary signal sources. Moreover, we examined whether a distant source of "constant" noise, like the magnetic fields produced by the heart, could be responsible for such contributions. Figure 7-10 shows time-depthplots for the small cylindrical source space during an epoch of a total 2.5 sec in association with the ECG signal. In the

---

* *The smoothing parameter was again 1.0; the decay factors of the Gaussian probability weight were* $\lambda_{1,2} = 0.025m$, $\lambda_3 = 0.038m$.

depthplot, a depth of 0.0 cm corresponds to the level of the left hippocampus (ipsilateral to the measurement side). Accordingly a depth of 5-6 cm corresponds to the level of the right hippocampus (contralateral to the measurements side). As the figure illustrates (especially the bottom half), the observation of firing in the right hippocampal area is not related to the heart cycle.

As mentioned before, the combination of solutions from the two source space models allowed an additional study of the spatio-temporal evolution of activity, namely, the interactions between left superficial cortex, left hippocampus, and right hippocampal area. We pursued this by means of the familiar activation curves making use of the following ROIs: for the left hippocampal and left temporal cortex those used before (i.e. Figure 7-3), while for the right hippocampus the whole bottom level of the cylindrical source space. It would be especially interesting to see whether there would be a constant time relation between the left and right hippocampal firings. Results for three typical interictal events are presented in Figure 7-11. Although sequences of successive activations are visible, no systematic time relation in the onset and offset of activity of the two hippocampi was identified.

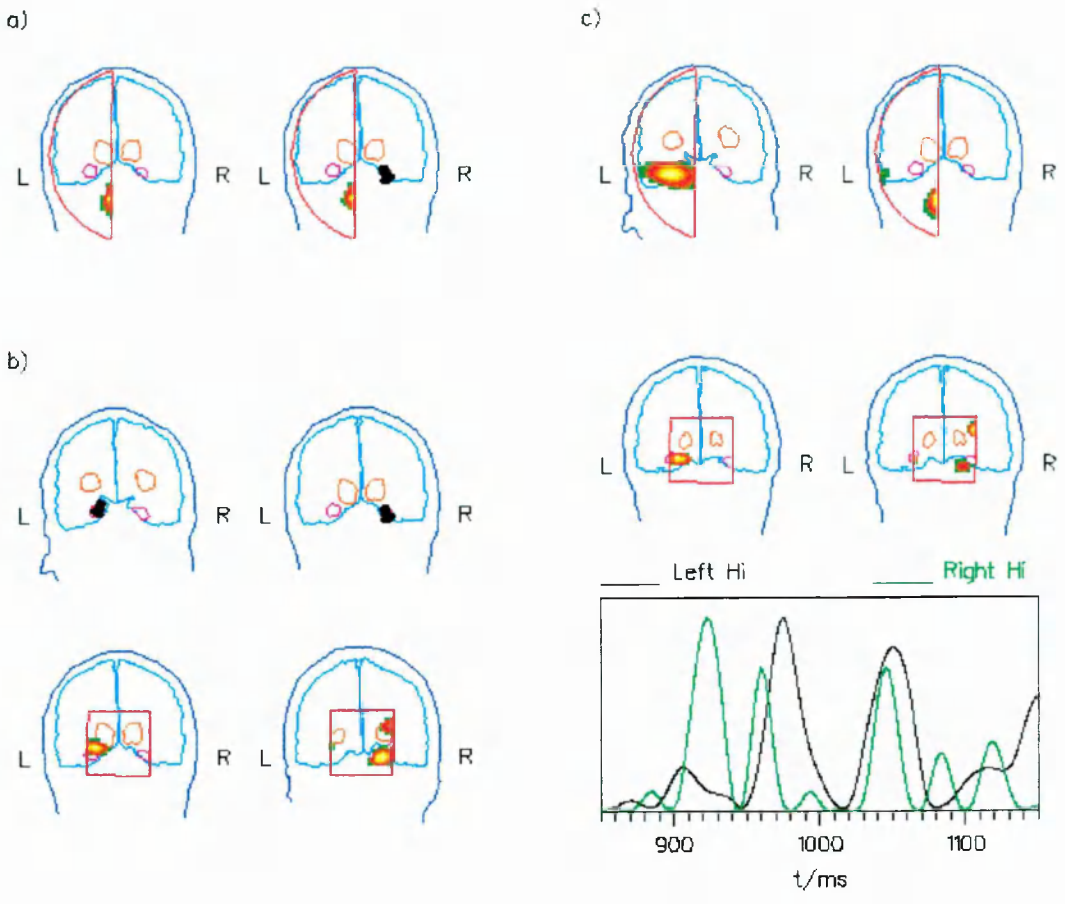

Figure 7-9: Examples of localised deep sources for Pat2. Coronal sections. **a)** Instantaneous MFT estimates (left) of recorded focal deep activity and computer generated data with a single dipole placed in the right hippocampus (right). Hemispherical source space is used. **b)** MFT estimates for source space shifted medially (see text; also tests in Chapter 5). *Top part*: locales of test dipoles (one in each hippocampus). *Bottom part*: MFT estimates from these two sets of simulated signals. **c)** Real data for the original hemispherical source space (top), and for the deep cylindrical source space (middle) for two specific instances: on the left, with activity localised at the left hippocampal region, and on the right with focal deeper activity identified. *Bottom*: temporal evolution of activity in the left (black) and right (green) hippocampal regions. The hemispherical source space model was used to obtain the activation within the left hippocampal ROI (see, for instance, Figure 7-3), while the cylindrical model for the right hippocampal activations (ROI covering the whole bottom level of the cylinder).

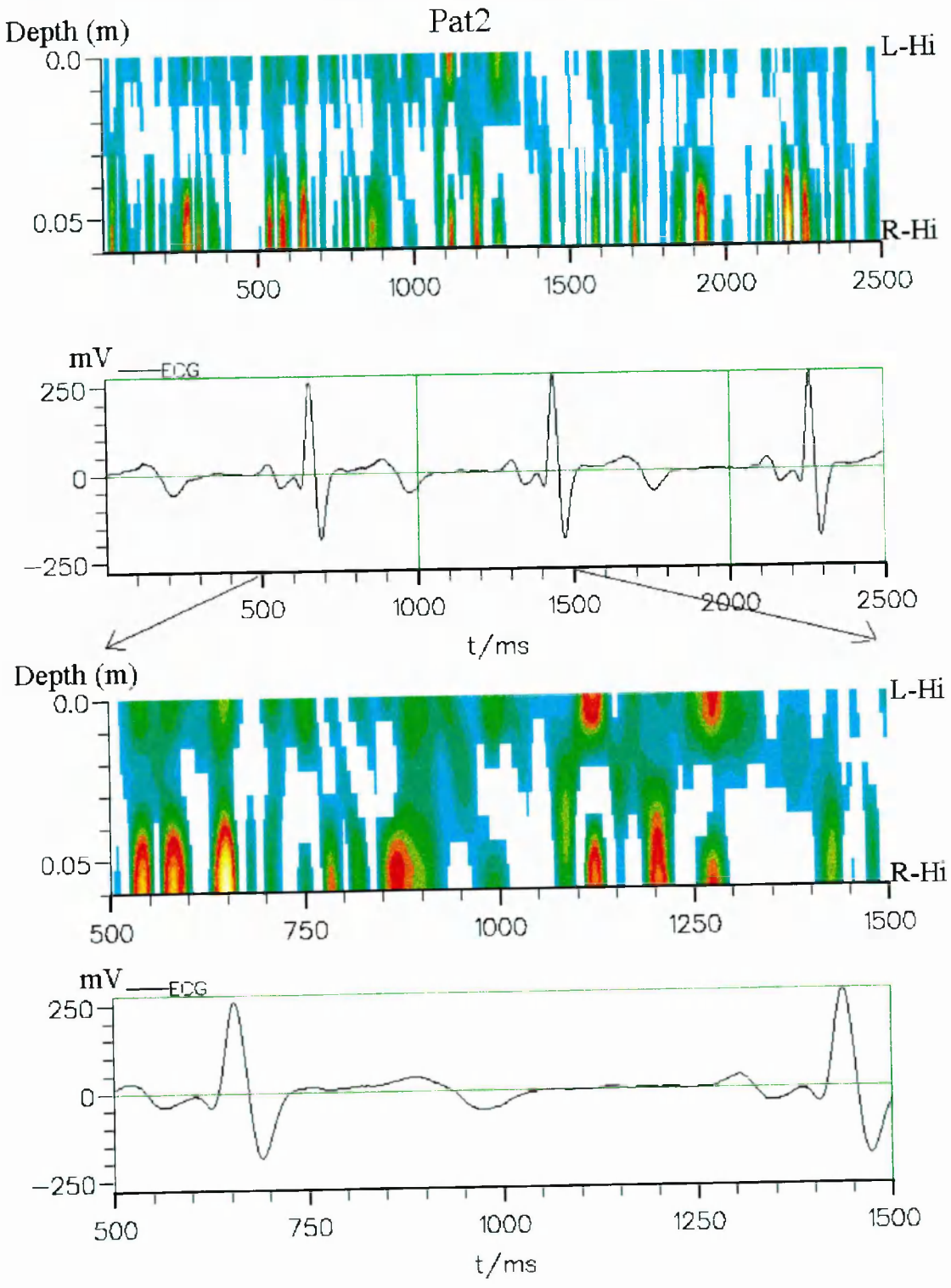

Figure 7-10: Top half: Time-depthplots for the small cylindrical source space (top) along with the ECG signal (bottom) for Pat2. Zero depth corresponds to L-Hi, while 5-6 cm depth corresponds to R-Hi. Bottom half: an expanded time segment of the above period. The firing of the R-Hi area is clearly independent of the heart cycle.

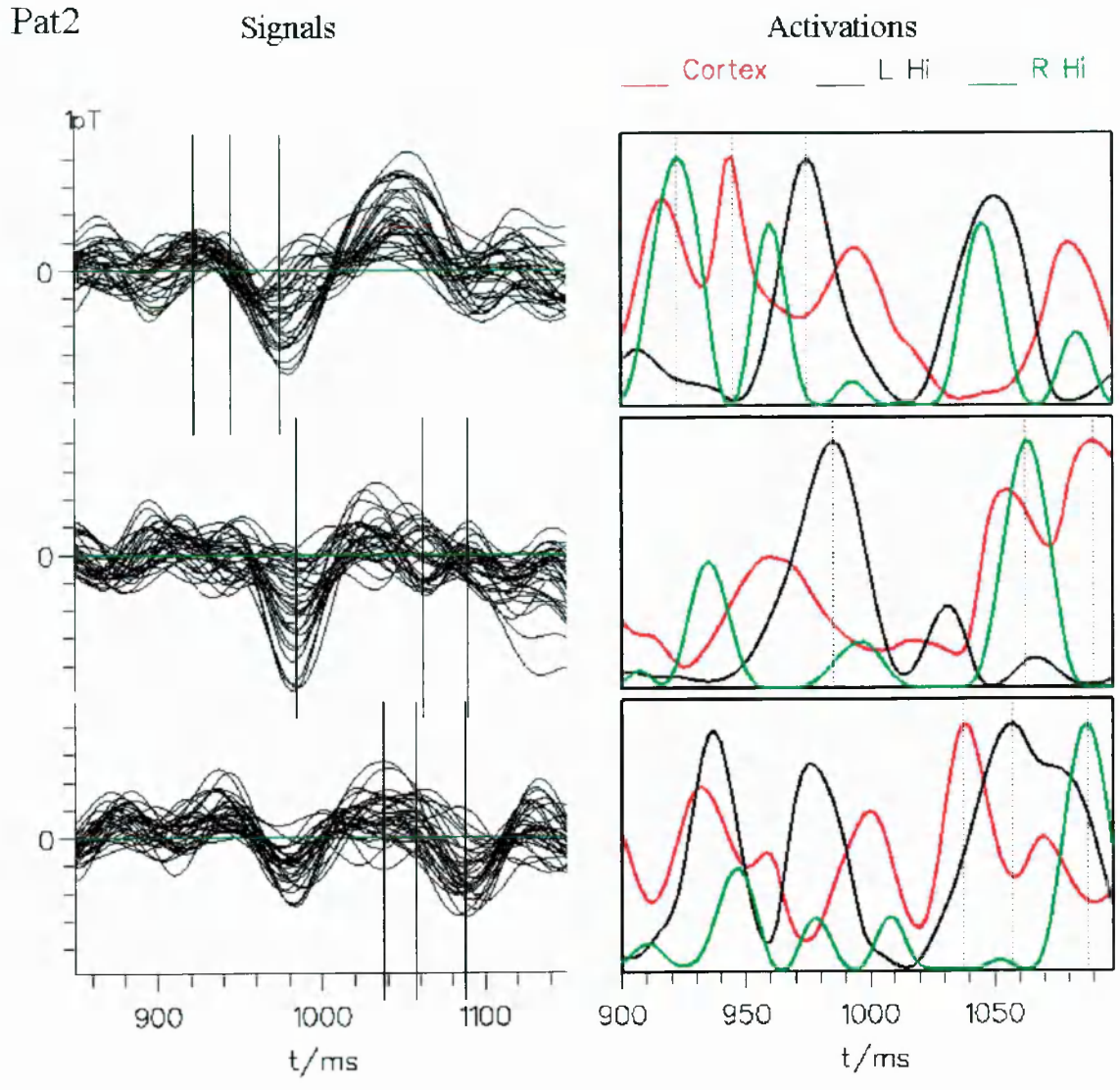

Figure 7-11: Pat2: Left: superimposed signals for three interictal events. Right: activations in the left cortex (red) and the two hippocampi (black and green) for the same three interictal events, after combining the two source space models. Activations of the right Hi were derived from the bottom level of the "deep" cylinder, while those for left cortex and left Hi within the same ROIs shown in previous figures. Note light vertical bars indicating the maxima of each activation curve. Despite sequences of successive activations, no systematic time relation in the activation onset and offset of the two hippocampi could be observed.

7.4 Discussion

The commonly used ECD model can provide fits with exceptional accuracy, provided the activity is isolated and highly focal. Co-activations within several regions and noisy signals usually shift the ECD solution away from the true centre of activity (cf section 6.4.2, and also Ioannides et al 1993c). In contrast, MFT allows for noisy data through the use of a regularisation parameter (Ioannides 1994). Tolerance to noise is gained at the expense of spatial resolution (at least in the depth), but, the actual shape of the activated area is reflected in the MFT solutions (Ioannides 1995a,b). Therefore, MFT makes possible the analysis of single trial, non-averaged data, avoiding the shortfalls produced by signal averaging. The analyses presented in the current as well as the previous chapter provide substantial evidence that MFT can be applied to unaveraged epileptic MEG signals and produce "sensible views" of both superficial and deep brain activity.

There has recently been an increasing interest in the study of unaveraged epileptic data (e.g. Lewine et al 1995), but using the ECD model and explaining, at each case, only small segments of the unaveraged record, usually around the peaks of spikes or sharp waves, thereby leaving parts of the event unexplained. We have used a more general method (MFT) to obtain estimates of activity throughout the whole time period of the various events, that is, from the rising phase of a spike to its peak, and beyond. In doing so, we have observed the interactions between neocortical areas and deep temporal structures during a number of unaveraged interictal spikes in 2 epileptic patients: superficial activity was seen to precede and follow deep activity. The time differences of the activations from cortical to deep or deep to cortical areas varied in the range between 10-60 ms. Back-averaging of the individual solutions was performed to enhance any orderly series of activations. The mean time delay from the cortical to hippocampal activation as given by the back-averaged record was some 30 ms for Pat2 and some 20 ms for Pat3. Two rather extended cortical areas in each patient emerged after back-averaging. Interplays of activity were consistently found between these two cortical sites, and between the most anterior cortical area and the hippocampal complex. We reiterate here, that the image revealed from the back-averaged solution (cf. schematics in Figure 7-5) may not necessarily represent the actual sequence of activations in each individual event, but it does indicate a frequently occurring and, therefore, non-random pattern in each patient.

Sutherling and Barth (1989) used scalp electrodes together with sphenoidal wires in combined EEG-MEG recordings to trigger the averaging of the MEG spikes in an effort to distinguish between deep and superficial epileptic activity. In the margins of their

findings they also reported that the cortical areas activated could be rather extended, since a single (least-squares) dipole model was resulting in deeper localisations when compared with subdural electrode spike occurrences; they confirmed this claim on the basis of "double-dipole" modelling - two dipoles end-to-end simulating an extended source - and use of the peak separation localisation method (see Chapter 2). In the temporal lobe they additionally measured a time delay of 30-35 ms between superficial and deep activation. These findings are in accordance with the findings presented here, but different from some earlier reported results by use of intracranial electrodes (Buser et al 1973; Buser and Bancaud 1983), where no significant propagations between neocortex and hippocampus were found. Given the relatively large distances and the fairly extended cortical regions involved, however, one can argue that the latter recordings simply missed the cortical activation because of insufficient spatial sampling.

Discharges in both neocortical and limbic structures have been shown for quite some time in temporal lobe epilepsies by means of electrocorticography and depth electrode recordings (Penfield and Jasper 1954). Spatio-temporal distributions of intracellular potentials (Chervin et al 1988) as well as cortical travelling waves (Petsche and Sterc 1967) have been observed in animal experiments. Cortical travelling was also identified in epileptic potential field analysis of human EEG records (Lemieux and Blume 1986). Such findings indicated that epileptic cortical fields might not be stationary. More recently "transitional stages" were noticed in the majority of examined patients suggesting the existence of an "evolutionary interictal process" (Nakasato et al 1994). It is, therefore, reasonable and typical for an interictal spike to travel, for instance, between the baso-mesial temporal cortex, anterior temporal lip, and anterior-posterior lateral temporal cortex within some 40 ms (Ebersole 1995). In addition, intracranial chronic depth records have also shown that neocortical activity may frequently spread to the mesiobasal limbic "stations", which can then act as a pacemaker zone with further distribution and maintenance of the ictal event according to observations by Wieser and Müller (1987).

One early MEG study discussing such issues was reported by Stefan et al (1991). Using the ECD model they found propagation of epileptic activity from lateral neocortical to mesio-basal limbic structures in 3 epileptic patients. More recently, Baumgartner et al (1995) suggested propagation of interictal MEG epileptic activity from the mesiobasal to the lateral temporal lobe in a study involving 4 epileptic patients. In the latter, it was found that activation of the mesial source was leading the lateral one by some 40 ms (the two "point" sources were separated in space by some 45 mm).

Moreover, investigations carried out in rats have revealed that spikes may not only arise from different areas within the epileptogenic zone ("focus"), but the pacemaker activity

for the interictal spikes may actually reside outside the focus itself within the so-called "inhibitory surround" (Witte et al 1992). Thus, topographically different areas may be involved in the generation of interictal discharge patterns. Witte and co-authors (1992) have also concluded from the above investigations, that localisation of activity for onset and maximum (peak) of epileptic spikes may yield completely different results. The same authors also emphasised that analysis of individual spikes is preferable since spikes of similar shapes may arise from different cortical areas and also use different propagation pathways and directions within the epileptogenic region.

Our results for the neocortical to mesiobasal propagation fit nicely with the points raised in the above discussion. One could attempt a step further by conversing on the possible architectonic mechanisms of such interactions on the basis of cortico-cortical association fibres, conduction velocities and so forth (Alarcon et al 1994; Burkitt et al 1996), as well as introducing a model on epileptogenesis. We are aware, though, that such efforts would mandate the availability of similar studies on a larger group of patients. For the purposes of the present study we place our findings within the context of other neurophysiological results on epilepsy.

We finally have to stress that the persistent shift in the maximum of the MFT estimates over time in an interictal sharp wave or spike occurs consistently in different epochs. However, the evolution of activity in different areas of the brain such as superficial cortical structures and deep situated amygdala-hippocampus areas may not necessarily indicate an established anatomical pathway - intermediate steps may be missing. This might in part be due to the set-up of sensors (i.e. recordings only from one side at a time), which together with the usually low signal-to-noise ratio, calls for a cautious interpretation of these data.

For both patients studied herein, the MFT estimates at the peaks of the signals indicate activation at the depth of the left (Pat2) or right (Pat3) temporal lobe. The shapes of the solutions are consistent with activation of the hippocampal area. With the activity integrated over relatively long time periods, such as 60 ms (e.g. Figure 7-6), a pattern of activation appears, indicating propagation from the anterior parts of the temporal lobe towards the posterior ones. This might mirror a spread of activity from amygdala to hippocampus, as observed in most of the events studied for each patient (12/26 for Pat2, 7/15 for Pat3). Sequential anterior-posterior-anterior shifts or vice versa were also identified in both patients (8/26 for Pat2, 4/15 for Pat3). Finally, propagations from posterior to anterior were occurring less frequently in both cases (4/26 for Pat2, 4/15 for Pat3). Such propagation characteristics have also been reported by others.

For instance, Sutherling et al. (1991) also indicated propagation of spikes in an anterior to posterior direction in a combined MEG (multiple single-channel placements), EEG, and ECoG study, in agreement with depth stereoelectroencephalography (SEEG) findings (Buser et al 1973; Buser and Bancaud 1983). More recently, Emerson et al (1995) noted after studying with EEG the spike propagation (i.e. time-dependent changes in spike topography) characteristics, that the pattern of anterior to posterior propagation was observed in 15/16 of their patients, while the reverse was less common, being present in only 6 out of the 16 patients; only one of their patients showed posterior to anterior propagations exclusively. Moreover, recent intracranial recordings and cross-correlation studies also confirmed that both the above patterns were detectable, but the anterior to posterior pattern was identified more often (Lopes da Silva 1996). It is worth noting a result from Buser and Bancaud (1983) stating that hippocampal responses to amygdala stimulation were displayed in all epileptic patients studied, but amygdala responses to hippocampal single shocks was a characteristic of temporal epileptics only.

A final noteworthy point on this topic is a very recently reported multidipole modelling of partial complex interictal spikes by Ebersole (1996). He claimed that by including two fixed position and orientation dipoles in a MEG modelling algorithm (BESA), he was able to explain the time-course of the amplitude of the recorded spikes: one of the dipoles was placed in the hippocampus having an anterior to posterior orientation, while the other one, with almost vertical orientation, was anterior and more medial to the first one (i.e. in the vicinity of amygdala). The activation of the latter source was leading that of the prior by some 6-9 ms.

The modelling of the very deep activity identified in the case of Pat2 using a deep source space proved to be helpful in separating activity from the two hippocampal structures. As discussed in Chapter 5, we do not advocate the use of a "deep source space" together with data from unilateral measurements. Realistic head modelling and use of bilateral recordings are certainly the way forward. With the new MEG hardware already available, where measurements are made simultaneously from both hemispheres, much more reliable data will appear for the studies of deep generators of epileptic activity. We have, nevertheless, proceeded with the deep source space analysis, since only unilateral data were available. The similarity of the model data to the actual solutions is encouraging. Furthermore, the fact that the activity was consistently observed in all epochs studied, and amplified when the stable integrals of intensity were considered, together with its apparent independence from heart-cycle activity, limits considerably the range of possible noise sources. In addition, the lack of a systematic time relation in the onset and offset of activity of the two hippocampal areas is concurring with findings in

depth electrode studies (Wilson et al 1990; Buser et al 1973), while the observed time delays from one hippocampus to the other (typical examples are shown in Figure 7-9 and Figure 7-11) are again within reasonable physiological limits.

Simultaneous bilateral - or whole head cover - recordings are, of course, available today. With bilateral data, one would, first, be able to study the neocortical and mesiobasal connections under a much more reliable view and investigate a more global model of inter-hemispheric interactions. Secondly, deep activity would be modelled more reliably, as mentioned above. Finally, the possibility of a secondary or mirror focus, like the one apparently seen for Pat2, would be pursued with more detail and accuracy. Such MEG studies, discussing the importance of the possibility to distinguish a secondary from a primary epileptogenic region have promptly appeared together with the availability of whole head cover systems (Hari et al 1993; Galen et al 1993). Hari et al (1993) used two (symmetric) dipole modelling in a single case study, and by plotting the amplitude profiles of the two dipolar sources, they succeeded in revealing the primary epileptogenic region: the right parietal dipole was much stronger a source, and was leading (latencywise) the left by some 17-20 ms.

The disadvantage of MFT - as applied at present - in such a case would have been the lack of absolute scale in the magnitude of the current density. That is, since arbitrary units are used for $|J^p|$, which depend on the inversion parameters (i.e. choice of probability decay factor and smoothing), and given that different parameters would have been chosen for either side (see following chapter), it would have been senseless to compare the intensity strengths of the two sources[+]. However, provided that the whole time course of the signal would have been accessible for MFT analysis, the time-activation curves of the two regions would have shown very clearly and robustly the temporal predominance of one region over the other, thereby, distinguishing the primary from the secondary epileptogenic region.

[+] *These defficiencies assume double Dewar modelling and not full head coverage.*

8. Bihemispheric MFT Studies

8.1 Introduction

The previous two chapters dealt with unaveraged interictal epileptic activity as recorded in unilateral MEG experiments which can at best only cover part of one hemisphere. Such measurements though, can only provide part of the picture for the on-going activity, since the hemisphere contralateral to the recording side is also activated throughout the time course of the recording sessions. Measurements conducted by use of modern systems (e.g. helmet-like and/or twin Dewar systems; see Chapter 1 and Appendix A) would hence inherently possess a much richer content of information. In addition, they would allow a much more reliable analysis of deep activity, as discussed in Chapter 5, the need for which was shown by analysis of real data in Chapter 7.

Thus, in the current chapter, we apply MFT analysis to simultaneous MEG recordings. Since no such measurements from patients suffering from partial complex epilepsy (CPE) were available to us, we switch to a clinically different example, namely myoclonic epilepsy. The sensors for the myoclonic case were not placed on symmetrical positions on either side: one of the Dewars is in a much more superior position than the sensor position (in one hemisphere) of our earlier CPE case. For this reason we have also included a short MFT study from the classic "auditory odd-ball" experiment[+] with frontolateral dual MAGNES probe placement.

[+] *This is the only part of the present thesis that involves actual data collection by the author.*

8.2 A case of Myoclonic Epilepsy

8.2.1 Motivation

In contrast to the cases of complex partial seizures, certain types of seizures, such as focal motor and psychomotor, are highly indicative of special cerebral areas, and hence are ideal for localisation studies. Similarly, interictal events associated with the appearance of certain symptoms would also be indicative of certain brain regions/zones. For instance, the twiching of fingers should involve the somatomotor cortex in some respect, since the latter is supposed to be involved in the execution of finger movement. Thus, analysis of pathological activity which is time-locked to a "motor-like" event (symptom) is of great interest.

The first part of this chapter deals with spontaneous myoclonic recorded simultaneously from two head aspects. Our initial goal was to use both averaged and single event datasets in our MFT analysis. Unaveraged datasets were not available to us though, and consequently our results and discussion will be drawn from the analysis of averaged data only.

8.2.2 General Terminology

Myoclonus is a very complex phenomenon; "it is characterised by a rapid involuntary muscle contraction, subtle or massive, usually with locomotor effects generalised or limited to certain muscular segments, mostly predominant in flexor muscles and more pronounced in upper extremities" (Niedermeyer, 1993c). Its symptoms, the resulting jerks, may be synchronous or moderately asynchronous. A considerable number of disorders with myoclonus are not classified as epileptic. Epileptic myoclonus is classically characterised by concomitant polyspikes or polyspike wave discharges in the EEG, of bilateral or generalised synchronous character, usually maximised over frontal regions (Niedermeyer 1993b).

It should emphasised that the term "myoclonic" refers to a single distinct jerk whereas "clonic" - a different type of seizure symptoms - refers to the repetitive type of muscular twiching. Progress in myoclonus research was sparked by the introduction of electromyographic (EMG) - myoclonus - triggered back-averaging of the EEG records, first suggested back in the seventies (Shibasaki and Kuroiwa 1975; Chadwick et al 1977). Jerk-locked averaging enabled the EEG observation of "positive-negative, biphasic, sharp potentials, either followed or not followed by a negative slow wave" having a close latency association with the myoclonic EMG discharges in large groups of patients (Shibasaki et al 1978).

The case studied in this chapter deals with a specific type of myoclonic epilepsy, the so-called "Epilepsia Partialis Continua" or "Koshevnikov Syndrome", named after the famous Russian doctor who investigated certain types of "Siberian" epilepsies some 100 years ago (Koshevnikov 1895).

8.2.3 The case

The patient (BN) was a girl at the age of 11 at the time of the MEG recordings. She was suffering from the syndrome of Koshevnikov, that is, she was experiencing focal motor seizures of the right body half with secondary generalisation for six months. Seizure frequency was up to 12 per hour regardless of high doses of various anticonvulsive drugs. A right side hemiparesis together continuous myoclonic twiching of the right fingers were revealed by neurological examinations. An MRI investigation had previously shown a diffuse oedema of the left sensorimotor and parietal cortex, but at the time of the MEG recording MRIs have been classified as normal[+]. Cerebrospinal fluid examination showed evidence of a chronic inflammation, but the aetiology of tissue changes remained unclear despite a brain biopsy. The possibility of a Rasmussen encephalitis was also hinted.

[^{18}F] fluoro-2-deoxy-D-glucose (FDG) PET scans were also performed (SCANDITRONIX PC 4096/7 WB, Düsseldorf, Germany); their analysis revealed increased FDG uptakes in the left inferior posterior parietal cortex, left dorsal thalamus, and right cerebellum. In addition, a focal hypermetabolism was shown in the precentral gyrus, surrounded by a decreased FDG uptake in the postcentral gyrus and frontal cortex.

8.2.4 Measurements and Analysis

The 2x37 channel, dual probe MEG system (BTi Twin MAGNES®, Jülich, Germany; see Appendix I) was used to record spontaneous interictal myoclonic activity. One MEG probe (probe B) was placed over the left temporo-parietal aspect of the patient's head, while the other (probe B) over the top-fronto-central, slightly to the right aspect (see Figure 8-1). EMG records of the m-flexor digitorum superficialis were also registered, and after being rectified, they were used as triggers for the backaveraging of 204 myoclonic events (Volkmann et al 1995, 1996).

Single dipole (ECD) analysis was performed by Volkmann et al (1995) for each of the 27 interactively identified interictal spikes, as well as the EMG triggered averaged signal.

[+] *For the analysis presented here though, only the earlier, "slightly" pathological MRIs were available, and are, therefore, the ones to be used.*

Dipole sources with a goodness of fit greater than 0.95 were clustered within a 60 cm^3 area within the left inferior parietal lobule (IPL). It was noted that, myoclonic activity was initiated by a dipolar source within IPL some 40 ms before the EMG onset, while around 80 ms after the EMG onset of activity, a "dipolar generator was observed in the left somatosensory cortex" (Volkmann et al 1995).

The MEG recordings were registered to the patient's MRIs using a combination of point and surface matching techniques (Bamidis and Ioannides 1996, Chapter 3* of this thesis): a registration using three fiducial points (nasion, left-right preauriculars) was first attempted; accuracy was subsequently improved using the surface matching methodology. This level of accuracy enabled a more confident description of the central sulcus in the MEG co-ordinate system and its subsequent fusion with the MFT solutions (see below).

Two separate, partial hemispherical source spaces, each associated with a specific probe, were used for the MFT analysis. Their orientations with respect to the MEG-defined head surface and the sensor positions, together with a plot of 4 of their levels are given in Figure 8-1 in three different perspective views. As seen in the drawings, the orientation of the Probe B-source space follows a medial-to-superficial direction (along the y-axis of the head defined MEG system), while that of Probe A follows the orientation of the third axis of the most central sensor (sensor 1). The distance from the most superficial to the deepest level measured some 59 mm in the latter and some 61 mm in the former source space.

The sphere model was used to model the conductivity profiles for each probe aspect. Each conducting sphere was fitted to the local (to the sensors) curvature of the inner skull surface (see pink circles and dots in Figure 8-1). Gaussian *a priori* probability weights were used, centred at the midpoints of the each conducting sphere; the decay factors were $\lambda_{1,2} = 0.048m$, $\lambda_3 = 0.047m$ in each case - adjusted to correctly recover point sources generated by the computer (see Chapter 5). In both cases, the smoothing parameter used was equal to 1.0.

Tracing of the central sulcus (CS) was attempted in sagittal slices - the only sections available to us - with an interslice distance of 1.17 mm, in an effort to help with the anatomical identification of the somatosensory, motor, and supplementary motor (SMA) areas. In doing so, the two most commonly used methodologies were followed: the midline sagittal method (Sobel et al 1993), and the lateral sagittal method (Ebelling et al

---

* *In fact, Figure 3-13 and Figure 3-14 were drawn from the analysis of the current case.*

1989). Tracing was also guided by means of referring to a "Co-planar Stereotactic Atlas" (Talaraich and Tournoux, 1988). The MRI co-ordinates of left and right hemisphere CS were transformed into the MEG system, thereby, allowing fusion with the MFT solutions.

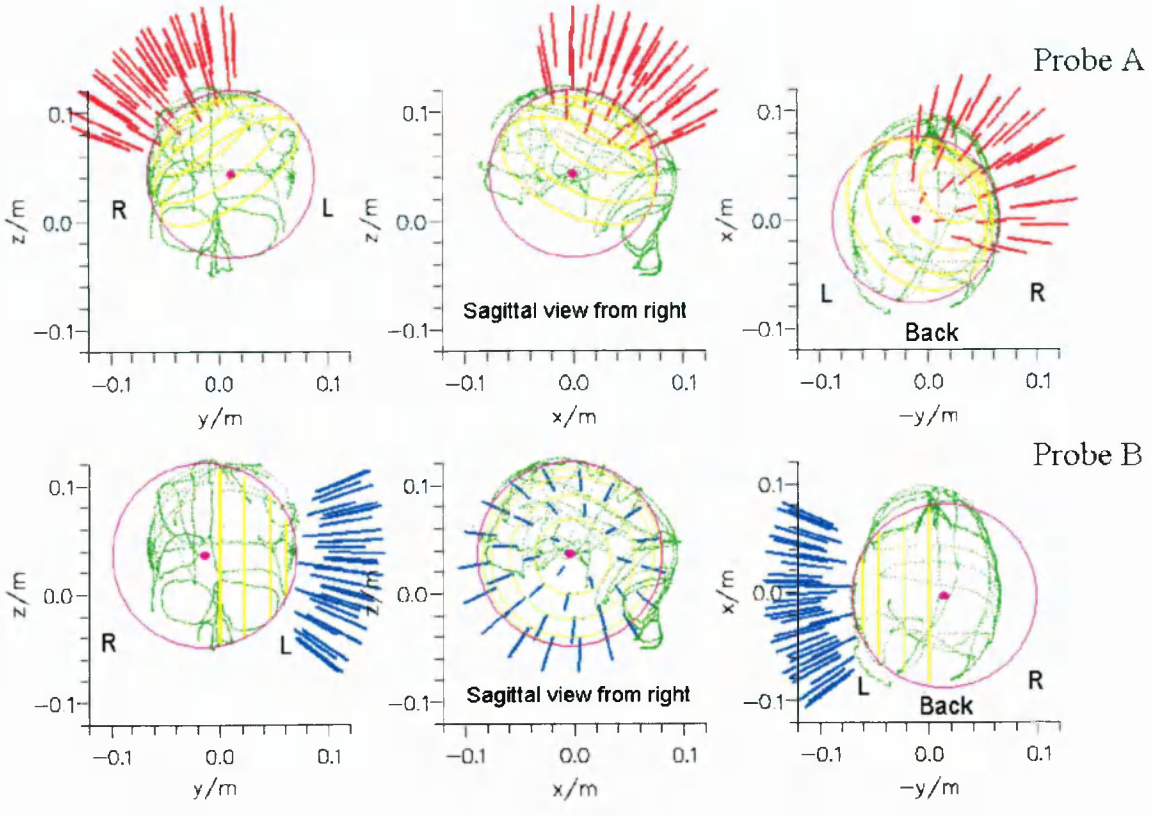

Figure 8-1: Experimental set up and analysis models for the myoclonic patient (BN). Two hemispherical source spaces were used in the MFT analysis, one for each probe. Note the source space orientations with respect to the MEG headshape outline (green) and the sensors (red and blue bars for probes A and B respectively). 4 levels are given for source space in three perspective views. The conducting spheres for each probe aspect are plotted as pink circles; pink dots denote the conducting centres.

8.2.5 Results

As mentioned already, our results will only be drawn from the analysis of averaged signals, which were also band-pass filtered in the range 3-45 Hz. We studied both the instantaneous and the temporal integrals of intensity over 20 and 50 ms. In addition, animated sequences of intensity as projected on specific MRI slices were reviewed on the dedicated transputer system of our lab (Liu et al 1993).

MFT analysis of the EMG-locked averaged data for the left probe (Probe B) revealed an area at the inferior-posterior portion of the left parietal lobe, in general agreement with the ECD analysis as conducted by Volkmann and colleagues. This area, we shall code it as IPL in the following, is responsible for producing the pre-spike signal some 40 ms before EMG onset. Figure 8-2 displays the MEG and (rectified) EMG signals. In addition, typical plots of intensity each projected on the nearest sagittal MRI slice are illustrating the location of the region: on the left part of the middle row, intensity is integrated over some 20 ms and about 40 ms prior to the EMG onset (actually from t=-50 to t=-30 ms), while on the right, an instantaneous display of the "local" maximum activation is shown. The bottom part of the figure, shows the chosen ROI together with a graph of its activation in time. One can note that this area is exhibiting a few "clear" peaks of activation at certain time instances which are always "dying out" smoothly, only to give rise to the next peak, acting like a "periodic" driving force of activation.

Despite the focal nature of the solutions in this region - which explains why the ECD model succeeds in describing well this data segment - activity is not stationary at exactly the same point. As the animated solutions and the connectivity plots revealed, there is a movement of activity towards more anterior and slightly deeper cerebral parts (see later in the results), which is again consistent with the observation that dipoles describing the various interictal spikes were scattered within a 60 cm^3 volume (Volkmann et al 1995).

We will simply describe the results from probe A as they appear in the MFT analysis of the averaged signal. A detailed explanation of the results necessitates commensurate MFT analysis of single trial data, which is both beyond the scope of this thesis and in any case impossible, since we have no access to the raw data. In Figure 8-3 we show 20 ms long integrals of intensity in two different views: in the top, through an oblique (tilted) axial slice coinciding with the 8th level of the source space for probe A, and in the bottom, on sagittal MRI slices nearest to the maximum of the displayed MFT activation. In either case, the location of the central sulcus is also given. As we can see, activity appears on either side of the central sulcus, consistent with activation within the pre- as well as the post-central gyrus, that is both somatosensory and motor cortices. We shall call this region sensorimotor (SM) region[+] . One can also see, that both the ipsilateral (R-

---

[+] *The plot showing activity in the left SM region in Figure 8-3, appears more on the motor area rather than somatosensory. However, one should be cautious in this case: the displayed activity is integrated over some 20 ms. During this interval, the maximum of activity may be found in either the motor or somatosensory cortices as can be seen in from the "connectivity" plot over a longer period in Figure 8-4. Furthermore, coregistration errors due to patient movement during the MEG acquisition impose extra limitations. For all*

SM) and contralateral (L-SM) - to the hand of myoclonic movement - areas become activated. However, activity in the contralateral area is preceding that in the ipsilateral as the activation curves in the middle portion of Figure 8-3 show. In fact, for the first nearly 90 ms after EMG onset activation of L-SM is dominating, and then activity is spread to the other side as well, while obtaining a much wider distribution though - note the co-activation of the two regions post-100 ms.

We also studied the connectivity plots - i.e. the sequential shifts of maximum intensity - throughout the first 100 ms following EMG onset. As Figure 8-4 illustrates, activity appears to be "jumping" across the central sulcus, indicating that both the somatosensory and somatomotor areas are involved. Such a "jump" across the central sulcus was observed in single trial MFT analysis of MEG signals, filtered around 25 Hz, prior to voluntary finger movement in normal subjects (Lado et al 1992; Lado 1993, Ioannides 1993). One could of course ask the question whether there is any time-relation in the activation of these two areas in this specific pathological case or not. Given the fact that we are only dealing with an averaged signal herein, we shall not pursue this issue any further. It is worth noting, however, that such oscillations are consistent with Ioannides's suggestion that the return currents may play an important functional role (Ioannides 1994, 1995a).

Areas anterior to the SM regions are also seen to be active, obtaining their maximal activations much later in the time course. At 160 ms after the EMG onset, very strong activity is seen around in the left frontal region probably coinciding with the anterior part of the left supplementary motor area (L-SMA). This region shows the strongest activation out of all the involved regions (see Figure 8-5). There is also an indication for involvement of a similar region on the ipsilateral side (R-SMA/frontal). However, its activation is maximal much later and with a much lower magnitude, and hence some of the observed activity variations might simply be due to noise. Plots of the two ROIs as well as their activations and projections on sagittal MRI slices are given in Figure 8-5. SMA activation precedes the movement onset when a complex voluntary movement is to be executed. The post movement activations observed here might be a consequence of pathology, or they may be weaker counterparts of pre-movement activations which are

---

these reasons, together with the fact that we are dealing only with an averaged signal, we have named this region sensorimotor (SM) just to be on the safe side, rather than attempting to distinguish between motor and somatosensory areas.

not precisely time-locked to the onset of movement and hence not surviving the averaging of MEG signal.

Figure 8-6 summarises the results described so far by displaying together the activations from all the previously mentioned regions. One can see that the first significant activation occurs in the left IPL region (some 40 ms before EMG onset) and after that, there is a whole sequence of events involving the SM and SMA regions in both the contralateral and ipsilateral hemispheres.

Finally, as mentioned in the beginning of this section, there is a movement of activity from the left IPL area towards more anterior and slightly deeper regions on the same side. This is depicted in Figure 8-7 where we show the integrated intensity between 70 and 90 ms after EMG onset (left) as well as the localisation of the instantaneous maximum of intensity. The location of the maximum (and the activated region in general) correspond to the location of the second somatosensory area (Nolte 1981; Forss et al 1995).

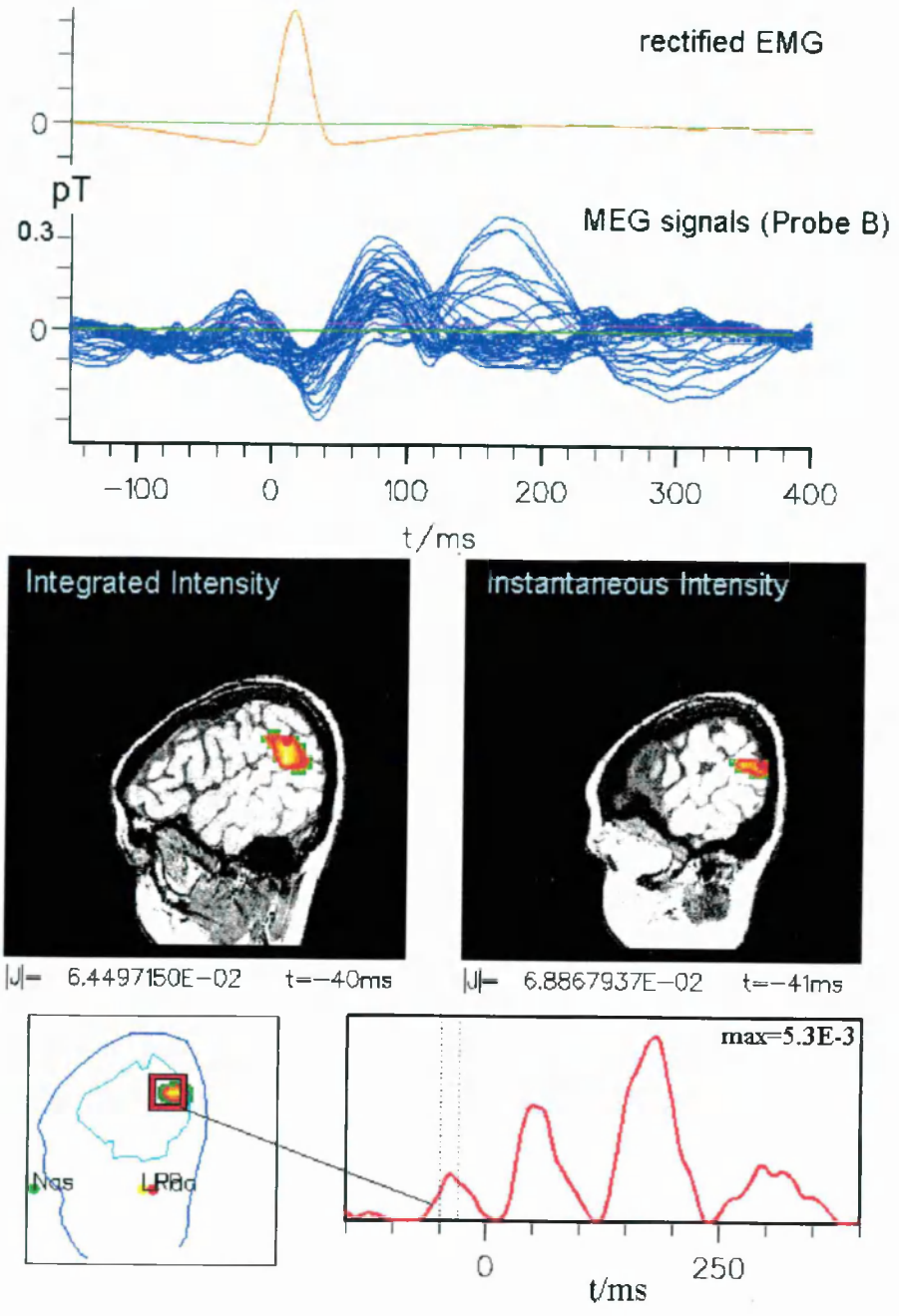

Figure 8-2: Analysis of Probe B signals. Top: rectified EMG (orange) and superimposed signals of all MEG channels (blue). Middle: plots of intensity projected on sagittal MRI slices revealing a region at the posterior-inferior part of the parietal lobe: on the left, intensity is integrated over 20 ms (from t=-50 to t=-30 ms); on the right, an instantaneous solution at the time of the first maximum activation. Bottom: MRI outline showing the chosen ROI (left) and graph of its activation in time (right). Note fiducials, dotted vertical lines denoting the integration period used above, and value of $|\mathbf{J}^p|$ in arbitrary units.

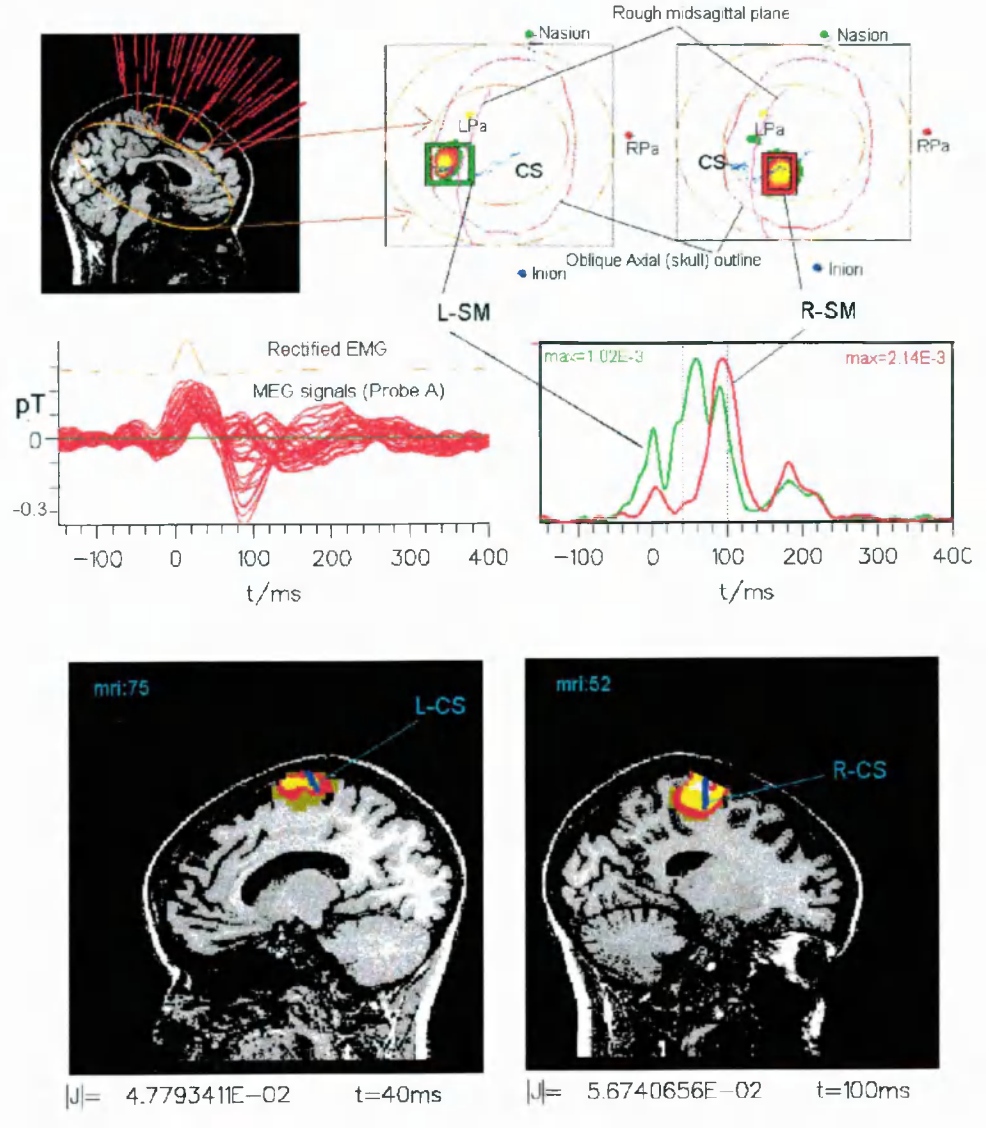

Figure 8-3: Top: *Left*: midsagittal MRI slice with sensor positions (red bars; probe A) and display of two source space levels (1 and 8; orange circles); *Middle and right*: 20 ms long integrals of intensity through an oblique axial slice at the plane of the 8th source space level showing activation of the left (30-50 ms post-EMG onset) and right (90-110 ms post-EMG onset) sensorimotor areas (L-SM and R-SM respectively). Note anatomical landmarks (coloured dots), central sulcus tracings (blue), L,R-SM ROIs, rough outline of the midsagittal slice (pink; see Figure 8-4 for more "orientation" details), and oblique axial skull outline (brown). Middle: *Left*: MEG signals from all channels of probe A (red) and rectified EMG (orange); *Right*: activation graphs for the L- and R-SM ROIs; dotted vertical lines show the periods used above. Bottom: the same 20 ms intensity integrals on sagittal MRI slices. Note location of central sulcus.

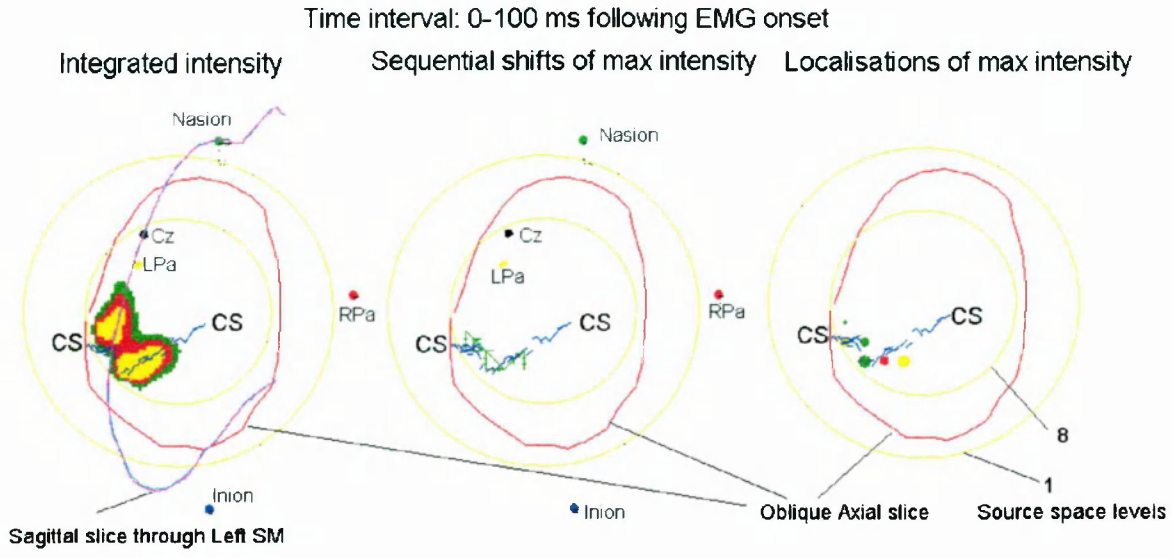

Figure 8-4: Study of the SM activations during the first 100 ms following EMG onset. Left: integrated intensity throughout 100 ms. Note orientation of a sagittal slice through L-SM (mid-sagittal plane is a few mm to the right of this slice, just where the central sulcus (CS) traces from left and right form an angle); see also anatomical landmarks, and source space levels (1 and 8). Middle: connectivity plots for the same period; the sequential shifts of maximum intensity criss-cross the central sulcus. Right: localisations of strong intensity maxima throughout the same period. Note their "distribution" on either side of the central sulcus; anatomical landmarks are not shown to avoid confusion. Dot colours correspond to different durations of activity in each point (yellow longer than red; red longer than green), while dot size different intensity strengths (the bigger the dot the stronger the intensity).

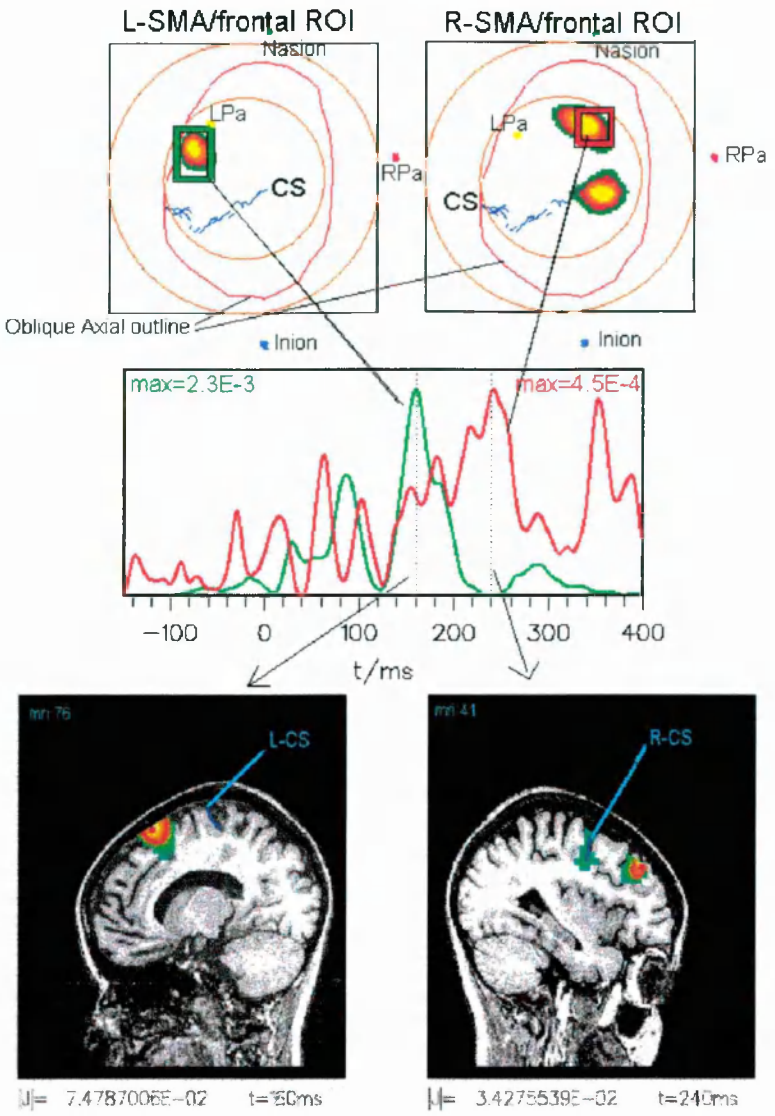

Figure 8-5: Top: 20 ms long integrals of intensity through an oblique axial slice at the plane of the 8th source space level; time intervals are between 150-170 ms (left) and 230-250 ms (right) after EMG onset. The regions revealed are anterior to the SM regions shown before, and are within the anterior parts of the supplementary motor and/or frontal areas (L,R-SMA/frontal). Note CS traces, source space levels, oblique axial skull outline, and anatomical landmarks. Middle: activation curves of the two ROIs. Note that the activation of L-SMA is much stronger than that of R-SMA. Bottom: the previous intensity integrals (shown on top) as projected on properly selected sagittal MRI slices. Note CS marks, and $|\mathbf{J}^P|$ in arbitrary units.

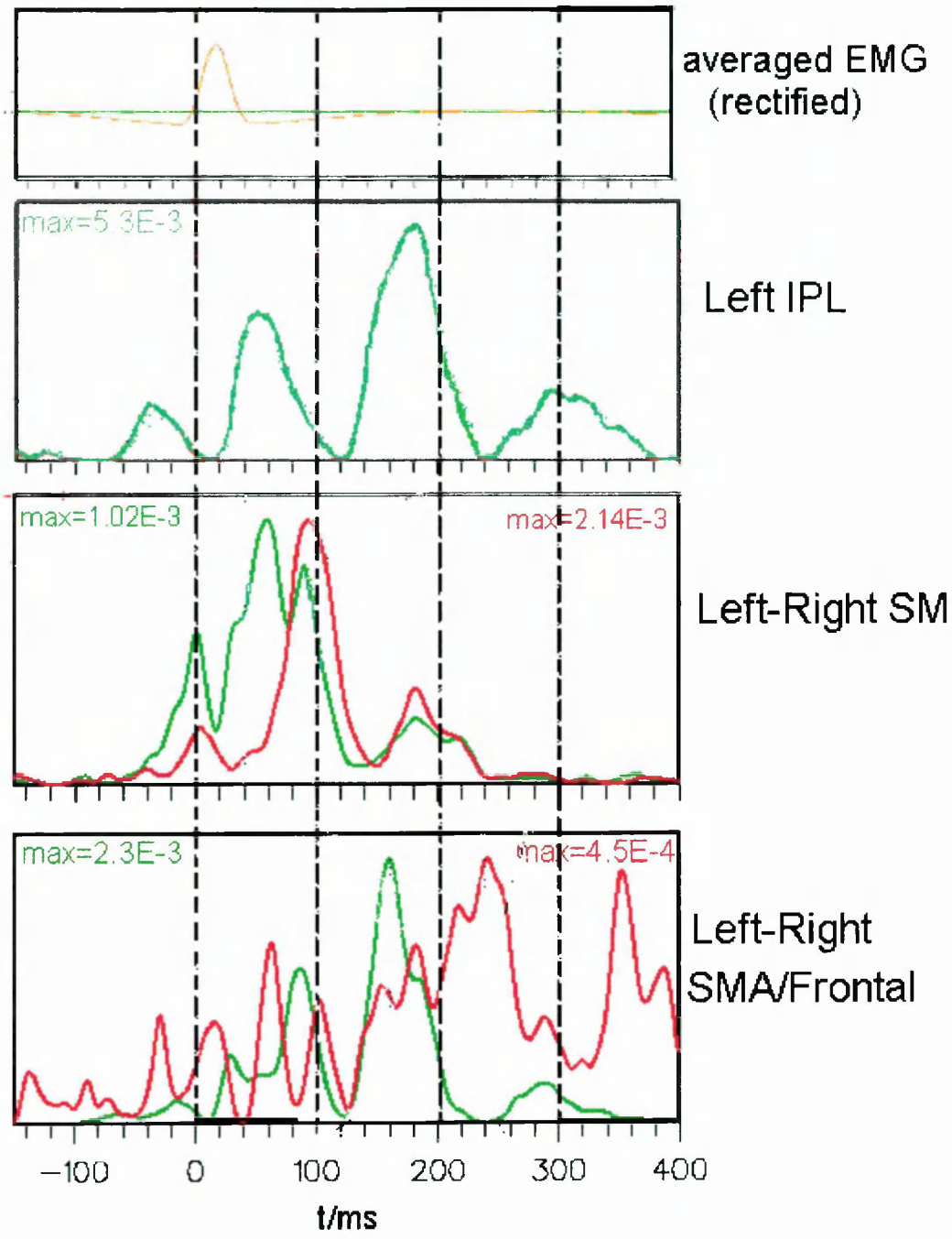

Figure 8-6: Activations within all the previously mentioned regions for summary and/or comparison purposes. Note that the first significant activation occurs in the left IPL region (some 40 ms before EMG onset) followed by a whole sequence of events involving the SM and SMA regions both contralaterally and ipsilaterally. Dashed vertical lines mark 100 ms apart latencies to aid comparisons.

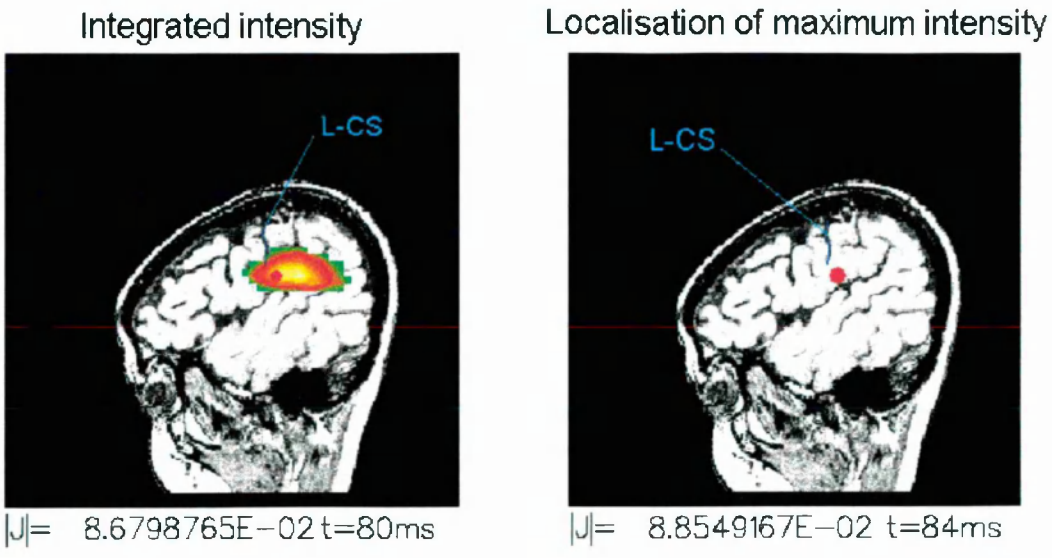

Figure 8-7: Left: integrated intensity between 70 and 90 ms after EMG onset. Right: localisation of the instantaneous maximum of intensity. The location of the maximum is in the second somatosensory area (SII).

8.2.6 Discussion

Before commenting on the aforepresented findings one should recall that the motivation for including this analysis of this dataset in the present thesis was to show that MFT does reveal pathological activity which is time-locked to an externally observed event, that is the EMG onset of myoclonic activity. Such a goal has been achieved since we have localised activity on the (left) sensorimotor cortex following (an averaged) spontaneous myoclonic movement of fingers as recorded with the EMG electrode.

However, the availability of a (twin Dewar) system capable of capturing activities from either side of the head made it possible to additionally identify the initiation of epileptic activity some 40 ms before the EMG onset in the left inferior parietal cortex. In other words, the use of the 2x37 channel MEG system which offered a partial bihemispheric coverage of the head enabled the simultaneous study of both the irritative (i.e. spike generating zone; left IPL area) and the symptomatogenic zone (i.e. the one responsible for the appearance of external symptoms; left SM area).

The MFT localisations of the left IPL area are in general agreement with those of the ECD analysis and also the PET results which indicated hypermetabolism in this region (Volkmann et al 1995, 1996). In their study, Volkmann et al mentioned that they could see a dipolar generator of activity in the left somatosensory area some 80 ms after EMG

onset, but they failed in the identification of (dipolar) activity in the precentral gyrus (motor) or frontal areas which were, however, identified in PET analysis. They speculated that there would be a polysynaptic transmission to the spinal cord, probably via activation of the hypermetabolic precentral gyrus (which showed no dipolar activation) and the feedback activity following the myocloni would fall within the hypometabolic somatosensory cortex.

The MFT analysis presented here though, not only identified activity within the pre- and post-central gyrus but also revealed the involvement of the frontal/SMA areas in agreement with the PET findings. The ECD failure was very likely due to the absence of a "focal image". Recalling that we only dealt with averaged signals that would not be surprising: single trial variability prior to movement could easily result in blurring (see for example Liu et al 1996). What additional goodies, though, could one have found by incorporating single trial analysis in this case?

The answer to this question can be speculated with the experience of unaveraged data analysis presented in this thesis, but also with reference to other recent single trial MFT reports (e.g. Liu and Ioannides 1996; Liu et al 1996). The most important piece of information would involve the latencies for the activations of the already identified areas (as appeared in the averaged record), as well as the order of activations in different single events (finger twichings). Since the areas revealed by MFT analysis of the averaged record are also identified by PET means that these areas are the "nodes" of activation in this case and, therefore, should also be activated in single epochs (Ioannides 1994). By averaging the signals, however, the inherent trial to trial variability is smoothed (if not completely lost) and one cannot maintain his confidence in the resulting sequence of events. It is for this reason that we did not pursue the issue of connectivity between somatosensory (postcentral gyrus) and somatomotor (precentral gyrus) areas any further in our analysis (refer to Figure 8-4), neither we attempted to say whether the observed activation of the SM region (e.g. Figure 8-3) is due to motor or somatosensory zones. We have shown that it should be due to both, and the PET results support this view. With single trial analysis though, we expect that we would have been able to clarify the issue considerably.

Finally, we should briefly comment on the rest of our findings. The involvement of the contralateral sensorimotor area is not surprising. As Shibasaki (1996) authoritatively states, "bilateral activation of motor cortices should be expected in both physiological and pathophysiological conditions". He further supports the view that movement of the intact hand would mainly involve contralateral activation, while movement of the "affected" hand would involve bilateral activation. Moreover, simple movements usually

comprise unilateral origin, while complex or sequential movements would necessitate bilateral activation (Shibasaki 1996). Despite the generally stronger appearance of activity in the ipsilateral sensorimotor area (right SM; see maximum of the activation curve in Figure 8-3) - which could be explained by the closer proximity of the sensors to the right SM than the left SM (see set up in Figure 8-1) - activation of the contralateral area (left SM) was seen to precede its homologous site, highlighting the temporal advantage of MEG.

8.3 Auditory Odd-ball Study

8.3.1 Aims and General Information

The observation of deep (contralateral to the measurements) activation in the analysis of interictal epileptic signals from one patient (Pat2) in the previous chapter opens up the question "how reliably can deep activity be extracted given bilateral sensor coverage". The dynamic simulations in the case of simultaneous bilateral measurements as presented in section 5.4.4 (and Figure 5-32 in specific) provide part of the answer. The full answer to this question is beyond the scope of the thesis; it requires an accurate modelling of the skull boundary - because the sphere model is almost certainly insufficient - and modifications to the main algorithm to deal simultaneously with bihemispheric and deep activity. We limit our task to addressing the question: given "real" bihemispheric recordings, how would the deep activity from the familiar "small deep cylinder" source space model compare with deep activity obtained with the modelling of each hemisphere separately?

For this part of work we shall use signals elicited under the classical "auditory odd-ball experiment", during which normal subjects are exposed to a series of "frequent" tones (of a certain frequency) interrupted by "infrequent" or "odd" tones (of a different frequency). The subject's task is "silently count" the presentations of the odd stimuli. This protocol produces "Endogenous" late sustained activity (Halgren et al 1980), known as P300 or P3, in addition to the "usual" main auditory evoked activity.

The family of late sustained potentials and magnetic fields associated with the P300 recorded on diverse population groups (normals, patients with lesions, epileptic patients) has been studied for many years using a variety of techniques (SEEG, EEG, MEG). A long list of candidates for the possible generator sites has been produced as a result, and when all the information is gathered together the list of sites implicated appears to cover a very wide network extending throughout the brain, including cortical regions in both hemispheres (frontal and parietal) as well as the limbic system, and the thalamus. As Halgren (1996) points out as an overall summary of his studies on odd-ball experiments, "many (and large) areas may be simultaneously activated from very soon after stimulus onset (<200 ms) till very late (>1 s)".

The specific MEG study of the odd-ball experiment involves considerable effort and it is part of an on-going research at Jülich since late 1994. The concern for this thesis is rather narrow and it is not, for example, intended to enter the "P300 generators debate". The interest is twofold: firstly, the ongoing experiments in late 1994 provided the opportunity for some experimental work to add to the mainly theoretical frame of research in the rest

of the thesis. Second reason is to merely exploit the fact that "deep activity" is expected to emerge from such a paradigm (especially at later latencies). We shall apply MFT to signals from left and right Dewar separately, as well as employing simultaneous bilateral MFT reconstructions as described in Chapter 5.

8.3.2 Experiment and Measurements

We used the standard odd-ball paradigm which consisted of monaural delivery of two tones, the frequent (1 kHz, 80% probability) and the odd (2 kHz, 20% probability), each 50 ms long (10 ms rise, 30 ms plateau, and 10 ms fall). The subject was instructed to count silently the odd tones and report their total at the end of each session. Measurements were performed with the Twin MAGNES BTi system (2x37 channels, Jülich, Germany); for each of the subjects* two different placements of the probes were used. For each placement the tones were delivered to the left and right ear in separate runs; some 300 tones (approximately 50 odd) were delivered in each run. Each epoch consisted of some 1042 timeslices covering the interval from 212 ms before, to 787 ms after the onset of the stimulus. A detailed description of the experimental protocol and the recording sessions is given in Appendix B.

8.3.3 Analysis

The signal was sampled at 1041.7 Hz (sample period 0.96 ms) with on-line (hardware) band-pass filters from 0.1 to 400 Hz; the raw signal was subsequently digitally band-pass filtered from 1 to 45 Hz. The resulting averaged signal (as computed for both odd and frequent responses) and individual single trials were then subjected to MFT analysis after registration of the MEG data with individual MRIs of each subject (using the methods presented in Chapter 3).

The signals from each probe were used in separate MFT analysis within partial hemispherical source spaces to provide a simultaneous, but independently derived view of activity in each hemisphere. Each source space covered almost the whole of its corresponding brain hemisphere. The source spaces had a common deep level (level 1) and were arranged symmetrically with their third axis along the y-direction of the head based MEG system. We have also used the signals from both probes together in a limited number of MFT reconstructions within a "small" deep cylindrical source space to

---

* *The series of experiments consisted of 6 subjects; MFT analysis has been performed for 4 of them. However, for the purpose of this thesis we are only going to use data from a single subject.*

specifically look at deep activity close to midline[+]. The conducting model used in all cases was a sphere fitted to the local (to the sensors) curvature of the inner skull surface, in the case of separate MFT analysis, and to the entire skull outline, in the combined case. Figure 8-8 illustrates the sensor positions relative to subject HMG, together with the source spaces and the conducting spheres in different perspective views. In all cases, Gaussian probability weightings with properly chosen decay factors were used and the smoothing parameter was kept equal to unity.

8.3.4 Results and discussion

Preliminary results from the averaged and single trial MFT analysis for two subjects of this experiment has already been reported in a meeting last year (Ioannides et al 1995d) and since then another two subjects have also been analysed. However, as mentioned in the introductory section, it is not our intention to present this analysis here, but to concentrate on a single aspect of it: the study of deep activity as conducted with the present facilities. The intention is to finish this thesis by identifying the problems and limitations associated with the analysis we have employed and indicate the directions for future research - some of which are already in progress in the MEG laboratory in Jülich.

We have selected three 20 ms long time intervals from the averaged odd and two single trial (also odd ones) records in which MFT reveals deep activity (always for subject HMG, and frontolateral Dewar placements). From the unlimited number of presentation options we have chosen to show the MFT solutions as projected on fixed axial and sagittal MRI slices: the axial slice contains both temporal lobes, the hippocampal-amygdala complexes, and the inferior parts of the anterior and posterior ends of the cingulate structures; the sagittal slices describe the cingulate system on the left and right side of the head and they only differ by some 12 mm from each other. The solutions for the averaged odd response as obtained from the separate modelling in the left and right source spaces respectively are given in Figure 8-9. Time runs from 325 ms to 340 ms after stimulus onset (to the left ear). Each display shows the instantaneous distribution of activity at a single timeslice. The $|\mathbf{J}^p|$ values printed beneath each axial slice correspond

---

[+] *MFT reveals activity in a number of deep areas. In the following we focus our attention on activity from the cingulate gyrus, this structure extends close to the brain midline, but it is still away from the centre of the conducting sphere that best fits the entire skull and the best sphere fitting the portion of the skull near each probe. Although we expect different choices for the conducting sphere centre in each of the three inversions (from signals from probe A, probe B, and both A and B) to lead to distortions, these will be less than what would be encountered if a structure closer to the head centre (e.g. thalamus) were considered.*

to the maximum of the distribution (at the specified time instants) throughout the whole of the left and right source spaces; in contrast, the values printed beneath each sagittal figurine give the maximum of levels 1 to 3 in each source space (i.e. 3 deepest levels only on either hemisphere). The actual MFT displays show the distribution at the displayed slice and do not necessarily contain the maximum throughout the whole volume in each case. One can see that there is progressive built up of activity at the posterior cingulate level which is identified by each reconstruction independently. The result looks more impressive in the axial projection where both MFT solutions (i.e. for left and right side) show activation at very similar locations.

The MFT reconstructions for the same time interval were repeated using the deep cylinder source space model and the results are shown in Figure 8-10. The same kind of display format is used there as well, with the only exception being the printed $|\mathbf{J}^p|$ values. In the latter figure, only the overall maxima throughout the whole cylinder are printed beneath each axial slice, and consequently the same cautions as before still apply. As one can notice in Figure 8-10, the cylinder also provides hints for activation at the posterior central region, but the axial projections are a little bit "fuzzy" and unclear. Given the inherent conducting modelling uncertainties one cannot be certain which structures exactly are activated. However, if with the existing modelling facilities is important to highlight that do get strong hints for an "activity crossover" between the two brain hemispheres occurring at the given time interval at the brain midline structures. This is clearly illustrated in Figure 8-11, where the time-depthplots for the specific MFT solution set are given for the deep cylinder model. One can note the aforementioned "crossover" happening around the latencies studied. Two scales are used in Figure 8-11: in the top part, the time-depthplot involves all 9 levels of the cylinder space (i.e. from fairly deep right to fairly deep left regions), while in the bottom part only the 5 deep levels of the cylindrical source space are involved in an effort to reduce the interference of any superficial activations (which are, of course, projected on the left and right extreme levels of the cylinder; see Chapter 5) and better focus on the more central (midline) activations.

Two more such examples drawn from the single epoch MFT analysis of the same dataset (i.e. frontolateral probe placements; subject HMG) are given in the four next figures. The first two of them (i.e. Figure 8-12 and Figure 8-13) involve the latencies from t=495 ms to t=510 ms in epoch 282 (odd one), while the following two (i.e. Figure 8-14 and Figure 8-15) involve the latencies from t=315 ms to t=330 ms in epoch 297 (an odd one as well). One can again note the general agreement between the two independent source spaces in the identification of deep, midline located activity. The set describing epoch 282 provides

hints for activation at the cingulate level with an "apparent" possible shift from anterior to posterior, while the set describing epoch 297 hints only posterior activation. The interpretation of MFT displays at fixed MRI slices must be done with caution, because one cannot be certain whether the observed activations are the true ones or just reflections of stronger activity in other areas and associated shifts due to conductivity modelling errors.

A critical appraisal of the "small deep cylinder" MFT inversions must conclude that they are distinctly less successful than the corresponding "small deep cylinder" MFT inversions in Chapter 5. A crucial difference between the two is the position of the sphere centre which for the bilateral measurements in this section was taken to be the geometric centre of the head, while for the unilateral measurements of Chapter 5 was well onto the other side. The need for a better conductivity model (e.g. spheroid; Fieseler et al 1995) is clearly evident.

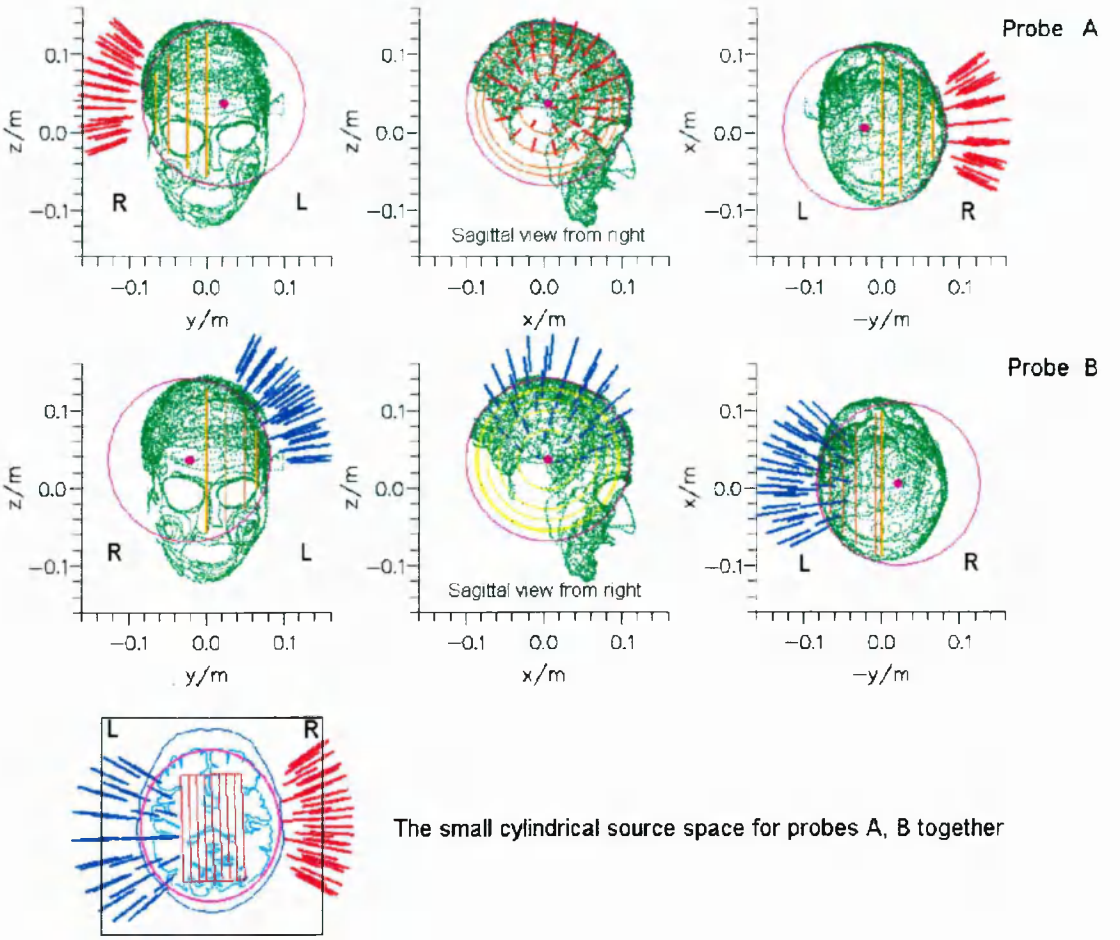

Figure 8-8: Experimental set up for subject HMG (frontolateral Dewar positions) and MFT source space models. Top and middle: two hemispherical source spaces were used in the MFT analysis, one for each probe. Note the source space orientations with respect to the MEG headshape outline (green) and the sensors (red and blue bars for probes A and B respectively). 4 levels are given for source space in three perspective views. Bottom: the "small" cylindrical source space used in the simultaneous study of both probes. In each plot, the conducting sphere is drawn as a pink circle with a pink dot marking the centre of the conducting sphere.

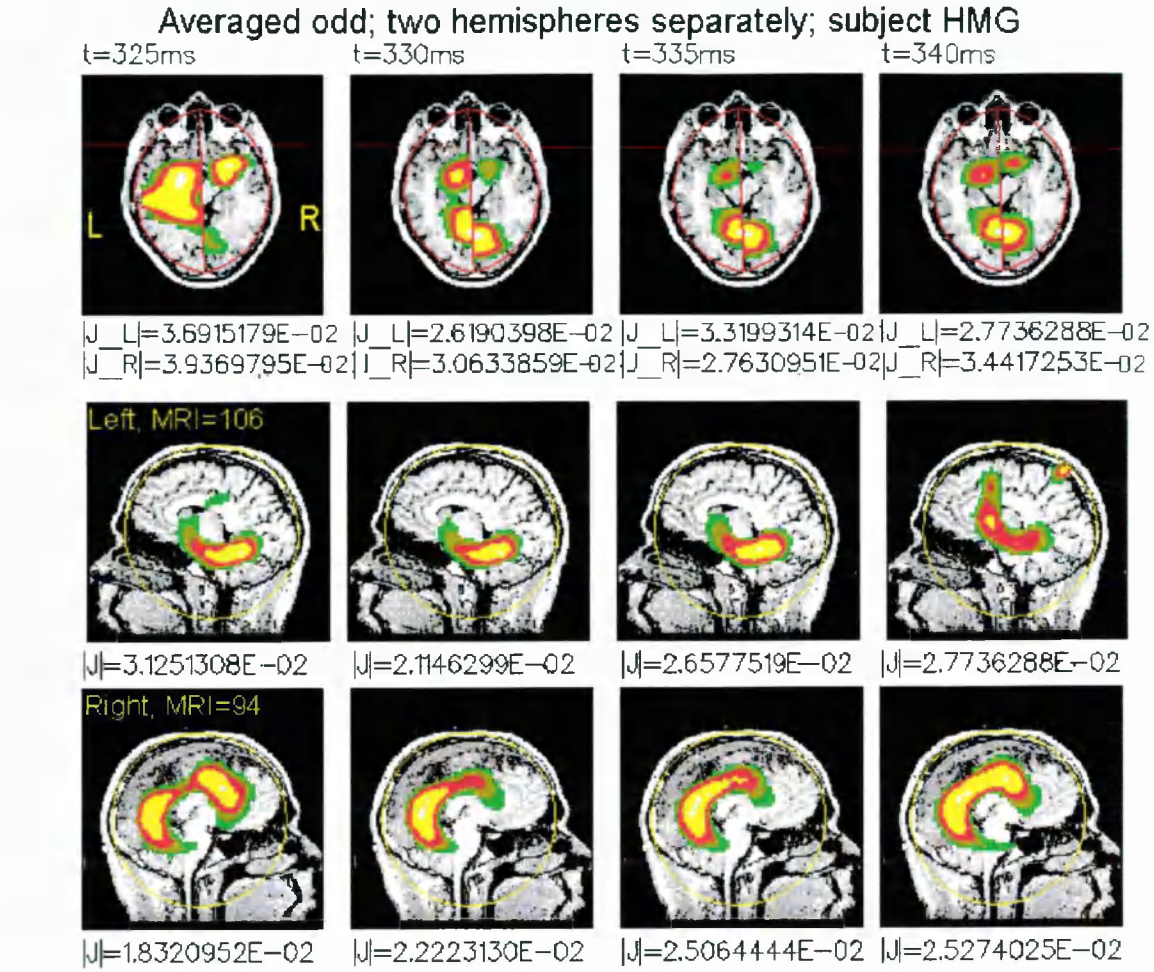

Figure 8-9: MFT Solutions for the averaged odd response obtained independently in the left and right source spaces between t= 325 ms and t=340 ms after stimulus onset (to the left ear). The $|\mathbf{J}^p|$ values beneath each axial slice correspond to the maximum of the distribution throughout the whole of the left and right source spaces at that time instant, while those beneath each sagittal to the maximum of the 3 deep levels only in each source space.

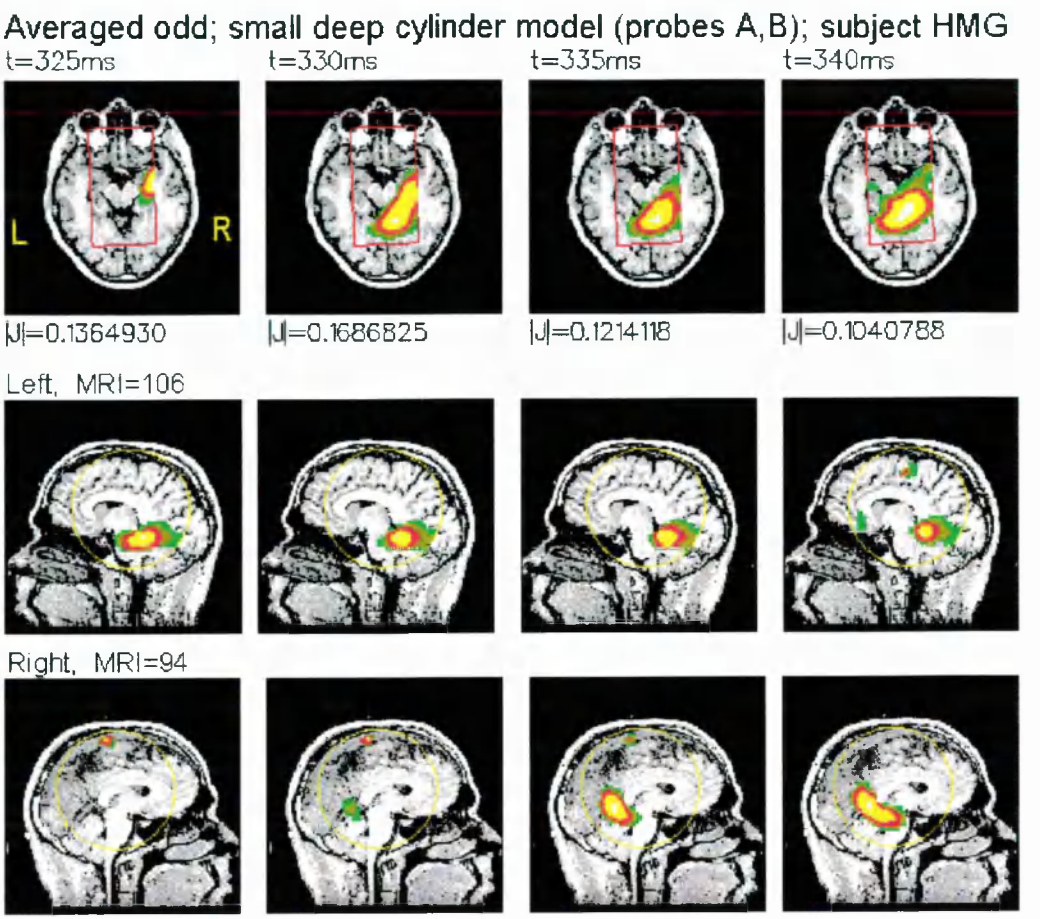

Figure 8-10: MFT reconstructions for the same time interval as that in Figure 8-9, but repeated using the deep cylinder source space model (both probes together; see bottom of Figure 8-8). The display format is the same used with that of Figure 8-9, except that only the overall maxima throughout the whole cylinder are printed beneath each axial slice.

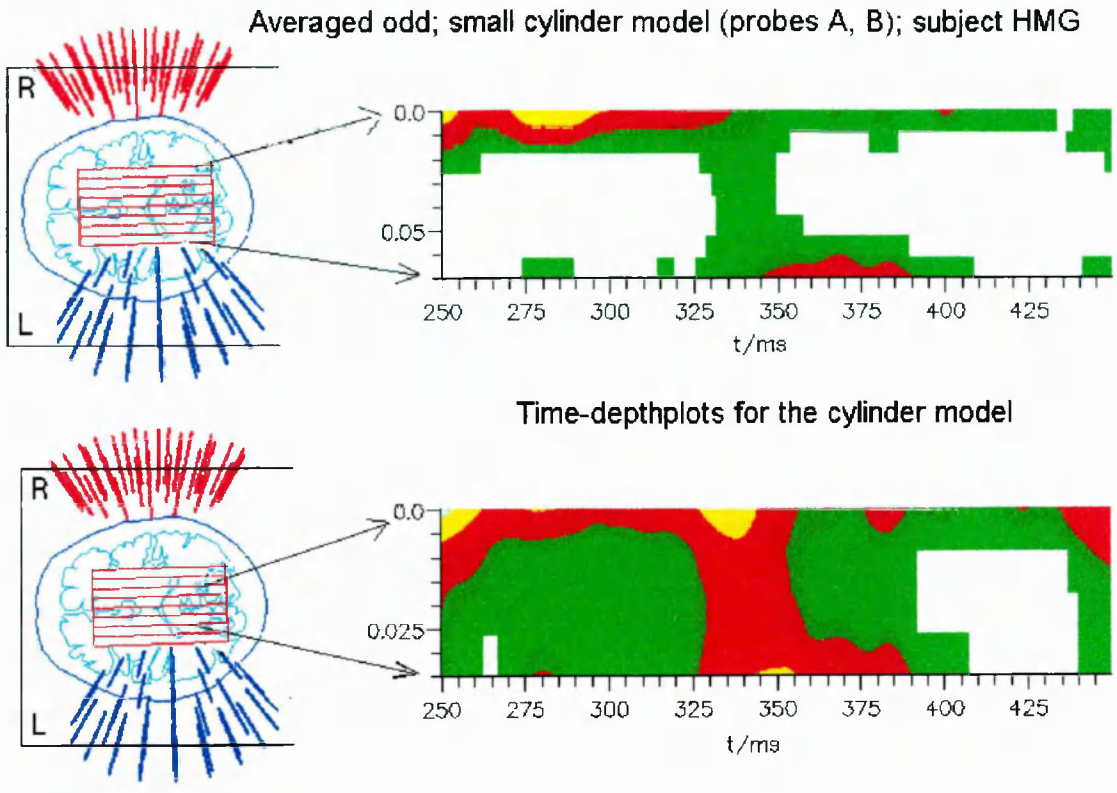

Figure 8-11: Left: the deep cylinder source space model. Right: time-depthplots for the MFT solutions presented in Figure 8-10 (i.e. using the deep cylinder model). Two scales are used: *in the top*, the time-depthplot involves all 9 levels of the cylinder space (i.e. from fairly deep right to fairly deep left regions), while in the *bottom*, only the 5 deep levels of the cylindrical source space are involved; arrows depict the association between the depthplot edges and the involved source space levels; (see text). One can note the aforementioned "crossover" happening around the latencies studied in the previous figure.

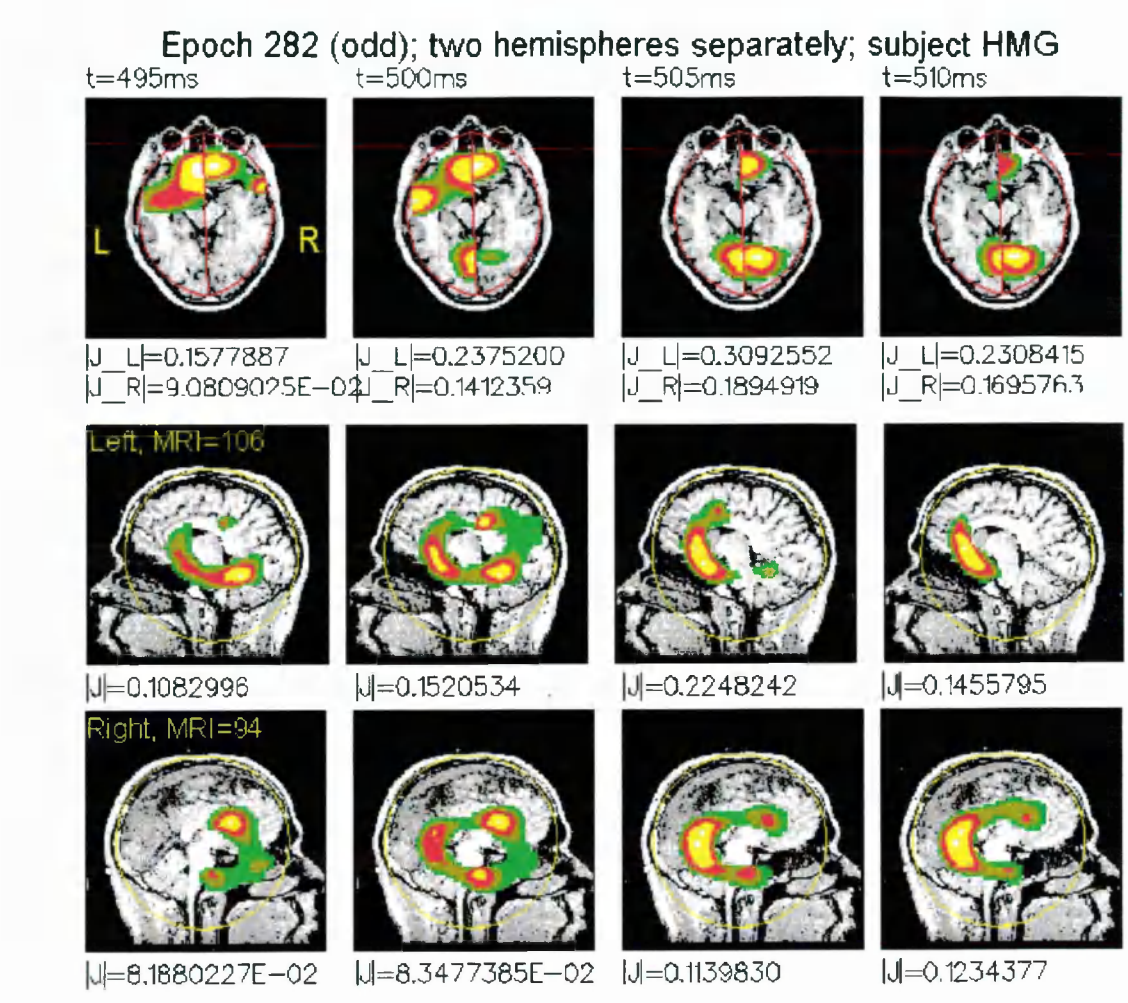

Figure 8-12: MFT displays involving the latencies from t=495 ms to t=510 ms during the odd epoch 282. The same conventions are used as for Figure 8-9. Note again the general agreement between the two independent MFT reconstructions (left and right) in the identification of deep midline activation. See also the corresponding deep cylinder reconstructions in Figure 8-13.

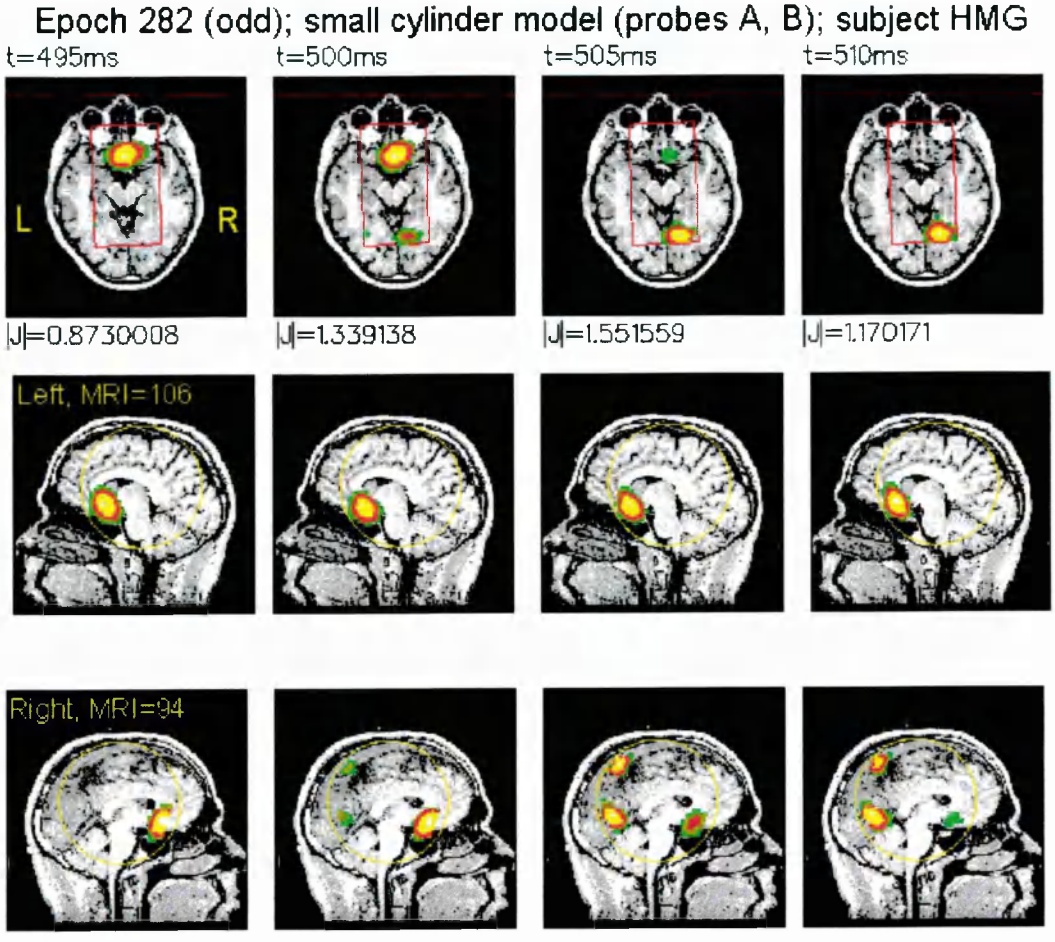

Figure 8-13: MFT reconstructions for the same time interval as that in Figure 8-12, but using the deep cylinder source space model. See Figure 8-10 for conventions. The displays are consistent with activation of the cingulate which shifts from anterior to posterior.

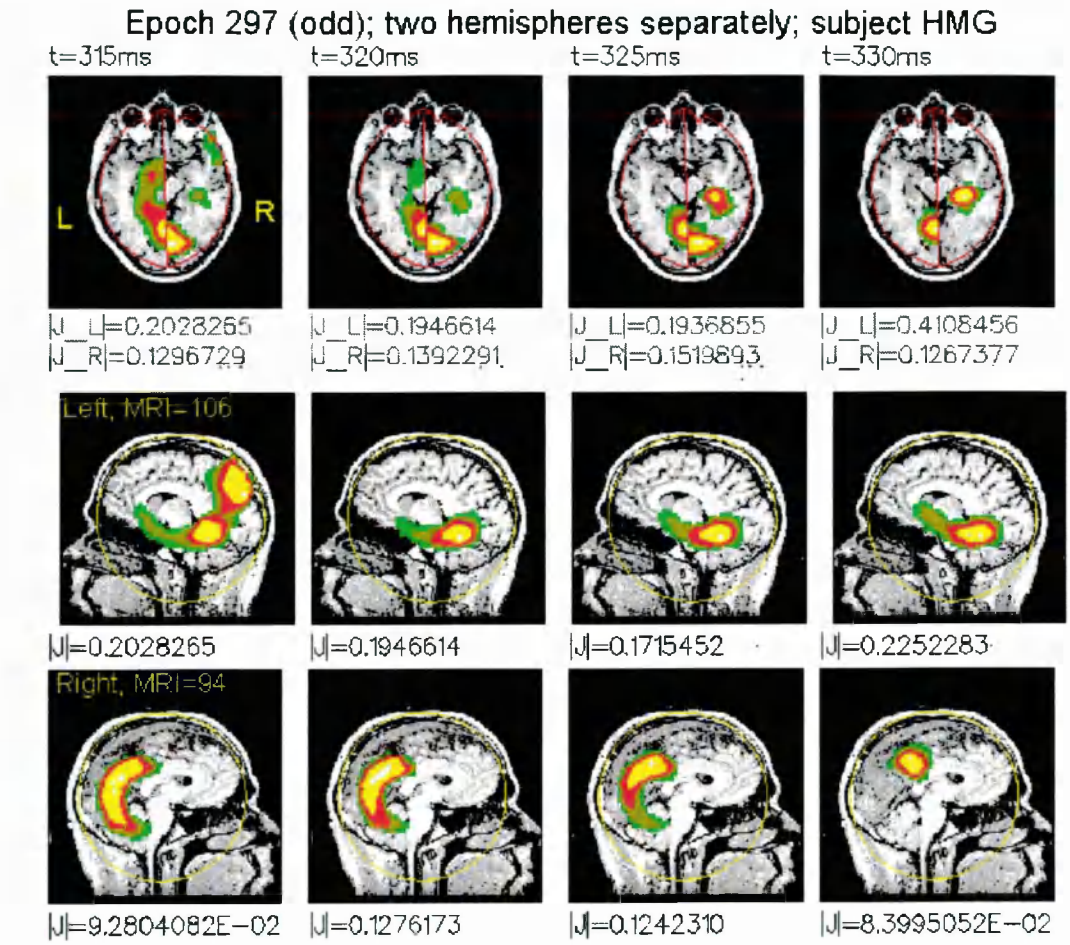

Figure 8-14: MFT displays involving the latencies from t=315 ms to t=330 ms during the odd epoch 297. The conventions valid in Figure 8-9 apply here too. Note again the general agreement between the two independent MFT reconstructions (left and right) in the identification of deep posterior midline activation. See also the corresponding deep cylinder reconstructions in Figure 8-15.

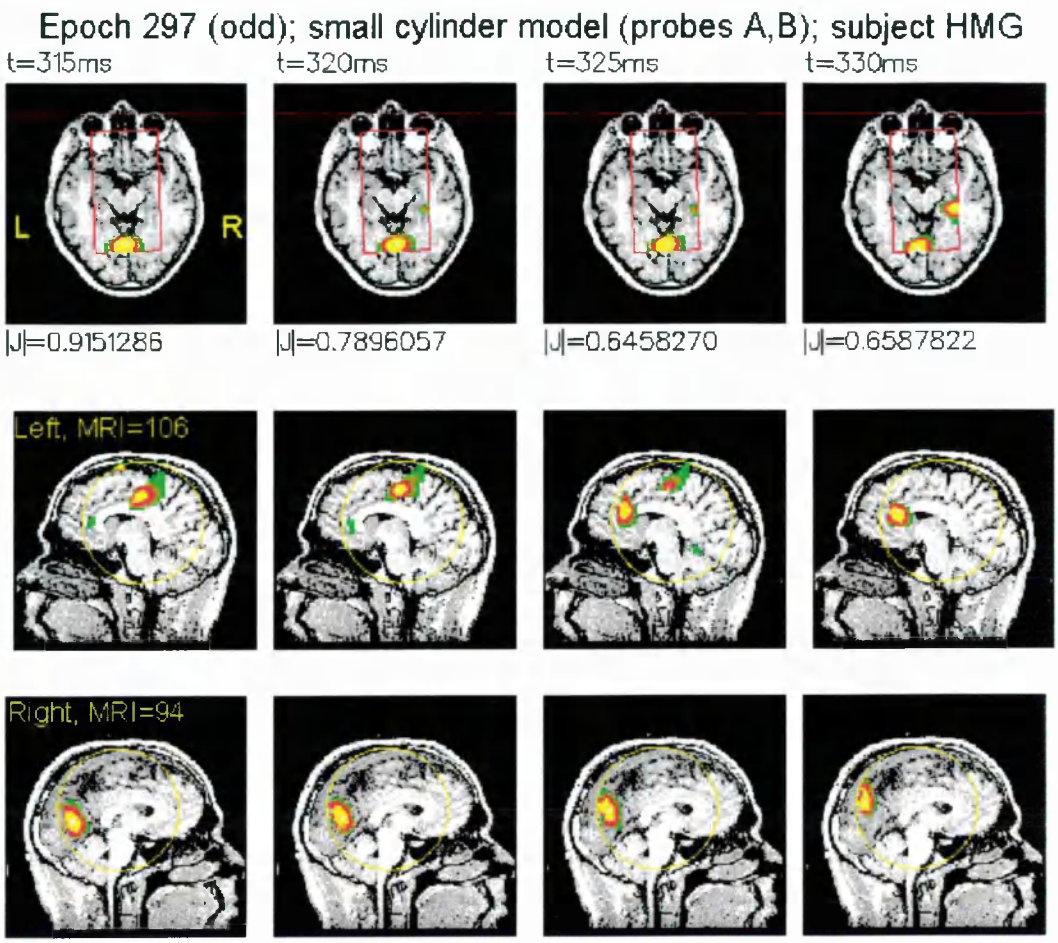

Figure 8-15: MFT reconstructions for the same time interval as that in Figure 8-12, but using the deep cylinder source space model. See Figure 8-10 for conventions. Hints are provided for activation at the posterior cingulate level especially in the axial projections.

9. General Discussion and Further Work

The work of this thesis has been mainly concerned with research into interictal epileptic activity as recorded by means of multichannel MEG systems and analysed using a source model employing current density distributions, namely MFT. The major aim has been to investigate whether or not MFT analysis of unaveraged MEG data (single epochs) is feasible in cases of pathophysiological signals and more specifically interictal signals from patients with epilepsy of a complex partial type. The investigation was undertaken against the old and "traditional" view of the impropriety and absurdity of using single epoch records in the MEG analysis due to noise dominance; it was, however, along and within the general concept adopted over the last few years here at the Open University that multichannel systems should provide the potential to study brain activity in "real time", if we may say so, but one would need a robust method to pursue such analysis. The research was initiated by a preliminary report (Ioannides et al 1993c) which showed that the 3d-distributed source model (i.e. MFT) was appropriate for studying deep and/or superficial activity extracted from averaged epileptic datasets. Moreover, another more recent MFT study hinted that MFT could be a valid method to use in unaveraged epileptic datasets (Ioannides et al 1995a). The project ran in parallel with other studies which tackled similar questions but under non-pathological frames, namely auditory evoked responses from normal subjects (Liu 1995) and responses during the Contingent Negative Variation (CNV) paradigm (Liu et al 1996).

To achieve the set goal we have started the research in Chapter 3 by trying to device strategies that would allow accurate registration of the MEG data with structural MEG

images, thereby improving the localisation capability of MEG/MFT, as well as, providing the prerequisite for advanced - future - modelling of specific brain structures. The registration methods attempted and developed were not a novelty as such, since ideas were borrowed from other relevant techniques of the brain imaging field in general. Some novelty could be, however, attributed to the demonstration of the need to move from the most common and easy point matching strategy to the more robust and less subjective methodology of surface matching through the use of practical visual examples. In addition, the combination of the two techniques (point and surface matching) was employed here for the first time. Moreover, all the attempted methods were implemented by developing software which did not make use of any already available commercial package (i.e. all the source code was "home-made" all the way through from beginning to end). The experiences collected throughout the development and application of these techniques will certainly provide a useful reference in future MEG research.

The first section of Chapter 5 has dealt with rudimentary MFT tests that are necessary before each MFT study, at least with existing tools. Some of the tests and simulations that followed, though, have been performed for the first time, but they should by no means regarded to be exhaustive. The main objective in undertaking them has been to identify the potential and some of the limitations of MFT, at least as far as the implementation that has followed in the rest of the thesis is concerned. In other words, the aim has been to provide support for the results obtained in the main bulk of the thesis from the MFT analysis of real datasets. Therefore, both the spatial and temporal aspects of MFT have been discussed and attention has also been paid on the "number of sensors effects" on the spatial resolution with special emphasis on the recovery of deep activity from both unilateral and (simultaneous) bilateral measurements. A novel way of conducting MFT studies in depth was suggested and implemented: the iterative use of a source space designed to cover deep situated structures on either side of the brain. This methodology is utilised in Chapters 7 and 8 in association with real data. Finally, utilities have been developed and used to allow for user-designed temporal evolutions of various source configurations to be incorporated in MFT simulations. Realistic sensor configurations and signals that were neurophysiologically pragmatic in terms of location and temporal characteristics have been employed to investigate the "dynamic" or temporal capacities of MFT, again in order to backup the results presented in Chapters 6 through to 8.

Real datasets from a SIEMENS 37 channel system were used in the following two chapters, the main ones in the current piece of work. Using these in Chapter 6, we have proved that MFT analysis of single, unaveraged epileptic spikes is indeed feasible: we have demonstrated spatio-temporal coherence in the MFT results of the various

("similar") single interictal events and showed that activity extracted from the "averaged event" is made up of activity contributions which occur intermittently and at variable latencies. Moreover, we have hinted that the averaged appeared to be the outcome of a higher aggregation of similar events in some epochs. Our statements were drawn from the study of both superficial and deep activity. We have shown that if the activity in an area is integrated over a period of time, then the averaged and single epoch integrals agree more and more as the interval of integration increases, despite huge variability from moment to moment in the course of single events. In addition, dominant features in the MFT solutions extracted from the averaged event have been identified in the MFT solutions of single, unaveraged events, although in the latter have usually been buried in a stronger and more variable background.

In Chapter 7, we further applied and exploited the above conclusions to study the spatio-temporal evolution of interictal activity during the course of unaveraged spike events in two cases of temporal lobe epilepsy. We have observed the interactions between superficial (neocortical) and deep temporal structures (hippocampus): superficial activity has been identified as preceding deep activity. These observations were reinforced using a novel technique of backavareging three dimensional MFT solutions. Furthermore, consistent propagation patterns of activation in the depth of the temporal lobe were revealed among the various spike events: at the hippocampal level, activity seemed to propagate mostly in the anterior-posterior direction suggesting spread from amygdala to hippocampus. However, sequential shifts of activity from anterior to posterior and then back to anterior (or vice versa) were also observed in this region. Finally, some focal deep activity in this region was seen to be initiated in the contralateral hemisphere (probably on the contralateral hippocampal region) and the deep cylindrical source space (archetype from Chapter 5) was called to model it.

These findings, although in agreement with depth electrode observations, have been quite novel in the sense that have not been demonstrated before using *unaveraged* interictal MEG signals. In addition, they provide further evidence that MFT can be applied to unaveraged MEG signals and produce a millisecond by millisecond "view" of superficial as well as deep brain activity, with minimal prior constraints in the spatial domain and no constraints on the temporal order of events. The clustering of sequences of events in space and time in the MFT solutions provides the most direct link to the evolution of events in the brain available so far, but we do not yet have enough experience to fully exploit the new information at our disposal. The experience gained from the analysis of averaged data is not always useful as the analysis of single trial data demonstrates, for both normal brain function (Ioannides et al 1995b) and pathology

(Bamidis et al 1995). Nevertheless, even at this early stage, single epoch analysis provides a potentially very useful tool. For the specific clinical use in epilepsy, the work we have reported suggests that, MEG offers a reliable technique to detect and localise epileptic activity within the human brain *completely non-invasively*. Its precision, when accompanied with a stereotactic system for the definition of brain structures, allows successful functional radiosurgery to be performed, with MEG-defined target zones (Hellstrand 1993, 1995). It remains to been seen whether further improvement in localisation can be achieved through the introduction of additional constraints from anatomical information and conductivity modelling. The MFT analysis has added further insights on the propagation of the epileptic activity within the brain and it, therefore, seems to be an ideal tool for studying the complex signal interplay making up the different spike types and kinds of epilepsy (Bamidis et al 1995). Concluding, we may state that, MEG measurements and MFT analysis offer the opportunity to non-invasively recover the functional connectivities of the various anatomical structures from single epoch data, avoiding the dangers associated with averaging.

Finally, simultaneous bilateral recordings conducted with modern MEG equipment (BTi, 2x37 channel system) have been utilised in the MFT analysis presented in Chapter 8 whose first part has dealt with a case of myoclonic epilepsy. The motivation has been to use this as an ideal localisation study and to show that MFT can reveal pathological activity which is time-locked to an externally observed event (i.e. EMG onset of myoclonic activity), a goal achieved by localising activity on the (left) sensorimotor cortex following (an averaged) spontaneous myoclonic movement of (right) fingers as recorded with the EMG electrode. Similar support for the correctness of the MFT analysis could, of course, be provided by means of a typical experimental set up of a "synthetic" dipole embedded in some kind of conducting medium and artificially activated in time. However, we believe the example used here to be more realistic and challenging and at the same time more interesting from the pathophysiology point of view.

The sensor configuration and the activations observed in the latter example, though, did not facilitate modelling of bilaterally recorded deep activity. Thus, the "MFT view" of deep activity (contralateral to the measurements side; case of unilateral recordings) - mostly undertaken in Chapters 5 and 7 as an academic exercise - has been applied in an actual situation of both averaged and single trial datasets in the second part of Chapter 8. The classical auditory odd-ball paradigm has been used in association with "more reliable" data from roughly symmetrical Dewar placements bihemispherically, to probe activity in depth. Hints for the suitability and usability of the novel iterative use of the

"small deep cylindrical source space model" in the study of deep activity have been provided therein.

So far, we have summarised the research undertaken in this thesis, highlighted the main findings, and provided a general discussion. In the following few lines we wish to suggest points and directions along which further research can be pursued.

One of the main drawbacks of the analysis presented throughout this thesis is the fact that, it was carried out in segmented time intervals of the overall dataset volume, which, however, comprised a considerably small percentage of the whole amount of the actual data[+] (e.g. some 30 sec were analysed with MFT for Pat2 in Chapter 7 as extracted from a 5 min MEG session). MFT analysis of long data sequences as currently facilitated is highly resource demanding (i.e. a substantially large amount of disk space storage needed, heavy and long computer engagement with extensive CPU usage for the inversions is mandated[*]) and, therefore, practically impossible. Simple vector signal transformations like the so-called $\mathbf{V}_3$ (Ioannides 1987, Ioannides et al 1990b) may prove particularly useful. Such an approach has already been developed and efficiently used here at the Open University to facilitate the analysis of single trial auditory evoked responses (Liu 1995). That implementation though, highlighted nearby (to the sensors) sources, providing an estimation of superficial generators of activity only. In order for the same approach to be applied in the study of epileptic data one needs to accommodate the requirement of highlighting deep sources too.

Simultaneous bilateral recordings would be very pertinent in such analysis. One could, for example, built signal transformations (templates) that would search for superficial activity on either side independently, and then use templates for both probes together to efficiently look for deep activations. The former task could exploit some kind of signal polarity inversion (like $\mathbf{V}_3$) around a specific (region of) sensor(s). The latter task would require searching for time segments where all (or many) channels would have the same sign on each probe but with opposite polarities between the two probes. Various other options could also be incorporated allowing for descriptions of stationary but rotating

---

[+] *The only justification though, is that we did use the results from the template correlation SIEMENS software to mark the "temporal whereabouts" of interesting events, and hence the time intervals studied were not concentrated in any particular edge of the dataset volume, but were spread throughout the it.*

[*] *The MFT inversion of 1s long signals (~1000 timeslices) from a 37-channel system would demand approximately 30Mb of disk storage and nearly 1½ - 2 hours of computing time on our dedicated transputer system.*

sources, moving or sequential superficial activations, or deep activity that is closer to one probe rather than the other. Some developments along these lines are already under exploration in the Jülich MEG laboratory.

Another way of examining long sequences of continuous epileptic data would be to apply the recently published ideas for signal-space projections (SSP, cf Tesche et al 1995). SSP can be used to detect and characterise simultaneous and/or sequential activation of neuronal distributions by studying the patterns of signals measured by a specific array of detectors (in either time or frequency domain). Such an approach would be directly applicable to the set of data analysed in this thesis, since having performed the MFT analysis for specific interictal events, we already have some idea of the sources involved in given time intervals. Thus, one could easily built up a spatio-temporal signal template (including, for instance, only signals from the detectors with strongest values) and browsing through the data to identify appearances of the specified pattern (and obviously the associated underlying neuronal generators) in time. One could assign different templates to different (assumed) neuronal populations: one to the intervals that indicated superficial activation and another one to those intervals that showed hippocampal activation. It would be very interesting to compare such results to those of Chapter 7 and study the interactions between neocortex and deep temporal structures over considerably long time segments.

Another straight forward task should be to combine the above lines with the modelling performed in Chapter 5 to use within any kind of paradigms. For instance, one could attach temporal information from animal experiments (conducted for same or similar conditions) to certain areas of activation. The "estimated" or anticipated signal shapes/patterns could then be used as seeds in the templates analysis. This is in fact similar to what Tepley and Wijesinghe (1996) attempted in an MEG study of spreading cortical depression: their simulations predicted additional waveforms which were not previously recognised but found in their data post-simulation. Moreover, such simulations could be used in association with the subject's MRIs prior to an experiment in order to predict the best probe placement positions. Of course, this is not necessary for the modern helmet-like systems in which the position subject is fixed in relation to the probe. In the latter case, however, simulations can be used to indicate the range of channels that will be involved in recording activations from certain areas, or in other words to produce so-called spatial filters.

Robust correlations in source space could also be developed to allowing for a fast and efficient analysis of the 3d MFT solutions. For example, one could follow ideas resembling those developed for $\mathbf{V}_3$ correlations (Liu LC and Ioannides 1995): identify a

time interval of interest in the MFT solution space (e.g. some 40-70 ms of hippocampal activations like those used in the connectivity plots in Chapter 7) and correlate the $\mathbf{J}^p$ quantity in a similar way to that used for $\mathbf{V}_j$ in order to reveal how often the same pattern repeats itself.

The latter could be used in conjunction with the 3d solution backaveraging technique: one could attempt a selective backaveraging considering only events with a specific type of propagation (e.g. anterior→posterior propagations or anterior→posterior→anterior shifts) and try to see whether the order of the identified superficial activations would continue to be the same or not, and whether or not there would be some kind of correlation between the appearing propagation patterns at the depth of the temporal lobe and those at the surface of it.

Moreover, we mentioned in Chapter 7 that spikes of similar shapes might involve different activation pathways and, therefore, spike averaging might embrace inherent caveats (Witte et al 1992). Our results indicate consistencies arising from the MFT analysis of unaveraged spikes, but we have observed that each spike may have a slightly different activation history to reveal. The overall localisation might be the same (e.g. integrated activity over relatively long time intervals) and might in fact agree with that of the averaged signal. But in order to investigate whether some credibility can be assigned to the pathway revealed by the averaged record or not, one may take up the following project:

- Conduct simulations with different pathways, that is, incorporate a few activation areas* - not only at the depth of the temporal lobe but also in superficial cortex - and assign different orders in the activation sequence (e.g. anterior cortex→posterior cortex→anterior hippocampus→posterior hippocampus etc.), as well as, different time constants in the individual activations.
- Compute the simulated signals from the above activations.
- Average the signals from similar, slightly different, and completely different pathways.
- Compute the MFT solutions for each of the individual signals, as well as, for the various averaged records.
- Perform the backaveraging of e.g. hippocampal activations (of similar or different implicated pathways

---

* *These can be simulated by dipoles or even distributions of current.*

- Study the "connectivity plots" extracted from the MFT solutions for the averaged signals and also the backaveraged solution set.
- Conduct a critical appraisal in terms of the advantages and disadvantages of signal averaging and solution backaveraging with respect to the revealed activation history.

Finally, research in modelling the conducting medium in association with deep cylindrical source space approaches has already been presented in Chapter 8. One may, however, recall that superficial activity is always interfering in the deep activations and is always projected on the first levels of the cylinder (on either side of the head in bilateral recordings). Therefore, one may combine some signal processing or template analysis techniques to eliminate this superficial interference directly from the signals and, therefore, study the deep activations from the "clean" signals more comfortably.

In conclusion, we have to mention that the real benefit for all this sort of studies, will come if processing is performed in real time, that is directly from the recorded signals ("on the fly") and not post-inversion. In this way limitations from the storage demands for the huge MFT solution files will be eliminated and studying long event sequences together with activation correlations will become practical. The use of high performance computers and advanced graphics representations is, however, mandatory. Such plans are already on the long term strategy of the MEG laboratory in Jülich.

Appendix A

The Siemens 37-channel KRENIKON system

The system was manufactured by Siemens AG in 1989. The first set of measurements used in this thesis were performed with a KRENIKON system in Erlangen, in late 1990. The second set of measurements were performed in Stockholm in 1992. Siemens has withdrawn the KRENIKON systems and hence moved out of biomagnetism (at least temporarily) in 1994. The KRENIKON system consists of 37 first order axial gradiometers fabricated on flexible printed-circuit boards and arranged in a flat hexagonal layout. The pickup and the compensation coils are arranged in two parallel planes 70 mm away (i.e. baseline=70 mm) both within a 19 cm-diameter cylinder. Each of the pickup coils possesses an area of 6 cm^2 and the gap between the liquid-helium space and the outer surface of the Dewar is 20 mm. Additional magnetometers measuring the x, y, and z components of the external magnetic field are also included for noise cancellation purposes. The system was designed for use inside a moderately shielded room and the noise of the system is typically less than $10\,fT\,/\,\sqrt{Hz}$ at frequencies over 10 Hz. The overall design was a compromise for brain and heart measurements.

Unlike the BTi system described below where the MEG co-ordinate system is subject specific, the KRENIKON MEG co-ordinate system defined in an experimental set up is dependent on the position of the probe. That is, the third axis of the most central coil of the array is defined as the third axis (z-axis) of the MEG system while the x and y axes are the ones defining the planar gradiometer arrangement as well. The origin of the co-

ordinate system is defined in association with a stereotactic frame consisting of watertubes visible on MR images.

The BTi MAGNES systems

BTi launched their first multichannel commercial gradiometer in 1985 (7-channels) introducing the curved-bottom Dewar. Their 37-channel version, consists of a hexagonal (Siemens-like) first order gradiometer arrangement, but the coils are wire-wound around 20 mm formers. The channel are 22 mm apart and are located on a spherical cap with a 120 mm radius of curvature. The coil array forms a cylinder with a 144 mm diameter and the gradiometer baseline is 50 mm. Eight additional SQUID-channels are also employed for noise cancellation. The system is designed for operation within a magnetically shielded room and its noise level is typically $10-20\,fT\,/\sqrt{Hz}$. With the curved Dewar bottom, the MAGNES system fits the human brain curvature better than the KRENIKON so it is believed to be more suitable for brain measurements rather than heart.

The MEG co-ordinate system is subject specific as mentioned above. That is, the system is defined in relation with the subject's/patient's own anatomical landmarks. These are the nasion, and the left and right preauricular points. The midpoint between the two preauriculars is defined as the origin of the system; the x-axis then points from the origin towards the nasion, while the y-axis towards the left preauricular. The z-axis is of course perpendicular to the xy-plane and points in the superior direction towards the Cz point.

Based on the MAGNES 37-channel system BTi developed recently the "twin MAGNES" system consisting of two 37-channel Dewars to facilitate simultaneous recordings over both hemispheres. One of the Dewars is floor based with limited angle flexibility while the other is driven by a gantry and allows much greater positioning flexibility (usually the subject's head is "placed" on the bottom Dewar and then the top one is positioned over it accordingly). The following two figures show the twin MAGNES system installed at Jülich, Germany in 1994, as well as a typical subject-system relative position for a simple experiment.

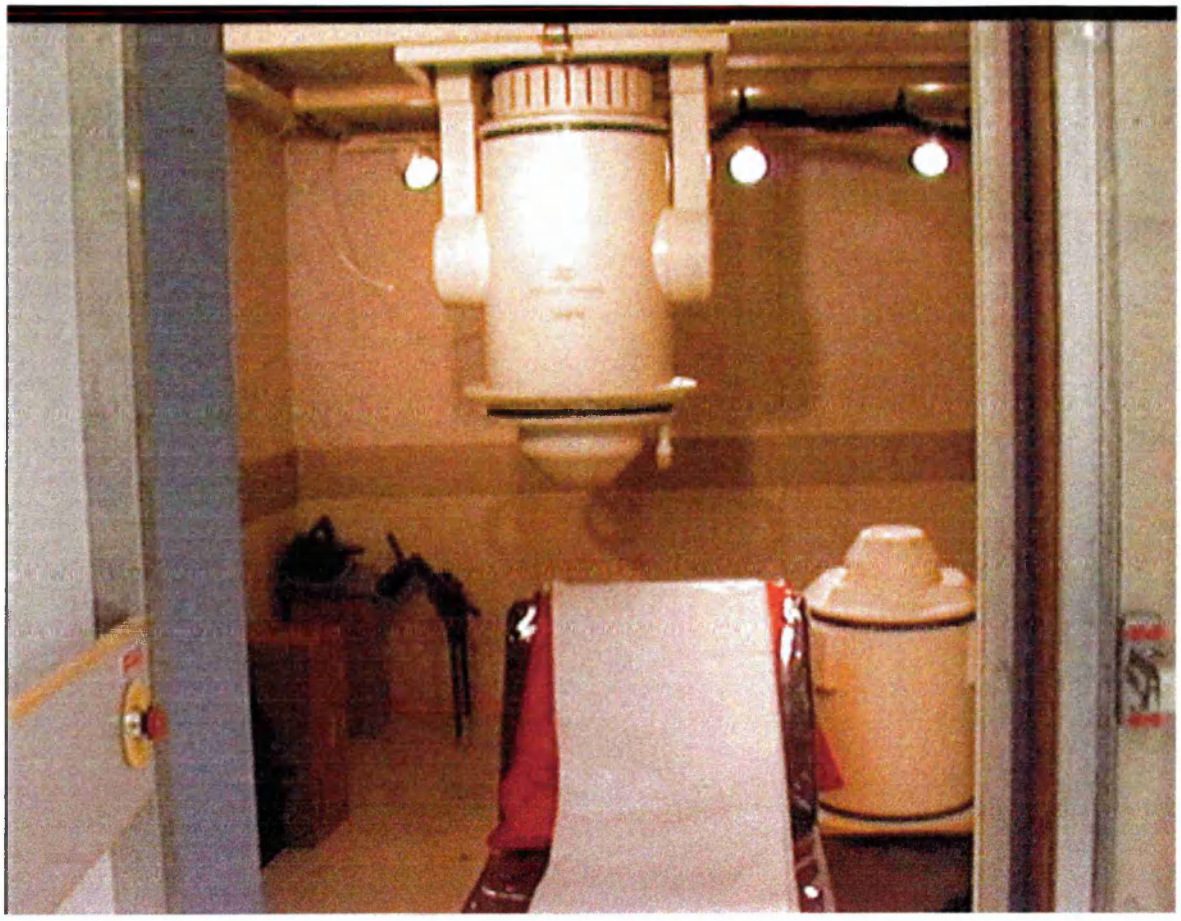

Figure A-1: The BTi twin MAGNES system (2x37 channels) inside the dedicated shielded magnetically room at Jülich Research Centre, Germany. The couch used as the subject "lying-bed" is seen between the two Dewars.

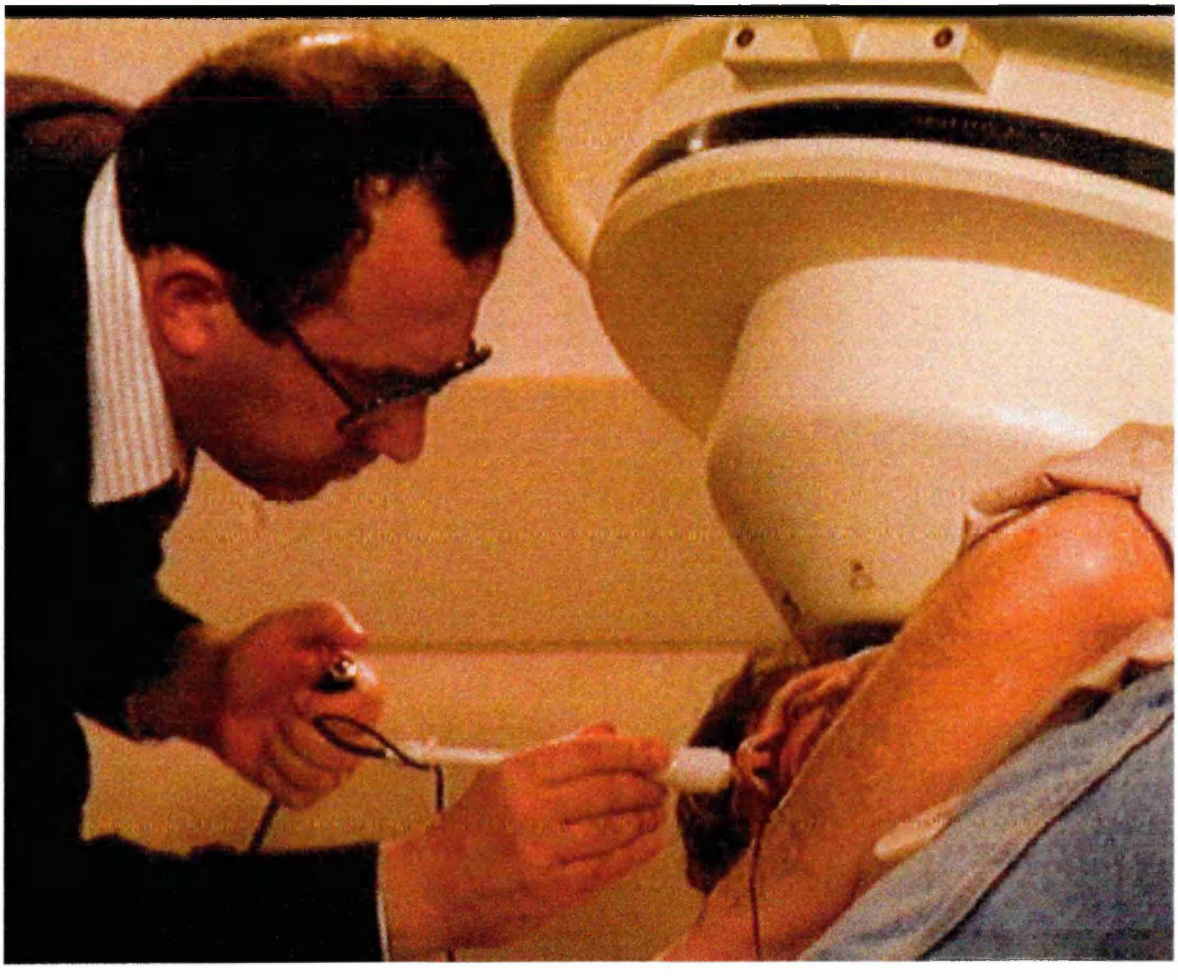

Figure A-2: A typical subject/probe positioning used for auditory recordings (temporal sensor placement) with the BTi twin MAGNES system (2x37 channels) at Jülich Research Centre, Germany. Note the probe position indicator (PPI) mentioned in Chapter 3 used for "clicking" (marking) anatomical landmarks (nasion in this specific case).

Appendix B

Auditory Odd-ball recordings (Jülich): Experimental Protocol

Subjects

Six unpaid male, right handed subjects with no past history of neurological disorder served as normal subjects (controls). All subjects were colleagues with some kind of relationship with the Institute of Medicine at Jülich.

Recording Preparation

A brief explanation of the entire procedure was given initially to each subject to put them at ease. It was essential for the subjects to be relaxed because muscular tension, often a physical manifestation of anxiety, might influence the character of the MEG signal. All subjects were asked to fill a questionnaire which included questions on their age and height, drinking and smoking habits, daily coffee consumption, sleeping conditions on the night before the experiment; the time of the experiment and food consumption just prior to it were controlled.

The first task was to define and mark with a pen the 5 fiducial points[+]: the left and right preauriculars, nasion, inion, and Cz. The Cz point was defined by the intersection of the curved-line connecting the two preauriculars and the curved-line connecting the nasion

---

[+] *In the BTi convention the MEG co-ordinate system is defined with respect to anatomical (external) head landmarks or fiduciary points (see Appendix A and Chapter 3).*

and the inion. The distances between the points were measured with a flexible ruler and noted down for future reference.

Two air-filled plastic tubes ending in an earphone were then fixed at each of the subject's ears and the sounds were delivered through them in an effort to determine the subject's hearing threshold. The auditory level for the tones to be used in the actual experiment were in this way adjusted (usually 30-40 dB above hearing threshold and in consensus with the subject's discretion).

With the 5 points marked on the subject's scalp, the following step involved the definition of the head-based MEG system and subsequently the headshape outline in relation to this system. The subject was seated comfortably on the couch in an upright position inside the shielded room. An inflatable/deflatable air-bag was used to help immobilise the subject. Although the subject had a partial freedom in moving his head despite the existence of the air-bag, he was requested to avoid any kind of head movements for a few minutes. With the top Dewar just above the subject's head, the head co-ordinate system (i.e. the MEG system in BTi's convention) was defined by clicking the aforementioned 5 anatomical points with a magnetic stylus (Probe Position Indicator, PPI); the whole head was then described by consecutive tracings of the stylus. At the end of the tracing, the 5 fiducial landmarks were "re-clicked" in order to observe any deviations from the previously obtained values. If the deviations were small enough (i.e. smaller than 1 mm overall) the headshape definition was accepted in confirmation of the fact that the subject had remained still during the procedure.

The subject was then released outside the shielded room for further preparations. Eyeblinks and eye movements were recorded from two electrodes placed laterally on the side of each eye-socket. Careful attention was paid to cleaning the skin area beneath each electrode with isopropyl alcohol. This procedure removed grease and desquamation, reducing skin resistance and improving tape adhesion. Conducting gel was also used to further reduce skin resistivity and allow for a "better" contact between skin and electrodes. The electrodes were fixed in position with surgical tape. Proper functioning of each electrode was secured by asking the subject to perform continuous blinks, "top-bottom" and "left-right" eye movements while the electrode outputs were monitored by means of an oscilloscope. An ECG electrode was similarly placed in the subject's chest to monitor heart activity.

Measurements

The subject was finally entered into the shielded room for the actual measurements: positioned on the couch (laterally lying posture), he was given the earphones again, and

he was placed between the two Dewars. The two probes were then positioned accordingly and the fiducial points were clicked again with the PPI to record the actual sensor positions with respect to the previously defined head-system. A final set of instructions was read to the subject; the shielded room door locked and the lighting inside it was deemed. A "control run" was then recorded consisting of 2 minutes of eye blinks (about one every 2 to 4 seconds), 2 minutes of rest with eyes closed and finally 2 minutes of rest with eyes open with the subject looking at a green patch inside the room* . It was during these control runs that any noise problems could be identified and resolved, if possible. For example, sometimes the channels of the reference coils were exhibiting an "harmonic noisy pattern" which was due to the EEG electrode which had been slightly removed from its proper position and was undergoing the inhalation/exhalation motion of the chest, with the result of producing magnetic fields!

For each of the subjects, two different placements of the probes were used: a lateral and a frontolateral placement. For each one, the tones were delivered to the left and right ear in separate runs; some 300 tones (approximately 50 odd) were delivered in each run. The subject was given a warning some 20 sec prior to the beginning of the recordings.

At the end of the first two runs (i.e. one placement; left and right ear tone presentations) the subject was repositioned, the sensor positions were re-defined, and the recordings repeated.

At the end of the experiment, the subject was removed from the shielded room and after being thanked he encouraged to provide any oral or written comments he wished to communicate. During this time, a recording of a five minute noise run was obtained to determine the actual environmental noise level for that specific day.

---

* *Sometimes, however, some of these test runs were performed at the end of all sessions to avoid subject exhaustion.*

References

Abraham-Fuchs K, Härer W, Schneider S, and Stefan H, (1990): "Pattern recognition in biomagnetic signals by spatio-temporal correlation and applications to the localization of propagating neural activity". Med. Biol. Eng. Comput. 28:398-406.

Abraham-Fuchs K, Lindner T, Wegener P, (1991): "Fusion of Biomagnetism with MR or CT Images by Contour-Fitting", Biomed. Eng., 1991, 36(Suppl): 88-89.

Abraham-Fuchs K, Strobach P, Härer W, and Schneider S, (1992): "Improvement of neuromagnetic localisation by MCG-artifact correction in MEG recordings". In: Hoke M, Erne SN, Okada YC, and Romani GL, (eds). "Biomagnetism: Clinical Aspects", Elsevier, Amsterdam, pp 787-791.

Ahlfors S, Ilmoniemi RJ, (1989): "Magnetometer position indicator for multichannel MEG". In Williamson SJ, Hoke M, Stroink G, and Kotani M, (eds), "Advances in Biomagnetism", Plenum Press, New York, pp 693-696.

Ahonen AI, Hämäläinen MS, Ilmoniemi RJ, Kajola MJ, Knuutila JET, Simola JT, and Vilkman VA, (1993): "Sampling theory for neuromagnetic detector arrays", IEEE Trans. Biomed. Eng., 40(9): 859-869.

Aine C, Supek S, George J, Ranken D, Best E, Tiee W, Vigil V, Flynn E, and Wood C, (1995): "MEG studies of human vision: retinotopic organisation of V1". In: Baumgartner C, Deecke L, Stroink G, and Williamson SJ, (eds), "Biomagnetism: Fundamental Research and Clinical Applications", Proceedings of the 9th International Conference on Biomagnetism, Studies in Applied Electromagnetics, 7, Elsevier, Amsterdam, pp 153-161.

Alarcon G, Guy CN, Binnie CD, Walker SR, Elwes RD, and Polkey CE, (1994): "Intracerebral propagation of interictal activity in partial epilepsy: implications for source localisation", J. Neurol. Neurosurg. Psychiatry, 57(4): 435-449.

Alavi FN, Taylor JG, and Ioannides AA (1993): "Estimates of current density distributions:I. Applying the principle of cross-entropy minimization to electrographic recordings". Inverse Problem, 9:623-639.

Anogianakis G, Badier JM, Barrett G, Erné S, Fenici R, Fenwick P, Grandori F, Hari R, Ilmoniemi R, Mauguière F, Lehmann D, Perrin F, Peters M, Romani GL, and Rossini PM, (1992): "A Consensus Statement on Relative Merits of EEG and MEG". Electroenceph. Clin. Neurophysiol., 82:317-319.

Baçar E, Baçar-Eroglu C, Röschke J, and Schütt, (1989): "The EEG is a quasideterministic signal anticipating sensory-cognitive tasks". In: Baçar E, and Bullock TH, (eds), "Brain Dynamics", Springer-Verlag, Berlin, Heidelberg, pp 43-71.

Bamidis PD, (1990): "Aspects of NMR imaging", Summer Student Report, Karyn Kupcinet International School, Weizmann Institute of Sciences, Rehovot, Israel.

Bamidis PD, and Ioannides AA, (1993): "Relating function (MEG) to structure (MRI)". In Deecke L, Baumgartner C, Stroink G, Williamson SJ (eds), "Recent Advances in Biomagnetism", 9th International Conference on Biomagnetism, Book of Abstracts , Vienna, pp 241-242.

Bamidis PD, and Ioannides AA, (1996): "Combination of point and surface matching techniques for accurate registration of MEG and MRI", Book of abstracts, 10th International Conference on Biomagnetism, Santa Fe, USA, February 1996, p. 14.

Bamidis PD, Hellstrand E, Lidholm H, Abraham-Fuchs K, and Ioannides AA, (1995): "MFT in complex partial epilepsy: spatio-temporal estimates of interictal activity", Neuroreport, 7(1): 17-23.

Bartestein P, Schober O, (1992): "PET as competitor for MEG?", In: Hoke M, Erne SN, Okada YC, and Romani GL, (eds). "Biomagnetism: Clinical Aspects", Elsevier, Amsterdam, pp 669-674.

Barth DS, Sutherling WW, Engel J, and Beatty J, (1982): "Neuromagnetic localization of epileptiform spike activity in the human brain", Science, 218:891-894.

Barth DS, Sutherling WW, Engel J, and Beatty J, (1984): "Neuromagnetic evidence of spatially distributed sources underlying epileptiform spikes in the human brain", Science, 223:293-296.

Baule GM, and McFee R, (1963): "Detection of the magnetic field of the heart", Am. Heart J., 66: 95-96.

Baumgartner C, Barth DS, Levesque MF, and Sutherling WW, (1992): "Detection of epileptiform discharges by magnetoencephalography in comparison to invasive measurements". In: Hoke M, Erne SN, Okada YC, and Romani GL, (eds). "Biomagnetism: Clinical Aspects", Elsevier, Amsterdam, pp 61-66.

Baumgartner C, Lindinger G, Ebner A, Aull S, Serles W, Olbrich A, Lurger S, Czech T, Burgess R, and Lüders H, (1995): "Propagation of interictal epileptic activity in temporal lobe epilepsy", Neurology, 45(1): 118-122.

Belliveau JW, Kennedy DN, McKinstry RC, Buchbinder BR, Weiskoff RM, Cohen MS, Venea JM, Brady TJ, and Rosen BR, (1991): "Functional Mapping of the human Visual Cortex by Magnetic Resonance Imaging", Science, 254: 716-719.

Bidaut L, (1991): "Composite PET and MRI for accurate localisation and metabolic modeling: a very useful tool for research and clinic", Proc. SPIE 1445 (Image Processing): 66-67.

Binder JR, Rao SM, Hammeke TA, Yetkin FZ, Jesmanowicz A, Bandettini PA, Wong EC, Estkowski LD, Goldstein MD, Haughton VM, and Hyde JS (1994): "Functional Magnetic Resonance Imaging of Human Auditory Cortex". Ann. Neurol., 35:662-672.

BioMagList, (1995), Biomagnetism research listserver, <BioMagList@plab.se>.

Bischof M, (1994): "The history of bioelectromagnetism". In: Ho MW, Popp FA, and Warnke U, (eds), "Bioelectrodynamics and Biocommunication" World Scientific, Singapore, pp 1-31.

Boon P, (1994): "MR-scan and focal lesions", Acta Neurol. Scand., 89(Suppl. 152): 106-108.

Boone KG, and Holder DS, (1995): "Design considerations and performance of a prototype system for imaging neuronal depolarisation in the brain using 'direct current' electrical resistance tomography", Physiol. Meas., 16: A87-A98.

Brankack J and Buzsaki G (1986): "Hippocampal Responses Evoked by Tooth Pulp and Acoustic Stimulation: Depth Profiles and Effect of Behaviour", Brain Research 378:303-314.

Brazier MAB, (1973): "Historical: the role of electricity in the exploration and elucidation of the epileptic seizure". In: Brazier MAB, (ed), "Epilepsy - its phenomena in man", Academic Press, New York, pp 67-97.

Brazier MAB, (1984): "A history of neurophysiology in the 17th and 18th centuries", Raven Press, New York.

Brazier MAB, (1988): "A history of neurophysiology in the 19th century", Raven Press, New York.

Brenner D, Lipton J, Kaufman L, and Williamson SJ, (1978): "Somatically evoked magnetic fields of the human brain", Science, 199: 81-83.

Brenner D, Williamson SJ, and Kaufman L, (1975): "Visually evoked magnetic fields of the human brain", Science, 190:480-482.

Burkitt GR, Silberstein RB, and Wood AW, (1996): "The steady state visual evoked response and estimates of phase velocity", Presented at the 10th International Conference on Biomagnetism, Santa Fe, USA, February 1996.

Buser P, and Bancaud J (1983): "Unilateral connections between amygdala and hippocampus in man. A study of epileptic patients with depth electrodes", Electroenceph. Clin. Neurophysiol. 55:1-12.

Buser P, Bancaud J, and Talairach J, (1973): "Depth recordings in man in temporal lobe epilepsy". In: Brazier MAB, (ed), "Epilepsy - its phenomena in man", Academic Press, New York, pp 67-97.

Chadwick D, Mallett M, Harris R, Jenner P, Reynolds EH, and Marsden CD, (1977): "Clinical biochemical and physiological features distinguishing myoclonus response to 5-hydroxytryptophan, tryptophan with a monoamino oxidase inhibitor and clonazepam", Brain, 100: 455-487.

Chapman RM, Ilmoniemi RJ, Barbanera S, and Romani GL, (1984): "Selective localisation of alpha brain activity with neuromagnetic measurements", Electroenceph. Clin. Neurophysiol. 58: 569-572.

Chervin RD, Pierce PA, and Connors BW, (1988): "Periodicity and directionality in the propagation of epileptiform discharges across neocortex", J. Neurophysiol., 60(5): 1695-1713.

Childers DG, (1986): "Single trial event-related potentials: statistical classification and topography". In: Duffy FH, (ed), "Topographic mapping of brain electrical activity", Butterworths, Boston, London.

Clarke CJS, and Janday BS, (1989): "Probabilistic methods in a biomagnetic inverse problem", Inverse Problems, 5:483-500.

Cohen D, (1972): "Magnetoencephalography: Detection of the brain's electrical activity with a superconducting magnetometer", Science, 175:664-666.

Cohen D, and Cuffin BN, (1983): "Demonstration of useful differences between magnetoencephalogram and electroencephalogram", Electroenceph. Clin. Neurophysiol., 56: 38-51.

Cohen D, Cuffin BN, Yunokuchi K, Maniewski R, Purcell C, Cosgrove GR, Ives J, Kennedy JG, and Schomer DL, (1990): "MEG versus EEG localization test using implanted sources in the human brain", Ann. Neurol., 28:811-817.

Cohen D, Edelsack EA, and Zimmerman JE, (1970): "Magnetocardiograms taken inside a shielded room with a superconducting point-contact magnetometer", Appl. Phys. Lett., 16:278-280.

Commission on Classification and Terminology of the International League Against Epilepsy, (1981), Epilepsia, 22: 489-501.

Commission on Revised Classification of Epilepsies and Epileptic Syndromes, (1989), Epilepsia, 30: 389-399.

Corbetta M, Miezin FM, Shulman GL, and Petersen SE, (1991): "Selective attention modulates extrastriate visual regions in humans during visual feature discrimination and recognition", in "Exploring Brain Functional Anatomy with PET", Ciba Foundation Symposium 163, J Wiley & Sons.

Crease RP, (1993): "Biomedicine in the age of imaging", Science, 261: 554-561.

Cuffin BN, and Cohen D, (1977): "Magnetic fields of a dipole in special volume conductor shapes", IEEE Trans. Biomed. Eng. BME-24(4): 372-381.

Curio G, Mackert BM, Burghoff M, Koetitz R, Abraham-Fuchs K, and Härer W, (1994): "Localisation of evoked neuromagnetic 600 Hz activity in the cerebral somatosensory system", Electroenceph. Clin. Neurophysiol., 91: 483-487.

Dallas WJ, (1985): "Fourier space solution to the magnetostatic imaging problem", Appl. Opt., 24(24): 4543-4546.

Dallas WJ, Schlitt HA, Cameron SA, and Kullmann WH, (1992): "Fourier methods in biomagnetic imaging". In: Hoke M, Erne SN, Okada YC, and Romani GL, (eds). "Biomagnetism: Clinical Aspects", Elsevier, Amsterdam, pp 773-777.

Dammers J, Bamidis PD, Gross J, Clewett BS, and Ioannides AA, (1996): "Optimisation of co-registration procedures for different biomagnetic probes", Book of abstracts, 10th International Conference on Biomagnetism, Santa Fe, USA, February 1996, p. 315.

De Munck JC, (1990): "The estimation of time-varying dipoles on the basis of evoked potentials", Electroenceph. Clin. Neurophysiol., 77: 156-160.

Dijkstra AM, Brown BH, Leathard AD, Harris ND, Barber DC, and Edbrooke DL, (1993): "Review: clinical applications of electrical impedance tomography", J. Med. Eng. Technol., 17(3): 89-98.

Ducla-Soares E, (1989): "Volume current effects on MEG and modeling". In Williamson SJ, Hoke M, Stroink G, and Kotani M, (eds), "Advances in Biomagnetism", Plenum Press, New York, pp 533-538.

Duncan R, Patterson J, Roberts R, Hadley DM, and Bone I, (1993): "Ictal/postictal SPECT in the pre-surgical localisation of complex partial seizures", J. Neurol. Neurosurg. Psychiatry, 56: 141-148.

Ebeling U, Steinmetz H, Huang Y, and Kahn T, (1989): "Topography and identification of the inferior precentral sulcus in MR imaging", AJNR: Am. J. Neuroradiol., 10: 937-942.

Ebersole JS, (1995): "Functional imaging of spike propagation using combined MEG and EEG dipole modelling", Human Brain Mapping, Suppl 1:1, p 419.

Ebersole JS, (1996), Personal notes from the "Workshop on MEG and epilepsy", 10th International Conference on Biomagnetism, Santa Fe, USA, February 1996.

Ebersole JS, and Smith JR, (1994): "MEG spike modelling differentiates baso-mesial from lateral cortical temporal epilepsy". In: "Program and abstracts of the American Electroencephalographic Society", p 65.

Ebersole JS, Squires KC, Eliashiv SD, and Smith JR, (1995): "Applications of magnetic source imaging in evaluation of candidates for epilepsy surgery", Neuroimaging Clinics of North America, 5(2): 267-288.

Elger CE, (1992): "Facts in epileptology which are of possible relevance for biomagnetism". In: Hoke M, Erne SN, Okada YC, and Romani GL, (eds). "Biomagnetism: Clinical Aspects", Elsevier, Amsterdam, pp 53-60.

Eliashiv SD, Velassco AL, Wilson CL, et al, (1994): "Magnetic source imaging as a predictor of invasive-electrode-defined irritative and ictal onset zones". In:

"Program and abstracts of the American Electroencephalographic Society", p 65.

Emerson RG, Turner CA, Pedley TA *et al, Electroenceph. Clin. Neurophysiol.* 94:338-348 (1995).

Emerson RG, Turner CA, Pedley TA, Walczak TS, and Forgione M, (1995): "Propagation patterns of temporal spikes", Electroenceph. Clin. Neurophysiol. 94:338-348.

Ernst T, and Hennig J, (1994): "Observation of a fast response in functional MR", Magn. Res. Med., 32: 146-149.

Evans AC, Marrett S, Collins L, and Peters TM, (1989): "Anatomical-functional correlative analysis of the human brain using 3D imaging systems", Proc. SPIE 1092 (Medical Imaging 3: Image processing): 264-274.

Fenwick P (1990): "The use of Magnetoencephalography in Neurology", in Advances in Neurology, Vol 54: "Magnetoencephalography", (ed) Sato S, Raven Press, New York.

Fenwick PBC, Ioannides AA, Fenton GW, Lumsden J, Grummich P, Kober H, Daun A, and Vieth J, (1993): "Estimates of Brain Activity using Magnetic Field Tomography in a GO/NOGO avoidance paradigm", Brain Topogr., 5:275-282.

Fieseler T, Ioannides AA, Liu MJ, and Nowak H, (1995): "Model studies of the accuracy of the conducting sphere model in magnetoencephalography using the spheroid". In: Baumgartner C, Deecke L, Stroink G, and Williamson SJ, (eds), "Biomagnetism: Fundamental Research and Clinical Applications", Proceedings of the 9th International Conference on Biomagnetism, Studies in Applied Electromagnetics, 7, Elsevier, Amsterdam, pp 445-449.

Foley JD, and Van Dam A (1989): "Fundamentals of Interactive Computer Graphics", Addison -Wesley Publishing Company.

Forss N, Jousmäki V, and Hari R, (1995): "Interaction between afferent input from fingers in human somatosensory cortex", Brain Res., 685: 68-76.

Fox PT, Lancaster JL, Davis G, and Mikiten SA, (1995): "BrainMap: a community database of human functional neuroanatomy", Human Brain Mapping, Suppl 1:1, p 74.

Fox PT, Raichle ME, Mintun MA, and Dence C, (1988): "Nonoxidative glucose consumption during focal physiologic neural activity", Science, 241: 462-464.

Franck G, Sadzot B, Salmon E, Depresseux JC, Grisar T, Peters JM, Guillaume M, Quaglia L, Delfiore G, and Lamotte D, (1986): "Regional cerebral blood flow and metabolic rates in human focal epilepsy and status epilepticus". In: Delgado-Escueta AV, Ward AA Jr, Woodbury DM, and Porter RJ, (eds), "Advances in Neurology", Vol 44, Raven Press, New York, pp 935-948.

Friberg L, and Lonborg-Jensen H, (1994): "Visual inspection versus quantified analysis of functional brain images", Acta Neurol. Scand., 89(Suppl. 152): 169-174.

Friston KJ, (1994): "Functional and effective connectivity in neuroimaging: a synthesis", Human Brain Mapping, 2: 56-78.

Friston KJ, Holmes AP, Poline JB, Grasby PJ, Williams SCR, Frackowiak RSJ, and Turner R, (1995): "Analysis of fMRI Time-Series Revisited", Neuroimage 2:45-53.

Friston KJ, Jezzard P, and Turner R, (1994): "Analysis of functional MRI time-series", Human Brain Mapping, 1: 153-171.

Frith CD, Friston K, Liddle PF, and Frackowiak RSJ (1991): "Willed action and the prefrontal cortex in man: a study with PET", Proc. R. Soc. Lond. B, 244:241-246.

Fuchs H, Levoy M, and Pizer SM (1990): "Interactive visualisation of 3D medical data". In Nielson GM et al (eds), "Visualisation in Scientific Computing", IEEE Computer Society Press, Los Alamitos, California.

Fuchs M, Wagner M, Wischmann HA, and Dössel O, (1995): "Cortical current imaging by morphologically constrained reconstructions". In: Baumgartner C, Deecke L, Stroink G, and Williamson SJ, (eds), "Biomagnetism: Fundamental Research and Clinical Applications", Proceedings of the 9th International Conference on Biomagnetism, Studies in Applied Electromagnetics, 7, Elsevier, Amsterdam, pp 320-325.

Gadian DG, (1993): "MRS and brain chemistry: clinical applications", Personal notes from the 'Glaxo advanced lecturee series on Neuroimaging', Spring Term, 10 February 1993, London.

Gadian DG, Connely A, Duncan JS, Cross JH, Kirkham FJ, Johnson CL, Vargha-Khadem F, Neville BGR, and GD Jackson, (1994): "^{1}H magnetic resonance spectroscopy in the investigation of intractable epilepsy", Acta Neurol. Scand., 89(Suppl. 152): 116-121.

Galen CC, Schwartz B, Pantev C, Hampson S, Sobel D, Hirschkoff E, Rieke K, Otis S, and Bloom F, (1992): "Detection and localisation of delta frequency activity in human strokes". In: Hoke M, Erne SN, Okada YC, and Romani GL, (eds). "Biomagnetism: Clinical Aspects", Elsevier, Amsterdam, pp 301-305.

Gallen CC, Gamelin JY, Lawson DS, et al, (1993): "Rapid localisation of multiple independent sources of epileptic activity using bilateral large array MEG", Epilepsia, 34(Suppl 6): 84.

Gallen CC, Hirschkoff EC, and Buchanan DS, (1995): "Magnetoencephalography and magnetic source imaging; capabilities and limitations", Neuroimaging Clinics of North America, 5(2): 227-249.

George JS, Aine CJ, Medvick PA, and Flynn ER, (1989): "Spatial/temporal resolution of multiple sources: paths of activation in human visual cortex", In Williamson SJ, Hoke M, Stroink G, and Kotani M, (eds), "Advances in Biomagnetism", Plenum Press, New York, pp 197-200.

George JS, Lewis PS, Schlitt HA, Kaplan L, Gorodnitsky IF, and Wood CC, (1995a): "Strategies for source space limitation in tomographic inverse procedures". In: Baumgartner C, Deecke L, Stroink G, and Williamson SJ, (eds), "Biomagnetism: Fundamental Research and Clinical Applications", Proceedings of the 9th International Conference on Biomagnetism, Studies in Applied Electromagnetics, 7, Elsevier, Amsterdam, pp 357-362.

George JS, Saunders JA, Lewine JD, Caprihan A, and Aine CJ, (1995b):: "Comparative studies of brain activation with MEG and Functional MRI", In: Baumgartner C, Deecke L, Stroink G, and Williamson SJ, (eds), "Biomagnetism: Fundamental Research and Clinical Applications", Proceedings of the 9th International Conference on Biomagnetism, Studies in Applied Electromagnetics, 7, Elsevier, Amsterdam, pp 60-65.

Gevins A, and Smith ME, (1995): "Subsecond dynamics of cortical networks of human working memory", Human Brain Mapping, Suppl 1:1, p 415.

Gevins A, Brickett P, Costales B, Le J, and Reutter B, (1990): "Beyond Topographic Mapping: towards Functional Anatomical Imaging with 124-Channel EEGs and 3-D MRIs", Brain Topography, 3(1): 53-64.

Gevins A, Le J, Brickett P, Reutter B, and Desmond J, (1991): "Seeing through the skull: advanced EEGs use MRIs to accurately measure cortical activity from the scalp", Brain Topography, 4(2): 125-131.

Gibbs FA, Davis H, and Lennox WG, (1935): "The electroencephalogram in epilepsy and in conditions of impaired consciousness", Arch. Neurol. Psychiatry (Chicago), 34: 1133-1148.

Gorodnitsky IF, (1995): "A novel class of recursively constrained algorithms for localised energy solutions: theory and application to magnetoencephalography and signal processing", PhD thesis, University of California, San Diego, USA.

Gorodnitsky IF, George JS, Schlitt HA, and Lewis PS, (1992): "A weighted iterative algorithm for neuromagnetic imaging". In: Dittmar A, and Froment JC, (eds), "IEEE/EMBS Symposium on Neuroscience and Technology", Lyon, France, pp 60-64.

Graf M, Niedermeyer J, Schiemann J, Uematsu S, Long DM, (1984): "Electrocorticography: information derived from intraoperative recordings during seizure surgery", Clin. Electroenceph. 15(2):83-91.

Greenblatt R, (1996), Presentation during the Workshop on the "Biomagnetic Inverse Problems", 10th International Conference on Biomagnetism, Santa Fe, USA, February 1996.

Greitz T, Bohm C, Holte S, and Eriksson L, (1991): "A Computerized Brain Atlas: Construction, Anatomical Content, and Some Applications", J. Comp. Assist. Tomography, 15(1): 26-38.

Grummich P, Kober H, and Vieth J, (1992): "Localisation of the underlying currents of magnetic barin activity using spatial filtering", Biomed. Eng., 37(Suppl. 2): 158-159.

Grynszpan F, and Geselowitz DB, (1973): "Model studies of the magnetocardiogram", Biophys. J., 13: 911-925.

Haig AR, Gordon E, Rogers G, and Anderson J, (1995): "Classification of single-trial ERP sub-types: application of globally optimal vector quantization using simulated annealing", Electroenceph. Clin. Neurophysiol., 94: 288-297.

Halgren E, (1996): "Depth recordings for MEG localisation", Personal notes from the invited presentation at the 10th International Conference on Biomagnetism, Santa Fe, USA, February 1996.

Halgren E, Squires NK, Wilson CL, Rohrbaugh JW, Babb TL, and Crandall PH, (1980): "Endogenous potentials generated in the human hippocampal formation and amygdala by infrequent events", Science, 210(14): 803-805.

Hämäläinen MS (1991): "Anatomical correlates for Magnetoencephalography: integration with magnetic resonance images", Clin. Phys. Physiol. Meas., 12(Sup A): 29-32.

Hämäläinen MS, and Ilmoniemi RJ, (1984): "Interpreting measured magnetic fields of the brain: estimates of current distributions", Technical report TKK-F-A559, Helsinki University of Technology, Finland.

Hämäläinen MS, and Ilmoniemi RJ, (1994): "Interpreting magnetic fields of the brain: minimum norm estimates", Med. Biol. Eng. & Comput., 32: 35-42.

Hämäläinen MS, and Sarvas J, (1987): "Feasibility of the homogeneous head model in the interpretation of neuromagnetic fields", Phys. Med. Biol., 32(1): 91-97.

Hämäläinen MS, and Sarvas J, (1989): "Realistic conductivity geometry model of the human head for interpretation of neuromagnetic data", IEEE Trans. Biomed. Eng., 36: 165-171.

Hämäläinen MS, Hari R, Ilmoniemi RJ, Knuutila J, and Lounasmaa OV, (1993):: "MEG-theory, intsrumentation, and applications to non-invasive studies of the working human brain", Reviews of Modern Physics, 65(2):413-497.

Hari R, (1990): "The neuromagnetic method in the study of the human auditory cortex". In: Grandori F, Hoke M, and Romani GL, (eds), "Auditory Evoked Magnetic Fields and Electric Potentials", Advances in Audiology, Vol 6, Karger, Basel, pp 222-282.

Hari R, (1993): "Magnetoencephalography as a tool of clinical neurophysiology". In: Niedermeyer E, and Lopez da Silva F, (eds), "Electroencephalography: basic principles, clinical applications, and Related Fields", 3rd Edition, Urban and Schwarzenberg, Baltimore, Münich, pp 1035-1061.

Hari R, Ahonen A, Forss N, Granström ML, Hämäläinen MS, Kajola M, Knuutila J, Lounasmaa OV, Mäkelä JP, Paetau R, Salmelin R, and Simola J, (1993): "Parietal epileptic mirror focus detected with a whole-head neuromagnetomer", NeuroReport, 5: 45-48.

Hari R, and Ilmoniemi RJ, (1986): "Cerebral magnetic fields", CRC Crit. Rev. Biomed. Eng., 14: 93-126.

Hari R, Hämäläinen MS, Ilmoniemi RJ, and Lounasmaa OV, (1991): Comment on "MEG versus EEG localisation test using implanted sources in the human brain", Letter to the Editor, Ann. Neurol., 30: 222-223.

Hari R, Reinikainen K, Kaukoranta E, Hämäläinen MS, Ilmoniemi RJ, Pentiinen A, Salminen J, and Teszner D, (1984): "Somatosensory evoked cerebral magnetic fields from SI and SII in man", Electroenceph. Clin. Neurophysiol., 57: 254-263.

Hashimoto T, Tayama M, Murakawa K, Yoshimoto T, Miyazaki M, Harada M, and Kuroda Y, (1995): "Development of the brain stem and cerebellum in autistic patients", J. Autism Dev. Disord., 25(1): 1-18.

Hasson R, (1991): "Mixed EEG/MEG imaging: a way forward". In "Biomagnetic localisation and 3d modelling", Report TKK-F-A689, Helsinki University of Technology, pp 125-136.

Haxby J, (1995): "Functional magnetic resonance imaging of the human brain: visual neuroanatomy", pp 297-298. In: Le Bihan D, moderator, "Functional magnetic resonance imaging of the brain", Ann. Intern. Med., 122: 296-303.

Heiken JP, Brink JA, and Vannier MW, (1993): "Spiral (helical) CT", Radiol., 189: 647-656.

Hellstrand E, (1995), Private Communication.

Hellstrand E, Abraham-Fuchs K, Jernberg B, Kihlström L, Knutsson E, Lindquist C, Schneider S, and Wirth A, (1993): "MEG localisation of interictal epileptic focal activity and concomitant stereotactic radiosurgery. A non-invasive approach for patients with focal epilepsy", Physiol. Meas., 14: 131-136.

Hellstrand E, Knutsson E, Schneider S, Striebel W, Gebhardt M, Liedholm H, Jernberg B, Lindquist C, and Kihlström L, (1995): "Magnetoencephalographic screening of children and adults: patients with signs and symptoms of epilepsy". In: Baumgartner C, Deecke L, Stroink G, and Williamson SJ, (eds), "Biomagnetism: Fundamental Research and Clinical Applications", Proceedings of the 9th International Conference on Biomagnetism, Studies in Applied Electromagnetics, 7, Elsevier, Amsterdam, pp 35-38.

Helmholtz H von, (1853): "Ueber einige gesetze der vertheilung elektrischer ströme in körperlichen leitern, mit anwendung auf die thierisch-elektrischen versuche", Ann. Phys. Chem., 89: 211-233, 353-377.

Hill DLG, Hawkes DJ, Crossman JE, Gleeson MJ, Cox TCS, Bracey EECMC, Strong AJ, and Graves P (1991): "Registration of MR and CT images for skull base surgery using point-like anatomical features", Br. J. Radiol., 64: 1030-1035.

Hoenig HE, Daalmans GM, Bär L, Bömmel F, Paulus A, Uhl D, Weisse HJ, Schneider S, Seifert H, Reichenberger H, and Abraham-Fuchs K, (1991): "Multi channel dc SQUID sensor array for biomagnetic applications", IEEE Trans. Magn., 27: 2777-2785.

Holder DS, (1993): "Opportunities for EIT in the nervous system". In: Holder DS, (ed), "Clinical and physiological applications of electrical impedance tomography", UCL, London, pp 166-176.

Hoshi Y, and Tamura M, (1993): "Detection of dynamic changes in cerebral oxygenation coupled to neuronal function during mental work in man", Neuroscience Letters, 150: 5-8.

Hounsfield GN, (1973): "Computerised transverse axial scanning (tomography). Part 1: description of system", Br. J. Radiol., 46: 1016-1022.

Ibanez V, Deiber MP, and Fischer C, (1989): "Middle latency auditory potentials in cortical lesions", Arch. Neurol. 46:1325-1332.

IFSECN, (1974): "A glossary of terms commonly used by clinical electroencephalographers", Electroenceph. Clin. Neurophysiol., 37: 538-548.

Ilmoniemi RJ, (1994): "Magnetic source imaging". In: Carpenter DO, and Ayrapetyan S, (eds), "Biological effects of electric and magnetic fields", Academic Press, San Diego, Vol 2, pp 49-79.

Ilmoniemi RJ, and Numminen JK, (1992): "Synthetic magnetometer channels for standrad representation of data". In: Hoke M, Erne SN, Okada YC, and Romani GL, (eds). "Biomagnetism: Clinical Aspects", Elsevier, Amsterdam, pp 793-796.

Ilmoniemi RJ, Hämäläinen MS, and Knuutila J, (1985): "The forward and inverse problems in the spherical model". In Weinberg H, Stroink G, and Katila T, (eds) "Biomagnetism: applications & theory", Pergamon, New York, pp 278-282.

Ioannides AA, (1987): "Graphical solutions and representations for the biomagnetic inverse problem". In: Sabatier PC, (ed), "Advances in Electronics

and Electron Physics Supplement 19, Inverse Problems: an Interdisciplinary Study", Academic Press, Orlando, pp 205-216.

Ioannides AA, (1991): "Comparison of MEG with other functional imaging techniques", Clinical Physics and Physiological Measurement, 12(supplA):23-28.

Ioannides AA, (1993): "Searchlights into the brain", Open University video, Milton Keynes, UK.

Ioannides AA, (1994): "Estimates of Brain Activity using Magnetic Field Tomography and large scale communication within the brain. In: Ho MW, Popp FA, and Warnke U, (eds), "Bioelectrodynamics and Biocommunication" World Scientific, Singapore, pp 319-353.

Ioannides AA, (1995a): "Estimates of 3D brain activity ms by ms from Biomagnetic signals: Method (MFT), results and their significance", In: Eiselt E, Zwiener U, and Witte H, (eds), "Quantitative and Topological EEG and MEG analysis", Universitätsverlag Druckhaus-Maayer GmbH, Jena, pp 59-68.

Ioannides AA, (1995b): "Distributed source analysis and Magnetic Field Tomography", In: Baumgartner C, Deecke L, Stroink G, and Williamson SJ, (eds), "Biomagnetism: Fundamental Research and Clinical Applications", Proceedings of the 9th International Conference on Biomagnetism, Studies in Applied Electromagnetics, 7, Elsevier, Amsterdam, pp 373-375.

Ioannides AA, Bolton JPR, and Clarke CJS, (1990): "Continuous Probabilistic Solutions to the biomagnetic inverse problem", Inverse Problems, 6:523-542.

Ioannides AA, Fenwick PBC, Lumsden J, Liu MJ, Bamidis PD, Squires KC, Lawson D, and Fenton GW, (1994): "Activation sequence of discrete brain areas during cognitive processes: Results from Magnetic Field Tomography", Electroenceph. Clin. Neurophysiol., 91: 399-402.

Ioannides AA, Hasson R, and Miseldine GJ, (1990): "Model-dependent noise elimination and distributed source solutions for the biomagnetic inverse problem". In: Gmitro AF, Idell PS, and LaHaie IJ, (eds), "Digital Image Synthesis and Inverse Optics", Proc. SPIE 1351 (Int. Soc. Opt. Eng.), Bellingham, San Diego, pp. 471-481.

Ioannides AA, Hellstrand E, and Abraham-Fuchs K, (1993c): "Point and distributed current density analysis of interictal epileptic activity recorded by Magnetoencephalography", Physiol. Meas., 14:121-130.

Ioannides AA, Hellstrand E, Bamidis PD, and Abraham-Fuchs K, (1995a): "Estimates of brain activity from unaveraged interictal multichannel magnetoencephalographic signals". In: Baumgartner C, Deecke L, Stroink G, and Williamson SJ, (eds), "Biomagnetism: Fundamental Research and Clinical Applications", Proceedings of the 9th International Conference on Biomagnetism, Studies in Applied Electromagnetics, 7, Elsevier, Amsterdam, pp 326-329.

Ioannides AA, Liu MJ, Liu LC, Bamidis PD, Hellstrand E, and Stephan KM, (1995b): "Magnetic Field Tomography of cortical and deep processes: examples of "real-time mapping" of averaged and single trial MEG signals", International Journal of Psychophysiology, 20(3):161-175.

Ioannides AA, Mueller-Gaertner HW, Bamidis PD, Weise F, Hacklaender T, Dammers J, and Liu MJ, (1995d), "The P300 Generators: where and when are they activated. An MFT investigation using bihemispheric MEG signals", Human Brain Mapping, Supplement 1:1, p 176.

Ioannides AA, Muratore R, Balish M, and Sato S, (1993b): "In vivo validation of distributed source solutions for the biomagnetic inverse problem", Brain Topography, 5:263-273.

Ioannides AA, Singh KD, Hasson R, Baumann SB, Rogers RL, Guinto FC, and Papanicolaou AC, (1993a): "Comparison of Current Dipole and Magnetic Field Tomography Analyses of the Cortical Response to Auditory Stimuli", Brain Topography, 6:27-34.

Ioannides AA, Stephan KM, Fenwick PBC, Lumsden J, Fenton GW, Liu MJ, Vieth J, Squires KC, Lawson D, Myers R, Fink GR, and Frackowiak RSJ, (1995c): "Analysis of MEG signals from a GO/NOGO avoidance paradigm and comparison of estimates of brain activity using PET", In: Baumgartner C, Deecke L, Stroink G, and Williamson SJ, (eds), "Biomagnetism: Fundamental Research and Clinical Applications", Proceedings of the 9th International Conference on Biomagnetism, Studies in Applied Electromagnetics, 7, Elsevier, Amsterdam, pp 262-265.

Jackson GD, Conelly A, Cross JH, Gordon I, and Gadian DG, (1994): "Functional magnetic resonance imaging of focal seizures", Neurology, 44:850-856.

Jones WHS, (1981): "Hippocrates Vol II; with an English translation". In: Goold GP, (ed), "The Loeb classical library", Vol 148, 6th Edition, Fletcher & Son Ltd, Norwich, UK.

Jongschaap HCN, Wytch R, Hutchison JMS, and Kulkarni V, (1994): "Electrical impedance tomography: a review of current literature", Europ. J. Radiol., 18: 165-174.

Josephs O, Fiaschi KA, Singh KD, and Swithenby SJ, (1995): "A multichannel tangential-field gradiometer system". In: Baumgartner C, Deecke L, Stroink G, and Williamson SJ, (eds), "Biomagnetism: Fundamental Research and Clinical Applications", Proceedings of the 9th International Conference on Biomagnetism, Studies in Applied Electromagnetics, 7, Elsevier, Amsterdam, pp 490-492.

Josephson BD, (1962): "Possible new effects in superconductive tunneling", Phys. Lett., 1: 251-253.

Kado H, (1995): "The national project of the superconducting sensor laboratory in Japan". In: Baumgartner C, Deecke L, Stroink G, and Williamson SJ, (eds), "Biomagnetism: Fundamental Research and Clinical Applications", Proceedings of the 9th International Conference on Biomagnetism, Studies in Applied Electromagnetics, 7, Elsevier, Amsterdam, pp 471-475.

Kamada K, Takeuchi F, Kuriki S, Oshiro O, Houkin K, Abe H, (1993): "Functional neurosurgical simulation with brain surface magnetic resonance images and magnetoencephalography", Neurosurgery, 33(2): 269-273.

Katila TE, (1983): "On the current multipole presentation of the primary current distributions", Nuovo Cimento D, 2: 660-664.

Kessler ML, (1989): "Integration of multimodality imaging data for radiotherapy treatment planning", PhD Thesis, University of California at Berkeley.

Kober H, Grummich P, and Vieth J (1995): "Fit of the digitized headsurface with surface reconstructed from MRI-Tomography", In: Baumgartner C, Deecke L, Stroink G, and Williamson SJ, (eds), "Biomagnetism: Fundamental Research and Clinical Applications", Proceedings of the 9th International Conference on Biomagnetism, Studies in Applied Electromagnetics, 7, Elsevier, Amsterdam, pp 309-312.

Koshevnikov, (1895): "Eine besondere form von corticaler epilepsie", Neurol. Centralbl., 14: 47-48.

Kraus N, Özdamar Ö, Hier D, and Stein L, (1982): "Auditory middle latency auditory evoked responses (MLRs) in patients with cortical lesions", Electroenceph. Clin. Neurophysiol., 54:275-287.

Kullmann W, and Dallas WJ, (1987): "Fourier imaging of electrical currents in the human brain from their magnetic fields", IEEE Trans. Biomed. Eng., BME-34(11): 837-842.

Kullmann W, Jandt KD, Rehm K, Schlitt HA, Dallas WJ, and Smith WE, (1989): "A linear estimation approach to biomagnetic imaging". In Williamson SJ, Hoke M, Stroink G, and Kotani M, (eds), "Advances in Biomagnetism", Plenum Press, New York, pp 571-574.

Kwong KK, Belliveau JW, Chesler DA, Goldberg IE, Weiskoff RM, Poncelet BP, Kennedy DN, Hoppel BE, Cohen MS, Turner R, Cheng HM, Brady T, and Rosen BR, (1992): "Dynamic magnetic resonance imaging of human brain activity during primary sensory stimulation", Proc. Natl. Acad. Sci. USA, 89:5675-5679.

Lado FA, (1993): "Coherent oscillations and the creation of functional states in the motor areas of the human brain", Disseration in the Basic Medical Sciences Program, Department of Physiology and Biophysics, The Sackler Institute of Graduate Biomedical Sciences, School of Medicine, Graduate School of Arts and Sciences, New York University, USA.

Lado FA, Ribary U, Ioannides AA, Volkmann J, Joliot M, Mogilner A, and Llinás R, (1992): "Coherent oscillations in primary motor and sensory cortices detected using MEG and MFT", Neuroscience Annual Meeting, Book of Abstracts.

Lagerlund TD, Sharbrough FW, Jack CR, Erickson BJ, Strelav DC, Cicora KM, and Busacker NE, (1993): "Determination of 10-20 system electrode locations using magnetic resonance imaging scanning with markers", Electroenc. Clin. Neurophysiology, 86: 7-14.

Laxer KD, Rowley HA, Novotny EJ, Gates JR, Sato S, Sutherling WW, Elger CE, Ebersole JS, and Stefan H, (1993): "Experimental technologies". In Engel J (ed), "Surgical treatment of the epilepsies", 2nd Edition, Raven Press, New York, pp 291-308.

Lehmann D, (1989): "Microstates of the brain in EEG and ERP mapping studies". In: Baçar E, and Bullock TH, (eds), "Brain Dynamics", Springer-Verlag, Berlin, Heidelberg, pp 72-83.

Leksell L, (1971): "Stereotaxis and Radiosurgery. An Operative System", Thomas, Springfield.

Lemieux JF, and Blume WT, (1986): "Topographical evolution of spike-wave complexes", Brain Res., 373: 275-287.

Lewine JD, Orrison WW Jr, Astur RS, Davis LE, Knight JE, Maclin EL, Reeve A, (1995): "Explorations of pathophysiological spontaneous activity by magnetic source imaging". In: Baumgartner C, Deecke L, Stroink G, and Williamson SJ, (eds), "Biomagnetism: Fundamental Research and Clinical Applications", Proceedings of the 9th International Conference on Biomagnetism, Studies in Applied Electromagnetics, 7, Elsevier, Amsterdam, pp 55-59.

Liégeois-Chauvel C, Musolino A, Badier JM, Marquis P, and Chauvel P, (1994): "Evoked potentials recorded from the auditory cortex in man: evaluation and topography of the middle latency components", Electroenceph. Clin. Neurophysiol., 92:204-214.

Liu LC, (1995): "Single epoch analysis and bi-hemispheric study of magnetoencephalographic (MEG) signals using vector signal transformation V3 and Magnetic Field Tomography (MFT)", PhD Thesis, The Open University, Milton Keynes, UK.

Liu LC, and Ioannides AA, (1995): "Single epoch analysis of MEG signals", In: Baumgartner C, Deecke L, Stroink G, and Williamson SJ, (eds), "Biomagnetism: Fundamental Research and Clinical Applications", Proceedings of the 9th International Conference on Biomagnetism, Studies in Applied Electromagnetics, 7, Elsevier, Amsterdam, pp 439-444.

Liu LC, and Ioannides AA, (1996): "A correlation study of averaged and single trial MEG signals: the average describes multiple histories each in a different set of single trials", Brain Topogr., In Press.

Liu MJ, and Ioannides AA, (1995): "Choice of source space for Magnetic Filed Tomography". In: Baumgartner C, Deecke L, Stroink G, and Williamson SJ, (eds), "Biomagnetism: Fundamental Research and Clinical Applications", Proceedings of the 9th International Conference on Biomagnetism, Studies in Applied Electromagnetics, 7, Elsevier, Amsterdam, pp 385-388.

Liu MJ, Fenwick PBC, Lumsden J, Lever C, Stephan KM, and Ioannides AA, (1996): "Averaged and single-trial analysis of cortical activation sequences in movement preparation, initiation, and inhibition", Submitted for publication in Human Brain Mapping, March 1996.

Liu MJ, Hasson R, and Ioannides AA, (1993): "A transputer-based system for Magnetic Field Tomography". In: Grebe R, Hektor J, Hilton SC, Jane M, and Welch PH, (eds.), "Transputer Applications and Systems '93", IOS Press, Amsterdam, Vol. 2, pp.1290-1297.

Lopez da Silva F, (1996), Private communication.

Lüders HO, and Awad I, (1992): "Conceptual considerations". In: Lüders HO, (ed), "Epilepsy Surgery", Raven Press, New York, pp 51-62.

Lüders HO, Engel J Jr, and Munari C, (1993): "General principles". In: Engel J Jr, (ed), "Surgical treatment of the epilepsies", 2nd Edition, Raven Press, New York, pp 137-153.

Lütkenhöner B, Pantev C, and Hoke M, (1990): "Comparison between different methods to approximate an area of the human head by a sphere". In: Grandori F, Hoke M, and Romani GL, (eds), "Auditory Evoked Magnetic Fields and Electric Potentials", Advances in Audiology, Vol 6, Karger, Basel, pp 103-118.

Mäkelä JP, Hämäläinen MS, Hari R, and McEvoy L, (1994): "Whole-head mapping of middle-latency auditory evoked magnetic fields", Electroenceph. Clin. Neurophysiol., 92:414-421.

Mazziotta JC, (1995), Personal notes from the discussion during the "Special Section: 'ICBM'", 1st Int. Conference on Functional Mapping of the Human Brain, Paris, June 27-30, 1995.

Mazziotta JC, Valentino D, Grafton S, Bookstein F, Pelizzari C, Chen C, and Toga AW, (1991): "Relating structure to function in vivo with tomographic imaging". In "Exploring Brain Functional Anatomy with PET", Ciba Foundation Symposium 163, J Wiley & Sons.

McGovern S, (1982): "The epilepsy handbook", Overcoming common problems: series, Sheldon Press, London.

Menon RS, Ogawa S, Hu X, Strupp JP, Anderson P, and Ugurbil K, (1995): "BOLD based functional MRI at 4 Tesla includes a capillary bed contribution: echo-

planar imaging correlates with previous optical imaging using intrinsic signals", Magn. Res. Med., 33(3): 453-459.

Mintun MA, Fox PT, and Raichle ME, (1989): "A highly accurate method of localising regions of neuronal activation in the human brain with positron emission tomography", J. Cereb. Blood Flow Metab., 9: 96-103.

Morris GL III, Mueller WM, Yetkin FZ, Haughton VM, Hammeke TA, Swanson S, Rao SM, Jesmanowicz A, Estkowski LD, Bandettini PA, Wong EC, and Hyde JS, (1994): "Functional magnetic resonance imaging in partial epilepsy", Epilepsia, 35(6): 1194-1198.

Mosher JC, (1993): "Localisation from near-source quasi-static electromagnetic fields", PhD thesis, University of California, Los Alamos National Laboratory, New Mexico, USA.

Mosher JC, Lewis PS, and Leahy RM, (1992): "Coherence and MUSIC in biomagnetic source localisation". In: Baumgartner C, Deecke L, Stroink G, and Williamson SJ, (eds), "Biomagnetism: Fundamental Research and Clinical Applications", Proceedings of the 9th International Conference on Biomagnetism, Studies in Applied Electromagnetics, 7, Elsevier, Amsterdam, pp 330-334.

Mosher JC, Lewis PS, and Leahy RM, (1992): "Multiple dipole modelling and localisation from spatio-temporal MEG data", IEEE Trans. Biomed. Eng., 39: 541-557.

Mosher JC, Lewis PS, Leahy RM, and Singh M, (1990): "Multiple dipole modelling of spatio-temporal MEG data". In: Gmitro GF, Idell PS, and LaHaie IJ, (eds), "Digital image synthesis and inverse optics", Proc. SPIE 1351 (Int. Soc. Opt. Eng.), Bellingham, San Diego, pp 364-375.

Nakasato N, Levesque MF, Barth DS, Baumgartner C, Rogers RL, and Sutherling WW, (1994): "Comparisons of MEG, EEG, and ECoG source localisation in neocortical partial epilepsy in humans", Electroenceph. Clin. Neurophysiol. 171:171-178.

Neiw HM, Chen CT, Lin WC, and Pelizzari CA, (1991): "Automated three-dimensional registration of medical images", Proc. SPIE 1445 (Image Processing): 259-264.

Neuro Scan News, (1995), Vol VI, No. 1.

Niedermeyer E, (1993a): "Historical aspects". In: Niedermeyer E, and Lopez da Silva F, (eds), "Electroencephalography: basic principles, clinical applications, and Related Fields", 3rd Edition, Urban and Schwarzenberg, Baltimore, Münich, pp 1-14.

Niedermeyer E, (1993b): "Abnormal EEG patterns: epileptic and paroxysmal". In: Niedermeyer E, and Lopez da Silva F, (eds), "Electroencephalography: basic principles, clinical applications, and Related Fields", 3rd Edition, Urban and Schwarzenberg, Baltimore, Münich, pp 217-239.

Niedermeyer E, (1993c): "Epileptic seizure disorders". In: Niedermeyer E, and Lopez da Silva F, (eds), "Electroencephalography: basic principles, clinical applications, and Related Fields", 3rd Edition, Urban and Schwarzenberg, Baltimore, Münich, pp 461-564.

Nolte J, (1981): "The human brain: an introduction to its functional anatomy", The C.V. Mosby Company, St. Luis, USA, pp 270-271.

Nyquist H, (1928): "Certain topics in telegraph transmission theory", Trans. AIEE, 47: 617-644.

Okada YC, and Nicholson C, (1988): "Magnetic evoked field associated with transcortical currents in turtle cerebellum", Biophys. J., 53: 723-731.

Okada YC, and Xu C, (1993): "Magnetocorticography", In Deecke L, Baumgartner C, Stroink G, Williamson SJ (eds), "Recent Advances in Biomagnetism", 9th International Conference on Biomagnetism, Book of Abstracts , Vienna, pp 408-409.

Okada YC, Kaufman L, and Williamson SJ, (1983): "The hippocampal formation as a source of the slow endogenous potentials", Electroenceph. Clin. Neurophysiol., 55:417-426.

Paetau R, Kajola M, Karhu J, Nousiainen U, Partanen J, Tiihonen J, Vapalahti M, and Hari R, (1992): "MEG localisation of epileptic cortex–impact on surgical treatment", Ann. Neurol. 32:106-109.

Papanicolaou AC, Rogers RL, Baumann SB, Saydjari C, and Eisenberg HM, (1990): "Source localization of two evoked magnetic field components using two alternative procedures", Exp. Brain Res., 80:44-48.

Pascual-Marqui RD, Michel CM, and Lehmann D, (1994): "Low resolution electromagnetic tomography: a new method for localising electrical activity in the brain", Int. J. Psychophysiol., 18: 49-65.

Pascual-Marqui RD, Michel CM, and Lehmann D, (1995): "Segmentation of brain electrical activity into microstates: model estimation and validation", IEEE Trans. Biomed. Eng., 42(7): 658-665.

Pelizzari CA, Chen GTY, Spelbring DR, Weichselbaum RR, and Chen CT, (1989): "Accurate 3D correlation of CT, PET, and/or MR images of the brain", J. Comp. Assist. Tomography, 13: 20-26.

Penfield W, and Jasper H, (1954): "Epilepsy and the functional anatomy of the human brain", Little, Brown, Boston.

Perrin F, Bertrand O, and Pernier J, (1987): "Scalp current density mapping: value and estimation of potential data", IEEE Trans. Biome. Eng., 34: 283-287.

Petche H, and Sterc J, (1967): "The significance of the cortex for the travelling phenomenon of brain waves", Electroenceph. Clin. Neurophysiol., 25: 11-22.

Peters TM, Clark JA, Olivier A, Marchand EP, Mawko G, Dieumegarde M, Muresan LV, and Ethier R, (1986): "Integrated Stereotaxic Imaging with CT, MR imaging, and Digital Substraction Angiography", Radiology, 161:821-826.

Pizella V, (1995): "The Italian biomagnetic projects". In: Baumgartner C, Deecke L, Stroink G, and Williamson SJ, (eds), "Biomagnetism: Fundamental Research and Clinical Applications", Proceedings of the 9th International Conference on Biomagnetism, Studies in Applied Electromagnetics, 7, Elsevier, Amsterdam, pp 476-482.

Plonsey R, (1981): "Magnetic field resulting from action currents on cylindrical fibres", Med. Biol. Eng. Comput., 19: 311-315.

Pockberger H, (1995): "Modern concepts in basic epileptology". In: Baumgartner C, Deecke L, Stroink G, and Williamson SJ, (eds), "Biomagnetism: Fundamental Research and Clinical Applications", Proceedings of the 9th International Conference on Biomagnetism, Studies in Applied Electromagnetics, 7, Elsevier, Amsterdam, pp 5-9.

Posche P, (1995), Private Communication.

Press WH, Flannery BP, Teulolsky SA, and Vetterling WF, (1988): "Numerical recipes in Fortran. The art of scientific computing", Cambridge University Press, New York.

Quesney LF, Risinger MW, and Shewmon DA, (1993): "Extracranial EEG evaluation". In: Engel J Jr, (ed), "Surgical treatment of the epilepsies", 2nd Edition, Raven Press, New York, pp 173-195.

Ribary U, Ioannides AA, Singh KD, Hasson R, Bolton JPR, Lado F, Mogilner A, and Llinàs R, (1991): "Magnetic Field Tomography (MFT) of coherent thalamo-cortical 40 Hz oscillations in humans", Proc. Nat. Acad. Sci. USA, 88:11037-11041.

Ribary U, Joliot M, Jagow R, and Llinàs R, (1995): "Oscillatory brain activity at around 40 Hz in humans: evidence for a major mechanism of higher brain function?". In: Baumgartner C, Deecke L, Stroink G, and Williamson SJ, (eds), "Biomagnetism: Fundamental Research and Clinical Applications", Proceedings of the 9th International Conference on Biomagnetism, Studies in Applied Electromagnetics, 7, Elsevier, Amsterdam, pp 286-291.

Rizzo G, Giraldi MC, Bettinardi V, Carutti S, and Fazio F, (1990): "Integration of multimodal medical images", Proc. Annual Conf. of the IEEE Engineering in Medicine and Biology Society 12(1): 145-146.

Robinson D, (1992): "Book 2; Neurobiology", The Open University series on "Biology: Brain and Behaviour", Course SD206, Milton Keynes, UK.

Robinson SE, (1989): "Theory and properties of lead field synthesis analysis". In Williamson SJ, Hoke M, Stroink G, and Kotani M, (eds), "Advances in Biomagnetism", Plenum Press, New York, pp 599-602.

Robinson SE, (1995): "Synthetic aperture magnetometry", Private Communication.

Robinson SE, and Rose DF, (1992): "Current source image estimation by spatially filtered MEG". In: Hoke M, Erne SN, Okada YC, and Romani GL, (eds). "Biomagnetism: Clinical Aspects", Elsevier, Amsterdam, pp 761-765.

Rogers RL, (1994): "Magnetoencephalographic imaging of cognitive processes". In: Thatcher RW, Hallet M, Zeffiro T, John ER, and Huerta M, (eds), "Functional Neuroimaging", Academic Press, San Diego, pp 289-297.

Rogers RL, Papanicolaou AC, Baumann SB, Bourbon TW, Alagarsamy S, and Eisenberg HM, (1990): "Localization of P3 sources using

magnetoencephalography and magnetic resonance imaging", Electroenceph. Clin. Neurophysiol., 79: 308-321.

Roy CS, Sherrington CS, (1890): "On the regulation of the blood-supply of the brain", J. Physiol., 11: 85-108.

Rueckert L, (1995): "Use of functional magnetic resonance imaging in language", pp 299-300. In: Le Bihan D, moderator, "Functional magnetic resonance imaging of the brain", Ann. Intern. Med., 122: 296-303.

Sadato N, (1995): "Functional magnetic resonance imaging of the motor cortex", pp 298-299. In: Le Bihan D, moderator, "Functional magnetic resonance imaging of the brain", Ann. Intern. Med., 122: 296-303.

Salmelin R, Hari R, Lounasmaa OV, and Sams M, (1994): "Dynamics of brain activation during picture naming", Nature, 368:463-465.

Santana de Sa - Bennet S, (1991): "Lectures on human anatomy and physiology", Personal notes, MSc Course on Medical Physics , University of Surrey, Guildford, UK.

Sarvas J, (1987): "Basic mathematical and electromagnetic concepts of the biomagnetic inverse problem", Phys. Med. Biol., 32: 11-22.

Sato S, (1992): "Current status of biomagnetic research in epileptology" In: Hoke M, Erne SN, Okada YC, and Romani GL, (eds). "Biomagnetism: Clinical Aspects", Elsevier, Amsterdam, pp 61-66.

Savic I, (1995): "[^{11}C]Flumazenil Positron Emission Tomography in human epilepsy", Abstracts from the 21st International Epilepsy Congress, Sydney, Australia, September 1995, Epilepsia, 36(Suppl. 3): S30.

Scherg M, (1990): "Fundamentals of dipole source potential analysis". In: Grandori F, Hoke M, and Romani GL, (eds), "Auditory Evoked Magnetic Fields and Electric Potentials", Advances in Audiology, Vol 6, Karger, Basel, pp 41-69.

Scherg M, and von Cramon D, (1985): "Two bilateral sources of the late AEP as identified by a spatio-temporal dipole model", Electroenceph. Clin. Neurophysiol., 62: 32-44.

Scherg M, Hari R, and Hämäläinen MS, (1989): "Frequency-specific sources of the auditory N19-P30 detected by a multiple source analysis of evoked magnetic

fields and potentials". In Williamson SJ, Hoke M, Stroink G, and Kotani M, (eds), "Advances in Biomagnetism", Plenum Press, New York, pp 97-100.

Schmidt RO, (1986): "Multiple emitter location and signal parameter estimation", IEEE Trans. Antennas Propag., AP-34: 276-280.

Shannon CE, (1949): "Communications in the presence of noise", Proc. IRE, 37: 10-21.

Shea TB, (1995): "Role of glial-derived nexin in neuronal differentiation and in acute brain injury and potential involvement in exacerbation of neurodegeneration in Alzheimer's disease", Brain Res. Brain Res. Rev. (BRS), 20(2): 171-184.

Shibasaki H, (1996): "Central motor control and its disorders studied by multidisciplinary approach", Personal notes from the invited presentation at the 10th International Conference on Biomagnetism, Santa Fe, USA, February 1996.

Shibasaki H, Yamashita Y, and Kuroiwa Y, (1978): "Electroencephalographic studies of myoclonus: myoclonus-related cortical spikes and high amplitude somatosensory evoked potentials", Brain, 101: 447-460.

Shin C, and McNamara JO, (1994): "Mechanism of epilepsy", Annu. Rev. Med., 45: 379-389.

Shulman RG, Blamire AM, Rothman DL, and McCarthy G, (1993): "Review: nuclear magnetic resonance imaging and spectroscopy of human brain function", Proc. Natl. Acad. Sci. USA, 90: 3127-3133.

Singh KD, Ioannides AA, Gray N, Kober H, Pongratz H, Grummich P, and Vieth J, (1994): "Distributed current analyses of bi-hemispheric magnetic N1m responses to ipsi/contralateral monaural stimuli from a single subject", Electroenceph. Clin. Neurophysiol., 92:365-368.

Singh KD, Ioannides AA, Hasson R, Ribary U, Lado F, Llinàs (1992): "Extraction of dynamic patterns from distributed current solutions of brain activity". In: Hoke M, Erne SN, Okada YC, and Romani GL, (eds). "Biomagnetism: Clinical Aspects", Elsevier, Amsterdam, pp 767-771.

Smith JR, Gallen CC, Orrison W, Lewine J, Murro AM, King DW, and Gallagher BB (1994): "Role of multichannel MEG in ablative seizure surgery candidates", Stereotact. Funct. Neurosurg., 62: 238-244.

Sobel DF, Gallen CC, Schwartz BJ, Waltz TA, Copeland B, Yamada S, Hirschkoff EC, and Bloom FE, (1993): "Locating the central sulcus: comparison of MR anatomic and magnetoencephalographic functional methods", AJNR: Am. J. Neuroradiol., 14: 915-925.

Speckmann EJ, Altrup U, Straub H, Bingmann D, Walden J, Lücke A, Pohl M, Wassmann H, and Moskopp D, (1992): "Pathophysiology of the epilepsies". In: Hoke M, Erne SN, Okada YC, and Romani GL, (eds). "Biomagnetism: Clinical Aspects", Elsevier, Amsterdam, pp 45-52.

Spencer SS, So NK, Engel J, Williamson PD, Levesque MF, and Spencer DD (1993): "Depth electrodes". In Engel J (ed). "Surgical treatment of the epilepsies", 2nd Edition, Raven Press, New York, pp 359-376.

Spinks TJ, Jones T, Gilard MC, and Heather JD, (1988): "Physical performance of the latest generation of commercial positron scanner", IEEE Transactions on Nuclear Science, 35(1):721-725.

Stefan H, Quesney LF, Feistel HK, Schüler P, Weis M, Hummel C, and Pauli E, (1995): "Presurgical evaluation in frontal lobe epilepsy: a multimethodological approach". In Jasper HH, Riggio S, Goldman-Rakic P (eds), "Epilepsy and functional anatomy of the frontal lobe", Advances in Neurology, Vol 66, Raven Press, New York, pp 213-222.

Stefan H, Schneider S, Abraham-Fuchs K, Pawlik G, Feistel H, Bauer J, Neubauer U, Huk WJ, and Holthoff V, (1991): "The neocortico to mesio-basal limbic propagation of focal epileptic activity during the spike-wave complex", Electroenceph. Clin. Neurophysiol., 79: 1-10.

Stefan H, Schneider S, FeistelH, Pawlik G, Schüler P, Abraham-Fuchs K, Schlegel T, Neubauer U, and Huk WJ, (1992): "Ictal and interictal activity in partial epilepsy recorded with multichannel MEG: correlation of EEG/ECoG, MRI, SPECT, and PET findings", Epilepsia, 33(5): 874-887.

Stefan H, Schüler P, Abraham-Fuchs K, Schneider S, Gebhardt M, Hummel C, Huk WJ, Thierauf P, (1994): "Magnetic source localisation and morphological changes in temporal lobe epilepsy: comparison of MEG/EEG, ECoG and volumetric MRI in presyrgical evaluation of operated patients", Acta Neurol. Scand., 89(Suppl. 152): 83-88.

Stok CJ, Meijs JWH, and Peters MJ, (1987): "Inverse solutions based on MEG and EEG applied to volume conductor analysis", Phys. Med. Biol., 32(1): 99-104.

Suk J, Ribary U, Cappell J, Yamamoto T, and Llinàs R, (1991): "Anatomical localization revealed by MEG recordings of the human somatosensory system", Electroenceph. Clin. Neurophysiol. 78:185-196.

Sutherling WW, and Barth DS, (1989): "Neocortical propagation in temporal lobe spike foci on Magnetoencephalography and Electroencephalography", Ann Neurology 25(4):373-381.

Sutherling WW, Crandall PH, Cahan LD, and Barth DS, (1988): "The magnetic field of epileptic spikes agrees with intracranial localisations in complex partial epilepsy", Neurology, 38: 778-786.

Sutherling WW, Levesque MF, Crandall PH, and Barth DS, (1991): "Localization of partial epilepsy using magnetic and electric measurements", Epilepsia 32(Suppl 5): S29-S40.

Talairach J, and Tournoux P, (1988): "Co-planar stereotaxic atlas of the human brain", Thieme, Stuttgart.

Tepley N, and Wijesinghe RS, (1996): "A dipole model for spreading cortical depression", Brain Topography, In Press.

Tesche CD, Uusitalo MA, Ilmoniemi RJ, Huotilaninen M, Kajola M, and Salonen O, (1995): "Signal-space projections of MEG data characterise both distributed and well-localised neuronal sources", Electroenceph. Clin. Neurophysiol., 95: 189-200.

The Lancet, Editorial, (1989): "SPECT and PET in epilepsy", 21 January 1989, pp 135-137.

Theodore WH, (1995): "Quantitative ictal and interictal metabolic and blood flow imaging", Abstracts from the 21st International Epilepsy Congress, Sydney, Australia, September 1995, Epilepsia, 36(Suppl. 3): S30.

Thomson RF, (1985): "The brain: an introduction to neuroscience", Freeman WH and Company, New York.

Tortora G, and Anagnostakos N, (1990): "Principles of anatomy and physiology", 6th Edition, Harper and Row Publishers, New York.

Towle VL, Bolaños, Suarez D, Tan K, Crzeszczuk R, Levin DN, Cakmur R, Frank SA, and Spire JP (1993): "The spatial location of EEG electrodes: locating the best-fitting sphere relative to cortical anatomy", Electroenc. Clin. Neurophysiology, 86: 1-6.

Tripp JH, (1983): "Physical concepts and mathematical models". In Williamson SJ, Romani GL, Kaufman L, and Modena I, (eds) "Biomagnetism: an interdisciplinary approach", Plenum Press, New York, pp 101-139.

Turner R, (1995): "Functional mapping of the human brain with magnetic resonance imaging", Seminars in The Neurosciences, 7: 179-194.

Turner R, and Jezzard P, (1994): "Magnetic resonance studies of brain functional activation using echo-planar imaging". In: Thatcher RW, Hallet M, Zeffiro T, John ER, and Huerta M, (eds), "Functional Neuroimaging", Academic Press, San Diego, pp 69-78.

Van den Elsen PA, and Viergever MA, (1991): "Marker guided registration of electromagnetic dipole data with tomographic images". In Colchester ACF, and Hawkes DJ (eds), "Information Processing in Medical Imaging", Springer, Berlin.

Vieth J, Kober H, Sack G, Grummich P, Friedrich S, Möger A, Weise E, Daun A, and Pongratz H, (1992): "The efficacy of the discrete and the quantified continuous dipole density plot (DDP) in multichannel MEG". In: Hoke M, Erne SN, Okada YC, and Romani GL, (eds). "Biomagnetism: Clinical Aspects", Elsevier, Amsterdam, pp 321-325.

Villringer A, Planck J, Hock C, Schleinkofer L, and Dirnagl U, (1993): "Near infrared spectroscopy (NIRS): a new tool to study hemodynamic changes during activation of brain function in human adults", Neuroscince Letters, 154: 101-104.

Volkmann J, Seitz RJ, Müller-Gärtner HW, and Witte O, (1996): "Extrarolandic origin of spike and myoclonus activity in a case of epilepsia partialis continua: a MEG and PET study", Submitted for publication to the Journal of Neuroimaging, March 1996.

Volkmann J, Witte O, Dammers J, Arnold S, Seitz RJ, Müller-Gärtner HW, and Freund HJ, (1995): "Relatioship between epileptogenic and symptomatogenic zone in epilepsia partialis continua: a MEG and PET study", ", Human Brain Mapping, Suppl 1:1, p 387.

Vrba J, Betts K, Burbank M, Cheung T, Cheyne D, Fife AA, Haid G, Kubik PR, Lee S, McCubbin J, McKay J, McKenzie D, Mori K, Spear P, Taylor B, Tillotson M, and Xu G, (1995): "Whole cortex 64 channel system for shielded and unshielded enviroments". In: Baumgartner C, Deecke L, Stroink G, and

Williamson SJ, (eds), "Biomagnetism: Fundamental Research and Clinical Applications", Proceedings of the 9th International Conference on Biomagnetism, Studies in Applied Electromagnetics, 7, Elsevier, Amsterdam, pp 521-525.

Wagner M, Fuchs M, Wischmann HA, Ottenberg K, and Dössel O, (1995): "Cortex segmentation from 3d MR images for MEG reconstructions". In: Baumgartner C, Deecke L, Stroink G, and Williamson SJ, (eds), "Biomagnetism: Fundamental Research and Clinical Applications", Proceedings of the 9th International Conference on Biomagnetism, Studies in Applied Electromagnetics, 7, Elsevier, Amsterdam, pp 433-438.

Walter H, Kristeva R, Know U, Schlaug G, Huang Y, Steinmetz H, Nebeling B, Herzog H, and Seitz RJ, (1992): "Individual somatotropy of primary sensorimotor cortex revealed by intermodal matching of MEG, PET, and MRI", Brain Topography, 5(2): 183-187.

Wang B, Toro C, Wassermann EM, Zeffiro TA, Thatcher RW, and Hallett M, (1994): "Multimodal integration of electrophysiological data and brain images: EEG, MEG, TMS, MRI, and PET". In: Thatcher RW, Hallet M, Zeffiro T, John ER, and Huerta M, (eds), "Functional Neuroimaging", Academic Press, San Diego, pp 251-257.

Wang JZ, (1993): "Minimum-norm least-squares estimation: magnetic source images for a spherical model head", IEEE Trans. Biomed. Eng., 39: 541-557.

Wang JZ, Kaufman L, and Williamson SJ, (1993): "Imaging regional changes in the spontaneous activity in the brain: an extension of the unique minimum-norm least-squares estimate", Electroenceph. Clin. Neurophysiol., 86: 36-50.

Wang JZ, Kaufman L, and Williamson SJ, (1995b): "MNLS inverse applied to complex source geometries". In: Baumgartner C, Deecke L, Stroink G, and Williamson SJ, (eds), "Biomagnetism: Fundamental Research and Clinical Applications", Proceedings of the 9th International Conference on Biomagnetism, Studies in Applied Electromagnetics, 7, Elsevier, Amsterdam, pp 394-397.

Wang JZ, Williamson SJ, and Kaufman L, (1992): "Magnetic Source images determined by a lead-field analysis: the unique minimum-norm least-squares estimation", IEEE Trans. Biomed. Eng, 39:665-675.

Wang JZ, Williamson SJ, and Kaufman L, (1995a): "Spatio-temporal model of neural activity of the human brain based on the MNLS inverse". In: Baumgartner C, Deecke L, Stroink G, and Williamson SJ, (eds), "Biomagnetism: Fundamental Research and Clinical Applications", Proceedings of the 9th International Conference on Biomagnetism, Studies in Applied Electromagnetics, 7, Elsevier, Amsterdam, pp 299-301.

Wang JZ, Williamson SJ, and Kaufman L, (1995c): "Kinetic images of neuronal activity of the human brain based on the spatio-temporal MNLS inverse: a theoretical study", Brain Topogr., 7(3): 193-200.

Webb S, (1988): "The Physics of Medical Imaging", Medical Science Series, Adam Hilger, UK, USA.

Webb S, (1993): "The Physics of three-dimensional radiation therapy; conformal radiotherapy, radiosurgery, and treatment planning", Medical Science Series, IOP Publishing Ltd, Bristol and Philadelphia.

Wikswo JP Jr, Barach JP, Freeman JA, (1980): "Magnetic field of a nerve impulse: first measurements", Science, 208: 53-55.

Wikswo JP Jr, Gevins A, and Williamson SJ, (1993): "Review article: The future of the EEG and MEG", Electroenc. Clin. Neurophysiology, 87:1-9.

Williamson SJ, (1991): "MEG versus EEG localisation test", Letter to the Editor, Ann. Neurol., 30: 222.

Williamson SJ, and Kaufman L, (1981): "Biomagnetism", J. Magn. Mat., 22: 129-201.

Williamson SJ, and Kaufman L, (1990): "Theory of neuroelectric and neuromagnetic fields". In: Grandori F, Hoke M, and Romani GL, (eds), "Auditory Evoked Magnetic Fields and Electric Potentials", Advances in Audiology, Vol 6, Karger, Basel, pp 1-39.

Wilson CL, Isokawa M, Babb TL, and Crandall PH, (1990): "Functional connections in the human temporal lobe. 1. Analysis of limbic system pathways using neuronal responses evoked by electrical stimulation", Exp. Brain Res. 82:279-292.

Wilson MW, and Mountz JM, (1989): "A reference system for neuroanatomical localisation on functional reconstructed cerebral images", J. Comp. Assist. Tomography, 13(1):174-178.

Wischmann HA, Fuchs M, Wagner M, and Dössel O, (1995): "Current density imaging: a time series reconstruction implementing a 'best fixed distributions' constraint". In: Baumgartner C, Deecke L, Stroink G, and Williamson SJ, (eds), "Biomagnetism: Fundamental Research and Clinical Applications", Proceedings of the 9th International Conference on Biomagnetism, Studies in Applied Electromagnetics, 7, Elsevier, Amsterdam, pp 427-432.

Witte OW, Dorn T, and Uhlig S, (1992): "Contribution of different areas of epileptic foci to the generation of interictal epileptic discharges". In: Hoke M, Erne SN, Okada YC, and Romani GL, (eds). "Biomagnetism: Clinical Aspects", Elsevier, Amsterdam, pp 73-77.

Wood CC, Cohen D, Cuffin BN, Yarita M, and Allison T, (1985): "Electrical sources in human somatosensory cortex: identification by combined magnetic and potential recordings", Science, 227: 1051-1053.

Woods DL, Clayworth CC, Knight RT, Simpson GV, and Naeser MA, (1987): "Generators of middle and long latency auditory evoked potentials: implications from studies of patients with bitemporal lesions", Electroenceph. Clin. Neurophysiol. 68:132-148.

Woods RP, Cherry SR, and Mazziotta JC, (1992): "Rapid automated algorithm for aligning and reslicing PET images", J. Comp. Assist. Tomography, 16(4): 620-633.

Worsley KJ, and Friston KJ, (1995): "Analysis of fMRI time-series revisited-again", Neuroimage, 2: 173-181.

Zimmerman JE, Thiene P, and Harding JT, (1970): "Design and operation of stable rf-biased superconducting point-contact quantum devices and a note on the properties of perfectly clean metal contacts", J. Applied Physics, 41:1572-1580.

Η γαρ σοφια του κοσμου τουτου, μωρια παρα τω Θεω εστι · γεγραπται γαρ · ο δρασσομενος τους σοφους εν τη πανουργια αυτων · και παλιν · Κυριος γιγνωσκει τους διαλογισμους των σοφων οτι εισι ματαιοι.

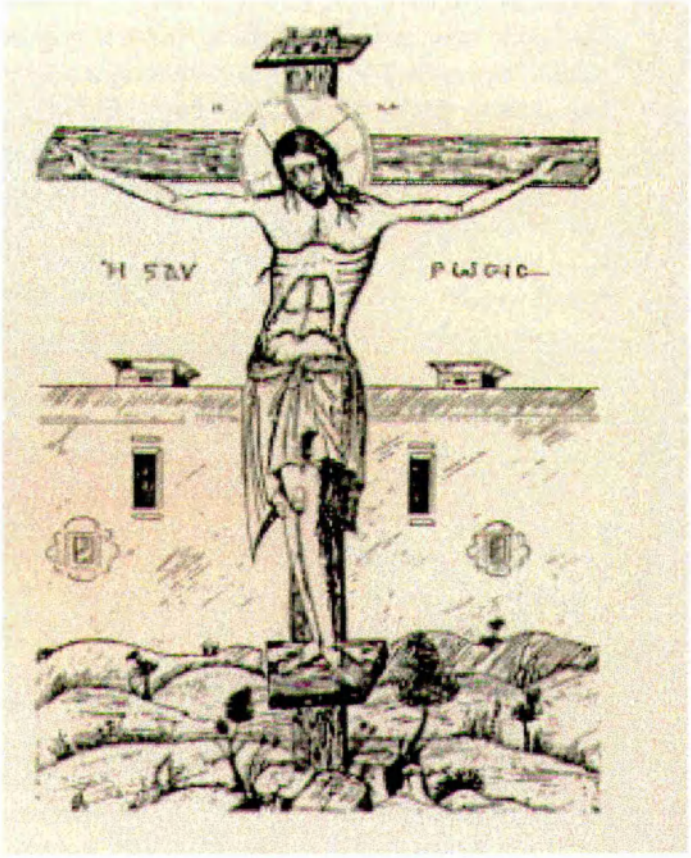

ΤΕΛΟΣ

ΚΑΙ ΔΟΞΑ ΤΩ ΔΙΔΟΝΤΙ ΗΜΙΝ ΖΩΗΝ